Analysis of the Intrinsic Visible V–Mid-infrared L Colors of Galaxies at Redshifts $z < 2$

by

Duho Kim

A Dissertation Presented in Partial Fulfillment
of the Requirements for the Degree
Doctor of Philosophy

Approved October 2019 by the
Graduate Supervisory Committee:

Rogier A. Windhorst, Chair
Rolf A. Jansen
Judd D. Bowman
Nathaniel R. Butler
Patrick A. Young

ARIZONA STATE UNIVERSITY

December 2019

©2019 Duho Kim

All Rights Reserved

ABSTRACT

Ultraviolet and optical light from stars is reddened and attenuated by interstellar dust, where different sightlines across a galaxy suffer varying amounts of extinction. Tamura *et al.* (2009) developed an approximate method to correct for dust extinction, dubbed the "β_V method," by comparing the observed to an empirical estimate of the intrinsic flux ratio of visible and $\sim$3.5 μm emission. Moving beyond that empirical approach, through extensive modeling, I calibrated the β_V-method for various filters spanning the visible through near-infrared wavelength range, for a wide variety of simple stellar populations (SSP) and composite stellar populations (CSP). Combining Starburst99 and BC03 models, I built spectral energy distributions of SSP and CSP for various realistic star formation histories, while taking metallicity evolution into account. I convolved various 0.44–1.65 μm filter throughput curves with each model spectral energy distribution (SED) to obtain intrinsic flux ratios, $\beta_{\lambda,0}$. To validate the modeling, I analyzed spatially resolved maps for the observed V- and g-band to 3.6 μm flux ratios and the inferred dust-extinction values A_V for a sample of 257 nearby galaxies. Flux ratio maps are constructed using point-spread function-matched mosaics of Sloan Digitial Sky Survey g- and r-band images and *Spitzer*/InfraRed Array Camera 3.6μm mosaics, with all of the pixels contaminated by foreground stars or background objects masked out. Dust-extinction maps for each galaxy were created by applying the β_V-method. The typical 1σ scatter in β_V around the average, both within a galaxy and in each morphological type bin, is $\sim$20%. Combined, these result in a $\sim$0.4 mag scatter in A_V. β_V becomes insensitive to small-scale variations in stellar populations once resolution elements subtend an area larger than 10 times that of a typical giant molecular cloud. I find noticeably redder $V-3.6$ μm colors in the center of star-forming galaxies and galaxies with a weak AGN. The derived intrinsic $V-3.6$ μm colors for each Hubble type are generally consistent with the modeling. Finally, I discuss the applicability of the β_V dust-correction method to more distant galaxies, for which large samples of

well-matched *Hubble Space Telescope* rest-frame visible and *James Webb Space Telescope* rest-frame $\sim 3.5\mu$m images will become available in the near future.

ACKNOWLEDGMENTS

I want to thank my advisors Rogier A. Windhorst and Rolf A. Jansen. Thank you for your support and discipline. I learned a lot from you in many ways. I thank all the former and current members in our research group Seth Cohen, Michael Rutkowski, Hwihyun Kim, Mira Mechtley, Bhavin Joshi, Teresa Ashcraft, Brent Smith, and Peter Nguyen for helpful discussion, comments, and emotional supports. I thank Lillian Otteson for reviewing my dissertation and giving me helpful comments. I thank committee members Judd Bowman, Nathaniel Butler, and Patrick Young for reviewing my work annually. I thank Chris Groppi and Tom Mozdzen for buying me countless beers on Fridays, and all friends who I had chats with over beers, Cheers! I want to thank my Korean friends, my roommates Miyuki Sawahara and Jeffery Wang, and my family Mom, Dad, and Brother for their support and caring.

This work was funded by NASA/ADAP grant NNX12AE47G (PI: Rolf A. Jansen). Rogier A. Windhorst acknowledges support from NASA JWST grants NAGS-12460 and NNX14AN10G, and 80NSSC18K0200.

This work is based in part on observations made with the *Spitzer* Space Telescope, which is operated by the Jet Propulsion Laboratory, California Institute of Technology under a contract with NASA. *Spitzer* Enhanced Imaging Product is provided by The *Spitzer* Science Center (SSC) and the Infrared Science Archive (IRSA).

This work also used images from the Sloan Digital Sky Survey (SDSS). Funding for the Sloan Digital Sky Survey has been provided by the Alfred P. Sloan Foundation, the U.S. Department of Energy Office of Science, and the Participating Institutions. SDSS acknowledges support and resources from the Center for High-Performance Computing at the University of Utah. SDSS is managed by the Astrophysical Research Consortium for the Participating Institutions of the SDSS Collaboration including the Brazilian Participation Group, the Carnegie Institution for Science, Carnegie Mellon University, the Chilean Participation Group, the French

Participation Group, Harvard-Smithsonian Center for Astrophysics, Instituto de Astrofísica de Canarias, The Johns Hopkins University, Kavli Institute for the Physics and Mathematics of the Universe (IPMU) / University of Tokyo, the Korean Participation Group, Lawrence Berkeley National Laboratory, Leibniz Institut für Astrophysik Potsdam (AIP), Max-Planck-Institut für Astronomie (MPIA Heidelberg), Max-Planck-Institut für Astrophysik (MPA Garching), Max-Planck-Institut für Extraterrestrische Physik (MPE), National Astronomical Observatories of China, New Mexico State University, New York University, University of Notre Dame, Observatário Nacional / MCTI, The Ohio State University, Pennsylvania State University, Shanghai Astronomical Observatory, United Kingdom Participation Group, Universidad Nacional Autónoma de México, University of Arizona, University of Colorado Boulder, University of Oxford, University of Portsmouth, University of Utah, University of Virginia, University of Washington, University of Wisconsin, Vanderbilt University, and Yale University.

This research has made use of the NASA/IPAC Extragalactic Database (NED), which is operated by the Jet Propulsion Laboratory, California Institute of Technology, under contract with the National Aeronautics and Space Administration.

PyRAF is a product of the Space Telescope Science Institute, which is operated by AURA for NASA.

TABLE OF CONTENTS

CHAPTER Page

LIST OF TABLES

LIST OF FIGURES

Figure Page

Figure Page

Figure Page

Figure Page

Figure Page

Figure Page

Figure | Page

Figure Page

Figure Page

Figure Page

Figure Page

Figure		Page

LIST OF ACRONYMS

ACS - Advanced Camera for Surveys

AGN - Active Galactic Nuclei

ASCII - American Standard Code for Information Interchange

B/T - Bulge-to-Total light ratio

BC03 - Bruzual and Charlot (2003)

BCD - Blue Compact Dwarf

BPT - Baldwin *et al.* (1981)

CALIFA - Calar Alto Legacy Integral Field Area (Sánchez *et al.*, 2012)

CANDELS - Cosmic Assembly Near-infrared Deep Extragalactic Legacy Survey

CLASH - Cluster Lensing And Supernova Survey

COSMOS - The Cosmic Evolution Survey

CSP - Composite Stellar Population

DR - Data Release

ETG - Early-Type Galaxy

ERS - Early Release Science

FITS - Flexible Image Transport System

FOV - Field Of View

FWHM - Full-Width at Half Maximum

GALEX - *GALaxy Evolution eXplorer*

GD15 - González Delgado *et al.* (2015)

GOODS - Great Observatories Origins Deep Survey

HLR - Half-Light Radius

HST - *Hubble Space Telescope*

IFU - Integral Field Unit

IGM - Inter-Galactic Medium

IMF - Initial Mass Function

IPAC - Infrared Processing and Analysis Center

IR - InfraRed

IRAC - InfraRed Array Camera

IRAS - *InfraRed Astronomical Satellite*

ISM - InterStellar Medium

ISO - *Infrared Space Observatory*

JWST - *James Webb Space Telescope*

K17 - Kim *et al.* (2017)

K19 - Kim *et al.* (2019)

LERG - Low-Excitation Radio Galaxy

LINER - Low-Ionization Nuclear Emission-line Region

LIRG - Luminous InfraRed Galaxy

LMC - Large Magellanic Cloud

LTG - Late-Type Galaxy

MIR - Mid-InfraRed

MIRI - Mid-InfraRed Instrument

MW - Milky Way

NASA - National Aeronautics and Space Administration

NED - NASA/IPAC Extragalactic Database

NGC - New General Catalogue

NIR - Near-InfraRed

NIRCam - Near-InfraRed Camera

NLAGN - Narrow-Line AGN

NLRG - Narrow emission-Line Radio Galaxy

PA - Position Angle

PAH - Polycyclic Aromatic Hydrocarbon

pCCD - Pixel Color-Color Diagram

PNG - Portable Network Graphics

PSF - Point-Spread Function

RC3 - The third Reference Catalogue of Bright Galaxies (de Vaucouleurs *et al.*, 1991)

RMS - Root Mean Square

RSG - Red SuperGiant

S18 - Steinicke (2018); Revised NGC/IC Catalog

S/N - Signal-to-Noise ratio

SB99 - Starburst99 (Leitherer *et al.*, 1999)

SDSS - Sloan Digital Sky Survey

SED - Spectral Energy Distribution

SEIP - *Spitzer* Enhanced Imaging Product

SHA - *Spitzer* Heritage Archive

SMC - Small Magellanic Cloud

sSFR - specific SFR

SSP - Simple (or Single) Stellar Population

SF - Star Formation

SFH - Star Formation History

SFR - Star Formation Rate

UV - UltraViolet

UVIS - UV/VISible

WFC - Wide Field Camera

WISE - Wide-field Infrared Survey Explorer

ΛCDM - Lambda Cold Dark Matter

Chapter 1

INTRODUCTION

1.1 What Do We Know About Galaxies?

According to the standard ΛCDM model of cosmology, the universe started from a minuscule dot followed by rapid expansion (Planck Collaboration *et al.*, 2016). When the temperature cooled down to below 4000 K by expanding to the size of $\sim$1/1400 of the current universe, free electrons started to be captured by protons (Ryden, 2003). Expansion itself also decreased free electron density. Photons could travel freely without being scattered by free electrons. Being that the outward pressure created by photon-matter interactions was relieved, matters started to collapse inward gravitationally. The energy density of the dark matter was three times larger than the one of the photons, electrons, and protons together (Ryden, 2003). Acoustic oscillations of the photon-baryon fluid by the non-uniform dark matter density were frozen by sudden decoupling of the photons. Baryonic matters fell to troughs of these density fluctuations and formed stars, black holes, and galaxies.

A galaxy is a gravitationally bound system that consists of dark matters, stars, gas, and dust. The galaxy we live in, the Milky Way, houses 200 billions of stars (Gott *et al.*, 2005) in a disk with a thickness and a diameter corresponding to 2,000 (Rix and Bovy, 2013) and 200,000 light years (López-Corredoira, M. *et al.*, 2018), respectively. Ten times more galaxies can be found elsewhere in the universe than the number of stars in the Milky Way galaxies ($\sim$2 trillion; Conselice *et al.*, 2016).

Edwin Hubble morphologically classified galaxies based on the structural forms of photographic images (Hubble, 1926). Astronomers still use his scheme (see Figure 1.1). The Milky

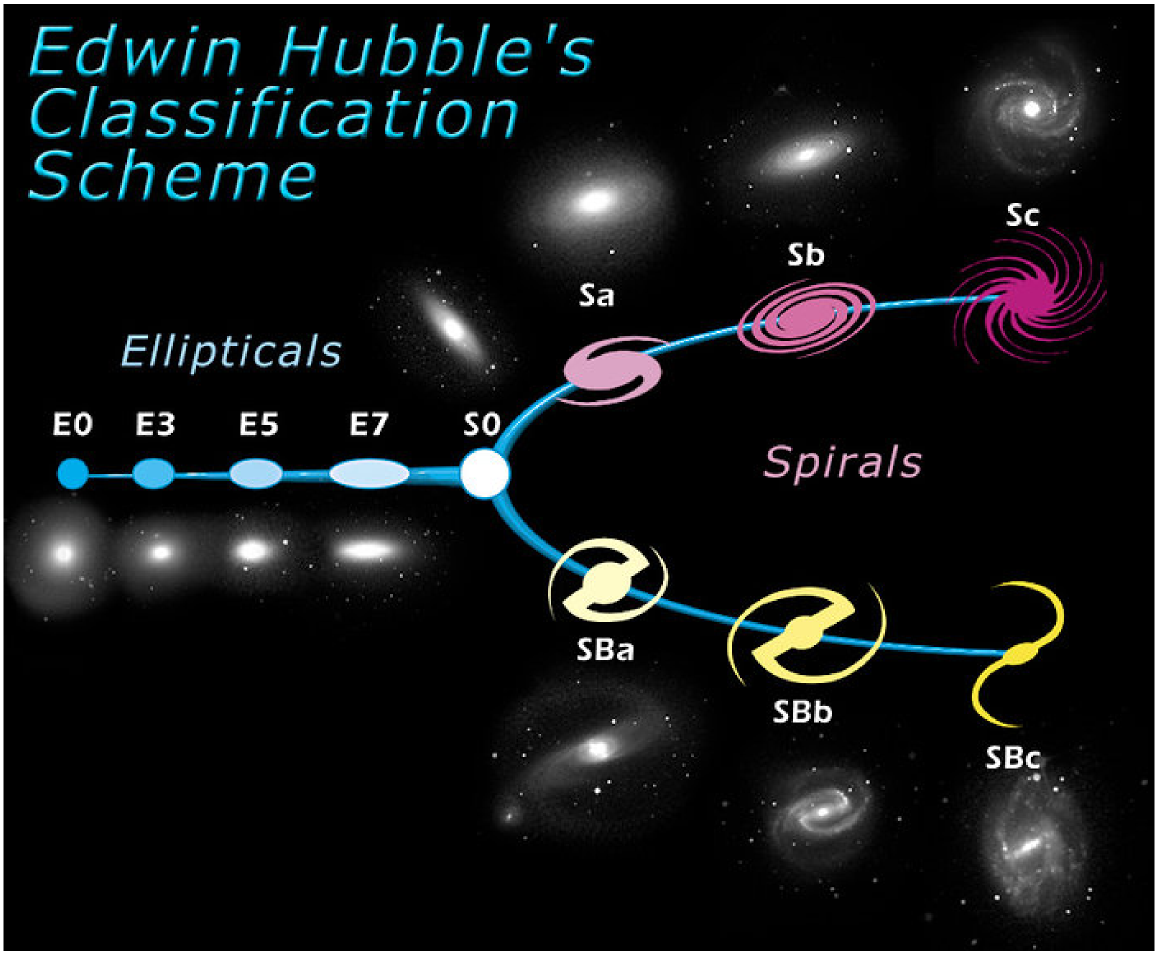

Figure 1.1: Morphological classification of galaxies by Hubble (1926) (Source: Wikipedia)

Way is a barred spiral galaxy "SBbc" type. Hubble (1926) thought elliptical galaxies formed first and evolved into spiral galaxies, so he called ellipticals "early types" and spirals "late types." Indeed, elliptical galaxies have older and redder stellar populations whereas thin-disky galaxies like Milky Way have younger and bluer stellar populations (Humason *et al.*, 1956). Nonetheless, there is no evidence that ellipticals evolve into spirals; in contrast, there are many pieces of counter evidence showing spirals merging and becoming ellipticals (Toomre, 1977; Kim and Im, 2013). As a matter of convention, astronomers still refer to ellipticals as early-type and spirals as late-type galaxies, and I will also follow this tradition throughout this dissertation.

1.2 Extinction by Interstellar Dust Hampers Studies of Galaxies

Dust in the interstellar medium (ISM) of galaxies effectively scatters or absorbs light at shorter wavelengths, such as UV and visible photons, and reradiates the absorbed energy in the far-infrared (see Figure 1.2; e.g., Buat and Xu, 1996; Charlot and Fall, 2000; Dale *et al.*, 2001; Bell *et al.*, 2002; Panuzzo *et al.*, 2003; Boissier *et al.*, 2004; Buat *et al.*, 2005). Accordingly, dust transforms the shape of the galaxy spectral energy distributions (SEDs), making it harder to study the intrinsic properties of astronomical sources (e.g., Trumpler, 1930; Mathis *et al.*, 1977; Viallefond *et al.*, 1982; Caplan and Deharveng, 1985, 1986; Roussel *et al.*, 2005; Driver *et al.*, 2008). Our rest-frame UV–visible view of distant galaxies is therefore modulated by dust extinction. The level of extinction varies across the face of a galaxy (Kreckel *et al.*, 2013) and differs from galaxy to galaxy. As a result, our interpretation of the distribution, evolution, and properties of stellar populations within a galaxy is significantly influenced by the intervening dust (e.g., Elmegreen, 1980; Kennicutt *et al.*, 2009). SED information across a wide frequency range can be used to infer the nature of the emitting source, and simultaneously the effect of the intervening ISM along the line of sight (e.g., Lindblad, 1941; Elmegreen, 1980; Walterbos and Kennicutt, 1988; Waller *et al.*, 1992; Witt *et al.*, 1992; Calzetti *et al.*, 1994; Boselli *et al.*, 2003; Deo *et al.*, 2006).

In order to directly account for the transformation of the SED of a galaxy or region therein by dust, it would be especially helpful to have UV data accompanied by far-infrared data (25–350 μm) at the same angular resolution (Calzetti *et al.*, 2000; Bell *et al.*, 2002; Boselli *et al.*, 2003; Boissier *et al.*, 2004; Buat *et al.*, 2005), UV to far-infrared multi-wavelength data in combination with SED fitting (Conroy, 2013, and references therein), or a full radiative transfer analysis (Steinacker *et al.*, 2013, and references therein). The Earth's atmosphere, however, is mostly opaque to the far-infrared (Elsasser, 1938), necessitating the use of space telescopes

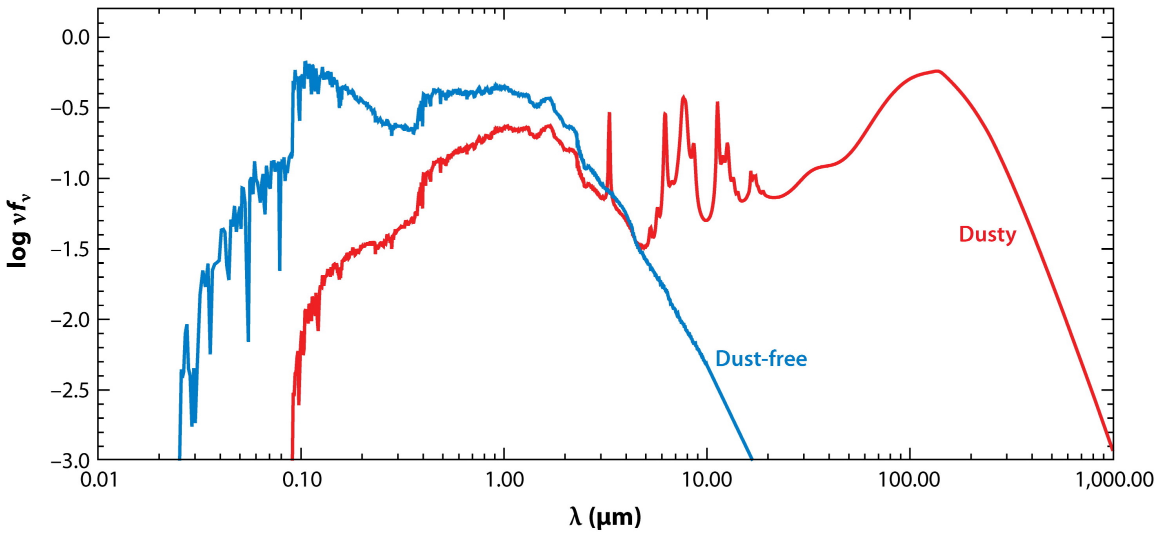

Figure 1.2: The UV–near-infrared range of an intrinsic galaxy SED as emitted by its stars (blue) is scattered and absorbed, and the absorbed energy is reradiated in the far-infrared (red). Image credit: Conroy (2013)

like *IRAS* (Neugebauer *et al.*, 1984), *ISO* (Kessler *et al.*, 1996), *Spitzer* (Werner *et al.*, 2004), and *Herschel* (Pilbratt, 2004; Kreckel *et al.*, 2013). Even then, it is challenging to build and operate far-infrared detector arrays, and for a given telescope aperture, the spatial resolution is $\sim$40–800 times worse than in the optical (Xu and Helou, 1996; Price *et al.*, 2002). For these reasons, shorter wavelength data have been used in various ways to correct for extinction by dust in many studies (e.g., Lindblad, 1941; Rudy, 1984; Calzetti *et al.*, 1994; Petersen and Gammelgaard, 1997; Meurer *et al.*, 1999; Scoville *et al.*, 2001; Bell *et al.*, 2002; Kong *et al.*, 2004; Maíz-Apellániz *et al.*, 2004; Calzetti *et al.*, 2005; Relaño *et al.*, 2006; Kennicutt *et al.*, 2009), each with their own advantages and disadvantages (see, e.g., Tamura *et al.*, 2009). One can correct for the effects of extinction by dust in HII regions within a galaxy, provided that suitable tracers exist, such as hydrogen recombination lines (e.g., Kreckel *et al.*, 2013) or helium recombination lines (Leitherer *et al.*, 2019).

1.3 The β_V Method, "An Approximate Method to Correct for Extinction"

Tamura *et al.* (2009, 2010) developed a simple, approximate, extinction-correction method, dubbed the "$\beta_V$method," which uses spatially-resolved surface photometry in two broadband filters at optical ($\lambda > 4000$Å; e.g., f_V) and mid-infrared (MIR) L-band ($\sim$3.5 μm) rest-frame wavelengths, respectively. The β_V method is primarily intended for the study of large numbers of spatially resolved galaxies at low to intermediate redshifts ($0.1 \lesssim z \lesssim 2$), for which multi-wavelength observations are too expensive and approximate dust corrections may still present a marked improvement over ignoring the effects of extinction altogether, or over adopting a single number as a canonical extinction value for a given galaxy. In particular, Tamura *et al.* (2009) applied the β_V method to one nearby late-type spiral galaxy, NGC 959, by using V-band images obtained from the ground and 3.6 μm images from space, and using ancillary far- and near-UV images from *GALEX* in order to better distinguish pixels dominated by younger stellar populations from those dominated by older ones. From an analysis of the histogram of the observed pixel flux ratios, they adopted values of 1.10 for "older" pixels and 1.32 for "younger" pixels for the extinction-free V to 3.6 μm flux ratio, $\beta_{V,0}$. By doing so, they were able to map the extinction across NGC 959, and obtain extinction-corrected images in which they discerned a hitherto unrecognized stellar bar. The $\beta_{V,0}$ values that they used for older pixels were consistent with the $0.5 \lesssim \beta_{V,0} \lesssim 2$ derived from the theoretical SED models for SSPs of Anders and Fritze-von Alvensleben (2003). The $\beta_{V,0}$ values for younger pixels, on the other hand, were significantly smaller than those expected from theory ($4 \lesssim \beta_{V,0} \lesssim 7$). The authors argued that the blending of light from underlying and neighboring older stellar populations was the likely origin of this discrepancy. This effect will be resolution-dependent and hence redshift-dependent because the poor spatial resolution will mix the light from a larger area within a galaxy.

Tamura *et al.* (2010) demonstrated that a pixel-to-pixel extinction correction based on the "$\beta_V$method" reveals galactic structures (both spatially, and in terms of a shared star formation history). Tamura *et al.* (2010) divided pixels of NGC 0959 into six groups based on the extinction-corrected pixel color ($B - 3.6\,\mu$m)-color (FUV $- U$) diagrams (pCCDs). Tamura *et al.* (2010) found six groups on pCCDs would not be readily discernible before the extinction correction, and locations of them on the galactic region are spatially coherent in the pixel coordinate map.

1.4 Extended Modeling and Evaluation of The β_V Method

Tamura *et al.* (2009) empirically adopted the 2σ-clipped mean (1.10) and the mode (1.32) of β_V values in older and younger pixels for their $\beta_{V,0}$ values, respectively. This was based on assumptions that the dust affects younger pixels more and is usually concentrated in relatively small regions so that the peak β_V value would be the extinction-free flux ratio for the younger pixels.

I extend the "β_V method" to the "β_λ method" by modeling the intrinsic L band to visible–NIR flux ratios using spectral synthesis models of CSP (see § 2), and compare with the observation at redshifts $z \simeq 0$ by analyzing the spatially-resolved $V - 3.6\,\mu$m colors and dust extinction in 257 nearby NGC and IC galaxies (see § 3).

The result will be relevant, particularly, for future surveys of intermediate-redshift ($z \lesssim 2$) galaxies that combine images from the *James Webb Space Telescope* (*JWST*; Gardner *et al.*, 2006) and the *Hubble Space Telescope* (*HST*) at rest-frame $\sim$3.5μm and visible–near-IR wavelengths, respectively. As the spatial resolution ($\propto \lambda/D$) of images from *JWST*/NIRCam at 3.5μm will be comparable to that of *HST*/ACS WFC and WFC3 UVIS in V to within a factor 2.5, combining rest-frame *JWST* $\sim$3.5μm and rest-frame *HST* V-band observations would extend the 'β_V method' from a redshift of $z \simeq 0$ to redshifts $z \lesssim 2$. With suitably chosen filter pairs and the previously computed intrinsic flux ratios, one could then approximately correct the surface photometry of large samples of galaxies for dust extinction.

1.5 Outline of This Dissertation

In Chapter 2, which was originally published in The Astrophysical Journal as Kim *et al.* (2017, hereafter K17), I describe how I analyzed the intrinsic mid-IR L band to visible-NIR flux ratios $\beta_{\lambda,0}$ in spectral synthesis models of composite stellar populations. The main results are: 1) Taking metallicity evolution into account results in significantly higher $\beta_{\lambda,0}$ values at higher redshifts. 2) The β_V method can infer A_V to a level of fidelity that is comparable to that of more established methods. All code, models, and a set of distinguishable spectral-energy distributions of simple-stellar populations are available online via http://lambda.la.asu.edu/betav/.

In Chapter 3, which was originally published in The Astrophysical Journal as Kim *et al.* (2019, hereafter K19), I describe how I analyzed the spatially resolved V-3.6 μm colors and dust extinction in 257 nearby NGC and IC galaxies. The main results are: 1) The $\beta_{V,0}$ values from Chapter 2 were confirmed by matching the $\beta_{V,0}$ values at a redshift of $z \simeq 0$ to those derived from the observation. For future reference, I also provide an atlas of 257 galaxies in Appendix C and D.

Last, In Chapter 4, I give a summary of my major findings and a short outline of future work and applications of the β_V method.

I adopt the Planck 2015 (Planck Collaboration et al. 2016) cosmology with (H_0 = 67.8 km s^{-1} Mpc^{-1}; Ω_m = 0.308; Ω_Λ = 0.692), and I will use AB magnitudes (Oke 1974; Oke & Gunn 1983) throughout.

Chapter 2

ANALYSIS OF THE INTRINSIC MID-INFRARED L BAND TO VISIBLE–NEAR-INFRARED FLUX RATIOS IN SPECTRAL SYNTHESIS MODELS OF COMPOSITE STELLAR POPULATIONS

In order to place the "β_V method" on a more secure theoretical footing, I build a library of SEDs by stacking the SEDs of SSPs—spectral snapshots of a coeval stellar population—for stellar populations with large ensembles of stochastic SFHs, various metallicities, and ages, in order to quantify how the intrinsic optical to mid-IR flux ratio, $\beta_{\lambda,0}$, will vary. The SFHs are designed to reproduce the mean observed SFH as a function of morphological class, assuming open-box metallicity evolution. All the work in this chapter is published in K17.

2.1 SED Models

2.1.1 Combining the SSP Model SEDs of Starburst99 and BC03

The first step of my computational analysis is to build a large family of SSP model SEDs. Each SSP represents a single generation of stars of the same age and chemical composition, with stellar masses that were distributed according to an adopted IMF (Salpeter, 1955; Kroupa, 2002; Chabrier, 2003) at birth. There are several stellar population synthesis codes available in the literature (e.g., Fioc and Rocca-Volmerange, 1997; Leitherer *et al.*, 1999; Bruzual and Charlot, 2003; Maraston, 2005; Vazdekis *et al.*, 2010). I select Starburst99 (Leitherer *et al.*, 1999; Vázquez and Leitherer, 2005) for very young ($\lesssim$30 Myr) stellar populations, as the stellar evolutionary tracks of the Geneva group (Schaller *et al.*, 1992; Schaerer *et al.*, 1993b,a;

Charbonnel *et al.*, 1993; Meynet *et al.*, 1994) adopted by Starburst99 are optimized for massive young stars, and include, e.g., the Wolf-Rayet phase. Starburst99 also includes the nebular continuum from the gas enshrouding the stellar populations, as is the general case for newborn and young stars. On the other hand, the stellar evolutionary tracks of the Padova group (Girardi *et al.*, 2000; Marigo *et al.*, 2008) are a good match to observations of intermediate- and low-mass stars that dominate older stellar populations (Vázquez and Leitherer, 2005). I therefore adopt the Padova1994 tracks in BC03 (Bruzual and Charlot, 2003) for older ($\gtrsim$100 Myr) stellar populations. Below, I describe how I combine the two sets of SED models into a database that can be used for stellar populations of any age. The age grid of the BC03 code is fixed as 221 logarithmic steps between 10^5 and 10^{10} years. In the Starburst99 code, however, the user can specify the age step and scale, so I set 1000 logarithmic time steps between 10^6 and 10^{10} years to provide a finer grid than BC03. For both codes, I adopted a Salpeter (1955) stellar IMF, with a power-law slope of -2.35, and with minimum and maximum stellar masses of 0.1 and 100 $M_\odot$. Each code has a different set of metallicities: $Z = 0.001$, 0.004, 0.008, 0.02, and 0.04 for Starburst99 and $Z = 0.0001$, 0.0004, 0.004, 0.008, 0.02, and 0.05 for BC03. I extrapolate the Starburst99 SEDs to match the metallicities of BC03 using the method described in the following. For each code, I log-exponentially extrapolated in $[Z] = \log_{10}(Z/Z_\odot)$ (where $Z_\odot = 0.02$) from the two SEDs that are closest in metallicity to the desired value. For example, to obtain my $Z = 0.0004$ SED in Starburst99, I combined SEDs for $Z = 0.001$ and $Z = 0.004$ in Starburst99 with relative weights of 1.40 and -0.40, which are derived from $F_1 = (F_2 - w \cdot F_3)/(1 - w)$, where F_1, F_2, and F_3 denote the logarithm of the wavelength-dependent flux densities of SEDs with metallicities of Z_1, Z_2, and Z_3 (with $Z_1 < Z_2 < Z_3$), and where the weight $w = (e^{Z_2} - e^{Z_1})/(e^{Z_3} - e^{Z_1})$. Similarly, when interpolating F_2 into F_1 and F_3, I use $F_2 = (1 - w) \cdot F_1 + w \cdot F_3$. Note that the SEDs F_1, F_2, and F_3 and metallicities

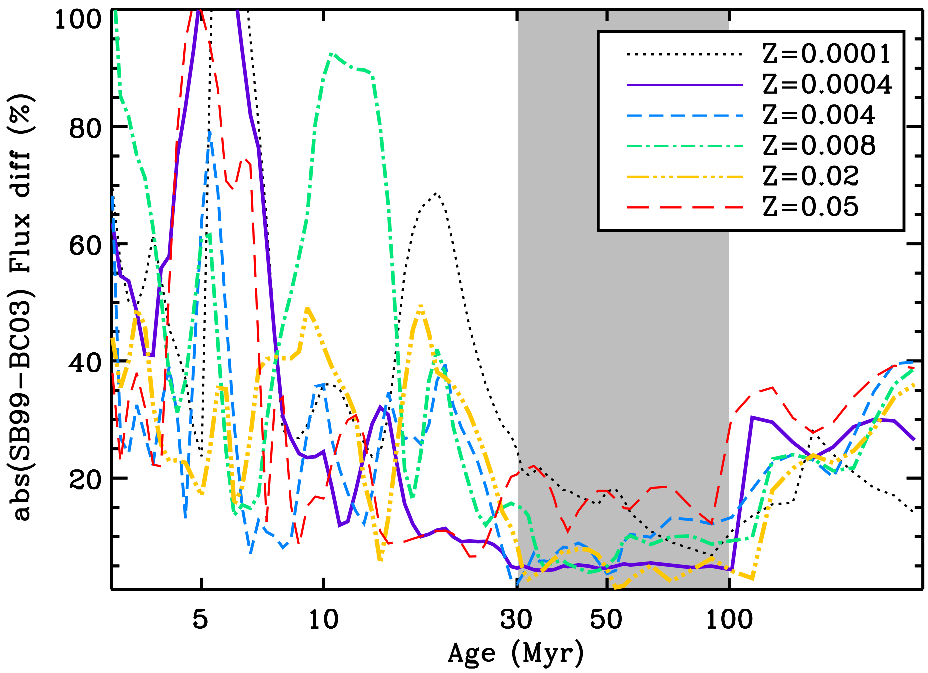

Figure 2.1: Integrated absolute flux difference over the 0.4–3.75 μm wavelength range between Starburst99 and BC03 SEDs (see Equation 2.1) as a function of SSP age for various metallicities. There is no specific age where both codes converge on an identical SED, but the percentage difference reaches a general minimum between ∼30 and ∼100 Myr, where they are mostly $\lesssim$10%.

Z_1, Z_2, and Z_3 are in log scale, with the latter all known (e.g., 0.0004, 0.001, and 0.004 giving $w = 0.285$ in the example).

For intermediate ages ($30 \lesssim \text{Age} \lesssim 100$ Myr), I interpolate the results of the two codes onto the BC03 Age grid as follows. To minimize discontinuities and sudden changes of SEDs for intermediate ages, I inspected the integrated absolute flux differences between Starburst99 and BC03 SEDs over the 0.4–3.75 μm wavelength range (the relevant range for the β_V method). This quantity is for a given age given by

$$\frac{\int_{\lambda_1}^{\lambda_2} \left| F_{SB99}(\lambda) - F_{BC03}(\lambda) \right|}{0.5 \left(\int_{\lambda_1}^{\lambda_2} F_{SB99}(\lambda) + \int_{\lambda_1}^{\lambda_2} F_{BC03}(\lambda) \right)}, \tag{2.1}$$

with $(\lambda_1, \lambda_2) = (0.4, 3.75)$ μm, and its dependence on age and metallicity is shown in Figure 2.1.

Table 2.1: Transition Age Range Adopted when Combining Starburst99 and BC03 Stellar Population Synthesis Model SEDs for Various Metallicities, Z.

Z	Age Range (Myr)	Min. Diff. (%)	Max. Diff. (%)	Mean Diff. (%)	RMS (%)
0.0001	30–100	7	25	17	5.0
0.0004	30–100	4	5	5	0.3
0.004	30–100	2	13	7	3.0
0.008	30–100	4	15	8	3.3
0.02	30–100	1	9	5	2.1
0.05	30–100	11	22	17	3.2

Note. Minimum, maximum, and mean relative flux differences of the two SEDs in the transition age range, and rms thereof are also tabulated.

Table 2.1 lists the minimum, maximum, mean, and rms differences. At 30 Myr, 100% of the Starburst99 SED and 0% of the BC03 SED is used, and the contributions are linearly reduced (increased) to 0% (100%) at 100 Myr. Interpolating using $\log(\text{Age})$ instead of Age yields nearly identical results, since the age ranges are relatively narrow.

Figure 2.2 shows examples of the combined SSP SEDs for six metallicities and 16 ages. I use this set of ages and metallicities when we calculate the L band to visible–near-IR flux ratios of stellar populations with various SFHs described in § 2.2. I also use the same parameter set when I select a manageably small but comprehensive set of SSP SEDs, which I extend with additional extinction-related parameters in Appendix A.

2.1.2 SFH, Metallicity Evolution, and Construction of CSP SEDs

Whereas an SSP consists of purely coeval stars, realistic star formation within galaxies is characterized by stochastic and/or temporally extended, possibly spatially propagating, episodes of star formation. The CSP of a larger region within a galaxy therefore effectively records its SFH. If I denote that SFH as the time-dependent star formation rate, $\psi(t)$, and the

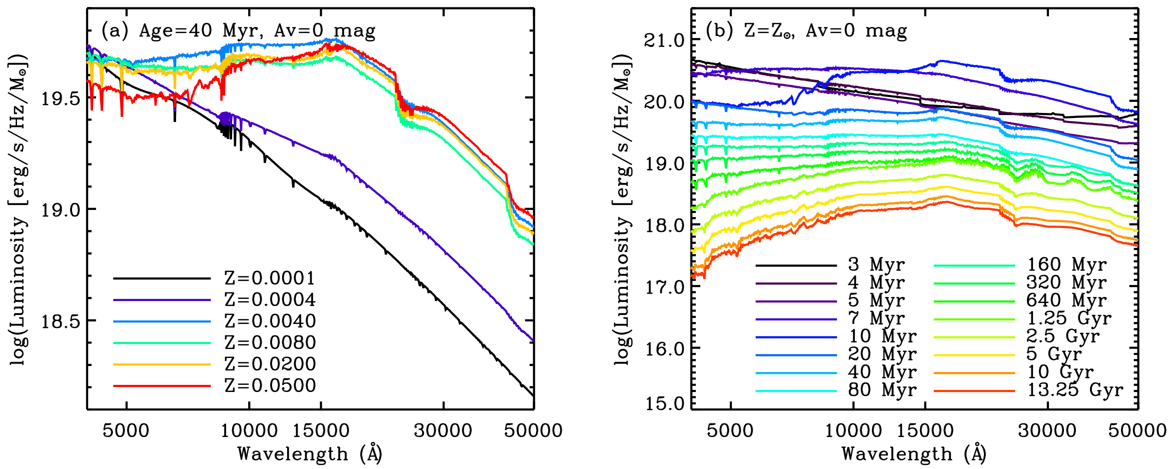

Figure 2.2: Examples of my adopted combined array of SSP SEDs. (a) SEDs for a 40 Myr old stellar population, for six different metallicities and no extinction; (b) SEDs for 16 different ages with fixed solar metallicity ($Z_\odot = 0.02$) and zero extinction.

SED of an SSP as a function of its age, t, and metallicity, Z, by $F_{\lambda,SSP}(t, Z)$, then I can express the SED of a CSP as the superposition of multiple SSPs:

$$F_{\lambda,CSP}(t, Z) = \sum_{t'=t_0}^{t} F_{\lambda,SSP}(t - t', Z(t'))\, \psi(t')\, \delta t' \,, \tag{2.2}$$

where $F_{\lambda,SSP}$ is derived by interpolating my combined SSP SEDs to generate a set of SEDs with 28 logarithmic steps in metallicity (between $Z = 0.0001$ and $Z = 0.05$) and 1000 logarithmic steps in Age (between $t = 1$ Myr and $t = 13.8$ Gyr), $Z(t')$ is used to explicitly denote the time-dependence of the metallicity, and t_0 denotes the time of the first episode of star formation. The metallicity at time step t' results from metal-enriched gas returned to the ISM by stars from previous generations of stellar populations, and from the accretion of gas from other nearby galaxies or from the inter-galactic medium and circum-galactic medium (whether more enriched, or diluted) by the end of time step $(t - \delta t)$. Note that this implies that the metallicity of the resulting CSP differs from that of the metallicity of (most of) its constituent SSPs, and that the chemical evolution of the CSP will not be entirely self-consistent with the choice of the SFH. It does account, however, for the open-box, rather than closed-box, nature of a galaxy or galaxy region in an empirical way. I return to the functional form of $Z(t')$ shortly.

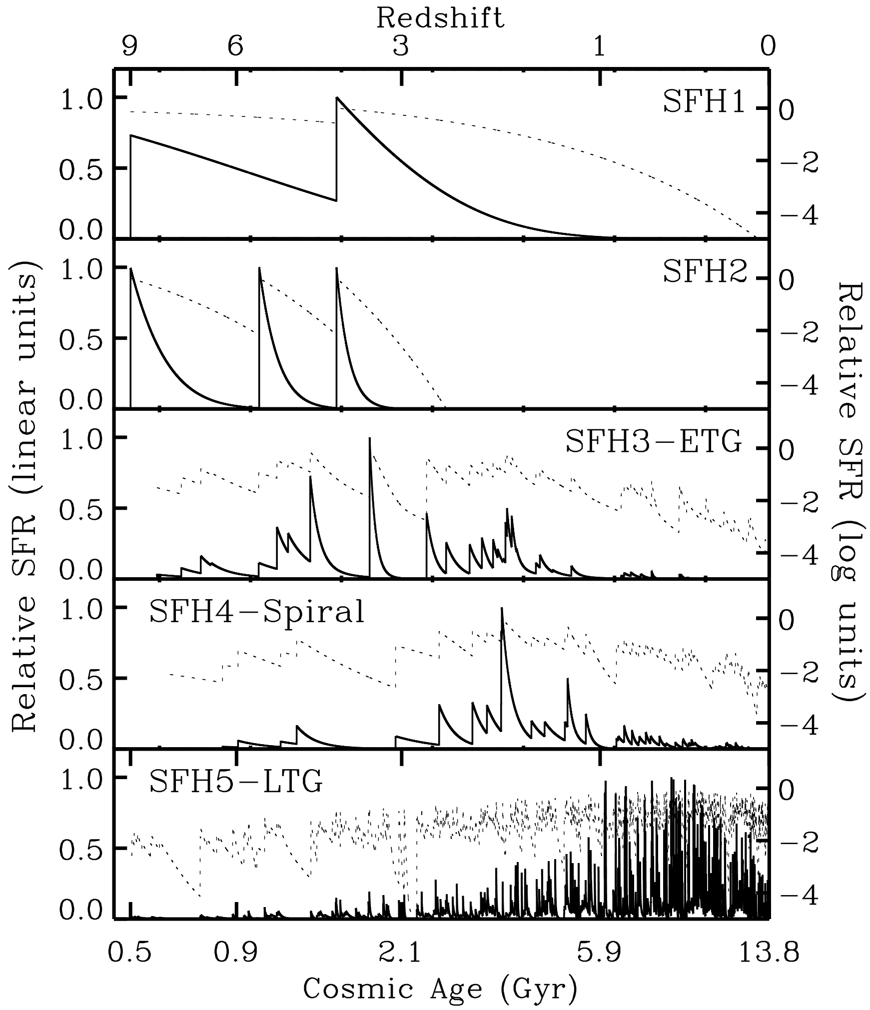

Figure 2.3: Examples of 5 arbitrary scenarios of stochastic SFHs. Relative star formation rates (ψ, normalized to the peak of the strongest star formation episode) are plotted as a function of cosmic time (bottom axis) and redshift (top axis) in both linear (solid curves; left axis) and logarithmic (dotted; right axis) units. SFH1 and 2 represent the cases of two and three bursts with long (1 Gyr) and shorter (0.5 Gyr) e-folding times, respectively. SFH3, 4, and 5 represent simulated CSPs of early-type (E, S0), spiral (Sa–Sbc) and late-type (Sc, Sd) galaxies, respectively.

I started by building CSP SEDs for stellar populations with exponentially declining SFRs, $\psi(t) = \psi_0\, e^{-t/\tau}$ for various values of the e-folding time τ (100, 250, 500 Myrs, 1, 2, 5, and 10 Gyr, where the latter two approach the case of a *constant* SFR). Note that for these exponentially declining SFHs, which were merely meant to test the effect of combining SSPs of different ages, I did not yet take metallicity evolution into account. I then produced SEDs for

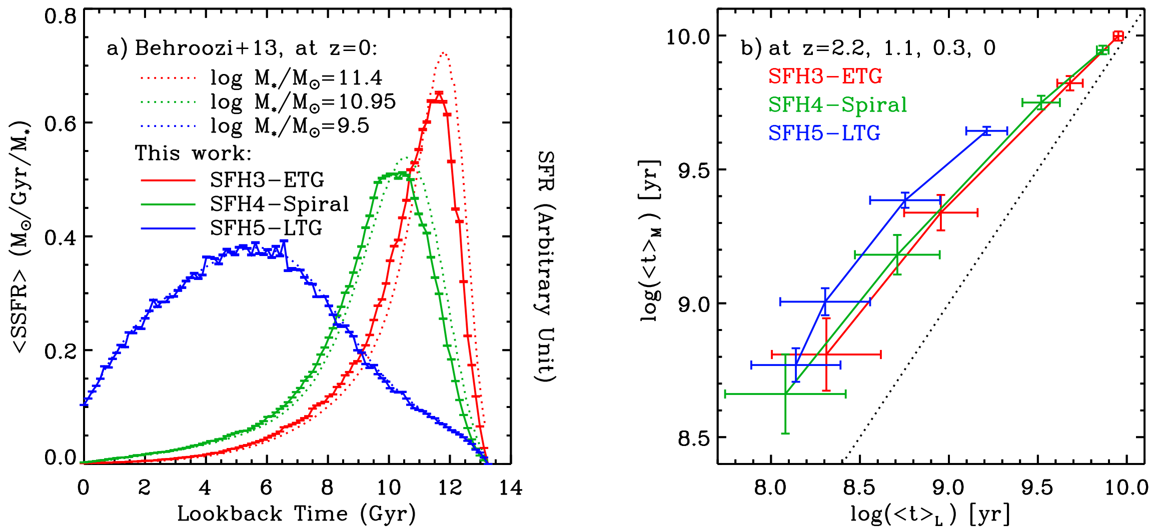

Figure 2.4: (a) Specific SFR versus lookback time for my families of stochastic SFHs. I show the mean and standard deviation of the mean SFR normalized by the total stellar mass built up at $z = 0$ for 1000 random realizations each of SFH3, SFH4, and SFH5 (solid distributions). The dotted curves represent the models of Behroozi et al. (2013) for present-day stellar masses of 2.5×10^{11}, 8.9×10^{10}, and 3.1×10^{9} $M_\odot$, representative of early-type (E), spiral (Sb), and late-type (Sd) galaxies, respectively. (b) Mean and scatter of the light- and mass-weighted ages of my stochastic SFHs at redshifts of 0 (upper right), 0.3, 1.1, and 2.2 (lower left). The mass-weighted ages are always larger than the light-weighted ones, but the gap between them decreases from redshift $z = 2$ to the present ($z = 0$).

more realistic stochastic SFHs, built from multiple, partially overlapping exponentially declining starbursts with onset times $t_{0,i}$, e-folding time τ_i, and peak amplitude $\psi_{0,i}$ from

$$\psi(t) = \sum_{i}^{n} \psi_{0,i}\, e^{-(t - t_{0,i})/\tau_i} \; . \tag{2.3}$$

I adopt five different families of stochastic SFHs (five examples of which are shown in Figure 2.3). SFH1 and SFH2 are simple test cases with $n = 2$ long ($\tau_i = 1$ Gyr) and $n = 3$ short ($\tau_i = 100$ Myr) bursts, respectively. For each of SFH3, SFH4, and SFH5, I randomly generated 1000 stochastic composite SFHs by combining multiple exponentially declining starbursts with different constraints in order to simulate galaxies of different (Hubble) types and present-day stellar masses. For SFH3, I restrict e-folding times τ_i to 50 Myr $< \tau_i <$ 1 Gyr, for SFH4 100 Myr $< \tau_i <$ 500 Myr, and for SFH5 to 5 Myr $< \tau_i <$ 100 Myr, representative of likely starbursts in early-type, spiral, and late-type galaxies. The mean e-folding times are $\sim$300 Myr,

Table 2.2: Log-linear Metallicity Evolution Parameters, Fit to the Results of Maiolino *et al.* (2008) Combined with My Stochastic SFHs

$\log \mathrm{M}/\mathrm{M}_\odot$	SFH3-ETG		SFH4-Spiral		SFH5-LTG	
	a	b	a	b	a	b
9.50	−0.37	0.25	−0.49	0.29	(−0.58)	0.22
10.95	−0.23	0.49	(−0.30)	0.52	−0.36	0.50
11.40	(−0.18)	0.49	−0.24	0.52	−0.30	0.51

Note. I approximate that evolution by $\log Z(z) = a \cdot z + b$. The rms of the fit in each of a and b is $<$0.01. I adopt the slopes in parentheses: −0.18 for SFH3, −0.30 for SFH4, and −0.58 for SFH5.

$\sim$250 Myr, and $\sim$30 Myr, respectively. I then estimate the number of starburst episodes required for each SFH family by dividing the Hubble time (13.8 Gyr) by these mean e-folding times, giving 44, 53, and 427 for SFH3, SFH4, and SFH5.

I furthermore adopt the model SFHs of Behroozi *et al.* (2013) to define constraints for my mean starburst amplitudes $\psi_{0,i}$ as a function of time of onset $t_{0,i}$. I chose model SFHs resulting in present-day stellar masses of 2.5×10^{11}, 8.9×10^{10}, and 3.1×10^{9} $\mathrm{M}_\odot$ ($\log(\mathrm{M}/\mathrm{M}_\odot)$ of 11.4, 10.95, and 9.5) for SFH3, SFH4, and SFH5, respectively, to match the distribution of stellar masses for Hubble types E, Sb, and Sd found by GD15 in the CALIFA IFU survey of 300 local galaxies (see their Figure 2). Figure 2.4*a* compares the mean sSFRs as a function of lookback time for each of my SFH families and for the corresponding Behroozi *et al.* (2013) models. For SFH3, I find that the results shown in Figure 2.4*a* are sensitive to the choice of lower bound on τ_i, such that for longer minimum burst durations I would fail to reproduce the steep rise and relatively fast decline in SF for massive (early-type) galaxies in the Behroozi *et al.* (2013) models. The resulting SF peak is reached at $z = 3.0$ for SFH3, at $z = 2.1$ for SFH4, and at $z = 0.6$ for SFH5.

For all CSPs constructed as described above, the normalization of the SFH is such that $\sum \psi(t')\delta t' = \mathrm{M}$, the total mass in stars formed up to the present time, which will be higher than the current stellar mass because of mass returned by stellar winds and supernova explosions,

Table 2.3: The Mean, Standard Deviation, Minimum and Maximum of $\beta_{V,0}$ Values Inferred for our SSPs and CSPs with Exponentially Declining SFHs (2nd column in Figure 2.5) for all Z, and Separately for Z=0.004, Z=0.008, and $Z = Z_\odot = 0.02$, Respectively

SFH	$0.0001 \leqslant Z \leqslant 0.05$			$Z = 0.004$			$Z = 0.008$			$Z = 0.02$		
	$\langle\beta_{V,0}\rangle$	Min	Max	$\langle\beta_{V,0}\rangle$	Min	Max	$\langle\beta_{V,0}\rangle$	Min	Max	$\langle\beta_{V,0}\rangle$	Min	Max
SSP	3.84±3.57	0.10	23.64	3.06±2.10	1.03	8.99	2.41±1.65	0.73	7.79	2.06±1.67	0.37	7.77
τ=100 Myr	2.74±1.37	0.35	6.05	2.67±1.22	1.04	4.71	2.13±0.89	0.73	3.89	1.86±0.92	0.55	4.13
τ=250 Myr	2.80±1.36	0.35	5.88	2.75±1.20	1.04	4.67	2.18±0.87	0.73	3.87	1.90±0.90	0.55	4.11
τ=500 Myr	2.85±1.35	0.35	5.82	2.82±1.17	1.04	4.65	2.22±0.85	0.73	3.86	1.93±0.84	0.56	4.11
τ=1 Gyr	2.92±1.33	0.36	5.78	2.88±1.13	1.04	4.64	2.26±0.82	0.74	3.86	1.97±0.84	0.56	4.10
τ=2 Gyr	2.98±1.29	0.37	5.77	2.95±1.06	1.06	4.64	2.31±0.76	0.77	3.86	2.02±0.79	0.59	4.10
τ=5 Gyr	3.05±1.24	0.48	5.76	3.02±0.98	1.24	4.64	2.37±0.69	0.96	3.86	2.07±0.73	0.76	4.10
τ=10 Gyr	3.08±1.22	0.57	5.75	3.05±0.95	1.38	4.64	2.39±0.66	1.11	3.85	2.09±0.70	0.89	4.10

but by no more than ∼30% (see Vázquez and Leitherer, 2005). The more recent SF in low-mass (late-type) galaxies, i.e., downsizing, results in younger ages, especially light-weighted ages (see Figure 2.4*b*). Mass-weighted ages are always larger than light-weighted ones, but Figure 2.4*b* shows that the gap between them decrease from a factor of 3 at $z = 2$ to ∼10% at $z = 0$ for SFH3 and SFH4. For SFH5, the difference remains a factor of ∼5 until $z \sim 0.3$ before decreasing to a factor of ∼3 at $z \simeq 0$.

To account for metallicity evolution and arrive at a functional form for $Z(t')$ in Equation 2.2, I combine my stochastic SFHs with the mass-metallicity relations at $z \simeq 0$, 0.3, 1.1, and 2.2 presented by Maiolino *et al.* (2008). At $z = 0$, I assume stellar masses of 2.5×10^{11}, 8.9×10^{10}, and 3.1×10^{9} $M_\odot$ for early-type, spiral, and late-type galaxies as above. I find that I can approximate the metallicity evolution as $\log Z(z) = a \cdot z + b$, and fit slopes a for each of these present-day stellar masses and SFHs (see Table 2.2). I adopt $a = -0.18$, -0.30, and -0.58 for the metallicity evolution of SFH3, SFH4, and SFH5, respectively. Note that while I list fitted values in the final column of Table 2.2 for SFH5 for each of my three stellar masses, late-type galaxies with $M > 10^{10}$ are extremely rare in nature (e.g., Kelvin *et al.*, 2014).

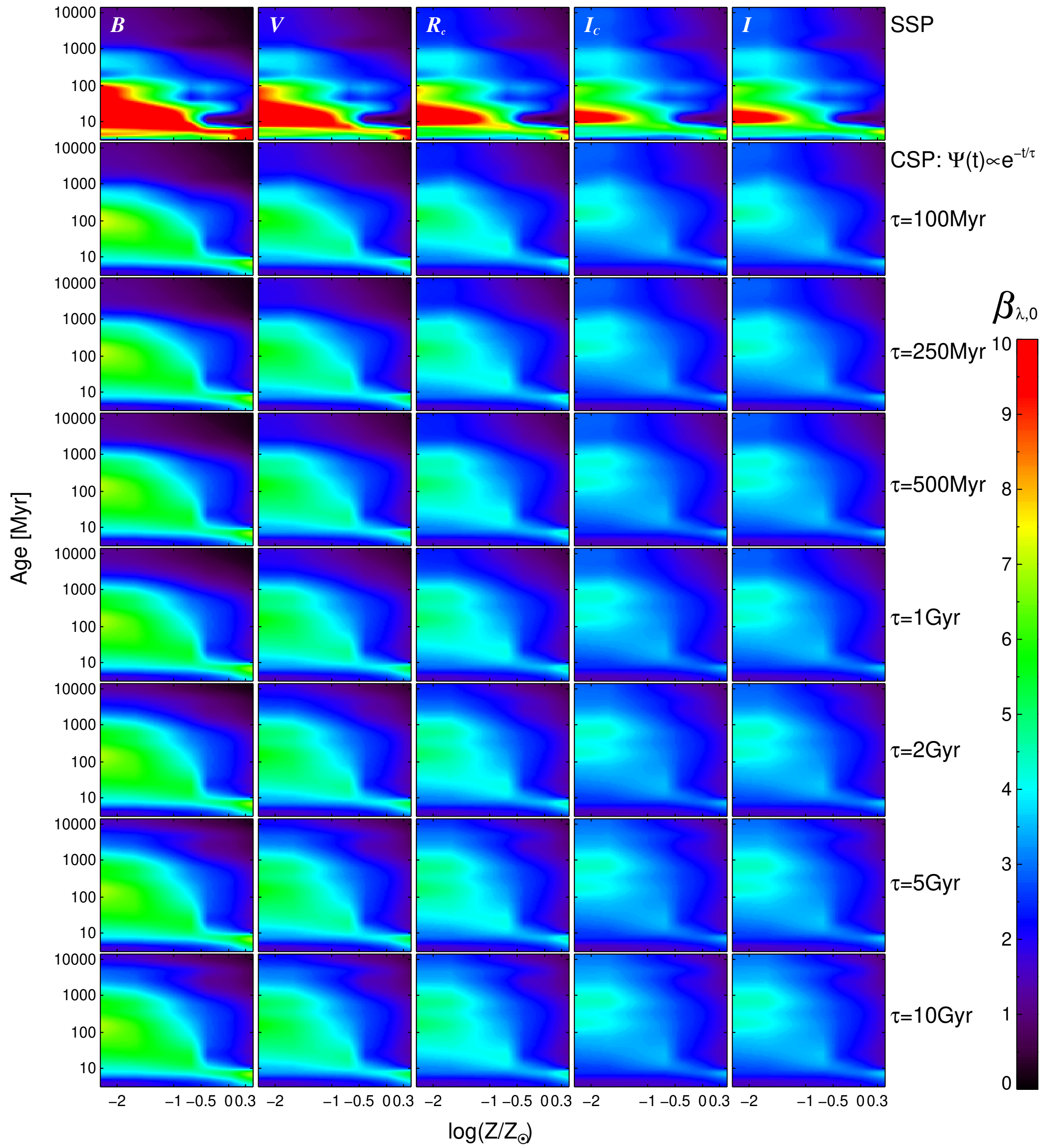

Figure 2.5: Maps of $\beta_{\lambda,0}$ values referenced to the Johnson L band as a function of metallicity $(Z/Z_{\odot})$ and age of the stellar populations for the (left to right) Johnson B, V, Kron-Cousins-Glass R_c, I_c, and Johnson I filters for (top to bottom) SSPs, and for seven CSPs resulting from exponentially declining SFHs with $\tau = 100$, 250, 500 Myr, 1, 2, 5, and 10 Gyr.

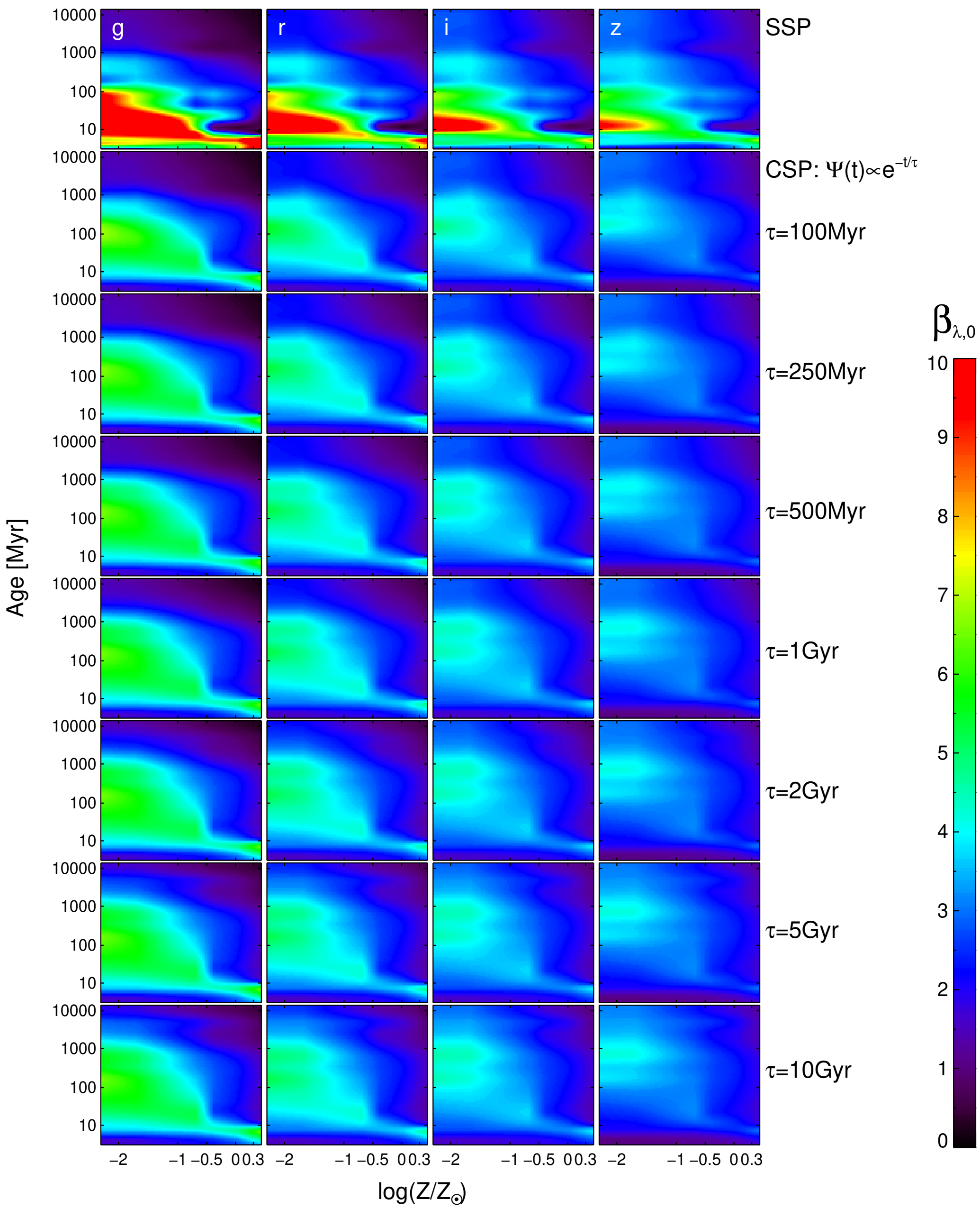

Figure 2.6: Same as Figure 2.5 for the SDSS g, r, i, and z filters.

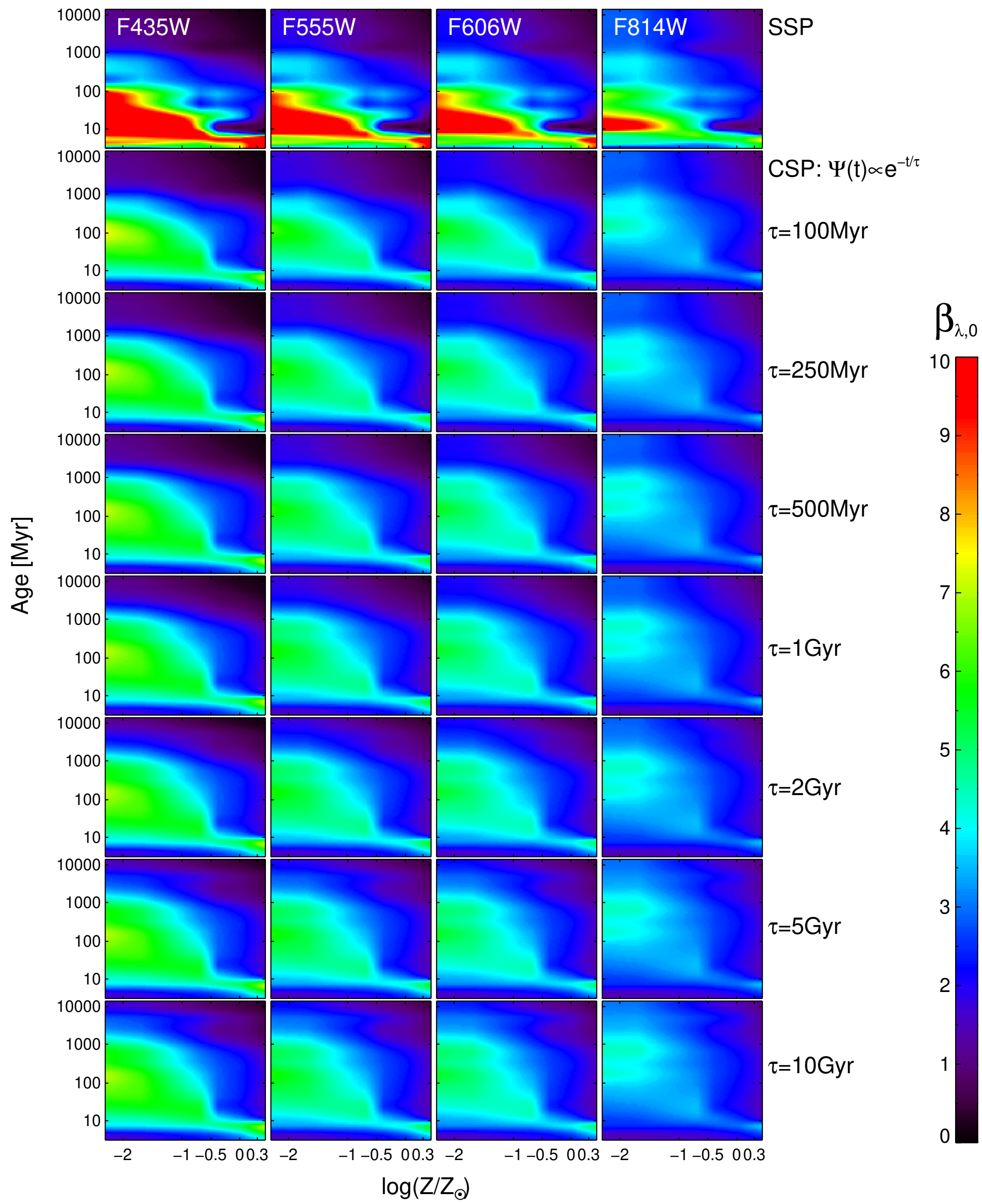

Figure 2.7: Same as Figure 2.5 for the *HST*/ACS WFC *F435W*, *F555W*, *F606W*, and *F814W* filters.

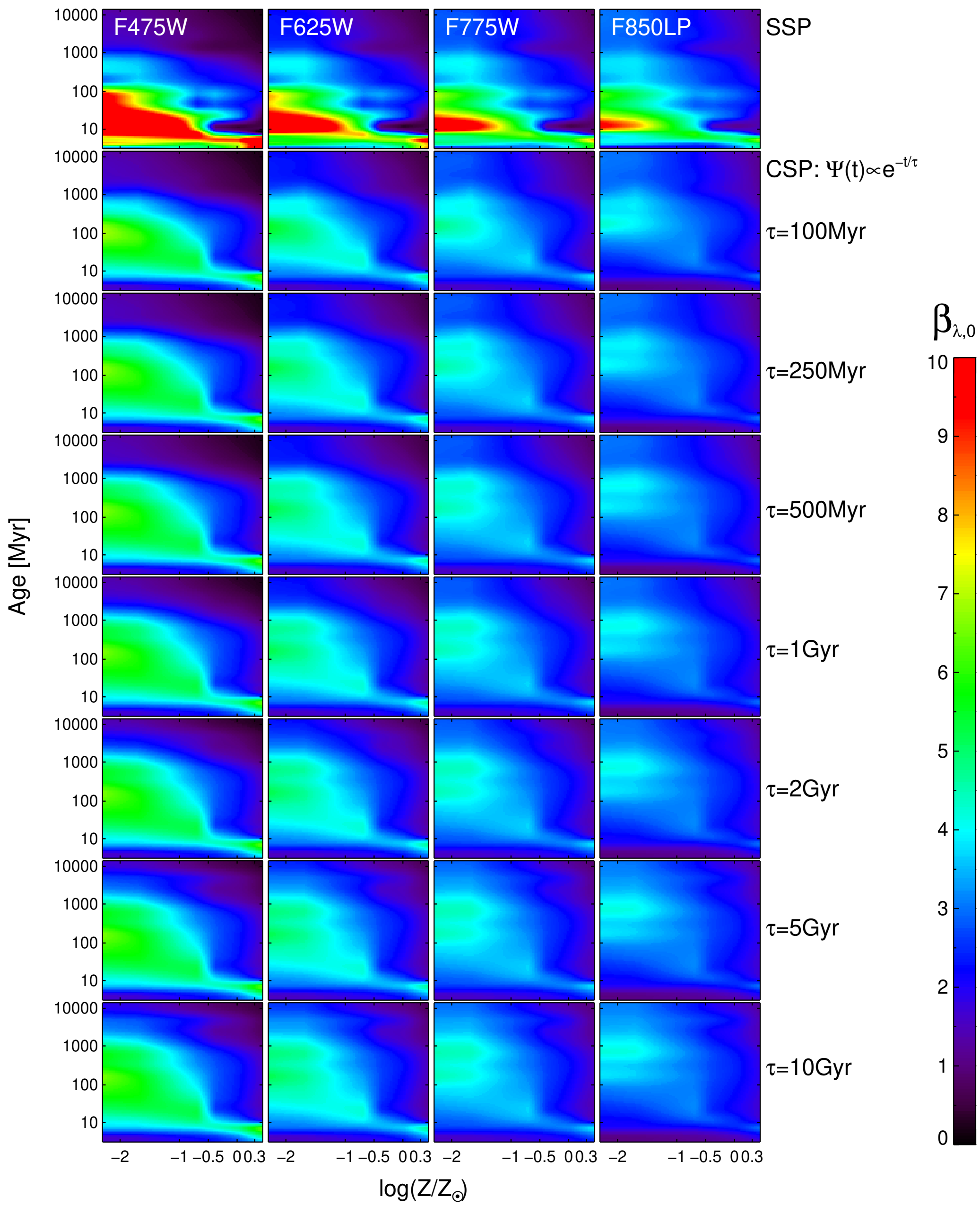

Figure 2.8: Same as Figure 2.5 for the *HST*/ACS WFC *F475W*, *F625W*, *F775W*, and *F850LP* filters.

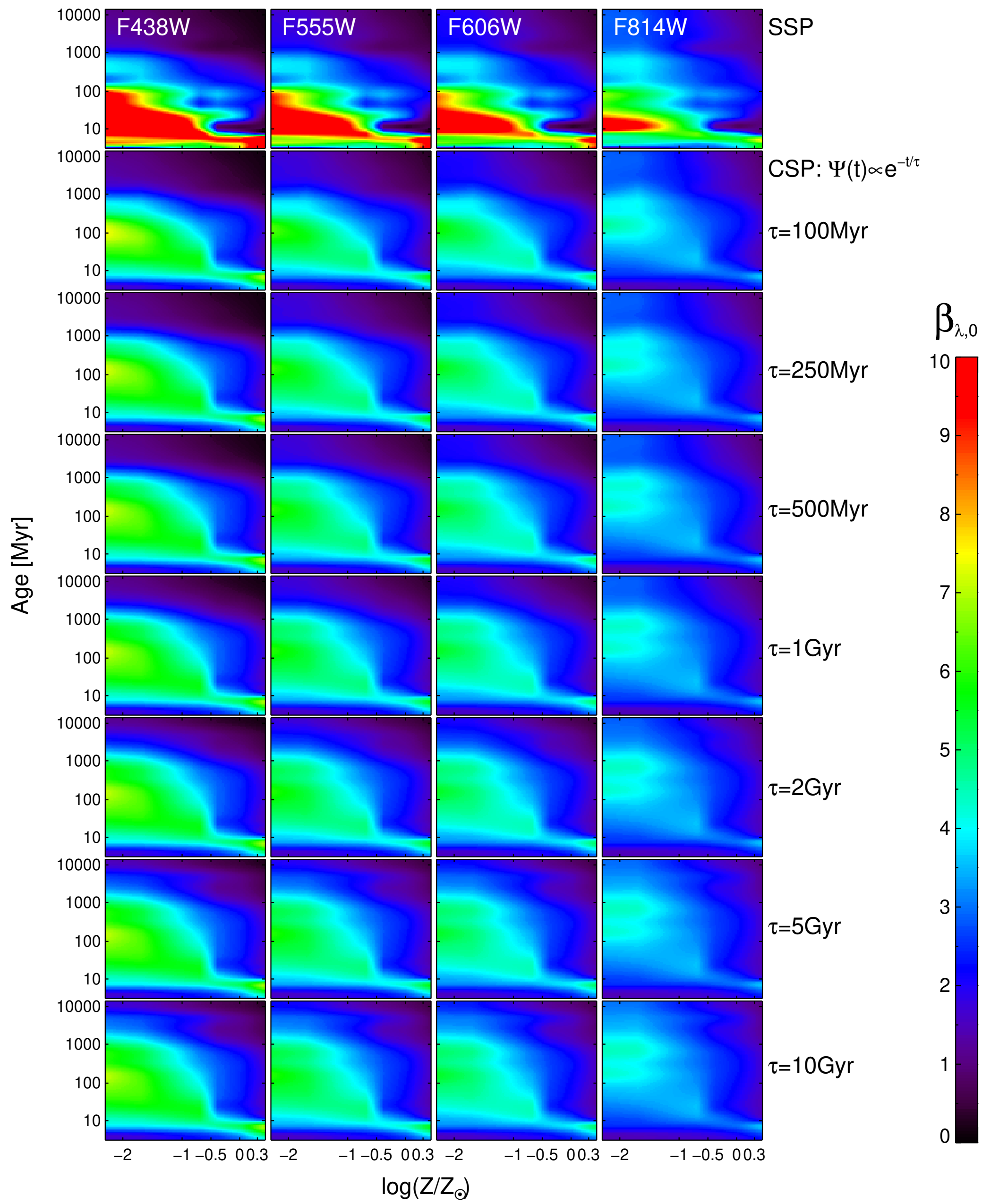

Figure 2.9: Same as Figure 2.5 for the *HST*/WFC3 UVIS *F438W*, *F555W*, *F606W*, and *F814W* filters.

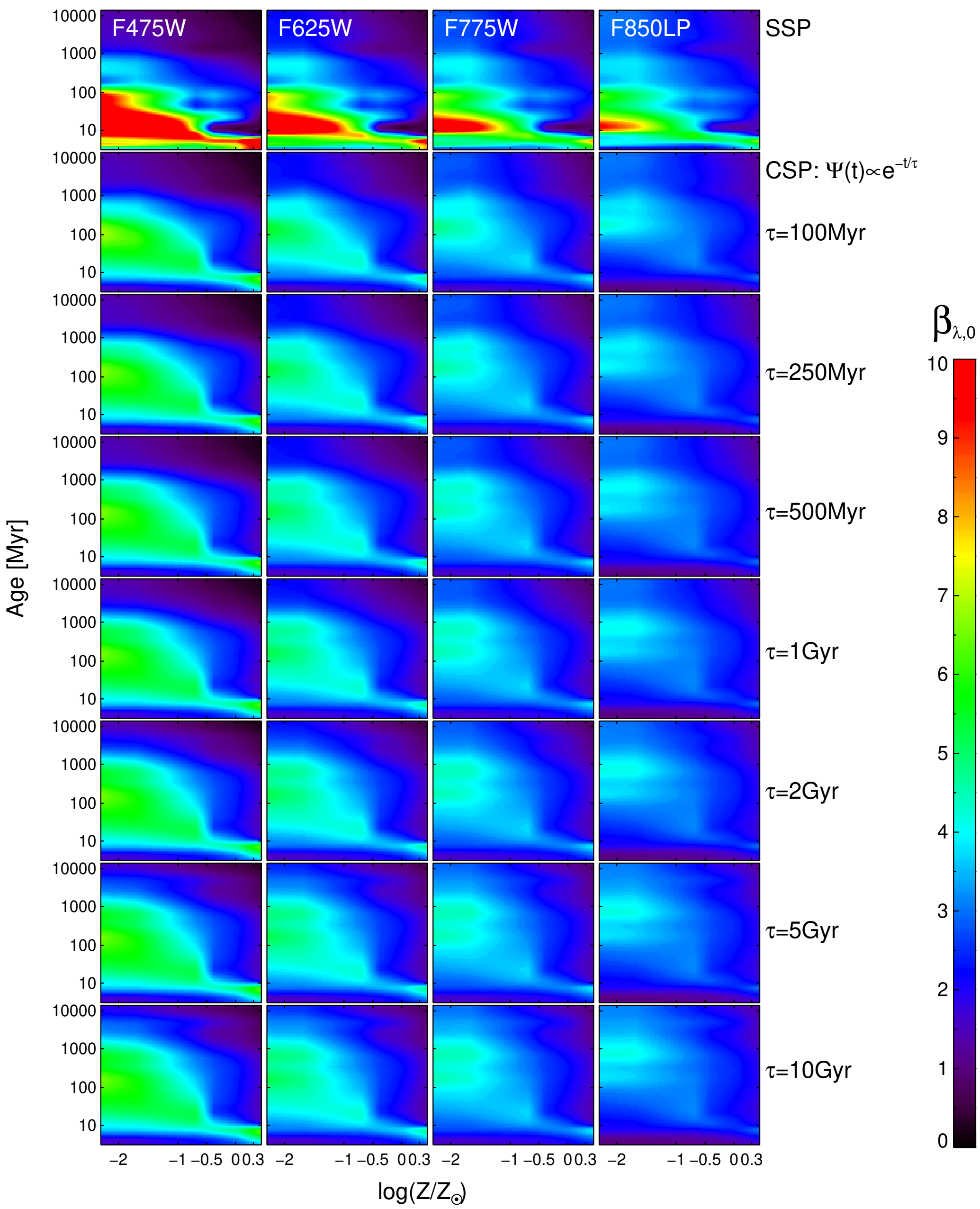

Figure 2.10: Same as Figure 2.5 for the *HST*/WFC3 UVIS *F475W*, *F625W*, *F775W*, and *F850LP* filters.

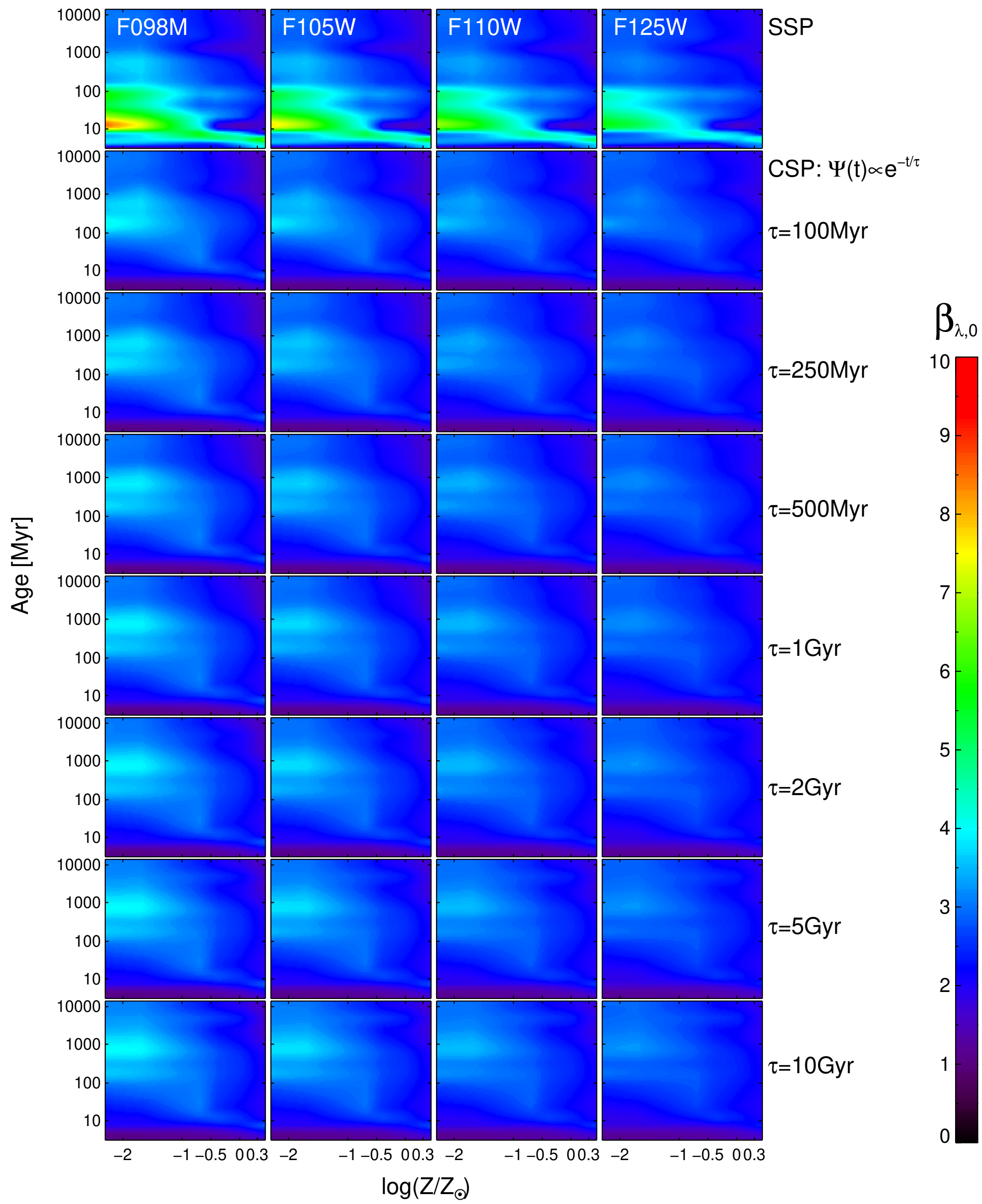

Figure 2.11: Same as Figure 2.5 for the *HST*/WFC3 IR *F098M*, *F105W*, *F110W*, and *F125W* filters.

2.2 Intrinsic $\beta_{\lambda,0}$ Flux Ratios from Model SEDs

Tamura *et al.* (2009) developed the β_V method to estimate the amount of dust extinction in a galaxy using images through just two broadband filters: one visible (V) and one in the mid-IR near 3.5 μm (L band), specifically, the IRAC (Fazio *et al.*, 2004) Channel 1 onboard the *Spitzer* Space Telescope (Werner *et al.*, 2004) centering around 3.6 μm in their case. The L band is where the extinction by dust reaches a minimum, and where there is still little emission from warm dust, PAHs, and silicates (although there is a significant C–H stretching PAH feature near 3.3 μm; see Figure 1.1; Leger and Puget, 1984; Allamandola *et al.*, 1989). If I have knowledge of the intrinsic SED of a simple or CSP, then I can calculate the intrinsic flux ratio $\beta_{V,0} = f_{V,0}/f_{L,0}$. This ratio will be a function of age t, metallicity Z, and SFH $\psi(t)$. If $\beta_{V,0}$ values were to fall in a very narrow range for a wide range of such CSP parameters, and if my model SEDs were accurate representations of observed stellar populations, then comparing the observed (β_V) and the intrinsic ($\beta_{V,0}$) flux ratios would allow us to infer the missing flux in the V band. I furthermore assume that the extinction in bandpasses centered near 3.5 μm (L) is negligible. The extinction in magnitudes is given by $A_V = (m_V - m_{V,0})$, which can be rewritten in terms of the observed L band flux and the intrinsic V-to-L-band flux ratio $\beta_{V,0}$ as

$$A_V \simeq m_V - [-2.5 \log(\beta_{V,0} \times f_L) - V_{zp}] , \tag{2.4}$$

where $f_L \simeq f_{L,0}$, V_{zp} is the zero-point magnitude for the V filter, and the $\simeq$ -symbol serves to recall the approximate nature of this method.

Here, I consider a more general extension of the β_V method, the β_λ method, where I compute $\beta_{\lambda,0}$ for a large selection of filter pairs in the rest-frame optical ($\lambda \sim 0.4$–$1\ \mu$m) and rest-frame mid-IR ($\lambda \sim 3.4$–$3.6\ \mu$m). In total, 29 visible–near-IR and 5 mid-IR filter throughput curves were convolved[1] with the simple and composite SEDs I constructed as described in § 2.1 to obtain the $\beta_{\lambda,0}$ values for each SED.

I make all models and derived data available on our website[2] as ASCII text tables and as 2D maps of $\beta_{\lambda,0}(Z,t)$ in both PNG[3] and FITS[4] format.

2.2.1 SSP and Exponentially Declining SFHs

Figure 2.5 depicts an example of 2D maps of $\beta_{\lambda,0}$ ratios as a function of metallicity and stellar population age (or time since the onset of SF) for the Johnson B, V, Kron-Cousins-Glass R_c, I_c, and Johnson I filter (Bessell, 1990), when referenced to the Johnson L band (Bessell and Brett, 1988). From top to bottom, I show the results for SSPs and for seven exponentially declining SFHs with $\tau = 100$, 250, and 500 Myr, and 1, 2, 5, and 10 Gyr. The final row approximates a continuous nearly constant star formation rate. For each panel, I started with a 2D array of SEDs that has six rows and 16 columns, corresponding to the metallicity and age values of Figure 2.2, for which I computed $\beta_{\lambda,0}$ values by convolving each of the filter curves with each of the 6×16 SEDs. The resulting array of $\beta_{\lambda,0}$ values was expanded through log–log cubic-spline interpolation into the finer 100×100 grids of metallicity and age as shown. SSPs show the highest dispersion and widest range of $\beta_{V,0}$ values (see Table 2.3). For exponentially

[1]While I mean the product $T(\lambda)\cdot F(\lambda)$ of the filter throughput $T(\lambda)$ and SED $F(\lambda)$, rather than the convolution operation $T(\lambda) * F(\lambda)$, the term "convolution" has become the accepted terminology and is used throughout.

[2]http://lambda.la.asu.edu/betav/

[3]Portable Network Graphics (Duce et al. 2004 [ISO/IEC 15948:2004]).

[4]Flexible Image Transport System (Wells *et al.*, 1981; Hanisch *et al.*, 2001).

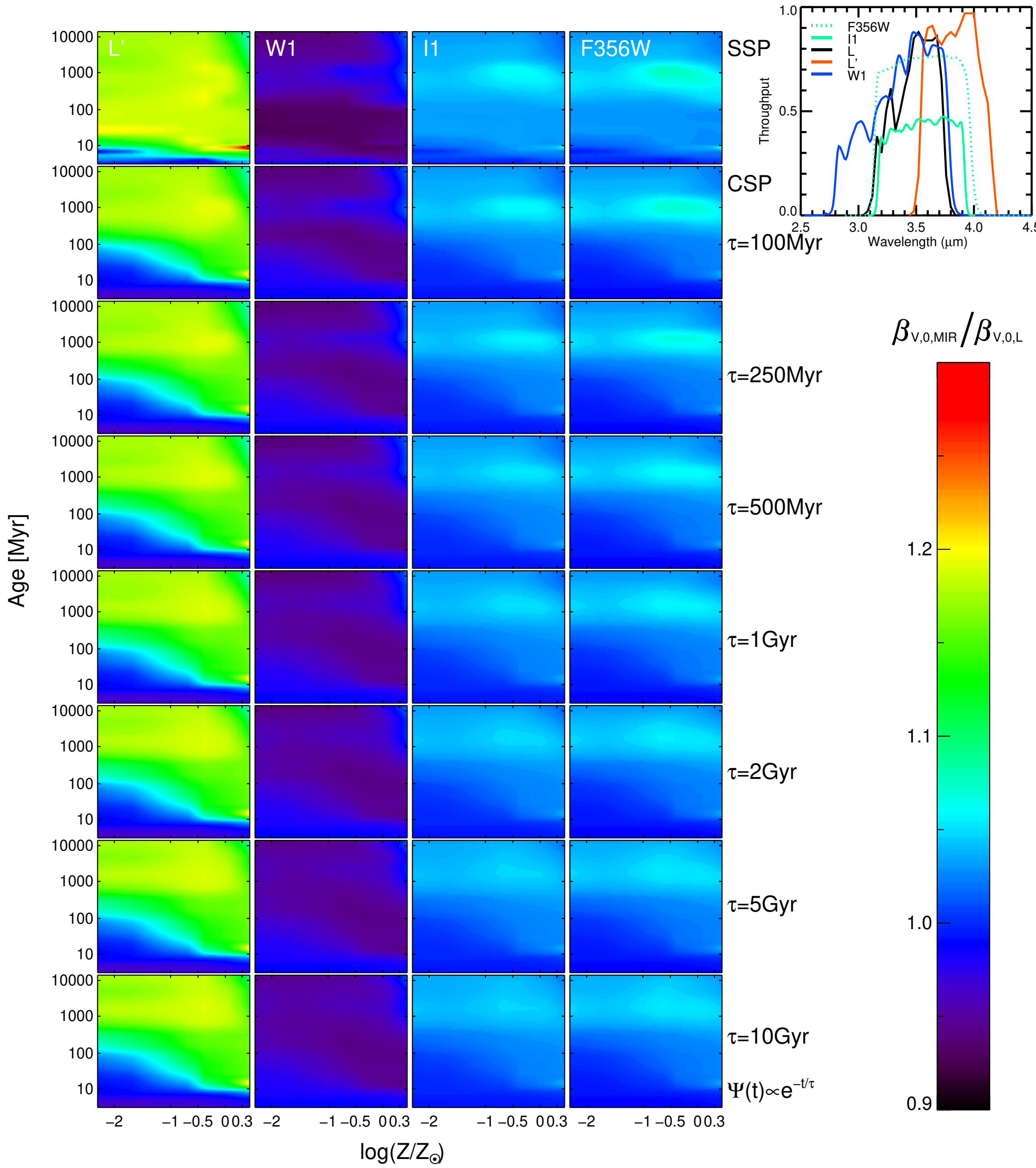

Figure 2.12: Maps of ratios $r_{\beta}(MIR, L) = F(L)/F(L')$, $F(L)/F(W1)$, $F(L)/F(I1)$, and $F(L)/F(\text{F356W})$ as a function of metallicity ($Z/Z_{\odot}$) and age t of the stellar populations and stellar population models as shown in Figure 2.5. $r_{\beta}(MIR, L)$ gradually increases as stellar populations age and decreases again for super-solar metallicity. The color bar in this figure spans a much narrower range than the one in Figure 2.5–2.11. For reference, I plot the throughput curves of each MIR bandpass in the inset at the upper right.

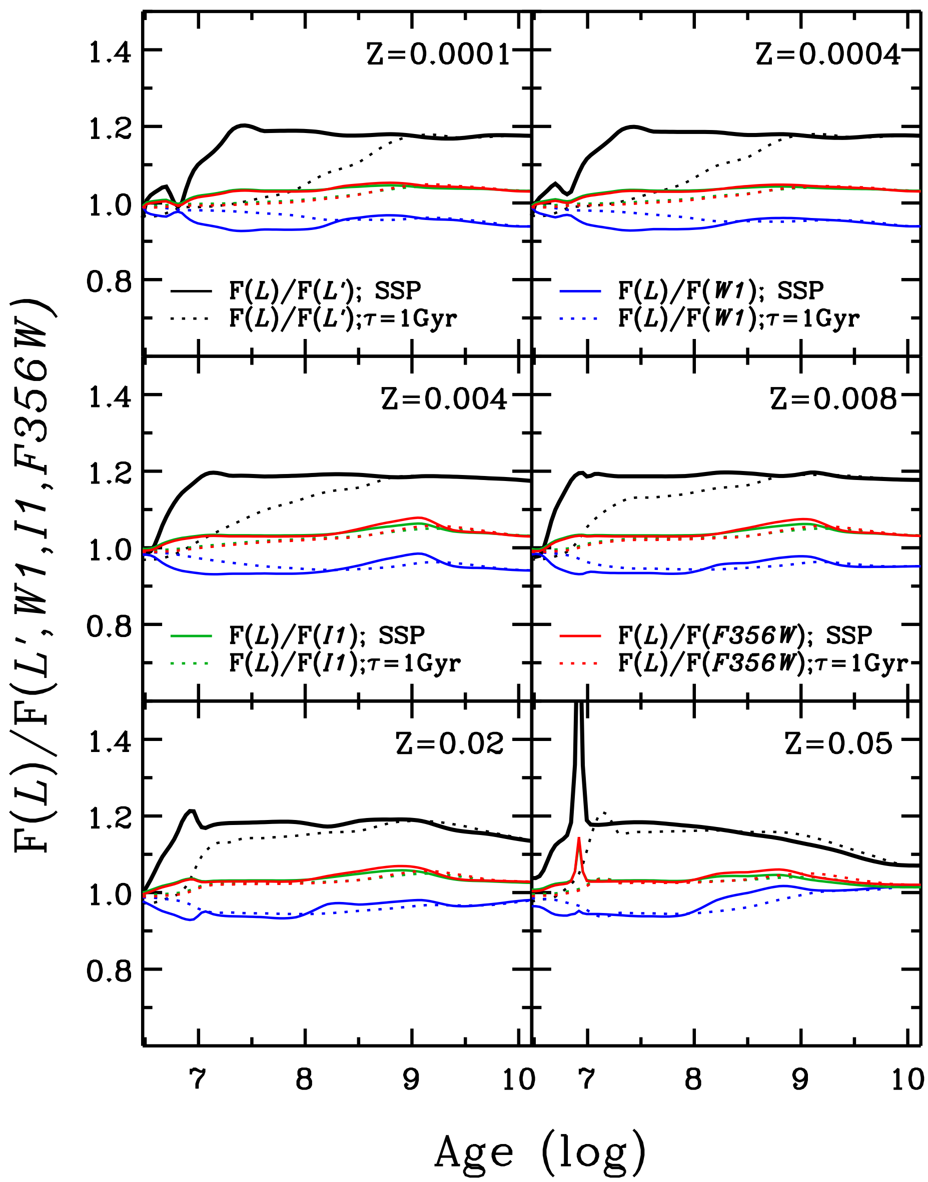

Figure 2.13: Flux ratios between different choices of mid-IR reference filters as a function of the age of the stellar populations for various metallicities. Solid curves are for SSPs and dotted curves are for exponentially declining SFHs with a 1 Gyr e-folding time. The ratio generally remains stable in the 0.9–1.2 range for ages larger than a few tens of Myr. While the $\beta_{\lambda,0}$ value to adopt depends on the choice of mid-IR reference filter, it is *predictable*, so any of the filters considered will be similarly valid for the application of the β_λ method.

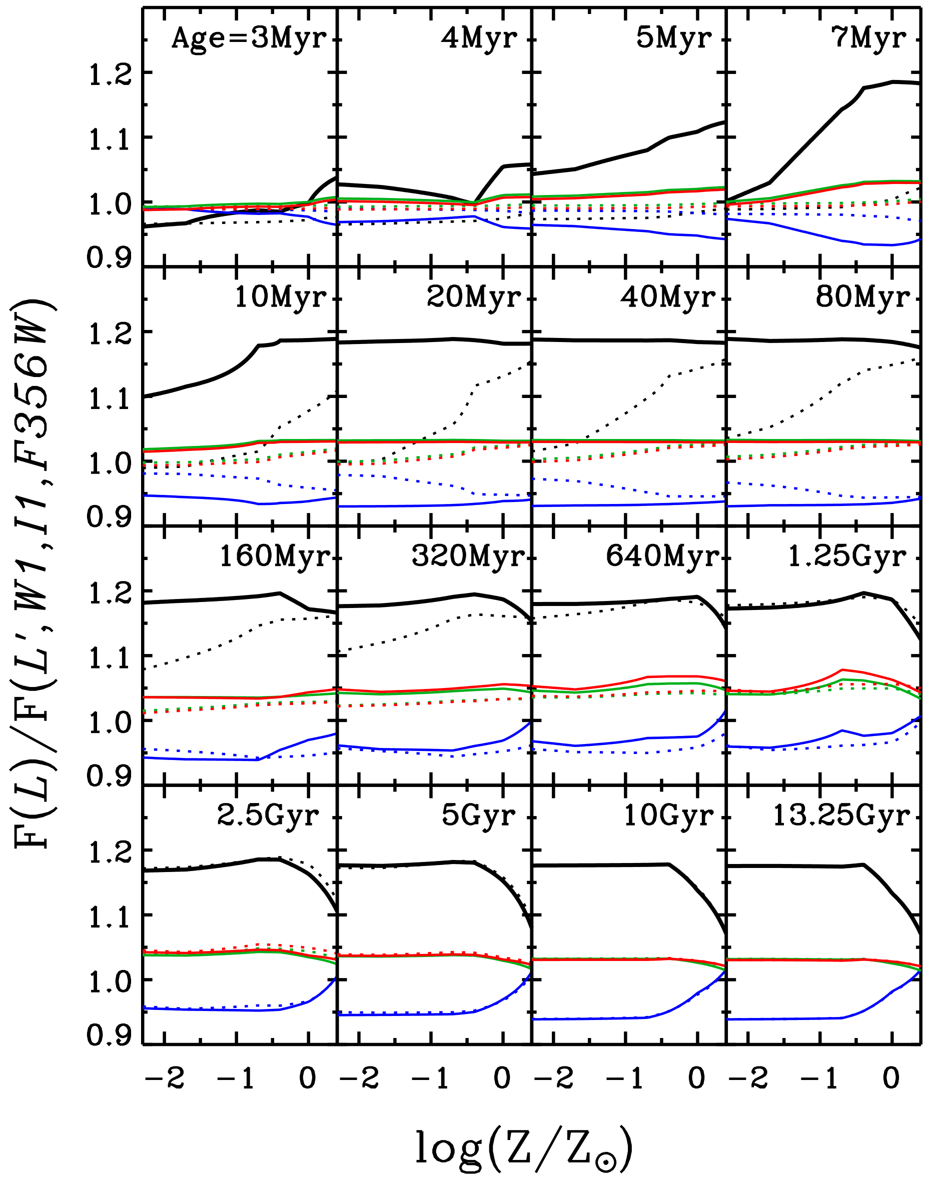

Figure 2.14: Flux ratios between different choices of mid-IR reference filters as a function of the metallicity of the stellar populations for various ages. Line and color schemes are the same as in Figure 2.13. If I exclude the red supergiants feature at ages of ∼5–10 Myr and high metallicity, the choice of mid-IR reference filter affects $\beta_{\lambda,0}$ at the $\lesssim$20% level, and for a given reference filter, much less than that over most of the range in age and metallicity.

Table 2.4: Comparison of the Mean Values and Standard Deviations of $r_\beta(MIR, L) = \beta^{MIR}_{\lambda,0}/\beta^{L}_{\lambda,0} = F(L)/F(MIR)$, before and after 3σ Rejection, For my SSPs and CSPs with Exponentially Declining SFHs (First and Fifth Rows in Figure 2.12).

MIR	SSP		τ=1 Gyr	
	Mean	Robust mean	Mean	Robust mean
L'	1.16±0.05	1.18±0.01	1.11±0.07	1.11±0.08
$W1$	0.95±0.02	0.95±0.02	0.96±0.01	0.96±0.02
$I1$	1.03±0.01	1.04±0.01	1.02±0.02	1.02±0.02
F356W	1.03±0.02	1.03±0.02	1.02±0.02	1.02±0.02

declining SFHs, as τ increases, the standard deviations and min–max ranges decrease, while the mean $\beta_{V,0}$ values themselves slightly increase ($\lesssim$11%). The lower metallicity population has higher $\beta_{V,0}$ values as well (~50% for $Z = 0.0004$ compared to $Z = 0.02$).

Similarly, in Figure 2.5–2.10, I show $\beta_{\lambda,0}$ referenced to the same Johnson L band for the SDSS g, r, i, and z filters (Gunn *et al.*, 1998), as well as for eight *HST*/ACS WFC (Ford *et al.*, 2003; Avila *et al.*, 2015) and eight *HST*/WFC3 UVIS (Dressel *et al.*, 2015) filters. The choice of filters was motivated by their common use for *HST* deep and medium-deep surveys, such as the GOODS (Dickinson *et al.* 2003, p. 324; Giavalisco *et al.* 2004), the CANDELS (Grogin *et al.*, 2011; Koekemoer *et al.*, 2011), the COSMOS (Scoville *et al.*, 2007), the CLASH (Postman *et al.*, 2012), and the *HST*/WFC3 ERS program (Windhorst *et al.*, 2011). In Figure 2.11, moreover, I extend our coverage to the NIR with four WFC3/IR filters.

One might wonder how sensitive the β_λ method is to the exact choice of the mid-IR reference filter. I thus considered the ground-based Johnson L and L' filters, the space-based *WISE* $W1$ bandpass ($\lambda_{eff} = 3.3526\ \mu$m, $\Delta\lambda = 0.66\ \mu$m; Wright *et al.*, 2010; Jarrett *et al.*, 2011), the *Spitzer*/IRAC $I1$ bandpass ($\lambda_{eff} = 3.550\ \mu$m, $\Delta\lambda = 0.75\ \mu$m; Fazio *et al.*, 2004), and the *JWST*/NIRCam (Horner and Rieke, 2004; Gardner *et al.*, 2006; Rieke, 2011) F356W filter

($\lambda_{eff} = 3.568\,\mu$m, $\Delta\lambda = 0.781\,\mu$m)[5]. In Figure 2.12 and Table 2.4, I compare the ratios of $\beta_{\lambda,0}$ computed relative to each mid-IR (MIR) band and to the L band: $r_\beta(MIR, L) = \beta^{MIR}_{\lambda,0}/\beta^{L}_{\lambda,0}$ $= F(L)/F(MIR)$. The ratios get closer to unity and the range in values decreases for the exponentially declining SFHs with $\tau = 1$ Gyr. The $\beta_{\lambda,0}$ values referenced to the $I1$ and F356W filters are similar to those referenced to the L band, whereas $\beta_{\lambda,0}$ values referenced to L' and $W1$ were higher and lower, respectively. The $r_\beta(L', L)$ values tend to be higher than 1 (i.e., $\beta^{L'}_{\lambda,0} > \beta^{L}_{\lambda,0}$), because I am sampling the Rayleigh-Jeans tail of the stellar SED and the central wavelength of the L' filter is longer than that of the L filter. Conversely, the central wavelength of the $W1$ bandpass lies shortward of that of L, resulting in $r_\beta(W1, L)$ smaller than 1. Except for a difference in the overall throughput, the $I1$ and F356W bandpasses have very similar shapes and similar central wavelengths to the L filter, as shown in the inset at the upper right side of Figure 2.12.

In Figure 2.13, I plot $r_\beta(L', L)$ as a function of age for six different metallicities for SSPs (black solid curves) and for exponentially declining SFHs (black dotted curves). At low metallicities, $r_\beta(L', L)$ is seen to be remarkably independent of age for ages older than 10 Myr for SSPs. For CSPs with an exponentially declining SFR and an e-folding time of 1 Gyr, $r_\beta(L', L)$ stabilizes around 500–600 Myr. At solar metallicity and above, and particularly for SSPs, sharp features become noticeable around 10 Myr of age in both Figure 2.12 and 2.13. These features correspond to the appearance and demise of red supergiants (RSGs; Walcher *et al.*, 2011). The strength or absence of these RSG features at low metallicity remains uncertain (see, e.g., discussions in Cerviño and Mas-Hesse, 1994; Leitherer *et al.*, 1999; Vázquez and Leitherer, 2005). The flux ratios for different mid-IR filters are similar at early ages ($\sim$3 Myr), but diverge until an age of $\sim$10 Myr before stabilizing again for ages larger than 1 Gyr in the case of super-solar metallicities. This pattern is more clearly shown in Fig 2.14, which plots $r_\beta(MIR, L)$ as a func-

[5] http://www.stsci.edu/jwst/instruments/nircam/instrumentdesign/filters/

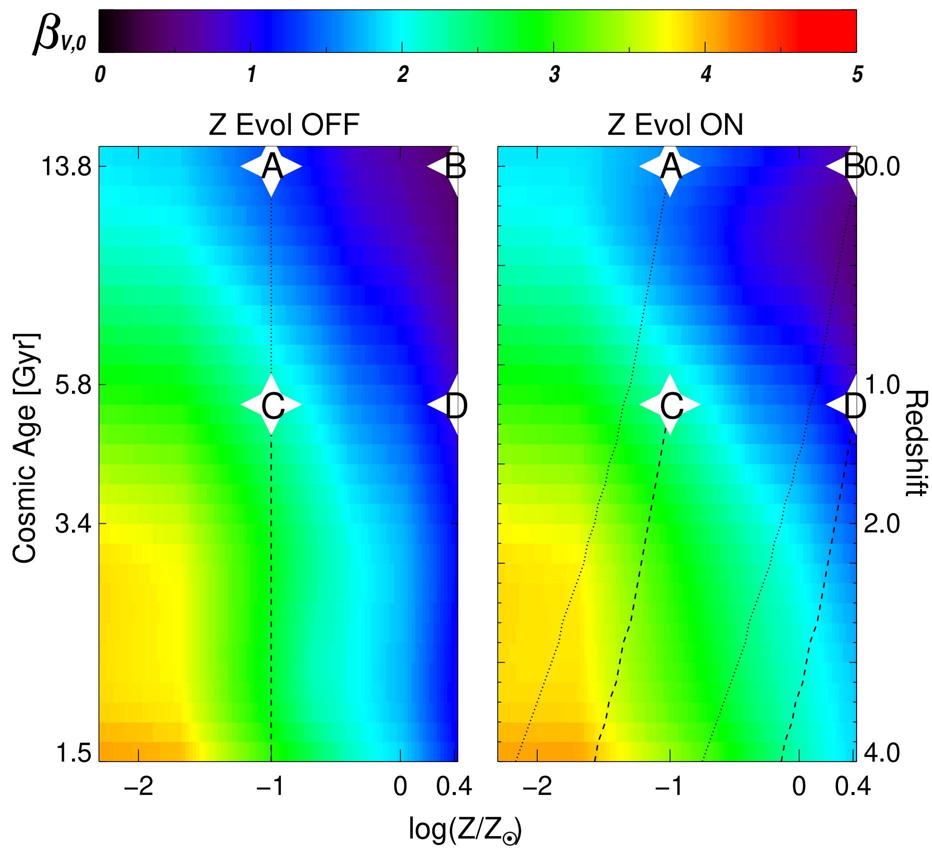

Figure 2.15: Comparison of $\beta_{V,0}$ values when metallicity evolution *is* (right) and *is not* (left) taken into account for the CSPs characterized by SFH4 (spiral galaxies). For four specific realizations of SFH4, I show the metallicity tracks as a function of cosmic age of the SSP SEDs, which are stacked to generate CSP SEDs at that age. The endpoints (z, Z) for tracks A, B, C, and D are $(0.0, 0.002)$, $(0.0, 0.05)$, $(1.0, 0.002)$, and $(1.0, 0.05)$, respectively. When I include metallicity evolution, I find a stronger dependence of $\beta_{V,0}$ on redshift, with higher $\beta_{V,0}$ values for the progenitors of present-day galaxies than in the no-evolution case.

tion of metallicity at 16 different ages. $r_\beta(MIR, L)$ is insensitive to metallicity at most stellar population ages (the curves in Fig 2.14 are nearly flat for most ages $\gtrsim$10 Myr and for most sub-solar metallicities). If I exclude the RSG feature at high metallicity, the choice of mid-IR filter affects $\beta_{\lambda,0}$ at the $\lesssim$20% level overall, while reference filter-dependent variations with respect to the L band are much smaller than that over most of the range in age and metallicity. One can gauge the impact of a given choice of mid-IR reference filter using Figs. 2.12–2.14.

2.2.2 Stochastic Multiburst SFHs

The β_V method was originally developed as an approximate dust extinction correction method for large surveys of spatially resolved galaxies with *unresolved* stellar populations. The light from the unresolved stellar populations will have more complex SFHs than SSP or exponentially declining SFHs (Gerola and Seiden, 1978; Kauffmann *et al.*, 2006; da Silva *et al.*, 2012). Hence, building SEDs for complex SFHs with stochastic starbursts and inspecting the resulting $\beta_{\lambda,0}$ values will be essential to determine whether the β_V method (or its extension, the β_λ method) is applicable. As mentioned in § 2.1.2, metallicity evolution is taken into account when I build the SED arrays for stochastic SFHs, which moves the metallicity range toward higher values when cosmic age increases and redshift decreases (read more in § 2.2.2.1 and see Figure 2.25). When metallicity evolution is taken into account, initial metallicities for cosmic ages less than 1.5 Gyr ($z > 4$) may be below the lower limit ($Z = 0.0001$) of my SSP model SEDs. There, my CSPs will have an artificial lower limit in metallicity of $Z = 0.0001$, so I will not consider redshifts $z > 4$. Figure 2.15 shows the difference between $\beta_{V,0}$ values when metallicity evolution *is* (right) and *is not* (left) applied for the CSPs characterized by SFH4 (spiral galaxies; see Figure 2.3 and Figure 2.4*a*). I adopt a metallicity evolution of -0.30 per unit z, appropriate for SFH4 (see Table 2.2). To illustrate the effect of metallicity evolution for four specific realizations of SFH4, I show the metallicity tracks as a function of cosmic age of the SSP SEDs, which are stacked to generate CSP SEDs at that age. The effects of metallicity evolution become evident at $z \gtrsim 1$ (cosmic age $\lesssim$5.8 Gyr). For the progenitors of galaxies at a given redshift, significantly higher values of $\beta_{V,0}$ must be assumed at longer lookback times than in the no-evolution case, so that there is a stronger dependence of $\beta_{V,0}$ on redshift.

In Figure 2.16 I present maps of $\beta_{\lambda,0}$ as a function of cosmic age and metallicity, and 1D profiles of $\beta_{\lambda,0}$ values as a function of redshift. The $\beta_{\lambda,0}$ values without metallicity evolution are overplotted in each 1D profile panel for comparison. Each curve in the panels for SFH3, SFH4, and SFH5 represents the median $\beta_{\lambda,0}$ values of 1000 randomly generated stochastic SFHs in that family. Comparing the solid to the dotted profiles in Figure 2.16*b*, I find that the $\beta_{\lambda,0}(z)$ values are higher when metallicity evolution is taken into account, and progressively more so for higher present-day metallicity values (at low present-day metallicities the difference must necessarily be small). The spread in $\beta_{\lambda,0}$ at a given redshift due to metallicity differences tends to be smaller than in the no-evolution case. While the range in $\beta_{\lambda,0}$ values at $z \simeq 0$ is comparable in both the evolution and no-evolution cases for each of SFH3, SFH4 and SFH5, this range becomes narrower toward higher redshifts for SHF4, and especially for SFH5. For these two SFH families, more of the stars formed relatively recently, with much (or even most) of the metallicity evolution taking place in the redshift range of interest (see my adopted slopes in Table 2.2). The range of $\beta_{V,0}$ for SFH3, SFH4, and SFH5 changes from 2.4–4.7 to 0.6–2.3 as the redshift decreases from 4 to 0. If I impose a minimal constraint on the redshift range without assuming any particular SFH family, I find allowed ranges for $\beta_{V,0}$ of 0.6–3.4 when $0 < z < 1$, and 0.90–3.85 when $1 < z < 2$. When the redshift is known, I find narrower ranges of 0.57–2.30, 0.70–2.93, 0.90–3.35, 1.17–3.58, and 1.52–3.85 for $\beta_{V,0}$ at z=0, 0.5, 1.0, 1.5, and 2.0, respectively. In § 2.2.3, I will show that these $\beta_{\lambda,0}$ ranges are further reduced once I can also constrain the range of likely SFHs and metallicities. For my full set of visible–near-IR filters, I refer the reader to Figures 2.17–2.22.

In Figure 2.23 (top panel) I show the dependence of the $-1\,\sigma$ to $+1\,\sigma$ range of $\beta_{\lambda,0}$ and β_λ values on the bandpass (wavelength) when the redshift is only minimally constrained to fall in the $0 < z < 1$ interval. The scatter in $\beta_{\lambda,0}$ was derived from the same 1000 randomly generated SFHs per SFH family as used for Figure 2.16. The visible filters show significant ranges of allowed $\beta_{\lambda,0}$ values, especially for SFHs with recent SF such as SFH5. The near-IR

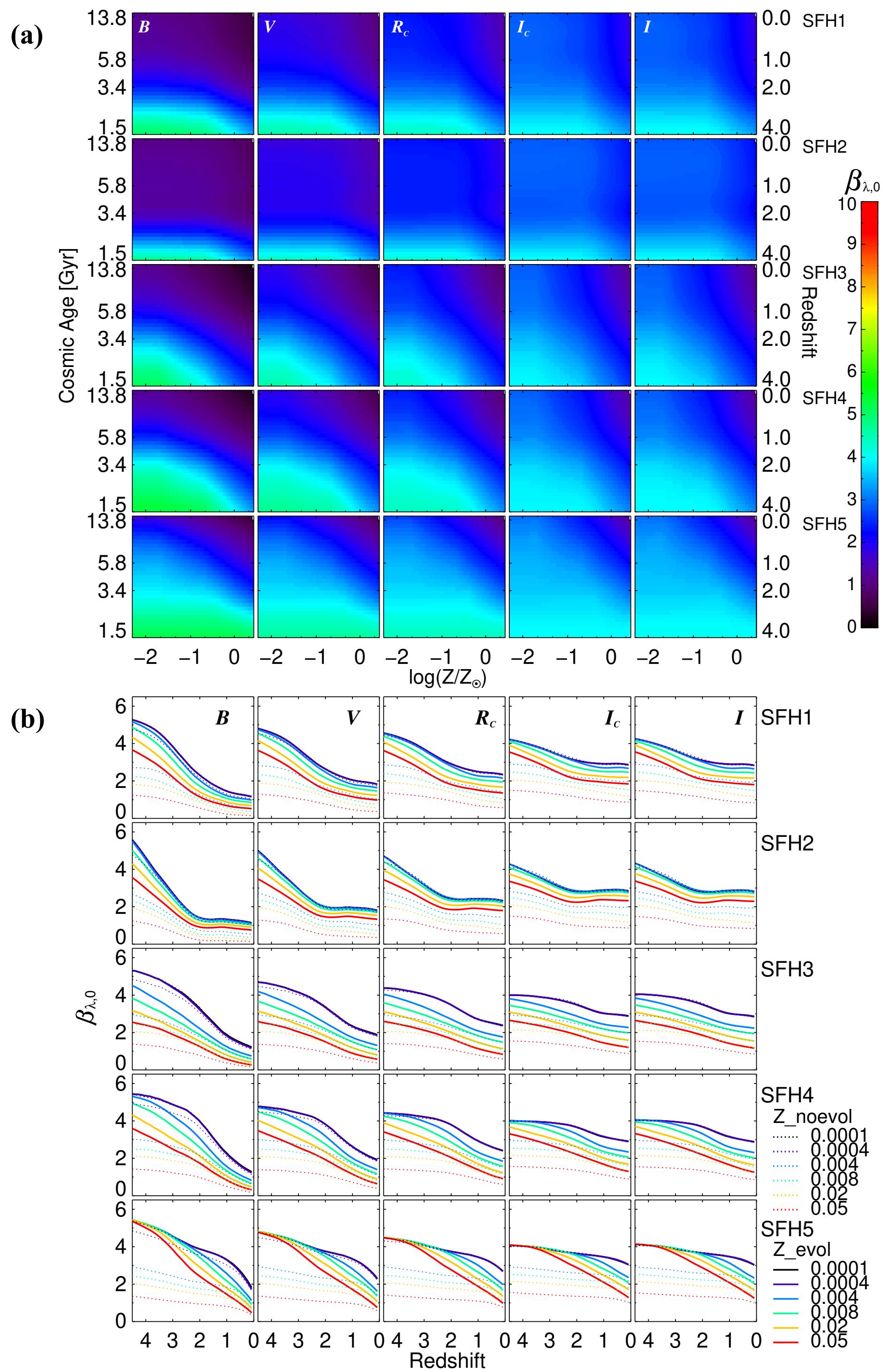

Figure 2.16: (a) Maps of $\beta_{\lambda,0}$ values referenced to the Johnson L band as a function of metallicity ($Z/Z_{\odot}$) and cosmic age for the (left to right) Johnson B, V, Kron-Cousins-Glass R_c, I_c, and Johnson I filters for (top to bottom) stochastic (multiburst) SFHs (see Figure 2.3) with metallicity evolution taken into account. (b) $\beta_{\lambda,0}$ profiles of stellar populations with various present-day (z=0) metallicities that have different stochastic SFHs as a function of redshift. For comparison, I overplot the no-evolution case (dotted curves). Each map and each curve in the panels for SFH3, SFH4, and SFH5 represents the median $\beta_{\lambda,0}$ values of 1000 randomly generated SFHs in that family.

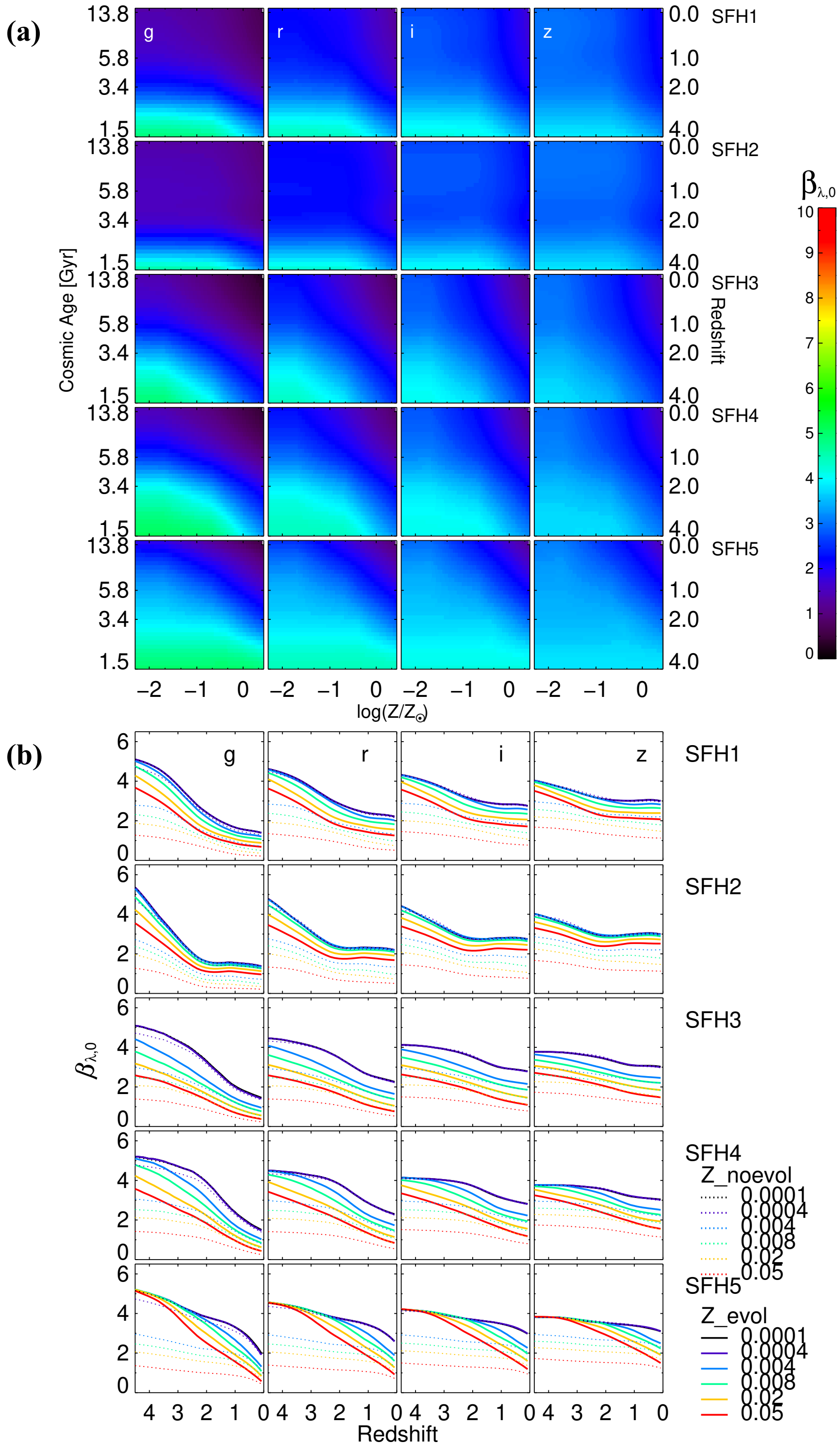

Figure 2.17: Same as Figure 2.16 for the SDSS g, r, i, and z filters.

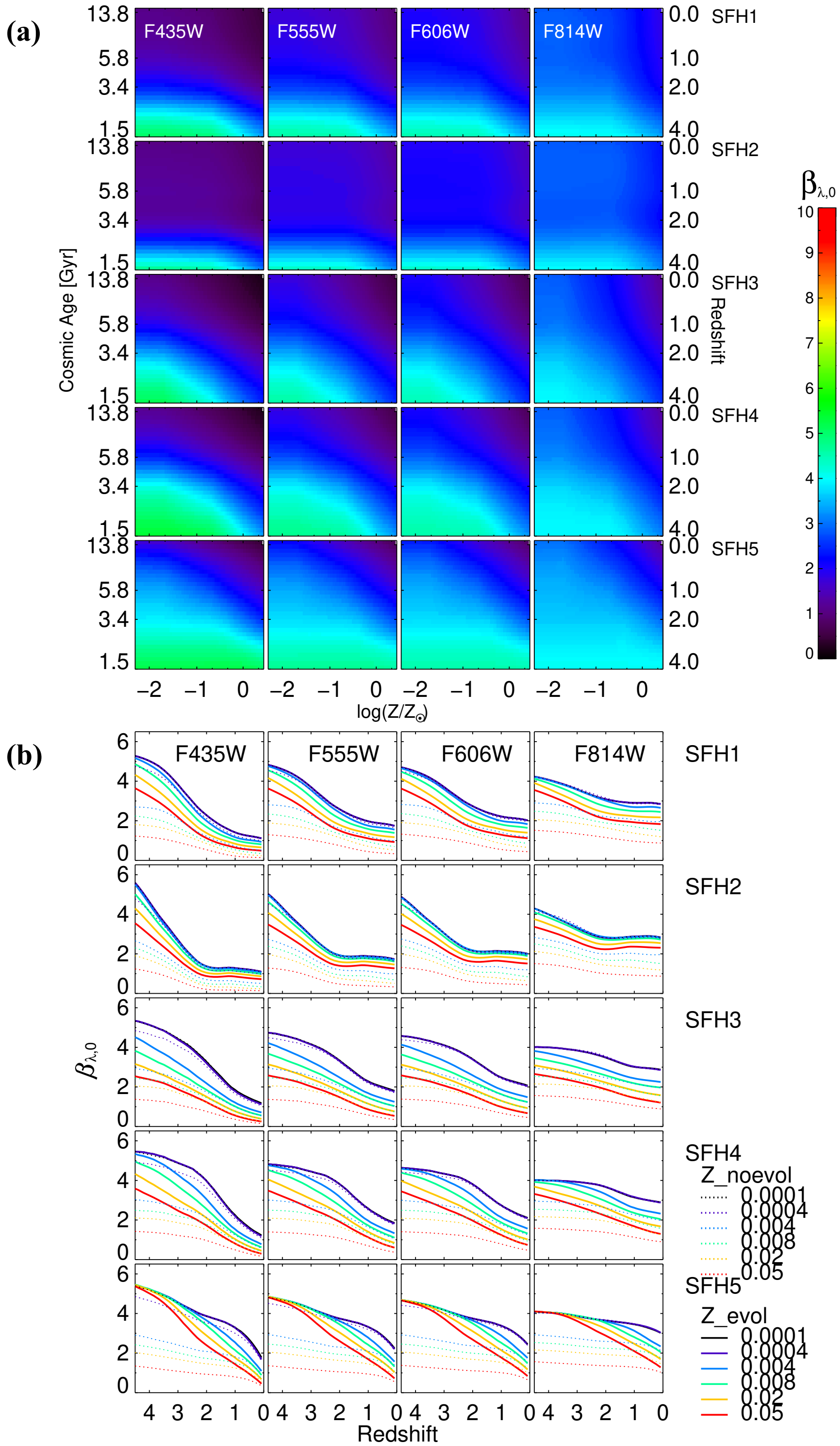

Figure 2.18: Same as Figure 2.16 for the *HST*/ACS WFC *F435W*,*F555W*, *F606W*, and *F814W* filters.

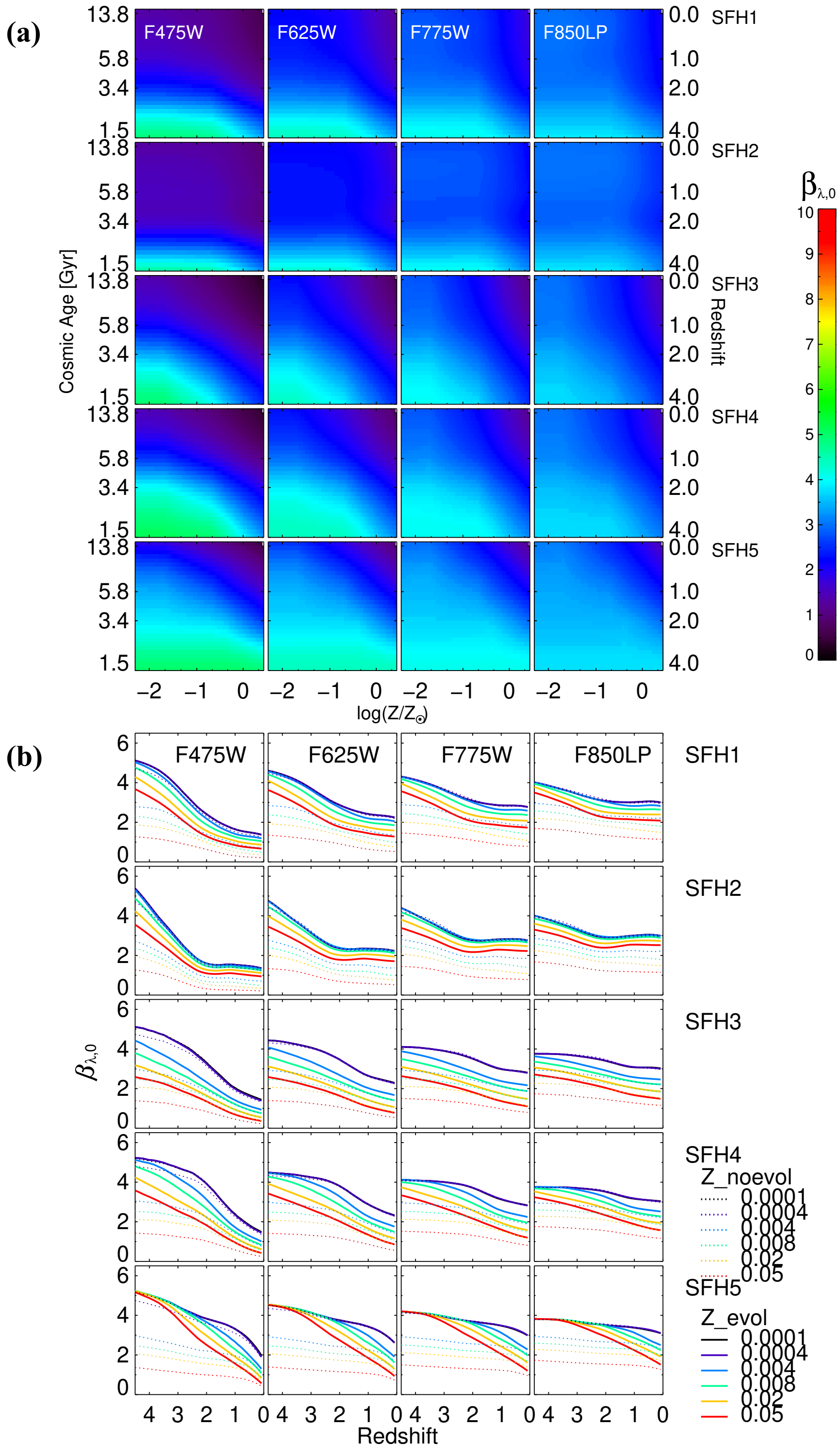

Figure 2.19: Same as Figure 2.16 for the *HST*/ACS WFC *F475W*, *F625W*, *F775W*, and *F850LP* filters.

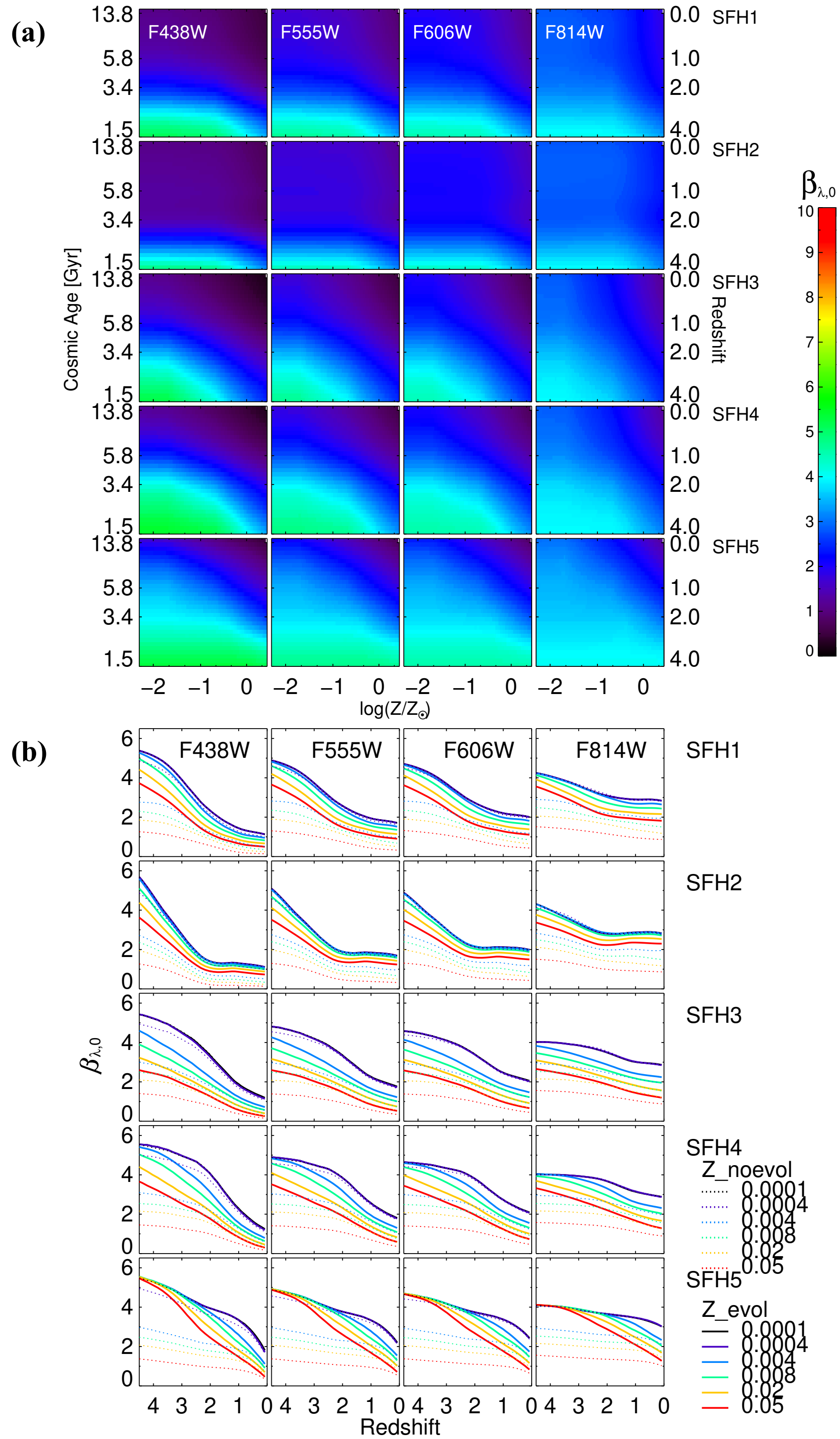

Figure 2.20: Same as Figure 2.16 for the *HST*/WFC3 UVIS *F438W*, *F555W*, *F606W*, and *F814W* filters.

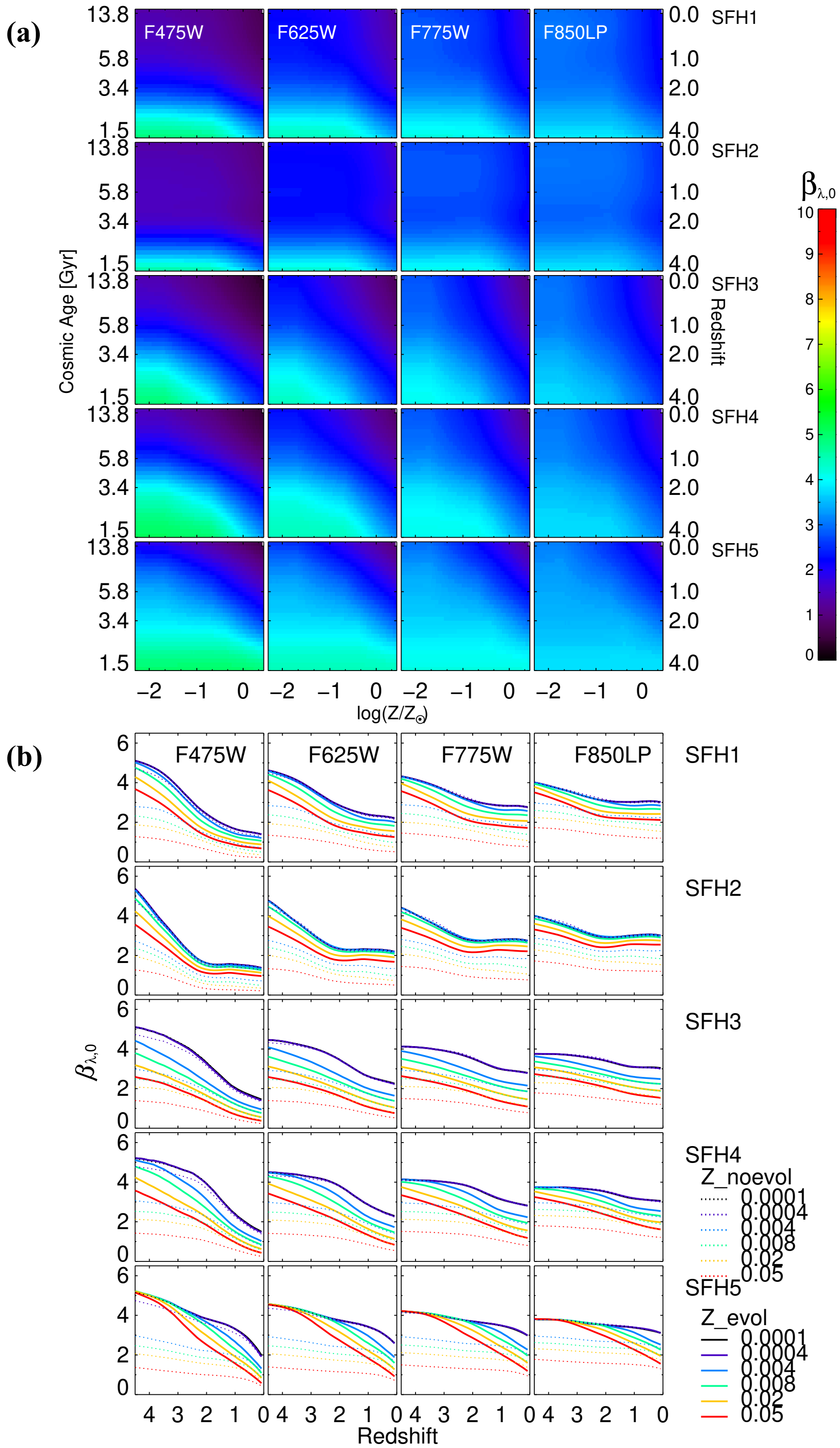

Figure 2.21: Same as Figure 2.16 for the *HST*/WFC3 UVIS *F475W*, *F625W*, *F775W*, and *F850LP* filters.

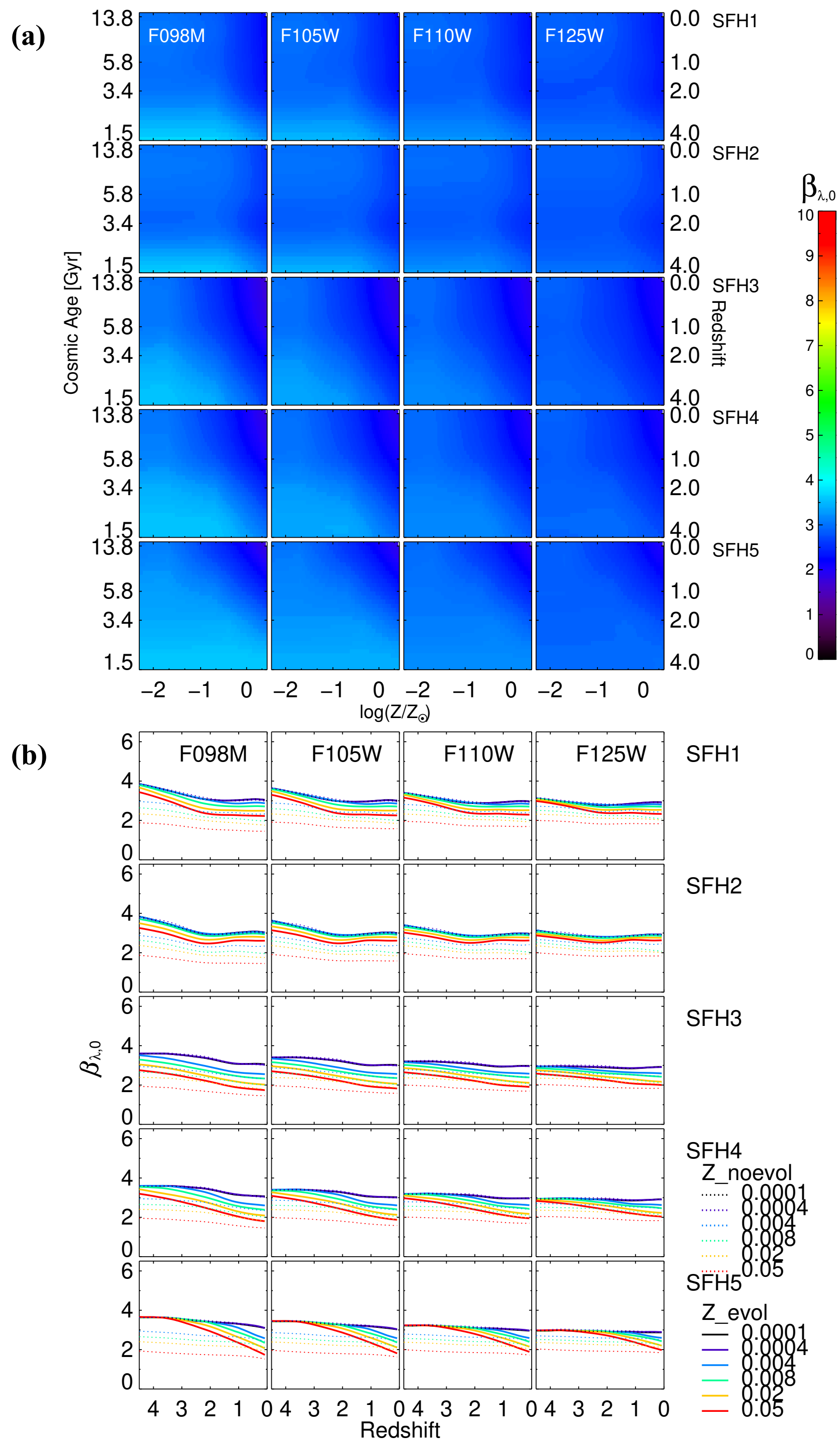

Figure 2.22: Same as Figure 2.16 for the *HST*/WFC3 IR *F098M*, *F105W*, *F110W*, and *F125W* filters.

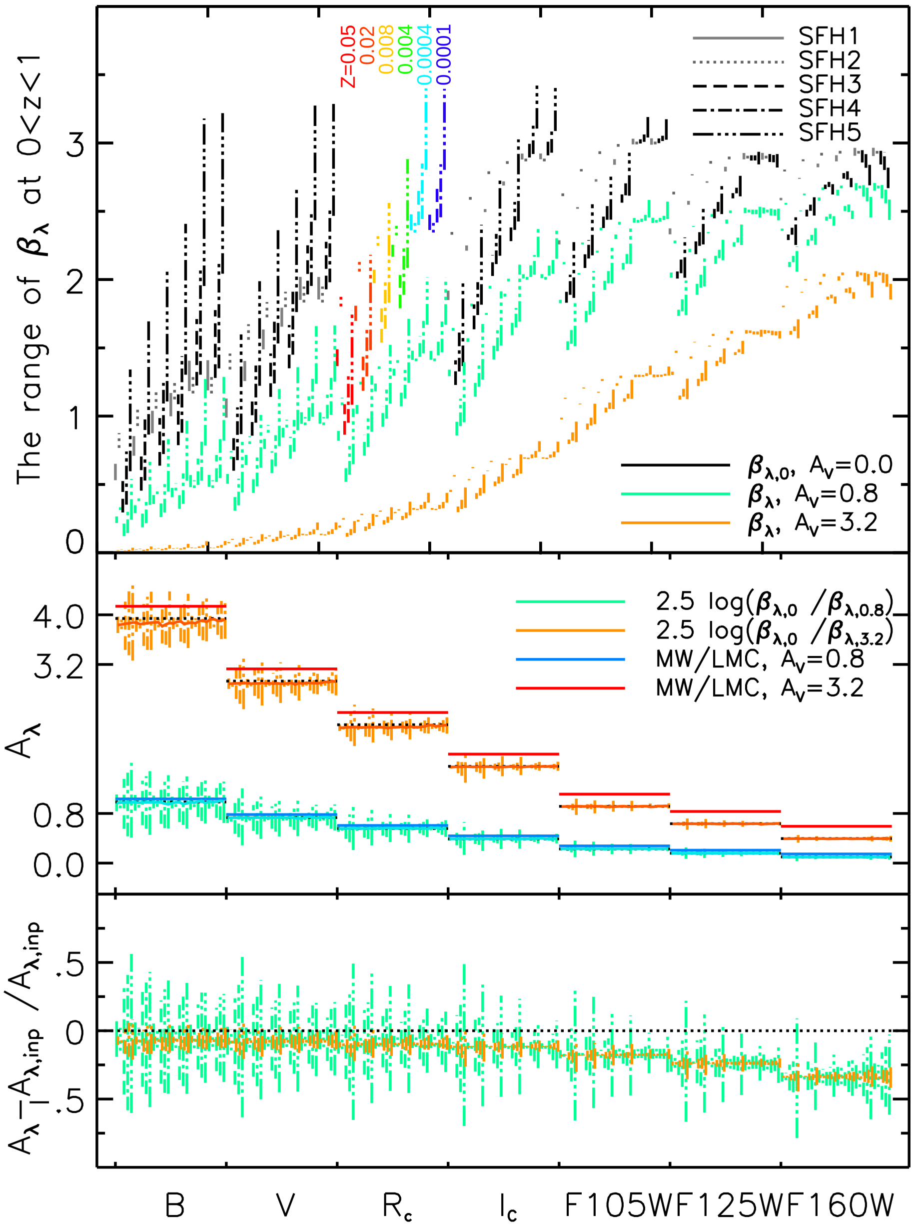

Figure 2.23: (top) The $\pm 1\,\sigma$ ranges of β_λ values, referenced to L, for CSPs at $0 < z < 1$ for different choices of the optical–NIR filters (bottom axis) for various metallicities, SFHs, and dust extinction values. (middle) Comparison between dust extinction values calculated using the ratio of $\beta_{\lambda,0}$ and β_λ values (center values are connected), and dust extinction values, $A_{\lambda,\mathrm{inp}}$, using the MW/LMC extinction law (red and blue horizontal lines). Dotted black lines indicate $A_{\lambda,\mathrm{inp}}$ values with -0.05 and -0.19 mag offsets for $A_V = 0.8$ and $A_V = 3.2$, respectively (see text), which arise from neglecting the residual extinction in the L filter. (bottom) Normalized ranges of recovered A_λ with respect to $A_{\lambda,\mathrm{inp}}$. For high extinction values (orange), the β_λ method can recover $A_{\lambda,\mathrm{inp}}$ to better than $\sim$20% for individual resolved galaxies when the redshift is only minimally constrained and when allowing a wide range in SFHs and metallicity. For large samples of galaxies, the β_V method recovers the *mean* extinction to better than 10%.

filters show much narrower ranges of $\beta_{\lambda,0}$. As these filters are closer to the L band, this can be understood as sampling the light from similar stellar populations.

In the middle panel of Figure 2.23, I compare the range of extinction values, A_λ, recovered from the β_λ method:

$$A_\lambda = 2.5 \log \left(\beta_{\lambda,0}/\beta_\lambda\right) , \tag{2.5}$$

to the extinction values $A_{\lambda,\mathrm{inp}}$ imposed as

$$F_{\lambda,\mathrm{ext}} = F_{\lambda,\mathrm{int}} \cdot 10^{-0.4 \cdot A_{\lambda,\mathrm{inp}}} \tag{2.6}$$

where $F_{\lambda,\mathrm{int}}$ and $F_{\lambda,\mathrm{ext}}$ are intrinsic and attenuated fluxes in each bandpass. These input extinction values are indicated by the horizontal red ($A_V = 3.2$ mag) and blue ($A_V = 0.8$ mag) lines. There are small systematic offsets of the median recovered A_λ (indicated by the dark orange and cyan horizontal lines) from the $A_{\lambda,\mathrm{inp}}$ values (red and blue horizontal lines). In V, these offsets are -0.05 and -0.24 mag for $A_V = 0.8$ and $A_V = 3.2$ mag, respectively, of which -0.05 and -0.19 mag results from the assumption of the β_λ method that the extinction in the L band is negligible. The relative error due to this assumption becomes more obvious in the near-IR, where the extinction values are also small. In fact, in the near-IR filters, this can account for the full offset observed. The additional $\sim$0.05 mag offset observed for $A_V = 3.2$ mag originates from the non-normal distribution of A_λ values (I plot the center value of the range, not the mid-point).

In order to determine whether the near-IR filters are a better choice for the β_λ technique over the optical filters, I compare their normalized scatter of A_λ values in the bottom panel of Figure 2.23. After normalization, the level of scatter is consistent from the optical through the near-IR filters, but the assumption of negligible extinction in L leads to a progressively worse underestimation of A_λ in a relative sense. To have a sufficient handle on the extinction over a wide range of extinction values, it is therefore recommended to use the bluest filter available. From this panel we also see that the minimum scatter in the recovered A_λ values

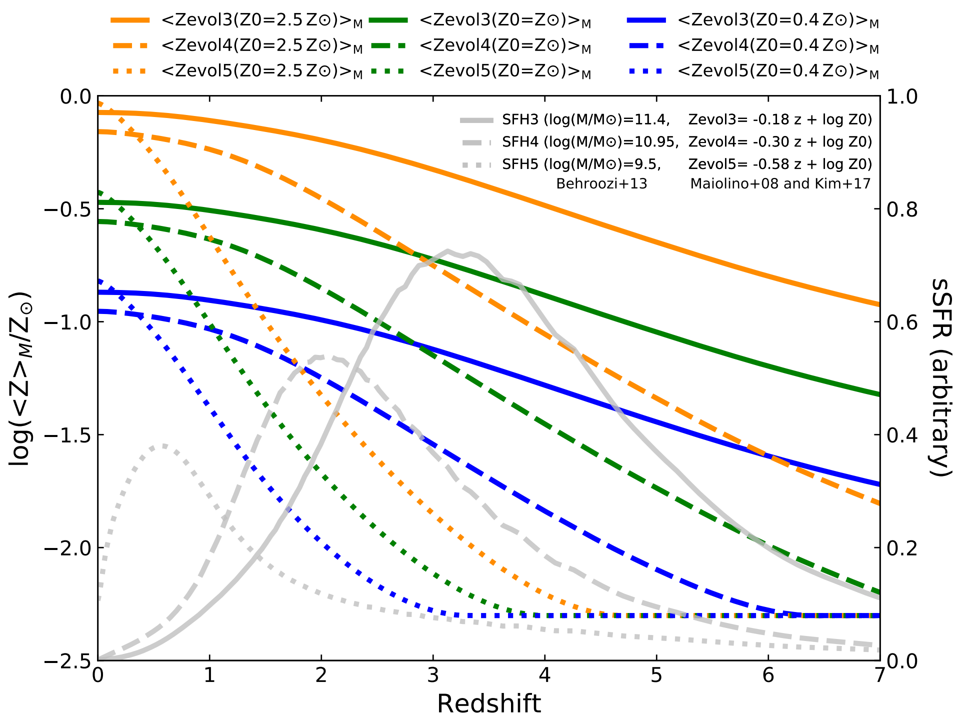

Figure 2.24: Mass-weighted metallicities, $\langle Z\rangle_{\rm M}$, and specific SFRs (sSFRs) as a function of redshift are indicated by the colored and gray lines, respectively. For sSFRs, I adopted SFRs of galaxies with stellar masses of $10^{11.4}$ (SFH3), $10^{10.95}$ (SFH4), and $10^{9.5}$ M$\odot$ (SFH5) from Behroozi *et al.* (2013). Linear metallicity evolution as a function of redshift was derived from these SFRs and the mass-metallicity relation of Maiolino *et al.* (2008). The $\langle Z\rangle_{\rm M}$ at a certain redshift, z_c, is the sum of the product of metallicity and SFR divided by the sum of the SFRs in the redshift range $z > z_c$. The lower metallicity limit at $\log Z/Z\odot \cong -2.3$ was set by the lowest metallicity available from SED models of simple stellar populations from BC03 and Starburst99.

consistently occurs for the lowest metallicity values and for SFHs characterized by little recent star formation (e.g., SFH3).

2.2.2.1 Mass-weighted Metallicity

Figure 2.24 shows the specific SFRs (sSFRs), and the mass-weighted metallicity, $\langle Z\rangle_{\rm M}$, as a function of redshift. The gray solid, dashed, and dotted lines indicate amplitudes of multiple exponentially declining star-formation episodes for early-type (SFH3), spiral (SFH4), and late-type (SFH5) galaxies, respectively. The SFH3, SFH4, and SFH5 models are from Behroozi *et al.* (2013) for galaxies with stellar masses of $10^{11.4}$, $10^{10.95}$, and $10^{9.5}$ M$\odot$, respectively.

The $\langle Z \rangle_{\rm M}$ value is the sum of the products of SFR and metallicity divided by the sum of the SFRs up to a certain redshift ($z > x$; see Equation 2.9). The colored solid, dashed, and dotted lines in Figure 2.24 are the $\langle Z \rangle_{\rm m}$ values of galaxies with SFH3, SFH4, and SFH5, respectively. I derived slopes for linear cosmic metallicity evolution as a function of redshift using the mass-metallicity relation from Maiolino *et al.* (2008) and three SFHs from Behroozi *et al.* (2013), which are -0.18 (SFH3), -0.03 (SFH4), and -0.58 (SFH5) (see also Figure 20 of Maiolino and Mannucci, 2019). The orange, green, and blue lines represent different metallicity offsets, $Z(z=0)$, of 2.5, 1.0, and 0.4 $Z\odot$, respectively. The lower limit of the metallicity evolution was selected as $Z = 0.0001$, which originated from the available SED models BC03 (Bruzual and Charlot, 2003) and Starburst99 (Leitherer *et al.*, 1999) that I used for young and old stellar populations. For example, the solid orange line represents the evolution of the $\langle Z \rangle_{\rm M}$ of a galaxy having SFH3 with a slope of the linear metallicity evolution of -0.18 (Zevol3) with a metallicity offset, $Z(z=0)$, of 2.5 $Z\odot$. Due to massive galaxies having high metallicities and dwarf galaxies having low metallicities on average, Figure 2.24 would not show many galaxies with dotted orange or solid blue lines. Nonetheless, I showed all these results for completeness.

Nine $\langle Z \rangle_{\rm M}$ values at $z=0$ are shown in Figure 3.12 either above or below each colored line with the same color and line type as the corresponding colored lines in Figure 2.24.

2.2.3 $\beta_{\lambda,0}$ for Galaxies of Different Hubble Type at $z \simeq 0$

Nearby galaxies have been characterized by their morphologies and studied separately ever since Hubble (1926) first classified them based on their morphologies (e.g., de Vaucouleurs, 1959; Odewahn, 1995; van den Bergh, 1998; Buta *et al.*, 2007). Morphology can be estimated from single-band imaging data, and is known to closely correlate with both structural properties of galaxies and their SFHs (e.g., Humason *et al.*, 1956; de Jong, 1996; Jansen *et al.*, 2000b,a; Windhorst *et al.*, 2002; Conselice *et al.*, 2004; Taylor *et al.*, 2005; Taylor-Mager *et al.*, 2007; Hoyos *et al.*, 2016). Examining the relationship between $\beta_{\lambda,0}$ values and the morphology of galaxies will therefore be useful.

To address this, I first generate multiple arrays of SEDs with different SFH criteria: 1000 SFH3-ETG, 1000 SFH4-Spiral, and 1000 SFH5-LTG (see § 2.1.2). GD15 presented integral field spectroscopy of 300 nearby galaxies of various Hubble types, and derived radial profiles of stellar population properties such as age, metallicity, and A_V. I adopt the mean of their weighted age and metallicity values for different Hubble types as a function of galactic radii. For spiral galaxies, I adopted the results of their face-on sample rather than edge-on sample, to minimize the effect of overlapping stellar populations and high mid-plane extinction. I then derive $\beta_{V,0}$ profiles for different Hubble types by comparing age and metallicity values of GD15 and my SEDs.

At each discrete Age step in Table A.1 for cosmic times later than 545 Myr ($z < 9$; see Figure 2.3), I calculated mass-weighted ages, $\langle t \rangle_M$, light-weighted ages, $\langle t \rangle_L$, and mass-weighted metallicities, $\langle Z \rangle_\mathrm{M}$, for consistency with GD15 as

$$\langle t \rangle_\mathrm{L} = \sum_{t'=t_0}^{t} \log t' \mathcal{F}(t') \psi(t') \delta t' \Big/ \sum_{t'=t_0}^{t} \mathcal{F}(t')\, \psi(t')\, \delta t', \tag{2.7}$$

$$\langle t \rangle_\mathrm{M} = \sum_{t'=t_0}^{t} \log t'\, \psi(t')\, \delta t' \Big/ \sum_{t'=t_0}^{t} \psi(t')\, \delta t', \tag{2.8}$$

$$\langle Z \rangle_\mathrm{M} = \sum_{t'=t_0}^{t} \log Z(t', Z_0)\, \psi(t')\, \delta t' \Big/ \sum_{t'=t_0}^{t} \psi(t')\, \delta t' \tag{2.9}$$

where $\mathcal{F}$ is the flux at 5635Å, and $\psi(t)$ denotes the SFR, Z_0 is the metallicity at $z = 0$, and metallicity is a function of cosmic time and Z_0, i.e., $Z(t', Z_0)$ (see Figure 2.24).

Table 2.5: $\beta_{V,0}$ Values at HLR R_e of Galaxies for each Hubble Type, Assuming either SSPs or CSPs with Stochastic SFHs

Hubble	SSP		Stochastic SFHs		
Type	$\langle t \rangle_{\mathrm{L}}$	$\langle t \rangle_{\mathrm{M}}$	$\langle t \rangle_{\mathrm{L}}$	$\langle t \rangle_{\mathrm{M}}$	Family
E0	$0.60^{+0.16}_{-0.14}$	$0.57^{+0.14}_{-0.13}$	$0.64^{+0.04}_{-0.07}$	$0.65^{+0.03}_{-0.07}$	SFH3
S0	$0.63^{+0.14}_{-0.13}$	$0.58^{+0.12}_{-0.11}$	$0.64^{+0.03}_{-0.07}$	$0.64^{+0.03}_{-0.07}$	SFH3
Sa	$0.74^{+0.17}_{-0.17}$	$0.61^{+0.17}_{-0.16}$	$0.74^{+0.14}_{-0.11}$	$0.65^{+0.14}_{-0.03}$	SFH4
Sb	$0.79^{+0.08}_{-0.09}$	$0.65^{+0.11}_{-0.10}$	$0.76^{+0.05}_{-0.03}$	$0.72^{+0.06}_{-0.09}$	SFH4
Sbc	$0.93^{+0.50}_{-0.13}$	$0.78^{+0.17}_{-0.17}$	$1.02^{+0.29}_{-0.27}$	$0.77^{+0.26}_{-0.12}$	SFH4
Sc	$1.65^{+0.49}_{-0.71}$	$0.88^{+0.22}_{-0.18}$	$1.09^{+0.37}_{-0.31}$	$1.06^{+0.30}_{-0.31}$	SFH5
Sd	$2.17^{+0.38}_{-0.62}$	$1.03^{+0.30}_{-0.17}$	$1.43^{+0.44}_{-0.36}$	$1.39^{+0.43}_{-0.34}$	SFH5

Note. The indicated ranges of $\beta_{V,0}$ for each model are derived from the uncertainties in the $\langle t \rangle_{\mathrm{L}}$, $\langle t \rangle_{\mathrm{M}}$, and $\langle Z \rangle_{\mathrm{M}}$ values. For each type of SFH, I compare mass- and luminosity-weighted $\beta_{V,0}$ values and ranges.

Figure 2.25*a* and *b* show smoothed median radial profiles of $\beta_{V,0}$ for galaxies modeled by SSP and stochastic SFHs, respectively, for different Hubble types. For stochastic SFHs, I used the SEDs of SFH3-ETG for E and S0, SFH4-Spiral for Sa–Sbc, and SFH5-LTG for Sc and Sd Hubble types, respectively. $\langle \beta_{V,0} \rangle$ in Figure 2.25*b* is the average β_V of 1000 randomly generated SFHs for each stochastic SFH family. In both panels, each profile was boxcar smoothed using a radial filter with a width corresponding to one half-light radius. Galaxies of E and S0 type have an almost constant $\beta_{V,0}$ value with increasing galactic radius for both SSPs and stochastic SFHs. Later types have higher and more fluctuating $\beta_{V,0}$ values and show a stronger dependence on radius. Table 2.5 lists representative mass- and light-weighted $\beta_{V,0}$ values at the HLR (R_e) for each Hubble type for both SSPs and CSPs resulting from stochastic SFHs. I derive uncertainties in the $\beta_{V,0}$ values from the 1 σ ranges presented in GD15 (their Figures 9, 15, and 18) by randomly varying the age and metallicity values in my models within these allowed ranges. The total range of luminosity-weighted $\beta_{V,0}$ values for nearby galaxies thus derived is 0.57–1.87 (the $\langle t \rangle_{\mathrm{L}}$ column for stochastic SFHs). For a galaxy of known morphological type, however, the likely range in $\beta_{V,0}$ is only $\sim\pm10\%$ with respect to the mean value

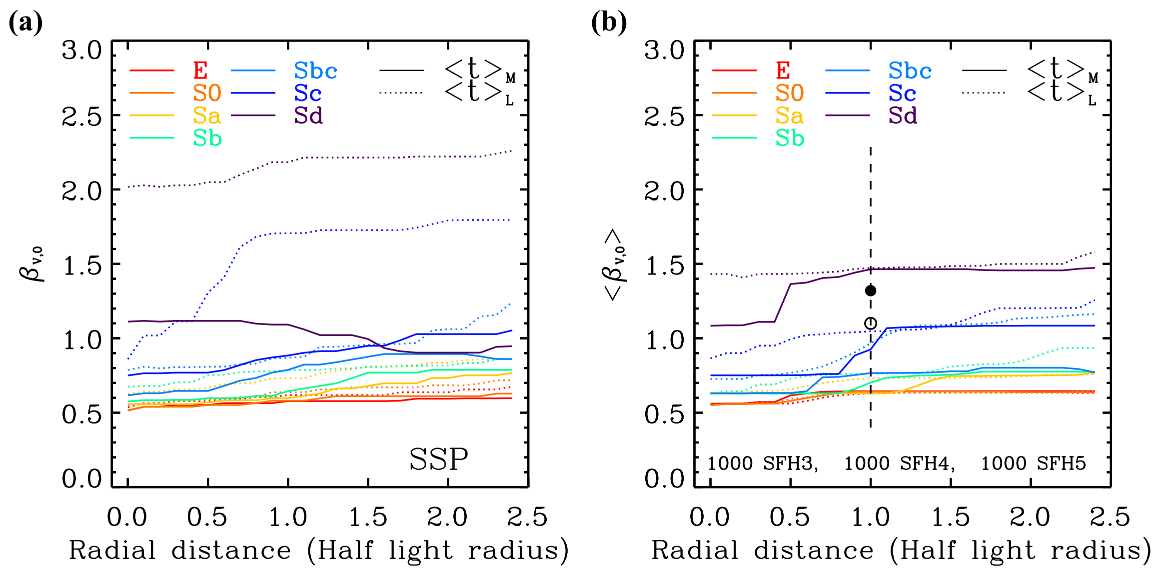

Figure 2.25: $\beta_{V,0}$ as a function of radius for galaxies of different Hubble type. (a) $\beta_{V,0}$ profiles derived from an array of SSP SEDs, and (b) mean $\langle\beta_{V,0}\rangle$ profiles resulting from 3000 arrays of stochastic SFH SEDs that I randomly generated using mass- (solid) and light-weighted (dotted) age and mass-weighted metallicity values from GD15. The solid (open) black circle indicates the value adopted by T09 for younger (older) stellar populations within NGC 959 (Sdm). For both SSP and stochastic SFH SEDs, I plot boxcar-smoothed radial profiles of $\beta_{V,0}$ and of average $\beta_{V,0}$ values, respectively (see text). The $\beta_{V,0}$ values vary little with radius for early-type galaxies for both SSPs and stochastic SFHs. For late-type galaxies, the presence of a bulge or older population would reduce the $\beta_{V,0}$ values within R_e.

for E, S0, Sa, and Sb galaxies, although late-type spiral and Magellanic-type galaxies display a wider ±30–50% range. Figure 2.25*b* also shows that the mean $\beta_{V,0}$ values beyond R_e in the case of (observed) light-weighted ages are similar, but systematically higher (by up to ∼8–20% at 2.5 R_e) than the (intrinsic) mass-weighted ages.

2.3 Discussion

I have generalized the β_V method to a β_λ method by placing the method on a more robust footing that does not require manual estimation of the intrinsic flux ratios from pixel histograms and that provides evaluation of the associated uncertainties for a large number of optical–near-IR and mid-IR filters. Stars with young ages and low metallicities emit light with SEDs that have high $\beta_{\lambda,0}$ values, and as stars age and as stars become more metal-rich, the $\beta_{\lambda,0}$ values decrease and stabilize. Tamura *et al.* (2009) also observed this trend in their 2D map of $\beta_{V,0}$ values (their Figure 2), which was based on SSPs and the model SEDs from Anders and Fritze-von Alvensleben (2003).

2.3.1 Application to Discrete Sets of Filters at $0 < z < 1.9$

While using near-IR filters results in a narrower $\beta_{\lambda,0}$ range over the redshift range 0 <z <1 (see Figure 2.23), after normalization, the relative dispersion in the simulated A_λ values is comparable in the optical and near-IR filters. One should be cautious about using near-IR bandpasses at low redshift, however, since the offset due to the residual extinction in the mid-IR reference filter becomes more noticeable (see Figure 2.23, bottom panel). Nonetheless, *HST*/WFC3 near-IR filters may be used to sample visible rest-frame wavelengths up to $z \sim 1.9$. In that case, one should use the filter nearest the corresponding rest-frame wavelength when applying the β_λ method. For instance, at $z \simeq 1.9$, the *HST*/WFC3 IR F160W filter would sample rest-frame V, and the *JWST*/MIRI F1000W bandpass would sample rest-frame 3.5 μm, so one can use the $\beta_{V,0}$ values presented in this paper and on my website[2].

Although the value of $\beta_{V,0}$ will depend on the detailed shape of the throughput curves of the filters sampling the rest-frame V and 3.5 μm light, Figures 2.13 and 2.14 show that such dependence for even quite mismatched filters (e.g., L' and *WISE* $W1$) affects $\beta_{V,0}$ at the $\lesssim$20% level. For bandpasses that are better matched to the L band, such as *Spitzer*/IRAC $I1$ and *JWST*/NIRCam F356W, the differences tend to be at the $\lesssim$5% level, except for very young ($<$ 10 Myr) stellar ages and for high metallicities ($Z >$ 0.02). A similar caution applies at redshifts where the bandpass sampling rest-frame V light differs very much from that of the V filter at $z \sim 0$. Nonetheless, the dependence of the accuracy of the β_λ technique on the choice of filters in both the optical–near-IR and mid-IR is weak.

2.3.2 Application to Galaxy Samples Using Realistic SFHs

I have extended my models from SSP to more complex SFHs. In real galaxies, the observed β_λ flux ratios are also affected by spatial resolution, as light from a broad region within a galaxy would result from a combination of various stellar populations, each resulting from different complex stochastic SFHs. For example, Galliano *et al.* (2011) obtained a ~50% difference in inferred dust mass when they used integrated SEDs with different spatial resolutions. The sharp features in a map of $\beta_{\lambda,0}$ values of SSPs in Figure 2.12 at young ($\lesssim$100 Myr) ages are smeared out when a galaxy has a more complex SFH, such as an exponentially declining SFH. In addition, I adopt five families of stochastic SFHs that are composed of multiple exponentially declining star formation episodes, and probe variations of $\beta_{\lambda,0}$ values over cosmic history. For a minimally constrained redshift range, $0 < z < 1$, the variation in β_λ is dominated by SFH5, representing late-type galaxies. The other SFH families show more modest variations for a given metallicity and choice of optical–near-IR filter (see Figures 2.16–2.23). Metallicity evolution is taken into account and makes a noticeable difference (Figures 2.15 and 2.16*b*), predicting higher $\beta_{\lambda,0}$ values than in the no-evolution case, especially at higher redshifts and for the higher-metallicity stellar populations at those redshifts.

I first consider the applicability of the β_λ method for a galaxy sample with a large effectively unconstrained redshift range ($0 \lesssim z \lesssim 4$). The $\beta_{V,0}$ values could span 0.6–4.7 in that case (see Figure 2.16 and § 2.2.2). For the minimally constrained $0 < \mathrm{z} < 1$ redshift range, the scatter in recovered A_λ is ~0.2 mag in V and decreases with increasing wavelength, but varies little with the amount of input extinction imposed (Figure 2.23, middle panel). The normalized difference of the recovered and input extinction, $(A_\lambda - A_{\lambda,\mathrm{inp}})/A_{\lambda,\mathrm{inp}}$, on the other hand, is $\sim$23% and $\sim$16% for $A_V = 0.8$ and $A_V = 3.2$ mag, respectively (see bottom panel of Figure 2.23). Note, however, that this reflects what one would expect for individual galaxies (or regions therein). The mean difference of the recovered and input extinction values is close to 0.0, suggesting that the β_λ method can accurately recover the mean extinction for a larger sample of galaxies spanning a range of redshifts, SFHs, and metallicities, and also of a population of galaxies of a given type within a narrow redshift range. The highly attenuated case ($A_V = 3.2$) has a smaller scatter, because the extinction dominates the shape of the SED more than any other factors, like stellar age or metallicity. For normal ($A_V \lesssim 1$) galaxies, I recommend using extra information, such as galaxy size and magnitudes, or if available, a photometric redshift estimate (or a spectroscopic redshift), for selecting the corresponding $\beta_{\lambda,0}$ value.

2.3.3 Dependence of $\beta_{\lambda,0}$ on Hubble Type and Weighting

Because one can classify the morphology of a galaxy with a single-band image (with the caveat of a slight rest-frame wavelength dependence of the morphology for different Hubble types, as found by Windhorst *et al.* 2002), studying the relationship between galactic morphology and $\beta_{\lambda,0}$ values can be useful, since the β_λ method is specifically designed as a dust-correction technique when a very limited number of filters are available. I used the SFH3–5 criteria (see § 2.1.2) to generate multiple arrays of SEDs combined with the stellar population parameters from GD15 to obtain the $\beta_{V,0}$ values for different Hubble types (see Figure 2.25*b*). For a given galaxy type, $\beta_{V,0}$ values vary little as a function of galactic radius. Later Hubble types typically have higher $\beta_{V,0}$ values (see also Table. 2.5), as their stellar populations tend to be younger and metallicities lower than earlier types (see Figure 17 in GD15). I also investi-

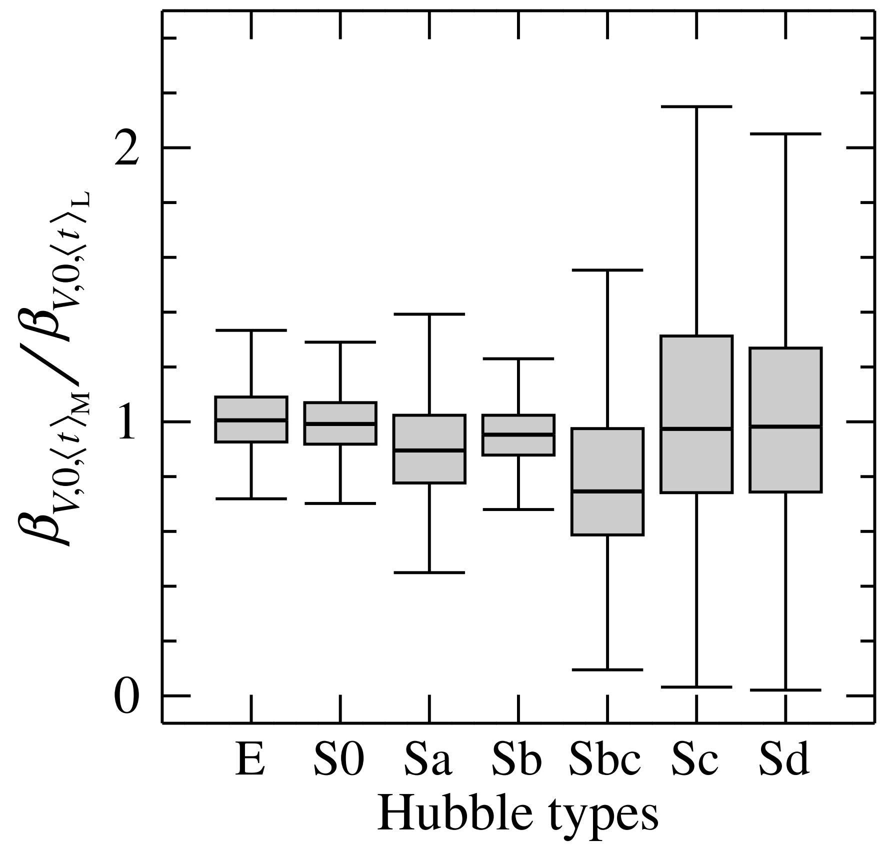

Figure 2.26: Ratio of $\beta_{V,0}$ values for mass- and light-weighted ages for different Hubble types. For each Hubble type, I randomly generated 1000 $\beta_{V,0}$ values each for both mass- and light-weighted ages, adopting the mean and 1 σ values at R_e listed in Table 2.5. The horizontal lines inside the boxes represent the median ratios. The gray boxes indicate the quartile range, while the error bars contain 99.7% of the distribution. The weighting method does not affect the inferred $\beta_{V,0}$ value for a given Hubble type in a systematic manner.

gate the effect of different weighting methods. The ratios between $\beta_{V,0}$ values resulting from using mass- and light-weighted ages are shown in Figure 2.26 as a function of Hubble type. I find no strong dependence of the median ratios of $\beta_{V,0}$ values with different weighting methods on Hubble type. Also indicated in Figure 2.26 are the quartile ranges and the $\pm 3\,\sigma$ range of these ratios. Light-weighted $\beta_{V,0}$ values are unlikely to differ by more than 10% (30%) from mass-weighted ones for early-type (late-type) galaxies.

To test the reliability of the β_λ method, in Figure 2.27, I compare the inferred β_V values

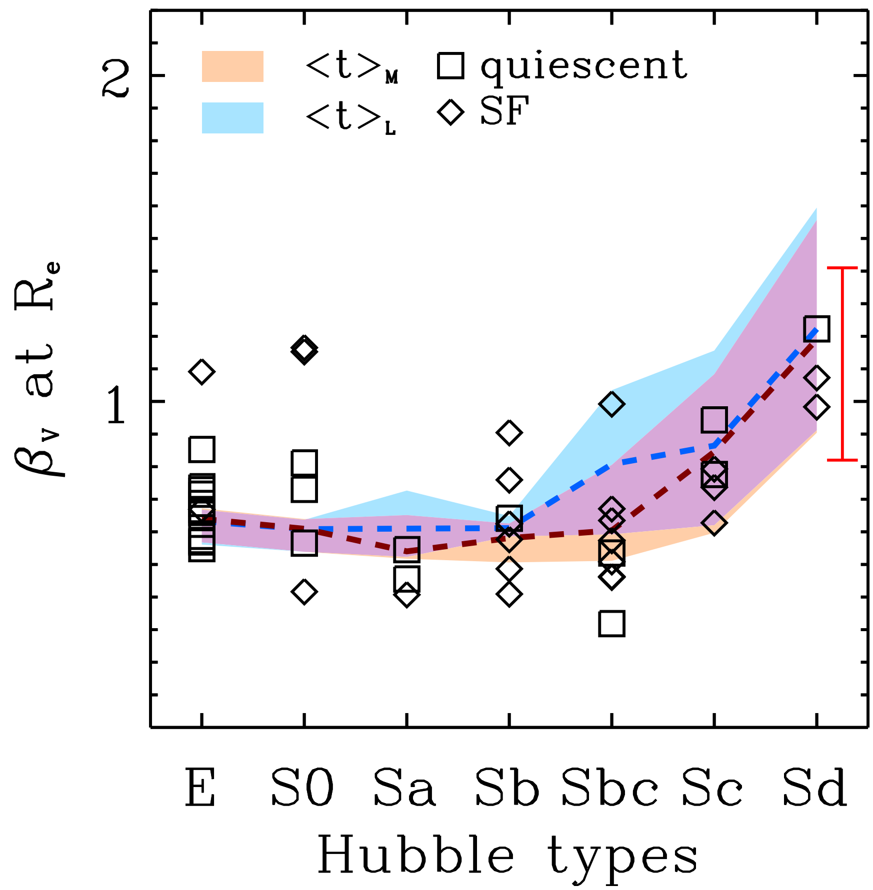

Figure 2.27: β_V values at the HLR, R_e, as a function of Hubble type (dashed lines) using mass- (dark brown), or light-weighted (blue) ages and A_V values. The shaded regions are the $\pm 1\,\sigma$ ranges of β_V values. I overplot the β_V values of nearby galaxies from Brown *et al.* (2014). The dashed curves represent median trends. The red error bar indicates the range of β_V values observed by T09 in NGC 959 (Sdm).

with observed β_V values for nearby galaxies. I used $\langle\beta_{V,0}\rangle$ values from Figure 2.25*b* at the half-light radius and the allowed 1 σ range therein computed by varying ages and metallicities within the 1 σ observed ranges of GD15 (see their Figures. 8, 11, and 18), coupled with the mean A_V values of the corresponding Hubble types at the half-light radii from GD15 ($\langle A_V \rangle$=0.01, 0.06, 0.22, 0.25, 0.27, 0.26, and 0.18 for E, S0, Sa, Sb, Sbc, Sc, and Sd galaxies) to derive the predicted ranges for the β_V values one would observe for each of the Hubble types (see also Figure 3.5). The dark brown (blue) dashed line and the orange (blue) shaded region indicate the median and 1 σ range of the β_V values when using mass- (light-) weighted ages, and the violet region represents the region of overlap. The β_V values of 23 nearby ($z \lesssim 0.05$) quiescent (limited star formation) and 28 normally star-forming galaxies from Brown *et al.* 2014 are overplotted. Galaxies with "peculiar" morphologies, and galaxies with "SF/AGN," or "AGN" BPT classes are excluded. Brown *et al.* (2014) combined multiple spectra and broadband data of nearby galaxies, and carefully performed aperture corrections in order to construct a template library. I used their aperture-corrected SDSS g, r band and the *Spitzer*/IRAC Channel 1 ($I1$) magnitudes to derive the β_V values. The SDSS g and r band magnitudes are converted into V-band magnitudes using the transformation equation from Jester *et al.* (2005). I take the *Spitzer* $I1$ magnitudes as proxy for L band magnitudes, since Figure 2.13 and 2.14 show that the resulting $\beta_{V,0}$ are at most $\lesssim$10% higher and show little structure. Our model and observation agree well, except in a few cases for star-forming galaxies with Hubble type E and S0, which seem to be outliers (see Section 2.1.4 of Brown et al. 2014). Last, I note that the 0.82–1.41 range of β_V values observed by T09 for Sdm galaxy NGC 959 is in good agreement with the trend in values inferred for the galaxy sample of Brown *et al.* (2014), as well as with the range predicted by my models in Figure 2.27, and that their empirical values adopted for the intrinsic $\beta_{V,0}$ ratios are consistent with those predicted in the present study (e.g., Figure 2.25*b* and Table 2.5 (Sd)).

2.3.4 Comparison with Other Methods

I next compare the β_V method to other established methods of correcting galaxy SEDs for attenuation by cosmic dust. In Figure 2.28*a*, I compare the relative differences between recovered and input extinction values (normalized to the input value, $A_{V,\mathrm{inp}}$) for (multiband)

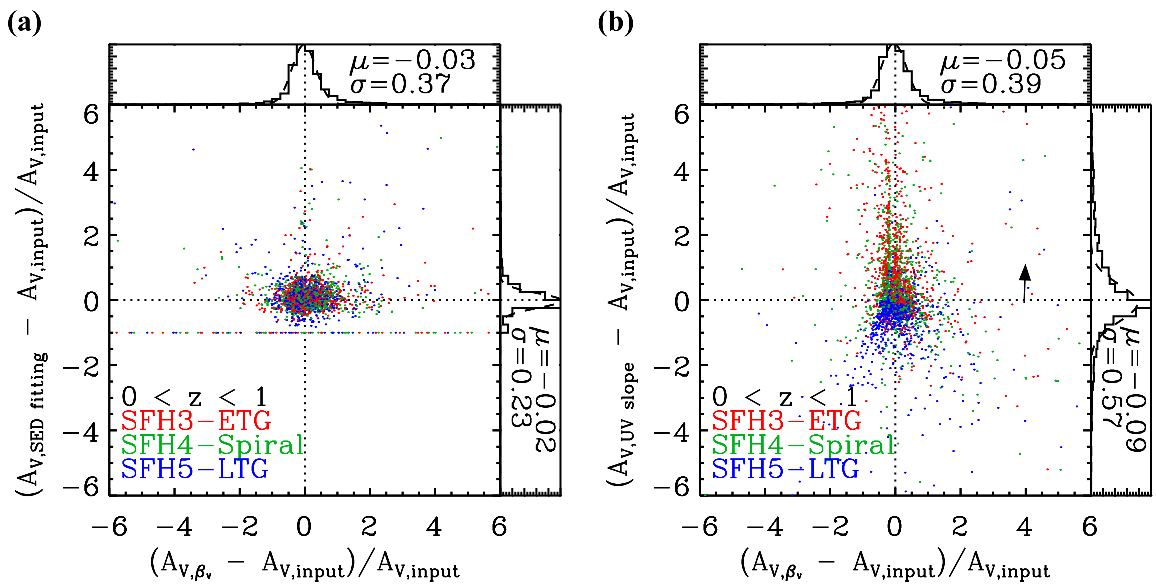

Figure 2.28: Comparison of the β_V method to other dust-correction methods. (a) Comparison of the normalized difference between recovered and input extinction values in V for both the SED-fitting and β_V methods. The β_V method shows a comparable average offset and scatter around the true value of A_V to the SED-fitting method, although it requires less information. To derive A_V for my families of stochastic SFHs, I used the $0 < z < 1$ average values of $\beta_{V,0}$ of 1.40, 1.48, and 1.78 for SFH3, SFH4, and SFH5, respectively. (b) As (a) for both the UV-slope and β_V methods. The A_V values recovered by the UV-slope method are systematically slightly lower than the $A_{V,\mathrm{inp}}$ values ($\mu = -0.10$ mag; for a MW/LMC extinction law as in Calzetti *et al.* (1994), and the scatter is larger than for the β_V method ($\sigma = 0.60$ vs. 0.38 mag). The black arrow shows how the offset would change if I adopted a Calzetti *et al.* (2000) extinction law ($\mu = +1.10$).

SED fitting and the β_V method. When I impose minimal constraints on the allowed redshift range ($0 < z < 1$), the SED-fitting method provides estimates that are closer to the true input value, $A_{V,\mathrm{inp}}$, on average ($\mu = -0.02$ vs. -0.03 mag), and with a smaller scatter ($\sigma = 0.23$ vs. 0.37 mag). The small fraction of data points for the SED-fitting method at a normalized difference of exactly -1 result where the best fit was for $A_V = 0$ mag (out of the finite set of discrete extinction values), when any non-zero extinction was imposed. These data points do not significantly broaden the distribution. The β_V method shows a somewhat larger scatter, but not by much, considering that the β_V method requires significantly less information than the SED-fitting method to correct for dust extinction. In order to make this comparison, I construct a large set of randomly generated SEDs for stochastic SFHs representing early-type, spiral, and late-type galaxies (my SFH families SFH3, SFH4, and SFH5; see § 2.1.2), sampled at random redshifts in the range $0 < z < 1$, and with random amounts of extinction ($0 \leqslant A_V \leqslant 2$ mag) applied and characterized by a randomly selected extinction law (MW/MW, SMC, or Calzetti). To apply the β_V method and recover A_V, I assume that the appropriate SFH family to use would be known *a priori* from the morphological type of an observed galaxy, and only minimally restrict the redshift to the same $0 < z < 1$ range. The average values of $\beta_{V,0}$ in this redshift range are 1.40, 1.48, and 1.78 for SFH3, SFH4, and SFH5, respectively. Using Equation 2.5, I then infer (recover) for each model SED an extinction value A_V from the appropriate mean $\beta_{V,0}$ value and the observed $(V - L)$ color (expressed as a flux ratio, i.e., β_V). As templates for the SED-fitting method, I used the same set of 724 unique and distinguishable SSP SEDs (see Appendix A), either used as is, or incorporated into CSP SEDs for seven exponentially declining SFHs, or into my suite of stochastic SFHs (§ 2.1.2) with 300 random realizations for each of the SFH3, SFH4, and SFH5 families. The comparison should therefore not be biased by differences in the adopted set of input galaxy SED templates. Using the full rest-frame $0.4 \leq \lambda \leq 3.75$ μm portion of each of the SEDs, I perform the SED fit to characterize both stellar population parameters and recover A_V. This represents a *best-case* scenario, the results of which are shown in Figure 2.28*a*. If, as would be the case for a more realistic galaxy survey, the SED is sampled through multiple filters, each resulting in a single flux density data point, the comparison is unlikely to be more favorable for the SED-fitting method, although the allowed redshift range may be narrowed for galaxies displaying a strong 4000Å break.

In Figure 2.28(b) I compare the relative differences between recovered and input extinction values for the UV continuum slope method and the β_V method. Calzetti *et al.* (1994) studied the effect of dust extinction on the UV continuum in spectra of local starburst galaxies, and provided a relationship between the UV power-law index β and the optical depth τ (their

Equation 4). For a *best-case* scenario, I use their fitting windows, sampling the 1268–2580Å wavelength range while excluding the interval that might be affected by a 2175Å-bump (if present), and adopt a MW/LMC extinction law to match Calzetti *et al.* (1994). The β_V method underestimates the extinction values in this test by $\sim$5% (compared to 9% for the UV continuum slope method) and shows a smaller scatter than the UV-slope method: $\sigma = 0.39$ mag for the β_V method versus 0.57 mag for the UV-slope method. Note, however, that if I were to adopt a Calzetti *et al.* (2000) extinction law instead, this would result in recovered extinction values for the UV-slope method that are systematically *higher* than the input values by an amount indicated by the black arrow in Figure 2.28*b*, whereas the mean difference μ would change by only $+0.04$ for the β_V method. I also note that the UV-slope method shows a stronger dependence of the recovered A_λ on SFH (galaxy type) than does the β_V method.

My tests therefore show that the β_V method can indeed be used to infer A_V and correct for dust extinction to a level of fidelity that is comparable to that of more established methods, with fewer or more readily obtainable data. In particular, I note that *systematic* offsets in the recovered extinction values are *no worse* than for these two commonly used methods. These properties make the β_V (β_λ) method a prime candidate for application to large imaging surveys with *JWST* of fields already observed with *HST* in the visible–near-IR.

2.3.5 $\beta_{\lambda,0}$ for Galaxies Observed with *HST* and *JWST*

For a $z \simeq 0.3$ galaxy, rest-frame optical images from *HST*/ACS WFC or WFC3 UVIS (F606W, ..., F850LP) and rest-frame $\sim$3.5 μm mid-IR images from *JWST*/NIRCam (F410M, F444W, F480M) will have resolutions of $\sim$0.″06–0.″09 and $\lesssim$0.″19, resolving regions of $\lesssim$875 pc in size. At $z \sim 2$, *HST*/WFC3 IR F160W and *JWST*/MIRI F1000W sample rest-frame V and 3.5 μm, but the resulting resolution of $\sim$0.″48 would not allow resolving regions

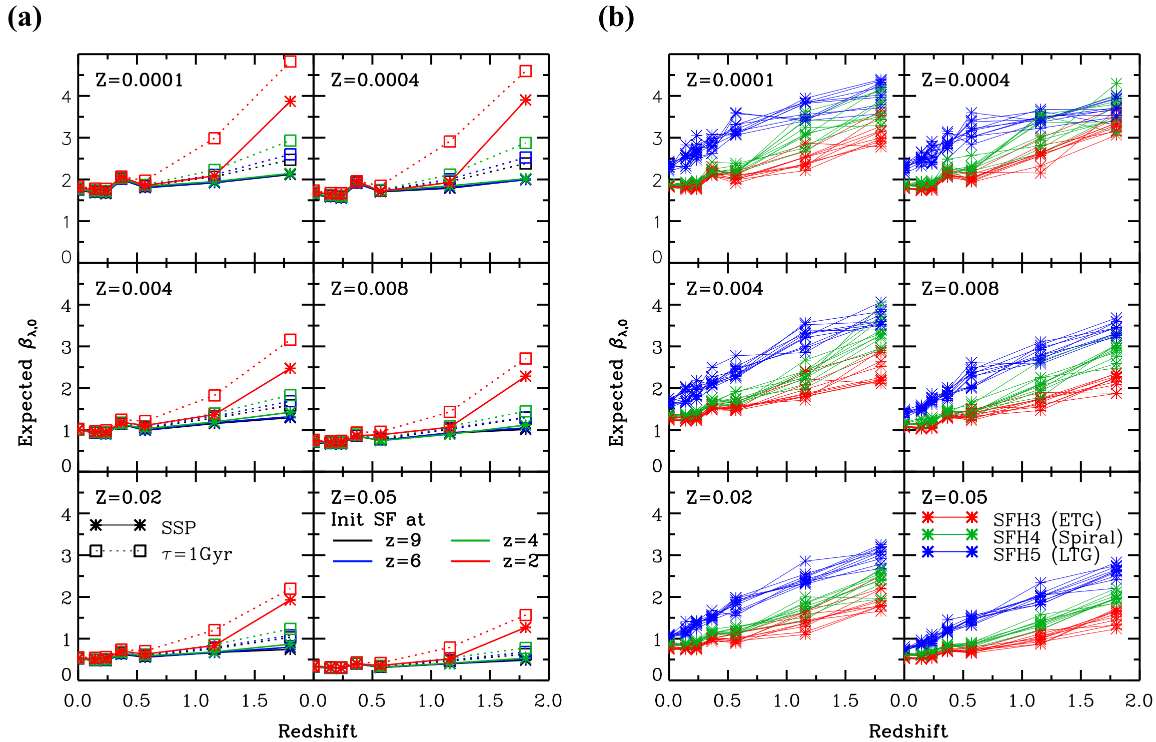

Figure 2.29: Expected intrinsic flux ratios $\beta_{\lambda,0}$ as a function of redshift for six metallicities and various SFHs, for redshifts where well-matched pairs of optical or near-IR *HST* and mid-IR *JWST* filters correspond to rest-frame V and 3.5 μm, respectively. (a) $\beta_{\lambda,0}$ for SSPs (solid) and exponentially declining SFHs with an e-folding time of 1 Gyr. Tracks are color-coded (as indicated in the lower right panel) according to the redshift of onset of the instantaneous (SSP) or extended star formation. At a fixed metallicity value and starburst onsets well before $z = 2$, $\beta_{\lambda,0}$ remains nearly constant over the entire $0 \leqslant z \leqslant 2$ redshift range. (b) The same as (a) for 10 examples of each of my three stochastic SFH families. Except for the two very lowest metallicities, $\beta_{\lambda,0}$ increases with redshift in a nearly linear fashion, with little overlap between the tracks for the three SFH families.

smaller than $\sim$4 kpc. The combination of these two space telescopes will make studies of galaxies over billions of years possible in unprecedented detail. Specifically for this purpose, I therefore generate model SEDs and calculate $\beta_{\lambda,0}$ values for a set of discrete redshifts at which well-matched *HST* and *JWST* filter pairs sample rest-frame V and 3.5 μm emission. At redshifts $z = 0$, 0.14, 0.24, and 0.37, well-matched *HST* and *JWST*/NIRCam filter pairs are (F555W, F356W), (F606W, F410M), (F625W, F444W), and (F775W, F480M), respectively. At $z = 0.57$, 1.16, and 1.8, suitable *HST* and *JWST*/MIRI filter pairs are (F814W, F560W), (F110W, F770W), and (F160W, F1000W). In Figure 2.29(a) I show the resulting tracks of $\beta_{\lambda,0}$ versus redshift for six different metallicities and both SSP and exponentially declining SFHs with an e-folding time of 1 Gyr, and do so for four different redshifts of onset of either the instantaneous or extended star formation. For SF onset times well before $z \sim 2$, the tracks remain nearly constant over the entire redshift range at a given metallicity, although the mean $\beta_{\lambda,0}$ values decrease systematically with increasing metallicity ($\langle\beta_\lambda\rangle_{z<1.2} \simeq 1.9$, 1.8, 1.0, 0.8, 0.5, and 0.4 for $Z = 0.0001$, 0.0004, 0.004, 0.008, 0.02, and 0.05, respectively). I similarly derive $\beta_{\lambda,0}$ for these *HST* and *JWST* filter pairs for our three families of stochastic SFHs. In Figure 2.29(b) I show $\beta_{\lambda,0}$ versus redshift for the same six metallicity values for 10 examples of each SFH family. The $\beta_{\lambda,0}$ tracks for each SFH family increase systematically and almost linearly with increasing redshift. The slopes of those tracks differ for each family, SFH5 (late-type) having the steepest slope and SFH3 (early-type) having the shallowest. Only at the two lowest metallicities do the late-type tracks start to deviate from their linear increase with redshift to overlap the tracks of spiral (at $z > 1$) and even early-type galaxies (for $z \gtrsim 1.5$). For higher metallicities there appears to be little overlap between the tracks for the three SFH families. With some constraints on the stellar metallicity, SFH, and redshift, the β_λ method can be a powerful tool to correct the spatially resolved images for large samples of galaxies observed with *HST* and *JWST* at moderate redshifts for the effects of extinction by dust.

2.4 Summary

I combined SSP SEDs from the Starburst99 and BC03 codes for young and old stellar ages, respectively, and generated arrays of CSP SEDs for a large variety of exponentially declining and stochastic SFHs by stacking SSP SEDs as a function of the adopted time-dependent SFRs. For my large suite of models with stochastic SFHs, I take the average metallicity evolution as a function of cosmic age into account. I calculated the intrinsic flux ratios $\beta_{\lambda,0}$ between rest-frame visible–near-IR and rest-frame mid-IR 3.5 μm on a grid of six metallicities and 16 ages of stellar populations for 13 different SFH families, for 29 visible–near-IR filters, and 5 mid-IR filters with central wavelengths near 3.5 μm. I find that taking metallicity evolution into account results in significantly higher $\beta_{\lambda,0}$ values at higher redshifts and for higher-metallicity stellar populations at those redshifts. I also provide the range of $\beta_{V,0}$ and β_V for different Hubble types of nearby galaxies, and confirm that my models agree with the observed β_V values. I demonstrated that the β_V method can infer A_V to a level of fidelity that is comparable to that of more established methods. I conclude that the β_V method and its extension, the β_λ method presented here, are valid as a first-order dust-correction method, when using the morphology and size of a galaxy as broad a priori constraints to its SFH and redshift, respectively. The β_λ method will be applicable to large samples of galaxies for which resolved imagery is available in one rest-frame visible–near-IR filter and one rest-frame $\lambda \sim 3.5\,\mu$m bandpass. I make my CSP synthesis models and all my results available via a dedicated website[2] in the form of FITS and PNG maps, and ASCII data tables of $\beta_{\lambda,0}$ values as a function of age and metallicity.

Chapter 3

ANALYSIS OF THE SPATIALLY RESOLVED $V-3.6\,\mu$m COLORS AND DUST EXTINCTION IN 257 NEARBY NGC AND IC GALAXIES

I then provide an extensive database of g- and V-band to 3.6 μm flux ratios for local galaxies and their corresponding dust-extinction maps. I analyze the results of the flux-ratios to evaluate the improvement, fidelity, and robustness offered by the approximate extinction corrections, as well as the nature of exceptional cases. I can then highlight coherent stellar structures previously hidden by dust, in addition to cases where the SED is non-thermal in nature, which can result from (weak) AGN. I also investigate the dependence on the physical resolution of a galaxy by comparing subsets of galaxies at different distances. I then compare my results with those obtained through multi-wavelength SED fitting found in the literature. All the work in this chapter is in press (K19).

3.1 Sample Selection and Data

I select my sample galaxies from the Revised New General and Index Catalog[6] (Steinicke 2018; hereafter S18), as it contained data necessary for our analysis of well-studied nearby galaxies. Of the 13,226 objects in the catalog, 9995 objects are classified as galaxies. Out of these 9995 galaxies, 568 had available *Spitzer* Enhanced Imaging Product (SEIP) Super Mosaics FITS images, which were observed with the IRAC Channel 1 on board the *Spitzer*. These observations were taken at a wavelength of 3.6 μm and have a FWHM resolution of $\sim 1\farcs6$. The galaxies in each mosaic were both well resolved (size $\gtrsim 100\times$ PSF, and roughly centered in

[6]http://www.klima-luft.de/steinicke/ngcic/ngcic.htm

the IRAC FOV (offset from the IRAC pointing center by $\lesssim 1\farcm0$). To avoid systematic uncertainties resulting from very large optical depths through a galactic disk, the 568 galaxies were reduced to 410 relatively face-on galaxies with axis ratio (b/a) larger than 0.5. Column 10 in Table 3.1 gives for b/a values for individual galaxies. Finally, the 257 galaxies which also had g- and r-band mosaics from the SDSS DR 12 server[7] were selected for the final sample. The SDSS mosaics have average FWHM values of $\sim 1\farcs2$.

Figure 3.1 shows the demographics of the 257 selected galaxies in our sample. The redshift, V-band magnitude, Hubble type, and star formation and/or nuclear activity type were determined from the NASA/IPAC Extragalactic Database[8] (NED), S18, The third Reference Catalogue of Bright Galaxies (de Vaucouleurs *et al.*, 1991, hereafter RC3), and from NED, respectively.

The Hubble type was determined from the RC3 numeric T type: E$= T < -3$, S0$= -3 \leqslant T < 0$, Sa$=$ $0 \leqslant T < 2$, Sb$=$ $2 \leqslant T < 4$, Sbc$=$ $4 \leqslant T < 5$, Sc$=$ $5 \leqslant T < 7$, Sd$=$ $7 \leqslant T < 9$, Irregular$=$ $9 \leqslant T < 91$, and Peculiar$=$ $91 \leqslant T < 100$. If the "T-type" from RC3 was missing, the value based on the 'Type' from S18 and the 'Classification' from NED was assigned. These are indicated with asterisks in Column 16 of Table C.1. Table C.1 also lists the celestial (J2000) coordinates, redshifts, magnitudes (B, V, and 3.6 μm), absolute magnitude (3.6 μm), major-axis size, r-band effective radius, Petrosian half-light radius in V band, position angle of the semi-major axis, Galactic extinction, bulge-to-total light ratio, T-type, T-type uncertainty, SF/AGN classification, and Figure number designation. For the SF and AGN classification, the "Classification" from NED was used to categorize the galaxies into six types: "not active," "Starburst," "LIRG," "LINER," "Seyfert 2," or "Seyfert 1." If the NED

[7]https://dr12.sdss.org/mosaics

[8]https://ned.ipac.caltech.edu/

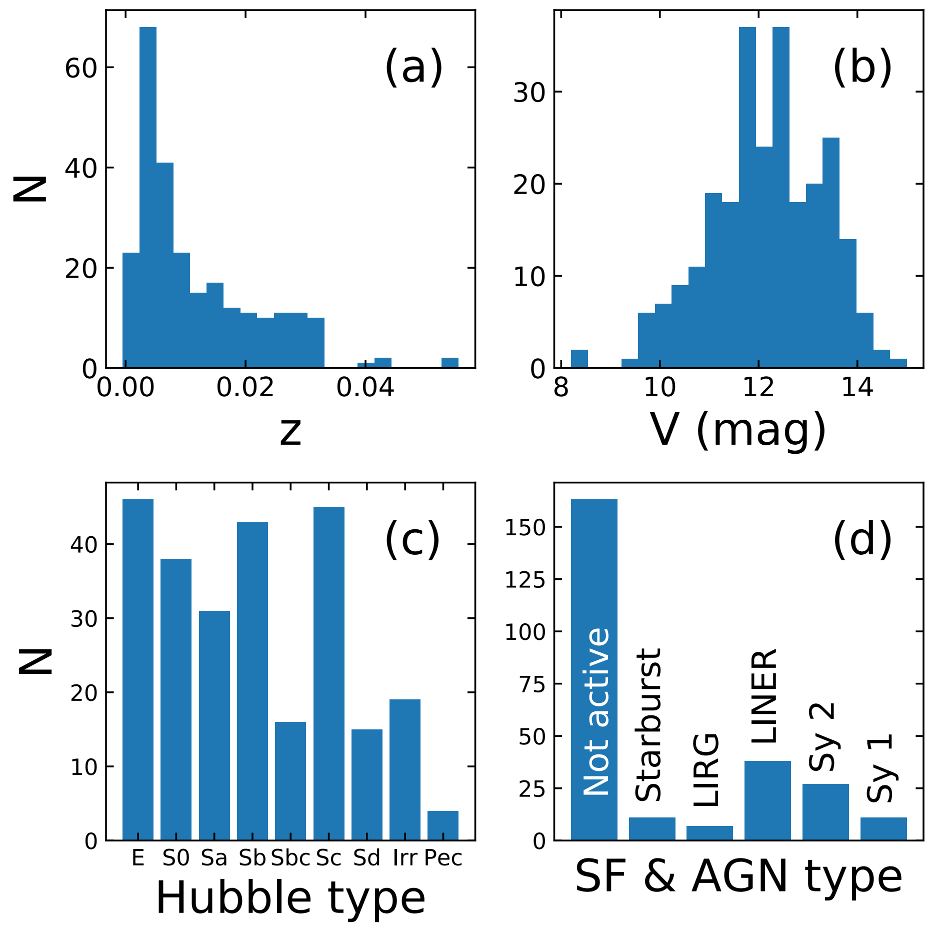

Figure 3.1: Demographics of the selected 257 NGC/IC sample galaxies containing both *Spitzer*/IRAC 3.6 μm and SDSS g and r mosaics. Distributions detailing the (a) redshifts, (b) V magnitudes, (c) Hubble type, and (d) SF and AGN types are shown for the sample galaxies. See § 3.1 and Table C.1 for details.

classification indicates more than one type, I categorize the galaxy with a preference toward later or more active types. For example, NED classifies NGC 0315 as "LINER," "Sy3b," and also "Sy1." Therefore, I classify NGC 0315 as "Seyfert 1." Galaxies without any classification are categorized as "not active."

For each of the 257 sample galaxies, the IRAC Channel 1 (3.6 μm) SEIP Cryogenic Release v3.0 Super Mosaics were downloaded from the SHA[9]. The data products called 'Mean mosaics'

[9]http://sha.ipac.caltech.edu/applications/Spitzer/SHA/

were used for the photometry, and those called the 'standard deviation maps' were used for S/N calculation; following the method detailed in the SEIP Explanatory Supplement[10]. For the V-band data, mosaic images of 257 NGC/IC galaxies were downloaded in both the g and r bands from the SDSS DR12 Science Archive Server. $30' \times 30'$ SDSS mosaics with a pixel scale of $0.''396$/pixel were selected, such that they had sufficiently larger FOV than the SEIP Super Mosaics. All SDSS images covering the area were used, even if they are not from the *primary*[11] SDSS data set anywhere.

3.2 Analysis

3.2.1 PSF Matching

One needs to match PSFs of the images from various facilities before performing any pixel-to-pixel analysis. A Python script[12] for modeling PSFs in the SDSS and *Spitzer* mosaics was written to perform the PSF matching. First, SExtractor (Bertin and Arnouts, 1996) was run on each mosaic to generate a background image, as well as a catalog of sources. These sources were then used as the input values of the PyRAF DAOPHOT package (Stetson, 1987). Stars having SExtractor parameter values listed below were selected and used to model the image PSF with the PyRAF task PSF:

1. FLAGS = 0
2. CLASS_STAR > 0.8 (0.7 for *Spitzer*)

[10] https://irsa.ipac.caltech.edu/data/SPITZER/Enhanced/SEIP/docs/seip_explanatory_supplement_v3.pdf

[11] https://www.sdss.org/dr12/help/glossary/#surveyprimary

[12] https://github.com/DuhoKim/PSFtractor

3. ELLIPTICITY < 0.1
4. mode(FWHM_IMAGE) $-$ σ(FWHM_IMAGE)
   $<$ FWHM_IMAGE $<$
   mode(FWHM_IMAGE) $+$ σ(FWHM_IMAGE).

A radius of 30 pixels was used for the PSF model, which was large enough to sample the wings of the PSF and small enough to exclude background objects. The generated PSF model was then fed into the task SUBSTAR, which subtracts background stars neighboring the stars used to create the PSF model. This cleans out the background and models the PSF to a higher degree of accuracy. This procedure was repeated one more time to finalize the modeling of each PSF.

PSF models of the *Spitzer* mosaics were consistent in shape, but with varying PAs. The PSF models were rotated to match the PAs, and then stacked to build a master PSF for the *Spitzer* mosaics. Before matching the PSFs of the SDSS mosaics, the PSFs needed to be rotated back to the original PA. The SDSS PSF model was constructed separately for each mosaic.

PyRAF task PSFMATCH was used to match the PSFs of the SDSS g and r mosaics to *Spitzer* 3.6 μm mosaics. PSFMATCH task convolves the input image with a convolution kernel to match a PSF of the input image to the corresponding PSF of the reference image (Phillips and Davis, 1995):

$$k = \mathscr{F}\left\{\frac{\mathscr{F}(\mathrm{PSF}_{\mathrm{ref}})}{\mathscr{F}(\mathrm{PSF}_{\mathrm{inp}})}\right\}, \tag{3.1}$$

where k is the convolution kernel and $\mathscr{F}$ indicates the Fourier transform.

For each galaxy, the PSFs of the SDSS g- and r-band mosaics were matched to the Spitzer 3.6 μm mosaic. The PyRAF DAOPHOT library was used to build model PSFs. Then, the tasks PSFMATCH and WREGISTER were used to match the SDSS and *Spitzer* PSFs, and then register the image relative to the 3.6 μm *Spitzer* mosaic. Nearly identical results were found regardless of the order that the tasks WREGISTER, PSF, and PSFMATCH were performed in. Color composite images in the R, G, and B channels are made from registered IRAC 3.6 μm, the SDSS g-, and r-band mosaics, respectively. See Figure 3.2 for example and see Appendix D for the entire sample.

3.2.2 β_V Map and Segmentation

After the PSFs were matched and the images were registered, we interpolated the V-band flux between the g- and r-band flux using the transformation formula from Jester *et al.* (2005) for all stars with $(R\text{-}I) < 1.15$ mag:

$$V = g - 0.59 \times (g - r) - 0.01 \text{ [mag]}. \tag{3.2}$$

The rms residual of this transformation equation is 0.01 mag (Jester *et al.*, 2005). The β_V FITS images were produced by dividing the *pseudo* V band co-registered FITS images by the 3.6 μm FITS images using the PyRAF task IMARITH. Examples of the resulting images are shown in the top middle panels of Figure 3.2. The β_g images are displayed next to the β_V image in each Figure for comparison.

The host galaxy's regions were selected using the segmentation map generated by SExtractor, which was obtained by setting "CHECKIMAGE_TYPE" as "SEGMENTATION." The SExtractor parameters "DETECT_THRESH," "BACK_TYPE," "BACK_SIZE," and "DETECT_NTHRESH" were carefully controlled to obtain an optimized segmentation map for each galaxy. Foreground stars and background galaxies were selected by visual inspection. Point sources, except the ones in the centers of galaxies, were marked. Extended sources with disparate colors and/or incoherent features were also marked. Their coordinates were recorded manually using the PyRAF DAOEDIT task, so that they could be removed from each segmen-

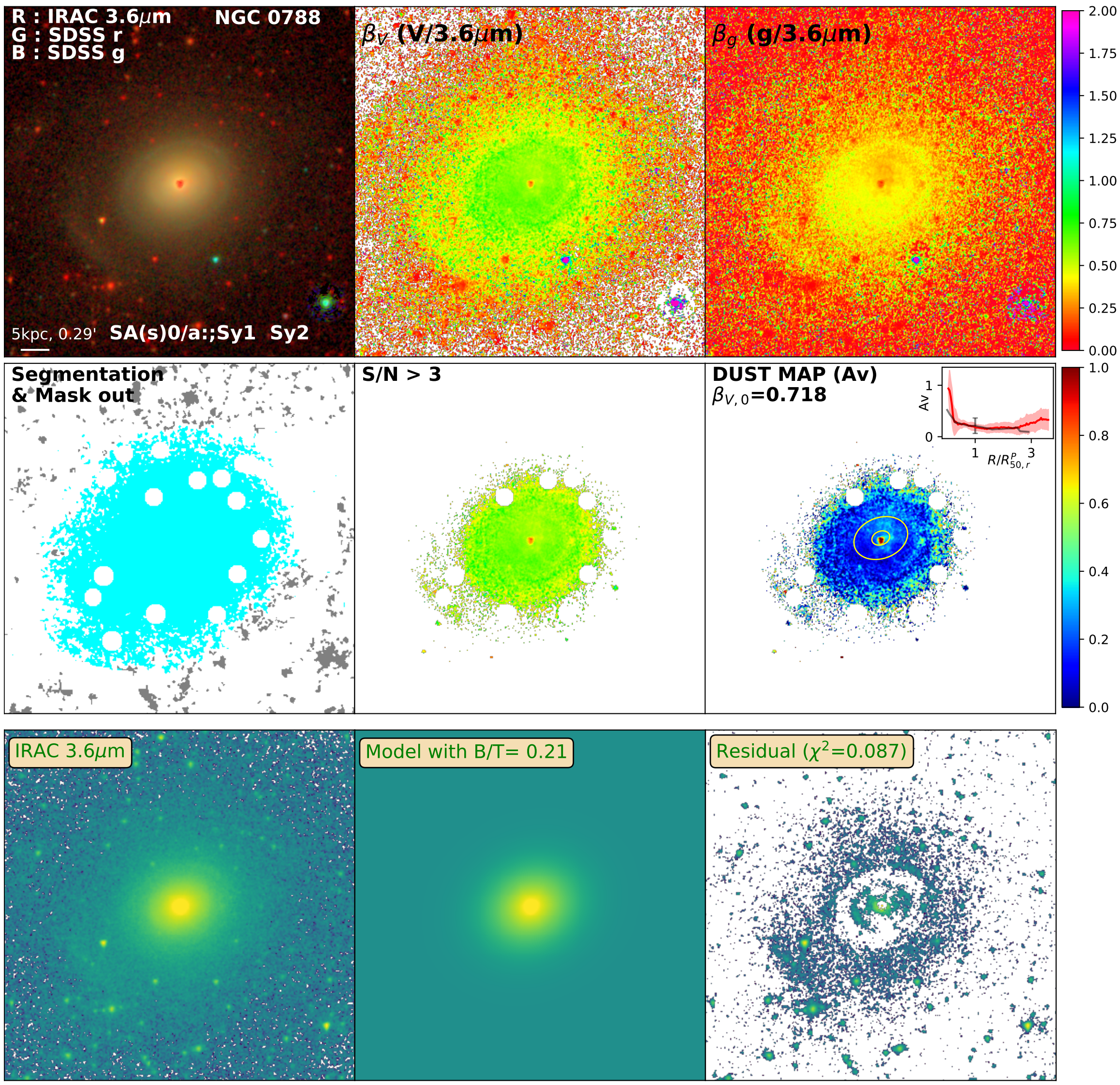

Figure 3.2: NGC 0788 example of (top left) RGB color composite from the IRAC 3.6 μm, SDSS r-, and SDSS g-band images, with the classification from NED on the bottom (top center) β_V-image. (top right) β_g-image. (middle left) SExtractor segmentation map masking out regions near Galactic stars from the galaxy of interest (cyan). (middle center) β_V-image of all pixels with a S/N greater than three in all mosaics for the region defined by the bottom-left segmentation map. (middle right) Dust A_V-map calculated by the ratio of the β_V to the $\beta_{V,0}$-values (see Equation 2.5). The A_V-profile (red) is plotted in the top right corner as a function of the normalized radius with the GD15 A_V-profile for the corresponding Hubble type (black). (bottom left) *Spitzer* 3.6 μm mosaics (bottom center) GALFIT model consists of bulge and disk components with the ratio between the bulge and the sum on top (bottom right) Residual with reduced χ^2 values on top (257 images for all my sample are available in Appendix D)

tation map. For each object removed from the segmentation map, all pixels within a radius of 10 pixels were set to zero. Finally, each segmentation map was individually analyzed and then edited, if necessary, using segeditor (Ryan, 2018). The resulting segmentation maps are shown in the lower-left panels of Figure 3.2. The cyan region is the galaxy of interest and the gray areas correspond to objects other than the galaxy.

Only the pixels with S/N >3 in all g-, r-band, and 3.6 μm FITS images were used for further analysis. Each 3.6 μm mosaic comes with an associated standard deviation map, which I used as a noise map. A similar data product is not available for the g- and r-band mosaics, so I measured the standard deviation of the background noise fluctuations and used it as the noise value of each mosaic. The final β_V and A_V maps used for our analysis are shown in the lower middle and right panels of Figure 3.2.

3.2.3 $\beta_{V,0}$ Derivation

A β_V-profile of a galaxy was built by taking the median of the β_V-values in elliptical annuli with major axes increasing from 1 pixel to the maximum visible size of a galaxy (“a” in Table C.1). This was done with a linear step size of one pixel, while the axis ratio and PA were fixed as “b/a” and “PA” in Table C.1. The outer ($r>20\%$ of “a”) annuli with more than half of pixels masked out were excluded from the β_V-profile.

The β_V-profiles were then converted into A_V-profiles using:

$$A_V(r) = 2.5 \times \log\left(\beta_{V,0}/\beta_V(r)\right) , \tag{3.3}$$

where $\beta_{V,0}$ is the global intrinsic β_V-value, assuming negligible extinction at 3.6 μm (see Equation 2.4).

The $\beta_{V,0}$-values for each galaxy or Hubble type were derived by grid-searching for the $\beta_{V,0}$-value which had the lowest χ^2 between A_V-profiles from Equation 3.3 and the average

A_V-profiles for each Hubble type from GD15 (see Figure 17 in GD15):

$$\chi^2 = \sum_{r=r0}^{r_n} \frac{(A_V^{\beta_\mathrm{V}}(r) - A_V^{GD15}(r))^2}{\sigma^{\beta_\mathrm{V}}(r)^2}, \tag{3.4}$$

where r is the linearly increasing galactic radius normalized by the Petrosian HLR (R_{50}^{P}; Blanton *et al.*, 2001; Yasuda *et al.*, 2001) (see § 3.2.3.1 for more details), ${A_V}^{\beta_\mathrm{V}}(r)$ is the individual or average A_V-profile from Equation 3.3 for a galaxy or Hubble type respectively, ${A_V}^{\mathrm{GD15}}(r)$ is the average A_V-profile for each Hubble type from GD15 for face-on ($b/a > 0.63$) galaxies, and $\sigma^{\beta_\mathrm{V}}(r)$ is the scatter in ${A_V}^{\beta_\mathrm{V}}(r)$. I interpolated over ${A_V}^{\beta_\mathrm{V}}(r)$, so that the number of radius bins ($r_n = 15$) was the same as in ${A_V}^{\mathrm{GD15}}(r)$ within a range of radius of $r = 0$–$3 \times R_{50,V}^{P}$. For 69 galaxies, the radial steps were less than the FWHM of the matched PSF ($1\farcs6$), which indicates that adjacent data points in the ${A_V}^{\beta_\mathrm{V}}(r)$ profiles are correlated. However, the $\beta_{V,0}$-values of interest are derived from the statistical average of multiple galaxies per Hubble type. The median β_V-profiles among $\geqslant$ five galaxies are used in Figures 3.7 and 3.8. Medians and 1σ ranges in the distribution of the resulting β_V-values are shown in Figure 3.9 and 3.12. I refer to § 3.3.3 for more details. I also verified that changing the value of r_n from 15 to 30 did not significantly change the $\beta_{V,0}$-values.

3.2.3.1 Petrosian Half-light Radius

The HLR was measured to normalize the radial profiles of the galaxies so that they could be compared with those from the literature.

GD15 collapsed the spectral cubes in the rest-frame window 5635±45 Å, which is near the central wavelength of the V filter (5448 Å, see the Table B.1) and then measured the HLR. Their HLR values thus measured are close to the Petrosian HLR (R_{50}^{P}; Blanton *et al.*, 2001; Yasuda *et al.*, 2001) from the SDSS data archive (see Appendix A in González Delgado *et al.*, 2014).

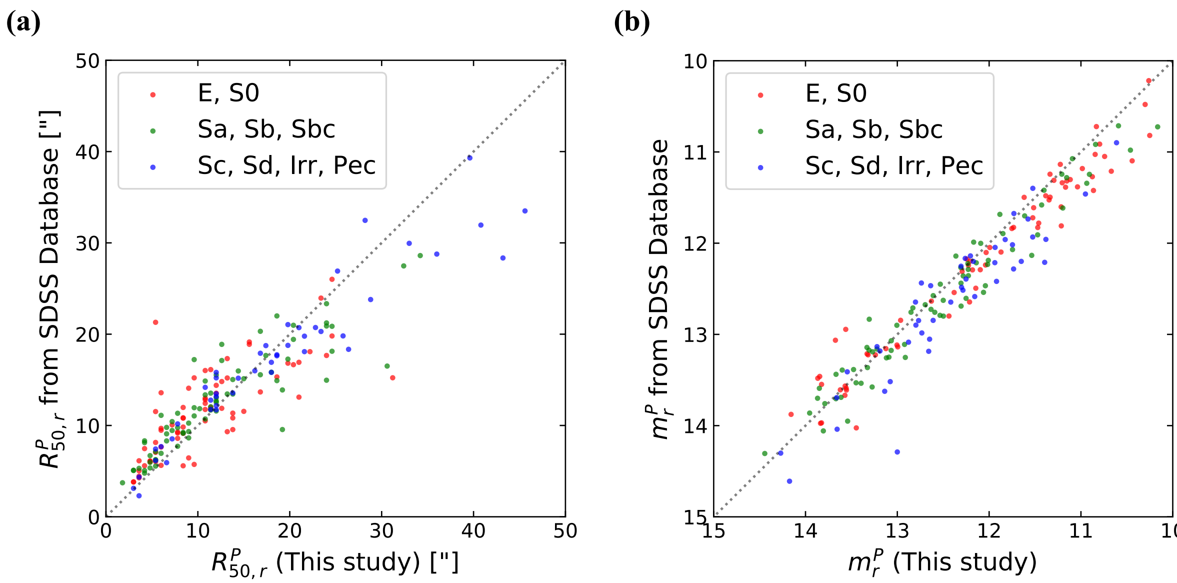

Figure 3.3: Comparison between (a) Petrosian half-light radii (*petroR50_r*) and (b) Petrosian magnitudes (*petroMag_r*) in r band from the catalog "Galaxy" in the SDSS archive and my measurements using downloaded SDSS mosaics. The morphological types of galaxies are color-coded. The almost one-to-one slope of my measurements and the SDSS measurements shows agreement with the archival catalog.

To be consistent, I followed the definition of the SDSS Petrosian HLR, R^P_{50}. A radial surface profile was first determined using the median values of circular annuli in a radius range from 1 pixel to the semi-major axis of the galaxy.

Next, the Petrosian radius, R^P, was calculated such that the flux within an annulus between $0.8R^P$ and $1.25R^P$ was less than 20% of the total flux within the radius R^P. The radius containing 50% of the flux within R^P was defined to be the Petrosian HLR, R^P_{50}. Figure 3.3 shows the comparison between my measurements and the SDSS data archive values of R^P_{50} in r ("petroR50_r") of 182 coordinate-matched galaxies in my sample. The values from the '*Galaxy*' catalog on SDSS SkyServer DR14[13] were queried using the coordinates of my galaxy sample with a $0'.5$ search radius. Overall, the galaxies match, so the R^P_{50} in the V band was used for the normalization of the radius in Figure 3.7.

[13] https://skyserver.sdss.org/dr14/en/tools/crossid/crossid.aspx

3.2.4 A_V Map Using $\beta_{V,0}$

A_V-maps were generated using Equation 2.5 as a function of each pixel instead of as a function of radius (see the lower right panels of Figure 3.2; hereafter "DUST MAP").

The $\beta_{V,0}$-value for each galaxy was selected as the value with the lowest χ^2 in Equation 3.4. That $\beta_{V,0}$-value is printed in the top left corner of each "DUST MAP" panel. The inset in the top right corner of each "DUST MAP" panel shows ${A_V}^{\beta_{\rm V}}(r)$ (red) and ${A_V}^{\rm GD15}(r)$ (black) curves as a function of the normalized radius, where the shading represents the 1σ scatter in the β_V-profile. The errorbar at a radius of $R = R^P_{50,V}$ in the inset represents the uncertainty in the A_V-value at the HLR for the corresponding Hubble type from GD15.

Yellow ellipses with major axes values of R^P_{50} and $3 \times R^P_{50}$, corresponding to the tick marks on the A_V-profile plot, are overplotted on each "DUST MAP" image.

3.3 Results

3.3.1 β_V vs. T-type and z

The distribution of the β_V-values for my sample galaxies is shown in Figure 3.4 as a function of T-type. The uncertainty in the T-type and the 1σ error of the β_V-range are represented by the shape of the ellipses. Furthermore, SF/AGN types are represented by the color of each ellipse. For each integer T-type in my sample, a range of T-types was selected from $T - 0.5 < T < T + 0.5$. To investigate the trend in this plot, the following steps were taken. For each galaxy in every T-type range, a β_V-value was sampled from a random distribution of β_V-values created using the mean and 1σ error for each galaxy. This was repeated 1000 times to determine a more statistically significant average β_V-value for each T-type. In Fig-

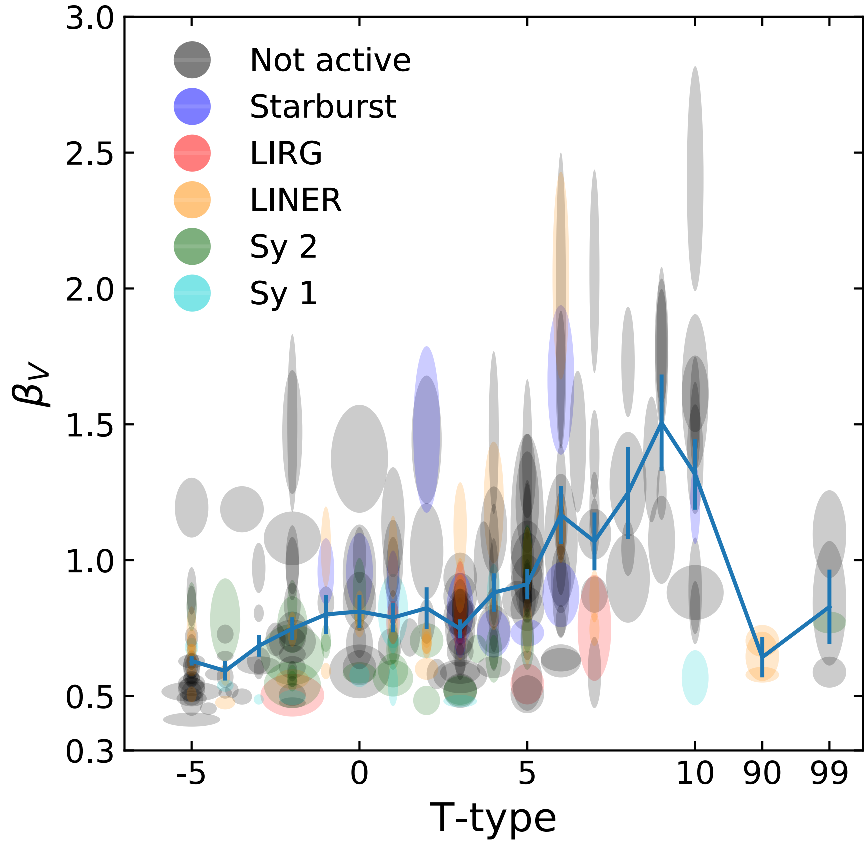

Figure 3.4: β_V-values as a function of T-type for my sample galaxies. The color of each ellipse represent the SF/AGN type of each galaxy, while the horizontal and vertical size represents the T-type and the 1σ β_V uncertainties, respectively. The solid line represents the mean and 1σ uncertainty for 1000 randomly generated β_V-values for $T - 0.5 < T < T + 0.5$. No relationship is seen between the SF/AGN types and their β_V-values within each type bin.

ure 3.4, this average is shown by the solid blue line, while the corresponding 1σ error range is illustrated by the vertical blue lines.

The global β_V-values (solid blue line) in Figure 3.4 are similar to Figure 2.27, which corresponds to the range of β_V-values derived from the SED models that adopted the observational stellar population properties from GD15. From both Figure 3.4 and 2.27, the average β_V-values, as well as the scatter of the values, increases with T-type. The observed 1σ scatter in β_V due to both the pixel-to-pixel variations within a galaxy, and from galaxy to galaxy within

Table 3.1: The Observed 1σ Scatter in β_V, $\beta_{V,0}$, and the Calculated 1σ Errors in A_V for Galaxies in each Hubble Type Bin.

	E (46)[a]	S0 (38)	Sa (31)	Sb (43)	Sbc (16)	Sc (45)	Sd (15)	Irr&Pec (23)
Within a galaxy[b]	0.08	0.15	0.20	0.18	0.24	0.30	0.31	0.33
From galaxy to galaxy[c]	0.15	0.19	0.16	0.19	0.17	0.27	0.32	0.45
1σ ranges of $\beta_{V,0}$[d]	0.15	0.25	0.38	0.38	0.35	0.63	0.45	
$\beta_{V,0}$[e]	$0.55^{+0.08}_{-0.07}$	$0.64^{+0.13}_{-0.12}$	$0.72^{+0.11}_{-0.27}$	$0.68^{+0.19}_{-0.19}$	$0.89^{+0.15}_{-0.20}$	$0.96^{+0.37}_{-0.26}$	$1.14^{+0.29}_{-0.16}$	
Expected ΔA_V[f]	0.30	0.36	0.36	0.38	0.38	0.45	0.45	0.53

Notes.

[a] The number of galaxies in each Hubble type bin.

[b] The mean of 1σ scatter in the pixel-to-pixel β_V-values within each galaxy (half vertical sizes of the ellipses in Figures 3.4 and 3.5) in each Hubble type bin.

[c] The standard deviation of the galaxy-by-galaxy average β_V-values (central vertical values of the ellipses in Figure 3.4) in each Hubble type bin.

[d] The 1σ scatter of the inferred $\beta_{V,0}$-values for galaxies in each Hubble type bin. See § 3.3.3 and Figure 3.9 for more details.

[e] The median and the 1σ ranges of the inferred $\beta_{V,0}$-values.

[f] The calculated 1σ scatters of A_V-values using the derivatives of Equation 3.3 [$\frac{dA(x)}{dx} = 2.5 \times \frac{d\beta_V(x)/dx}{ln(10)\beta_V(x)}$, where I adopt (d) for $d\beta_V(x)/dx$ and the average β_V-values for each Hubble type bin for β_V(x))].

a Hubble type bin are listed in Table 3.1. Within individual galaxies, the pixel-to-pixel scatter increases toward later Hubble types, from 0.08 for E to 0.18 for Sb and to 0.33 for Irr&Pec. From galaxy to galaxy, the spread within a Hubble type bin also increases from 0.17 for E through Sbc to 0.45 for Irr&Pec. On average, the spread in β_V around the average, both within a galaxy and for each morphological type bin, are ∼20%, which results in a ∼0.4 mag scatter in A_V. Slowly evolving old and metal-enriched stellar populations in early-type galaxies tend to be more similar compared with more dynamically evolving young and low-metallicity galaxies of later types, resulting in a wider β_V-range for the latter. However, spiral types with β_V-values less than 0.5 from Brown *et al.* (2014) in Figure 2.27, are not seen in this sample. This difference seems to originate from an intrinsic difference in the type of galaxies from my sample compared with the sample in Brown *et al.* (2014). Almost all of Brown *et al.* (2014)'s galaxies have low resolution 5–38μm spectra from the *Spitzer* Infrared Spectrograph (Houck *et al.*, 2004). This wavelength range is where the re-radiation from dust clouds dominates.

Furthermore, these differences can also be attributed to the majority of the galaxies in Brown *et al.* (2014) being of the SF/AGN class, while the majority of my sample galaxies are listed as "not active."

PSFs of registered image data are matched with an FWHM of $1.''6$ of the PSF modeled from the *Spitzer*/IRAC 3.6 μm mosaics. The $1.''6 \times 1.''6$ corresponds to a galaxy surface area of 34^2, 340^2, 670^2, and 990^2 pc^2 at $z = 0.001$, 0.01, 0.02, and 0.03, respectively. Statistically, as redshift increases, the sample surface area increases by factors of $\sim$100 ($z = 0.01$), 390 ($z = 0.02$), and 850 ($z = 0.03$) times compared with a galaxy at a redshift of $z = 0.001$. This reduces the scatter of any measurements taken by $\sim$10, 20, and 30 times compared with the measurement taken at a redshift of $z = 0.001$ for a completely random sample. This trend is illustrated in Figure 3.5, where the median and the scatter in β_V-values decreases significantly as the redshift increases. For redshifts less than $z \lesssim 0.02$, this trend holds. This trend can be interpreted as the β_V-values arising from stellar populations not being well-mixed (i.e., being spatially correlated among adjacent pixels), as well as spatial resolution effects, which cause less variance in β_V at $z \gtrsim 0.02$. Murray (2011) shows sizes of giant molecular clouds are less than 200 pc. Stochasticity of stellar population seems to subside when the PSF becomes larger than at least ten times the size of the giant molecular clouds.

3.3.2 Central β_V vs. SF and AGN Activity

In Figure 3.4, SF/AGN galaxies are seen to have randomly distributed global β_V-values. However, they do have characteristically lower β_V-values in their centers. Figure 3.6 shows histograms of the mean β_V-values of the central 3×3 pixels for various SF/AGN galaxies—"Not active," "LINER," "Starburst," "Sy 2," "Sy 1," and "LIRG"—from top to bottom in order of

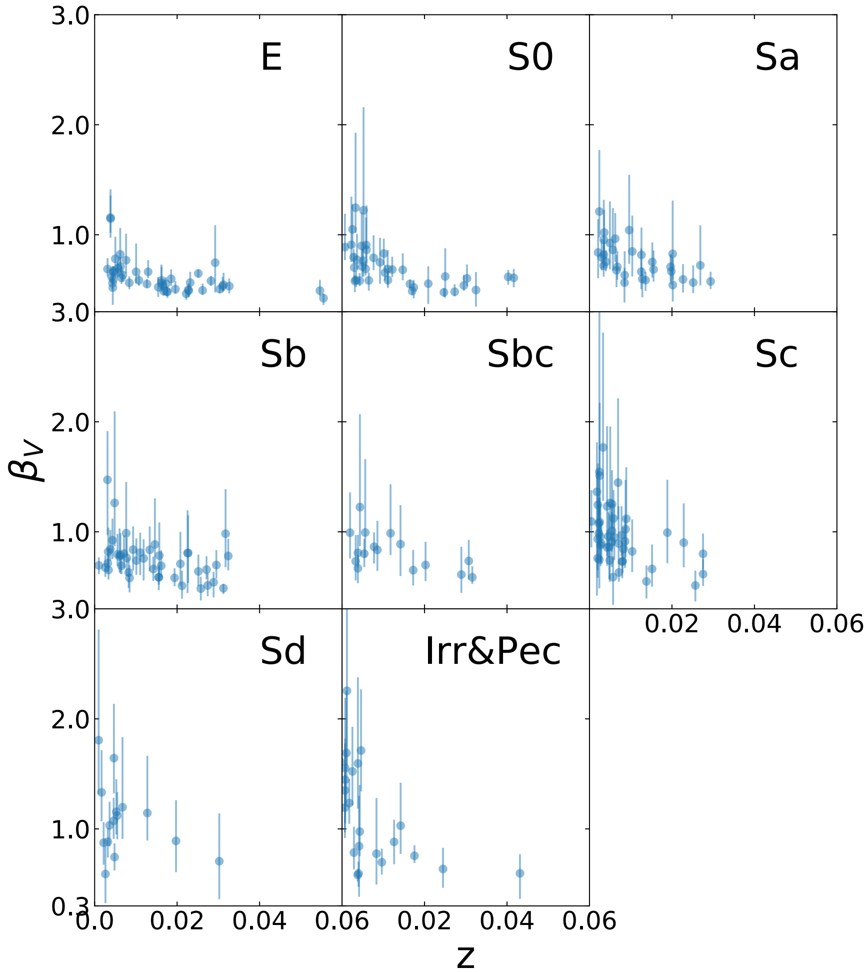

Figure 3.5: Median and 1σ range of β_V-values as a function of redshift for each Hubble type in my sample. The scatter in β_V-values for a single galaxy and the width of the distribution for a specific Hubble type decreases as redshift increases, which can be understood as a spatial resolution effect. The trend seems to level out at $z \gtrsim 0.02$, which corresponds to the spatial resolution achieved by *HST* and *JWST* at a redshift of $z \simeq 0.2$.

decreasing median central β_V-values. Nine galaxies, whose central 3×3 pixels are masked out, are excluded. Central star-forming regions are thought to be enshrouded by molecular clouds, while accretion disks surrounding supermassive black holes are thought to be surrounded by a dust torus (Urry and Padovani, 1995). Relatively low β_V-values in the centers of active galaxies support this idea of dusty environments of active SF regions and AGN.

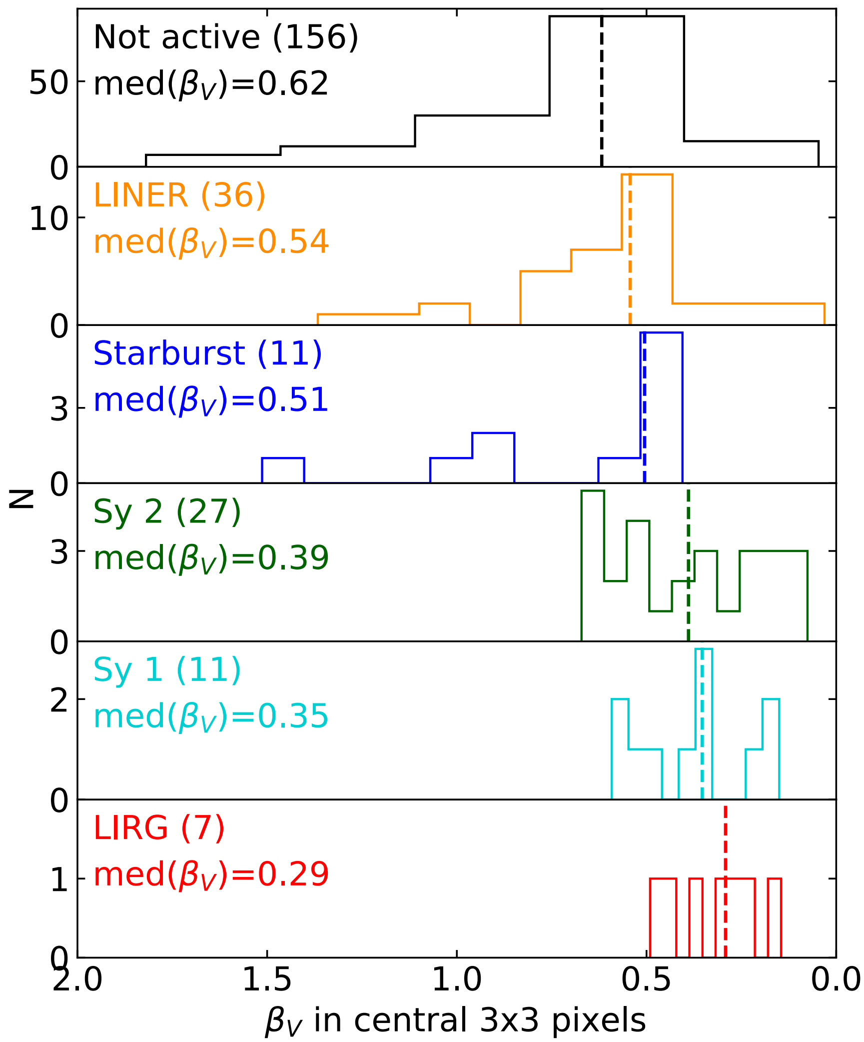

Figure 3.6: Histograms showing the mean β_V-values for the central 3x3 pixels of each galaxy. From top to bottom, this is done for 248 NGC/IC galaxies with different SF/AGN types: Not active, LINER, Starburst, Seyfert type 2, Seyfert type 1, and LIRG. Compared with average (Not active) galaxies, galaxies with increasing star-formation and/or nuclear activity have decreasing central β_V-values, which implies an increasing amount of dust.

3.3.3 $\beta_{V,0}$-values and A_V-profiles

Figure 3.7 shows A_V-profiles for each Hubble type, corresponding to the least square fitting of the median-combined β_V-profile to the average A_V-profile from GD15. The $\beta_{V,0}$-values and numbers of galaxies for each Hubble type are also listed. Spiral (Sa, Sb) galaxies have

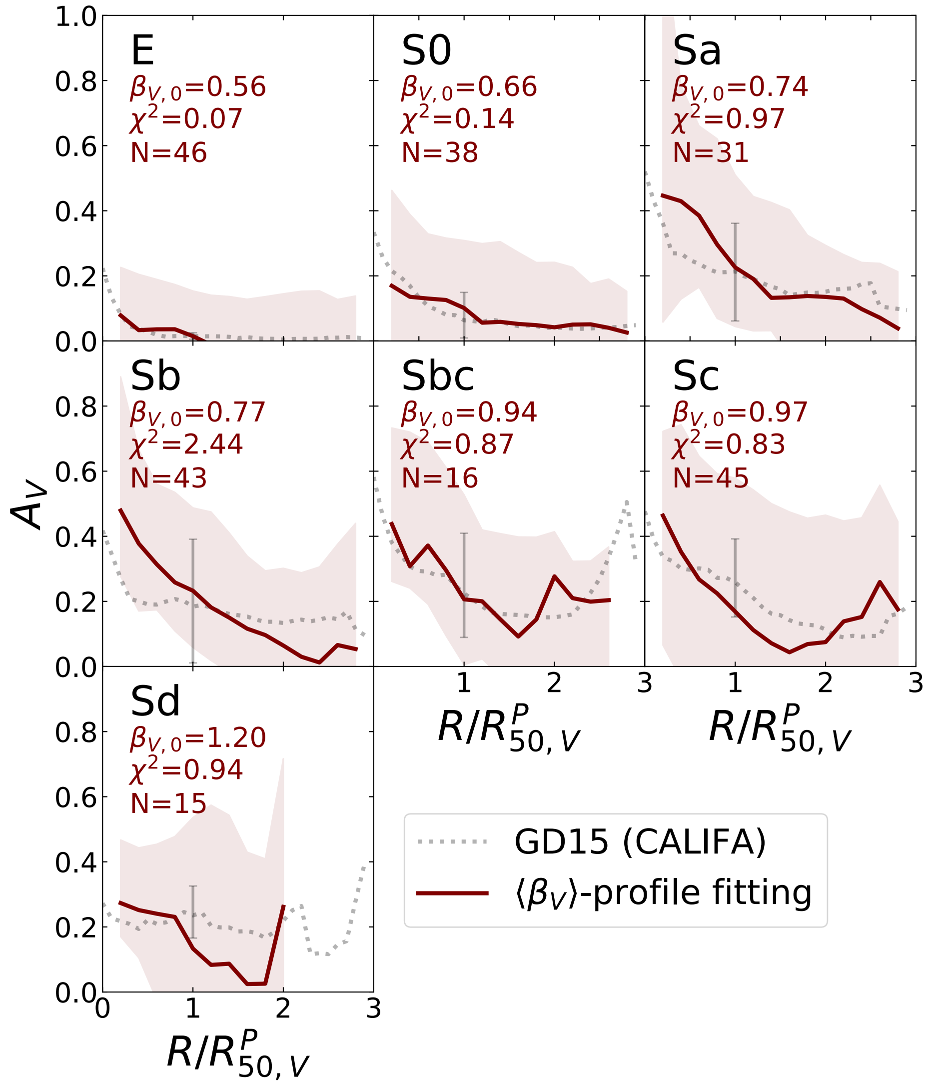

Figure 3.7: A_V-profiles as a function of galactic radius normalized by the Petrosian HLR for different Hubble types. The gray dotted lines are the averaged A_V-profiles of face-on ($b/a > 0.63$) galaxies as a function of Hubble type from the CALIFA survey of GD15. The error bars at a radius of $R = R^P_{50}$ indicate the measurement errors at the HLR for each Hubble type from GD15 (see their Figure 14), while the solid, dark brown lines are A_V-profiles generated from Equation 3.3 using the median β_V-profile for each Hubble type. The $\beta_{V,0}$-value with the smallest χ^2 in Equation 3.4 is grid-searched, and the results are detailed on each panel along with the number of galaxies for each type. The light brown shaded regions represent the 1σ ranges of the β_V-profiles. Sections of the A_V-profiles where the number of available β_V-profiles less than five are excluded from the χ^2 fitting. This is the case for the outskirts of the Sd types. Overall, the profiles agree with the CALIFA survey results from GD15. Slight deviations are seen in the slopes of spiral galaxies (Sa, Sb) and in the stochastic fluctuations of galaxies with small sample sizes (Sbc, Sd).

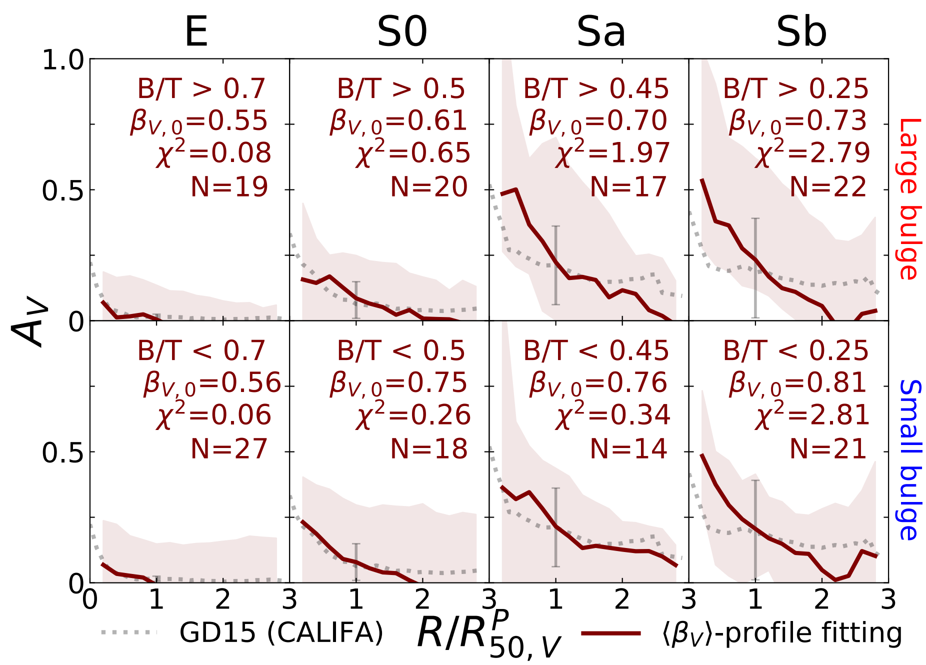

Figure 3.8: Same as Figure 3.7, but with each Hubble type divided into large and small bulge subgroups. The subgroups are defined by bulge-to-total light ratios larger or smaller than 0.7, 0.5, 0.45, and 0.25 for the E, S0, Sa, and Sb types, respectively. A_V-profiles for Sa type galaxies are in closer agreement for the small-bulge subgroup, which is a direct result of a more uniform stellar population within that subgroup.

steeper A_V-profiles than what was calculated in GD15. Sbc and Sd types show larger stochastic fluctuations, because they have fewer than half of the number of objects compared with other galaxy type bins. The scatter in the β_V-profiles results in larger uncertainties than what was derived from the measurement error at $R = R^P_{50}$ from GD15. This is expected, as the β_V-method uses only two broadband images and a single color $\beta_{V,0}$, whereas GD15 used three-dimensional spectral images and a library of SED models.

The E–Sb types were subgrouped into "Large bulge" and "Small bulge" categories by their bulge-to-total light ratios (B/T) derived using GALFIT (Peng *et al.*, 2002, 2010) (see next section for details). The B/T threshold values were arbitrarily chosen, so that there were comparable numbers in each of the two subgroups. The A_V-profile fitting process was then repeated (see Figure 3.8), which significantly reduced the χ^2 for the small-bulge subgroup of the Sa type.

More uniform stellar populations of galaxies in a subgroup result in more reliable A_V-profiles using the β_V-method. This is discussed in § 3.4.

Figure 3.9 shows the histograms of the $\beta_{V,0}$-values derived individually for each galaxy. I obtained the $\beta_{V,0}$-values for each galaxy by least-square fitting its β_V-profile to the average A_V-profile of the corresponding Hubble type from GD15. The β_V-profile is converted to the A_V-profile with a reference $\beta_{V,0}$-value (see Equation 3.3). The median and 1σ ranges are shown as dotted-dashed and dotted green vertical lines, while the $\beta_{V,0}$-values derived from the median-combined β_V-profiles are shown as dark brown dashed lines. The median values and associated ranges are listed in Table 3.1. The 1σ ranges are comparable to the quadratic sum of the pixel-to-pixel and the galaxy-to-galaxy β_V-variations in Figure 3.4. The median values derived with these complementary methods agree to within $\pm\, 1\,\sigma$.

3.3.3.1 Bulge-to-total Light Ratio

GALFIT (version 3; Peng *et al.*, 2002, 2010) was used to measure the B/T of the sample galaxies (see bottom rows of Appendix D for the fitting result). The segmentation map generated for the β_V analysis was used for the "Bad pixel mask." The 3.6 μm mosaics for each galaxy, the master PSF of the 3.6 μm mosaics, and the 'Bad pixel mask' were used as inputs for GALFIT. The "Image region" and "Size of the convolution box" were set to the same as the images shown in Figure 3.2), which is twice the semi-major axis (column 7 in Table C.1).

Three components, the disk "expdisk," the bulge "devauc," and "sky," were input to the fitting procedure to decompose the galaxy light into the light from the disk, the bulge, and the background, respectively. When a bright central point source was found and the galaxy is known to have an embedded AGN (column 19 and 20 in Table C.1), I allowed for an additional 'psf' component and excluded that in the calculation of the B/T.

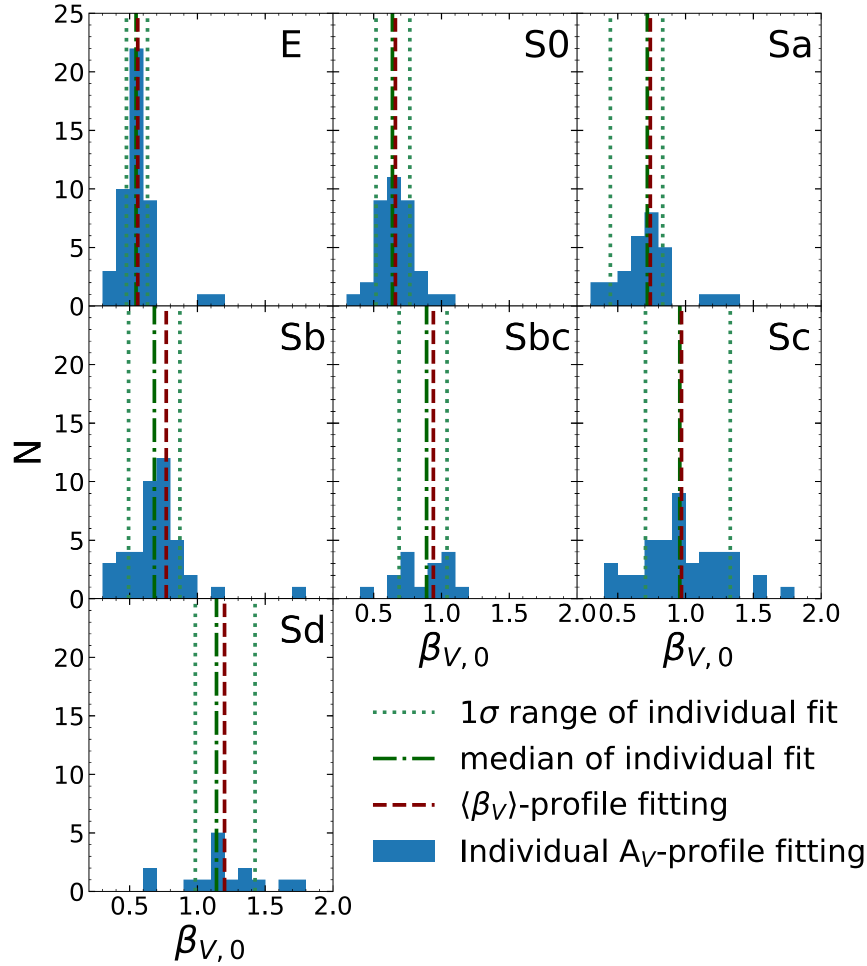

Figure 3.9: Histograms of the $\beta_{V,0}$-values corresponding to the least square fitting of the A_V-profiles of each galaxy to the average A_V-profile of each Hubble type from GD15. The green dotted-dashed and dotted lines represent the median and 1σ ranges, respectively. The brown dashed lines show the least square fitting result of median-combined β_V-profiles for each Hubble type (see Figure 3.7).

The following were used as the initial guesses for the GALFIT parameters:

1. "position" = the physical pixel position converted from R.A. and decl.
2. "Integrated magnitude" = the magnitude in V
3. "R_e" = one fifth of the semi-major axis
4. "b/a" = from Table C.1,
5. "PA" = from Table C.1.

These parameters were then set as free, so they could be varied during the fitting process. I chose one fifth of the semi-major axis as the initial guess of the effective radius “R_e”.

Upon visual inspection, any parameters that seemed unreasonable were fixed, and GALFIT was rerun. For the case when either the bulge or disk moved toward the outer part of the galaxy, the “position” argument of GALFIT was set as fixed for both components. For the case where the bulge parameter, “devauc,” was seen to dominate the GALFIT fitting, a smaller effective radius, “R_e,” was forcefully set for the ‘devauc’ component to prevent unphysical fitting at large “R_e.” This was seen to be the case for some late-type galaxies in the sample.

Figure 3.10 shows the “absolute magnitudes” (a) and the B/T (b) as a function of T-types in the RC3 catalog, excluding irregular and peculiar galaxies (T$\geqslant$9). The ‘Integrated magnitude’ output from the GALFIT fitting for each of the ‘expdisk’ and ‘devauc’ components was converted from magnitudes to flux units. The summed flux values were converted back to the total magnitude of the entire galaxy. The distance modulus, which was determined from the redshift, was added to the total magnitude of the entire galaxy to determine the “absolute magnitude” for each galaxy. The reduced χ^2 value of each B/T fit is shown in different colors. The bulge component, “devauc,” dominates in the ETGs ($T<0$), while the disk component, “expdisk,” gradually increases with T-type. The B/T was used to subdivide the E–Sb galaxies in Figure 3.8, which show different shapes of A_V-profiles between this study and IFU-SED-fitting method used in GD15. E, S0, Sa, and Sb galaxies were divided using boundary B/T values of $\simeq$0.7, 0.5, 0.45, and 0.25, respectively. Each group is shown in Figure 3.10 (b) with colored boxes for galaxies with larger (red) and smaller (blue) bulges than the dividing B/T values.

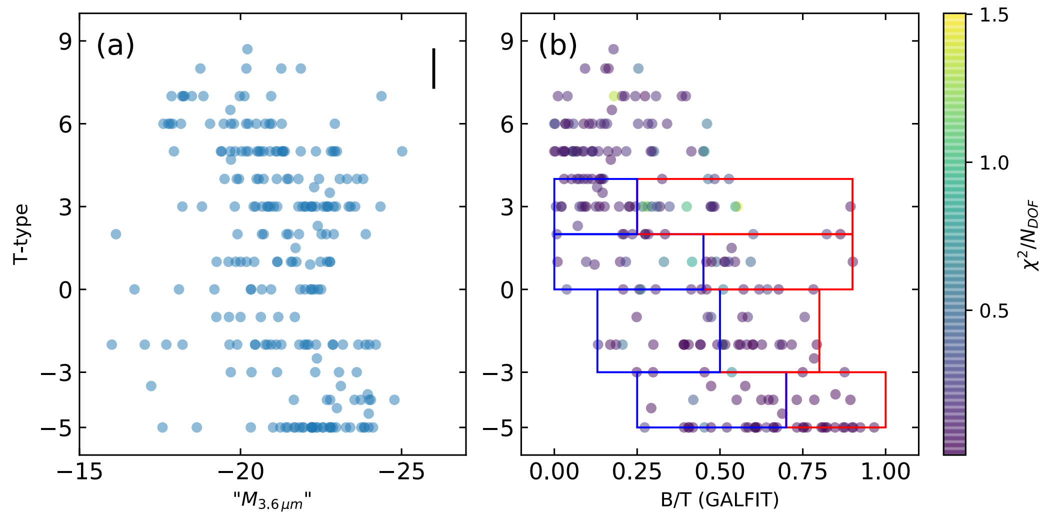

Figure 3.10: (a) RC3 T-type vs. total magnitude + distance modulus; (b) The bulge-to-total light ratios (B/T) measured using GALFIT versus RC3 T-type (excluding irregular and peculiar galaxies) of 239 galaxies. The colors of the dots in (b) represent the χ^2 divided by the number of pixels. The red (blue) boxes contain galaxies whose B/T values higher (lower) than 0.7, 0.5, 0.45, and 0.25 for E, S0, Sa, and Sb type galaxies, respectively, which consists of the "Large bulge" (red) and "Small bulge" (blue) subgroups for each Hubble types in Figure 3.8.

3.3.4 β_V vs. Axis Ratio

To avoid potential systematic uncertainties originating from a wide range of optical depths through edge-on galactic disks, I selected only face-on galaxies having axis-ratios (b/a) larger than 0.5. Figure 3.11 shows the relationship between β_V-values and their axis-ratio values. No significant correlation between β_V and the axis ratio was seen in our sample to within the 1σ errors (blue shaded regions). Sbc, Sd, and Irr&Pec types may show at best a hint of a positive correlation, although this is not significant within the current uncertainties.

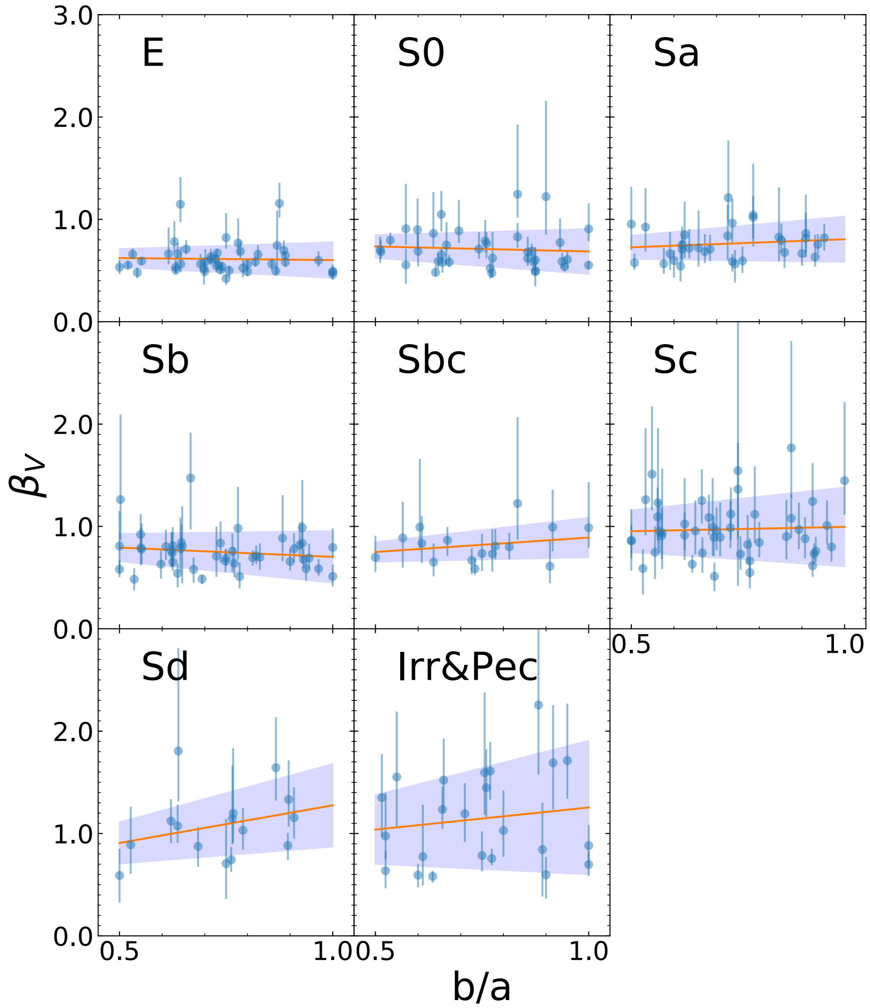

Figure 3.11: β_V versus b/a of the individual galaxies for each in morphological type bin. Galaxies with $b/a < 0.5$ are not included in my sample. The best-fit regression is overlaid as orange lines, while the shaded region represents the $\pm 1\sigma$ range. Only Sbc, Sd, and Irr&Pec galaxies in my sample show hints of a correlation between the β_V-value and the axis ratio for my sample. However, within the uncertainties, this correlation does not seem to be statistically significant.

3.3.5 Hidden Coherent Features

Coherent features buried in a single band or even in composite images (such as top left panel of Figure 3.2) stand out in color images, such as in the β_V, β_g, and/or A_V-maps. The features found in these color maps are detailed in Table 3.2, along with notes on their corresponding galaxies.

Star-forming regions and dust lanes are the most common features, which have bluer and redder ($V-3.6\,\mu$m) colors, respectively.

LIRG-like galaxies are dominated by optically thick dust clouds that are likely to be undergoing cold gas accretion from the cosmic web, harboring an AGN (see Müller-Sánchez *et al.*, 2018; Saito *et al.*, 2018, for e.g., the case of NGC 6240), or experiencing the aftermath of a recent merger (see Pingel *et al.*, 2018, for e.g., the case of NGC 4414).

AGN appear to have at least local dust clouds such as NGC 1275 (Tanada *et al.*, 2018) and NGC 985 (Appleton and Marcum, 1993), except the active, dustless, bulgeless, intermediate-mass black hole in NGC 3319 (see Jiang *et al.*, 2018).

Inner and outer rings in NGC 3011 have been found by Gil de Paz *et al.* (2003). The inner ring could have been produced by a starburst-driven shock interacting with the surrounding medium (Marino *et al.*, 2013).

Dust rings in NGC 2844 and NGC 3032 are also found and included in the Atlas of Resonance Rings As Known In S^4G (ARRAKIS; Comerón *et al.*, 2014). These rings appear to be formed by a dynamical resonance resulting from non-axisymmetries in galaxy disks (Comerón *et al.*, 2014).

NGC 2685 (Arp 336, also known as “The Helix Galaxy”) is a well-known polar ring galaxy (Sandage, 1961; Eskridge and Pogge, 1997), which has an outer ring perpendicular to the galactic disk. This is seemingly the remains of a merger with a polar-orbiting smaller galaxy.

NGC 3801 could be at an earlier stage of an NGC 2685-like merger (Hota *et al.*, 2012). The merging event $\sim$2–3 Gyr ago is presumably responsible for nuclear-ring in NGC 7742 (Martinsson *et al.*, 2018), while the minor merger $\sim$200 Myr ago (Knierman *et al.*, 2012, 2013) is responsible for the central dust in NGC 2782 and in NGC 4194 (König *et al.*, 2018).

Table 3.2: Coherent Features Revealed in the β_V, β_g, and/or A_V Images and Lists of Galaxies Containing the Features

Features (Number of Galaxies)	Galaxies (In the Order of ID)
Star-forming regions (15)	**NGC** 14, 337, 2500, 2552, 2730, 3020, 3381,3395, 3622, 3794, 3870, 3906, 5668, 5669, 5691
Dust lanes (43)	**IC** 676, 1065, 2239, 1551, 2637, **NGC** 23, 266, 275, 1667, 2512, 2608, 2712, 2731, 2742, 2750, 2776, 2782, 2824, 2893, 2906, 3015, 3049, 3055, 3265, 3349, 3351, 3489, 3655, 3720, 3726, 3799, 3801, 3811, 3921, 4194, 5631, 5633, 5992, 7080, 7177, 7479, 7653, 7798
Star-forming regions and dust lanes (30)	**IC** 1076, **NGC** 275, 309, 337, 2403, 2415, 2731, 2742, 2776, 2906, 3020, 3055, 3184, 3192, 3212, 3239, 3310 (pec), 3344, 3370, 3381, 3395 (pec), 3486, 3646, 3659, 3686, 3726, 3794, 3799, 3811, 3870, 4234, 4420, 4449 (Sbrst), 5660, 5691, 5936, 5992, 7714 (pec), 7741, 7753
LIRG-like thick dusty cloud (18)	**IC** 214, 730, 2520 (with blue halo), **NGC** 992, 1144 (pec,Sy2), 3593 (Sy2), 3655, 3683, 3822 (Sy2), 3839, 3934, 4207 (elongated), 4414 (LINER), 5541, 5653, 5953, 5990, 6240
Central dust torus (10)	**IC** 730, 2551, 2637 (Sy1.5), **NGC** 383 (LERG[1]), 3015 (NLAGN[2]), 3349, 3921 (pec), 4014, 4290, 7742 (LINER)
Central dust cloud	**IC** 486 (Sy1), 676, 691, 3050, 5298 (Sy2), **NGC** 788 (Sy1,2), 985 (Sy1), 1275 (cD;pec;NLRG[3];Sy2;LEG), 2782 (Sy1, Arp 215), 2824 (Sy?), 2831, 3212, 3561, 3720, 3781, 3839 (with blue disk), 3928, 4150, 4162 (AGN), 4194 (pec), 4335, 4369 (intertwined with blue), 4378 (point-like; Sy2), 4412 (LINER), 7177 (LINER), 7674 (Sy2)
Star-forming ring with outer dust ring (1)	**NGC** 3011
Dust ring (2)	**NGC** 2844, 3032
Polar dust ring (2)	**NGC** 2685(Arp 336)[14], 3801
Outer blue ring (3)	**NGC** 3938, 4162, 7217
Dusty disk in E type (1)	**NGC** 3656 (Arp 155, pec, LINER)
Blue disk in E type (2)	**IC** 692, **NGC** 3011
Central blue region (2)	**NGC** 3773 (H ii), 7077 (H ii)
M82-like outflow (?) (1)	**NGC** 3622
Green center bluer outskirt region (Negative color gradient) (32)	**IC** 208, 2239, 3050, **NGC** 274 (pec), 275 (pec), 309, 428, 2043, 2500, 2604, 2730, 2750, 2776, 2893, 3032, 3049, 3055, 3162, 3319, 3344, 3370, 3489, 3646 (ring), 3659, 3773, 4136, 4234, 4412, 4420, 5584, 5585, 7731
Blue center with green outskirt (3) (Positive color gradient)	**NGC** 3741 (BCD[4]), 4068, 6789

Notes: (1) Low-excitation radio galaxy; (2) Narrow-line AGN; (3) Narrow emission-line radio galaxy; (4) Blue compact dwarf; pec: peculiar, Sbrst: Starburst. ID numbers following the **NGC** are included in the New General Catalog and the **IC** are included in the Index Catalog.

Balcells (1997) argues that the dusty disk, two tidal tails, and shells in E-type NGC 3656 is the outcome of a disk-disk major merger. Conversely, the blue disk in the E-type, but low-mass, "blue sequence" galaxy IC 692 is from cold-mode gas accretion (Moffett *et al.*, 2012).

Both NGC 3773 and NGC 7077 have central blue features that are classified as H ii regions, which are probably caused by Wolf–Rayet stars (Miralles-Caballero *et al.*, 2016).

The sandglass-shaped feature in NGC 3622, which resembles the outflow of M82, has never been reported. SDSS DR12 classifies this galaxy as a starburst galaxy, which reinforces the idea of an outflow-like feature. Strong Hα and O iii emission lines might be the cause of this particular feature[15].

In total, 32 galaxies have noticeable negative color gradients, while 3 have positive color gradients. The color gradients of NUV(*GALEX*) / 3.6 μm (S^4G) observations for the disks of 1931 nearby galaxies ($z < 0.01$) also show negative color gradients (see Figure 6 in Bouquin *et al.*, 2018, see also de Jong 1996, Taylor *et al.* 2005, Kim and Im 2013). These color gradients are in agreement with the global scenario of the inside-out formation of disks.

3.4 Discussion and Conclusion

Studying PSF-matched images of 257 NGC/IC galaxy mosaics in the SDSS g and r filters and *Spitzer* 3.6 μm mosaics, I conclude the following:

1. *Early-type galaxies have lower and narrower ranges of β_V and $\beta_{V,0}$-values than later type galaxies* (see Figures 3.4 and 3.9). This trend can be explained by an increased amount of old stellar populations with quenched SF in ETGs.
2. *Spiral galaxies have steeper A_V-profiles.* The A_V-profiles for Sa galaxies with small

[15] http://skyserver.sdss.org/dr12/en/tools/explore/Summary.aspx?id=1237651273508651034

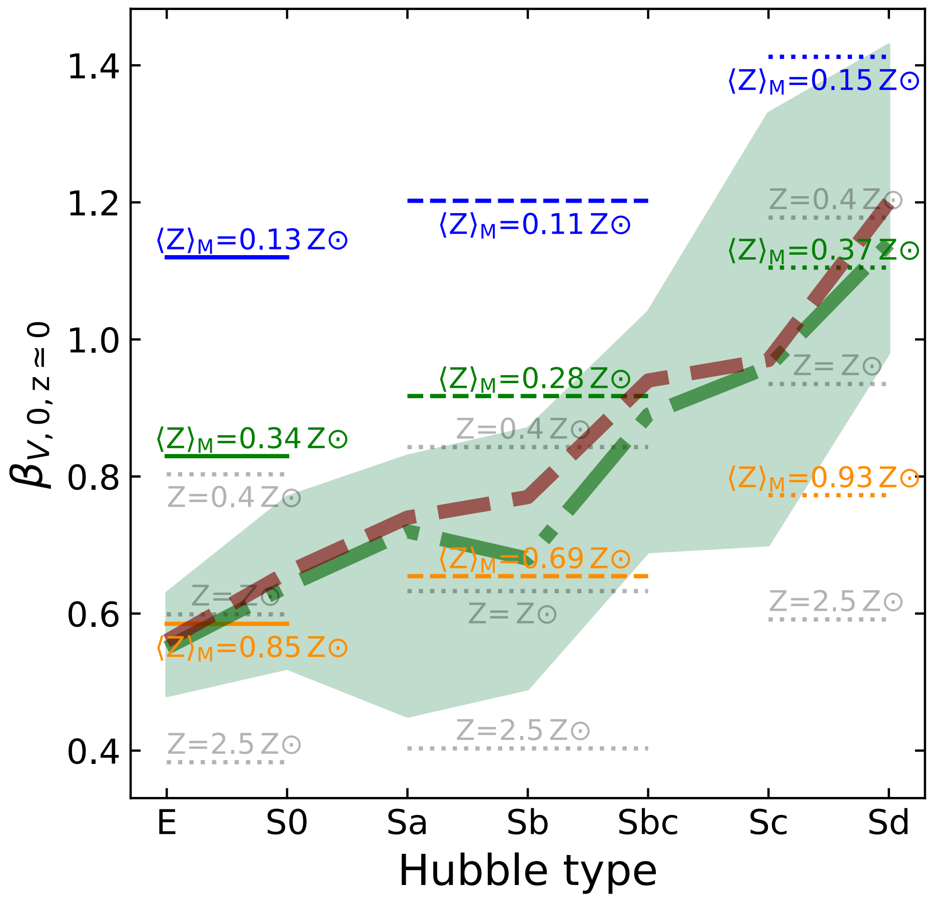

Figure 3.12: $\beta_{V,0}$-values at $z \simeq 0$ for galaxies of Hubble type E–Sd. The green dotted-dashed line and shaded region indicate the median and 1σ limits of the $\beta_{V,0}$-values for galaxies in each Hubble type bin (see Figure 3.9). The thick brown dashed line indicates the $\beta_{V,0}$ values derived from the median combined $\langle\beta_V\rangle$-profiles for each Hubble type. Horizontal lines show the expected model values from Chapter 2 (K17), where the colors and line styles correspond to those from Figure 2.24. Mass-weighted metallicities for models at a redshift of $z = 0$ are shown above or below each line. $\beta_{V,0}$-values with no metallicity evolution are plotted as light gray dotted lines. Mass-weighted metallicity ranges for each Hubble type from GD15 (see their Figure 11) match well to the mass-weighted metallicity range, where $\beta_{V,0}$-values are distributed throughout the green shaded region.

bulges agree better with what was published in GD15 than for the ones with large bulges. The steeper A_V-profile slopes are the result of the red-bulge population in their galaxy centers, which increases the inferred extinction values. Before using the β_V-method for spiral galaxies with large bulges, these larger gradients need to be taken into account.

3. *The K17 model holds for nearby galaxies.* I published the intrinsic flux ratios of various visible–NIR filters ($\beta_{\lambda,0}$) with respect to the L filter (∼3.5μm) as a function of redshift for galaxies having SFHs characteristic of early-types (E and S0), spirals (Sa–Sbc), and late-types (Sbc–Sd) (Kim *et al.*, 2017, Chapter 2 in this dissertation). I approximated metallicity evolution by stacking the SEDs of SSPs as a function of SFH, which is different for each SFH type. Figure 3.12 shows the $\beta_{V,0}$-values at a redshift of $z \simeq 0$ from the K17 model, as well as the observed data from this Chapter. The model values are indicated by colored lines for early-types, spirals, and late-types with metallicity offsets: $Z(z{=}0) = 2.5$, 1.0, and 0.4 $Z_\odot$ from bottom to top. K17 selected the metallicity offset values arbitrarily, matching the metallicities of the empirical SED model of SSP. Metallitiicy offsets result in mass-weighted metallicities, $\langle Z \rangle_m$ at $z = 0$, as indicated above or below each line (see Figure 2.24). The gray dotted lines are $\beta_{V,0}$-values without any metallicity evolution taken into account. The $\beta_{V,0}$-values derived through A_V-profile matching are plotted on top of the horizontal lines from Chapter 2. The thick green dashed line and the corresponding green shaded region represent the median and 1σ ranges of the $\beta_{V,0}$-values derived from the β_V-profiles of individual galaxies in each Hubble type bin, respectively (see Figure 3.9). The thick brown dashed line shows the $\beta_{V,0}$-values derived from the average β_V-profile of all galaxies in each Hubble type bin. The $\beta_{V,0}$-values fall within a range of observed $\langle Z \rangle_m$ from GD15 of $1.3^{+0.7}_{-0.5}$, $1.2^{+0.6}_{-0.4}$, $0.9^{+0.5}_{-0.4}$, $0.8^{+0.4}_{-0.3}$, $0.6^{+0.4}_{-0.2}$, $0.4^{+0.3}_{-0.2}$, and $0.3^{+0.3}_{-0.1}\,Z\odot$ for the E, S0, Sa, Sb, Sbc, Sc, and Sd types, respectively (see Figure 11 of GD15).

The $\beta_{V,0}$-values from Chapter 2 were confirmed by matching the $\beta_{V,0}$-values at a redshift of $z \simeq 0$ to the observations. I derived $\beta_{V,0}$-values using empirical models that were developed based upon observations of galaxies including a sample at redshifts $z \gtrsim 2$. The model at a redshift of $z \simeq 0$ is the end-product of an accumulation of SEDs of SSPs as a function of SFH and metallicity evolution. Any discrepancy at the intermediate redshift would have resulted in the mismatch at redshift $z \simeq 0$. Therefore, with *HST* and future *JWST* data, I expect the β_V-method would work for galaxies at a redshift $z \lesssim 2$ with a careful classification of galaxy morphology and metallicities.

JWST/NIRCam's images are Nyquist sampled at 4 μm with $0''.0647$ pixels in the long-wavelength arm (Beichman *et al.*, 2012). PSF FWHM ~2 pixels correspond to $\sim 0''.13$ which is comparable to the one of *HST* at 1 μm. The scale corresponds to ~440, 600, and 720 pc at redshifts of $z = 0.2$, 0.3, and 0.4, respectively. At $z \sim 0.3$, a square with a side of PSF FWHM size becomes about ten times the size of the giant molecular clouds (~200 pc). The same galaxies at these redshifts observed with both *HST* and *JWST* would look similar to galaxies observed at a redshift of $z = 0.02$ by *Spitzer* at IRAC's 3.6 μm resolution, such as NGC 1016, IC 2239, NGC 2832, NGC 2892, and NGC 2937 from my sample. The large variation not only inside a galaxy but also global pixel-to-pixel values of the β_V due to the stochasticity of individual stellar population, that we have seen in Figure 3.5, would subside at the redshift larger than $z > 0.3$ in the galaxy survey of the *HST* and *JWST*.

In addition to dust correction via the β_V-map, the β_V-method may also serve as a detection tool for AGN and bluer/redder coherent features. Because AGN are typically surrounded by thick dust tori, central β_V-values lower than the rest of the galaxy could serve as an indication of AGN activity. This method was able to find previously known features, such as resonance rings and H ii regions, and also an outflow-like feature that has not been observed before.

I conclude that the β_V-method can serve as a simple dust-correction method for large galaxy surveys in the redshift range $0.3 < z < 2$, where *JWST* observations will sample rest-frame ~3.5 μm, and *HST* observations sample rest-frame visible wavelengths. This will become particularly useful when no, or only a limited number of, other broadband images are available.

Chapter 4

REVIEW AND FUTURE WORK

4.1 Review

My goal of this dissertation was to model the $\beta_{\lambda,0}$ values as accurate as possible and evaluate the uncertainties of the β_λ method.

To model the $\beta_{\lambda,0}$ values, I stacked SSP SEDs as a function of 1000 SFHs and 6 metallicities for each of three galaxy types. Each SFH consists of randomly-generated multiple exponentially-declining star-forming episodes. Six metallicity tracks evolve with different slopes for each SFH type. The throughput curves of each filter pair then convolved to calculate the $\beta_{\lambda,0}$ values at a certain redshift.

To evaluate the $\beta_{V,0}$ values at redshift $z \simeq 0$, I derived those by measuring the β_V profiles of ~250 nearby galaxies using the SDSS and the *Spitzer* mosaics and using the A_V profiles from the literature.

I found an agreement between metallicity ranges of the model $\beta_{V,0}$ values which are close to the derived values and those obtained directly from SED fitting of nearby galaxies. Figure 4.1 shows the mass-weighted metallicities of nearby 300 galaxies from González Delgado *et al.* (2015), and on top of those, the mass-weighted metallicities of stacked SEDs which resulted in the best fit between the $\beta_{V,0}$ values at a redshift $z = 0$ of the SEDs and the calculated $\beta_{V,0}$ values from the observed β_V profiles and the A_V profiles are also depicted (see also Figure 3.12). Solid dots and vertical error bars are average mass-weighted metallicities at the half-light radii for each Hubble type from González Delgado *et al.* (2015). A red thick rugged line is the

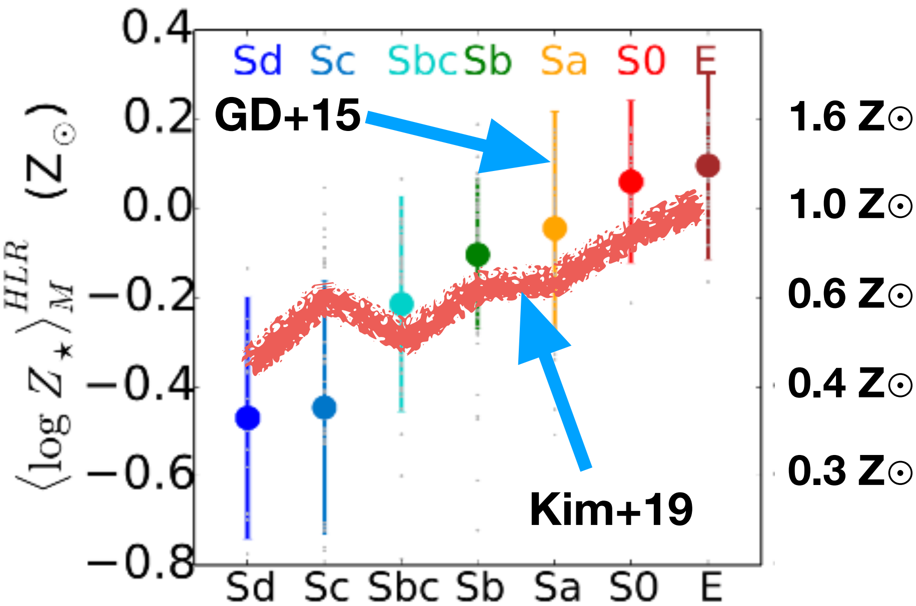

Figure 4.1: Comparison between the mass-weighted metallicities of nearby 300 galaxies from the literature and my model values of $\beta_{V,0}$ best fit to the observed β_V profiles associated with the A_V profiles (see Figure 3.12). Solid dots and vertical error bars are average mass-weighted metallicities at the half-light radii for each Hubble type from González Delgado *et al.* (2015). A red thick rugged line is the result of fitting the β_V profiles to the model $\beta_{V,0}$ values associated with the A_V profiles from González Delgado *et al.* (2015). Two results agree with each other within the uncertainty. This validates my model of the $\beta_{\lambda,0}$ values.

result of fitting the β_V profiles to the model $\beta_{V,0}$ values associated with the A_V profiles from González Delgado *et al.* (2015). Two results agree with each other within the uncertainty.

I conclude my model of the $\beta_{\lambda,0}$ values are valid within the uncertainties of $\sim$30% at a redshift $z = 0$. The uncertainties are from 1σ scatter in β_V around the average both within a galaxy and each morphological type bin is $\sim$20%. These result in a $\sim$0.4 mag scatter in A_V.

Figure 4.2 is flow-chart guidance for users of the β_λ method. A user needs to derive morphological types, redshifts, and metallicities of galaxies to determine the $\beta_{\lambda,0}$ values in Figures 2.16–2.22. Galaxy morphologies assist in the selection of an appropriate SFH among SFH3, SFH4, and SFH5. Redshifts could be derived from the fitting of photometric measurements or the galaxy size evolution (e.g., Furlong *et al.*, 2017). Redshifts are crucial to the choice of a filter pair which is nearest to the rest-frame λ and $\sim$3.5μm for using the $\beta_{\lambda,0}$ values for correcting for extinction by dust. I recommend using the $\beta_{\lambda,0}$ values with the metallicity offsets between $Z(z=0)=0.05$ and 0.02 because their $\beta_{V,0}$ values agreed with the observation at $z\simeq 0$ in Figure 3.12.

4.2 Future Work

In Chapter 3, the β_V method on 257 nearby galaxies resulted in $\sim$0.4 mag uncertainties in the A_V values with prior knowledge of morphological types and redshifts. At a redshift range $0.3 < z < 2$, the uncertainties in the A_V values would be increased from the additional uncertainties in morphological types and redshifts. Future work on how to minimize the uncertainties by choosing right $\beta_{\lambda,0}$ values would be beneficial.

In the following sections, I will briefly highlight the prospects of some lines of future investigation into new questions that have arisen.

4.2.1 Shallow Gradients in $\beta_{V,0}$ Profiles?

In Chapter 2, I found that the $\beta_{V,0}$ profile varies <20% across the radius $0 < R < 2.5\times$half-light radius (HLR) of elliptical galaxies in Figure 2.25. Opposite signs between age and metallicity gradients could have leveled off the $\beta_{V,0}$ profiles (e.g., the ones of elliptical galaxies in Kim and Im, 2013). Similar A_V profiles in Figure 3.7–3.8 between the IFU-SED-fitting result and the β_V method also suggest flat $\beta_{V,0}$ profiles, because any gradients in the $\beta_{V,0}$ profiles would have resulted disagreements. In other words, the similarity in Figure 3.7–3.8 is telling us that the variations of the β_V profiles are most significantly originated from the dust extinction, except Sa and Sb types with big bulges. I propose research focusing on the gradients of the

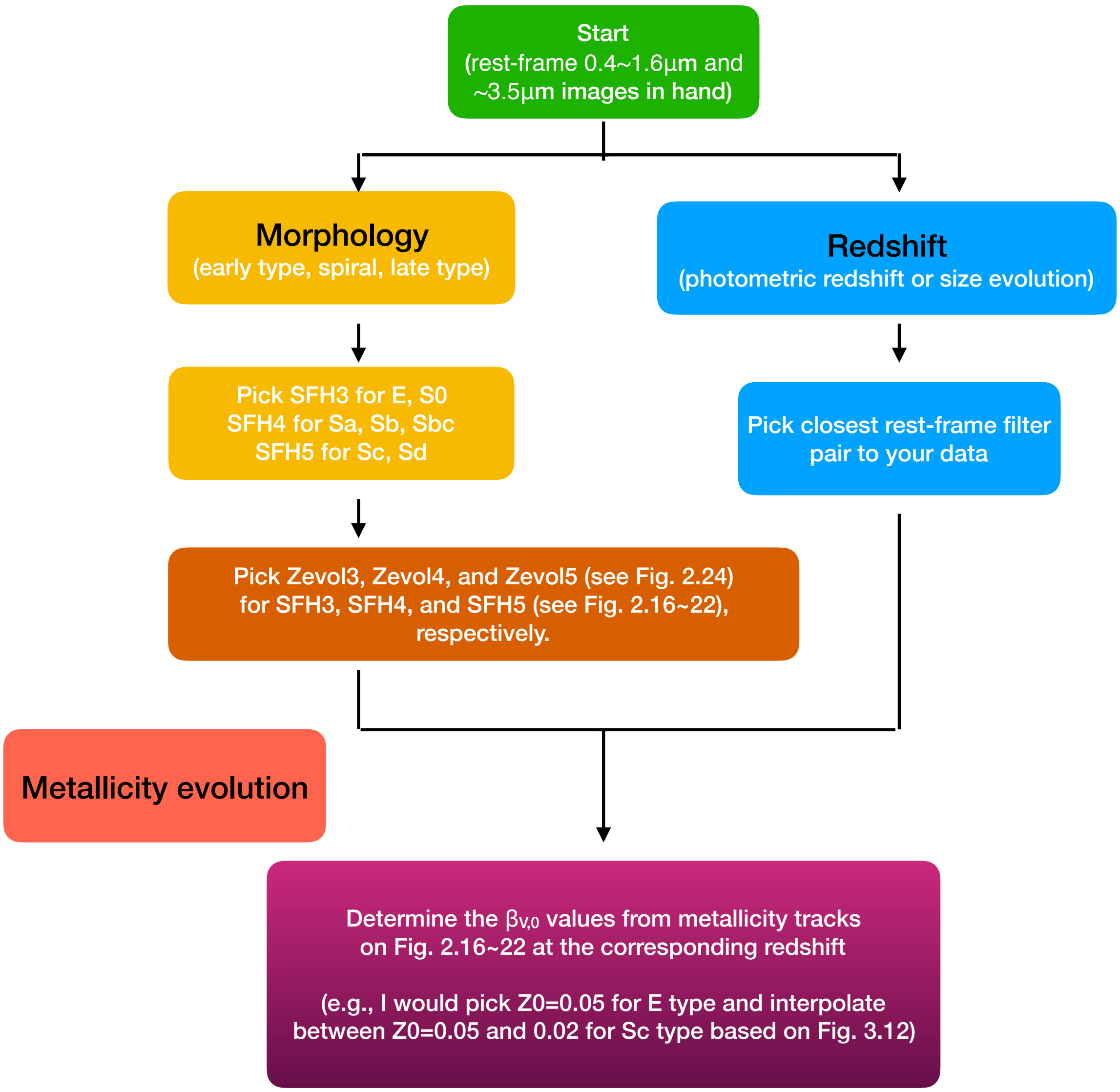

Figure 4.2: Flow-chart guidance for users of the β_V method. A user needs to obtain morphological types, redshifts, and metallicities of galaxies to determine the $\beta_{\lambda,0}$ values in Figures 2.16–2.22. Morphological types are used to select either SFH3, SFH4, or SFH5. Redshifts are used to select a filter pair that has effective rest-frame wavelengths closest to λ and $\sim$3.5μm. Comparison between mass-weighted metallicities of my model and those of nearby galaxies in Figure 3.12 suggests that the evolutionary tracks with metallicity offsets between $Z(z=0) = 0.05 \sim 0.02$ are suitable.

intrinsic colors after the correction for the extinction by interstellar dust. Shallow gradients in the $\beta_{V,0}$ profiles would make the β_V method a more powerful dust-correction method.

4.2.2 Correlation between A_V and GALFIT Residual Map

Laurikainen *et al.* (2010, 2011) used the residual images after subtracting the bulge and disk model functions to identify the structural components: bars, ovals, and lenses. Rothberg and Joseph (2004) used the residual images created by subtracting a galaxy model generated from IRAF tasks ELLIPSE and BMODEL from the actual data image for identifying large-scale fine merger remnants structure.

My residual images after subtracting the bulge and disc models from GALFIT from the 3.6 μm images (see Appendix D) seem to coincide with high-extinction regions in the A_V map. Especially, spiral arms, where stars are formed out of thick dust clouds so distinctive on the A_V map, are not symmetric so are usually remained on the residual images. More quantitative analyses into the correlation between the residual images and the dust extinction maps could be an insightful study for the asymmetric distribution of the insterstellar dust.

REFERENCES

Allamandola, L. J., A. G. G. M. Tielens and J. R. Barker, "Interstellar Polycyclic Aromatic Hydrocarbons: The Infrared Emission Bands, the Excitation/Emission Mechanism, and the Astrophysical Implications", Astrophysical Journal, Supplement **71**, 733 (1989).

Anders, P. and U. Fritze-von Alvensleben, "Spectral and photometric evolution of young stellar populations: The impact of gaseous emission at various metallicities", Astronomy and Astrophysics **401**, 1063–1070 (2003).

Appleton, P. N. and P. M. Marcum, "Infrared Observations of the Seyfert Ring Galaxy NGC 985", Astrophysical Journal **417**, 90 (1993).

Avila, R. *et al.*, *ACS Instrumend Handbook, Version 14.0* (Baltimore, MD: STScI, 2015), URL https://hst-docs.stsci.edu/display/ACSIHB/.

Balcells, M., "Two Tails in NGC 3656 and the Major Merger Origin of Shell and Minor-Axis Dust Lane Elliptical Galaxies", Astrophysical Journal, Letters **486**, L87–L90 (1997).

Baldwin, J. A., M. M. Phillips and R. Terlevich, "Classification parameters for the emission-line spectra of extragalactic objects", Publication of the ASP **93**, 5–19 (1981).

Behroozi, P. S., R. H. Wechsler and C. Conroy, "The Average Star Formation Histories of Galaxies in Dark Matter Halos from z = 0-8", Astrophysical Journal **770**, 57 (2013).

Beichman, C. A., M. Rieke, D. Eisenstein, T. P. Greene, J. Krist, D. McCarthy, M. Meyer and J. Stansberry, "Science opportunities with the near-IR camera (NIRCam) on the James Webb Space Telescope (JWST)", in "Space Telescopes and Instrumentation 2012: Optical, Infrared, and Millimeter Wave", edited by M. C. Clampin, G. G. Fazio, H. A. MacEwen and J. M. O. Jr., vol. 8442, pp. 973 – 983, International Society for Optics and Photonics (SPIE, 2012), URL https://doi.org/10.1117/12.925447.

Bell, E. F., K. D. Gordon, J. Kennicutt, Robert C. and D. Zaritsky, "The Effects of Dust in Simple Environments: Large Magellanic Cloud H II Regions", Astrophysical Journal **565**, 2, 994–1010 (2002).

Bertin, E. and S. Arnouts, "SExtractor: Software for source extraction.", Astronomy and Astrophysics, Supplement **117**, 393–404 (1996).

Bessell, M. S., "UBVRI photometry II: the Cousins VRI system, its temperature and absolute flux calibration, and relevance for two-dimensional photometry.", Publication of the ASP **91**, 589–607 (1979).

Bessell, M. S., "UBVRI passbands.", Publication of the ASP **102**, 1181–1199 (1990).

Bessell, M. S., "Standard Photometric Systems", Annual Review of Astron and Astrophys **43**, 1, 293–336 (2005).

Bessell, M. S. and J. M. Brett, "JHKLM Photometry: Standard Systems, Passbands, and Intrinsic Colors", Publication of the ASP **100**, 1134 (1988).

Blanton, M. R., J. Dalcanton, D. Eisenstein, J. Loveday, M. A. Strauss, M. SubbaRao, D. H. Weinberg, J. E. Anderson, Jr., J. Annis, N. A. Bahcall, M. Bernardi, J. Brinkmann, R. J. Brunner, S. Burles, L. Carey, F. J. Castander, A. J. Connolly, I. Csabai, M. Doi, D. Finkbeiner, S. Friedman, J. A. Frieman, M. Fukugita, J. E. Gunn, G. S. Hennessy, R. B. Hindsley, D. W. Hogg, T. Ichikawa, Ž. Ivezić, S. Kent, G. R. Knapp, D. Q. Lamb, R. F. Leger, D. C. Long, R. H. Lupton, T. A. McKay, A. Meiksin, A. Merelli, J. A. Munn, V. Narayanan, M. Newcomb, R. C. Nichol, S. Okamura, R. Owen, J. R. Pier, A. Pope, M. Postman, T. Quinn, C. M. Rockosi, D. J. Schlegel, D. P. Schneider, K. Shimasaku, W. A. Siegmund, S. Smee, Y. Snir, C. Stoughton, C. Stubbs, A. S. Szalay, G. P. Szokoly, A. R. Thakar, C. Tremonti, D. L. Tucker, A. Uomoto, D. Vanden Berk, M. S. Vogeley, P. Waddell, B. Yanny, N. Yasuda and D. G. York, "The Luminosity Function of Galaxies in SDSS Commissioning Data", Astronomical Journal **121**, 2358–2380 (2001).

Boissier, S., A. Boselli, V. Buat, J. Donas and B. Milliard, "The radial extinction profiles of late-type galaxies.", Astronomy and Astrophysics **424**, 465–476 (2004).

Boselli, A., G. Gavazzi and G. Sanvito, "UV to radio centimetric spectral energy distributions of optically-selected late-type galaxies in the Virgo cluster", Astronomy and Astrophysics **402**, 37–51 (2003).

Bouquin, A. Y. K., A. Gil de Paz, J. C. Muñoz-Mateos, S. Boissier, K. Sheth, D. Zaritsky, R. F. Peletier, J. H. Knapen and J. Gallego, "The GALEX/S^{4}G Surface Brightness and Color Profiles Catalog. I. Surface Photometry and Color Gradients of Galaxies", Astrophysical Journal, Supplement **234**, 18 (2018).

Brown, M. J. I., J. Moustakas, J.-D. T. Smith, E. da Cunha, T. H. Jarrett, M. Imanishi, L. Armus, B. R. Brandl and J. E. G. Peek, "An Atlas of Galaxy Spectral Energy Distributions from the Ultraviolet to the Mid-infrared", Astrophysical Journal, Supplement **212**, 18 (2014).

Bruzual, G. and S. Charlot, "Stellar population synthesis at the resolution of 2003", Monthly Notices of the RAS **344**, 1000–1028 (2003).

Buat, V., J. Iglesias-Páramo, M. Seibert, D. Burgarella, S. Charlot, D. C. Martin, C. K. Xu, T. M. Heckman, S. Boissier, A. Boselli, T. Barlow, L. Bianchi, Y. I. Byun, J. Donas, K. Forster, P. G. Friedman, P. Jelinski, Y. W. Lee, B. F. Madore, R. Malina, B. Milliard, P. Morissey, S. Neff, M. Rich, D. Schiminovitch, O. Siegmund, T. Small, A. S. Szalay, B. Welsh and T. K. Wyder, "Dust Attenuation in the Nearby Universe: A Comparison between Galaxies Selected in the Ultraviolet and in the Far-Infrared", Astrophysical Journal, Letters **619**, 1, L51–L54 (2005).

Buat, V. and C. Xu, “Star formation and dust extinction in disk galaxies. Comparison between the UV non-ionizing and the FIR emissions”, Astronomy and Astrophysics **306**, 61 (1996).

Buta, R. J., H. G. Corwin and S. C. Odewahn, *The de Vaucouleurs Atlas of Galaxies* (2007).

Calzetti, D., L. Armus, R. C. Bohlin, A. L. Kinney, J. Koornneef and T. Storchi-Bergmann, “The Dust Content and Opacity of Actively Star-forming Galaxies”, Astrophysical Journal **533**, 2, 682–695 (2000).

Calzetti, D., J. Kennicutt, R. C., L. Bianchi, D. A. Thilker, D. A. Dale, C. W. Engelbracht, C. Leitherer, M. J. Meyer, M. L. Sosey, M. Mutchler, M. W. Regan, M. D. Thornley, L. Armus, G. J. Bendo, S. Boissier, A. Boselli, B. T. Draine, K. D. Gordon, G. Helou, D. J. Hollenbach, L. Kewley, B. F. Madore, D. C. Martin, E. J. Murphy, G. H. Rieke, M. J. Rieke, H. Roussel, K. Sheth, J. D. Smith, F. Walter, B. A. White, S. Yi, N. Z. Scoville, M. Polletta and D. Lindler, “Star Formation in NGC 5194 (M51a): The Panchromatic View from GALEX to Spitzer”, Astrophysical Journal **633**, 2, 871–893 (2005).

Calzetti, D., A. L. Kinney and T. Storchi-Bergmann, “Dust Extinction of the Stellar Continua in Starburst Galaxies: The Ultraviolet and Optical Extinction Law”, Astrophysical Journal **429**, 582 (1994).

Caplan, J. and L. Deharveng, “Absolute H-alpha and H-beta photometry of LMC HII regions.”, Astronomy and Astrophysics, Supplement **62**, 63–104 (1985).

Caplan, J. and L. Deharveng, “Extinction and reddening of H II regions in the Large Magellanic Cloud.”, Astronomy and Astrophysics **155**, 297–313 (1986).

Cerviño, M. and J. M. Mas-Hesse, “Metallicity effects in star-forming regions.”, Astronomy and Astrophysics **284**, 749–763 (1994).

Chabrier, G., “Galactic Stellar and Substellar Initial Mass Function”, Publication of the ASP **115**, 809, 763–795 (2003).

Charbonnel, C., G. Meynet, A. Maeder, G. Schaller and D. Schaerer, “Grids of stellar models. III. From 0.8 to 120 Msolar at Z=0.004”, Astronomy and Astrophysics, Supplement **101**, 415 (1993).

Charlot, S. and S. M. Fall, “A Simple Model for the Absorption of Starlight by Dust in Galaxies”, Astrophysical Journal **539**, 2, 718–731 (2000).

Cohen, M., W. A. Wheaton and S. T. Megeath, “Spectral Irradiance Calibration in the Infrared. XIV. The Absolute Calibration of 2MASS”, Astronomical Journal **126**, 2, 1090–1096 (2003).

Colina, L. and R. C. Bohlin, “Absolute Flux Calibration of Optical Spectrophotometric Standard Stars”, Astronomical Journal **108**, 1931 (1994).

Comerón, S., H. Salo, E. Laurikainen, J. H. Knapen, R. J. Buta, M. Herrera-Endoqui, J. Laine, B. W. Holwerda, K. Sheth, M. W. Regan, J. L. Hinz, J. C. Muñoz-Mateos, A. Gil de Paz, K. Menéndez-Delmestre, M. Seibert, T. Mizusawa, T. Kim, S. Erroz-Ferrer, D. A. Gadotti, E. Athanassoula, A. Bosma and L. C. Ho, "ARRAKIS: atlas of resonance rings as known in the S^4G", Astronomy and Astrophysics **562**, A121 (2014).

Conroy, C., "Modeling the panchromatic spectral energy distributions of galaxies", Annual Review of Astronomy and Astrophysics **51**, 1, 393–455, URL https://doi.org/10.1146/annurev-astro-082812-141017 (2013).

Conselice, C. J., N. A. Grogin, S. Jogee, R. A. Lucas, T. Dahlen, D. de Mello, J. P. Gardner, B. Mobasher and S. Ravindranath, "Observing the Formation of the Hubble Sequence in the Great Observatories Origins Deep Survey", Astrophysical Journal, Letters **600**, 2, L139–L142 (2004).

Conselice, C. J., A. Wilkinson, K. Duncan and A. Mortlock, "THE EVOLUTION OF GALAXY NUMBER DENSITY AT z less 8 AND ITS IMPLICATIONS", The Astrophysical Journal **830**, 2, 83, URL https://doi.org/10.3847%2F0004-637x%2F830%2F2%2F83 (2016).

da Silva, R. L., M. Fumagalli and M. Krumholz, "SLUG—Stochastically Lighting Up Galaxies. I. Methods and Validating Tests", Astrophysical Journal **745**, 2, 145 (2012).

Dale, D. A., G. Helou, A. Contursi, N. A. Silbermann and S. Kolhatkar, "The Infrared Spectral Energy Distribution of Normal Star-forming Galaxies", Astrophysical Journal **549**, 1, 215–227 (2001).

de Jong, R. S., "Near-infrared and optical broadband surface photometry of 86 face-on disk dominated galaxies. IV. Using color profiles to study stellar and dust content of galaxies.", Astronomy and Astrophysics **313**, 377–395 (1996).

de Vaucouleurs, G., "Classification and Morphology of External Galaxies.", Handbuch der Physik **53**, 275 (1959).

de Vaucouleurs, G., A. de Vaucouleurs, H. G. Corwin, Jr., R. J. Buta, G. Paturel and P. Fouqué, *Third Reference Catalogue of Bright Galaxies. Volume I: Explanations and references. Volume II: Data for galaxies between* 0^h *and* 12^h*. Volume III: Data for galaxies between* 12^h *and* 24^h. (P.. Springer, New York, NY (USA), 1991).

Deo, R. P., D. M. Crenshaw and S. B. Kraemer, "The Host Galaxies of Narrow-Line Seyfert 1 Galaxies: Nuclear Dust Morphology and Starburst Rings", Astronomical Journal **132**, 1, 321–346 (2006).

Dickinson, M., M. Giavalisco and GOODS Team, "The Great Observatories Origins Deep Survey", in "The Mass of Galaxies at Low and High Redshift", edited by R. Bender and A. Renzini, p. 324 (2003).

Dressel, L. *et al.*, *Wide Field Camera 3 Instrument Handbook, Version 7.0* (Baltimore, MD: STScI, 2015), URL https://hst-docs.stsci.edu/display/WFC3IHB.

Driver, S. P., C. C. Popescu, R. J. Tuffs, A. W. Graham, J. Liske and I. Baldry, "The Energy Output of the Universe from 0.1 to 1000 μm", Astrophysical Journal, Letters **678**, 2, L101 (2008).

Elmegreen, D. M., "An optical analysis of dust complexes in spiral galaxies", Astrophysical Journal, Supplement **43**, 37–56 (1980).

Elsasser, W. M., "Far Infrared Absorption of Atmospheric Water Vapor", Astrophysical Journal **87**, 497 (1938).

Eskridge, P. B. and R. W. Pogge, "H II Region Abundances in the Polar Ring of NGC 2685", Astrophysical Journal **486**, 259–267 (1997).

Fazio, G. G., J. L. Hora, L. E. Allen, M. L. N. Ashby, P. Barmby, L. K. Deutsch, J.-S. Huang, S. Kleiner, M. Marengo, S. T. Megeath, G. J. Melnick, M. A. Pahre, B. M. Patten, J. Polizotti, H. A. Smith, R. S. Taylor, Z. Wang, S. P. Willner, W. F. Hoffmann, J. L. Pipher, W. J. Forrest, C. W. McMurty, C. R. McCreight, M. E. McKelvey, R. E. McMurray, D. G. Koch, S. H. Moseley, R. G. Arendt, J. E. Mentzell, C. T. Marx, P. Losch, P. Mayman, W. Eichhorn, D. Krebs, M. Jhabvala, D. Y. Gezari, D. J. Fixsen, J. Flores, K. Shakoorzadeh, R. Jungo, C. Hakun, L. Workman, G. Karpati, R. Kichak, R. Whitley, S. Mann, E. V. Tollestrup, P. Eisenhardt, D. Stern, V. Gorjian, B. Bhattacharya, S. Carey, B. O. Nelson, W. J. Glaccum, M. Lacy, P. J. Lowrance, S. Laine, W. T. Reach, J. A. Stauffer, J. A. Surace, G. Wilson, E. L. Wright, A. Hoffman, G. Domingo and M. Cohen, "The Infrared Array Camera (IRAC) for the Spitzer Space Telescope", Astrophysical Journal, Supplement **154**, 10–17 (2004).

Fioc, M. and B. Rocca-Volmerange, "PEGASE: a UV to NIR spectral evolution model of galaxies. Application to the calibration of bright galaxy counts.", Astronomy and Astrophysics **500**, 507–519 (1997).

Fitzpatrick, E. L., "Correcting for the Effects of Interstellar Extinction", Publication of the ASP **111**, 755, 63–75 (1999).

Ford, H. C., M. Clampin, G. F. Hartig, G. D. Illingworth, M. Sirianni, A. R. Martel, G. R. Meurer, W. J. McCann, P. C. Sullivan, F. Bartko, N. Benitez, J. Blakeslee, R. Bouwens, T. Broadhurst, R. A. Brown, C. J. Burrows, D. Campbell, E. S. Cheng, P. D. Feldman, M. Franx, D. A. Golimowski, C. Gronwall, R. A. Kimble, J. E. Krist, M. P. Lesser, D. Magee, G. Miley, M. Postman, M. D. Rafal, P. Rosati, W. B. Sparks, H. D. Tran, Z. I. Tsvetanov, P. Volmer, R. L. White and R. A. Woodruff, "Overview of the Advanced Camera for Surveys on-orbit performance", in "Proceedings of the SPIE ", edited by J. C. Blades and O. H. W. Siegmund, vol. 4854 of *Society of Photo-Optical Instrumentation Engineers (SPIE) Conference Series*, pp. 81–94 (2003).

Furlong, M., R. G. Bower, R. A. Crain, J. Schaye, T. Theuns, J. W. Trayford, Y. Qu, M. Schaller, M. Berthet and J. C. Helly, “Size evolution of normal and compact galaxies in the EAGLE simulation”, Monthly Notices of the RAS **465**, 1, 722–738 (2017).

Galliano, F., S. Hony, J. P. Bernard, C. Bot, S. C. Madden, J. Roman-Duval, M. Galametz, A. Li, M. Meixner, C. W. Engelbracht, V. Lebouteiller, K. Misselt, E. Montiel, P. Panuzzo, W. T. Reach and R. Skibba, “Non-standard grain properties, dark gas reservoir, and extended submillimeter excess, probed by Herschel in the Large Magellanic Cloud”, Astronomy and Astrophysics **536**, A88 (2011).

Gardner, J. P., J. C. Mather, M. Clampin, R. Doyon, M. A. Greenhouse, H. B. Hammel, J. B. Hutchings, P. Jakobsen, S. J. Lilly, K. S. Long, J. I. Lunine, M. J. McCaughrean, M. Mountain, J. Nella, G. H. Rieke, M. J. Rieke, H.-W. Rix, E. P. Smith, G. Sonneborn, M. Stiavelli, H. S. Stockman, R. A. Windhorst and G. S. Wright, “The James Webb Space Telescope”, Space Science Reviews **123**, 485–606 (2006).

Gerola, H. and P. E. Seiden, “Stochastic star formation and spiral structure of galaxies.”, Astrophysical Journal **223**, 129–139 (1978).

Giavalisco, M., H. C. Ferguson, A. M. Koekemoer, M. Dickinson, D. M. Alexander, F. E. Bauer, J. Bergeron, C. Biagetti, W. N. Brandt, S. Casertano, C. Cesarsky, E. Chatzichristou, C. Conselice, S. Cristiani, L. Da Costa, T. Dahlen, D. de Mello, P. Eisenhardt, T. Erben, S. M. Fall, C. Fassnacht, R. Fosbury, A. Fruchter, J. P. Gardner, N. Grogin, R. N. Hook, A. E. Hornschemeier, R. Idzi, S. Jogee, C. Kretchmer, V. Laidler, K. S. Lee, M. Livio, R. Lucas, P. Madau, B. Mobasher, L. A. Moustakas, M. Nonino, P. Padovani, C. Papovich, Y. Park, S. Ravindranath, A. Renzini, M. Richardson, A. Riess, P. Rosati, M. Schirmer, E. Schreier, R. S. Somerville, H. Spinrad, D. Stern, M. Stiavelli, L. Strolger, C. M. Urry, B. Vandame, R. Williams and C. Wolf, “The Great Observatories Origins Deep Survey: Initial Results from Optical and Near-Infrared Imaging”, Astrophysical Journal, Letters **600**, 2, L93–L98 (2004).

Gil de Paz, A., B. F. Madore, K. Noeske, L. M. Cairós, P. Papaderos and S. A. Silich, “Discovery of a Double Ring in the Dwarf Galaxy Markarian 409”, Astrophysical Journal **596**, L179–L182 (2003).

Girardi, L., A. Bressan, G. Bertelli and C. Chiosi, “Evolutionary tracks and isochrones for low- and intermediate-mass stars: From 0.15 to 7 M_{sun}, and from Z=0.0004 to 0.03”, Astronomy and Astrophysics, Supplement **141**, 371–383 (2000).

González Delgado, R. M., R. García-Benito, E. Pérez, R. Cid Fernandes, A. L. de Amorim, C. Cortijo-Ferrero, E. A. D. Lacerda, R. López Fernández, N. Vale-Asari, S. F. Sánchez, M. Mollá, T. Ruiz-Lara, P. Sánchez-Blázquez, C. J. Walcher, J. Alves, J. A. L. Aguerri, S. Bekeraité, J. Bland-Hawthorn, L. Galbany, A. Gallazzi, B. Husemann, J. Iglesias-Páramo, V. Kalinova, A. R. López-Sánchez, R. A. Marino, I. Márquez, J. Masegosa, D. Mast,

J. Méndez-Abreu, A. Mendoza, A. del Olmo, I. Pérez, A. Quirrenbach and S. Zibetti, “The CALIFA survey across the Hubble sequence. Spatially resolved stellar population properties in galaxies”, Astronomy and Astrophysics **581**, A103 (2015).

González Delgado, R. M., E. Pérez, R. Cid Fernandes, R. García-Benito, A. L. de Amorim, S. F. Sánchez, B. Husemann, C. Cortijo-Ferrero, R. López Fernández, P. Sánchez-Blázquez, S. Bekeraite, C. J. Walcher, J. Falcón-Barroso, A. Gallazzi, G. van de Ven, J. Alves, J. Bland-Hawthorn, R. C. Kennicutt, D. Kupko, M. Lyubenova, D. Mast, M. Mollá, R. A. Marino, A. Quirrenbach, J. M. Vílchez and L. Wisotzki, “The star formation history of CALIFA galaxies: Radial structures”, Astronomy and Astrophysics **562**, A47 (2014).

Gordon, K. D., G. C. Clayton, K. A. Misselt, A. U. Land olt and M. J. Wolff, “A Quantitative Comparison of the Small Magellanic Cloud, Large Magellanic Cloud, and Milky Way Ultraviolet to Near-Infrared Extinction Curves”, Astrophysical Journal **594**, 1, 279–293 (2003).

Gott, J. R., M. Jurić, D. Schlegel, F. Hoyle, M. Vogeley, M. Tegmark, N. Bahcall and J. Brinkmann, “A map of the universe”, The Astrophysical Journal **624**, 2, 463–484, URL https://doi.org/10.1086%2F428890 (2005).

Grogin, N. A., D. D. Kocevski, S. M. Faber, H. C. Ferguson, A. M. Koekemoer, A. G. Riess, V. Acquaviva, D. M. Alexander, O. Almaini, M. L. N. Ashby, M. Barden, E. F. Bell, F. Bournaud, T. M. Brown, K. I. Caputi, S. Casertano, P. Cassata, M. Castellano, P. Challis, R.-R. Chary, E. Cheung, M. Cirasuolo, C. J. Conselice, A. Roshan Cooray, D. J. Croton, E. Daddi, T. Dahlen, R. Davé, D. F. de Mello, A. Dekel, M. Dickinson, T. Dolch, J. L. Donley, J. S. Dunlop, A. A. Dutton, D. Elbaz, G. G. Fazio, A. V. Filippenko, S. L. Finkelstein, A. Fontana, J. P. Gardner, P. M. Garnavich, E. Gawiser, M. Giavalisco, A. Grazian, Y. Guo, N. P. Hathi, B. Häussler, P. F. Hopkins, J.-S. Huang, K.-H. Huang, S. W. Jha, J. S. Kartaltepe, R. P. Kirshner, D. C. Koo, K. Lai, K.-S. Lee, W. Li, J. M. Lotz, R. A. Lucas, P. Madau, P. J. McCarthy, E. J. McGrath, D. H. McIntosh, R. J. McLure, B. Mobasher, L. A. Moustakas, M. Mozena, K. Nandra, J. A. Newman, S.-M. Niemi, K. G. Noeske, C. J. Papovich, L. Pentericci, A. Pope, J. R. Primack, A. Rajan, S. Ravindranath, N. A. Reddy, A. Renzini, H.-W. Rix, A. R. Robaina, S. A. Rodney, D. J. Rosario, P. Rosati, S. Salimbeni, C. Scarlata, B. Siana, L. Simard, J. Smidt, R. S. Somerville, H. Spinrad, A. N. Straughn, L.-G. Strolger, O. Telford, H. I. Teplitz, J. R. Trump, A. van der Wel, C. Villforth, R. H. Wechsler, B. J. Weiner, T. Wiklind, V. Wild, G. Wilson, S. Wuyts, H.-J. Yan and M. S. Yun, “CANDELS: The Cosmic Assembly Near-infrared Deep Extragalactic Legacy Survey”, Astrophysical Journal, Supplement **197**, 2, 35 (2011).

Gunn, J. E., M. Carr, C. Rockosi, M. Sekiguchi, K. Berry, B. Elms, E. de Haas, Ž. . Ivezić, G. Knapp, R. Lupton, G. Pauls, R. Simcoe, R. Hirsch, D. Sanford, S. Wang, D. York, F. Harris, J. Annis, L. Bartozek, W. Boroski, J. Bakken, M. Haldeman, S. Kent, S. Holm, D. Holmgren, D. Petravick, A. Prosapio, R. Rechenmacher, M. Doi, M. Fukugita, K. Shimasaku, N. Okada, C. Hull, W. Siegmund, E. Mannery, M. Blouke, D. Heidtman, D. Schneider,

R. Lucinio and J. Brinkman, “The Sloan Digital Sky Survey Photometric Camera”, Astronomical Journal **116**, 6, 3040–3081 (1998).

Hanisch, R. J., A. Farris, E. W. Greisen, W. D. Pence, B. M. Schlesinger, P. J. Teuben, R. W. Thompson and A. Warnock, III, “Definition of the Flexible Image Transport System (FITS)”, Astronomy and Astrophysics **376**, 359–380 (2001).

Hayes, D. S. and D. W. Latham, “A rediscussion of the atmospheric extinction and the absolute spectral-energy distribution of Vega.”, Astrophysical Journal **197**, 593–601 (1975).

Horner, S. D. and M. J. Rieke, “The near-infrared camera (NIRCam) for the James Webb Space Telescope (JWST)”, in “Proceedings of the SPIE ”, edited by J. C. Mather, vol. 5487 of *Society of Photo-Optical Instrumentation Engineers (SPIE) Conference Series*, pp. 628–634 (2004).

Hota, A., S.-C. Rey, Y. Kang, S. Kim, S. Matsushita and J. Chung, “NGC 3801 caught in the act: a post-merger star-forming early-type galaxy with AGN-jet feedback”, Monthly Notices of the RAS **422**, L38–L42 (2012).

Houck, J. R., T. L. Roellig, J. van Cleve, W. J. Forrest, T. Herter, C. R. Lawrence, K. Matthews, H. J. Reitsema, B. T. Soifer, D. M. Watson, D. Weedman, M. Huisjen, J. Troeltzsch, D. J. Barry, J. Bernard-Salas, C. E. Blacken, B. R. Brandl, V. Charmandaris, D. Devost, G. E. Gull, P. Hall, C. P. Henderson, S. J. U. Higdon, B. E. Pirger, J. Schoenwald, G. C. Sloan, K. I. Uchida, P. N. Appleton, L. Armus, M. J. Burgdorf, S. B. Fajardo-Acosta, C. J. Grillmair, J. G. Ingalls, P. W. Morris and H. I. Teplitz, “The Infrared Spectrograph (IRS) on the Spitzer Space Telescope”, Astrophysical Journal, Supplement **154**, 18–24 (2004).

Hoyos, C., A. Aragón-Salamanca, M. E. Gray, C. Wolf, D. T. Maltby, E. F. Bell, A. Böhm and S. Jogee, “Linking the structural properties of galaxies and their star formation histories with STAGES”, Monthly Notices of the RAS **455**, 1, 295–307 (2016).

Hubble, E. P., “Extragalactic nebulae.”, Astrophysical Journal **64**, 321–369 (1926).

Humason, M. L., N. U. Mayall and A. R. Sandage, “Redshifts and magnitudes of extragalactic nebulae.”, Astronomical Journal **61**, 97–162 (1956).

Jansen, R. A., D. Fabricant, M. Franx and N. Caldwell, “Spectrophotometry of Nearby Field Galaxies: The Data”, Astrophysical Journal, Supplement **126**, 2, 331–397 (2000a).

Jansen, R. A., M. Franx, D. Fabricant and N. Caldwell, “Surface Photometry of Nearby Field Galaxies: The Data”, Astrophysical Journal, Supplement **126**, 2, 271–329 (2000b).

Jarrett, T. H., M. Cohen, F. Masci, E. Wright, D. Stern, D. Benford, A. Blain, S. Carey, R. M. Cutri, P. Eisenhardt, C. Lonsdale, A. Mainzer, K. Marsh, D. Padgett, S. Petty, M. Ressler, M. Skrutskie, S. Stanford, J. Surace, C. W. Tsai, S. Wheelock and D. L. Yan, “The Spitzer-WISE Survey of the Ecliptic Poles”, Astrophysical Journal **735**, 2, 112 (2011).

Jester, S., D. P. Schneider, G. T. Richards, R. F. Green, M. Schmidt, P. B. Hall, M. A. Strauss, D. E. Vanden Berk, C. Stoughton, J. E. Gunn, J. Brinkmann, S. M. Kent, J. A. Smith, D. L. Tucker and B. Yanny, “The Sloan Digital Sky Survey View of the Palomar-Green Bright Quasar Survey”, Astronomical Journal **130**, 873–895 (2005).

Jiang, N., T. Wang, H. Zhou, X. Shu, C. Yang, L. Dou, L. Sun, X. Dong, S. Wang and H. Yang, “Discovery of an active intermediate-mass black hole candidate in the barred bulgeless galaxy NGC 3319”, The Astrophysical Journal **869**, 1, 49, URL https://doi.org/10.3847%2F1538-4357%2Faaeb90 (2018).

Kauffmann, G., T. M. Heckman, G. De Lucia, J. Brinchmann, S. Charlot, C. Tremonti, S. D. M. White and J. Brinkmann, “Gas infall and stochastic star formation in galaxies in the local universe”, Monthly Notices of the RAS **367**, 4, 1394–1408 (2006).

Kelvin, L. S., S. P. Driver, A. S. G. Robotham, E. N. Taylor, A. W. Graham, M. Alpaslan, I. Baldry, S. P. Bamford, A. E. Bauer, J. Bland -Hawthorn, M. J. I. Brown, M. Colless, C. J. Conselice, B. W. Holwerda, A. M. Hopkins, M. A. Lara-López, J. Liske, Á. R. López-Sánchez, J. Loveday, P. Norberg, S. Phillipps, C. C. Popescu, M. Prescott, A. E. Sansom and R. J. Tuffs, “Galaxy And Mass Assembly (GAMA): stellar mass functions by Hubble type”, Monthly Notices of the RAS **444**, 2, 1647–1659 (2014).

Kennicutt, R. C., Jr., C.-N. Hao, D. Calzetti, J. Moustakas, D. A. Dale, G. Bendo, C. W. Engelbracht, B. D. Johnson and J. C. Lee, “Dust-corrected Star Formation Rates of Galaxies. I. Combinations of Hα and Infrared Tracers”, Astrophysical Journal **703**, 1672–1695 (2009).

Kessler, M. F., J. A. Steinz, M. E. Anderegg, J. Clavel, G. Drechsel, P. Estaria, J. Faelker, J. R. Riedinger, A. Robson, B. G. Taylor and S. Ximenez de Ferran, “The Infrared Space Observatory (ISO) mission.”, Astronomy and Astrophysics **500**, 493–497 (1996).

Kim, D. and M. Im, “Optical-Near-infrared Color Gradients and Merging History of Elliptical Galaxies”, Astrophysical Journal **766**, 109 (2013).

Kim, D., R. A. Jansen and R. A. Windhorst, “Analysis of the Intrinsic Mid-infrared L band to Visible-Near-infrared Flux Ratios in Spectral Synthesis Models of Composite Stellar Populations”, Astrophysical Journal **840**, 28 (2017).

Kim, D., R. A. Jansen, R. A. Windhorst, S. H. Cohen and T. McCabe, “Analysis of the spatially-resolved V-3.6μm colors and dust extinction in 257 nearby NGC and IC galaxies”, arXiv e-prints p. arXiv:1901.00565 (2019).

Knierman, K., P. M. Knezek, P. Scowen, R. A. Jansen and E. Wehner, “Tidal Tails of Minor Mergers: Star Formation Efficiency in the Western Tail of NGC 2782”, Astrophysical Journal, Letters **749**, L1 (2012).

Knierman, K. A., P. Scowen, T. Veach, C. Groppi, B. Mullan, I. Konstantopoulos, P. M. Knezek and J. Charlton, "Tidal Tails of Minor Mergers. II. Comparing Star Formation in the Tidal Tails of NGC 2782", Astrophysical Journal **774**, 125 (2013).

Koekemoer, A. M., S. M. Faber, H. C. Ferguson, N. A. Grogin, D. D. Kocevski, D. C. Koo, K. Lai, J. M. Lotz, R. A. Lucas, E. J. McGrath, S. Ogaz, A. Rajan, A. G. Riess, S. A. Rodney, L. Strolger, S. Casertano, M. Castellano, T. Dahlen, M. Dickinson, T. Dolch, A. Fontana, M. Giavalisco, A. Grazian, Y. Guo, N. P. Hathi, K.-H. Huang, A. van der Wel, H.-J. Yan, V. Acquaviva, D. M. Alexander, O. Almaini, M. L. N. Ashby, M. Barden, E. F. Bell, F. Bournaud, T. M. Brown, K. I. Caputi, P. Cassata, P. J. Challis, R.-R. Chary, E. Cheung, M. Cirasuolo, C. J. Conselice, A. Roshan Cooray, D. J. Croton, E. Daddi, R. Davé, D. F. de Mello, L. de Ravel, A. Dekel, J. L. Donley, J. S. Dunlop, A. A. Dutton, D. Elbaz, G. G. Fazio, A. V. Filippenko, S. L. Finkelstein, C. Frazer, J. P. Gardner, P. M. Garnavich, E. Gawiser, R. Gruetzbauch, W. G. Hartley, B. Häussler, J. Herrington, P. F. Hopkins, J.-S. Huang, S. W. Jha, A. Johnson, J. S. Kartaltepe, A. A. Khostovan, R. P. Kirshner, C. Lani, K.-S. Lee, W. Li, P. Madau, P. J. McCarthy, D. H. McIntosh, R. J. McLure, C. McPartland, B. Mobasher, H. Moreira, A. Mortlock, L. A. Moustakas, M. Mozena, K. Nandra, J. A. Newman, J. L. Nielsen, S. Niemi, K. G. Noeske, C. J. Papovich, L. Pentericci, A. Pope, J. R. Primack, S. Ravindranath, N. A. Reddy, A. Renzini, H.-W. Rix, A. R. Robaina, D. J. Rosario, P. Rosati, S. Salimbeni, C. Scarlata, B. Siana, L. Simard, J. Smidt, D. Snyder, R. S. Somerville, H. Spinrad, A. N. Straughn, O. Telford, H. I. Teplitz, J. R. Trump, C. Vargas, C. Villforth, C. R. Wagner, P. Wand ro, R. H. Wechsler, B. J. Weiner, T. Wiklind, V. Wild, G. Wilson, S. Wuyts and M. S. Yun, "CANDELS: The Cosmic Assembly Near-infrared Deep Extragalactic Legacy Survey—The Hubble Space Telescope Observations, Imaging Data Products, and Mosaics", Astrophysical Journal, Supplement **197**, 2, 36 (2011).

Kong, X., S. Charlot, J. Brinchmann and S. M. Fall, "Star formation history and dust content of galaxies drawn from ultraviolet surveys", Monthly Notices of the RAS **349**, 3, 769–778 (2004).

König, S., S. Aalto, S. Muller, J. S. Gallagher, III, R. J. Beswick, E. Varenius, E. Jütte, M. Krips and A. Adamo, "Major impact from a minor merger. The extraordinary hot molecular gas flow in the Eye of the NGC 4194 Medusa galaxy", Astronomy and Astrophysics **615**, A122 (2018).

Kreckel, K., B. Groves, E. Schinnerer, B. D. Johnson, G. Aniano, D. Calzetti, K. V. Croxall, B. T. Draine, K. D. Gordon, A. F. Crocker, D. A. Dale, L. K. Hunt, R. C. Kennicutt, S. E. Meidt, J. D. T. Smith and F. S. Tabatabaei, "Mapping Dust through Emission and Absorption in Nearby Galaxies", Astrophysical Journal **771**, 1, 62 (2013).

Kroupa, P., "The Initial Mass Function of Stars: Evidence for Uniformity in Variable Systems", Science **295**, 5552, 82–91 (2002).

Kurucz, R. L., *SYNTHE spectrum synthesis programs and line data* (1993).

Laurikainen, E., H. Salo, R. Buta and J. H. Knapen, "Near-infrared atlas of S0-Sa galaxies (NIRS0S)", Monthly Notices of the RAS **418**, 3, 1452–1490 (2011).

Laurikainen, E., H. Salo, R. Buta, J. H. Knapen and S. Comerón, "Photometric scaling relations of lenticular and spiral galaxies", Monthly Notices of the RAS **405**, 2, 1089–1118 (2010).

Leger, A. and J. L. Puget, "Identification of the "unidentified" IR emission features of interstellar dust ?", Astronomy and Astrophysics **500**, 279–282 (1984).

Leitherer, C., J. C. Lee and A. Faisst, "He II Emission from Wolf-Rayet Stars as a Tool for Measuring Dust Reddening", arXiv e-prints p. arXiv:1909.07246 (2019).

Leitherer, C., D. Schaerer, J. D. Goldader, R. M. G. Delgado, C. Robert, D. F. Kune, D. F. de Mello, D. Devost and T. M. Heckman, "Starburst99: Synthesis Models for Galaxies with Active Star Formation", Astrophysical Journal, Supplement **123**, 3–40 (1999).

Lindblad, B., "On the distribution of light-intensity and colour in the spiral nebula NGC7331", Stockholms Observatoriums Annaler **13**, 8.1–8.32 (1941).

López-Corredoira, M., Allende Prieto, C., Garzón, F., Wang, H., Liu, C. and Deng, L., "Disk stars in the milky way detected beyond 25 kpc from its center", A&A **612**, L8, URL https://doi.org/10.1051/0004-6361/201832880 (2018).

Maiolino, R. and F. Mannucci, "De re metallica: the cosmic chemical evolution of galaxies", The Astronomy and Astrophysics Review **27**, 1, 3, URL https://doi.org/10.1007/s00159-018-0112-2 (2019).

Maiolino, R., T. Nagao, A. Grazian, F. Cocchia, A. Marconi, F. Mannucci, A. Cimatti, A. Pipino, S. Ballero, F. Calura, C. Chiappini, A. Fontana, G. L. Granato, F. Matteucci, G. Pastorini, L. Pentericci, G. Risaliti, M. Salvati and L. Silva, "AMAZE. I. The evolution of the mass-metallicity relation at z larger than 3", Astronomy and Astrophysics **488**, 463–479 (2008).

Maíz-Apellániz, J., E. Pérez and J. M. Mas-Hesse, "NGC 604, the Scaled OB Association (SOBA) Prototype. I. Spatial Distribution of the Different Gas Phases and Attenuation by Dust", Astronomical Journal **128**, 3, 1196–1218 (2004).

Maraston, C., "Evolutionary population synthesis: models, analysis of the ingredients and application to high-z galaxies", Monthly Notices of the RAS **362**, 3, 799–825 (2005).

Marigo, P., L. Girardi, A. Bressan, M. A. T. Groenewegen, L. Silva and G. L. Granato, "Evolution of asymptotic giant branch stars. II. Optical to far-infrared isochrones with improved TP-AGB models", Astronomy and Astrophysics **482**, 3, 883–905 (2008).

Marino, A., H. Plana, R. Rampazzo, L. Bianchi, M. Rosado, D. Bettoni, G. Galletta, P. Mazzei, L. Buson, P. Ambrocio-Cruz and R. F. Gabbasov, “Galaxy evolution in nearby loose groups - II. Photometric and kinematic characterization of USGC U268 and USGC U376 group members in the Leo cloud”, Monthly Notices of the RAS **428**, 476–501 (2013).

Martinsson, T. P. K., M. Sarzi, J. H. Knapen, L. Coccato, J. Falcón-Barroso, B. G. Elmegreen and T. de Zeeuw, “MUSE observations of the counter-rotating nuclear ring in NGC 7742”, Astronomy and Astrophysics **612**, A66 (2018).

Mathis, J. S., W. Rumpl and K. H. Nordsieck, “The size distribution of interstellar grains.”, Astrophysical Journal **217**, 425–433 (1977).

Meurer, G. R., T. M. Heckman and D. Calzetti, “Dust Absorption and the Ultraviolet Luminosity Density at z $\sim$3 as Calibrated by Local Starburst Galaxies”, Astrophysical Journal **521**, 1, 64–80 (1999).

Meynet, G., A. Maeder, G. Schaller, D. Schaerer and C. Charbonnel, “Grids of massive stars with high mass loss rates. V. From 12 to 120 $M_{sun\_}$ at Z=0.001, 0.004, 0.008, 0.020 and 0.040”, Astronomy and Astrophysics, Supplement **103**, 97–105 (1994).

Miralles-Caballero, D., A. I. Díaz, Á. R. López-Sánchez, F. F. Rosales-Ortega, A. Monreal-Ibero, E. Pérez-Montero, C. Kehrig, R. García-Benito, S. F. Sánchez, C. J. Walcher, L. Galbany, J. Iglesias-Páramo, J. M. Vílchez, R. M. González Delgado, G. van de Ven, J. Barrera-Ballesteros, M. Lyubenova, S. Meidt, J. Falcon-Barroso, D. Mast, M. A. Mendoza and Califa Collaboration, “First survey of Wolf-Rayet star populations over the full extension of nearby galaxies observed with CALIFA”, Astronomy and Astrophysics **592**, A105 (2016).

Misselt, K. A., G. C. Clayton and K. D. Gordon, “A Reanalysis of the Ultraviolet Extinction from Interstellar Dust in the Large Magellanic Cloud”, Astrophysical Journal **515**, 1, 128–139 (1999).

Moffett, A. J., S. J. Kannappan, A. J. Baker and S. Laine, “Extended Ultraviolet Disks and Ultraviolet-bright Disks in Low-mass E/S0 Galaxies”, Astrophysical Journal **745**, 34 (2012).

Müller-Sánchez, F., R. Nevin, J. M. Comerford, R. I. Davies, G. C. Privon and E. Treister, “Two separate outflows in the dual supermassive black hole system NGC 6240”, Nature **556**, 345–348 (2018).

Murray, N., “Star Formation Efficiencies and Lifetimes of Giant Molecular Clouds in the Milky Way”, Astrophysical Journal **729**, 133 (2011).

Neugebauer, G., H. J. Habing, R. van Duinen, H. H. Aumann, B. Baud, C. A. Beichman, D. A. Beintema, N. Boggess, P. E. Clegg, T. de Jong, J. P. Emerson, T. N. Gautier, F. C. Gillett, S. Harris, M. G. Hauser, J. R. Houck, R. E. Jennings, F. J. Low, P. L. Marsden, G. Miley, F. M. Olnon, S. R. Pottasch, E. Raimond, M. Rowan-Robinson, B. T. Soifer, R. G. Walker,

P. R. Wesselius and E. Young, “The Infrared Astronomical Satellite (IRAS) mission.”, Astrophysical Journal, Letters **278**, L1–L6 (1984).

Odewahn, S. C., “Automated galaxy classification with the APS digitization of POSS I”, Astrophysical Letters and Communications **31**, 55 (1995).

Oke, J. B., “Absolute Spectral Energy Distributions for White Dwarfs”, Astrophysical Journal, Supplement **27**, 21 (1974).

Oke, J. B. and J. E. Gunn, “Secondary standard stars for absolute spectrophotometry”, Astrophysical Journal **266**, 713–717 (1983).

Panuzzo, P., A. Bressan, G. L. Granato, L. Silva and L. Danese, “Dust and nebular emission. I. Models for normal galaxies”, Astronomy and Astrophysics **409**, 99–114 (2003).

Peng, C. Y., L. C. Ho, C. D. Impey and H.-W. Rix, “Detailed Structural Decomposition of Galaxy Images”, Astronomical Journal **124**, 266–293 (2002).

Peng, C. Y., L. C. Ho, C. D. Impey and H.-W. Rix, “Detailed Decomposition of Galaxy Images. II. Beyond Axisymmetric Models”, Astronomical Journal **139**, 2097–2129 (2010).

Petersen, L. and P. Gammelgaard, “Dust extinction of HII regions in NGC 598 and NGC 5457.”, Astronomy and Astrophysics **323**, 697–706 (1997).

Phillips, A. C. and L. E. Davis, “Registering, PSF-Matching and Intensity-Matching Images in IRAF”, in “Astronomical Data Analysis Software and Systems IV”, edited by R. A. Shaw, H. E. Payne and J. J. E. Hayes, vol. 77 of *Astronomical Society of the Pacific Conference Series*, p. 297 (1995).

Pilbratt, G. L., “Herschel mission: status and observing opportunities”, in “Proceedings of the SPIE ”, edited by J. C. Mather, vol. 5487 of *Society of Photo-Optical Instrumentation Engineers (SPIE) Conference Series*, pp. 401–412 (2004).

Pingel, N. M., D. J. Pisano, G. Heald, T. H. Jarrett, W. J. G. de Blok, G. I. G. Józsa, E. Jütte, R. J. Rand, T. Oosterloo and B. Winkel, “A GBT Survey of the HALOGAS Galaxies and Their Environments. I. Revealing the Full Extent of H I around NGC 891, NGC 925, NGC 4414, and NGC 4565”, Astrophysical Journal **865**, 36 (2018).

Planck Collaboration, P. A. R. Ade, N. Aghanim, M. Arnaud, M. Ashdown, J. Aumont, C. Baccigalupi, A. J. Banday, R. B. Barreiro, J. G. Bartlett and et al., “Planck 2015 results. XIII. Cosmological parameters”, Astronomy and Astrophysics **594**, A13 (2016).

Postman, M., D. Coe, N. Benítez, L. Bradley, T. Broadhurst, M. Donahue, H. Ford, O. Graur, G. Graves, S. Jouvel, A. Koekemoer, D. Lemze, E. Medezinski, A. Molino, L. Moustakas, S. Ogaz, A. Riess, S. Rodney, P. Rosati, K. Umetsu, W. Zheng, A. Zitrin, M. Bartelmann,

R. Bouwens, N. Czakon, S. Golwala, O. Host, L. Infante, S. Jha, Y. Jimenez-Teja, D. Kelson, O. Lahav, R. Lazkoz, D. Maoz, C. McCully, P. Melchior, M. Meneghetti, J. Merten, J. Moustakas, M. Nonino, B. Patel, E. Regös, J. Sayers, S. Seitz and A. Van der Wel, "The Cluster Lensing and Supernova Survey with Hubble: An Overview", Astrophysical Journal, Supplement **199**, 2, 25 (2012).

Price, S. D., S. J. Carey and M. P. Egan, "The MSX galactic plane survey submillimeter results", Advances in Space Research **30**, 9, 2027–2036 (2002).

Relaño, M., U. Lisenfeld, J. M. Vilchez and E. Battaner, "Distribution of extinction and star formation in NGC 1569", Astronomy and Astrophysics **452**, 2, 413–421 (2006).

Rieke, M., "The JWST-NIRCam View of Galaxy Evolution", in "Galaxy Evolution: Infrared to Millimeter Wavelength Perspective", edited by W. Wang, J. Lu, Z. Luo, Z. Yang, H. Hua and Z. Chen, vol. 446 of *Astronomical Society of the Pacific Conference Series*, p. 331 (2011).

Rix, H.-W. and J. Bovy, "The milky way's stellar disk", The Astronomy and Astrophysics Review **21**, 1, 61, URL https://doi.org/10.1007/s00159-013-0061-8 (2013).

Rothberg, B. and R. D. Joseph, "A Deep K-Band Photometric Survey of Merger Remnants", Astronomical Journal **128**, 5, 2098–2143 (2004).

Roussel, H., A. Gil de Paz, M. Seibert, G. Helou, B. F. Madore and C. Martin, "Extinction Law Variations and Dust Excitation in the Spiral Galaxy NGC 300", Astrophysical Journal **632**, 1, 227–252 (2005).

Rudy, R. J., "Effects of dust on the infrared emission, selected line ratios, and polarization of Seyfert 1 galaxies, broad-line radio galaxies, and quasars.", Astrophysical Journal **284**, 33–43 (1984).

Ryan, R. E., Jr, "A Graphical-User Interface for Editing Segmentation Images", ArXiv e-prints (2018).

Ryden, B., *Introduction to cosmology* (2003).

Saito, T., D. Iono, J. Ueda, D. Espada, K. Sliwa, K. Nakanishi, N. Lu, C. K. Xu, T. Michiyama, H. Kaneko, T. Yamashita, M. Ando, M. S. Yun, K. Motohara and R. Kawabe, "Imaging the molecular outflows of the prototypical ULIRG NGC 6240 with ALMA", Monthly Notices of the RAS **475**, L52–L56 (2018).

Salpeter, E. E., "The Luminosity Function and Stellar Evolution.", Astrophysical Journal **121**, 161 (1955).

Sánchez, S. F., R. C. Kennicutt, A. Gil de Paz, G. van de Ven, J. M. Vílchez, L. Wisotzki, C. J. Walcher, D. Mast, J. A. L. Aguerri, S. Albiol-Pérez, A. Alonso-Herrero, J. Alves, J. Bakos, T. Bartáková, J. Bland-Hawthorn, A. Boselli, D. J. Bomans, A. Castillo-Morales, C. Cortijo-Ferrero, A. de Lorenzo-Cáceres, A. Del Olmo, R. J. Dettmar, A. Díaz, S. Ellis, J. Falcón-Barroso, H. Flores, A. Gallazzi, B. García-Lorenzo, R. González Delgado, N. Gruel, T. Haines, C. Hao, B. Husemann, J. Iglésias-Páramo, K. Jahnke, B. Johnson, B. Jungwiert, V. Kalinova, C. Kehrig, D. Kupko, Á. R. López-Sánchez, M. Lyubenova, R. A. Marino, E. Mármol-Queraltó, I. Márquez, J. Masegosa, S. Meidt, J. Mendez-Abreu, A. Monreal-Ibero, C. Montijo, A. M. Mourão, G. Palacios-Navarro, P. Papaderos, A. Pasquali, R. Peletier, E. Pérez, I. Pérez, A. Quirrenbach, M. Relaño, F. F. Rosales-Ortega, M. M. Roth, T. Ruiz-Lara, P. Sánchez-Blázquez, C. Sengupta, R. Singh, V. Stanishev, S. C. Trager, A. Vazdekis, K. Viironen, V. Wild, S. Zibetti and B. Ziegler, "CALIFA, the Calar Alto Legacy Integral Field Area survey. I. Survey presentation", Astronomy and Astrophysics **538**, A8 (2012).

Sandage, A., *The Hubble Atlas of Galaxies* (Washington: Carnegie Institution, 1961).

Schaerer, D., C. Charbonnel, G. Meynet, A. Maeder and G. Schaller, "Grids of stellar models. IV. From 0.8 to 120 M_solar at Z=0.040", Astronomy and Astrophysics, Supplement **102**, 339 (1993a).

Schaerer, D., G. Meynet, A. Maeder and G. Schaller, "Grids of stellar models. II. From 0.8 to 120 M_solar at Z=0.008", Astronomy and Astrophysics, Supplement **98**, 523 (1993b).

Schaller, G., D. Schaerer, G. Meynet and A. Maeder, "New grids of stellar models from 0.8 to 120 M_solar at Z=0.020 and Z=0.001", Astronomy and Astrophysics, Supplement **96**, 269 (1992).

Scoville, N., R. G. Abraham, H. Aussel, J. E. Barnes, A. Benson, A. W. Blain, D. Calzetti, A. Comastri, P. Capak, C. Carilli, J. E. Carlstrom, C. M. Carollo, J. Colbert, E. Daddi, R. S. Ellis, M. Elvis, S. P. Ewald, M. Fall, A. Franceschini, M. Giavalisco, W. Green, R. E. Griffiths, L. Guzzo, G. Hasinger, C. Impey, J. P. Kneib, J. Koda, A. Koekemoer, O. Lefevre, S. Lilly, C. T. Liu, H. J. McCracken, R. Massey, Y. Mellier, S. Miyazaki, B. Mobasher, J. Mould, C. Norman, A. Refregier, A. Renzini, J. Rhodes, M. Rich, D. B. Sanders, D. Schiminovich, E. Schinnerer, M. Scodeggio, K. Sheth, P. L. Shopbell, Y. Taniguchi, N. D. Tyson, C. M. Urry, L. Van Waerbeke, P. Vettolani, S. D. M. White and L. Yan, "COSMOS: Hubble Space Telescope Observations", Astrophysical Journal, Supplement **172**, 1, 38–45 (2007).

Scoville, N. Z., M. Polletta, S. Ewald, S. R. Stolovy, R. Thompson and M. Rieke, "High-Mass, OB Star Formation in M51: Hubble Space Telescope Hα and Paα Imaging", Astronomical Journal **122**, 6, 3017–3045 (2001).

Steinacker, J., M. Baes and K. D. Gordon, “Three-dimensional dust radiative transfer”, Annual Review of Astronomy and Astrophysics **51**, 1, 63–104, URL https://doi.org/10.1146/annurev-astro-082812-141042 (2013).

Stetson, P. B., “DAOPHOT - A computer program for crowded-field stellar photometry”, Publication of the ASP **99**, 191–222 (1987).

Tamura, K., R. A. Jansen, P. B. Eskridge, S. H. Cohen and R. A. Windhorst, “Lifting the Veil of Dust from NGC 0959: The Importance of a Pixel-based Two-dimensional Extinction Correction”, Astronomical Journal **139**, 2557–2565 (2010).

Tamura, K., R. A. Jansen and R. A. Windhorst, “Mapping the Spatial Distribution of Dust Extinction in NGC 959 Using Broadband Visible and Mid-Infrared Filters”, Astronomical Journal **138**, 1634–1654 (2009).

Tanada, K., J. Kataoka, M. Arimoto, M. Akita, C. C. Cheung, S. W. Digel and Y. Fukazawa, “The Origins of the Gamma-Ray Flux Variations of NGC 1275 Based on Eight Years of Fermi-LAT Observations”, Astrophysical Journal **860**, 74 (2018).

Taylor, V. A., R. A. Jansen, R. A. Windhorst, S. C. Odewahn and J. E. Hibbard, “UBVR and Hubble Space Telescope Mid-Ultraviolet and Near-Infrared Surface Photometry and Radial Color Gradients of Late-Type, Irregular, and Peculiar Galaxies”, Astrophysical Journal **630**, 784–803 (2005).

Taylor-Mager, V. A., C. J. Conselice, R. A. Windhorst and R. A. Jansen, “Dependence of Galaxy Structure on Rest-Frame Wavelength and Galaxy Type”, Astrophysical Journal **659**, 1, 162–187 (2007).

Toomre, A., “Mergers and Some Consequences”, in “Evolution of Galaxies and Stellar Populations”, edited by B. M. Tinsley and R. B. G. Larson, D. Campbell, p. 401 (1977).

Trumpler, R. J., “Absorption of Light in the Galactic System”, Publication of the ASP **42**, 248, 214 (1930).

Urry, C. M. and P. Padovani, “Unified Schemes for Radio-Loud Active Galactic Nuclei”, Publication of the ASP **107**, 803 (1995).

van den Bergh, S., *Galaxy Morphology and Classification* (1998).

Vazdekis, A., P. Sánchez-Blázquez, J. Falcón-Barroso, A. J. Cenarro, M. A. Beasley, N. Cardiel, J. Gorgas and R. F. Peletier, “Evolutionary stellar population synthesis with MILES - I. The base models and a new line index system”, Monthly Notices of the RAS **404**, 4, 1639–1671 (2010).

Vázquez, G. A. and C. Leitherer, “Optimization of Starburst99 for Intermediate-Age and Old Stellar Populations”, Astrophysical Journal **621**, 2, 695–717 (2005).

Viallefond, F., W. M. Goss and R. J. Allen, “The giant spiral galaxy M 101. VIII - Star formation in H I-H II associations”, Astronomy and Astrophysics **115**, 2, 373–387 (1982).

Walcher, J., B. Groves, T. Budavári and D. Dale, “Fitting the integrated spectral energy distributions of galaxies”, Astrophysics and Space Science **331**, 1–52 (2011).

Waller, W. H., M. Gurwell and M. Tamura, “Circumnuclear Pileups of Dust and Gas in M82”, Astronomical Journal **104**, 63 (1992).

Walterbos, R. A. M. and J. Kennicutt, R. C., “An optical study of stars and dust in the Andromeda galaxy.”, Astronomy and Astrophysics **198**, 61–86 (1988).

Wells, D. C., E. W. Greisen and R. H. Harten, “FITS - a Flexible Image Transport System”, Astronomy and Astrophysics, Supplement **44**, 363 (1981).

Werner, M. W., T. L. Roellig, F. J. Low, G. H. Rieke, M. Rieke, W. F. Hoffmann, E. Young, J. R. Houck, B. Brandl, G. G. Fazio, J. L. Hora, R. D. Gehrz, G. Helou, B. T. Soifer, J. Stauffer, J. Keene, P. Eisenhardt, D. Gallagher, T. N. Gautier, W. Irace, C. R. Lawrence, L. Simmons, J. E. Van Cleve, M. Jura, E. L. Wright and D. P. Cruikshank, “The Spitzer Space Telescope Mission”, Astrophysical Journal, Supplement **154**, 1–9 (2004).

Windhorst, R. A., S. H. Cohen, N. P. Hathi, P. J. McCarthy, J. Ryan, Russell E., H. Yan, I. K. Baldry, S. P. Driver, J. A. Frogel, D. T. Hill, L. S. Kelvin, A. M. Koekemoer, M. Mechtley, R. W. O’Connell, A. S. G. Robotham, M. J. Rutkowski, M. Seibert, A. N. Straughn, R. J. Tuffs, B. Balick, H. E. Bond, H. Bushouse, D. Calzetti, M. Crockett, M. J. Disney, M. A. Dopita, D. N. B. Hall, J. A. Holtzman, S. Kaviraj, R. A. Kimble, J. W. MacKenty, M. Mutchler, F. Paresce, A. Saha, J. I. Silk, J. T. Trauger, A. R. Walker, B. C. Whitmore and E. T. Young, “The Hubble Space Telescope Wide Field Camera 3 Early Release Science Data: Panchromatic Faint Object Counts for 0.2-2 μm Wavelength”, Astrophysical Journal, Supplement **193**, 2, 27 (2011).

Windhorst, R. A., V. A. Taylor, R. A. Jansen, S. C. Odewahn, C. A. T. Chiarenza, C. J. Conselice, R. de Grijs, R. S. de Jong, J. W. MacKenty, P. B. Eskridge, J. A. Frogel, I. Gallagher, John S., J. E. Hibbard, L. D. Matthews and R. W. O’Connell, “A Hubble Space Telescope Survey of the Mid-Ultraviolet Morphology of Nearby Galaxies”, Astrophysical Journal, Supplement **143**, 1, 113–158 (2002).

Witt, A. N., J. Thronson, Harley A. and J. Capuano, John M., “Dust and the Transfer of Stellar Radiation within Galaxies”, Astrophysical Journal **393**, 611 (1992).

Wright, E. L., P. R. M. Eisenhardt, A. K. Mainzer, M. E. Ressler, R. M. Cutri, T. Jarrett, J. D. Kirkpatrick, D. Padgett, R. S. McMillan, M. Skrutskie, S. A. Stanford, M. Cohen, R. G. Walker, J. C. Mather, D. Leisawitz, I. Gautier, Thomas N., I. McLean, D. Benford, C. J. Lonsdale, A. Blain, B. Mendez, W. R. Irace, V. Duval, F. Liu, D. Royer, I. Heinrichsen, J. Howard, M. Shannon, M. Kendall, A. L. Walsh, M. Larsen, J. G. Cardon, S. Schick,

M. Schwalm, M. Abid, B. Fabinsky, L. Naes and C.-W. Tsai, “The Wide-field Infrared Survey Explorer (WISE): Mission Description and Initial On-orbit Performance”, Astronomical Journal **140**, 6, 1868–1881 (2010).

Xu, C. and G. Helou, “High-Resolution IRAS Maps and Infrared Emission of M31. I. Morphology and Sources”, Astrophysical Journal **456**, 152 (1996).

Yasuda, N., M. Fukugita, V. K. Narayanan, R. H. Lupton, I. Strateva, M. A. Strauss, Ž. Ivezić, R. S. J. Kim, D. W. Hogg, D. H. Weinberg, K. Shimasaku, J. Loveday, J. Annis, N. A. Bahcall, M. Blanton, J. Brinkmann, R. J. Brunner, A. J. Connolly, I. Csabai, M. Doi, M. Hamabe, S.-I. Ichikawa, T. Ichikawa, D. E. Johnston, G. R. Knapp, P. Z. Kunszt, D. Q. Lamb, T. A. McKay, J. A. Munn, R. C. Nichol, S. Okamura, D. P. Schneider, G. P. Szokoly, M. S. Vogeley, M. Watanabe and D. G. York, “Galaxy Number Counts from the Sloan Digital Sky Survey Commissioning Data”, Astronomical Journal **122**, 1104–1124 (2001).

APPENDIX A

A SET OF DISTINGUISHABLE SSPS

I construct my combined model SSP SEDs for a manageably small, yet comprehensive set of parameters that span the range of representative SP properties and dust extinction. I consider six metallicity and 16 age values of the SP, four extinction laws, and eight V-band extinction values A_V (see Table A.1). I adopted a grid of 16 SP ages between 3 Myr and 13.25 Gyr [16] in steps that roughly double for ages between 10 Myr and 10 Gyr. This allows me to follow the rapid evolution of massive stars, without reserving too many SEDs for the slow evolution of low-mass stars. Because the MW and both the LMC2 Supershell and LMC Average extinction laws are nearly indistinguishable in the 0.4–3.75 μm wavelength range of interest for the present study (see Figure A.1(a)), I averaged both into a single "MW/LMC" extinction law and adopt $R_V = 3.1$. I furthermore consider the SMC bar extinction law with $R_V = 2.74$, and the law appropriate for starburst galaxies of Calzetti *et al.* (2000), which has less reddening per unit extinction, for which I adopt $R_V = 4.33$. I substitute the MW/LMC curve for the SMC extinction law at $\lambda > 1$ μm, where no SMC data is available. The Calzetti extinction law is also only defined to 2.2 μm, so I extrapolated to 3.75 μm, imposing a minimum residual attenuation of 5% of that in V. For each of these three extinction laws, I select seven extinction values between $A_V = 0.1$ and $A_V = 6.4$ mag, each double the value of the previous one, plus the trivial case of zero extinction ($A_V = 0$ mag), generating 22 SSP SEDs for each of the six metallicity values and 16 ages, i.e., a total of 2112 unique SSP SEDs. Figure 2.2 and Fig. A.1 shows example SEDs for different metallicities, ages, extinction laws, and extinction values.

Within typical observational uncertainties, many of these unique SSP SEDs will be indistinguishable from one or more of the others over the wavelength range of interest. I quantified the differences between each pair of SEDs, where I only need to consider differences in SED shape, not in the absolute flux scale (which depends on the total mass of stars formed). I first divide the 0.4–3.75 μm wavelength range into 10 equal linear bins and normalize the integrated flux in each bin to the mean integrated flux in all bins. For each pair of SEDs, (i, j), and each wavelength bin, k, I compare the difference between normalized integrated fluxes as

$$\Delta_k^{ij} = \left| \int_k F_i(\lambda) \Big/ \overline{\int_k F_i(\lambda)} \; - \int_k F_j(\lambda) \Big/ \overline{\int_k F_j(\lambda)} \right| . \tag{A.1}$$

I reject SED j as indistinguishable from SED i when both the maximum difference, $\max\{\Delta_k^{ij}\}$, and the mean$\{\Delta_k^{ij}\}$ are smaller than 5%. Using this criterion, I rejected 1388 of my 2112 SSP SEDs, leaving a set of 724 unique and distinguishable SEDs for further analysis of the β_V method and its comparison with the SED-fitting method, and for fitting observed SEDs of individual regions within galaxies. Figure A.2 shows two examples of pairs of SEDs that were deemed to be *just* distinguishable (>5%) over the 0.4–3.75μm interval.

---

[16] In Planck 2015 cosmology (Planck Collaboration XIII, 2016), the Hubble time $t_H \simeq 13.8$ Gyr. Hence, $t = 13.25$ Gyr corresponds to 0.55 Gyr after the Big Bang or $z_f \simeq 9$, consistent with the Planck Collaboration (Paper 2016) results of $\tau = 0.058$ and $z_{\rm reion} \simeq 8$, so this maximum age is a deliberate choice.

Table A.1: Parameter Set of the Combined SSP Model SEDs

Parameter	Values
Z	0.0001, 0.0004, 0.004, 0.008, 0.02, 0.05
Age (Myr)	3, 4, 5, 7, 10, 20, 40, 80, 160, 320, 640, 1250, 2500, 5000, 10000, 13250
Extinction law	MW[a]/LMC[b], SMC[c], Calzetti[d]
A_V (mag)	0.0, 0.1, 0.2, 0.4, 0.8, 1.6, 3.2, 6.4

Notes. [a]Fitzpatrick (1999), [b]Misselt *et al.* (1999), [c]Gordon *et al.* (2003), [d]Calzetti *et al.* (2000).

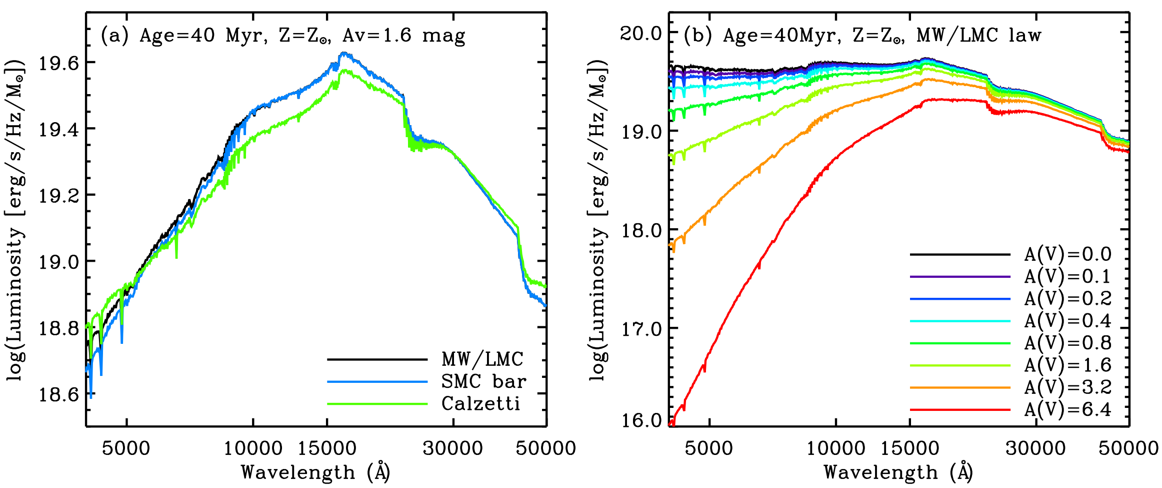

Figure A.1: Examples of my adopted combined array of SSP SEDs. (a) SEDs for a 40 Myr old SSP with $Z = Z_\odot$, for three different extinction laws and $A_V = 1.6$ mag. Note that over the wavelength range of interest (0.4–3.75 μm), the MW and LMC extinction laws are essentially indistinguishable and were combined; (b) SEDs for a 40 Myr old SSP with $Z = Z_\odot$, for eight different extinction values and a MW/LMC extinction law.

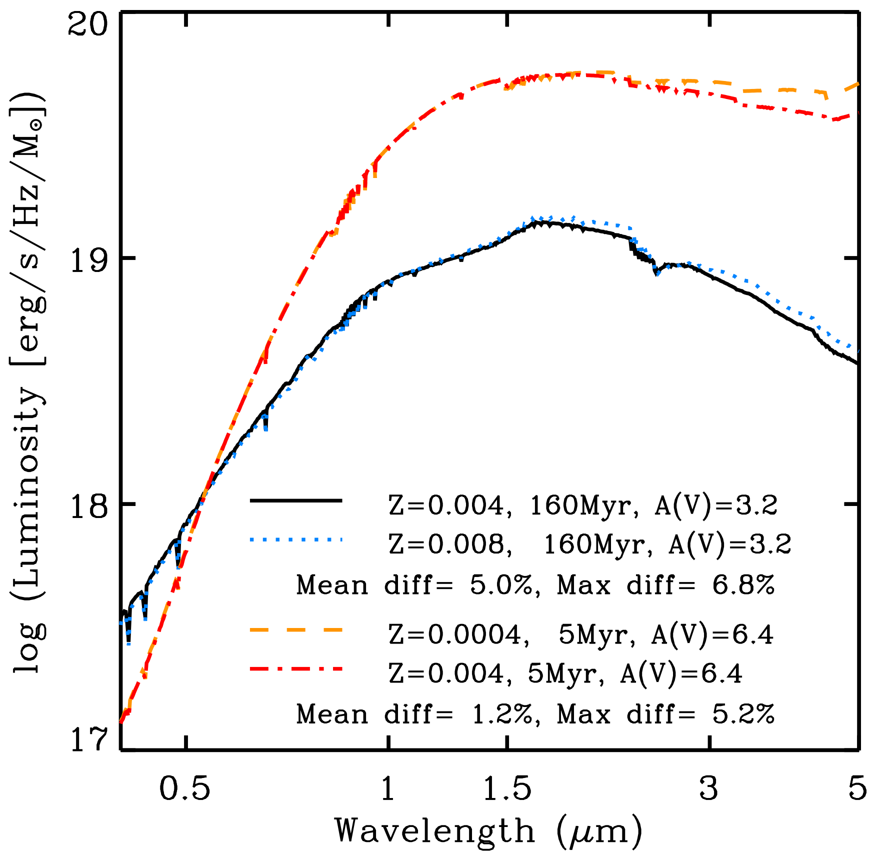

Figure A.2: Examples of two pairs of SSP model SEDs that *just* meet my $\max\{\Delta_k^{ij}\}$ or mean$\{\Delta_k^{ij}\}$ $> 5\%$ criteria for being distinguishable over the 0.4–3.75 μm wavelength range, each normalized at $\lambda = 1$ μm. The lower pair (black/blue) is for mean$\{\Delta_k^{ij}\} > 5\%$ and therefore also has $\max\{\Delta_k^{ij}\}$ greater than 5%, and the upper pair (red/orange) is for $\max\{\Delta_k^{ij}\} > 5\%$.

APPENDIX B

THE MAGNITUDE OFFSETS BETWEEN AB AND VEGA MAGNITUDE SYSTEMS FOR VARIOUS FILTERS

Throughout this dissertation, I use the AB magnitude system (Oke, 1974; Oke and Gunn, 1983). For observers with data calibrated onto the Vega magnitude system, I here provide magnitude offsets between AB and Vega magnitudes, derived using the Kurucz (1993) Vega spectrum as available in STSDAS 3.16 (www.stsci.edu/institute/software_hardware/stsdas/). I also list the central wavelength, λ_c, and bandwidth (FWHM), $\Delta\lambda$, of each filter in Table B.1.

Table B.1: Central Wavelengths, Bandwidths, And Magnitude Offsets Between AB And Vega Magnitudes For Each Of The Filters Used In The Present Study

Filter	λ_c[a][Å]	$\Delta\lambda$[b][Å]	$m_{\lambda,\mathrm{AB}}-m_{\lambda,\mathrm{Vega}}$[c]	Filter	λ_c[a][Å]	$\Delta\lambda$[b][Å]	$m_{\lambda,\mathrm{AB}}-m_{\lambda,\mathrm{Vega}}$[c]
B	4361[d]	890[d]	−0.098	WFC3 UVIS F475W	4773[e]	1344[e]	−0.088
V	5448[d]	840[d]	0.022	WFC3 UVIS F555W	5308[e]	1562[e]	−0.013
R_c	6400[f]	1500[f]	0.213	WFC3 UVIS F606W	5887[e]	2182[e]	0.096
I_c	7900[f]	1500[f]	0.455	WFC3 UVIS F625W	6242[e]	1463[e]	0.163
I	7980[d]	1540[d]	0.436	WFC3 UVIS F775W	7647[e]	1171[e]	0.396
SDSS g	4774[g]	1377[g]	−0.085	WFC3 UVIS F814W	8024[e]	1536[e]	0.433
SDSS r	6231[g]	1371[g]	0.167	WFC3 UVIS F850LP	9166[e]	1182[e]	0.536
SDSS i	7615[g]	1510[g]	0.394	WFC3 IR F098M	9864[e]	1570[e]	0.576
SDSS z	9132[g]	940[g]	0.530	WFC3 IR F105W	10552[e]	2650[e]	0.660
ACS WFC F435W	4297[h]	1038[h]	−0.094	WFC3 IR F110W	11534[e]	4430[e]	0.775
ACS WFC F475W	4760[h]	1458[h]	−0.088	WFC3 IR F125W	12486[e]	2845[e]	0.916
ACS WFC F555W	5346[h]	1193[h]	0.006	WFC3 IR F160W	15369[e]	2683[e]	1.267
ACS WFC F606W	5907[h]	2342[h]	0.100	J	12546	1620[i]	0.909
ACS WFC F625W	6318[h]	1442[h]	0.178	H	16487	2510[i]	1.383
ACS WFC F775W	7764[h]	1528[h]	0.403	K_S	21634	2620[i]	1.853
ACS WFC F814W	8333[h]	2511[h]	0.438	K	22053	3889	1.886
ACS WFC F850LP	9445[h]	1229[h]	0.536	K'	21218	3404	2.800
WFC3 UVIS F438W	4325[e]	618[e]	−0.144				
L	34831	5103	2.760	NIRCam F410M	40820[j]	4380[j]	3.087
L'	38333	5880	2.954	NIRCam F444W	44080[j]	10290[j]	3.224
WISE W1	33836	7934	2.681	NIRCam F480M	48740[j]	3000[j]	3.423
Spitzer I1	35466	7432	2.797	MIRI F560W	56000[k]	12000[k]	3.732
NIRCam F200W	19890[j]	4570[j]	1.691	MIRI F770W	77000[k]	22000[k]	4.352
NIRCam F356W	35680[j]	7810[j]	2.793	MIRI F1000W	100000[k]	20000[k]	4.921

Notes.

[a] Central wavelength.

[b] Width of the bandpass (FWHM).

[c] Magnitude offset between AB and Vega magnitude system; $m_{\lambda,\mathrm{AB}}-m_{\lambda,\mathrm{Vega}}=-2.5\ \log\left(F_{\lambda,\mathrm{Vega}}\right)-48.585$ (Hayes and Latham, 1975; Bessell and Brett, 1988; Bessell, 1990; Colina and Bohlin, 1994).

[d] Bessell (2005).

[e] Dressel *et al.* (2015).

[f] Bessell (1979).

[g] Gunn *et al.* (1998).

[h] Avila *et al.* (2015).

[i] Cohen *et al.* (2003).

[j] http://www.stsci.edu/jwst/instruments/nircam/instrumentdesign/filters/

[k] http://ircamera.as.arizona.edu/MIRI

APPENDIX C

TABLE FOR 257 NGC AND IC GALAXIES

Table C.1: The List of NGC/IC Galaxy Sample

ID	R.A.(J2000) (deg)	Decl.(J2000) (deg)	z	B (mag)	V (mag)	3.6μm (mag)	3.6μm (Mag)	a ($'$)	b/a	$\mathrm{r_{eff}}$ ($''$)	$R^P_{50,V}$ ($''$)	PA (deg)	Gal. Ext. (mag)	B/T	T	eT	Type	SF & AGN	Classification	Figure D.#
(1)	(2)	(3)	(4)	(5)	(6)	(7)	(8)	(9)	(10)	(11)	(12)	(13)	(14)	(15)	(16)	(17)	(18)	(19)	(20)	(21)
NGC 0014	2.193333	15.815556	0.002885	12.7	12.1	12.7	–17.8	2.8	0.75	44.4	24.0	25.0	0.117	0.19	10.0	0.3	IBm	0	(R)IB(s)m pec	1
NGC 0023	2.472542	25.923778	0.015231	12.9	12.0	11.5	–22.7	2.1	0.62	14.4	4.2	8.0	0.145	0.49	1.0	0.4	SBa	2	SB(s)a;HII;LIRGSbrst	2
NGC 0193	9.827458	3.331111	0.014723	13.3	12.3	11.7	–22.4	1.4	0.86	19.5	13.8	55.0	0.061	0.78	–2.5	0.6	E/SB0	0	SAB(s)0-:	3
NGC 0266	12.449167	32.277722	0.015547	12.5	11.6	10.3	–23.9	3.0	0.97	42.3	31.2	99.0	0.217	0.28	2.0	0.7	SBab	3	SB(rs)ab LINER	4
NGC 0274	12.757750	–7.056944	0.005837	12.8	11.8	11.7	–20.3	1.5	1.00	*	7.8	25.0	0.211	0.45	–3.0	0.4	E/SB0	0	SAB(r)0- pec	5
NGC 0275	12.767500	–7.066667	0.005817	13.2	12.5	12.3	–19.8	1.5	0.73	*	18.0	126.0	0.211	0.00	6.0	0.4	SBcd/P	0	SB(rs)cd pec	6
NGC 0309	14.177750	–9.913861	0.018886	12.5	11.9	11.8	–22.9	1.94	0.69	44.4	31.2	175.0	0.156	0.06	5.0	0.3	SBc	0	SAB(r)c HII	7
NGC 0315	14.453667	30.352444	0.016485	12.2	11.2	10.3	–24.0	2.08	0.74	36.9	23.4	43.0	0.261	0.78	–4.0	0.5	E2	5	E+:;LINER;Sy3b Sy1	8
NGC 0337	14.958708	–7.577972	0.00549	12.1	11.6	11.0	–21.0	2.9	0.62	31.5	25.8	141.0	0.316	0.31	7.0	0.3	SBcd	0	SB(s)d HII	9
NGC 0382	16.849458	32.403861	0.017442	14.2	13.2	12.3	–22.2	0.7	1.00	*	5.4	*	0.173	0.61	–5.0	0.5	E0	0	E: HII	10
NGC 0383	16.854000	32.412556	0.017005	13.2	12.2	10.8	–23.6	1.6	0.87	*	15.0	30.0	0.173	0.75	–3.0	0.3	E-S0	5	SA0-:;BrClG;Sy LERG	11
NGC 0410	17.745417	33.151889	0.017659	12.5	11.5	11.0	–23.5	2.4	0.54	34.5	16.2	30.0	0.189	0.55	–4.0	0.6	cD	3	E+:;LINER HII	12
NGC 0428	18.232125	0.981556	0.003843	11.9	11.5	12.2	–19.0	4.1	0.76	49.8	34.2	120.0	0.025	0.00	9.0	0.3	SBm	0	SAB(s)m HII	13
NGC 0507	20.916292	33.256056	0.016458	12.2	11.2	10.5	–23.9	3.1	1.00	53.4	37.8	*	0.165	0.39	–2.0	0.3	E-S0	0	SA(r)0^0^;BrClG	14
NGC 0514	21.016250	12.917389	0.008246	12.2	11.7	11.7	–21.1	3.5	0.80	65.7	36.0	110.0	0.073	0.03	5.0	0.3	SBc	0	SAB(rs)c	15
NGC 0596	23.217000	–7.031833	0.006258	11.8	10.9	10.6	–21.7	3.2	0.66	27.3	16.8	40.0	0.107	0.62	–4.0	0.5	E4	0	E+ pec:	16
NGC 0636	24.777208	–7.512611	0.006204	12.4	11.5	11.0	–21.2	2.8	0.75	19.5	10.8	40.0	0.119	0.61	–5.0	0.3	E3	0	E3	17
NGC 0695	27.809333	22.582361	0.032472	13.8	12.8	11.6	–24.2	0.8	0.87	*	6.0	40.0	0.297	0.68	–2.0	1.9	S0/P	2	S0? pec;LIRG HII	18
NGC 0741	29.087625	5.628944	0.018549	12.2	11.1	10.8	–23.8	3.0	0.97	52.2	25.2	90.0	0.133	0.81	–5.0	0.4	E0	0	E0:	19
NGC 0772	29.831583	19.007528	0.008246	11.1	10.3	9.5	–23.4	7.2	0.60	77.1	43.2	130.0	0.157	0.24	3.0	0.3	Sb	0	SA(s)b HII	20
NGC 0777	30.062083	31.429583	0.016728	12.5	11.5	11.0	–23.4	2.5	0.80	34.5	11.4	155.0	0.145	0.66	–5.0	0.3	E1	3	E1 Sy;LINER	21
NGC 0788	30.276875	–6.815528	0.013603	13.0	12.1	11.6	–22.3	1.9	0.74	17.7	12.0	111.0	0.067	0.21	-.0	0.6	S0-a	5	SA(s)0/a:;Sy1 Sy2	22
IC 0195	30.935875	14.709278	0.012168	14.0	13.0	12.7	–21.0	1.17	0.51	*	3.6	126.0	0.137	0.72	–2.0	0.8	S0	0	SAB0^0^	23
IC 0208	32.115583	6.394917	0.011755	14.2	13.4	12.9	–20.7	1.8	1.00	*	19.8	*	0.133	0.03	4.0	0.8	Sbc	0	SAbc	24
IC 0214	33.523292	5.173250	0.030224	14.7	14.2	11.3	–24.4	0.8	0.75	*	3.0	162.0	0.109	0.18	7.0*	*	Sd	2	I? LIRG	25
NGC 0985	38.657375	–8.787611	0.043143	14.0	13.4	12.8	–23.6	1.0	0.90	13.2	8.4	69.0	0.093	0.73	10.0	0.8	Ring/P	5	SBbc? p (Ring) Sy1	26
NGC 0992	39.356208	21.100833	0.013813	13.7	12.8	11.6	–22.3	0.9	0.78	*	5.4	7.0	0.409	0.45	5.0*	*	Sc	2	S? LIRG	27
NGC 1016	39.581500	2.119250	0.022209	12.6	11.6	11.0	–24.0	2.4	1.00	36.0	19.2	*	0.053	0.69	–4.5	0.5	E0	0	E	28
NGC 1143	43.790458	–0.177861	0.028216	14.1	13.1	12.5	–23.0	0.9	0.89	*	8.4	110.0	0.177	0.29	–4.3	0.6	Ring A	0	S0 pec (Ring A)	29
NGC 1144	43.800833	–0.183556	0.028847	13.8	13.0	12.0	–23.6	1.1	0.64	16.8	9.0	130.0	0.177	0.40	3.0*	*	Ring B	4	S pec (Ring B) Sy2	30
NGC 1265	49.565250	41.857750	0.025137	14.4	13.4	11.3	–24.0	1.8	0.89	41.4	12.0	125.0	0.753	0.66	–4.0	0.5	E5	0	E+ LERG	31
NGC 1275	49.950667	41.511694	0.017559	12.6	11.9	10.8	–23.7	2.2	0.77	16.8	22.2	110.0	0.697	0.29	99.0	*	S0/P	4	cD;pec;NLRG;Sy2;LEG	32
NGC 1667	72.154750	–6.319972	0.015167	12.8	12.1	11.4	–22.8	1.8	0.78	18.6	12.6	20.0	0.221	0.05	5.0	0.4	SBc	4	SAB(r)c Sy2	33
NGC 1700	74.234625	–4.865778	0.012972	12.2	11.2	10.5	–23.3	3.3	0.64	18.6	9.0	120.0	0.113	0.82	–5.0	0.3	E4	0	E4	34
NGC 2403	114.214167	65.602556	0.000445	8.9	8.5	8.6	–17.9	21.9	0.56	143.7	126.0	127.0	0.157	0.00	6.0	0.3	SBc	3	SAB(s)cd;HII LINER	35
NGC 2415	114.236208	35.241972	0.012622	12.8	12.4	11.6	–22.2	0.9	1.00	*	7.2	*	0.161	0.37	10.0	1.7	Im	0	Im?	36
IC 0486	120.087417	26.613528	0.026875	14.6	13.7	12.6	–22.8	1.11	0.66	*	6.0	139.0	0.049	0.59	1.0	0.9	SBa	5	Sy1	37
NGC 2500	120.471708	50.737111	0.001681	12.2	11.6	11.1	–18.2	2.9	0.90	*	40.8	48.0	0.129	0.21	7.0	0.3	SBcd	0	SB(rs)d HII	38
NGC 2512	120.782708	23.391833	0.015684	13.9	13.1	12.3	–21.9	1.4	0.64	12.9	11.4	113.0	0.161	0.31	3.0	0.8	SBb	1	SBb Sbrst	39

continuted …

…continued

ID	R.A.(J2000)	Decl.(J2000)	z	B	V	3.6μm	3.6μm	a	b/a	r$_{\rm eff}$	$R^P_{50,V}$	PA	Gal. Ext.	B/T	T	eT	Type	SF &	Classification	Figure
	(deg)	(deg)		(mag)	(mag)	(mag)	(Mag)	($'$)		($''$)	($''$)	(deg)	(mag)					AGN		Set 2 #
(1)	(2)	(3)	(4)	(5)	(6)	(7)	(8)	(9)	(10)	(11)	(12)	(13)	(14)	(15)	(16)	(17)	(18)	(19)	(20)	(21)
IC 2239	123.528292	23.866361	0.020174	14.6	13.6	12.9	–21.9	1.3	0.85	*	4.8	168.0	0.185	0.46	0.0*	*	S0	0	S0?	40
NGC 2552	124.835542	50.009639	0.001748	12.6	12.1	13.1	–16.4	3.5	0.66	68.7	43.2	57.0	0.165	0.00	9.0	0.3	SBm	0	SA(s)m?	41
IC 0505	125.840292	4.372472	0.031232	14.9	14.0	12.9	–22.9	1.24	0.69	*	9.6	143.0	0.033	0.23	3.0*	*	S	5	S;BrClG AGN	42
NGC 2604	128.346417	29.538806	0.00693	13.3	12.6	13.0	–19.5	2.1	1.00	*	25.2	*	0.105	0.14	6.0	0.8	SBc	1	SB(rs)cd;WR;HIISbrst	43
NGC 2608	128.822208	28.473417	0.007122	13.0	12.3	11.5	–21.0	2.3	0.61	25.5	18.6	60.0	0.109	0.09	3.0	0.5	SBb	0	SB(s)b:	44
NGC 2685	133.894625	58.734389	0.002945	12.1	11.3	10.9	–19.6	4.5	0.51	32.1	10.2	38.0	0.149	0.76	–1.0	0.3	SB0-a	4	(R)SB0+ pec;RETSy2	45
NGC 2712	134.876958	44.913889	0.006054	12.8	12.1	11.3	–20.9	2.9	0.55	27.9	18.6	178.0	0.037	0.15	3.0	0.5	SBb	0	SB(r)b:	46
NGC 2731	135.535042	8.301667	0.008616	14.4	13.7	12.9	–20.0	0.8	0.62	*	7.2	70.0	0.177	0.11	5.0*	*	Sc	0	S?	47
NGC 2730	135.565958	16.838306	0.012782	13.6	13.0	12.5	–21.3	1.7	0.76	*	19.8	80.0	0.077	0.09	8.0	1.1	SBdm	0	SBdm:	48
NGC 2750	136.449625	25.437417	0.00892	12.6	11.9	11.7	–21.3	1.9	0.79	*	30.6	81.0	0.133	0.22	5.0	0.7	Sc	0	Sc	49
NGC 2740	136.520792	51.735306	0.029516	14.8	14.0	14.2	–21.4	0.76	0.83	*	8.4	45.0	0.017	0.21	2.0*	*	Sab	4	S? NLAGN	50
NGC 2742	136.889708	60.479333	0.0043	12.0	11.4	10.8	–20.6	3.0	0.50	45.3	28.2	87.0	0.185	0.00	5.0	0.5	Sc	0	SA(s)c:	51
NGC 2768	137.906250	60.037222	0.004513	10.8	9.9	9.6	–21.9	8.1	0.53	64.2	24.0	95.0	0.161	0.61	–5.0	0.3	E6	3	S0_1/2_ LINER	52
NGC 2776	138.060458	44.954833	0.008759	12.1	11.6	11.6	–21.3	2.32	0.62	33.6	24.0	0.0	0.037	0.09	5.0	0.3	SBc	0	SAB(rs)c	53
NGC 2778	138.101542	35.027528	0.006835	13.4	12.4	12.1	–20.3	1.4	0.71	15.6	7.8	40.0	0.021	0.39	–5.0	0.8	E3	0	E	54
NGC 2782	138.521292	40.113694	0.008483	12.3	11.6	11.3	–21.6	3.5	0.74	23.4	19.8	74.0	0.0	0.55	1.0	0.3	SBa	5	SAB(rs)a;Sy1 Sbrst	55
NGC 2824	139.759292	26.269972	0.0092	14.2	13.3	12.6	–20.5	0.9	0.67	6.6	3.6	160.0	0.061	0.51	–2.0	0.9	S0	4	S0 Sy?	56
NGC 2831	139.939542	33.745000	0.017279	14.3	13.3	12.3	–22.2	0.71	0.73	*	5.4	*	0.0	0.27	–5.0	0.5	E0	0	E0	57
NGC 2832	139.945250	33.749750	0.023176	12.9	11.9	11.4	–23.7	1.71	0.69	25.5	12.0	160.0	0.0	0.73	–4.0	0.3	E2	3	E+2:;cD LINER	58
NGC 2844	140.450042	40.151250	0.004957	13.8	13.0	12.5	–19.3	1.5	0.53	*	8.4	13.0	0.0	0.46	1.0	0.6	Sa	0	SA(r)a: HII	59
NGC 2893	142.570667	29.539972	0.005667	13.9	13.2	12.8	–19.2	1.1	0.91	*	3.6	79.0	0.021	0.41	-.0	0.8	SB0-a	1	(R)SB0/a Sbrst	60
NGC 2906	143.025917	8.441778	0.007138	13.4	12.7	11.5	–21.0	1.4	0.64	*	12.0	75.0	0.073	0.09	6.0	1.2	Sc	0	Scd:	61
NGC 2892	143.220542	67.617389	0.022822	14.1	13.1	11.9	–23.1	1.4	1.00	*	13.2	*	0.157	0.58	–3.5	0.6	E0	0	E+ pec:	62
NGC 2937	144.437625	2.747361	0.022702	14.6	13.7	12.7	–22.3	0.7	0.76	9.9	3.0	0.0	0.085	0.59	–5.0	0.9	E3	0	E	63
IC 0559	146.182875	9.615000	0.001806	15.1	14.2	14.7	–14.8	0.8	0.75	*	10.2	90.0	0.033	0.00	5.0*	*	S?	0	Sc	64
NGC 3015	147.345500	1.145417	0.025017	14.5	13.5	12.9	–22.3	0.71	0.77	*	4.2	95.0	0.117	0.13	–2.0	1.9	S0	4	SAB0^0^ pec? NLAGN	65
NGC 3011	147.421667	32.221111	0.005147	14.3	13.3	13.6	–18.2	0.96	0.76	*	4.2	69.0	0.013	0.39	–2.0	0.9	S0	0	S0/a	66
NGC 3020	147.527500	12.813639	0.004803	12.6	11.9	13.5	–18.2	3.2	0.50	*	21.6	105.0	0.017	0.06	6.0	0.5	SBc	0	SB(r)cd:	67
NGC 3032	148.033958	29.236222	0.00521	13.2	12.5	12.2	–19.7	2.0	0.90	9.3	2.4	95.0	0.021	0.39	–2.0	0.3	SB0	0	SAB(r)0^0^ HII	68
NGC 3049	148.706500	9.271083	0.004854	12.9	12.1	11.8	–19.9	2.13	0.50	*	24.6	25.0	0.037	0.24	2.0	0.8	SBab	1	SB(rs)ab;HII Sbrst	69
NGC 3055	148.825250	4.270028	0.006021	12.7	12.1	11.9	–20.2	2.12	0.57	*	16.8	63.0	0.093	0.12	5.0	0.4	SBc	0	SAB(s)c WR	70
IC 2520	149.083833	27.227583	0.00413	14.4	13.4	12.4	–18.9	0.83	0.89	*	7.2	90.0	0.033	0.27	99.0	*	P	0	Pec HII	71
IC 2551	152.668000	24.414139	0.021185	14.4	13.6	12.9	–22.0	0.87	0.78	*	1.8	33.0	0.105	0.55	3.0*	*	S	0	S? WR?	72
NGC 3162	153.381625	22.737556	0.00433	12.2	11.6	11.9	–19.5	3.0	0.83	34.5	25.2	33.0	0.065	0.10	4.0	0.3	SBbc	0	SAB(rs)bc	73
NGC 3184	154.570250	41.424056	0.001975	10.4	9.8	8.9	–20.8	7.4	0.93	116.7	91.2	135.0	0.0	0.04	6.0	0.3	SBc	0	SAB(rs)cd HII	74
NGC 3192	154.771375	46.454111	0.030721	14.1	13.3	13.3	–22.4	0.8	0.75	*	7.8	5.0	0.0	0.08	4.0*	*	SBbc/P	0	SB(s)bc pec	75
NGC 3239	156.270375	17.163583	0.002512	11.7	11.3	8.5	–21.7	5.0	0.66	36.9	52.2	81.0	0.105	0.07	10.0	0.3	IBm/P	0	IB(s)m pec	76
NGC 3212	157.068583	79.823389	0.032402	14.0	13.2	13.6	–22.2	1.1	0.91	*	6.6	92.0	0.013	0.48	3.0*	*	SBb	0	S?	77
NGC 3215	157.169083	79.813083	0.031582	13.9	13.1	12.5	–23.3	1.5	0.73	*	12.0	52.0	0.013	0.14	4.0*	*	Sbc	0	SB?	78
NGC 3265	157.778208	28.796667	0.0044	13.9	12.9	12.8	–18.6	0.96	0.70	*	4.8	73.0	0.053	0.66	–5.0	0.7	E2	0	E:;WR? HII	79

continuted …

…continued

ID	R.A.(J2000)	Decl.(J2000)	z	B	V	3.6μm	3.6μm	a	b/a	r_{eff}	$R^{P}_{50,V}$	PA	Gal. Ext.	B/T	T	eT	Type	SF &	Classification	Figure
	(deg)	(deg)		(mag)	(mag)	(mag)	(Mag)	($'$)		($''$)	($''$)	(deg)	(mag)					AGN		Set 2 #
(1)	(2)	(3)	(4)	(5)	(6)	(7)	(8)	(9)	(10)	(11)	(12)	(13)	(14)	(15)	(16)	(17)	(18)	(19)	(20)	(21)
NGC 3310	159.691083	53.503389	0.003312	11.2	10.8	11.0	–19.9	3.1	0.77	12.3	9.6	156.0	0.0	0.46	4.0	0.3	SBbc/P	0	SAB(r)bc pec HII	80
NGC 3319	159.789417	41.686667	0.002465	11.5	11.1	9.3	–20.9	6.2	0.55	128.1	60.0	37.0	0.0	0.11	6.0	0.3	SBc	0	SB(rs)cd HII:	81
NGC 3344	160.879792	24.922222	0.001935	10.5	9.9	9.7	–20.0	7.1	0.92	88.5	61.2	18.0	0.025	0.09	4.0	0.3	SBbc	0	(R)SAB(r)bc HII	82
NGC 3349	160.960667	6.762972	0.027536	15.2	14.5	14.1	–21.4	0.65	0.97	*	5.4	*	0.053	0.19	5.0*	*	Sc	0	WR? HII	83
NGC 3351	160.990417	11.703806	0.002595	10.5	9.7	7.3	–23.0	3.07	0.93	64.2	60.0	13.0	0.045	0.13	3.0	0.3	SBb	1	SB(r)b;HII Sbrst	84
NGC 3370	161.766875	17.273611	0.004266	12.3	11.6	11.7	–19.7	3.2	0.56	*	18.6	148.0	0.037	0.45	5.0	0.3	Sc	0	SA(s)c	85
NGC 3381	162.103417	34.711417	0.005434	12.7	11.8	12.5	–19.4	1.46	0.96	*	19.8	60.0	0.0	0.29	5.0*	*	SB/P	0	SB pec;WR HII	86
NGC 3395	162.458792	32.982861	0.00542	12.4	12.1	12.2	–19.7	2.1	0.57	*	12.6	50.0	0.0	0.15	6.0	0.6	SBc	0	SAB(rs)cd pec: HII	87
NGC 3414	162.817542	27.975111	0.004903	12.0	11.0	10.6	–21.1	3.5	0.74	20.7	13.8	25.0	0.0	0.56	–2.0	0.3	SB0	3	S0 pec LINER	88
NGC 3419	162.823917	13.946000	0.010124	13.4	12.5	12.6	–20.6	1.2	0.83	*	4.2	115.0	0.045	0.47	–1.0	0.5	SB0-a	0	(R)SAB(r)0+	89
NGC 3489	165.077375	13.901222	0.002258	11.1	10.3	10.0	–20.0	3.5	0.57	20.4	9.0	70.0	0.021	0.57	–1.0	0.3	SB0-a	3	SAB(rs)0+ Sy;LINER	90
NGC 3486	165.099458	28.975139	0.002272	11.1	10.5	10.6	–19.4	7.1	0.73	62.7	39.0	80.0	0.015	0.41	5.0	0.3	SBc	4	SAB(r)c;HII Sy2	91
NGC 3561	167.805000	28.696472	0.029367	14.7	13.8	13.1	–22.5	1.36	0.51	*	8.4	*	0.0	0.44	0.0*	*	SB0-a	4	S0^0^: pec Sy3	92
IC 0676	168.165917	9.055833	0.004767	12.7	11.8	12.4	–19.3	1.72	0.60	*	14.4	10.0	0.061	0.46	–1.0	0.5	SB0-a	1	(R)SB(r)0+ Sbrst	93
IC 2637	168.457292	9.586306	0.02923	13.9	12.9	12.9	–22.7	0.92	0.87	*	3.6	*	0.017	0.42	–4.0	0.9	E0	4	E+ pec Sy1.5	94
NGC 3593	168.654167	12.817667	0.002095	11.9	10.9	9.5	–20.3	1.46	0.73	33.6	24.6	92.0	0.0	0.78	-.0	0.4	S0-a	4	SA(s)0/a;HII Sy2	95
NGC 3610	169.605292	58.786278	0.005694	11.7	10.8	10.4	–21.7	1.83	0.89	15.3	6.0	144.0	0.0	0.45	–5.0	0.4	E5	0	SB(r)0^0^ pec	96
NGC 3622	170.051542	67.241556	0.004325	13.7	13.2	13.2	–18.2	1.31	0.55	11.4	7.8	7.0	0.0	0.10	3.0*	*	S?	0	S?	97
NGC 3640	170.278542	3.234833	0.00433	11.4	10.4	9.7	–21.7	4.0	0.80	32.1	16.2	100.0	0.097	0.92	–5.0	0.3	E3	0	E3	98
NGC 3646	170.429500	20.169556	0.01417	11.8	11.1	10.4	–23.6	3.9	0.56	54.6	36.6	50.0	0.0	0.15	4.0	0.3	Sbc/P	0	SA:(r)bc pec (ring)	99
NGC 3655	170.727583	16.590028	0.004913	12.3	11.7	11.2	–20.5	1.5	0.67	*	11.4	30.0	0.0	0.11	5.0	0.4	Sc	0	SA(s)c: HII	100
NGC 3656	170.911042	53.842111	0.00964	13.3	12.3	11.6	–21.6	1.6	1.00	*	14.4	*	0.0	0.94	90.0	*	E?	3	(R')I0: pec LINER	101
NGC 3659	170.939750	17.818667	0.004287	12.8	12.2	12.8	–18.6	2.1	0.52	*	10.8	60.0	0.0	0.06	9.0	0.8	SBm	0	SB(s)m? HII	102
NGC 3664	171.101042	3.325000	0.004607	15.1	14.5	7.7	–23.9	2.0	0.95	35.1	19.2	15.0	0.109	0.01	9.0	0.4	SBm	0	SB(s)m pec	103
IC 0692	171.472792	9.987500	0.003858	14.4	13.6	13.6	–17.6	0.84	0.64	*	4.2	125.0	0.096	0.81	–5.0	*	S	0	E	104
IC 0691	171.684667	59.155417	0.003992	14.5	13.9	12.8	–18.5	0.9	0.60	*	3.6	150.0	0.0	0.59	99.0	*	P	0	I?;WR? HII	105
NGC 3683	171.882708	56.877056	0.005724	13.2	12.5	10.7	–21.3	1.84	0.53	*	8.4	128.0	0.0	0.30	5.0	0.9	SBc	0	SB(s)c? HII	106
NGC 3686	171.933208	17.224194	0.003856	11.9	11.3	10.6	–20.6	3.2	0.78	37.8	33.0	15.0	0.023	0.05	4.0	0.5	SBbc	0	SB(s)bc	107
NGC 3720	173.090000	0.804000	0.019837	13.7	13.0	12.6	–22.2	1.0	0.90	11.1	6.6	85.0	0.077	0.12	.9	0.7	Sa	0	SAa:	108
NGC 3726	173.338000	47.029194	0.002887	10.9	10.4	10.0	–20.6	6.2	0.69	*	61.2	10.0	0.008	0.03	5.0	0.3	SBc	0	SAB(r)c HII	109
NGC 3738	173.953292	54.523889	0.000764	12.1	11.7	12.2	–15.5	2.5	0.76	*	24.0	155.0	0.0	0.11	10.0	0.3	Im	0	Irr HII	110
NGC 3741	174.025750	45.283639	0.000764	14.3	14.0	15.6	–12.1	2.0	0.55	20.4	11.4	5.0	0.0	0.07	10.0	0.8	Im	0	ImIII/BCD	111
NGC 3750	174.465167	21.974250	0.030291	14.9	13.9	13.4	–22.3	0.8	0.87	*	6.6	132.0	0.0	0.88	–3.0	0.7	E-S0	0	SAB0-?	112
NGC 3773	174.553667	12.112056	0.003276	13.0	12.0	13.1	–17.7	1.2	0.83	*	9.0	165.0	0.089	0.52	–2.0	0.6	S0	0	SA0: HII	113
NGC 3781	174.765667	26.361750	0.022676	14.8	13.8	12.8	–22.2	0.71	0.76	*	4.8	30.0	0.0	0.51	0.0*	*	S0	0	S0/a	114
NGC 3794	175.222583	56.202028	0.00462	13.6	12.9	13.3	–18.3	2.2	0.64	*	24.0	120.0	0.0	0.20	7.0*	*	SBc	0	SAB(s)d	115
NGC 3799	175.039083	15.327306	0.011048	14.7	13.9	13.6	–19.8	0.8	0.62	*	6.0	114.0	0.055	0.02	3.0	0.5	SBb/P	0	SB(s)b: pec	116
NGC 3801	175.070583	17.728056	0.011064	13.0	12.0	11.5	–22.0	3.5	0.60	33.0	20.4	120.0	0.0	0.63	–2.0	1.4	S0	0	S0/a	117
NGC 3811	175.319292	47.690806	0.010357	12.9	12.3	12.0	–21.3	2.2	0.77	*	15.6	160.0	0.018	0.30	6.0	1.1	SBc/P	1	SB(r)cd: Sbrst	118
NGC 3822	175.546292	10.277778	0.020904	14.0	13.1	12.0	–22.9	1.4	0.57	*	6.0	178.0	0.122	0.19	–2.0	1.7	S0	4	Sb Sy2	119

continuted …

…continued

ID	R.A.(J2000)	Decl.(J2000)	z	B	V	3.6μm	3.6μm	a	b/a	$r_{\rm eff}$	$R^P_{50,V}$	PA	Gal. Ext.	B/T	T	eT	Type	SF &	Classification	Figure
	(deg)	(deg)		(mag)	(mag)	(mag)	(Mag)	($'$)		($''$)	($''$)	(deg)	(mag)					AGN		Set 2 #
(1)	(2)	(3)	(4)	(5)	(6)	(7)	(8)	(9)	(10)	(11)	(12)	(13)	(14)	(15)	(16)	(17)	(18)	(19)	(20)	(21)
NGC 3839	175.976375	10.784694	0.019734	13.9	13.3	12.9	–21.9	1.14	0.53	*	6.6	87.0	0.195	0.25	8.0	1.3	Sd	0	Sdm:	120
IC 0730	176.396875	3.231833	0.020198	14.6	13.7	12.8	–22.0	0.91	0.62	*	3.6	36.0	0.049	0.62	-.0	1.8	S0-a	0	S0/a pec?	121
NGC 3870	176.485833	50.199750	0.002522	13.5	13.0	13.2	–17.0	1.1	0.65	7.8	4.8	25.0	0.0	0.44	–2.0	1.7	S0	0	S0?	122
NGC 3906	177.418750	48.425972	0.0032	13.8	12.9	12.9	–17.9	1.9	0.89	*	22.2	0.0	0.027	0.04	7.0	0.8	SBcd	0	SB(s)d	123
NGC 3921	177.778625	55.078750	0.019667	13.1	12.4	12.6	–22.2	2.1	0.62	21.6	6.0	20.0	0.0	0.26	-.0	0.4	S0-a	0	(R')SA(s)0/a pec	124
NGC 3928	177.948417	48.683139	0.003296	13.2	12.6	12.0	–18.8	1.29	0.92	11.4	6.0	*	0.038	0.89	3.0*	*	E0	0	SA(s)b? HII	125
NGC 3934	178.052333	16.851444	0.012605	14.4	13.6	12.8	–20.9	1.1	0.91	*	10.8	66.0	0.135	0.68	0.0*	*	Sb	0	S0/a	126
NGC 3938	178.206042	44.120722	0.002699	10.9	10.4	10.2	–20.2	5.4	0.91	72.0	54.6	0.0	0.0	0.16	5.0	0.3	Sc	0	SA(s)c HII	127
NGC 3941	178.230667	36.986333	0.003102	11.3	10.3	9.9	–20.8	3.5	0.66	22.8	11.4	10.0	0.0	0.49	–2.0	0.3	SB0	4	SB(s)0^0^ Sy2	128
NGC 3945	178.307208	60.675556	0.004273	11.8	10.9	9.7	–21.7	5.2	0.67	22.8	10.2	160.0	0.073	0.58	–1.0	0.3	SB0	3	SB(rs)0+ LINER	129
NGC 4014	179.649208	16.177306	0.012552	13.2	12.3	11.3	–22.4	2.2	0.59	*	6.6	120.0	0.088	0.64	-.0	0.8	S0-a	0	S0/a	130
NGC 4068	181.003250	52.588278	0.0007	13.0	12.4	11.0	–16.4	3.3	0.52	*	1.8	30.0	0.0	0.09	10.0	0.5	Im	0	IAm	131
NGC 4073	181.112792	1.895972	0.019584	12.4	11.4	10.8	–23.9	1.93	0.63	47.4	24.0	105.0	0.008	0.85	–3.8	0.4	E3	0	E;BrClG	132
NGC 4125	182.025083	65.174139	0.004523	10.7	9.7	9.1	–22.4	5.8	0.55	58.5	21.6	81.0	0.037	0.82	–5.0	0.3	E6/P	3	E6 pec LINER	133
NGC 4136	182.323708	29.927611	0.002031	11.8	11.1	11.8	–17.9	4.0	0.93	*	40.2	90.0	0.022	0.03	5.0	0.5	SBc	0	SAB(r)c HII	134
NGC 4150	182.640208	30.401528	0.000694	12.4	11.6	11.4	–16.0	2.3	0.70	17.7	9.0	147.0	0.044	0.21	–2.0	0.4	S0	0	SA(r)0^0^?	135
NGC 4162	182.968625	24.123667	0.008569	12.9	12.2	11.8	–21.1	2.3	0.61	21.3	17.4	174.0	0.089	0.07	4.0	0.4	Sbc	5	(R)SA(rs)bc AGN	136
NGC 4168	183.071958	13.205194	0.007625	12.1	11.2	10.7	–22.0	2.03	0.78	28.5	21.0	120.0	0.026	0.90	–5.0	0.3	E2	4	E2 Sy1.9	137
IC 3050	183.446958	13.424806	0.007055	12.5	11.7	10.6	–21.9	2.4	0.71	*	29.4	85.0	0.025	0.02	5.0*	*	SBc	0	SAB(rs)cd? HII	138
NGC 4194	183.539458	54.526833	0.008342	13.0	12.5	12.0	–20.9	1.8	0.61	7.5	3.0	168.0	0.0	0.79	10.0	0.4	IBm/P	0	IBm pec;BlueCG HII	139
NGC 4207	183.877083	9.584889	0.001988	13.6	12.6	11.9	–17.8	1.59	0.57	*	12.6	124.0	0.0	0.25	6.0*	*	Scd	0	Scd HII	140
NGC 4234	184.288167	3.683056	0.006761	13.3	12.7	12.2	–20.2	1.37	0.77	*	16.2	*	0.014	0.18	8.7	0.5	SBm	0	(R')SB(s)m HII	141
NGC 4267	184.938500	12.798278	0.003406	11.9	10.9	9.8	–21.1	3.2	0.94	41.4	18.6	33.0	0.024	0.30	–3.0	0.3	E/SB0	0	SB(s)0-?	142
NGC 4290	185.198042	58.092500	0.010114	12.8	12.0	11.8	–21.5	2.02	0.62	*	19.8	90.0	0.0	0.21	2.0	0.5	SBab	0	SB(rs)ab: HII	143
NGC 4335	185.757833	58.444556	0.015417	13.4	12.4	11.6	–22.6	1.9	0.79	*	9.0	145.0	0.0	0.64	–5.0	0.8	E2	0	E	144
NGC 4365	186.117833	7.317667	0.004146	10.5	9.6	8.8	–22.6	6.9	0.72	49.8	42.0	40.0	0.0	0.67	–5.0	0.3	E3	0	E3	145
NGC 4369	186.150833	39.383000	0.003486	12.3	11.7	10.8	–20.2	2.1	0.95	16.5	13.2	127.0	0.0	0.90	1.0	0.3	Sa	0	(R)SA(rs)a HII	146
NGC 4378	186.325417	4.925139	0.008536	12.6	11.7	11.2	–21.7	2.9	0.93	18.6	13.2	167.0	0.0	0.47	1.0	0.3	Sa	4	(R)SA(s)a Sy2	147
NGC 4414	186.612917	31.223528	0.002388	11.0	10.1	9.4	–20.7	3.6	0.56	27.3	21.0	155.0	0.019	0.07	5.0	0.3	Sc	3	SA(rs)c?;HII LINER	148
NGC 4412	186.650333	3.964694	0.007652	13.2	12.4	12.2	–20.5	1.4	0.93	*	17.4	132.0	0.028	0.08	3.0	0.4	SBb/P	3	SB(r)b? pec LINER	149
NGC 4420	186.743750	2.494361	0.005621	12.8	12.1	11.5	–20.5	1.44	0.60	*	12.6	8.0	0.0	0.14	4.0	0.6	SBbc	3	SB(r)bc:;HII LINER	150
NGC 4449	187.046250	44.093639	0.00069	10.0	9.6	9.9	–17.5	6.2	0.71	48.6	43.2	45.0	0.0	0.11	10.0	0.3	IBm	1	IBm;HII Sbrst	151
NGC 4450	187.123458	17.084944	0.006518	10.9	10.1	9.7	–22.7	5.2	0.75	61.2	42.0	175.0	0.025	0.27	2.0	0.3	Sab	3	SA(s)ab;LINER Sy3	152
NGC 4457	187.245875	3.570583	0.002942	11.8	10.9	10.2	–20.3	2.7	0.85	17.4	10.8	66.0	0.035	0.57	-.0	0.3	SB0-a	3	(R)SAB(s)0/a LINER	153
NGC 4494	187.850417	25.775250	0.004476	10.7	9.8	9.3	–22.2	4.8	0.73	48.6	25.8	171.0	0.051	0.97	–5.0	0.3	E1	3	E1-2 LINER	154
NGC 4500	187.842333	57.964639	0.010377	13.1	12.5	12.2	–21.1	1.6	0.62	*	5.4	130.0	0.0	0.33	1.0	0.4	SBa	1	SB(s)a Sbrst	155
NGC 4498	187.914833	16.852778	0.005027	12.8	12.1	12.1	–19.7	3.0	0.53	*	25.8	133.0	0.026	0.17	6.5	0.5	SBc	0	SAB(s)d HII	156
NGC 4509	188.278292	32.091556	0.003125	14.3	13.5	14.6	–16.1	0.9	0.67	*	7.2	155.0	0.02	0.01	2.0	0.9	Sab/P	0	Sab pec? HII	157
IC 0800	188.486083	15.354833	0.007759	14.1	13.4	13.0	–19.7	1.51	0.67	*	20.4	157.0	0.043	0.17	4.7	0.9	SBc	0	SB(rs)c pec? HII	158
NGC 4561	189.034167	19.322917	0.004677	12.9	12.5	12.8	–18.8	1.5	0.87	28.5	18.0	30.0	–	0.16	8.0	0.4	SBcd	0	SB(rs)dm	159

continuted …

…continued

ID	R.A.(J2000)	Decl.(J2000)	z	B	V	3.6μm	3.6μm	a	b/a	$r_{\rm eff}$	$R^P_{50,V}$	PA	Gal. Ext.	B/T	T	eT	Type	SF &	Classification	Figure
	(deg)	(deg)		(mag)	(mag)	(mag)	(Mag)	($'$)		($''$)	($''$)	(deg)	(mag)					AGN		Set 2 #
(1)	(2)	(3)	(4)	(5)	(6)	(7)	(8)	(9)	(10)	(11)	(12)	(13)	(14)	(15)	(16)	(17)	(18)	(19)	(20)	(21)
NGC 4578	189.377333	9.555083	0.007645	12.4	11.5	10.6	–22.1	3.3	0.76	32.1	21.6	35.0	0.0	0.44	–2.0	0.5	S0	0	SA(r)0^0^:	160
NGC 4580	189.451625	5.368528	0.003449	12.3	11.8	11.3	–19.6	2.28	0.64	27.3	24.0	165.0	0.0	0.01	1.0	0.3	SBa/P	3	SAB(rs)a pec LINER	161
NGC 4612	190.386458	7.314889	0.005921	12.5	11.5	11.3	–20.8	2.17	0.64	*	13.2	145.0	0.009	0.30	–2.0	0.4	SB0	0	(R)SAB0^0^	162
IC 3687	190.562917	38.503333	0.001181	13.7	13.5	15.5	–13.1	3.4	0.88	41.4	23.4	9.0	0.0	0.00	10.0	0.5	IBm	0	IAB(s)m	163
NGC 4636	190.707625	2.687778	0.003129	10.4	9.5	8.9	–21.8	6.0	0.78	88.5	58.2	150.0	0.05	0.76	–5.0	0.3	E2	3	E/S0_1;LINER Sy3	164
NGC 4651	190.927625	16.393389	0.002628	11.4	10.8	10.5	–19.8	4.0	0.65	36.0	21.6	80.0	0.028	0.06	5.0	0.3	Sc/P	3	SA(rs)c LINER	165
NGC 4670	191.321125	27.125417	0.003566	13.1	12.7	12.9	–18.1	1.4	0.79	*	6.0	90.0	0.043	0.31	-.0	0.4	SB0-a	0	SB(s)0/a pec: BCDG	166
NGC 4688	191.943833	4.336056	0.003289	12.6	11.9	13.2	–17.6	3.2	0.87	*	24.6	123.0	0.013	0.34	6.0	0.5	SBc	3	SB(s)cd;LINER HII	167
NGC 4689	191.939833	13.762806	0.00539	11.6	11.0	10.5	–21.4	4.3	0.81	*	48.0	160.0	0.048	0.11	4.0	0.3	Sbc	3	SA(rs)bc;Sy LINER	168
NGC 4698	192.095458	8.487389	0.003366	11.5	10.6	10.2	–20.7	4.0	0.62	33.0	18.6	170.0	0.0	0.33	2.0	0.3	Sab	3	SA(s)ab;Sy2 LINER	169
NGC 4704	192.193458	41.921250	0.027132	14.5	13.7	12.7	–22.8	1.0	0.90	12.3	12.0	105.0	0.0	0.15	3.5	0.6	SBbc/P	4	Sbc pec;HII Sy2	170
NGC 4701	192.298292	3.388722	0.002406	12.8	12.4	12.4	–17.8	2.8	0.75	*	12.0	45.0	0.014	0.46	6.0	0.3	Sc	0	SA(s)cd HII	171
NGC 4713	192.491125	5.311417	0.002183	12.2	11.7	11.7	–18.2	2.28	0.68	32.1	25.8	100.0	0.0	0.01	7.0	0.3	SBcd	3	SAB(rs)d;HII LINER	172
NGC 4736	192.721083	41.120444	0.001027	9.0	8.2	7.6	–20.7	11.2	0.81	38.7	19.2	117.0	0.0	0.82	2.0	0.3	Sab	3	(R)SA(r)ab;Sy2 LINER	173
NGC 4765	193.310042	4.463111	0.002388	13.4	13.0	13.4	–16.7	1.1	0.73	7.8	6.0	80.0	0.006	0.04	-.0	1.7	S0-a	0	S0/a? HII	174
NGC 4772	193.371500	2.168389	0.003469	12.0	11.0	10.9	–20.0	3.4	0.50	23.7	21.0	147.0	0.0	0.51	1.0	0.3	Sa	3	SA(s)a;LINER Sy3	175
NGC 4868	194.787083	37.310333	0.015561	13.0	12.2	11.8	–22.4	1.6	0.94	*	13.2	90.0	0.0	0.07	2.3	0.6	Sab	0	SAab?	176
IC 4182	196.456417	37.604889	0.001071	11.8	11.1	14.1	–14.3	6.0	0.92	*	91.8	90.0	0.0	0.00	9.0	0.4	Sm	0	SA(s)m	177
NGC 4992	197.273333	11.634167	0.025137	14.3	13.4	12.8	–22.5	1.18	0.58	*	7.2	10.0	0.016	0.22	1.0	0.9	Sa	4	Sa;XBONG Sy2	178
NGC 5060	199.317583	6.037444	0.020791	14.1	13.3	12.2	–22.7	1.1	0.73	*	12.0	55.0	0.0	0.29	3.0	0.9	SBb	0	SB(s)b	179
NGC 5068	199.728375	–21.039111	0.002235	10.7	10.0	9.8	–20.2	7.2	0.88	73.5	84.0	110.0	0.309	0.28	6.0	0.3	SBc	0	SB(s)d	180
NGC 5123	200.793833	43.086250	0.027546	13.5	12.8	12.5	–22.9	1.2	0.93	*	12.6	174.0	0.0	0.16	6.0	1.2	Sc	0	Scd:	181
NGC 5127	200.937583	31.565750	0.016218	12.9	11.9	12.1	–22.3	1.54	0.70	*	13.2	75.0	0.023	0.52	–5.0	0.5	E2	0	E pec	182
NGC 5141	201.214333	36.378528	0.017379	13.8	12.8	12.3	–22.1	1.3	0.77	*	4.2	80.0	0.0	0.60	–2.0	0.8	S0	0	S0	183
NGC 5147	201.582208	2.100861	0.003629	12.3	11.8	10.9	–20.2	1.9	0.79	21.3	21.0	120.0	0.0	0.15	8.0	0.4	SBd	0	SB(s)dm HII	184
NGC 5198	202.547500	46.670778	0.008402	12.7	11.8	11.5	–21.4	2.1	0.86	25.5	10.8	0.0	0.0	0.42	–5.0	0.5	E1	0	E1-2:	185
NGC 5230	203.882833	13.676167	0.022856	12.8	12.1	12.1	–22.9	2.2	0.86	*	22.8	*	0.0	0.09	5.0	0.3	SBc	0	SA(s)c HII	186
NGC 5248	204.383417	8.885167	0.003839	11.0	10.3	9.7	–21.5	6.2	0.73	53.4	35.4	122.0	0.0	0.48	4.0	0.3	SBbc	4	(R)SB(rs)bc;Sy2HII	187
NGC 5257	204.970458	0.840000	0.022676	12.9	12.4	12.3	–22.7	1.8	0.50	*	9.6	121.0	0.009	0.27	3.0	0.4	SBb/P	2	SAB(s)b pec;HIILIRG	188
NGC 5258	204.990375	0.830944	0.022539	12.9	12.3	11.6	–23.4	1.7	0.65	*	9.0	22.0	0.009	0.27	3.0	0.4	SBb	3	SA(s)b: pec;HIILINER	189
NGC 5278	205.415083	55.670639	0.025154	13.7	12.9	10.9	–24.3	1.3	0.77	*	9.0	57.0	0.0	0.28	3.0	0.4	Sb/P	0	SA(s)b? pec	190
NGC 5273	205.534750	35.654222	0.003619	12.4	11.6	11.1	–19.9	1.94	0.93	30.6	23.4	10.0	0.0	0.17	–2.0	0.3	S0	4	SA(s)0^0^ Sy1.9	191
NGC 5313	207.434750	39.984778	0.008466	12.8	12.0	10.9	–22.0	1.41	0.67	*	12.6	43.0	0.0	0.08	3.0	1.6	Sb	0	Sb?	192
NGC 5368	208.621500	54.330667	0.015531	13.8	13.0	12.5	–21.7	1.16	0.67	*	6.0	10.0	0.0	0.54	1.5	0.6	SBab	0	(R’)SABab:	193
NGC 5363	209.030042	5.254778	0.003799	11.1	10.1	9.5	–21.6	4.1	0.63	36.0	27.0	135.0	0.038	0.82	90.0	*	S0-a	3	I0? LINER	194
NGC 5374	209.373458	6.097000	0.014617	13.3	12.5	11.8	–22.3	1.7	0.88	*	16.8	54.0	0.023	0.13	3.7	0.6	SBbc	0	SB(r)bc?	195
NGC 5414	210.514708	9.929333	0.014206	13.4	12.4	12.7	–21.3	1.0	0.80	*	4.8	172.0	0.006	0.28	99.0	*	P	0	PECULR	196
NGC 5448	210.708458	49.172694	0.006748	11.9	11.0	11.2	–21.1	1.49	0.68	72.0	15.6	115.0	0.041	0.20	1.0	0.3	SBa	5	(R)SAB(r)a AGN	197
NGC 5490	212.488708	17.545556	0.016195	13.1	12.1	11.5	–22.8	1.74	0.64	18.6	6.0	5.0	0.0	0.75	–5.0	0.5	E2	0	E	198
NGC 5520	213.094958	50.348417	0.006261	13.2	12.4	11.3	–20.9	2.0	0.55	*	7.8	66.0	0.0	0.47	3.0	0.8	Sb	0	Sb	199

continuted …

…continued

ID	R.A.(J2000) (deg)	Decl.(J2000) (deg)	z	B (mag)	V (mag)	3.6μm (mag)	3.6μm (Mag)	a ($'$)	b/a	r$_{\rm eff}$ ($''$)	$R^P_{50,V}$ ($''$)	PA (deg)	Gal. Ext. (mag)	B/T	T	eT	Type	SF & AGN	Classification	Figure Set 2 #
(1)	(2)	(3)	(4)	(5)	(6)	(7)	(8)	(9)	(10)	(11)	(12)	(13)	(14)	(15)	(16)	(17)	(18)	(19)	(20)	(21)
NGC 5515	213.159042	39.310278	0.025749	13.7	12.9	12.4	–22.9	1.31	0.53	*	4.8	108.0	0.0	0.27	2.0	0.8	Sab	4	Sab Sy1.9	200
NGC 5541	214.132500	39.589056	0.025678	13.6	12.7	12.3	–23.0	0.95	0.69	*	7.2	12.0	0.0	0.07	5.0*	*	S?	0	Sc HII	201
NGC 5532	214.220625	10.807389	0.024704	12.9	11.9	11.2	–24.0	1.32	0.77	23.4	12.6	*	0.0	0.79	–2.0	0.8	S0	0	FRI LEG	202
NGC 5557	214.607167	36.493556	0.010737	11.9	11.0	10.6	–22.8	1.93	0.82	30.0	13.8	105.0	0.0	0.61	–5.0	0.3	E1	0	E1	203
NGC 5585	214.950833	56.729056	0.000977	11.2	10.7	9.3	–18.8	5.8	0.64	101.7	45.6	30.0	0.0	0.39	7.0	0.3	SBcd	0	SAB(s)d HII	204
NGC 5576	215.265333	3.271000	0.005023	11.9	11.0	10.3	–21.5	3.5	0.63	18.0	7.8	95.0	0.037	0.73	–5.0	0.3	E3	0	E3	205
NGC 5584	215.599042	–0.387667	0.005464	12.1	11.4	11.4	–20.5	2.45	0.67	*	39.6	140.0	0.145	0.03	6.0	0.3	SBc	0	SAB(rs)cd	206
NGC 5596	215.619750	37.122194	0.010414	14.4	13.5	12.9	–20.5	1.13	0.65	9.6	6.0	100.0	0.0	0.41	–2.0	0.8	S0	0	S0	207
NGC 5631	216.638750	56.582639	0.006484	12.4	11.5	11.0	–21.3	1.86	0.87	18.9	12.0	*	0.0	0.56	–2.0	0.3	S0	4	SA(s)0^0^ Sy2	208
NGC 5633	216.868250	46.146528	0.007785	13.1	12.4	11.9	–20.8	1.56	0.62	15.6	10.2	10.0	0.039	0.01	3.0	0.4	Sb	0	(R)SA(rs)b	209
NGC 5660	217.457542	49.622667	0.007765	12.4	11.9	11.8	–20.9	2.8	0.89	25.5	24.0	90.0	0.0	0.30	5.0	0.3	SBc	0	SAB(rs)c	210
NGC 5653	217.543417	31.215500	0.011881	12.9	12.2	11.4	–22.2	1.7	0.76	*	8.4	125.0	0.0	0.35	3.0	0.4	Sb	2	(R')SA(rs)b;HIILIRG	211
NGC 5669	218.181208	9.890444	0.004563	12.0	11.3	12.5	–19.1	4.0	0.70	*	40.8	50.0	0.021	0.03	6.0	0.3	SBc	0	SAB(rs)cd	212
NGC 5668	218.351417	4.450444	0.00526	12.2	11.5	11.9	–20.0	3.3	0.91	37.8	32.4	*	0.053	0.40	7.0	0.3	Sd	0	SA(s)d	213
NGC 5691	219.472250	–0.398889	0.006238	12.3	11.8	12.4	–19.9	1.9	0.74	19.8	13.2	110.0	0.121	0.10	1.0	0.4	SBa/P	0	SAB(s)a: pec HII	214
IC 1065	222.339875	63.270556	0.041639	14.4	13.6	13.2	–23.2	0.8	0.95	11.4	5.4	141.0	0.029	0.51	–2.0	0.8	SB0	0	SB0;Radio galaxy	215
NGC 5778	223.631208	18.642306	0.055502	14.8	13.8	13.3	–23.7	1.2	0.75	*	11.4	10.0	0.025	0.47	–5.0	1.7	E3	0	cD;BrClG	216
IC 1076	223.748417	18.037333	0.020247	14.2	13.7	13.0	–21.8	1.0	0.50	*	5.4	5.0	0.025	0.33	4.0*	*	Sbc	1	SBc Sbrst	217
NGC 5820	224.665917	53.886083	0.011124	13.4	12.5	11.7	–21.8	1.7	0.65	*	5.4	87.0	0.025	0.69	–2.0	0.3	S0	0	S0	218
NGC 5813	225.296792	1.701972	0.006525	11.5	10.5	10.1	–22.2	4.2	0.71	57.3	31.8	145.0	0.149	0.41	–5.0	0.3	E1	3	E1-2 LINER	219
NGC 5831	226.029167	1.219917	0.005524	12.5	11.5	10.9	–21.0	1.94	0.82	25.5	14.4	55.0	0.137	0.58	–5.0	0.4	E3	5	E3 BLLAC	220
NGC 5936	232.503458	12.989333	0.013356	13.1	12.5	11.7	–22.2	1.4	0.93	*	14.4	36.0	0.093	0.20	3.0	0.4	SBb	2	SB(rs)b;LIRG HII	221
NGC 5953	233.634917	15.193778	0.006555	13.2	12.3	10.7	–21.6	1.35	0.86	*	4.8	169.0	0.093	0.53	1.0	0.4	S0-a	4	SAa: pec;LINER;Sy2	222
NGC 5964	234.400917	5.974028	0.004827	12.6	11.9	11.5	–20.1	4.2	0.76	*	52.8	145.0	0.145	0.24	7.0	0.3	SBcd	3	SB(rs)d AGN?	223
NGC 5982	234.665958	59.355833	0.010064	12.0	11.1	10.5	–22.7	2.26	0.62	23.7	11.4	110.0	0.013	0.87	–5.0	0.3	E3	3	E3 LINER	224
NGC 5992	236.089625	41.086361	0.031749	14.3	13.7	13.3	–22.5	0.9	0.78	*	4.2	175.0	0.053	0.60	2.0*	*	Sab	0	SBb HII	225
NGC 5990	236.568167	2.415417	0.012806	13.3	12.4	11.0	–22.8	1.5	0.60	*	9.0	115.0	0.293	0.42	1.0	1.2	Sa	4	(R')Sa pec?;Sy2LIRG	226
IC 1144	237.840375	43.417667	0.040291	14.5	13.5	13.3	–23.1	0.7	0.86	*	3.0	100.0	0.033	0.54	–3.0	1.3	E-S0	0	S0-:	227
NGC 6047	241.287458	17.729889	0.031262	14.6	13.5	13.0	–22.8	1.1	0.73	17.7	9.6	90.0	0.061	0.65	–4.0	0.5	E3	0	E+	228
NGC 6109	244.418833	35.004278	0.029544	13.8	12.7	12.8	–22.9	1.06	0.94	25.5	6.0	*	0.013	0.60	–2.0	*	S0	3	E/S0;BrClG;LERGLINER	229
NGC 6137	245.762917	37.922361	0.031031	13.4	12.4	11.6	–24.1	1.9	0.63	25.5	9.0	175.0	0.005	0.88	–5.0	0.8	E4	0	E	230
NGC 6166	247.160333	39.551556	0.030354	12.8	11.8	10.9	–24.8	1.9	0.74	47.4	16.2	35.0	0.0	0.89	–4.0	0.4	E3	0	cD;E;NLRG LEG	231
NGC 6240	253.245292	2.400917	0.02448	13.8	12.9	11.3	–23.9	2.1	0.52	*	12.0	20.0	0.285	0.48	90.0	*	E?	3	I0: pec;LINER Sy2	232
NGC 6340	257.603542	72.304444	0.003996	11.9	11.0	10.6	–20.7	3.2	0.94	42.3	25.2	120.0	0.197	0.26	-.0	0.3	S0-a	3	SA(s)0/a LINER	233
NGC 6338	258.845792	57.411194	0.027303	13.4	12.3	11.8	–23.7	1.56	0.64	28.5	12.6	15.0	0.073	0.58	–2.0	0.8	S0	5	cD;S0;PEG blazar	234
IC 1262	263.258417	43.759611	0.032649	14.7	13.6	12.9	–23.0	1.2	0.50	12.3	7.8	85.0	0.069	0.75	–5.0	0.8	E5	0	cD;E	235
NGC 6789	289.175667	63.971472	-0.00047	13.8	13.2	14.0	–13.8	1.3	0.77	*	16.8	60.0	0.325	0.00	10.0	0.8	Im	0	Im	236
NGC 7047	319.115208	–0.826500	0.019383	14.2	13.4	12.4	–22.3	1.38	0.50	*	12.0	107.0	0.149	0.02	3.0	1.2	SBb	0	SAB(r)b: HII	237
NGC 7077	322.498375	2.414167	0.003843	14.1	13.1	13.9	–17.2	0.8	0.87	*	5.4	37.0	0.165	0.47	–3.5	1.3	E1	0	BCD/E HII	238
NGC 7080	322.508125	26.717806	0.016141	13.1	12.3	11.6	–22.7	1.8	0.94	36.0	18.0	50.0	0.425	0.23	3.0	0.8	SBb	0	SB(r)b	239

continuted …

…continued

ID	R.A.(J2000)	Decl.(J2000)	z	B	V	3.6μm	3.6μm	a	b/a	$r_{\rm eff}$	$R^P_{50,V}$	PA	Gal. Ext.	B/T	T	eT	Type	SF &	Classification	Figure
	(deg)	(deg)		(mag)	(mag)	(mag)	(Mag)	($'$)		($''$)	($''$)	(deg)	(mag)					AGN		Set 2 #
(1)	(2)	(3)	(4)	(5)	(6)	(7)	(8)	(9)	(10)	(11)	(12)	(13)	(14)	(15)	(16)	(17)	(18)	(19)	(20)	(21)
NGC 7177	330.171833	17.738056	0.003803	12.0	11.2	10.7	–20.4	3.1	0.65	22.2	11.4	93.0	0.233	0.48	3.0	0.3	SBb	3	SAB(r)b; HII LINER	240
NGC 7217	331.968292	31.359333	0.003176	11.0	10.1	8.9	–21.8	3.9	0.82	45.3	34.2	83.0	0.413	0.86	2.0	0.3	Sb	3	(R)SA(r)ab;Sy LINER	241
NGC 7320	339.014083	33.948111	0.002622	16.0	15.0	11.8	–18.5	2.2	0.50	33.6	17.4	45.0	0.329	0.27	7.0	0.4	S0	0	SA(s)d HII	242
NGC 7385	342.477458	11.608556	0.026175	13.1	12.0	11.4	–24.0	1.5	0.87	37.8	15.0	36.0	0.149	0.90	–5.0	0.6	E2	0	cD;E pec:; LERG	243
NGC 7457	345.249708	30.144944	0.002815	12.1	11.2	10.8	–19.7	4.3	0.53	32.1	21.0	130.0	0.205	0.25	–3.0	0.3	E-S0	0	SA(rs)0-?	244
NGC 7479	346.236042	12.322889	0.007942	11.6	10.9	7.7	–25.0	4.1	0.76	57.3	45.0	25.0	0.161	0.06	5.0	0.3	SBc	4	SB(s)c;LINER Sy2	245
IC 5298	349.002917	25.556694	0.027422	14.9	14.0	12.9	–22.6	0.7	1.00	*	3.6	108.0	0.265	0.55	3.0*	*	S?	4	LINER;HII;SbrstSy2	246
NGC 7653	351.205667	15.275583	0.014227	13.4	12.7	12.2	–21.8	1.59	0.75	18.0	13.8	132.0	0.093	0.32	3.0	0.8	Sb	0	Sb	247
NGC 7674	351.986333	8.779028	0.028924	13.9	13.2	11.8	–23.8	1.1	0.91	12.6	10.8	150.0	0.101	0.53	4.0	0.5	SBbc	4	SA(r)bc pec;HIISy2	248
NGC 7714	354.058750	2.155167	0.009333	13.0	12.5	12.0	–21.1	1.9	0.74	11.1	12.6	79.0	0.153	0.47	3.0	0.5	SBb/P	3	SB(s)b:pec;HII LINER	249
IC 5338	354.126792	21.146000	0.054628	15.0	13.7	13.2	–23.8	1.0	0.70	*	11.4	30.0	0.105	0.40	–5.0	1.8	E3	0	cD;E?;BrClG	250
NGC 7731	355.371125	3.740028	0.009627	13.5	12.8	12.7	–20.4	1.4	0.79	15.3	4.2	95.0	0.153	0.52	1.0	0.7	SBa	0	(R)SBa pec:	251
NGC 7741	355.976542	26.075611	0.002502	11.8	11.3	10.0	–20.2	4.4	0.68	64.2	46.2	170.0	0.137	0.10	6.0	0.3	SBc	0	SB(s)cd HII	252
NGC 7742	356.065542	10.767083	0.005547	12.4	11.6	11.3	–20.7	1.7	1.00	15.0	9.6	*	0.101	0.14	3.0	0.4	Sb	3	SA(r)b;LINER HII	253
NGC 7743	356.088083	9.934083	0.005704	12.4	11.5	10.8	–21.2	3.0	0.87	35.1	24.6	80.0	0.173	0.25	–1.0	0.3	SB0-a	4	(R)SB(s)0+ Sy2	254
NGC 7753	356.770125	29.483444	0.017239	12.8	12.0	11.4	–23.1	3.3	0.64	*	24.6	50.0	0.193	0.14	4.0	0.3	SBbc	0	SAB(rs)bc	255
NGC 7785	358.829292	5.915833	0.012702	12.6	11.6	10.9	–22.9	2.5	0.52	23.4	9.0	143.0	0.165	0.85	–5.0	0.4	E5	0	E5-6	256
NGC 7798	359.856250	20.749861	0.008016	13.0	12.4	11.7	–21.1	1.4	0.93	15.3	12.0	51.0	0.145	0.13	5.0*	*	Sc	1	SBc Sbrst	257

My sample of 257 galaxies, sorted by R.A. Unless stated otherwise, all table entries are taken or derived from NASA/IPAC Extragalactic Database (NED)[a]

(1) Same as S18
(2) R.A. in degrees and in epoch J2000.0
(3) Decl. in degrees and in epoch J2000.0
(4) Redshift from NED
(5) Total B-band magnitude from Steinicke 2018
(6) Total V-band magnitude from Steinicke 2018
(7) Total 3.6 μm magnitude measured using GALFIT (AB mag; see Appendix C for more information)
(8) (7) + Distance Modulus from (4): not taking into account K-correction
(9) Major axis in arcminutes
(10) Axis-ratio
(11) Effective radius in r-band in arcseconds from RC3, but recomputed by RAJ from log(Ae) after accounting for the fact that the listed Ae values were diameters, not radii
(12) Petrosian Half-light radius measured in V-band in arcseconds
(13) Position angle from S18 from North through East
(14) Foreground Galactic extinction
(15) Bulge-to-total light ratio measured in 3.6 μm using GALFIT
(16) T-type from RC3 or assigned (with '*') based on (18) and (20)
(17) T-type error from RC3
(18) Morphological type from S18
(19) Assigned SF/AGN classification based on (20) [0 = Not active, 1 = Starburst, 2 = LIRG, 3 = LINER, 4 = Seyfert 2, 5 = Seyfert 1]
(20) Morphological and activity classification from NED

(21) Figure Set number

[a]The NASA/IPAC Extragalactic Database (NED) is operated by the Jet Propulsion Laboratory, California Institute of Technology, under contract with the National Aeronautics and Space Administration.

APPENDIX D

FIGURE 3-2 FOR 257 NGC AND IC GALAXIES

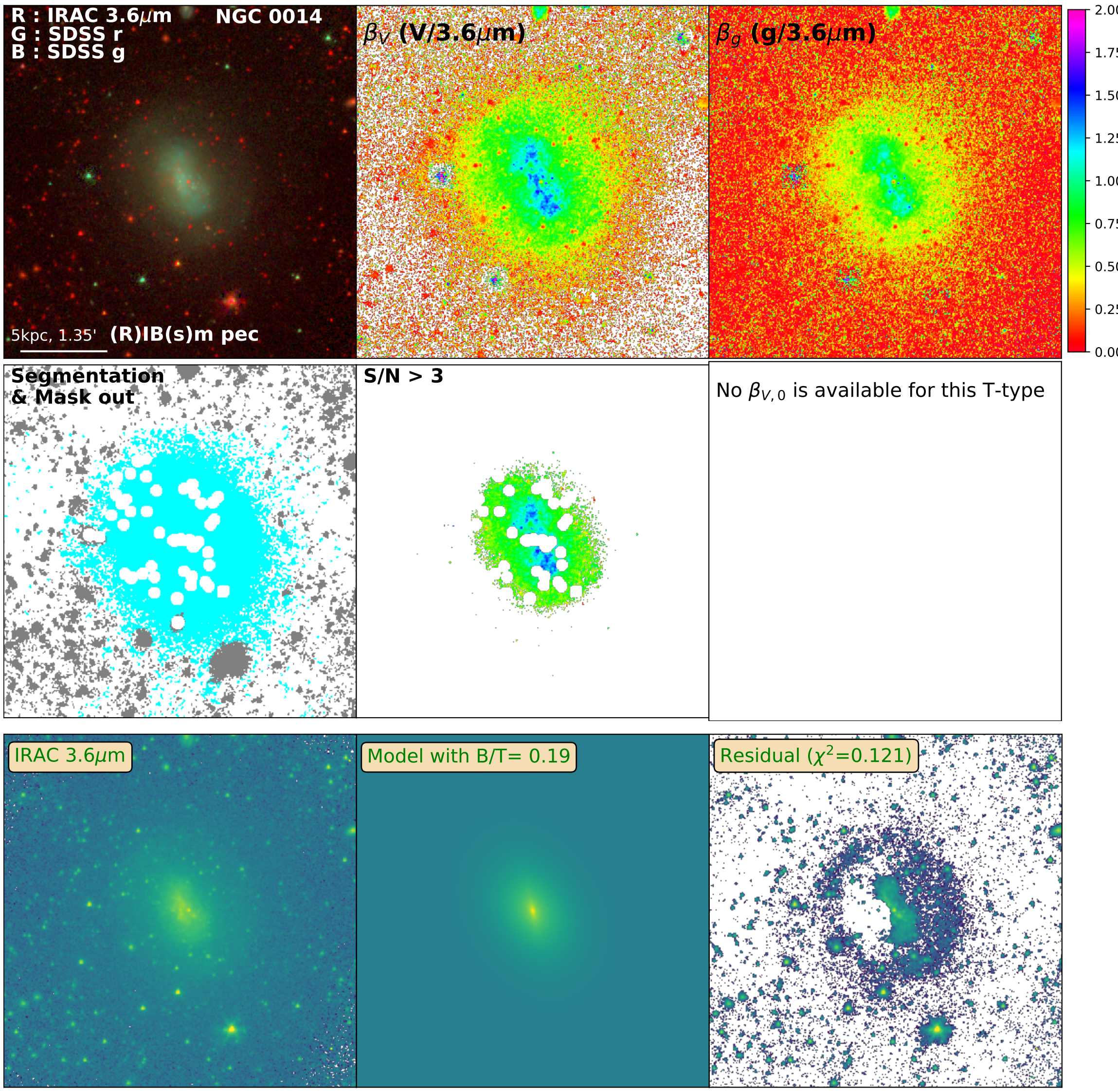

Figure D.1: Same as Figure 3.2 for NGC0014

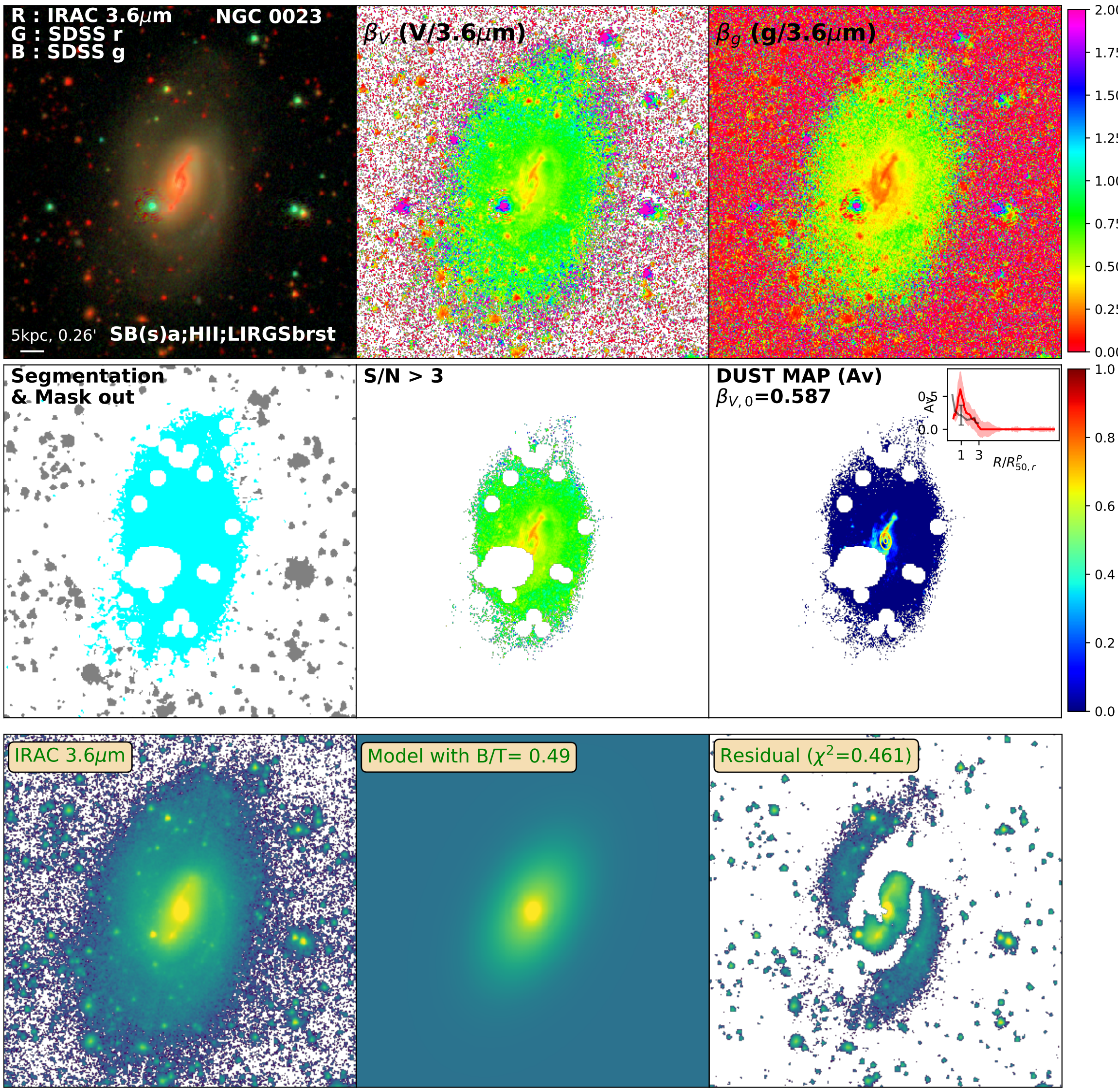

Figure D.2: Same as Figure 3.2 for NGC0023

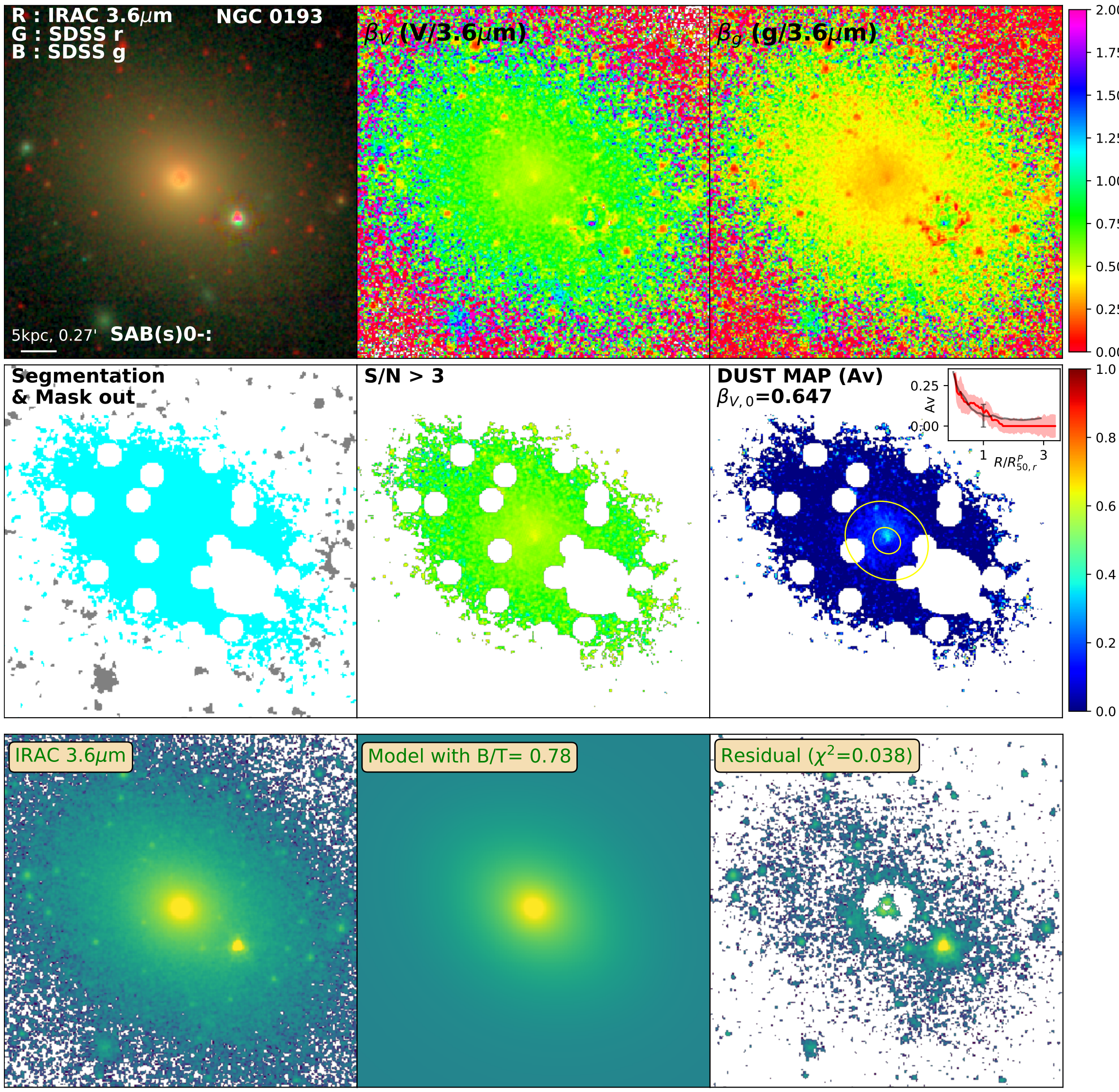

Figure D.3: Same as Figure 3.2 for NGC0193

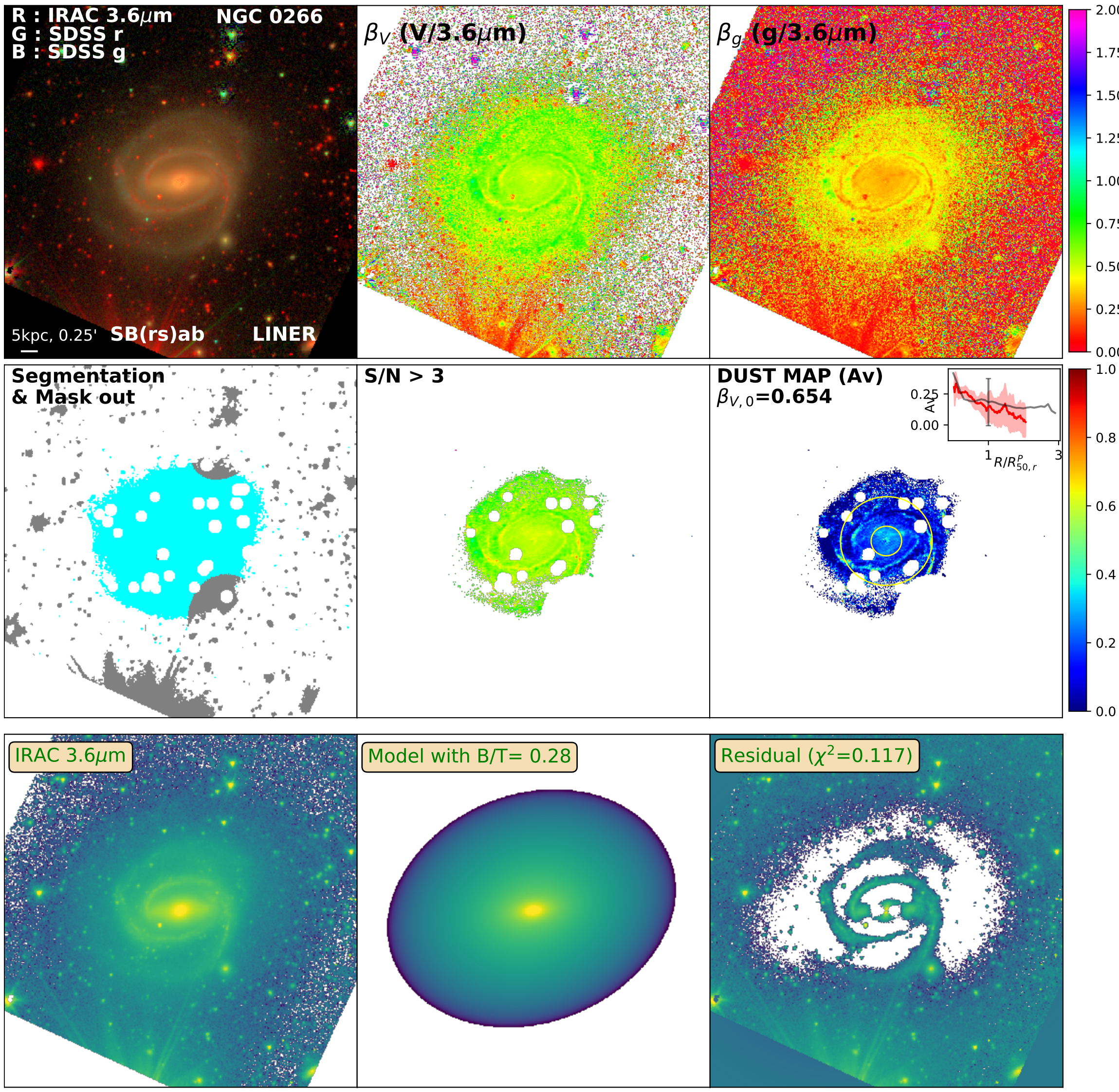

Figure D.4: Same as Figure 3.2 for NGC0266

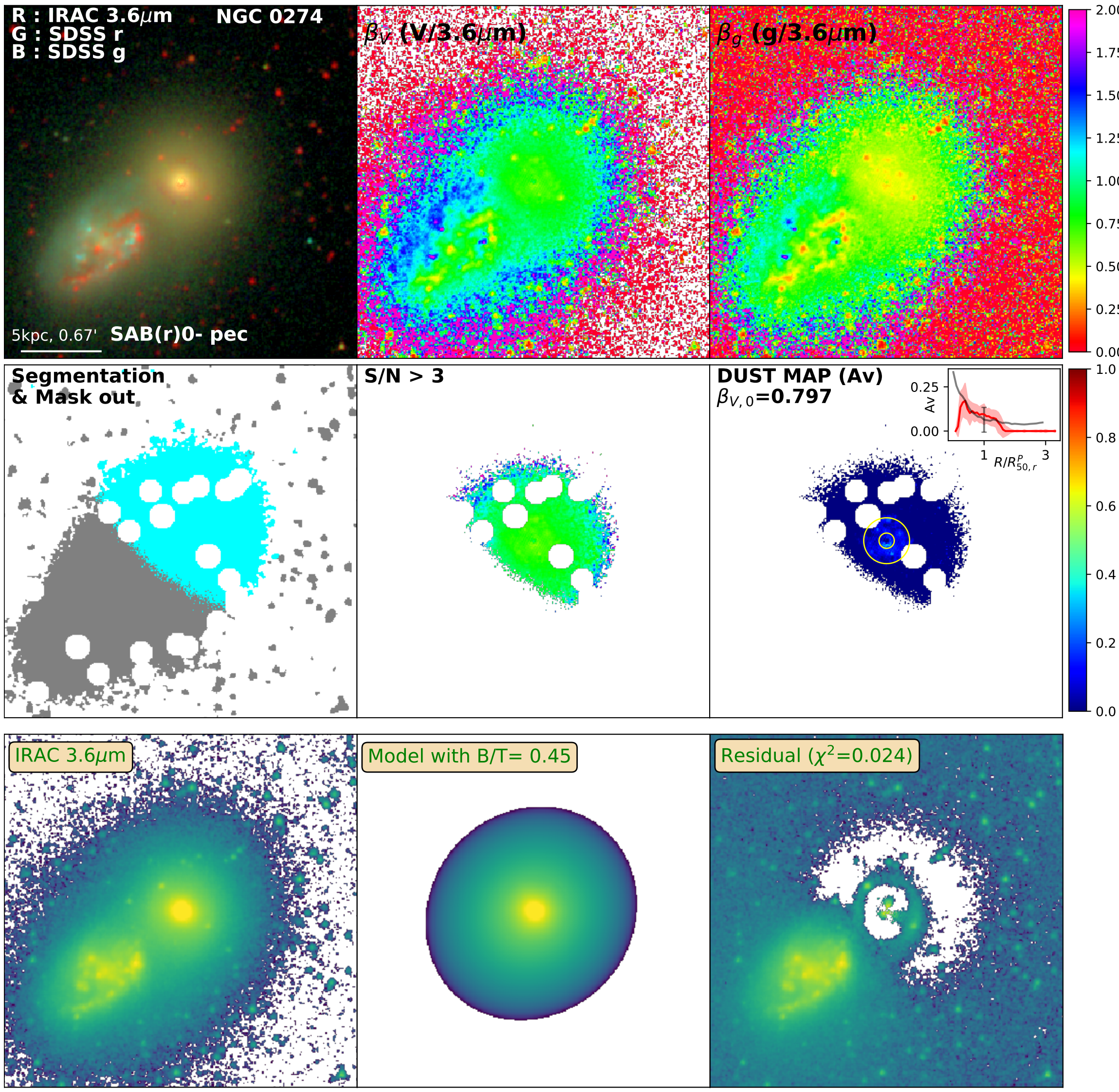

Figure D.5: Same as Figure 3.2 for NGC0274

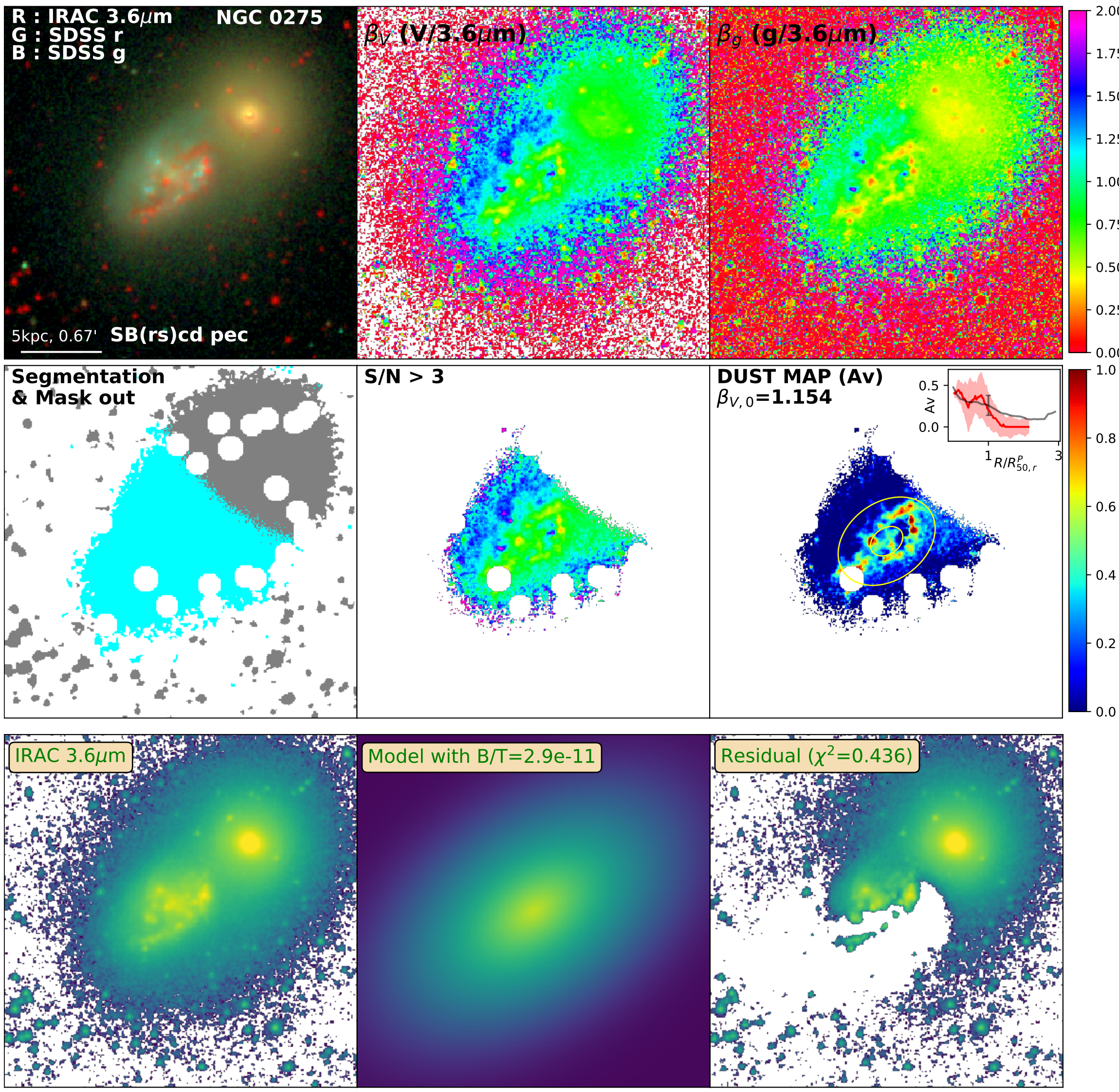

Figure D.6: Same as Figure 3.2 for NGC0275

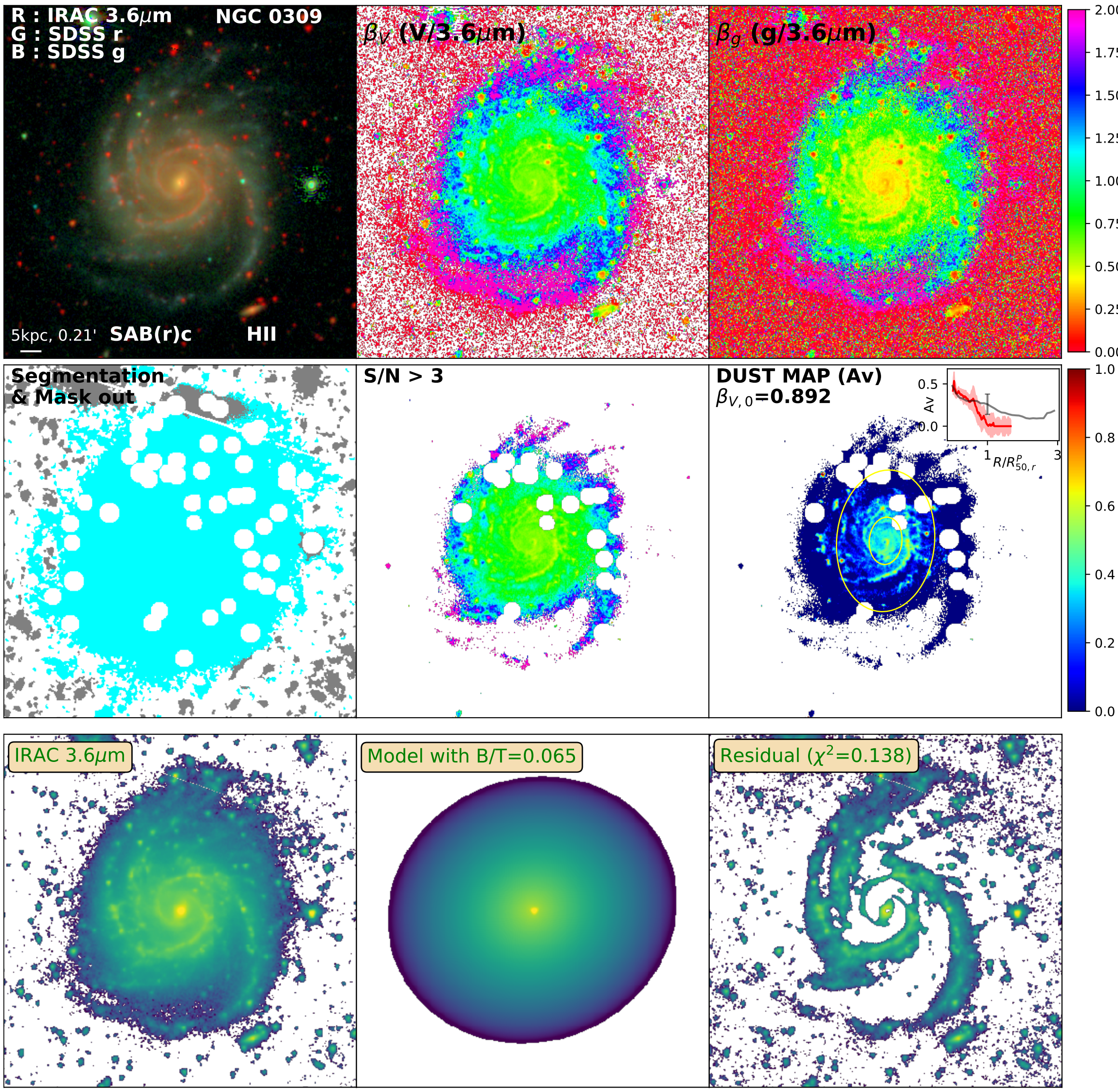

Figure D.7: Same as Figure 3.2 for NGC0309

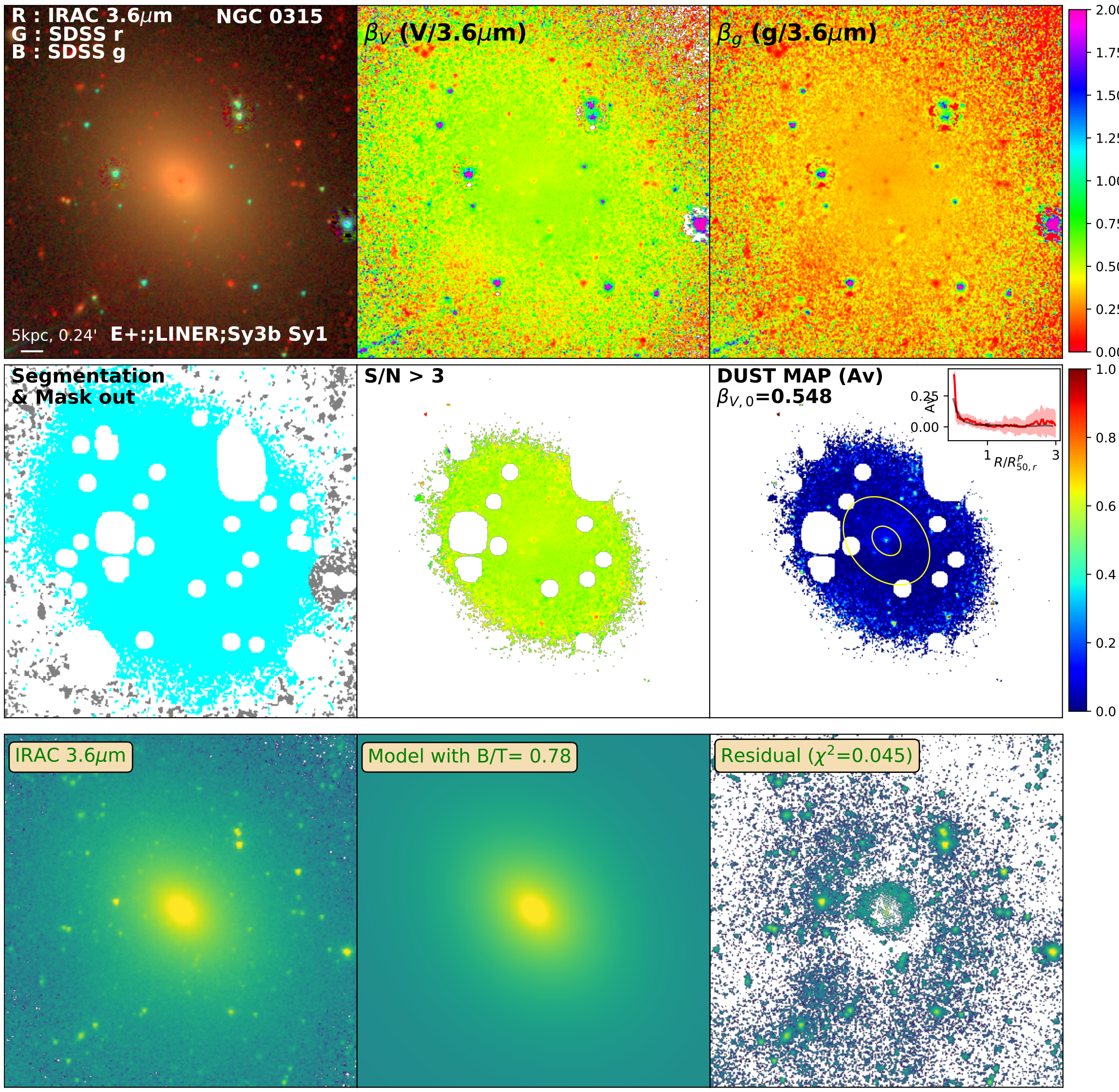

Figure D.8: Same as Figure 3.2 for NGC0315

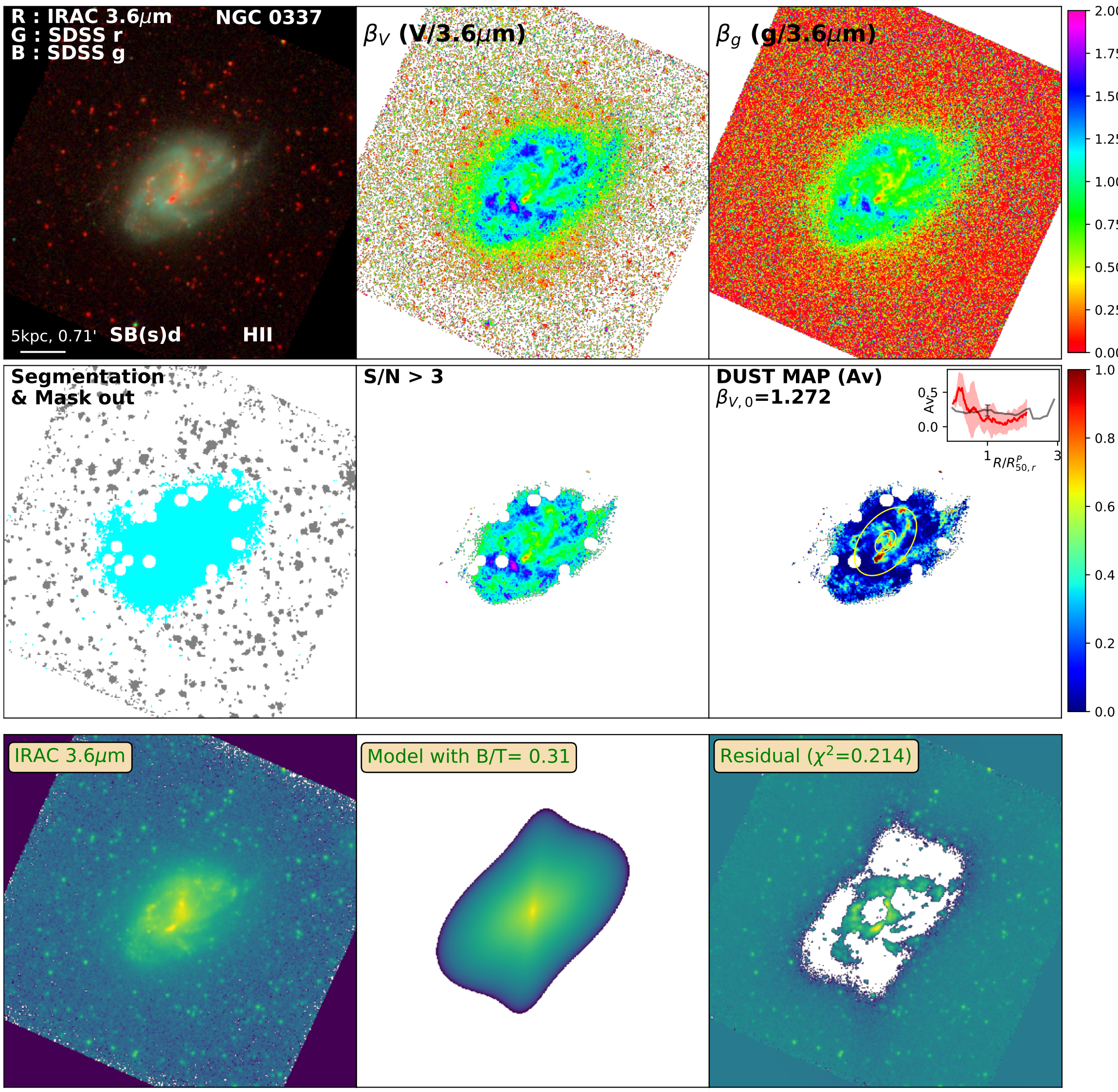

Figure D.9: Same as Figure 3.2 for NGC0337

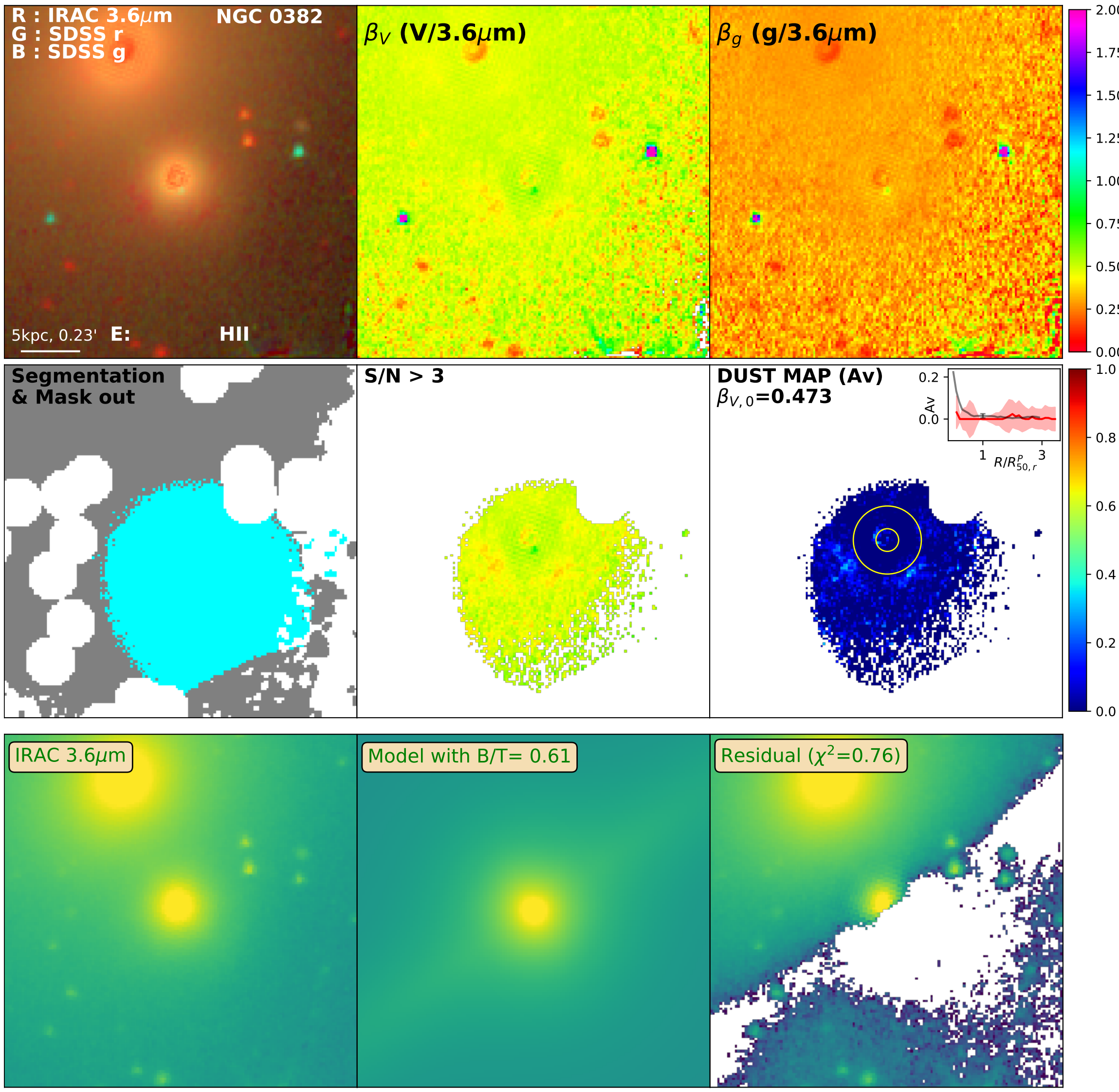

Figure D.10: Same as Figure 3.2 for NGC0382

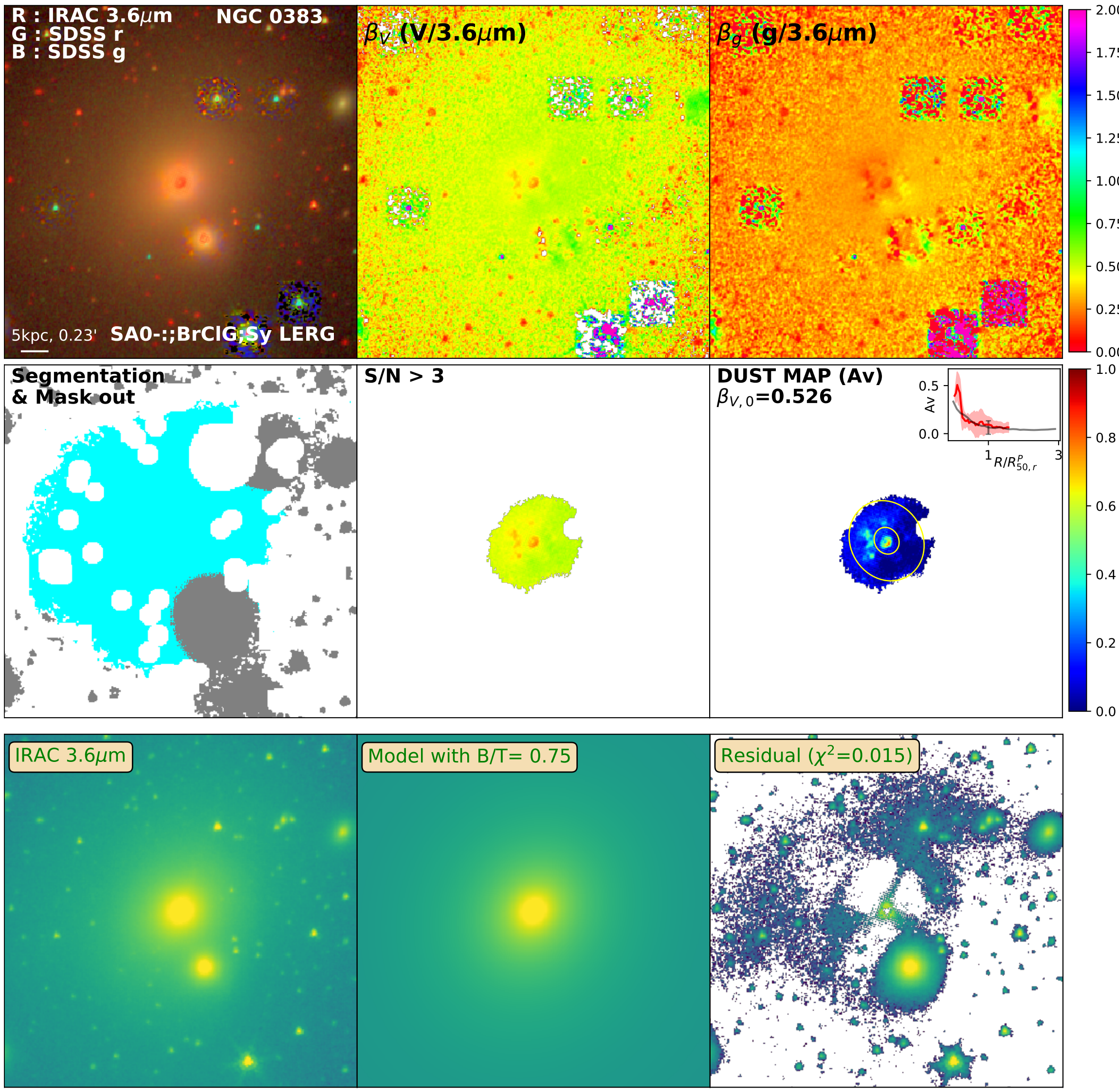

Figure D.11: Same as Figure 3.2 for NGC0383

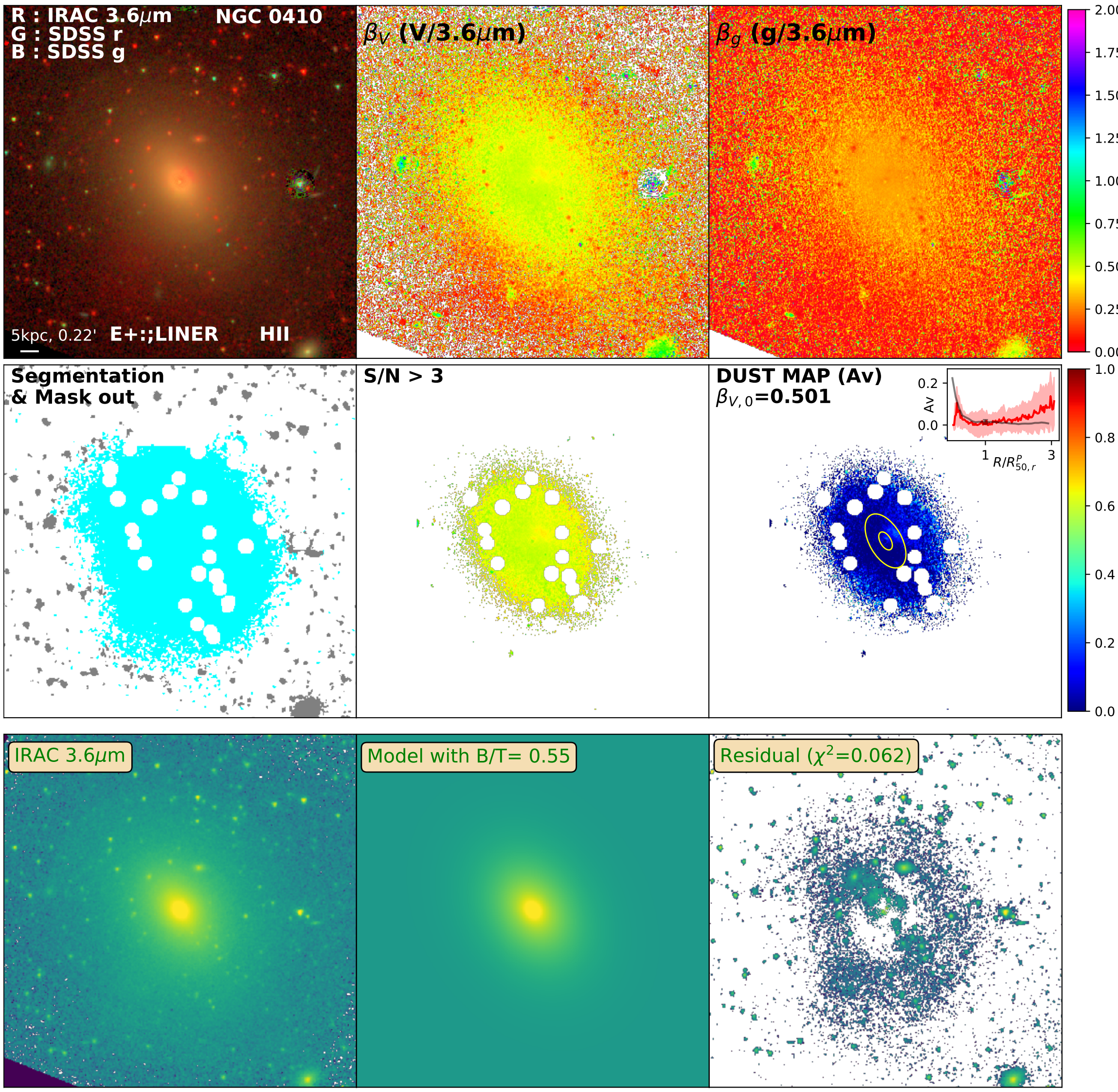

Figure D.12: Same as Figure 3.2 for NGC0410

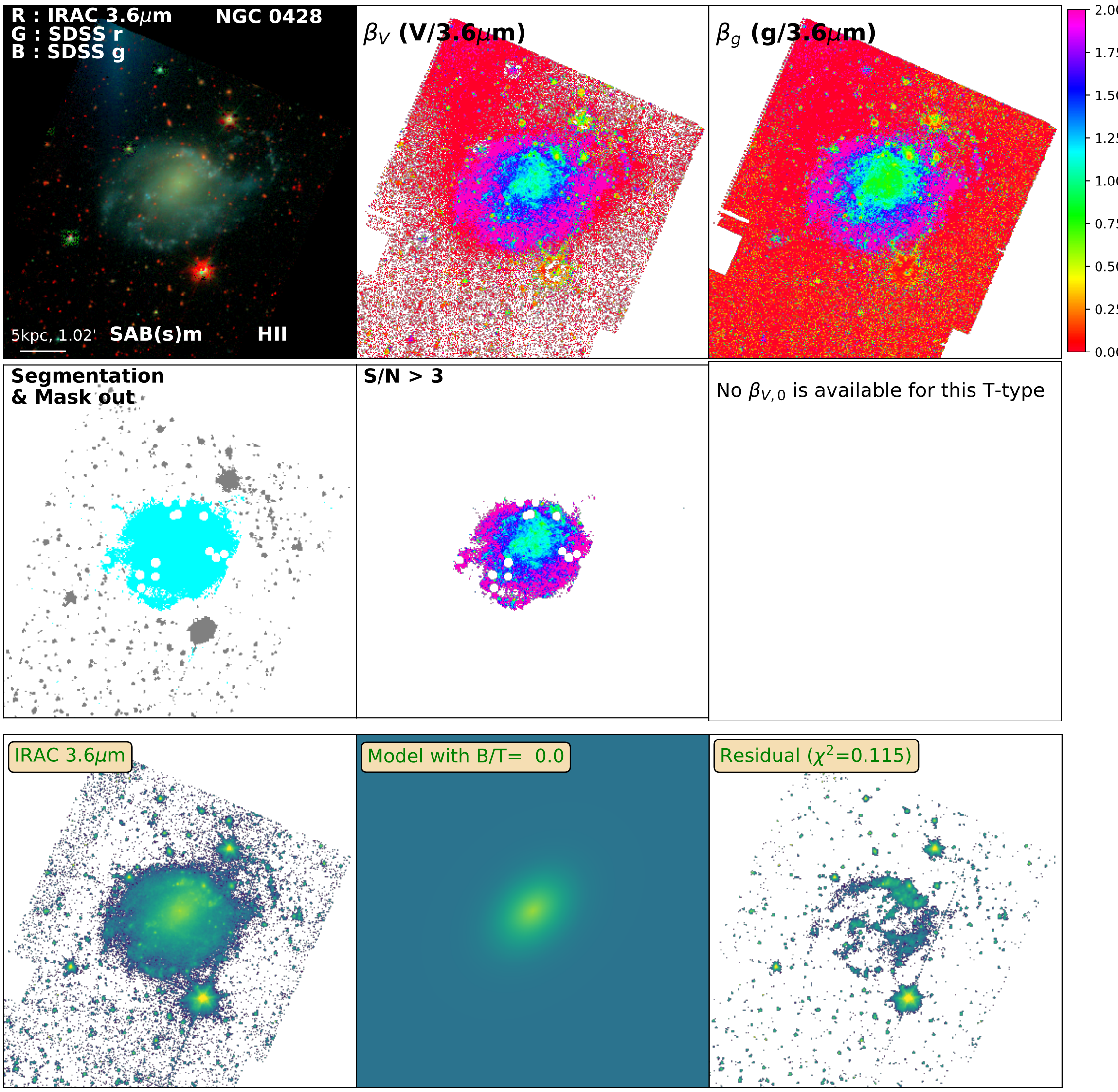

Figure D.13: Same as Figure 3.2 for NGC0428

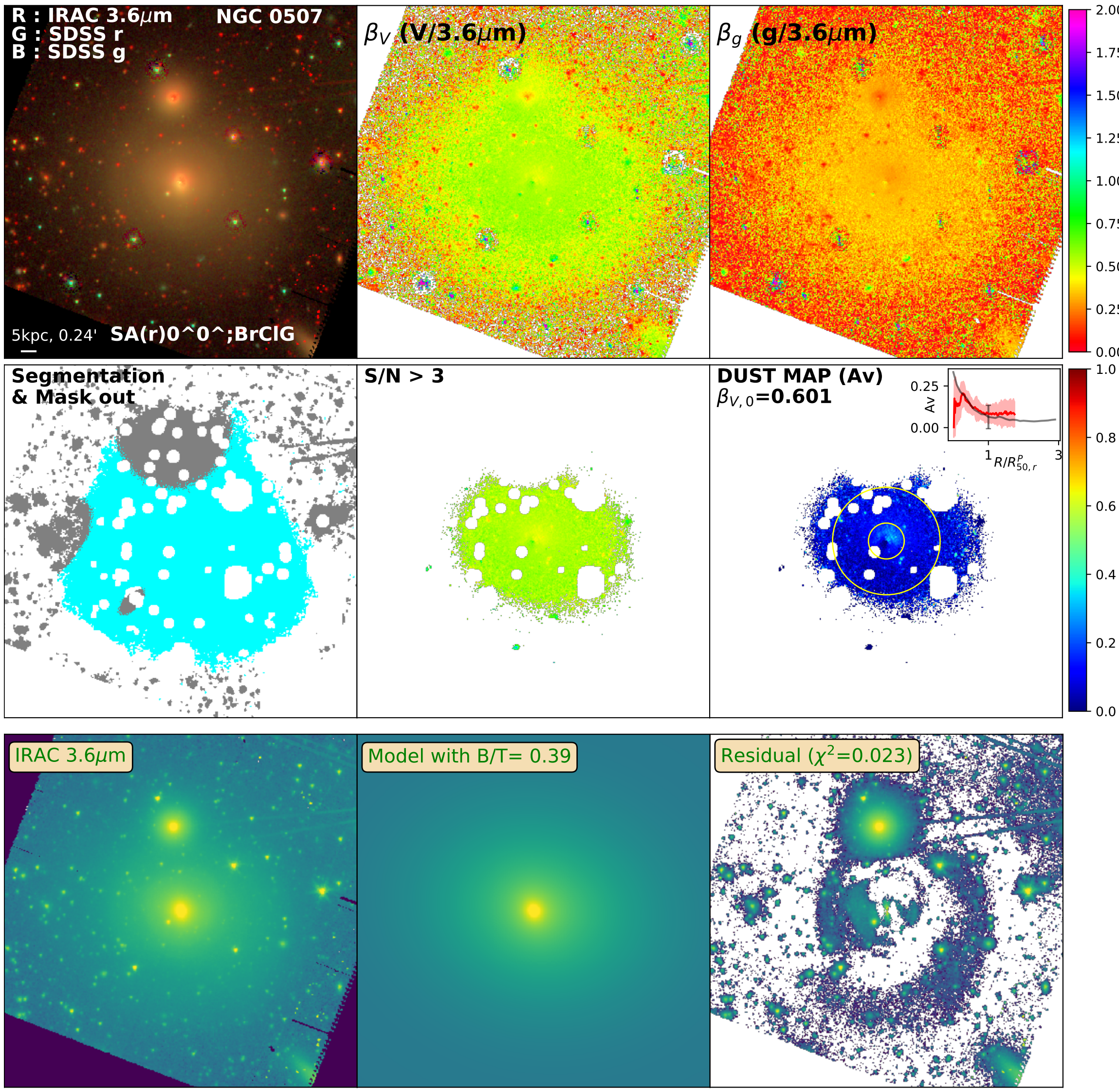

Figure D.14: Same as Figure 3.2 for NGC0507

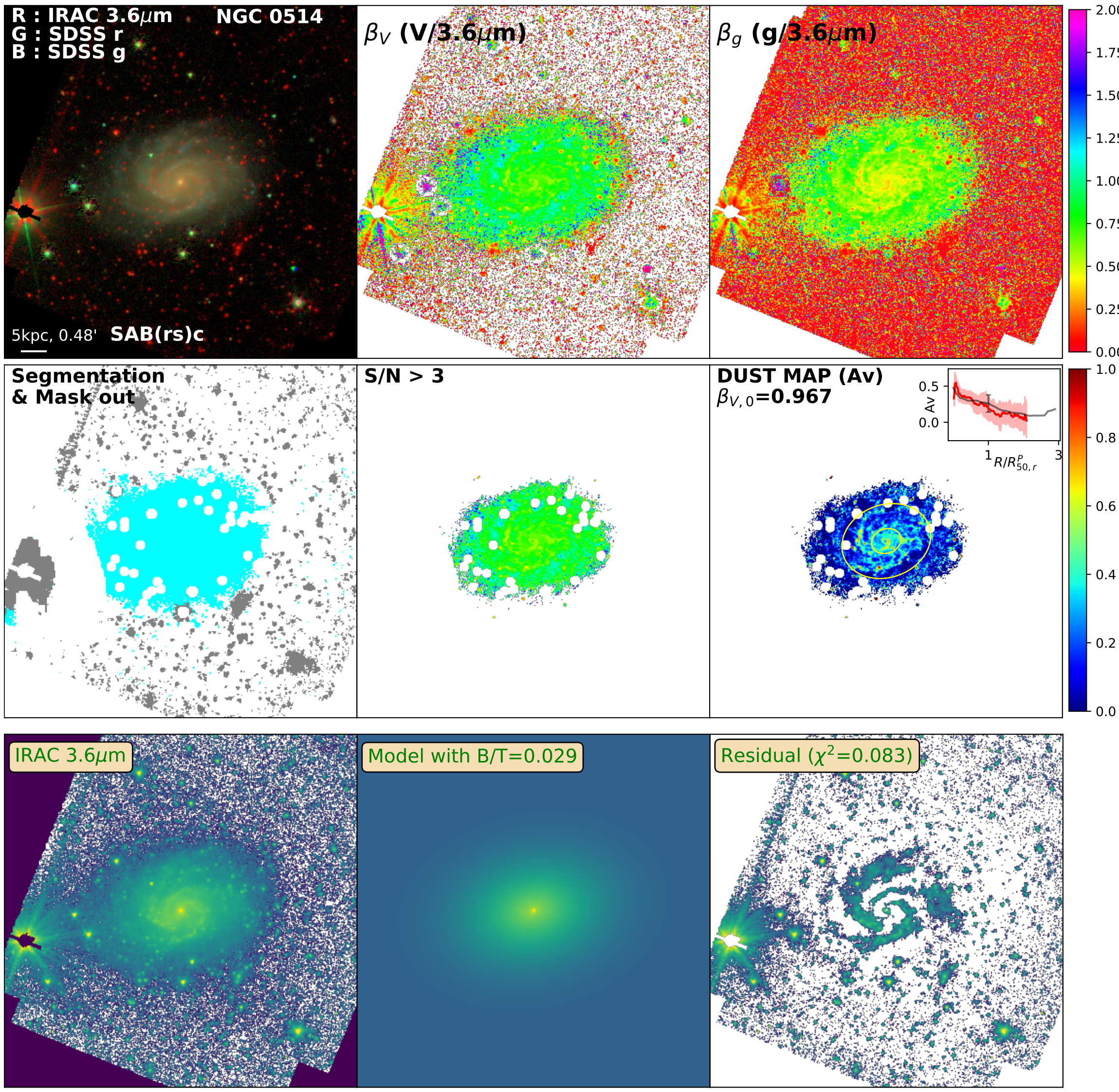

Figure D.15: Same as Figure 3.2 for NGC0514

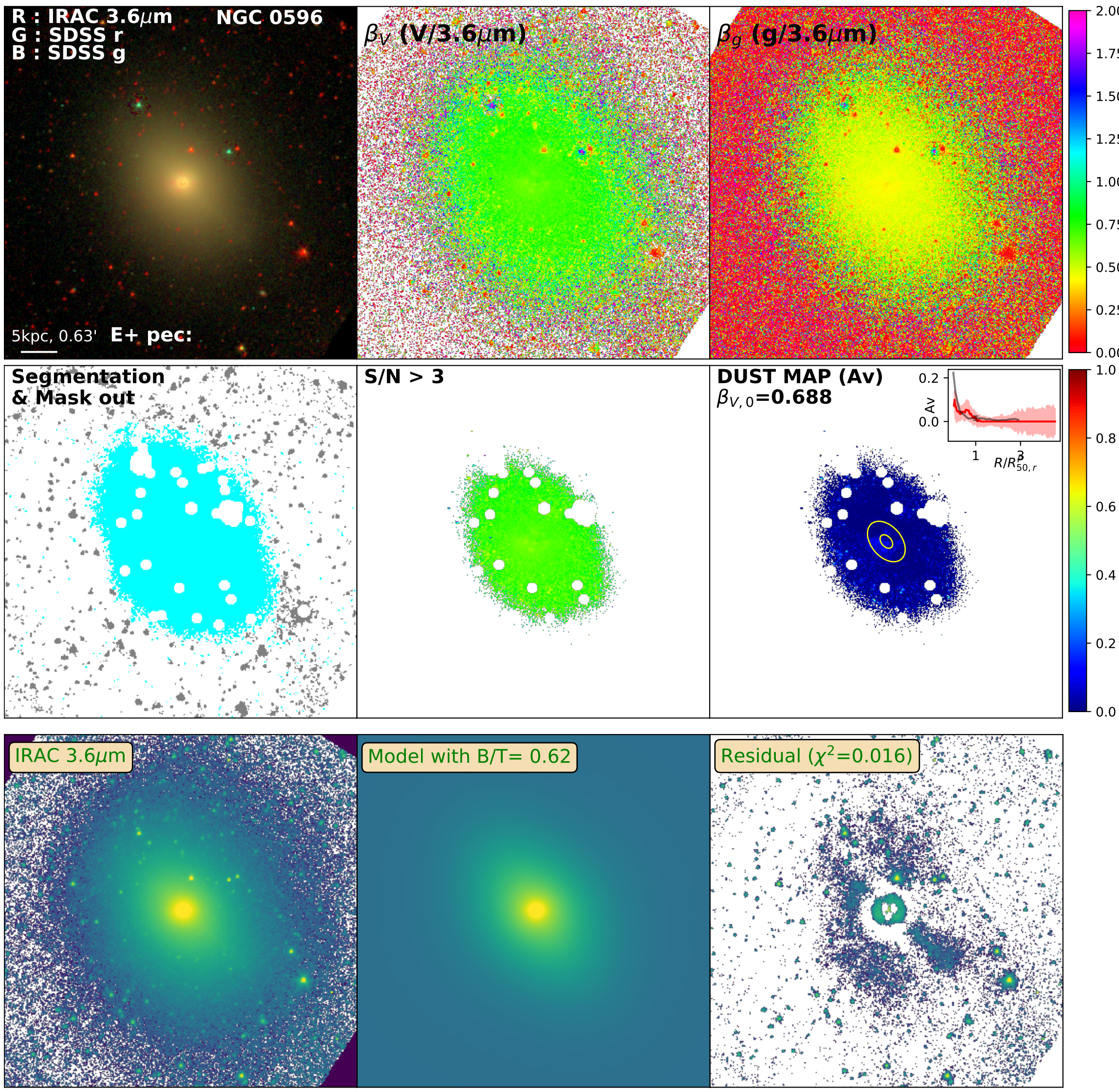

Figure D.16: Same as Figure 3.2 for NGC0596

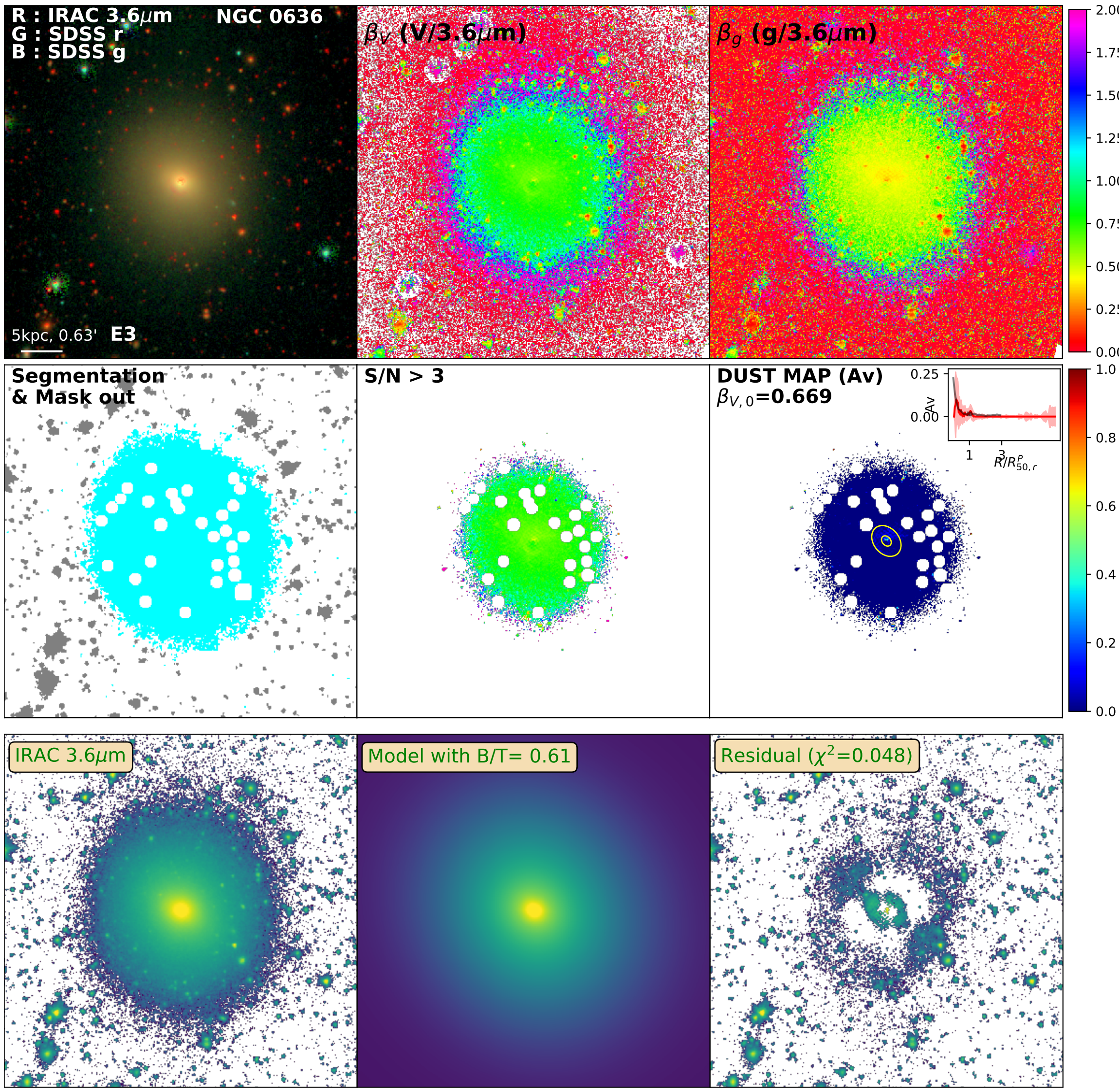

Figure D.17: Same as Figure 3.2 for NGC0636

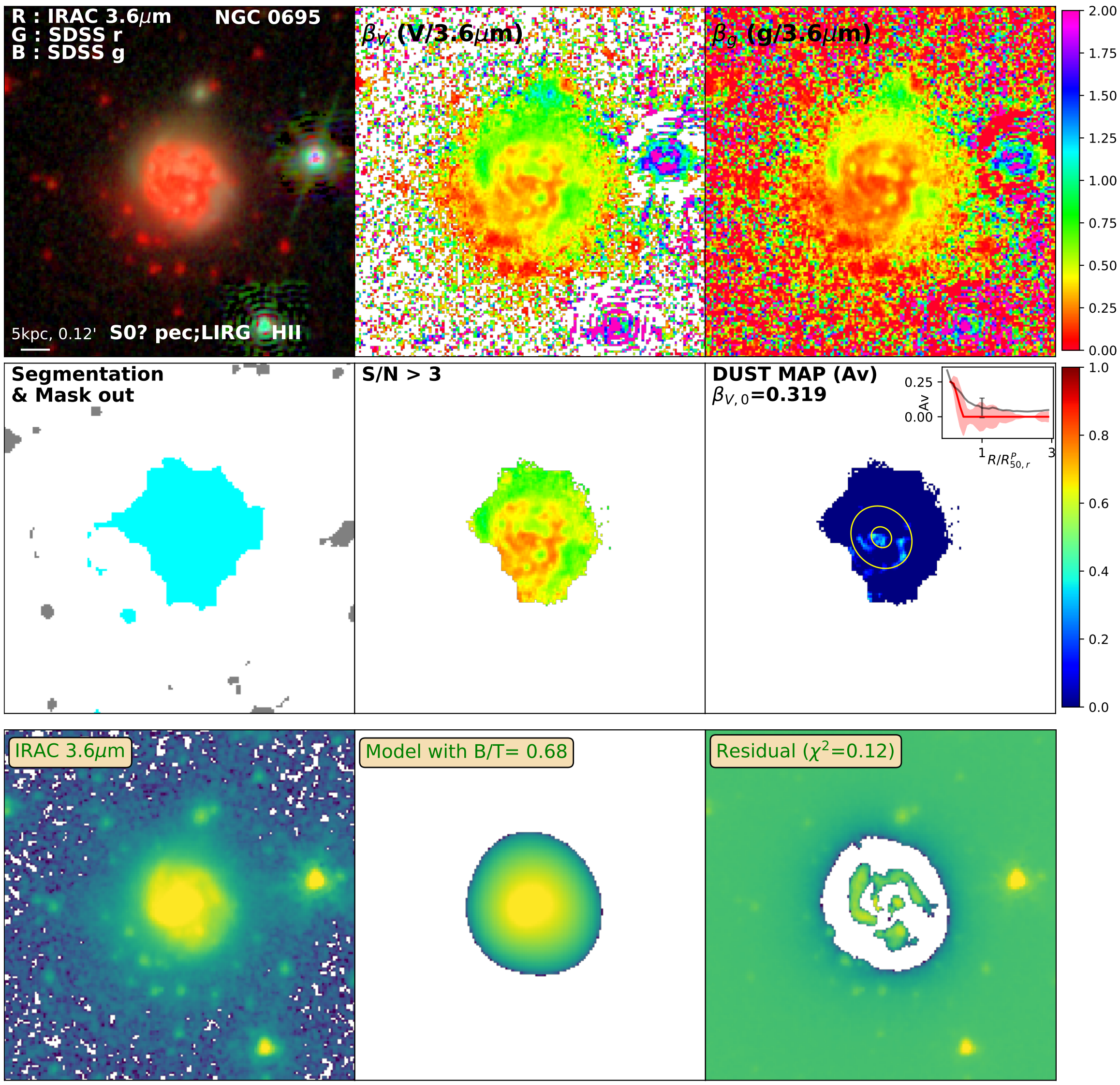

Figure D.18: Same as Figure 3.2 for NGC0695

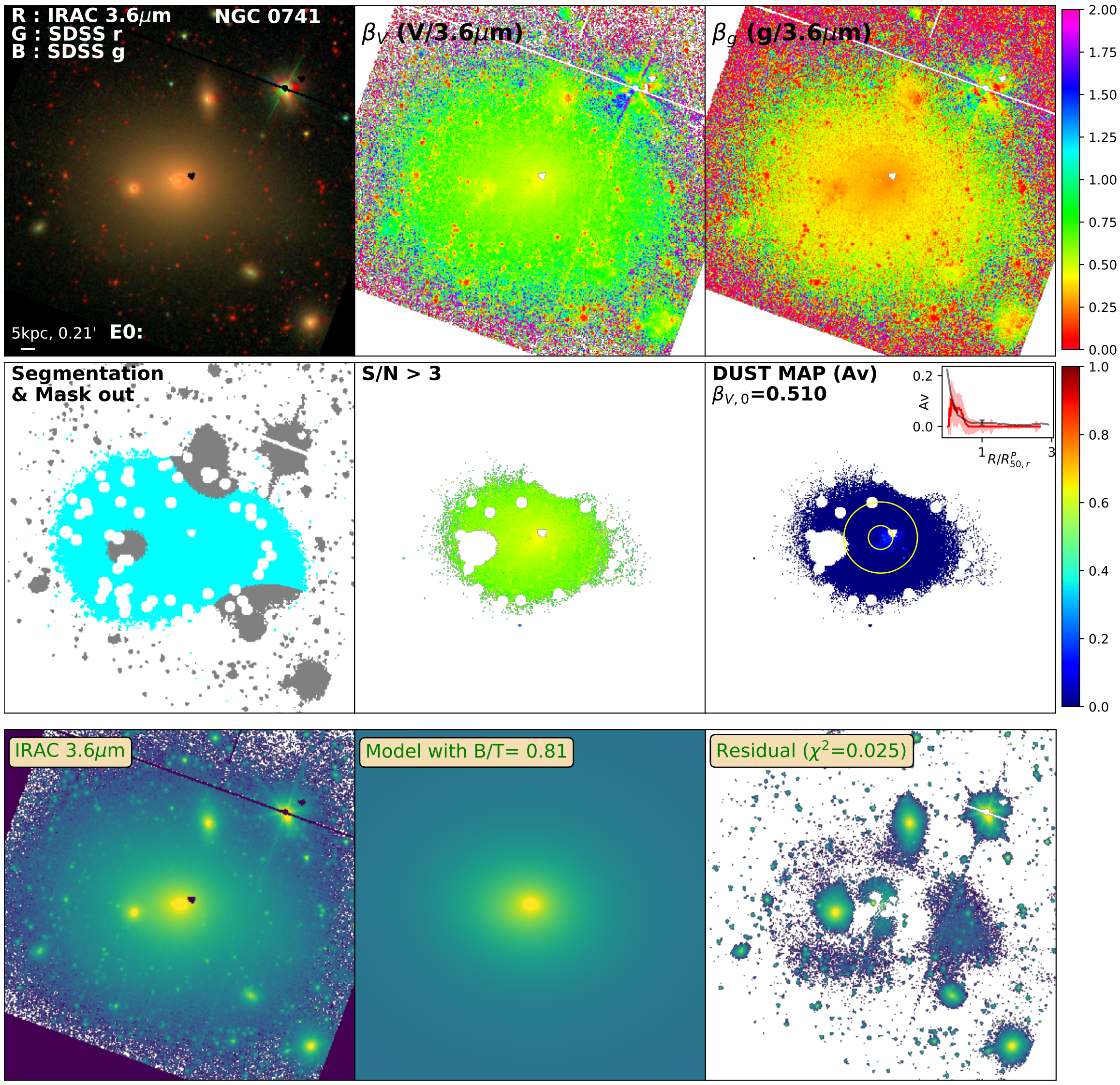

Figure D.19: Same as Figure 3.2 for NGC0741

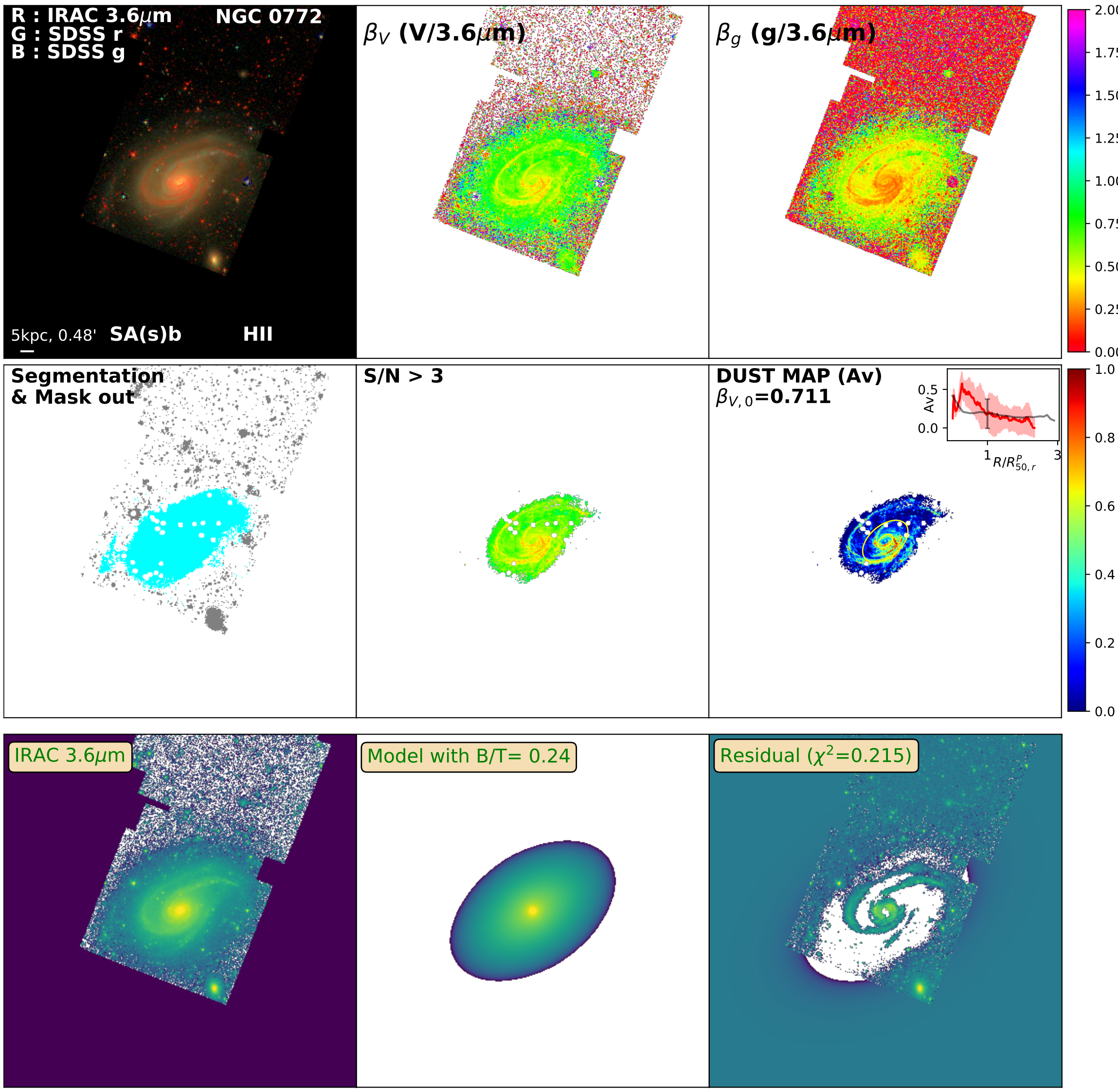

Figure D.20: Same as Figure 3.2 for NGC0772

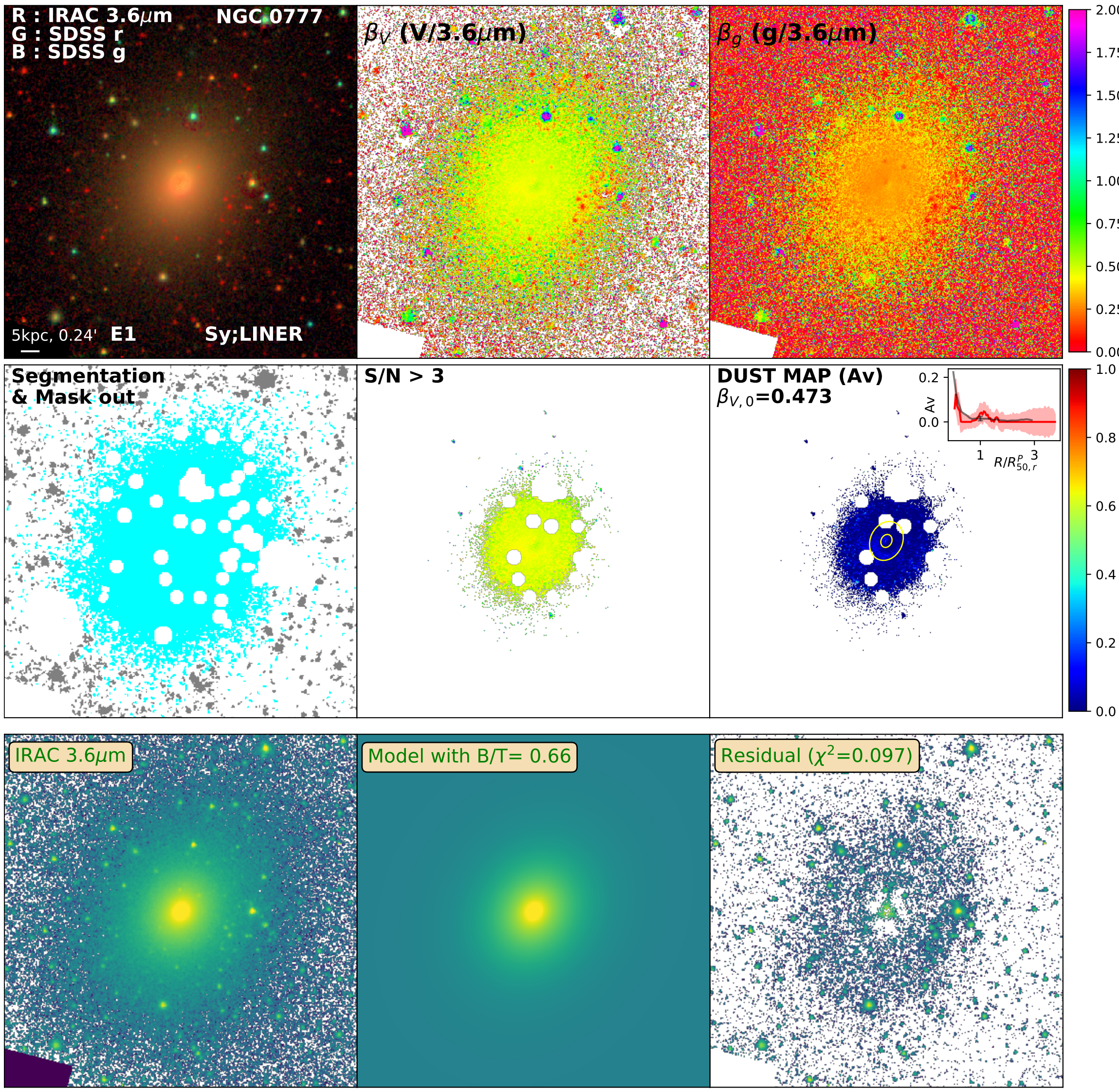

Figure D.21: Same as Figure 3.2 for NGC0777

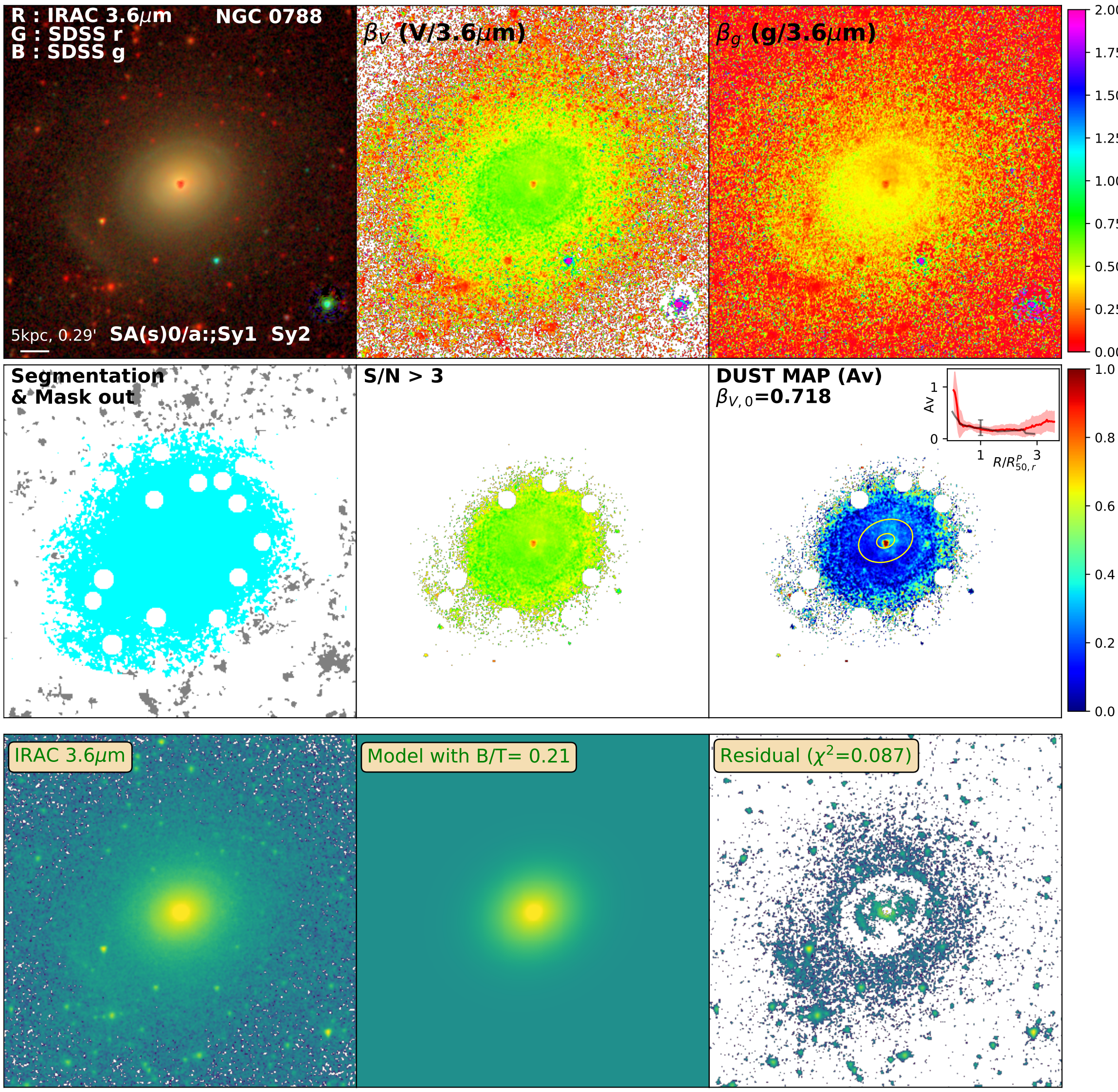

Figure D.22: Same as Figure 3.2 for NGC0788

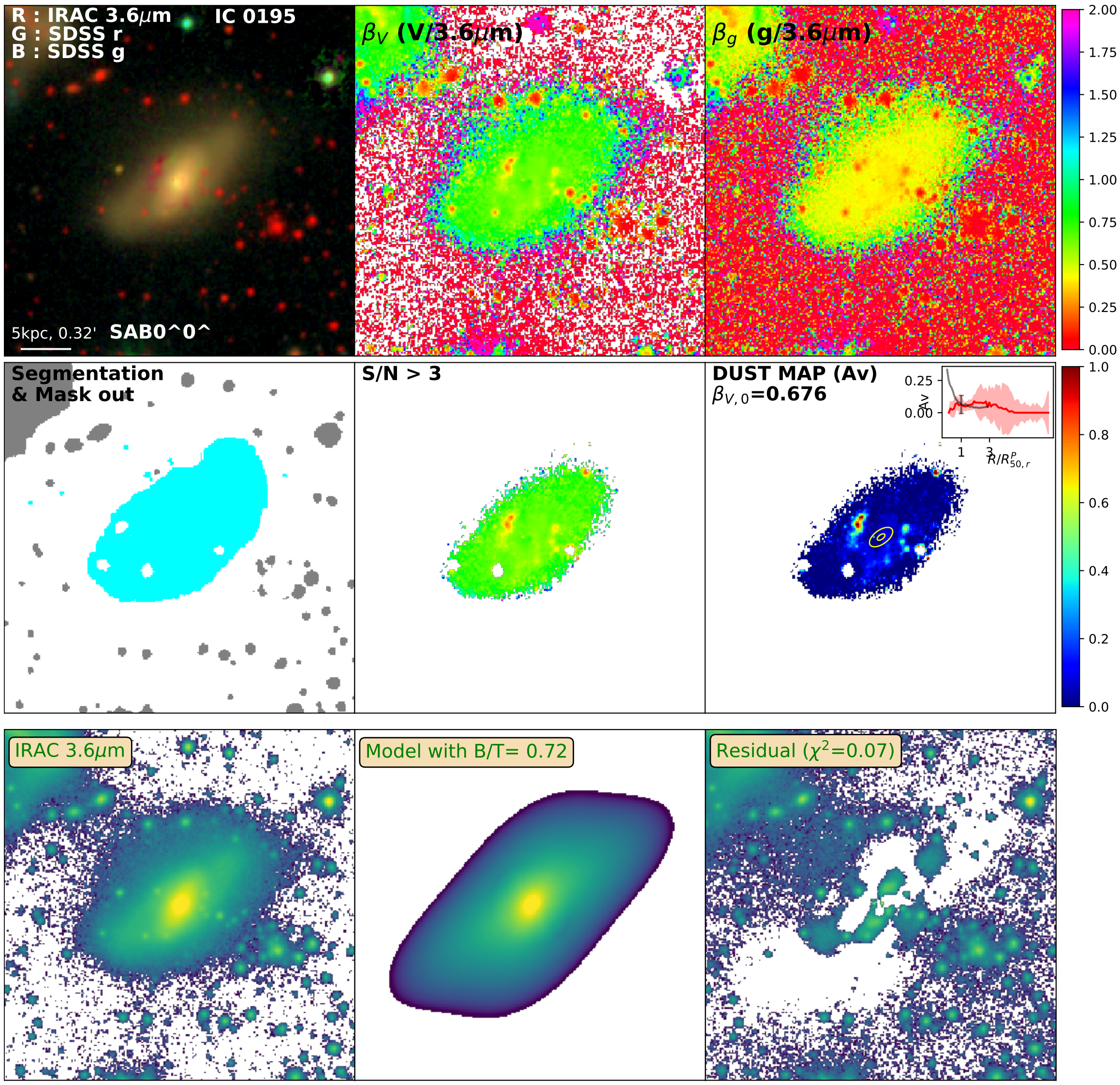

Figure D.23: Same as Figure 3.2 for IC0195

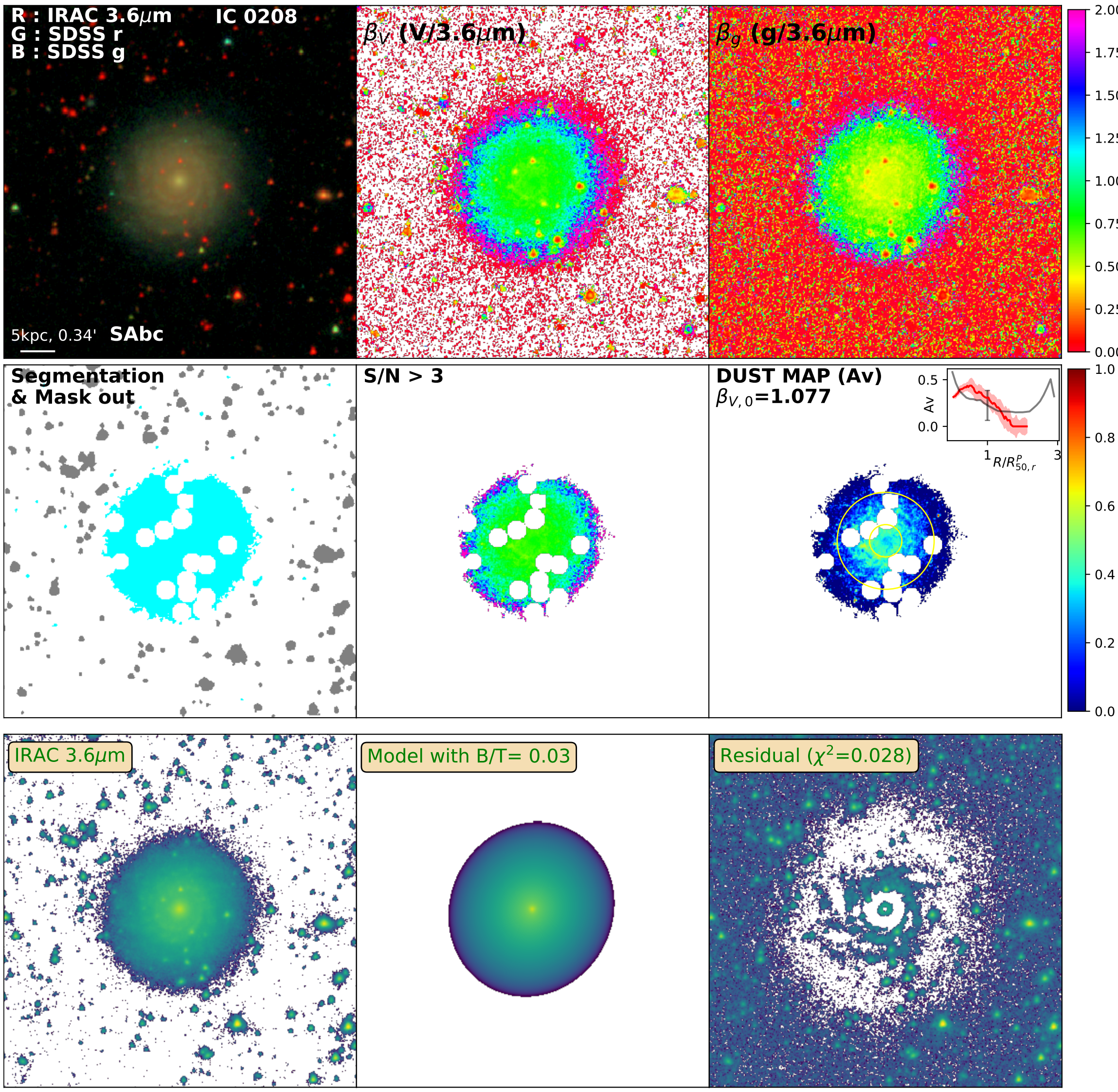

Figure D.24: Same as Figure 3.2 for IC0208

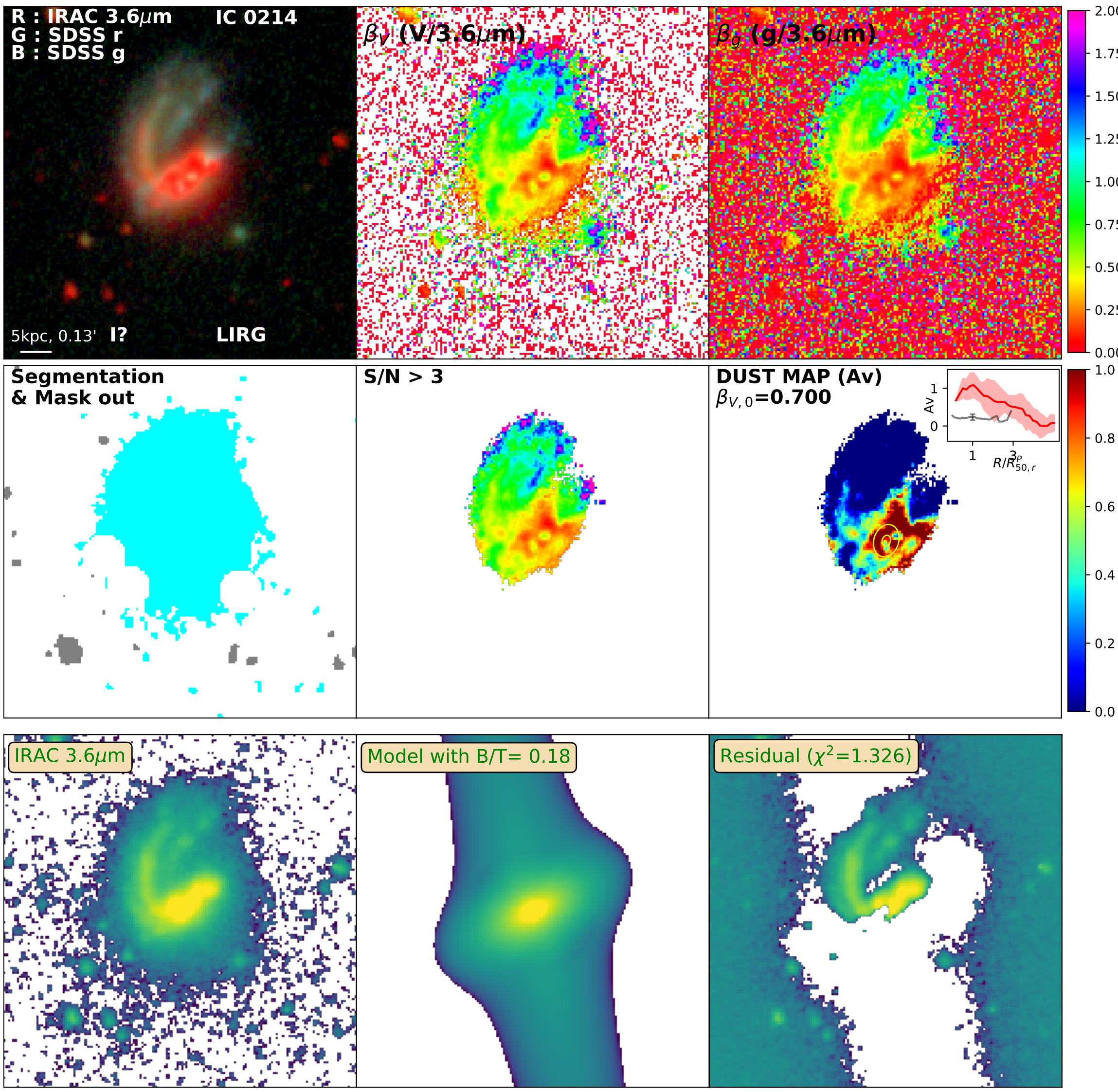

Figure D.25: Same as Figure 3.2 for IC0214

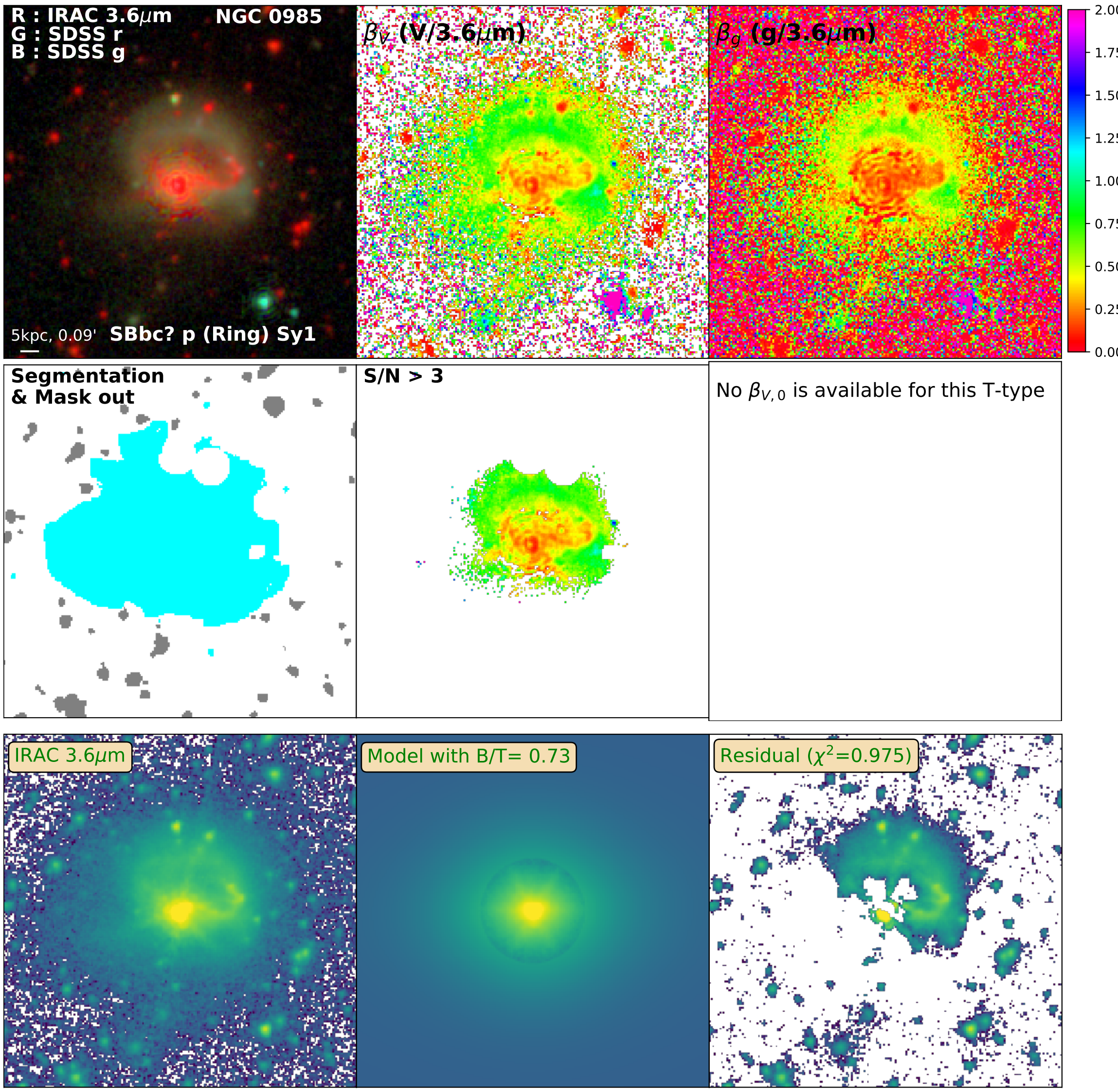

Figure D.26: Same as Figure 3.2 for NGC0985

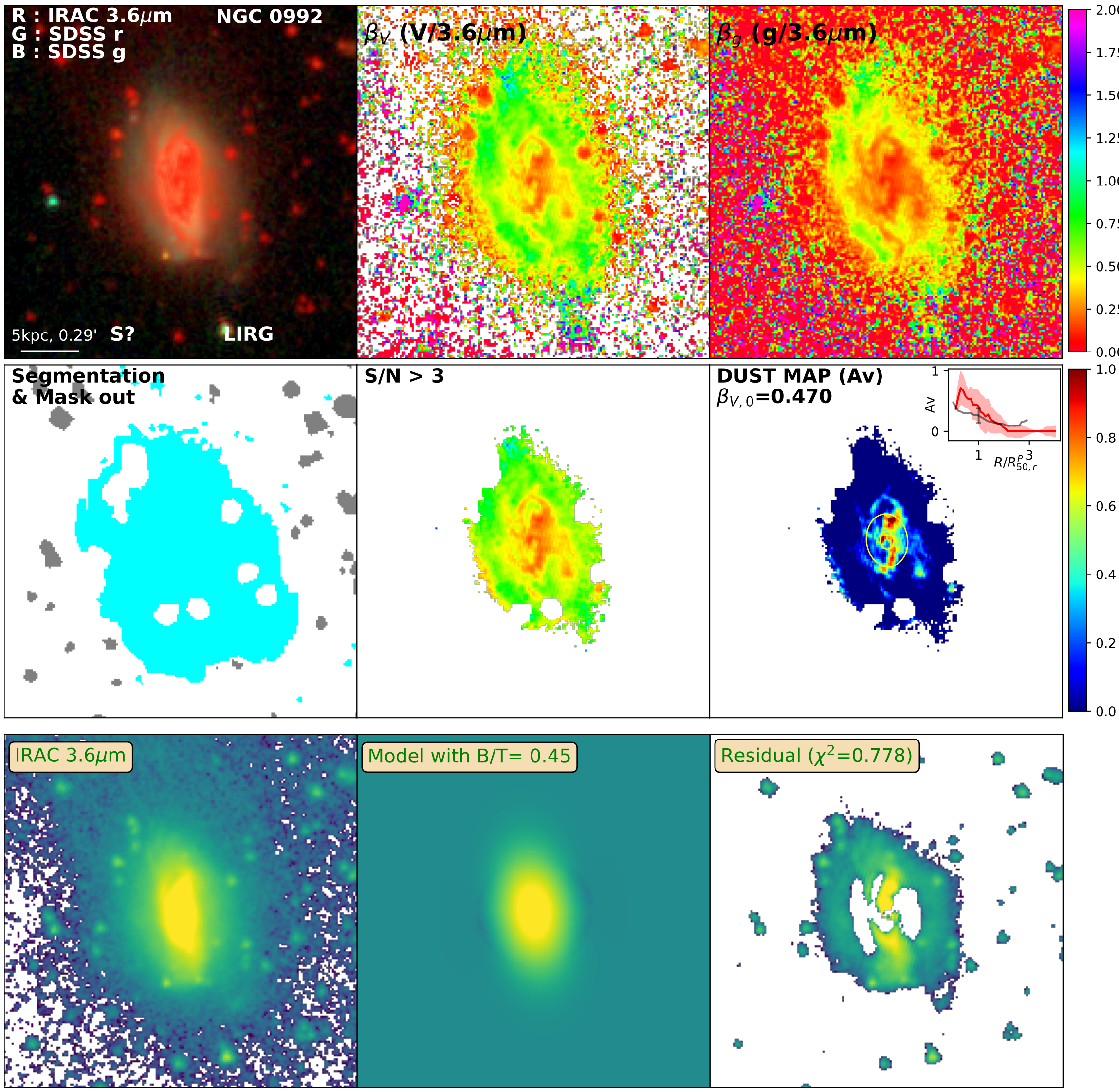

Figure D.27: Same as Figure 3.2 for NGC0992

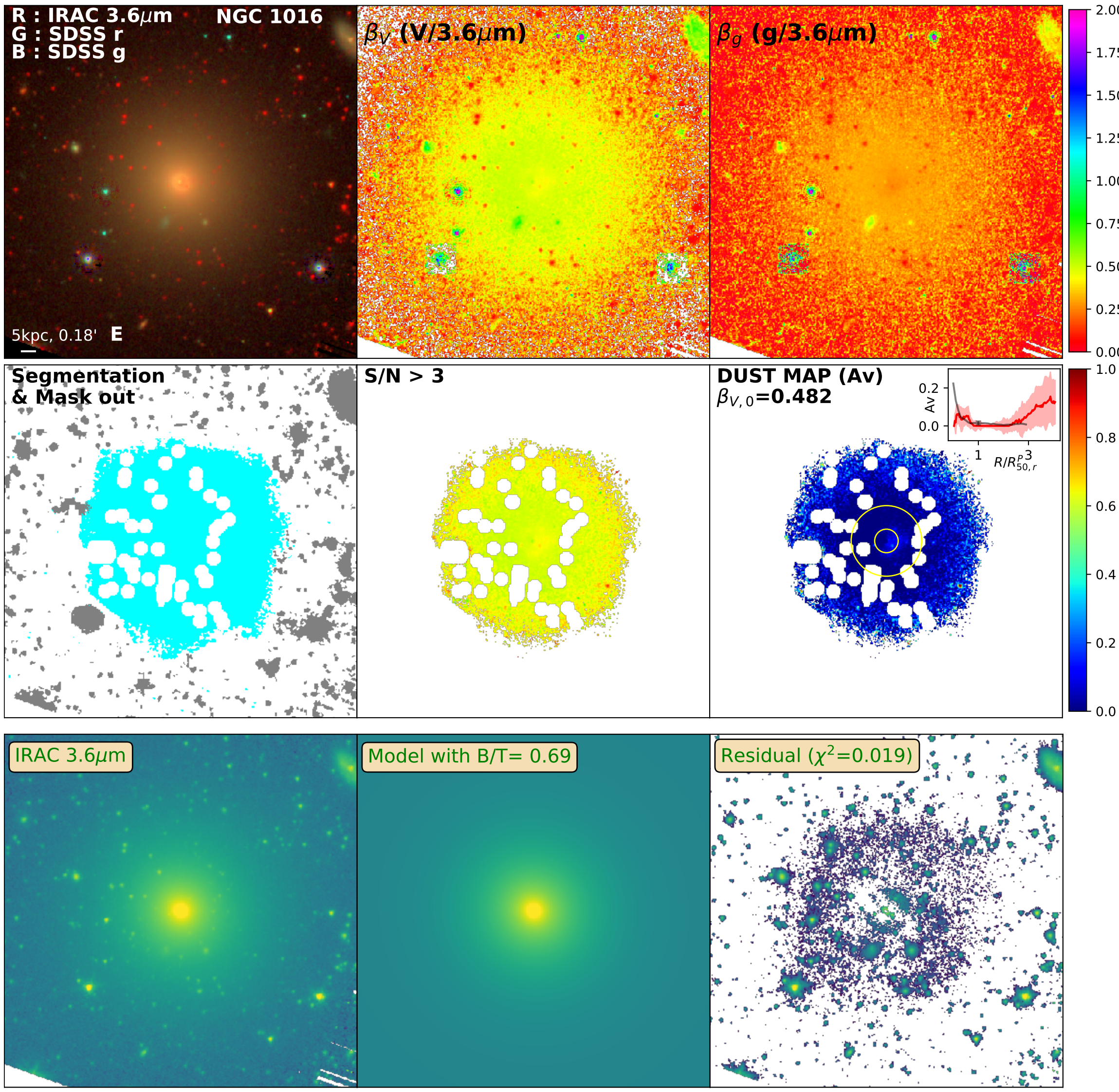

Figure D.28: Same as Figure 3.2 for NGC1016

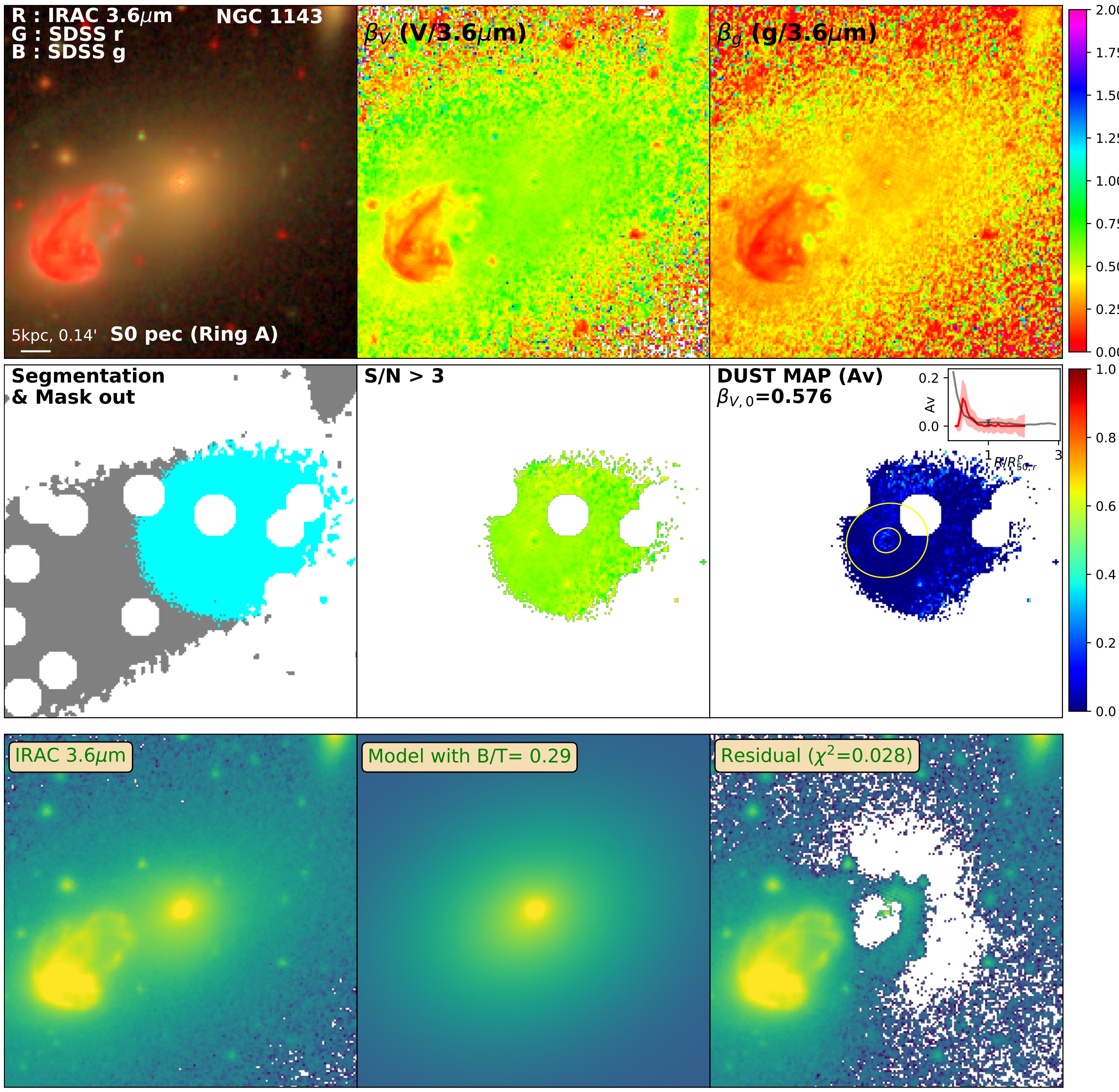

Figure D.29: Same as Figure 3.2 for NGC1143

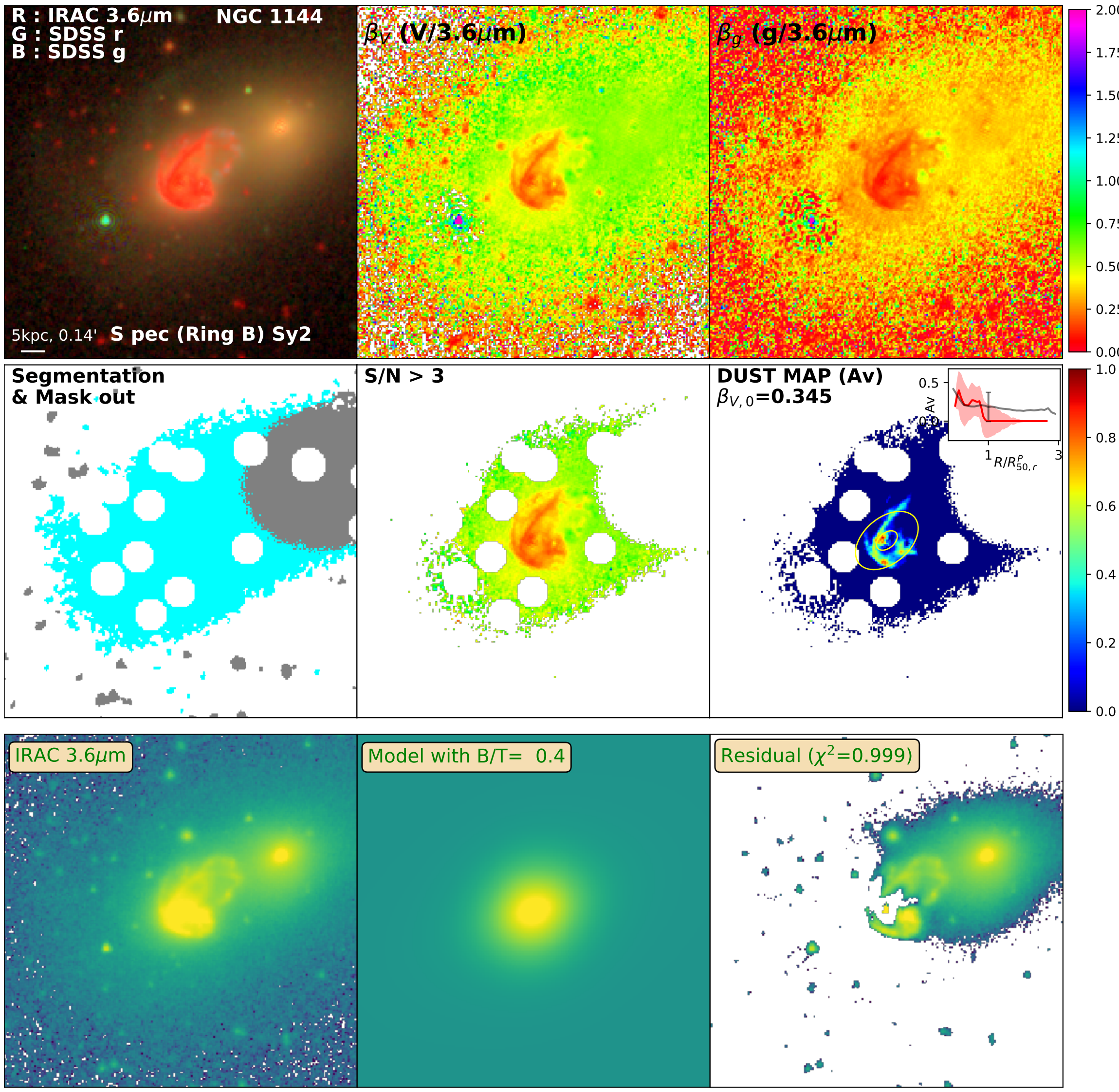

Figure D.30: Same as Figure 3.2 for NGC1144

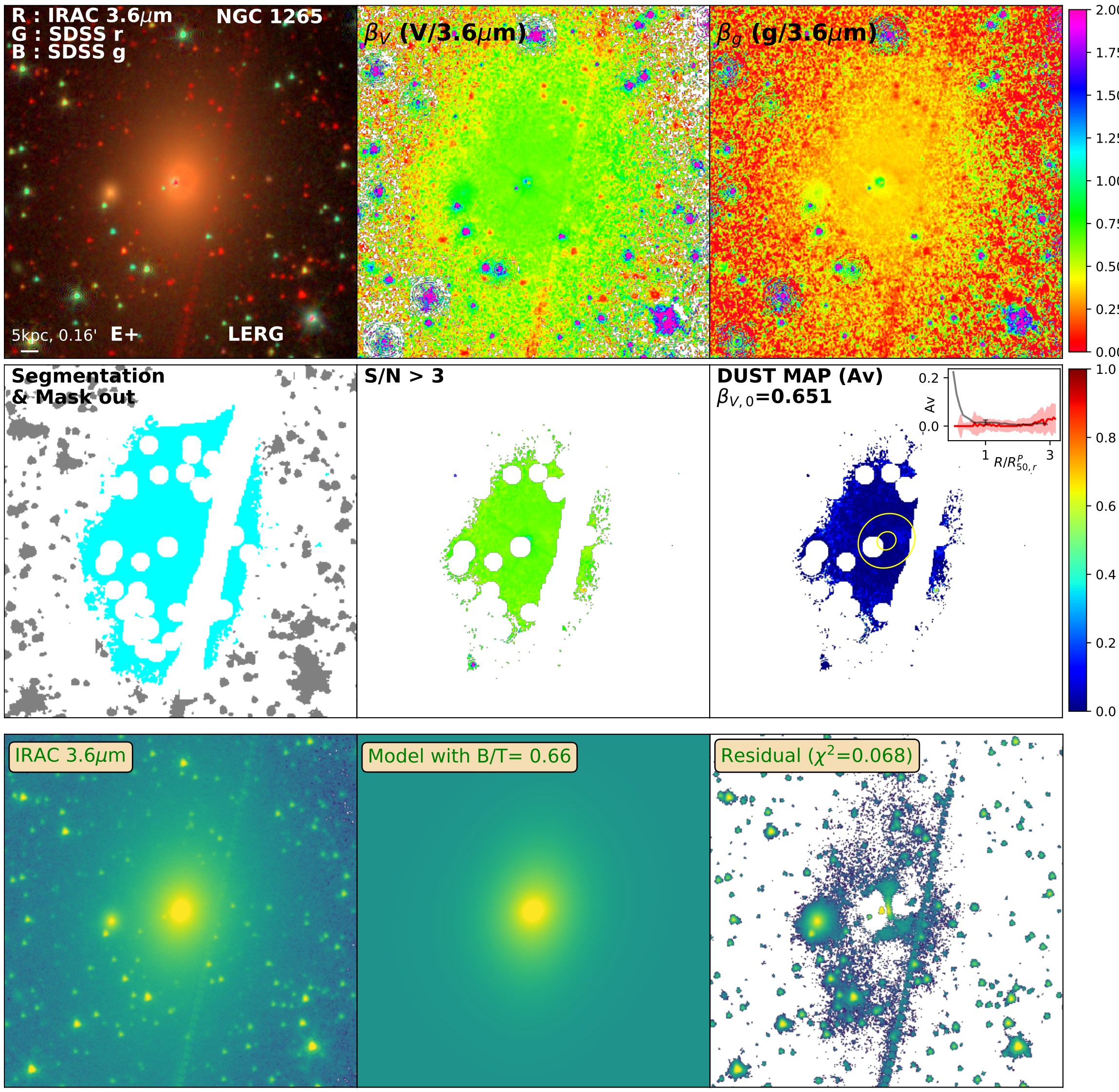

Figure D.31: Same as Figure 3.2 for NGC1265

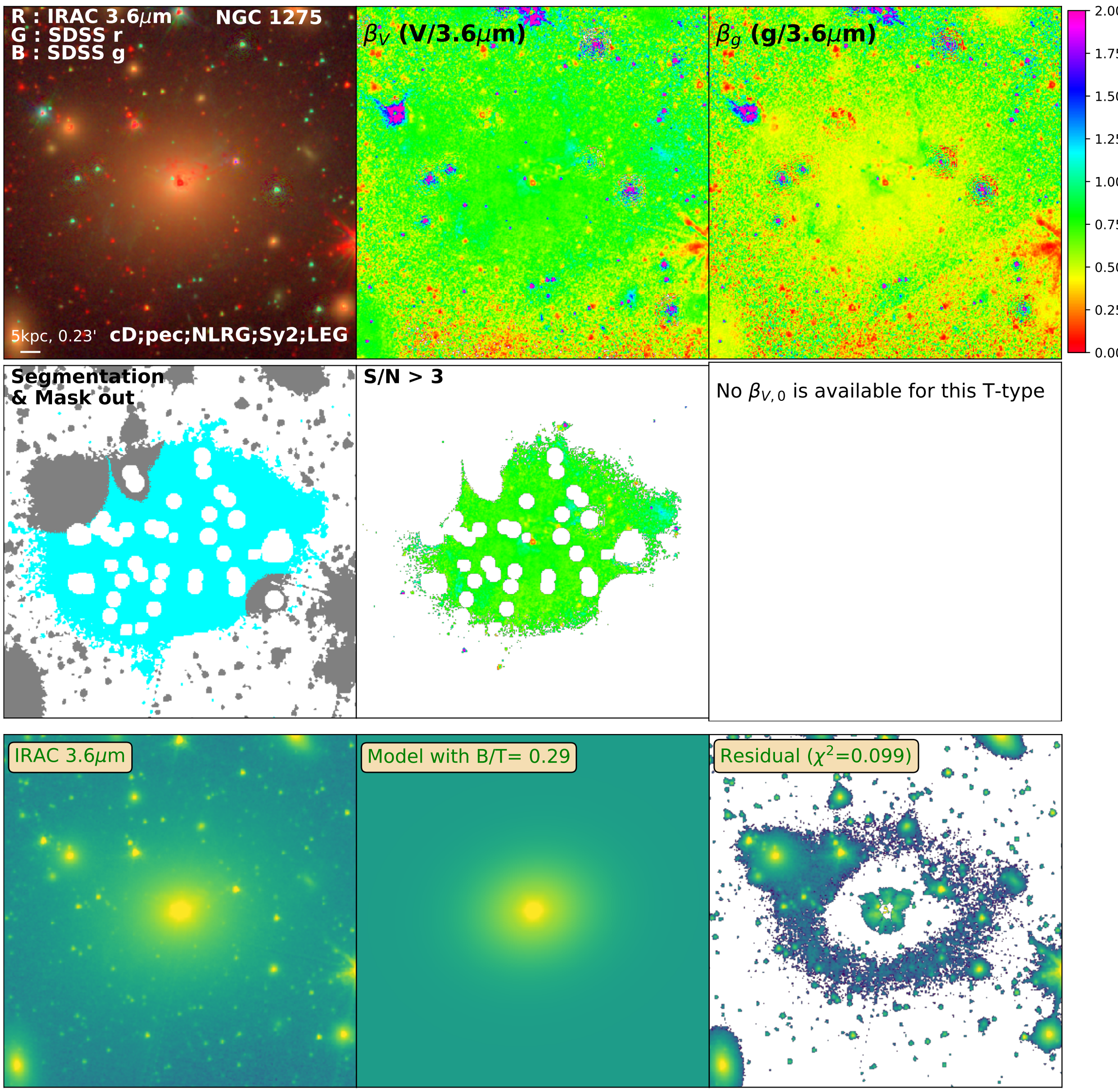

Figure D.32: Same as Figure 3.2 for NGC1275

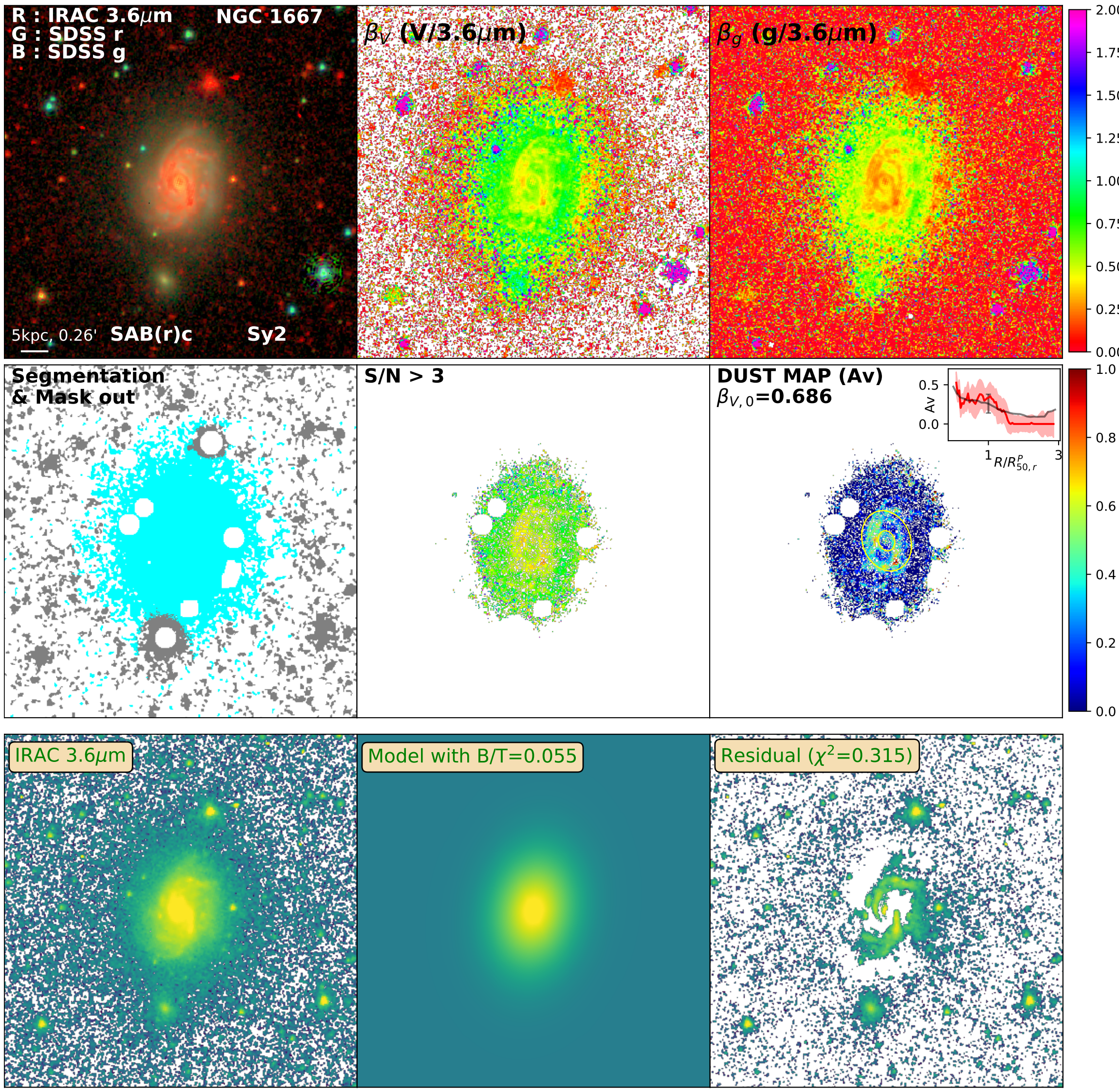

Figure D.33: Same as Figure 3.2 for NGC1667

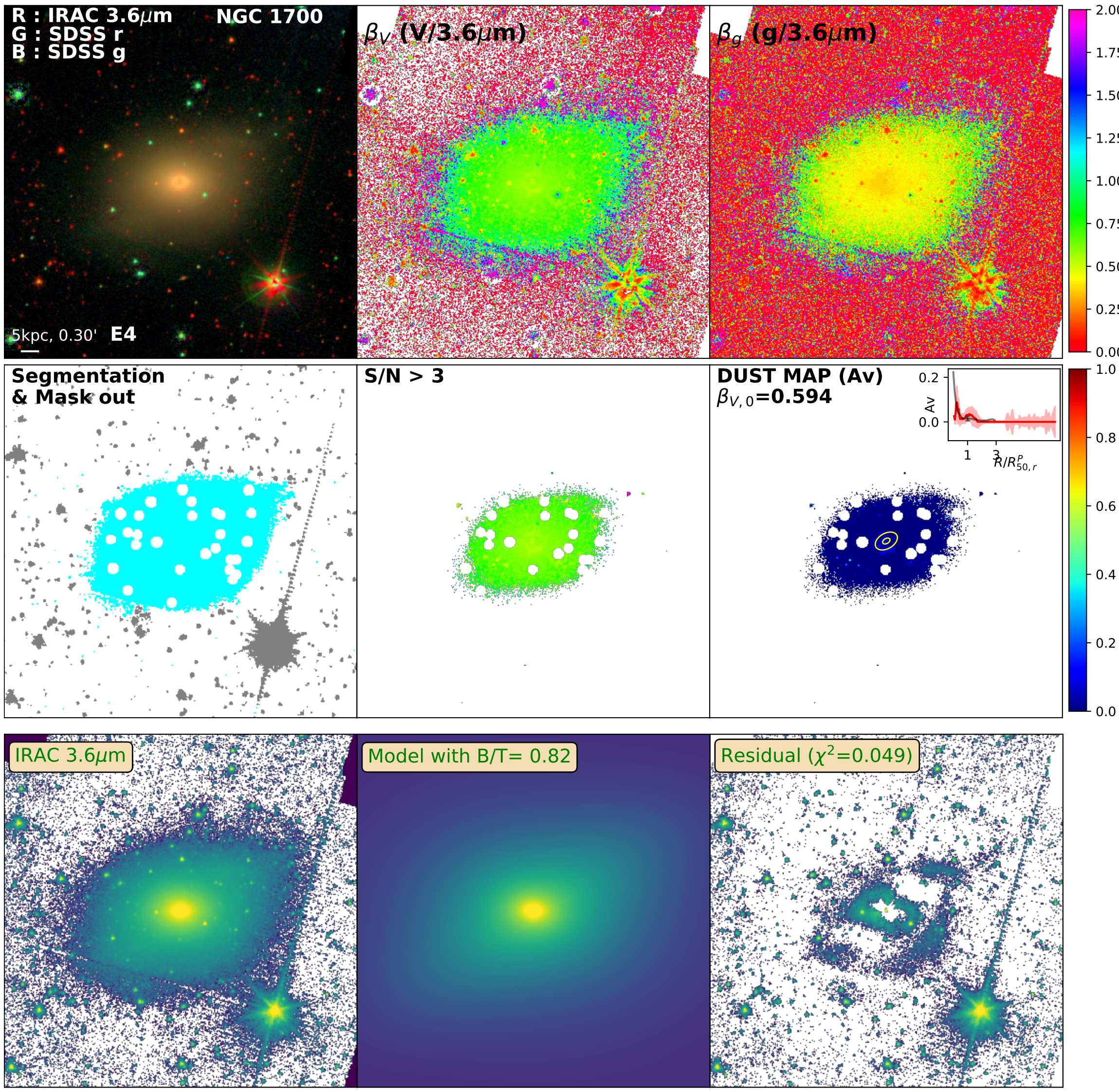

Figure D.34: Same as Figure 3.2 for NGC1700

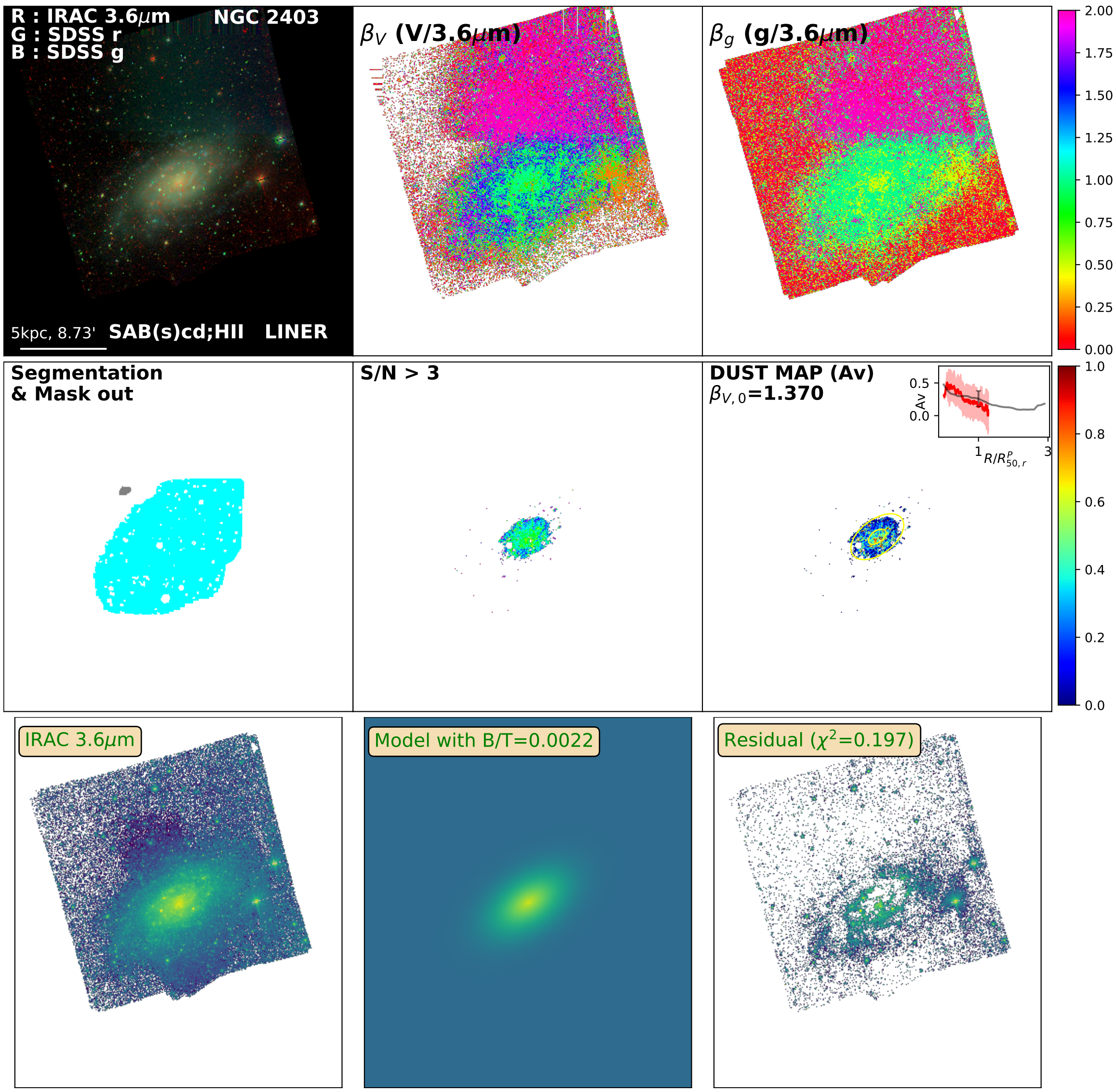

Figure D.35: Same as Figure 3.2 for NGC2403

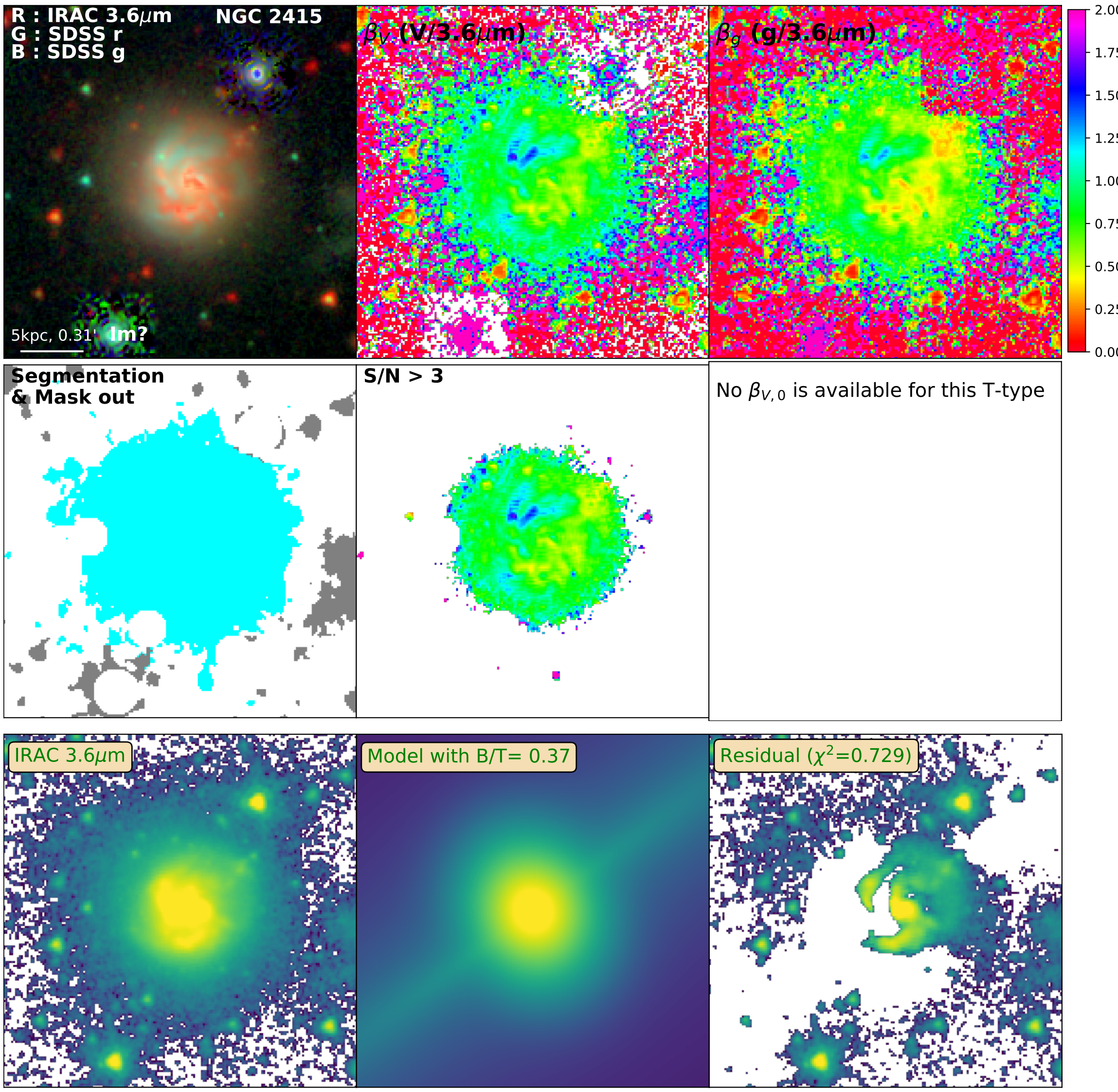

Figure D.36: Same as Figure 3.2 for NGC2415

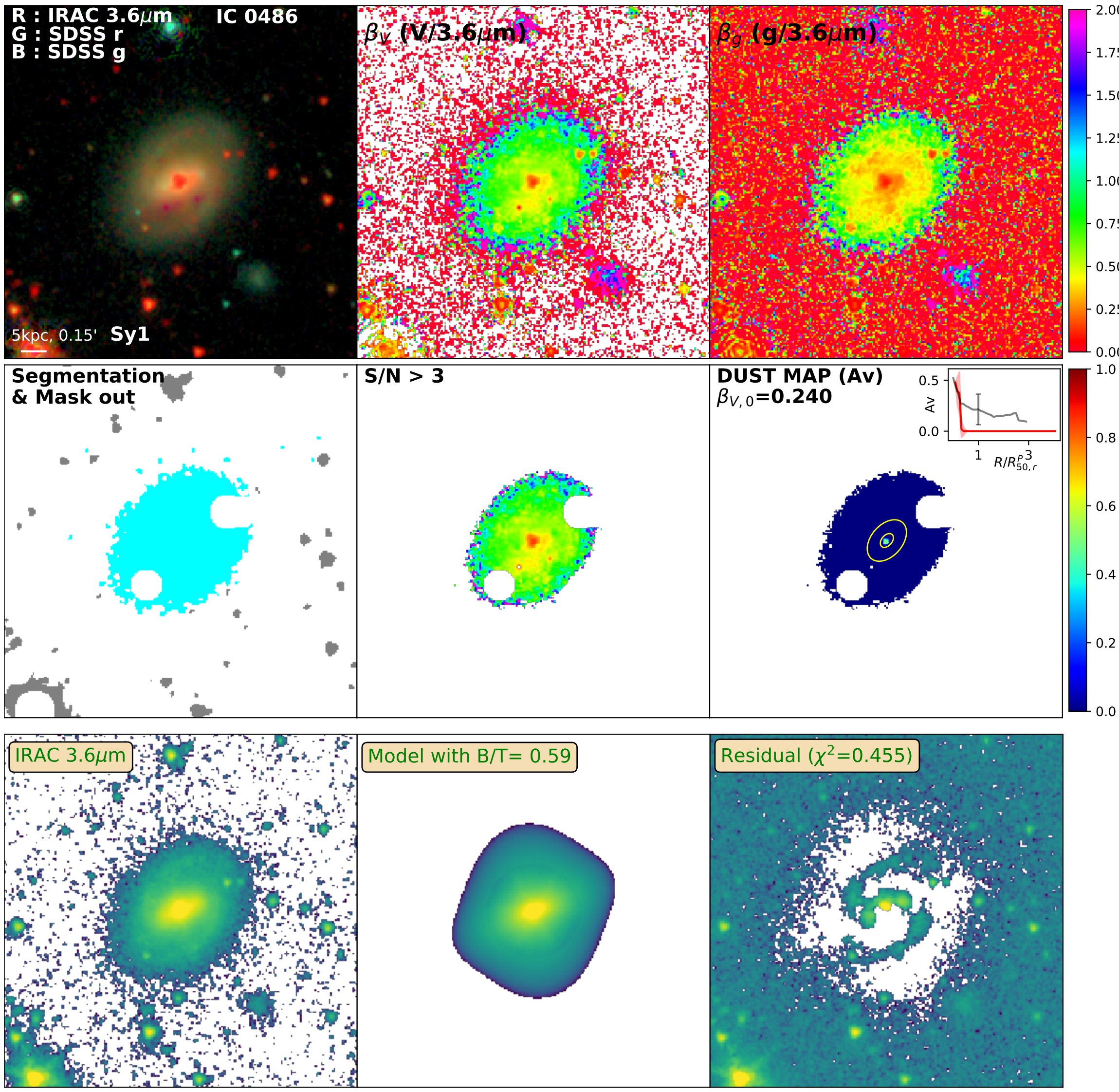

Figure D.37: Same as Figure 3.2 for IC0486

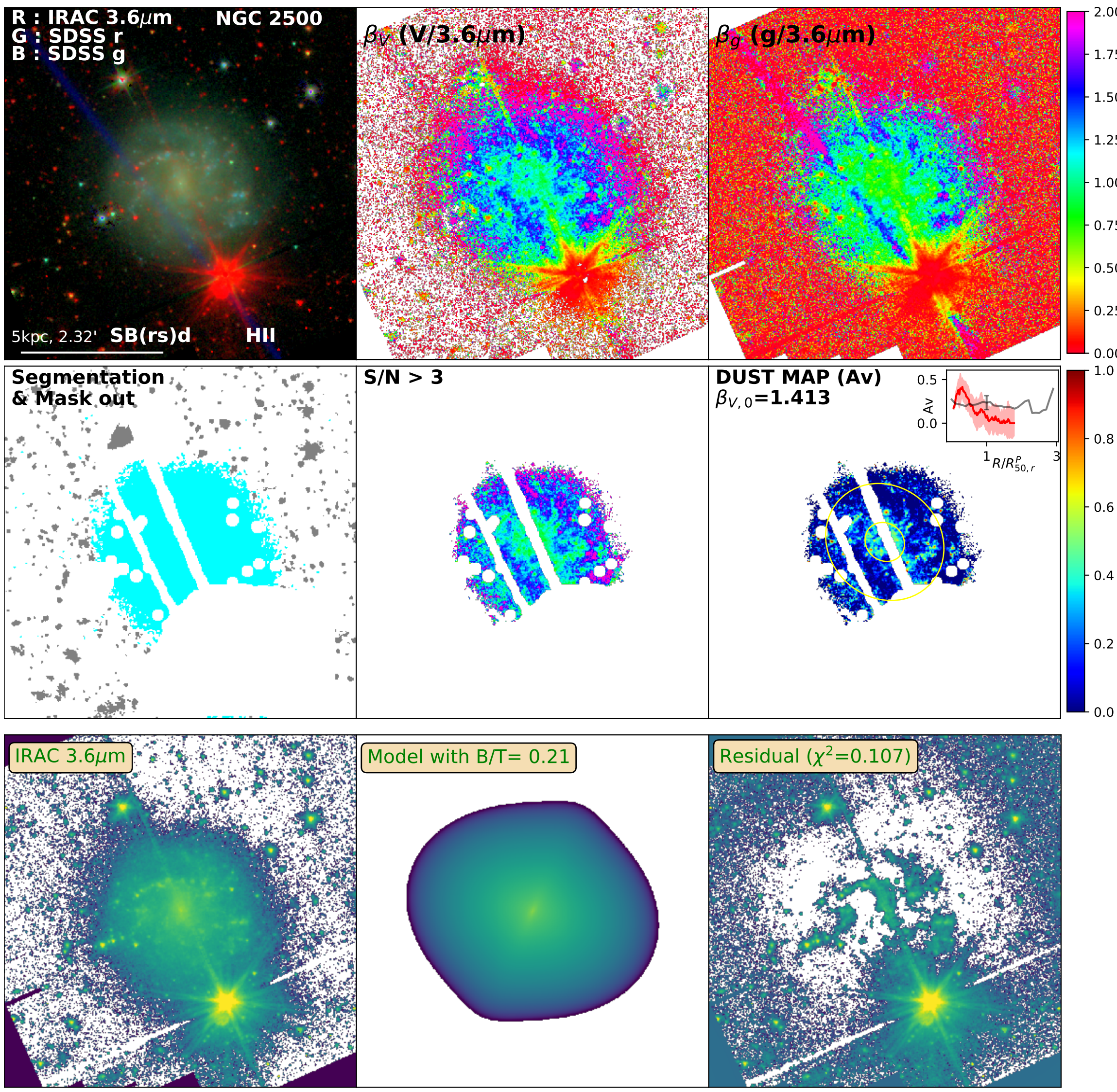

Figure D.38: Same as Figure 3.2 for NGC2500

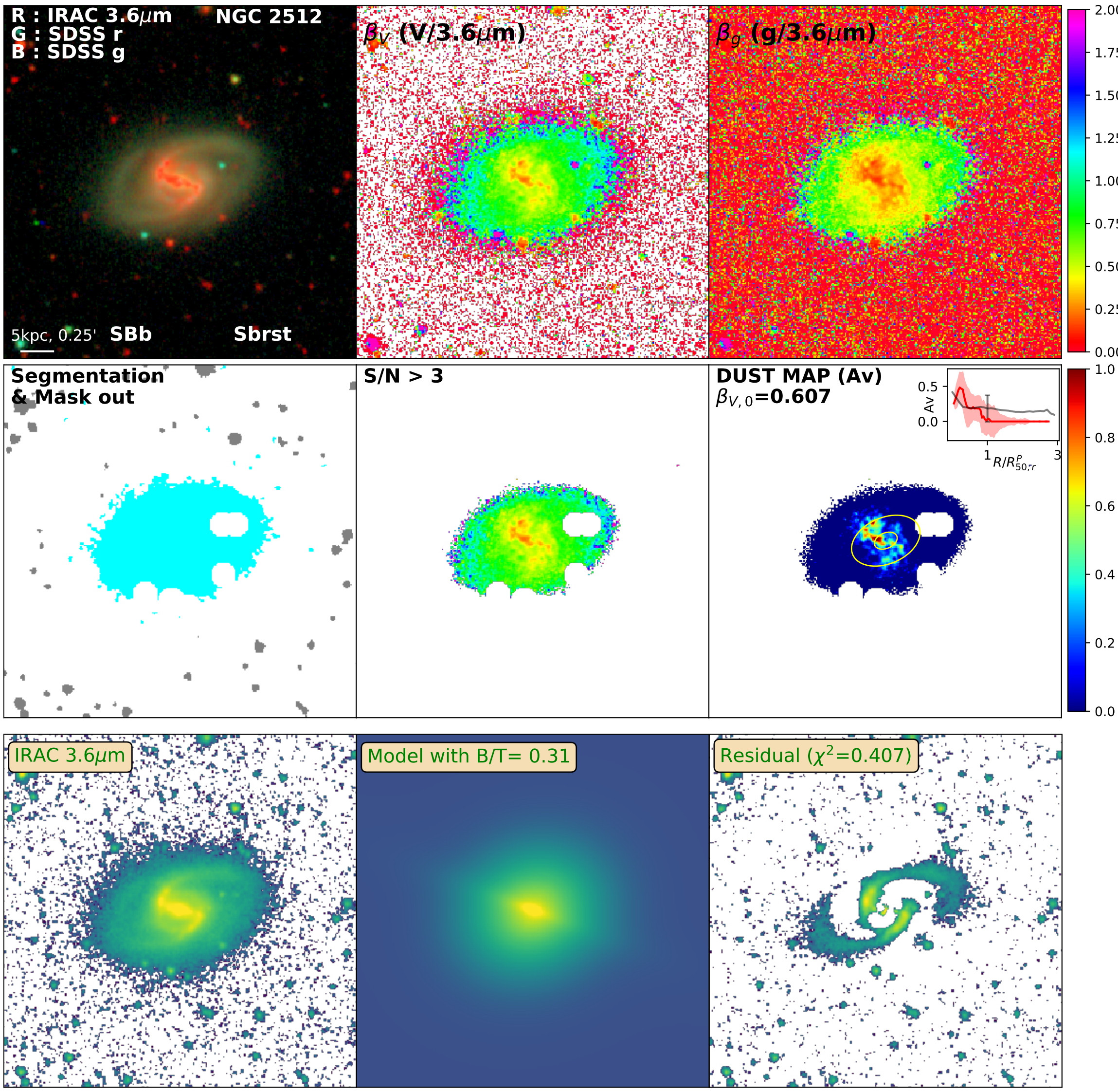

Figure D.39: Same as Figure 3.2 for NGC2512

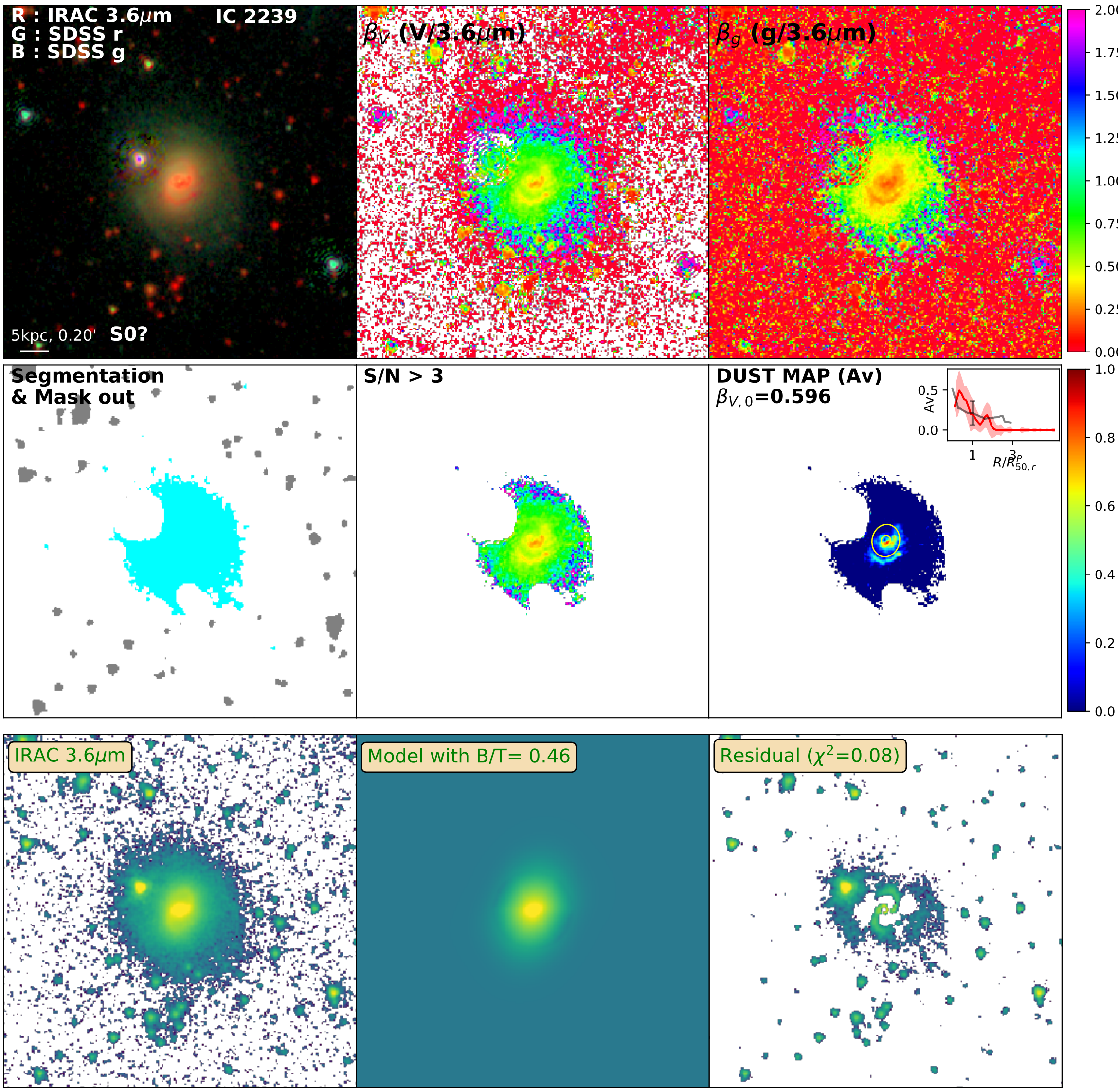

Figure D.40: Same as Figure 3.2 for IC2239

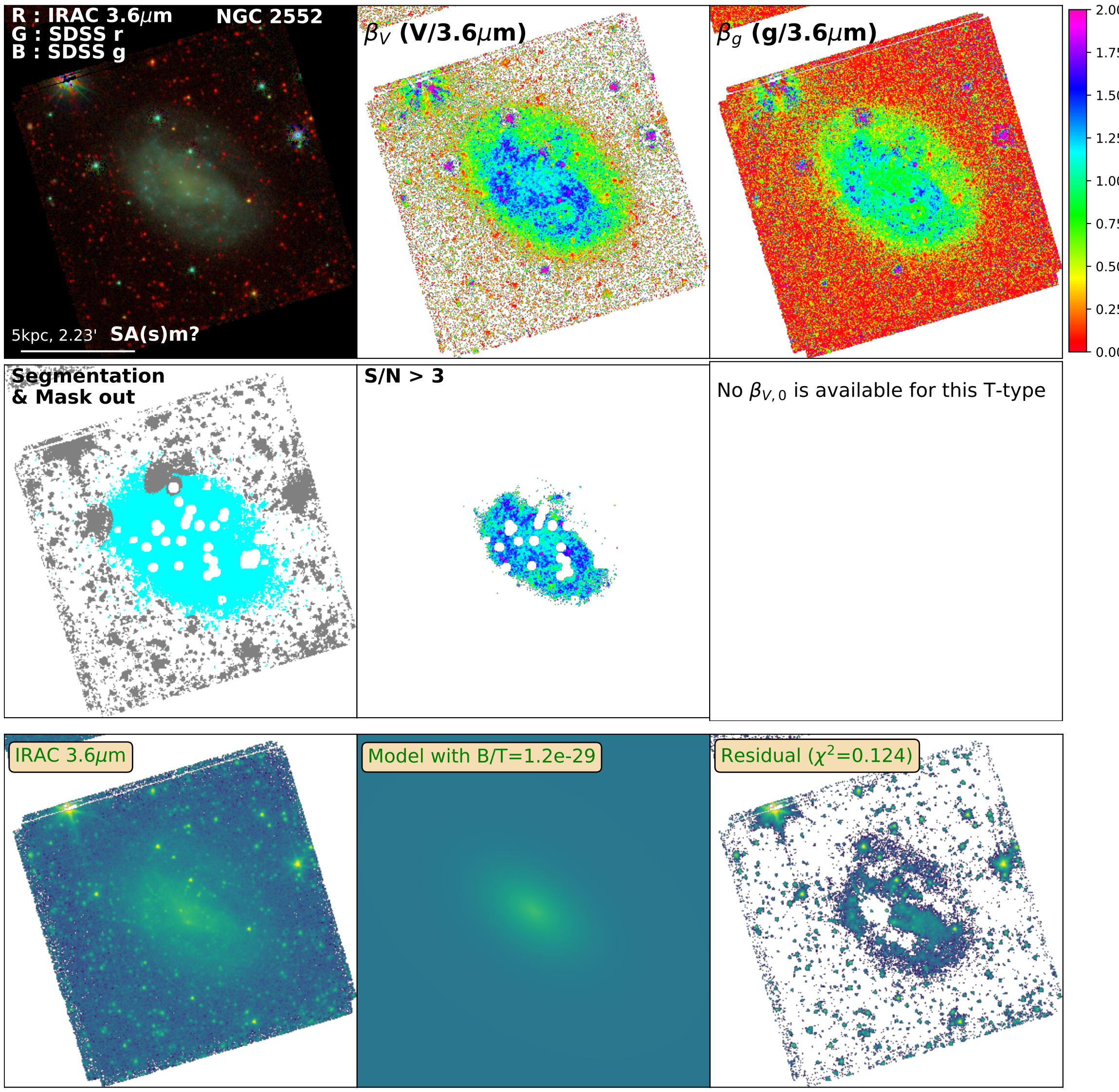

Figure D.41: Same as Figure 3.2 for NGC2552

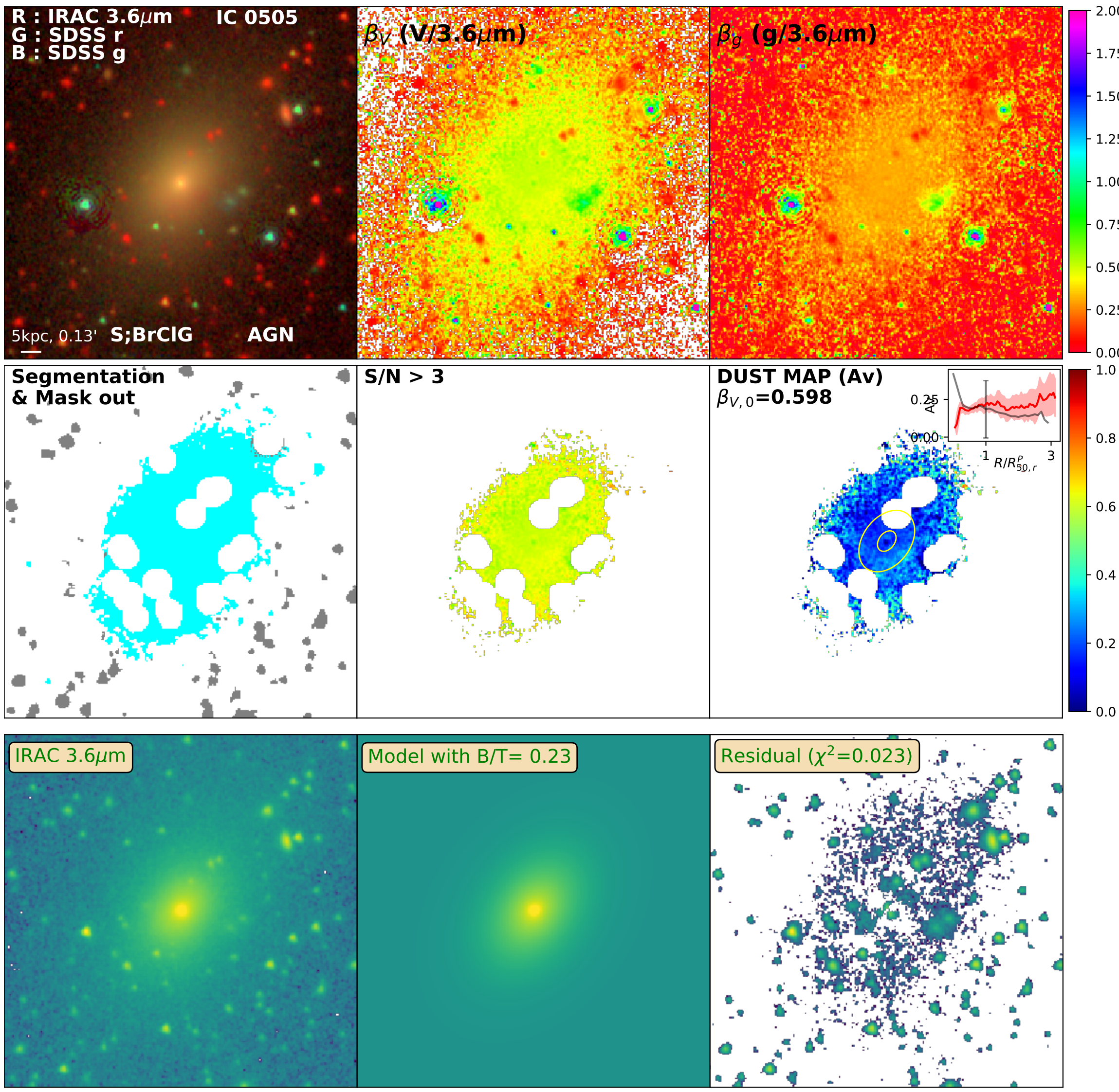

Figure D.42: Same as Figure 3.2 for IC0505

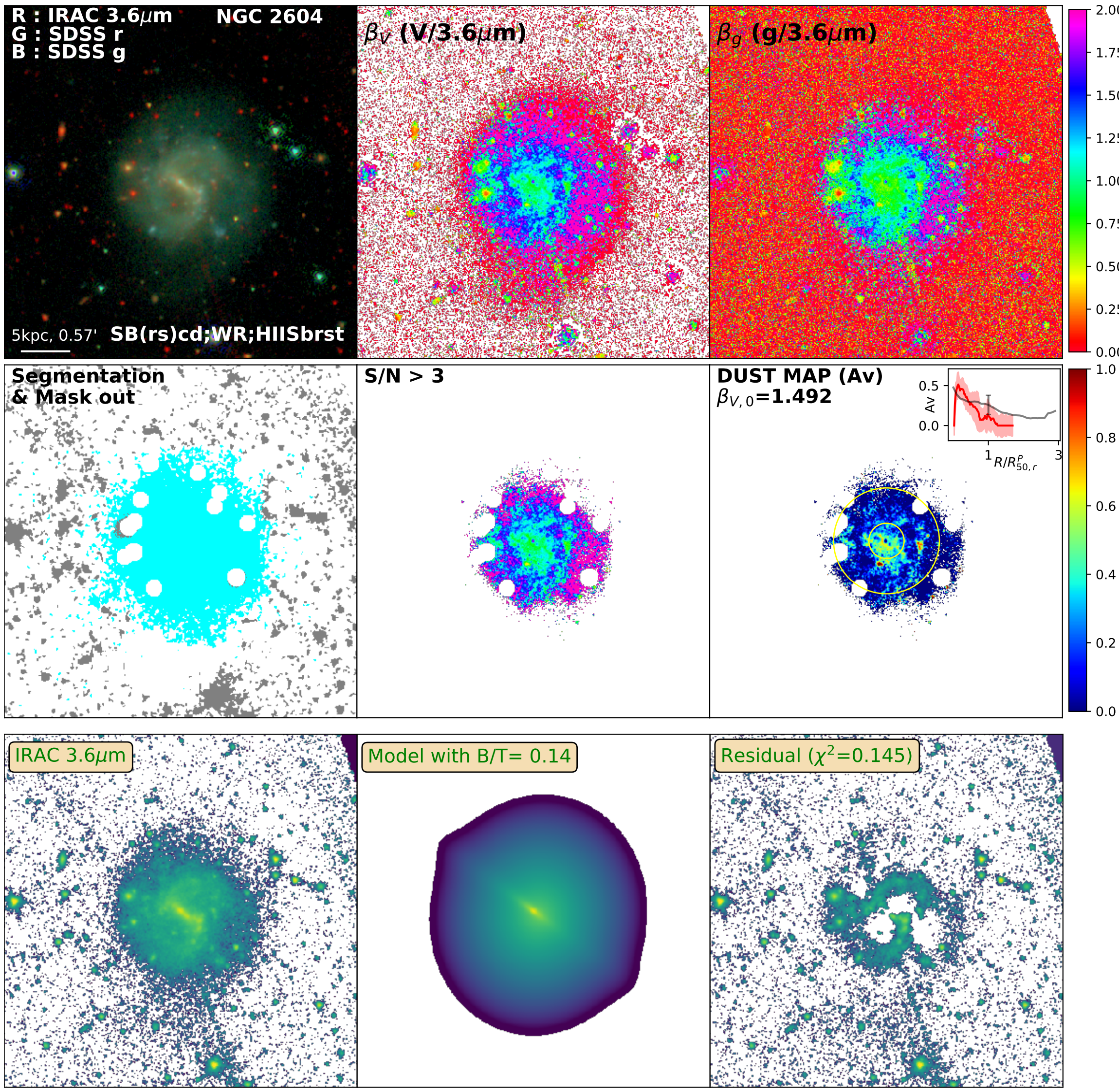

Figure D.43: Same as Figure 3.2 for NGC2604

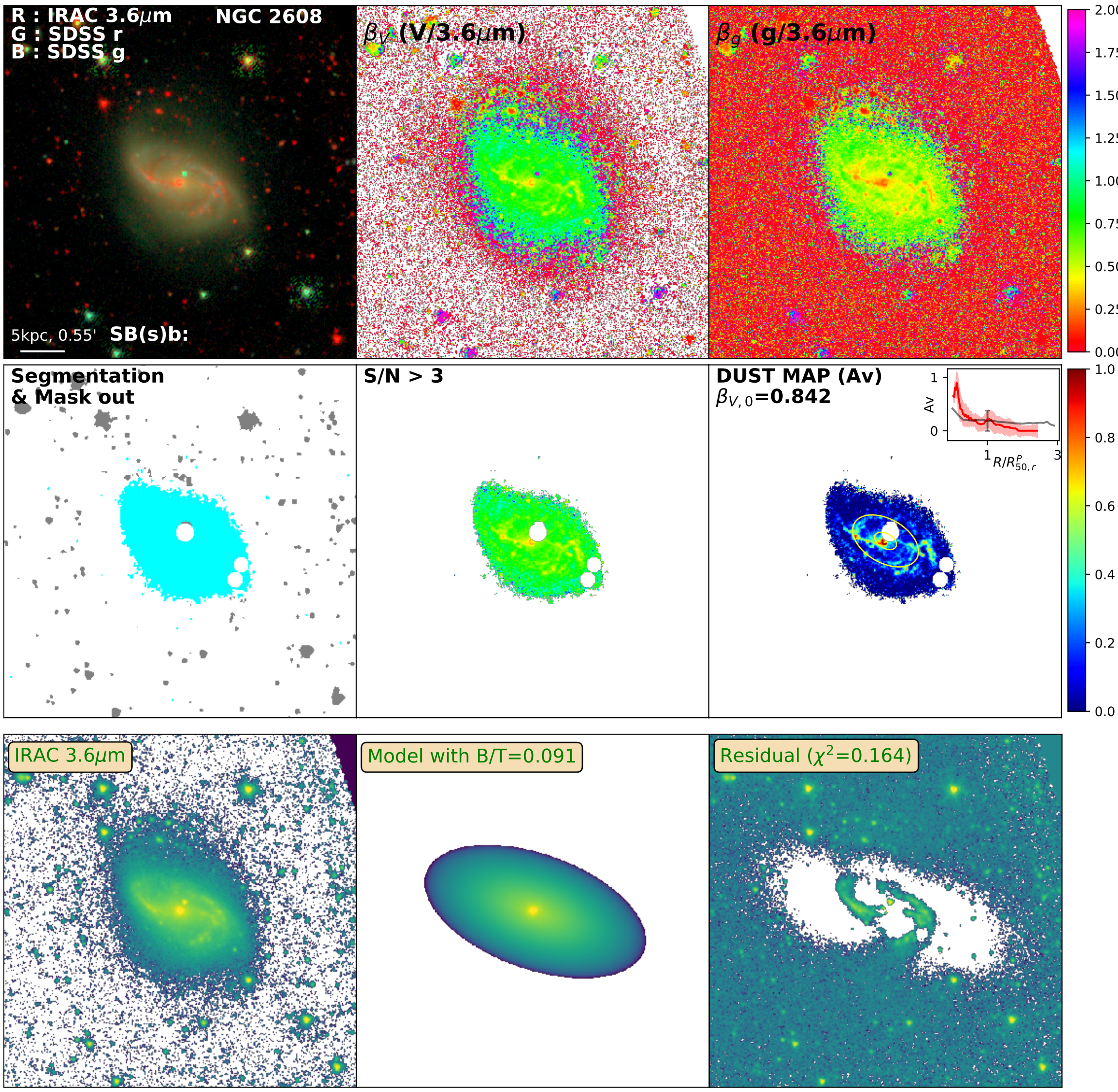

Figure D.44: Same as Figure 3.2 for NGC2608

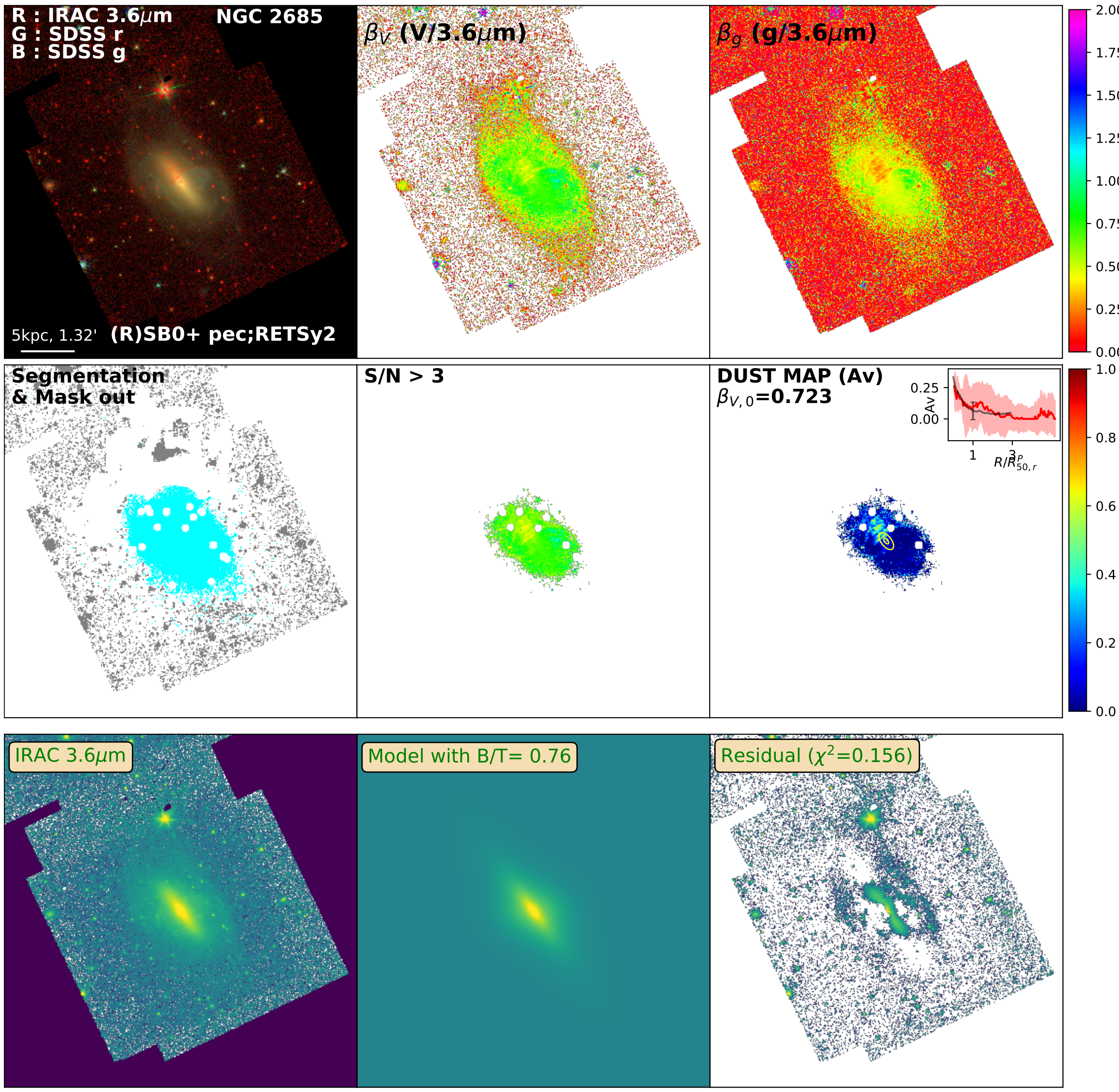

Figure D.45: Same as Figure 3.2 for NGC2685

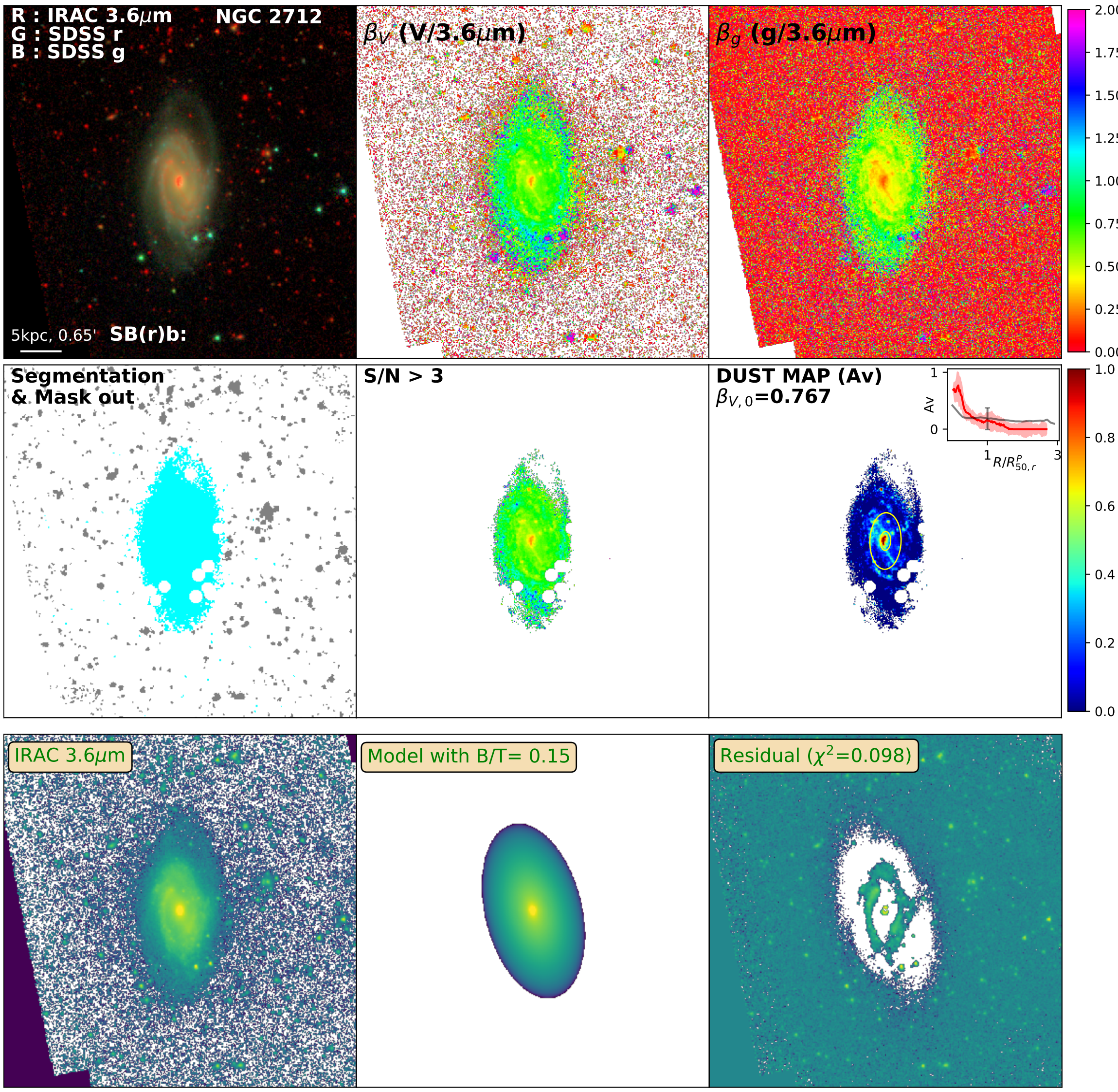

Figure D.46: Same as Figure 3.2 for NGC2712

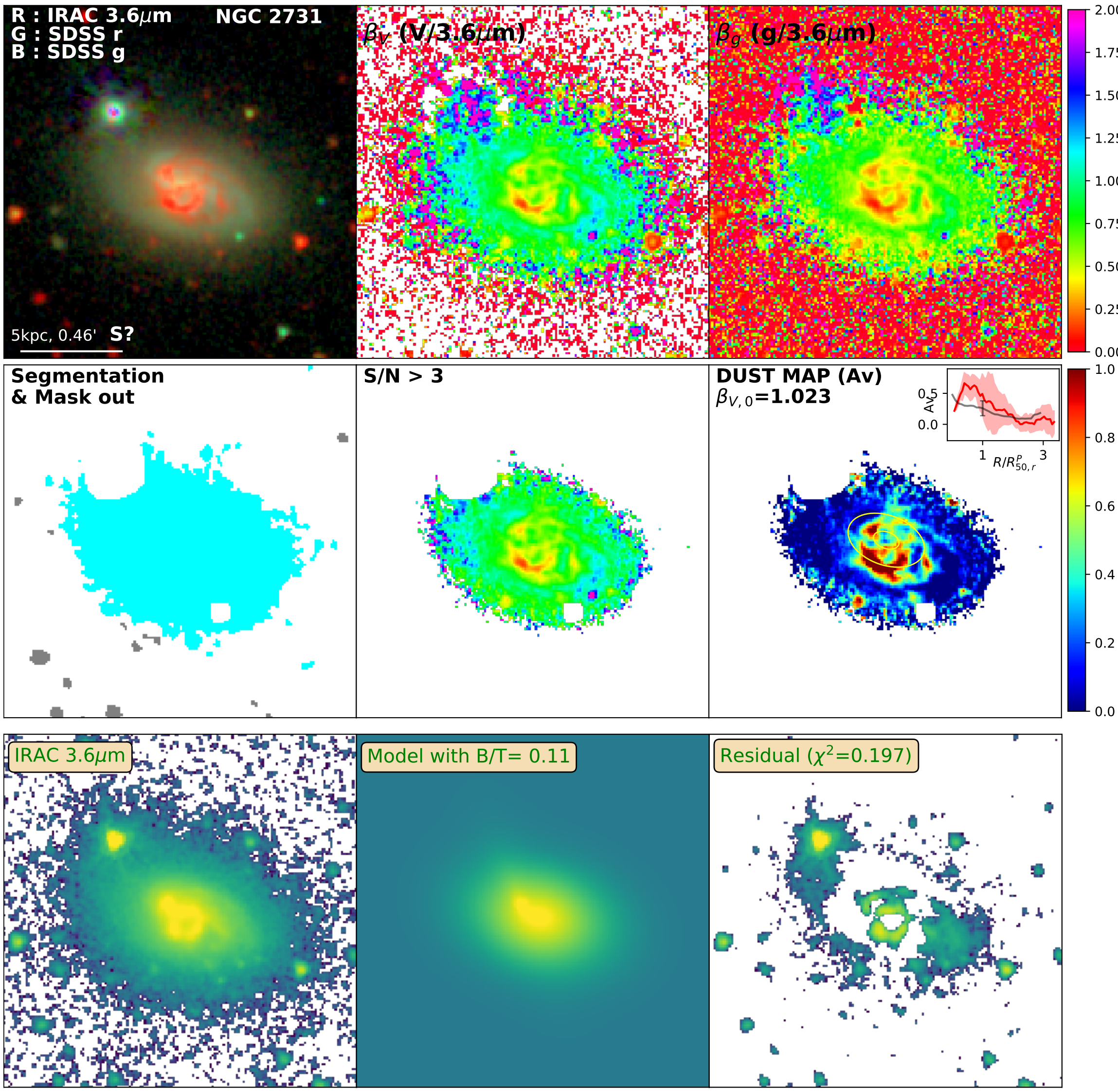

Figure D.47: Same as Figure 3.2 for NGC2731

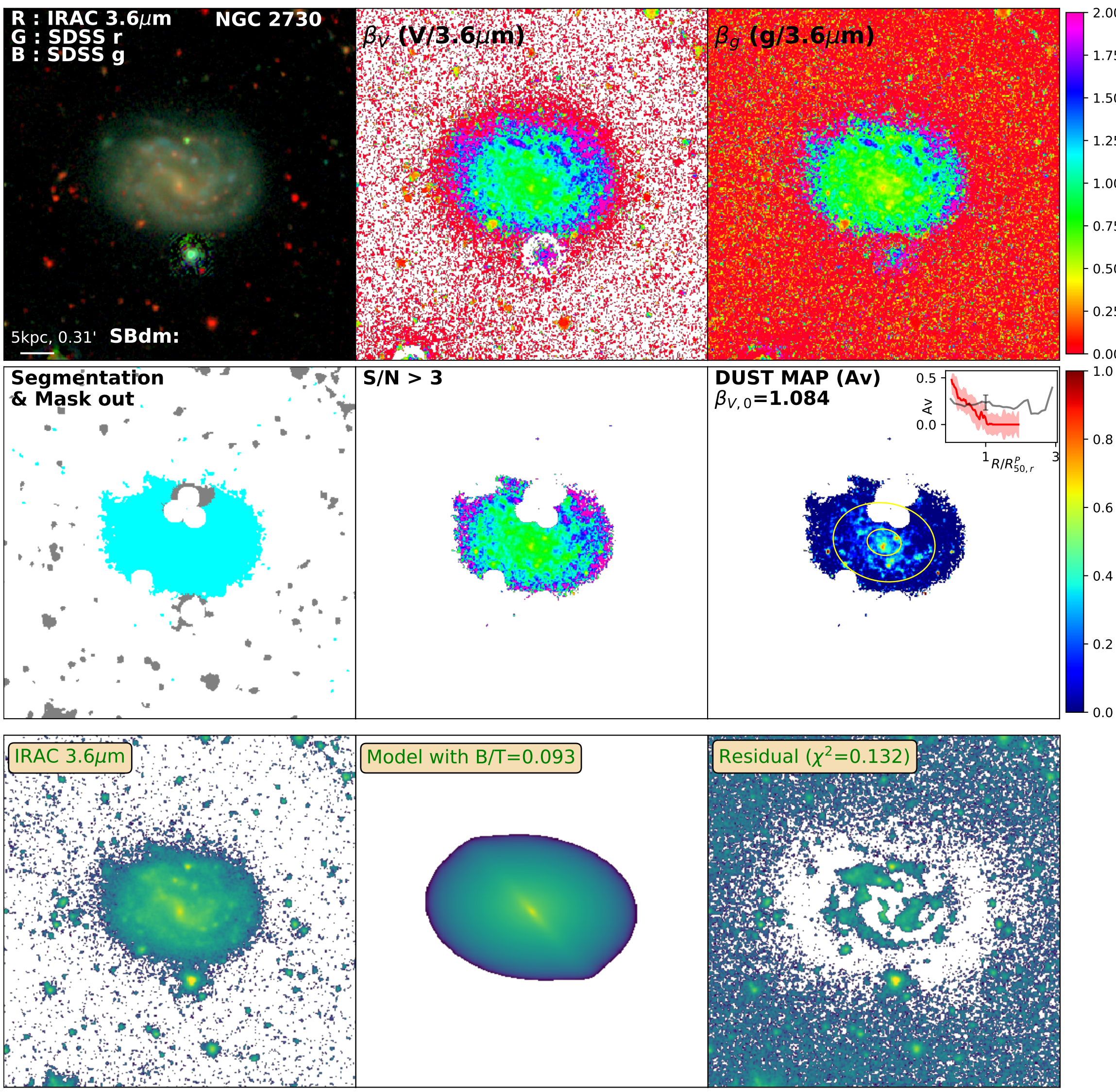

Figure D.48: Same as Figure 3.2 for NGC2730

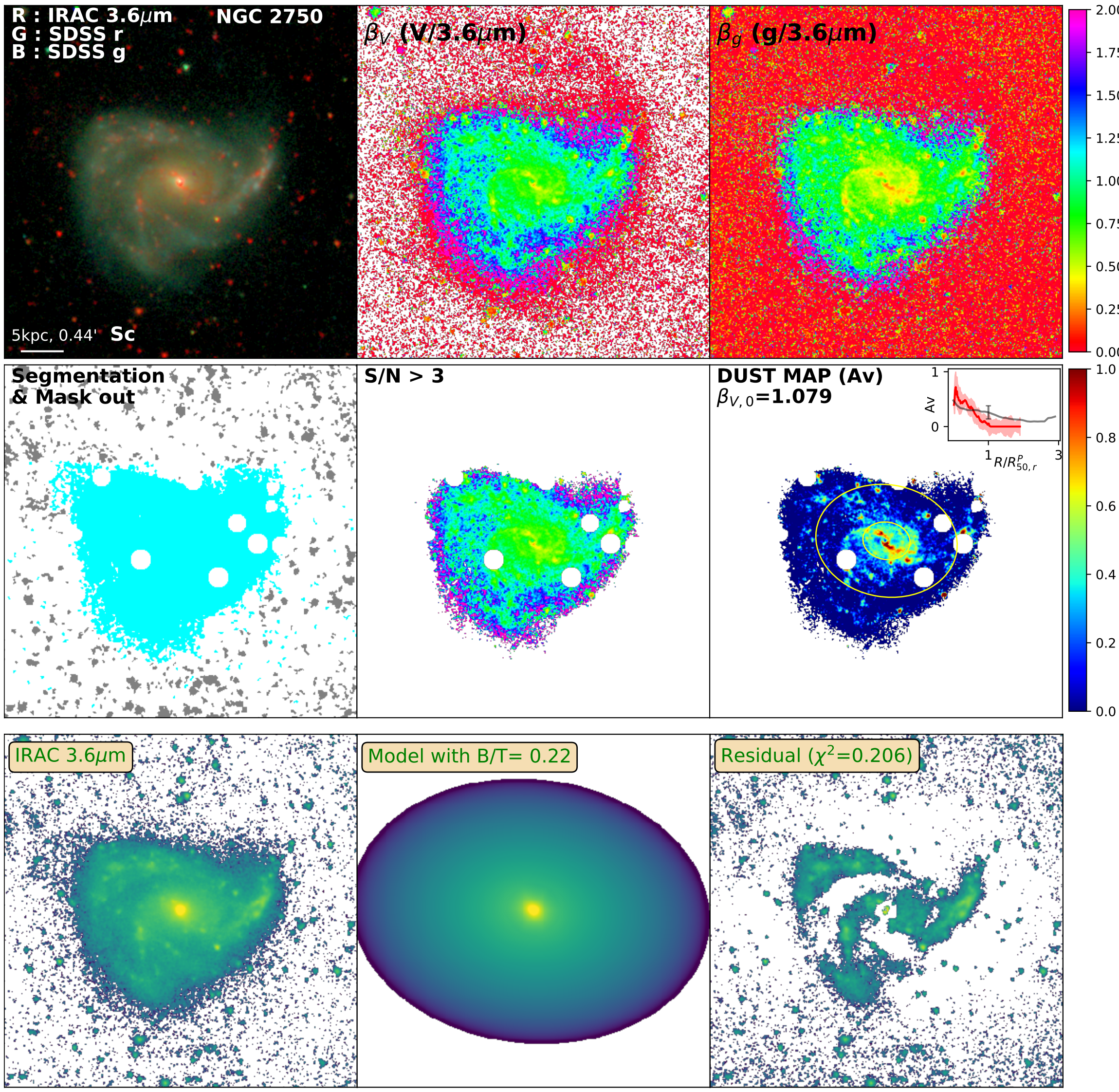

Figure D.49: Same as Figure 3.2 for NGC2750

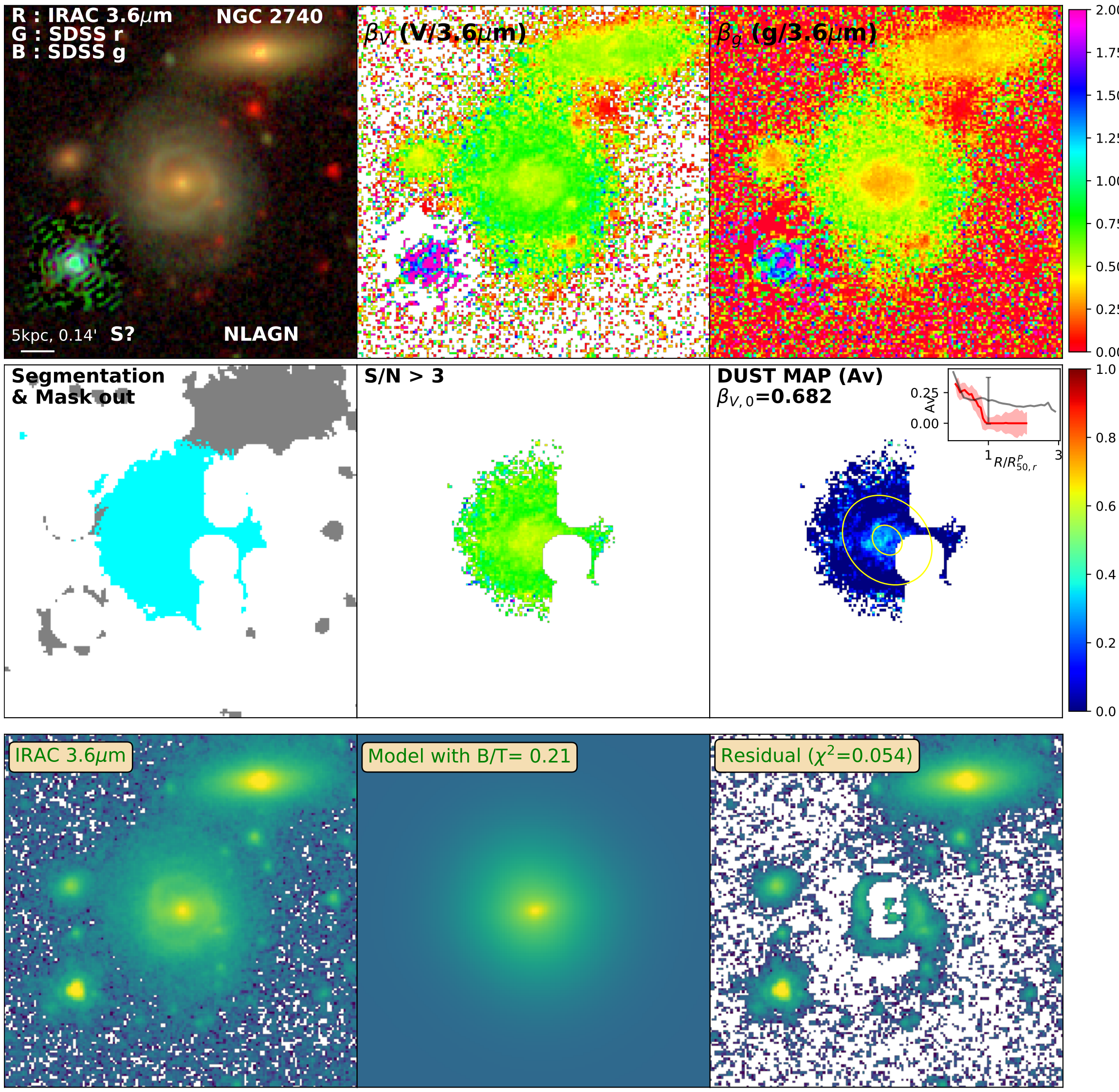

Figure D.50: Same as Figure 3.2 for NGC2740

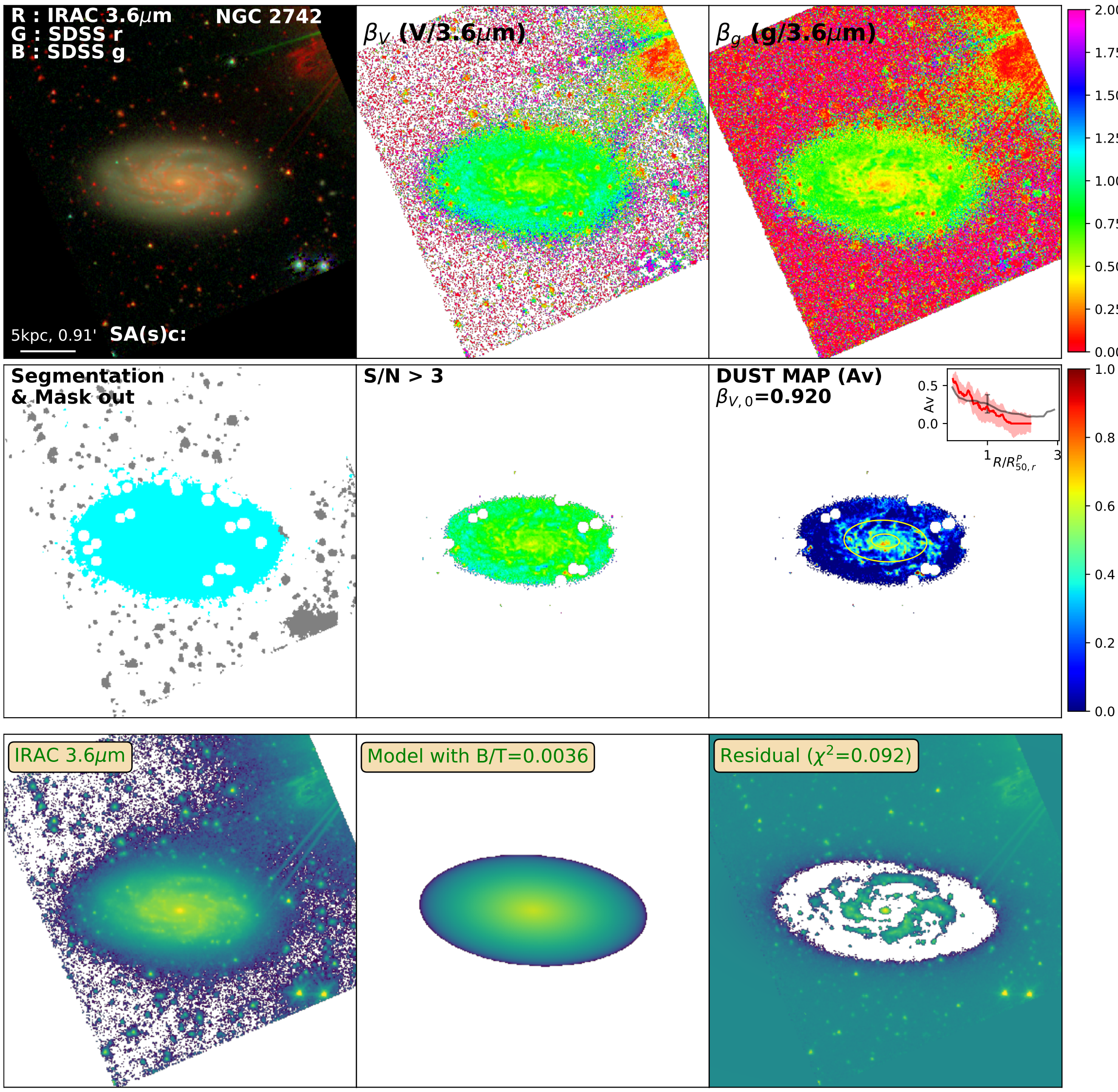

Figure D.51: Same as Figure 3.2 for NGC2742

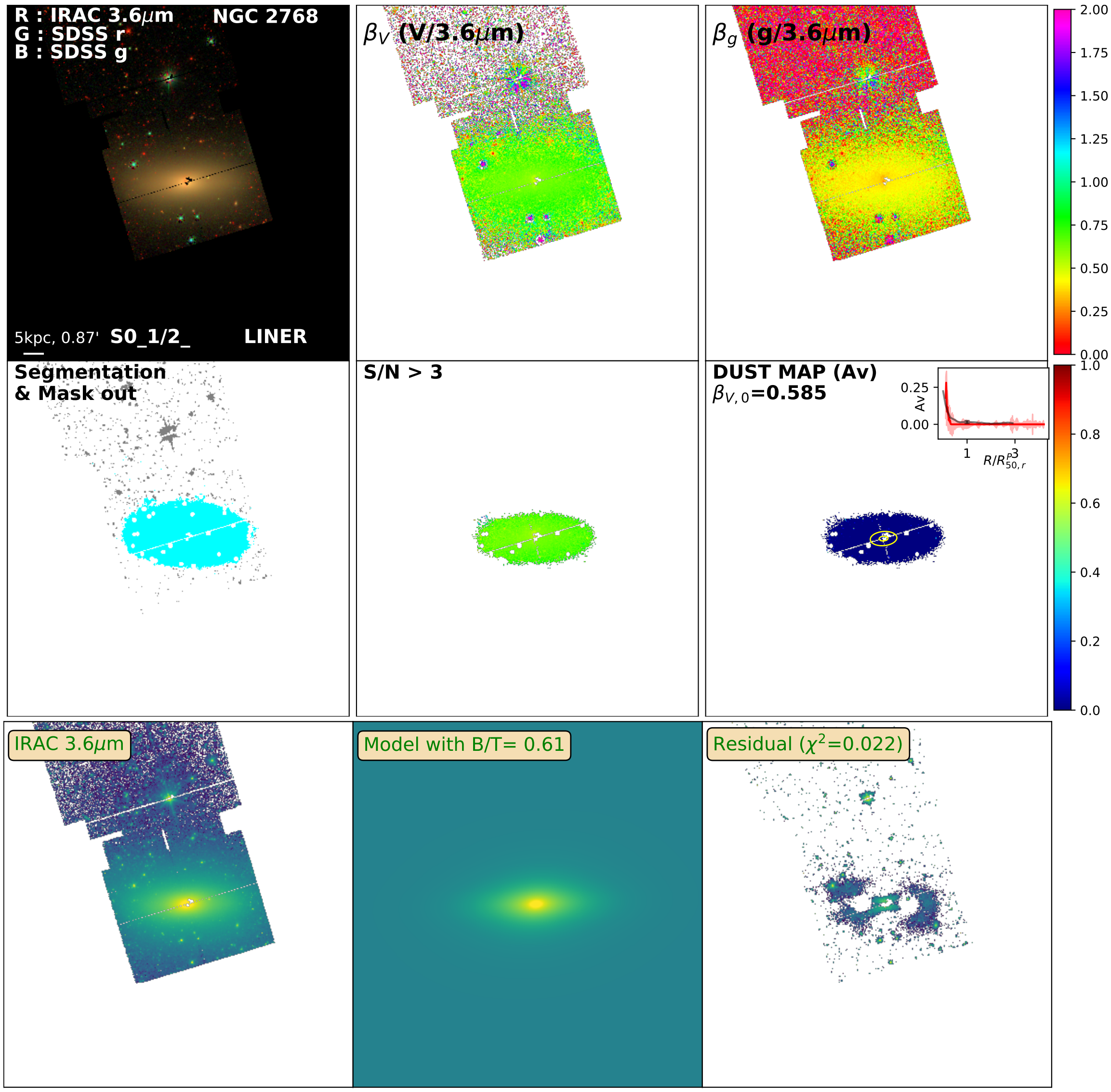

Figure D.52: Same as Figure 3.2 for NGC2768

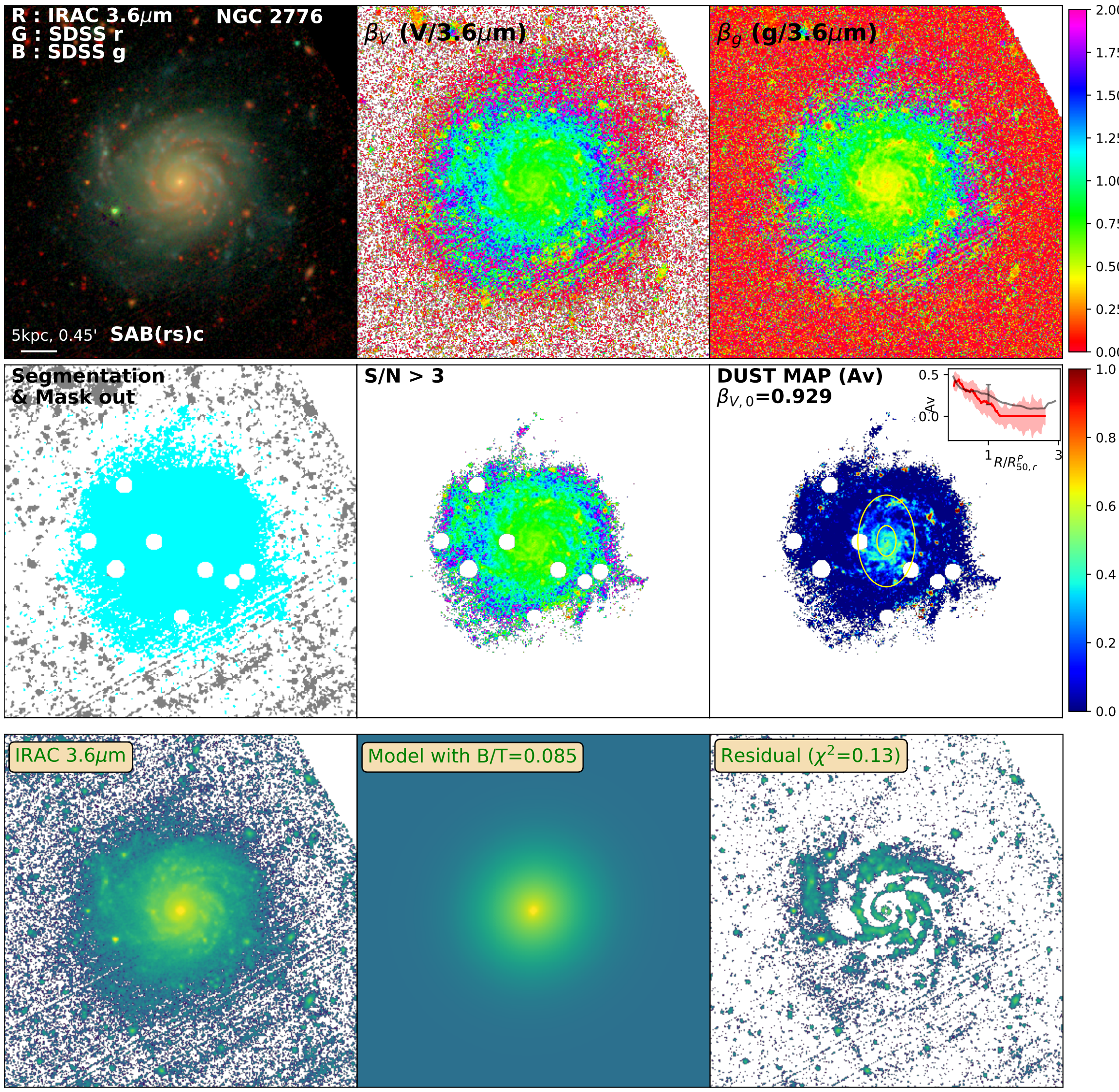

Figure D.53: Same as Figure 3.2 for NGC2776

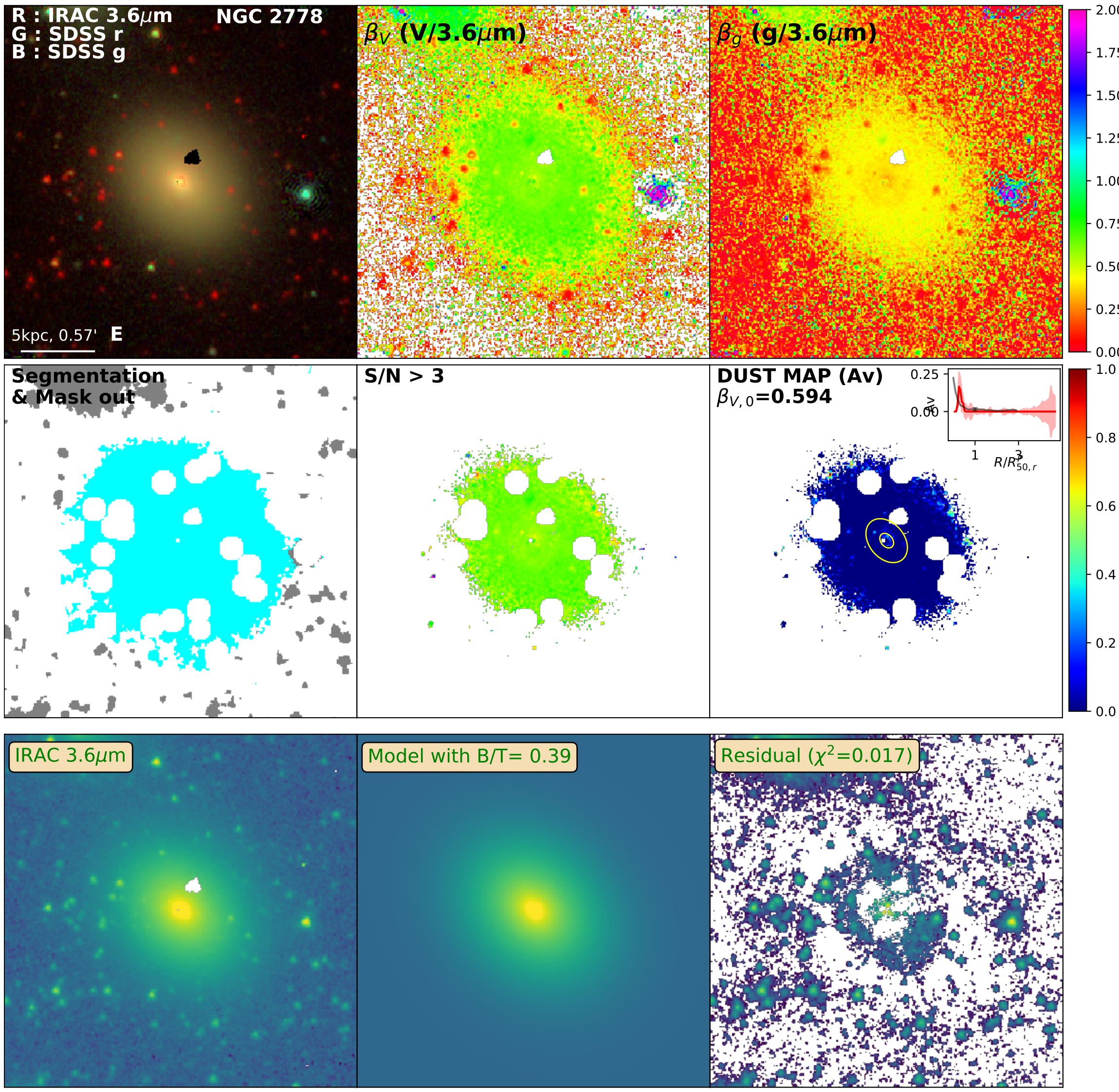

Figure D.54: Same as Figure 3.2 for NGC2778

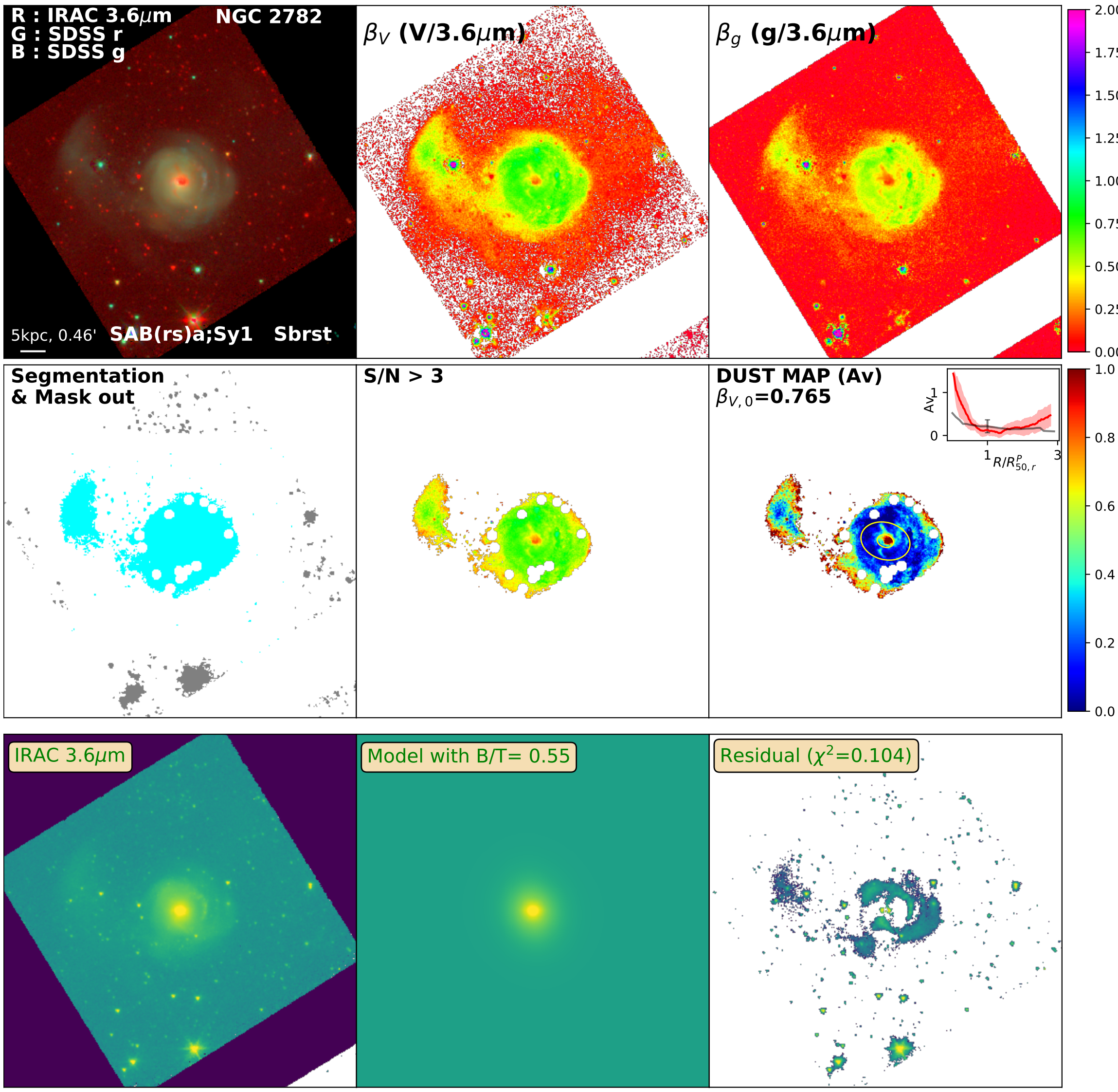

Figure D.55: Same as Figure 3.2 for NGC2782

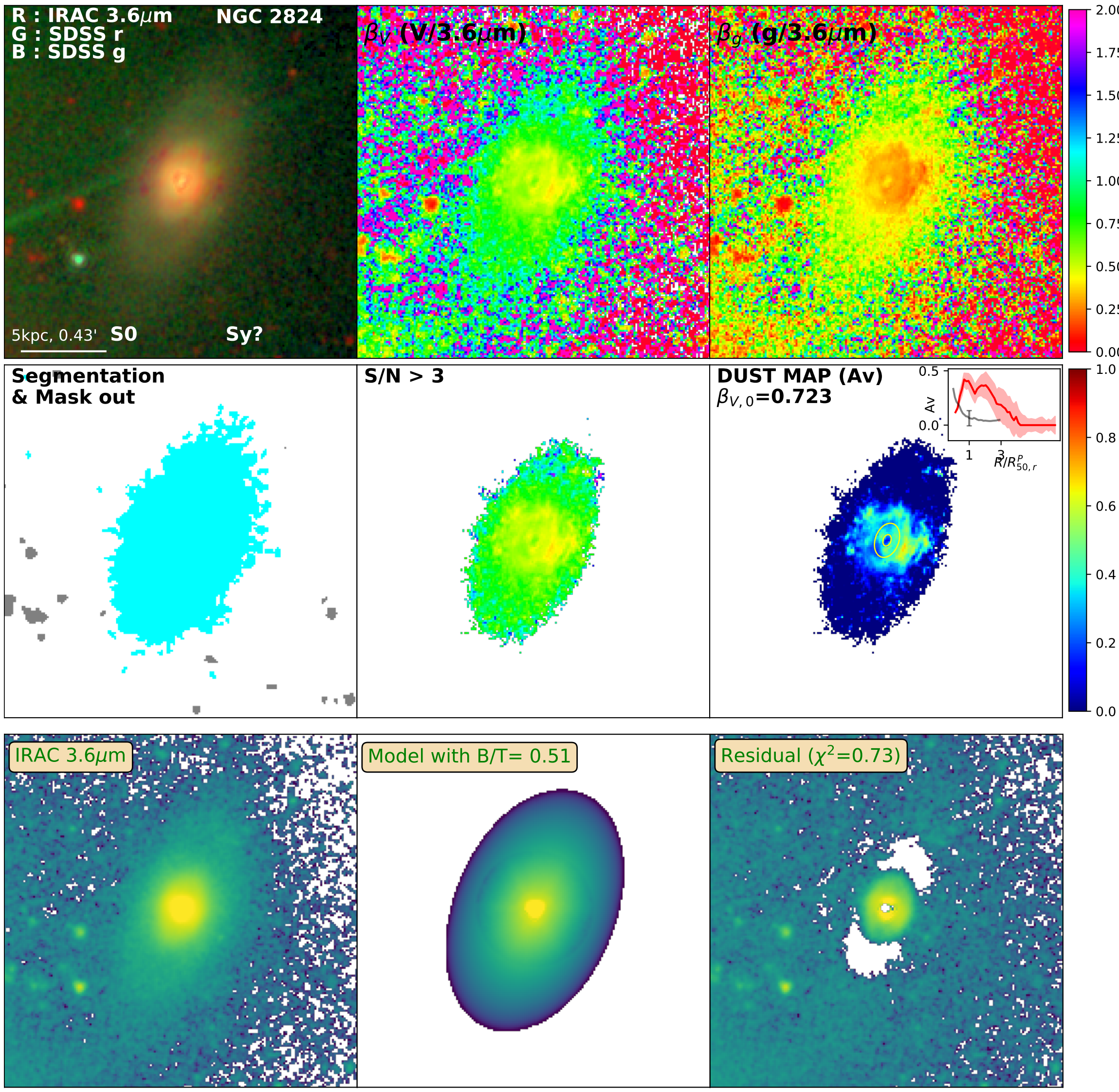

Figure D.56: Same as Figure 3.2 for NGC2824

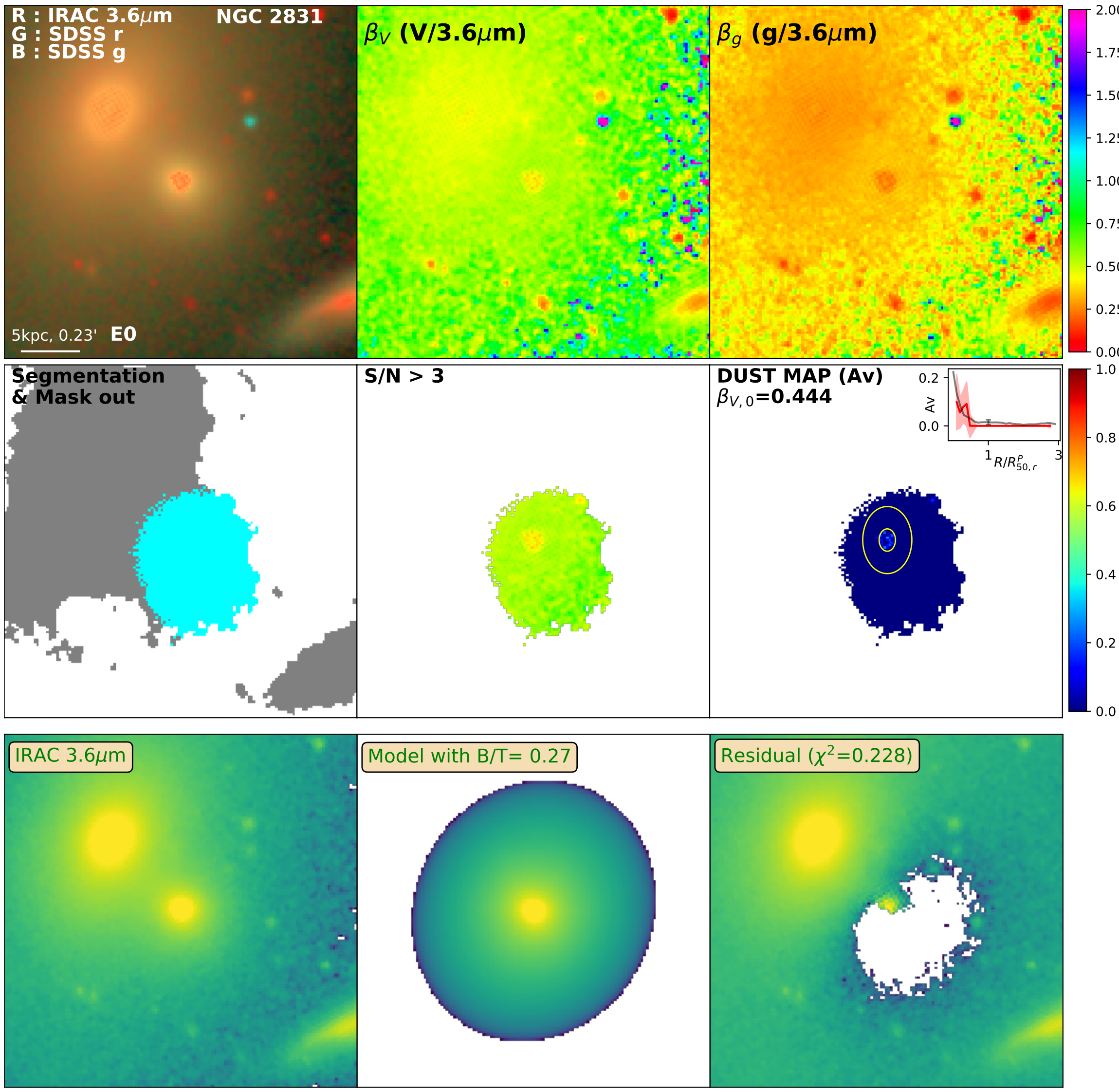

Figure D.57: Same as Figure 3.2 for NGC2831

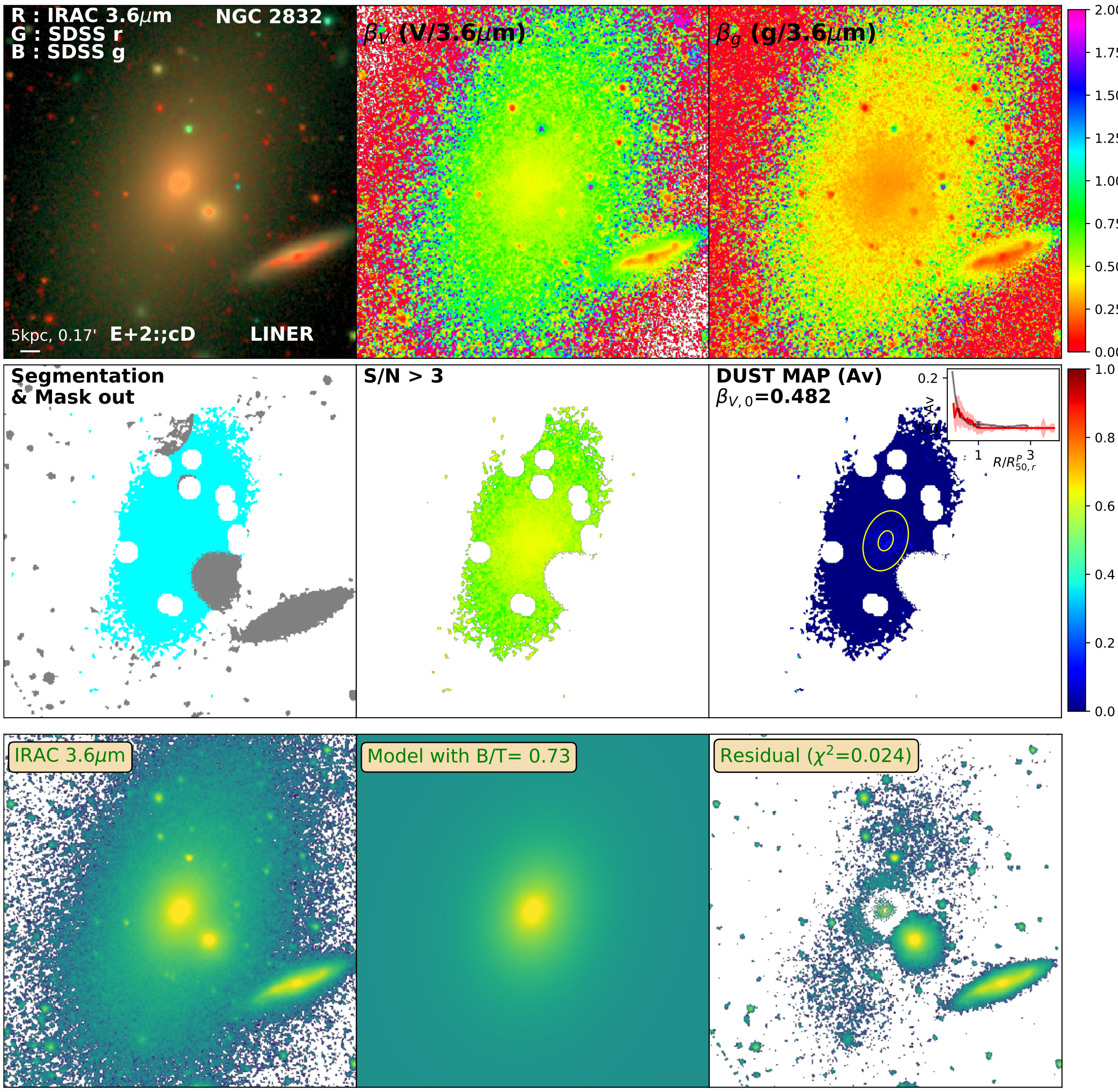

Figure D.58: Same as Figure 3.2 for NGC2832

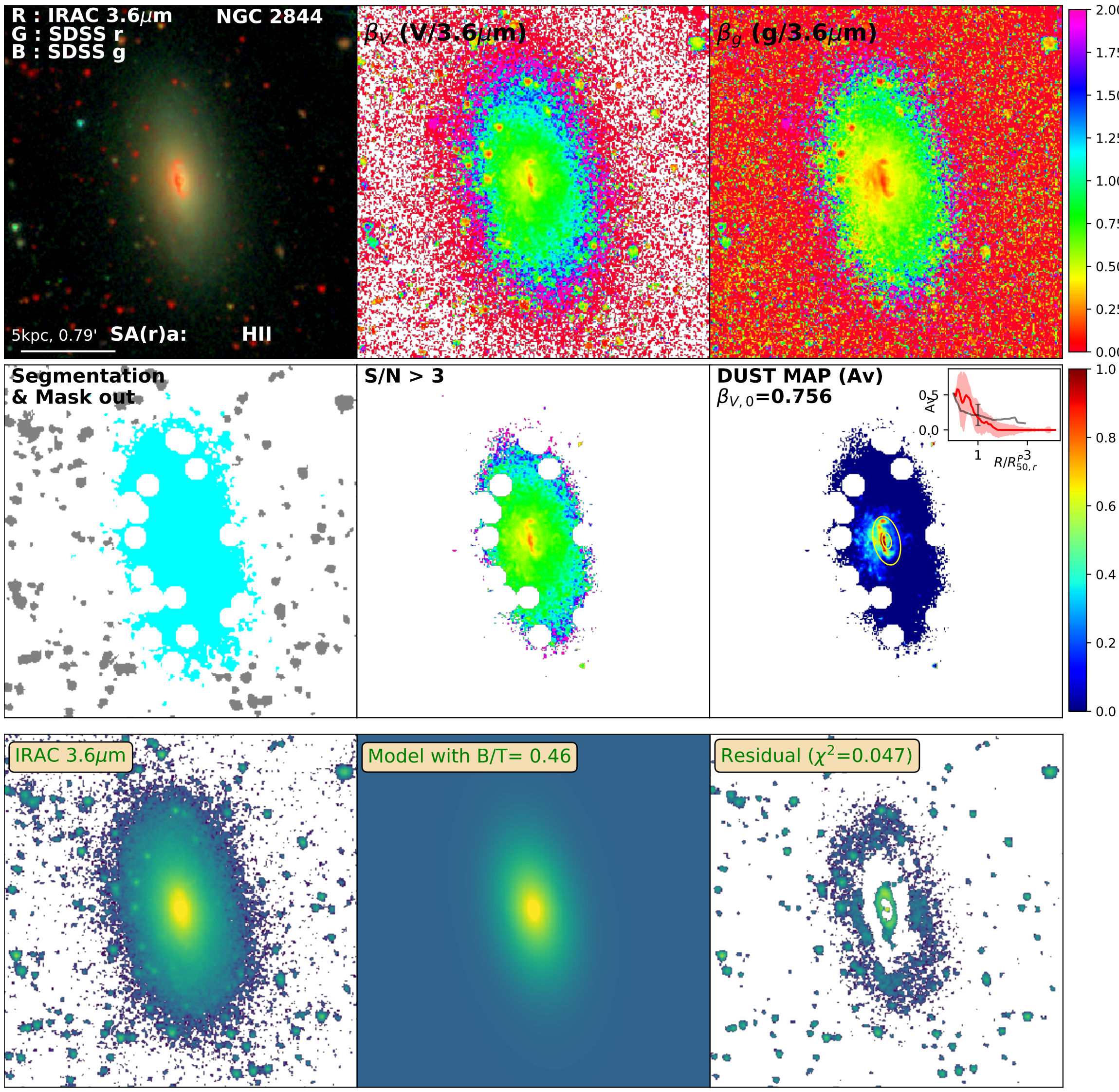

Figure D.59: Same as Figure 3.2 for NGC2844

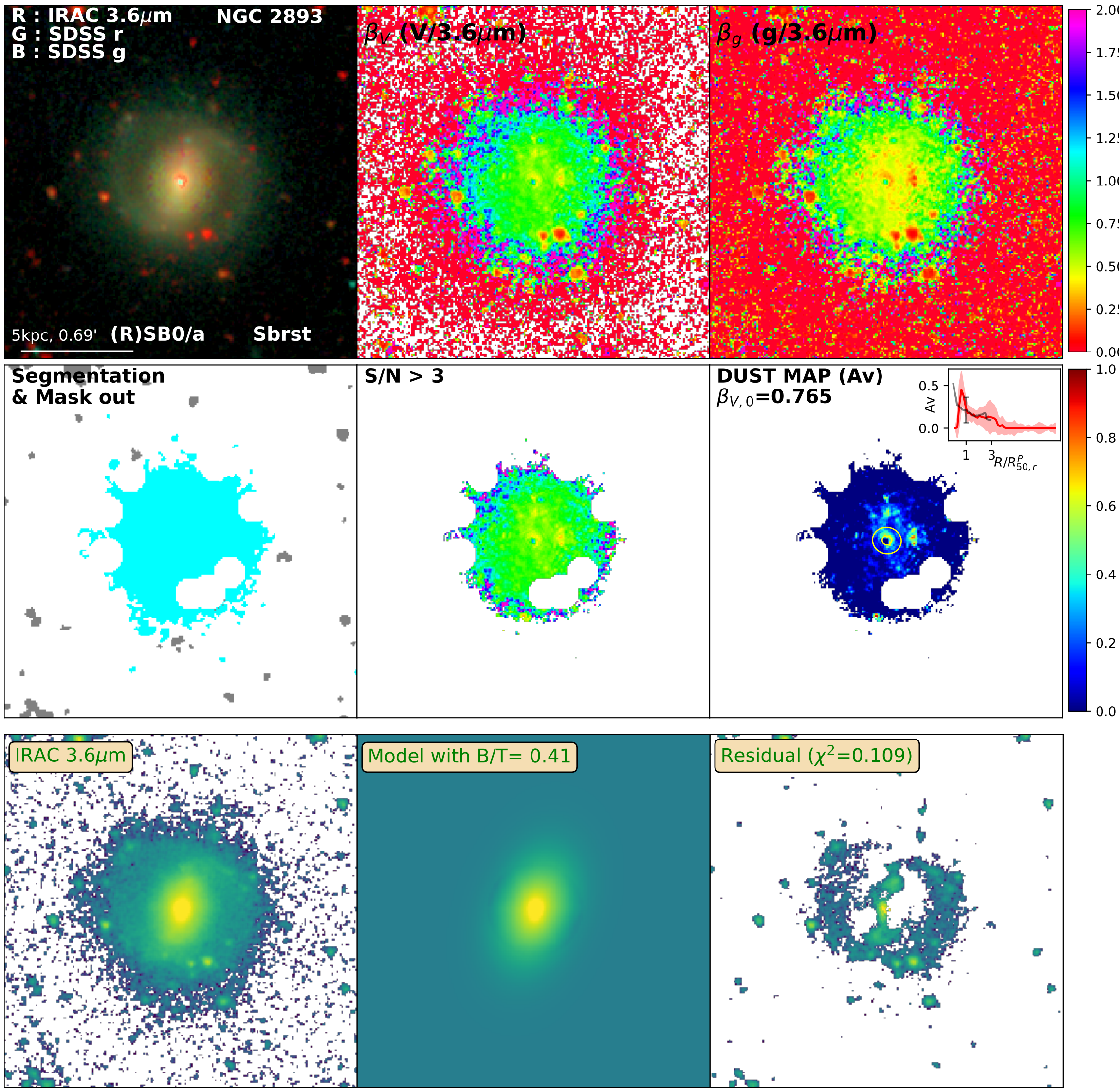

Figure D.60: Same as Figure 3.2 for NGC2893

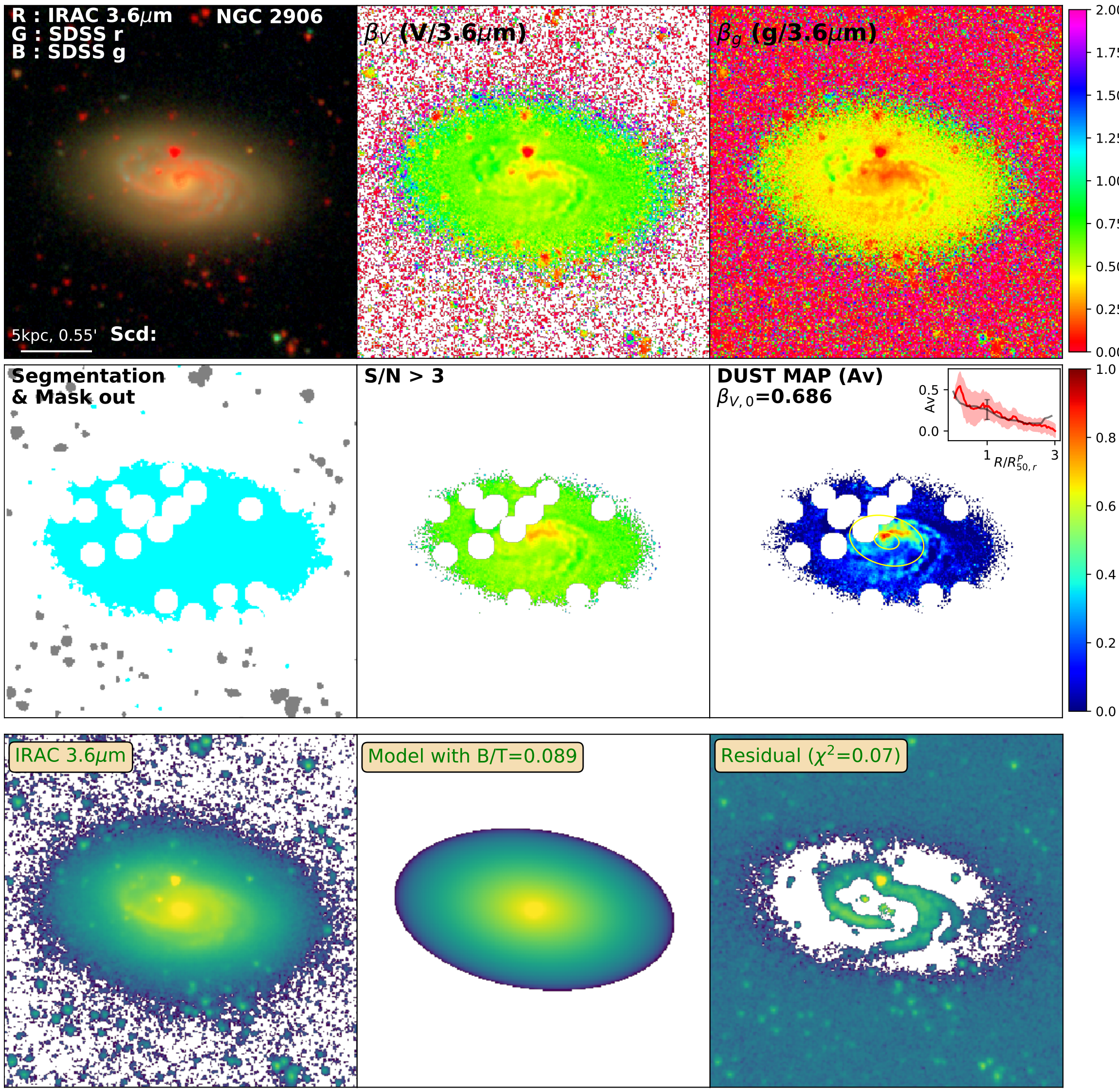

Figure D.61: Same as Figure 3.2 for NGC2906

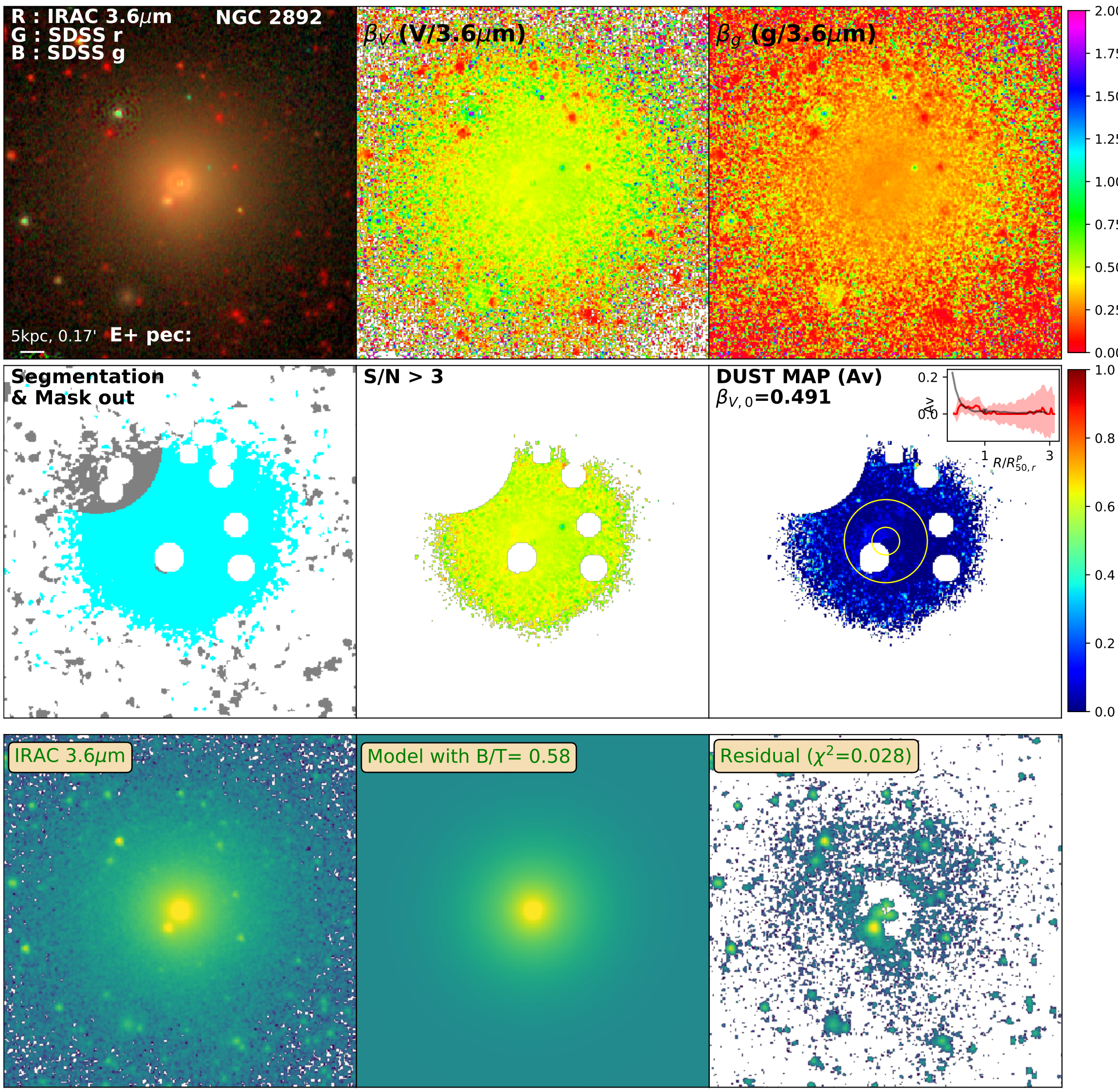

Figure D.62: Same as Figure 3.2 for NGC2892

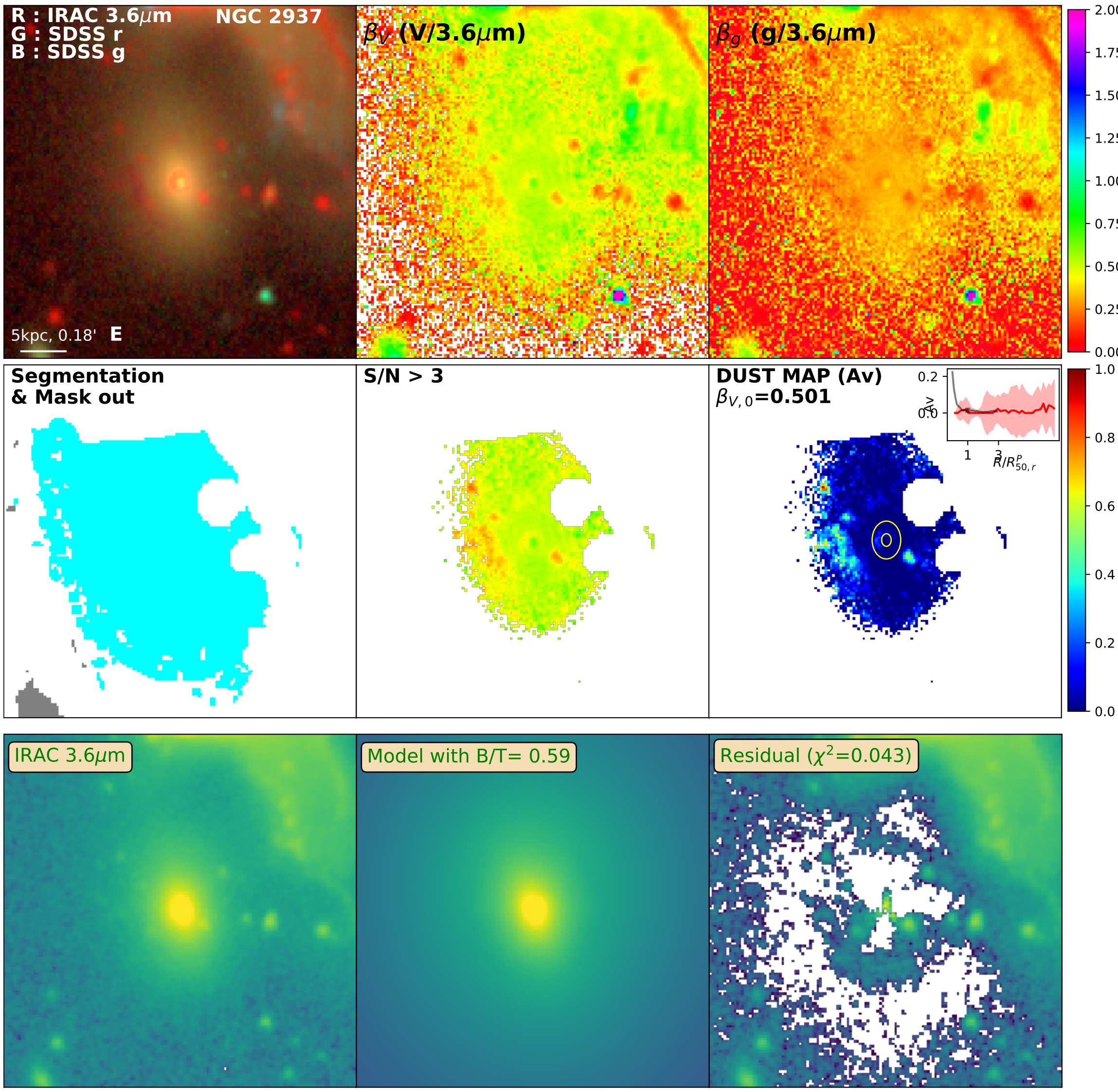

Figure D.63: Same as Figure 3.2 for NGC2937

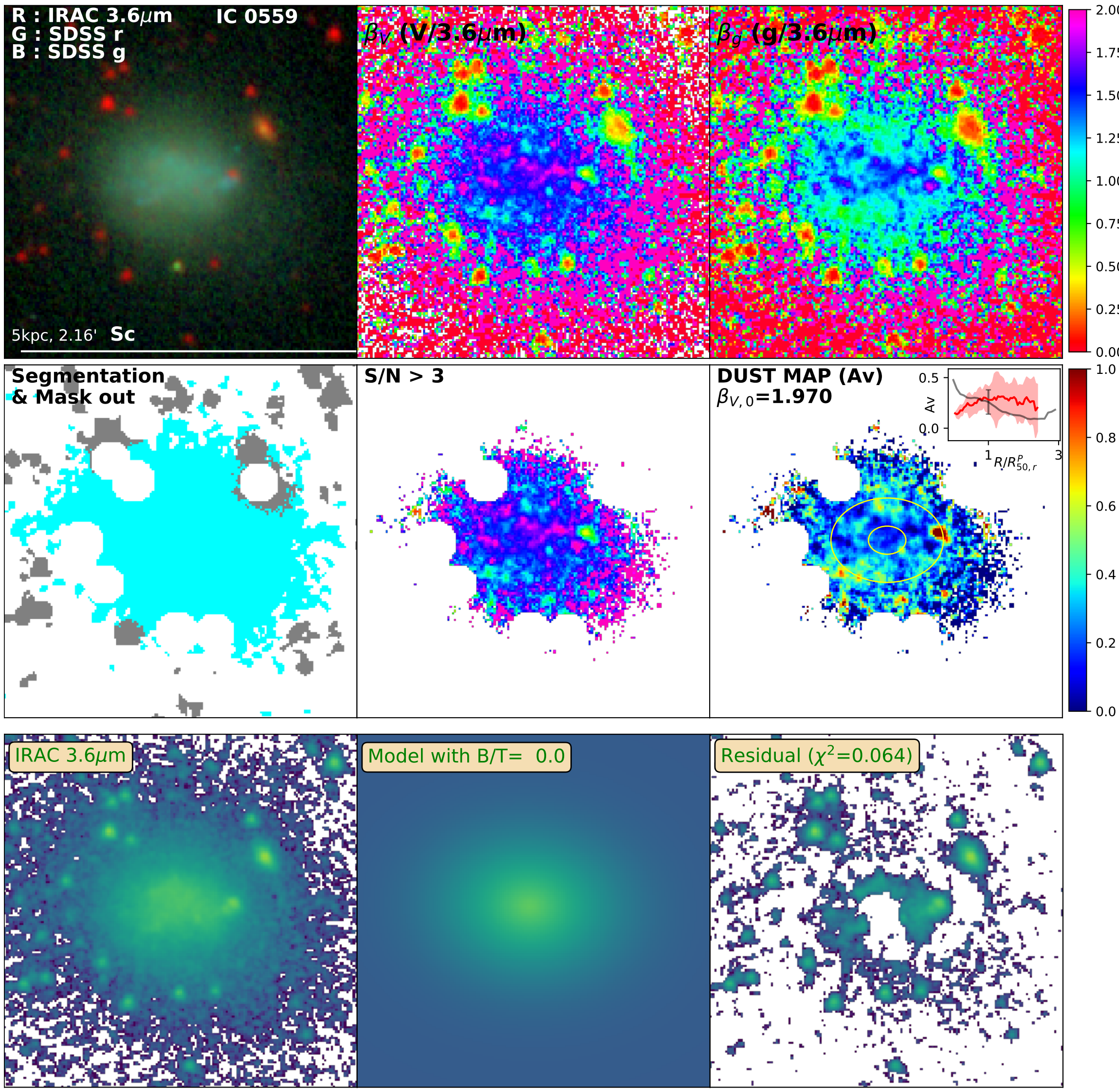

Figure D.64: Same as Figure 3.2 for IC0559

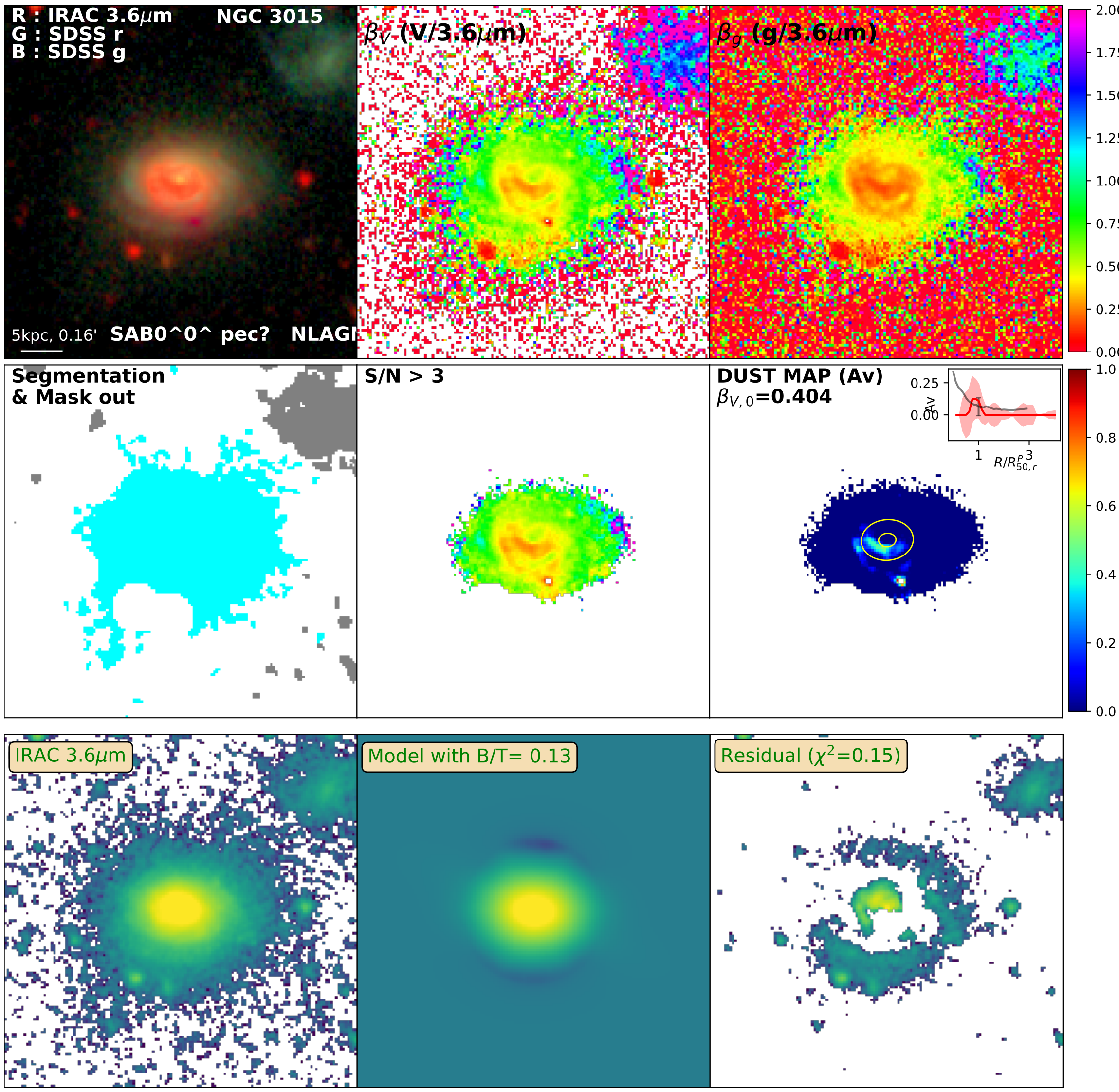

Figure D.65: Same as Figure 3.2 for NGC3015

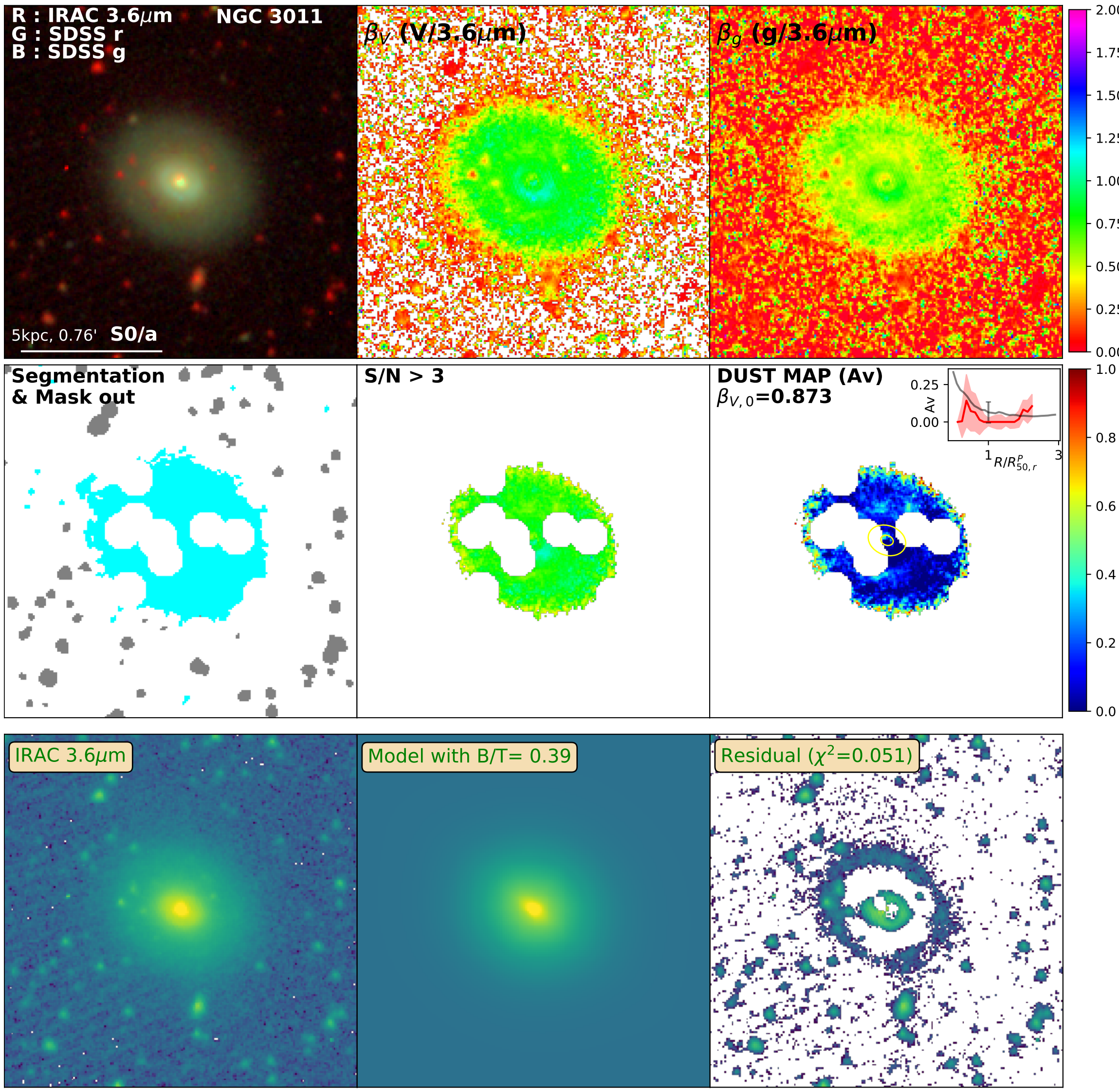

Figure D.66: Same as Figure 3.2 for NGC3011

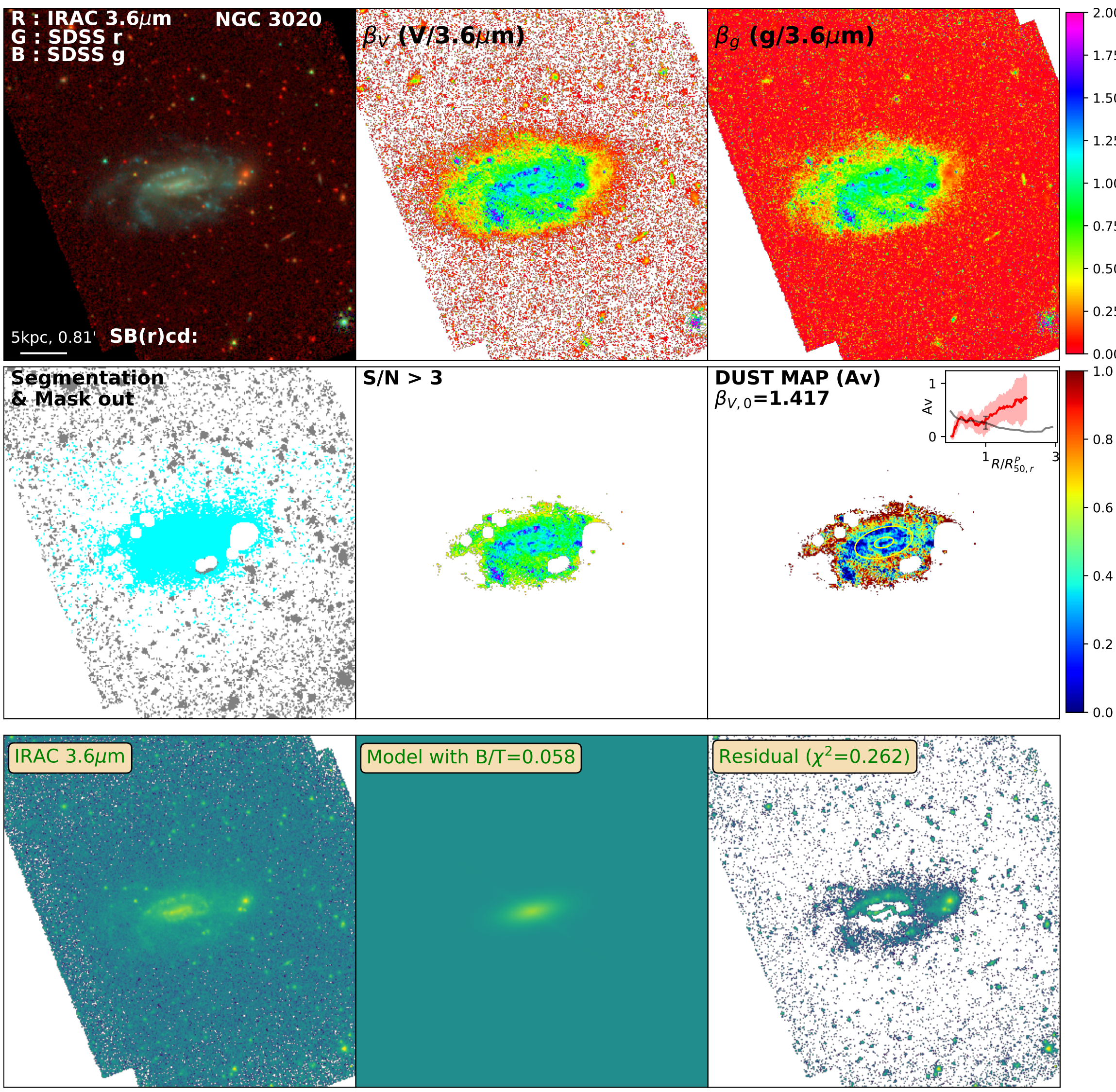

Figure D.67: Same as Figure 3.2 for NGC3020

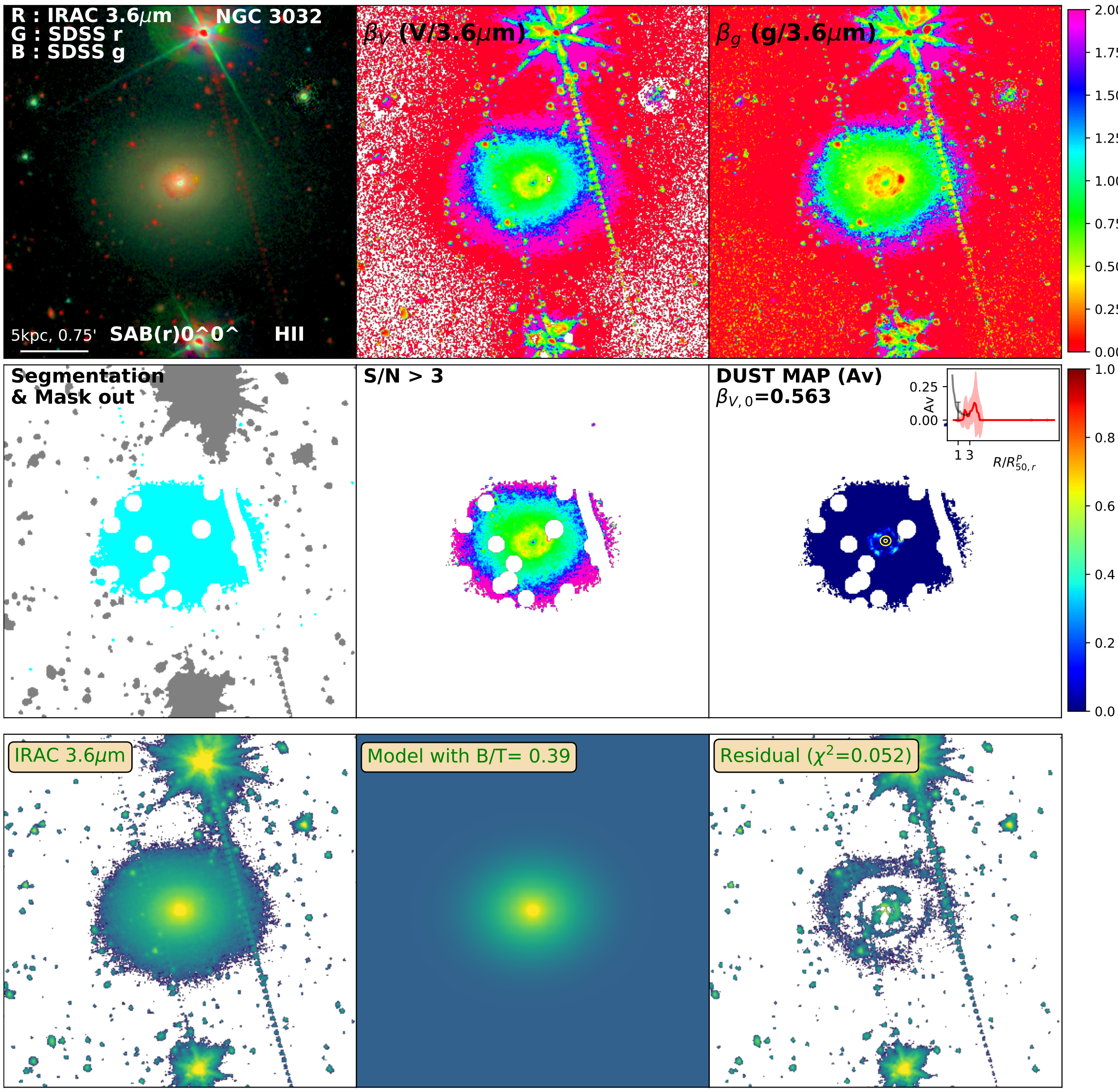

Figure D.68: Same as Figure 3.2 for NGC3032

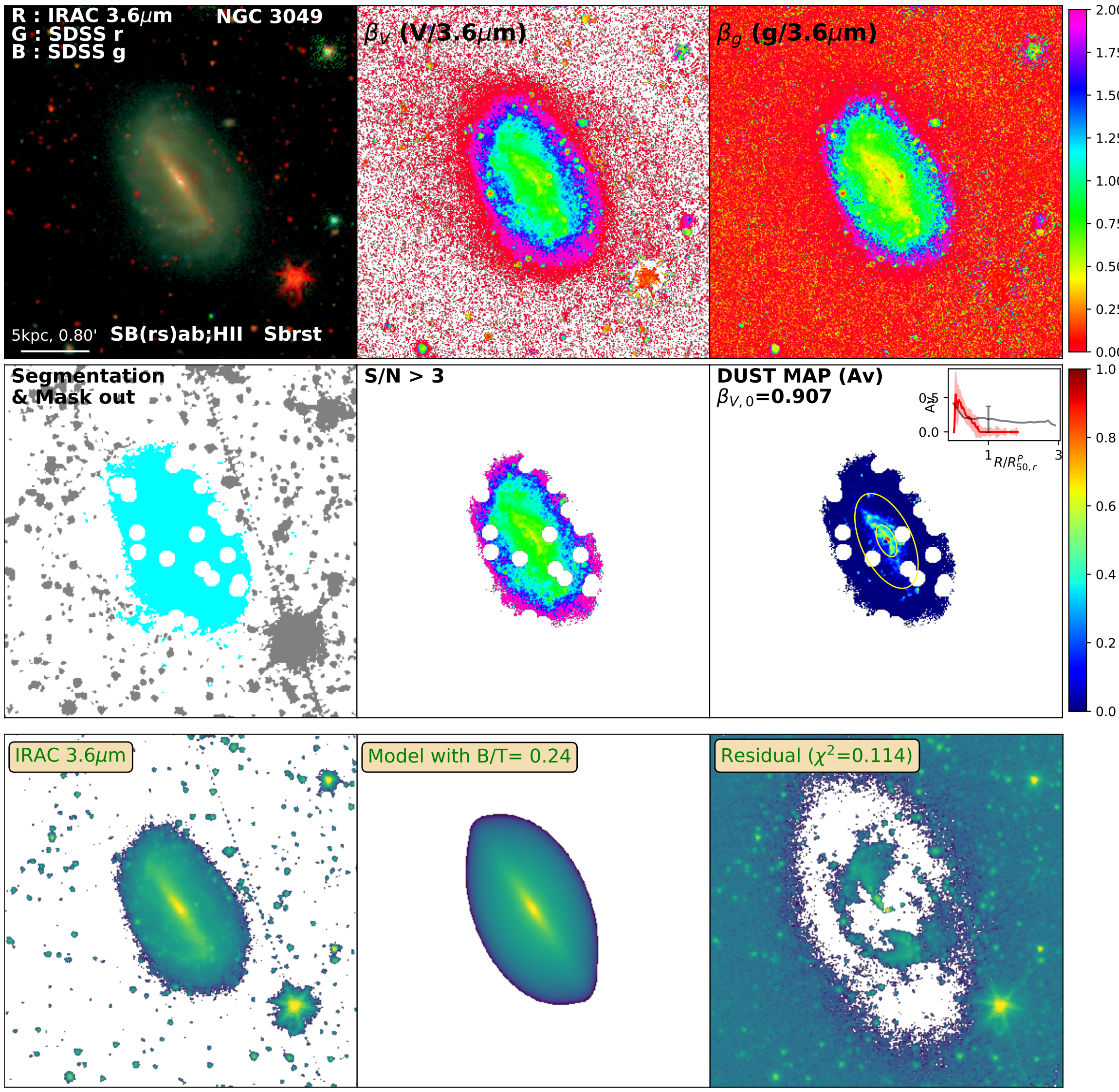

Figure D.69: Same as Figure 3.2 for NGC3049

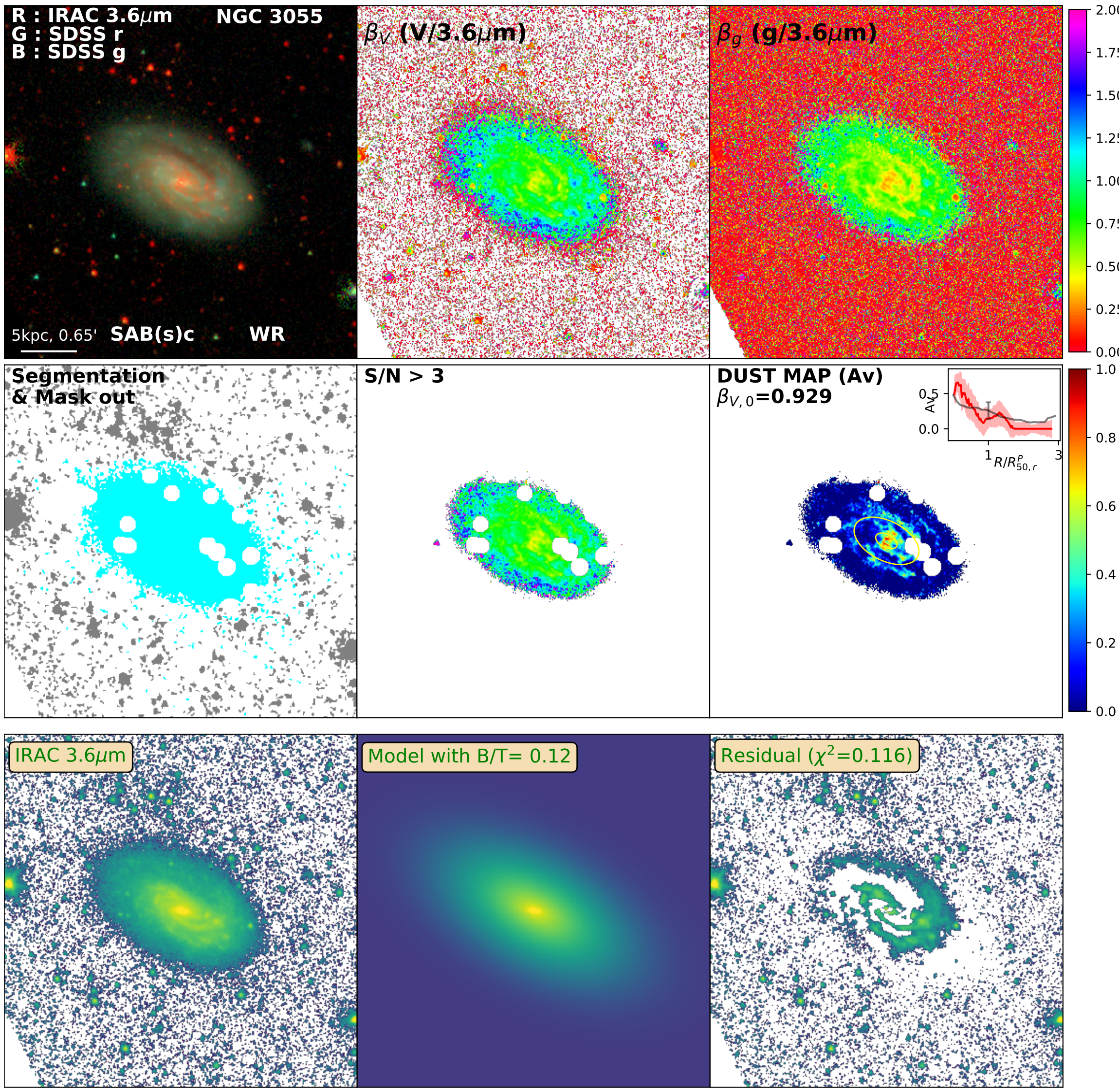

Figure D.70: Same as Figure 3.2 for NGC3055

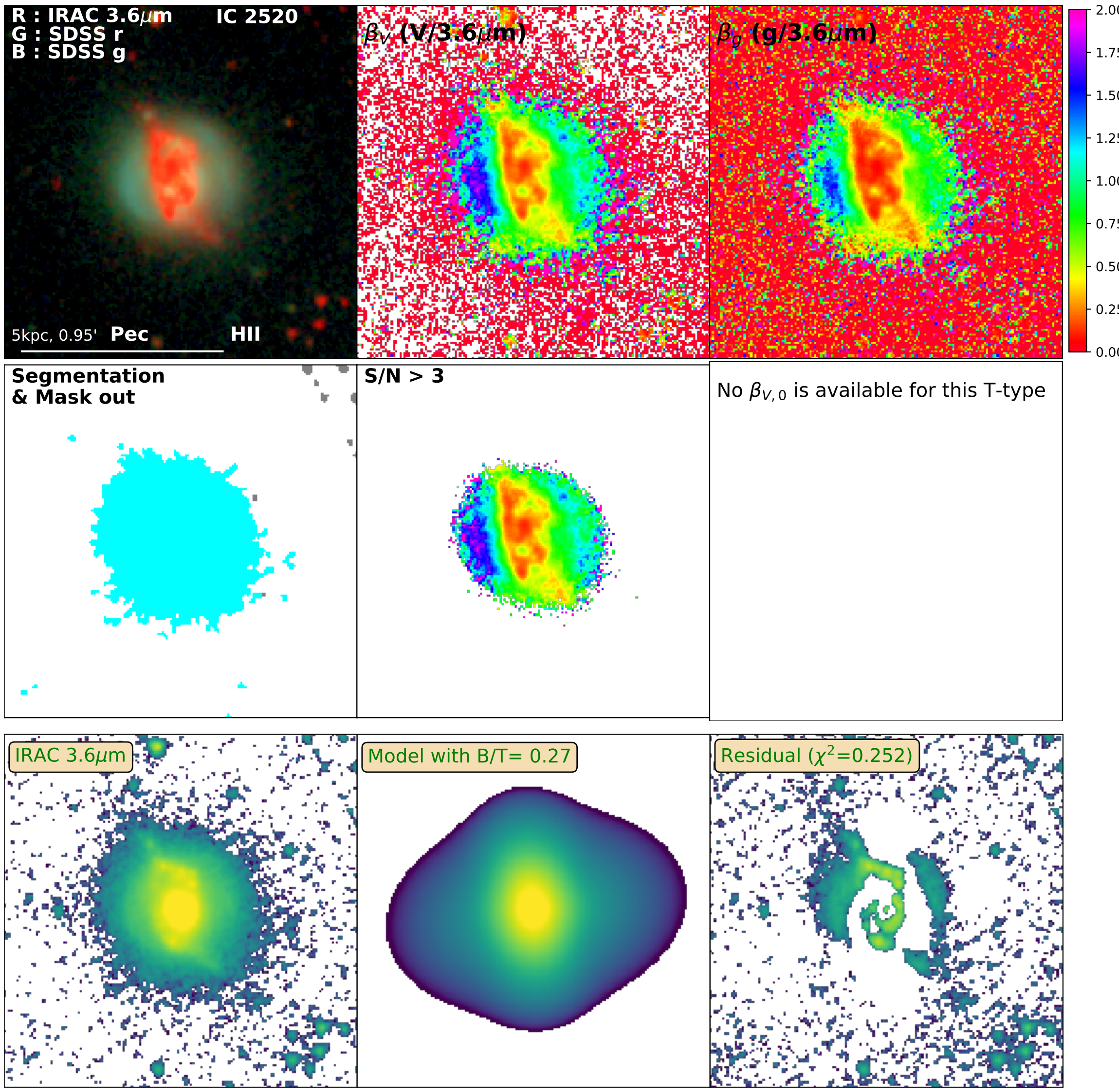

Figure D.71: Same as Figure 3.2 for IC2520

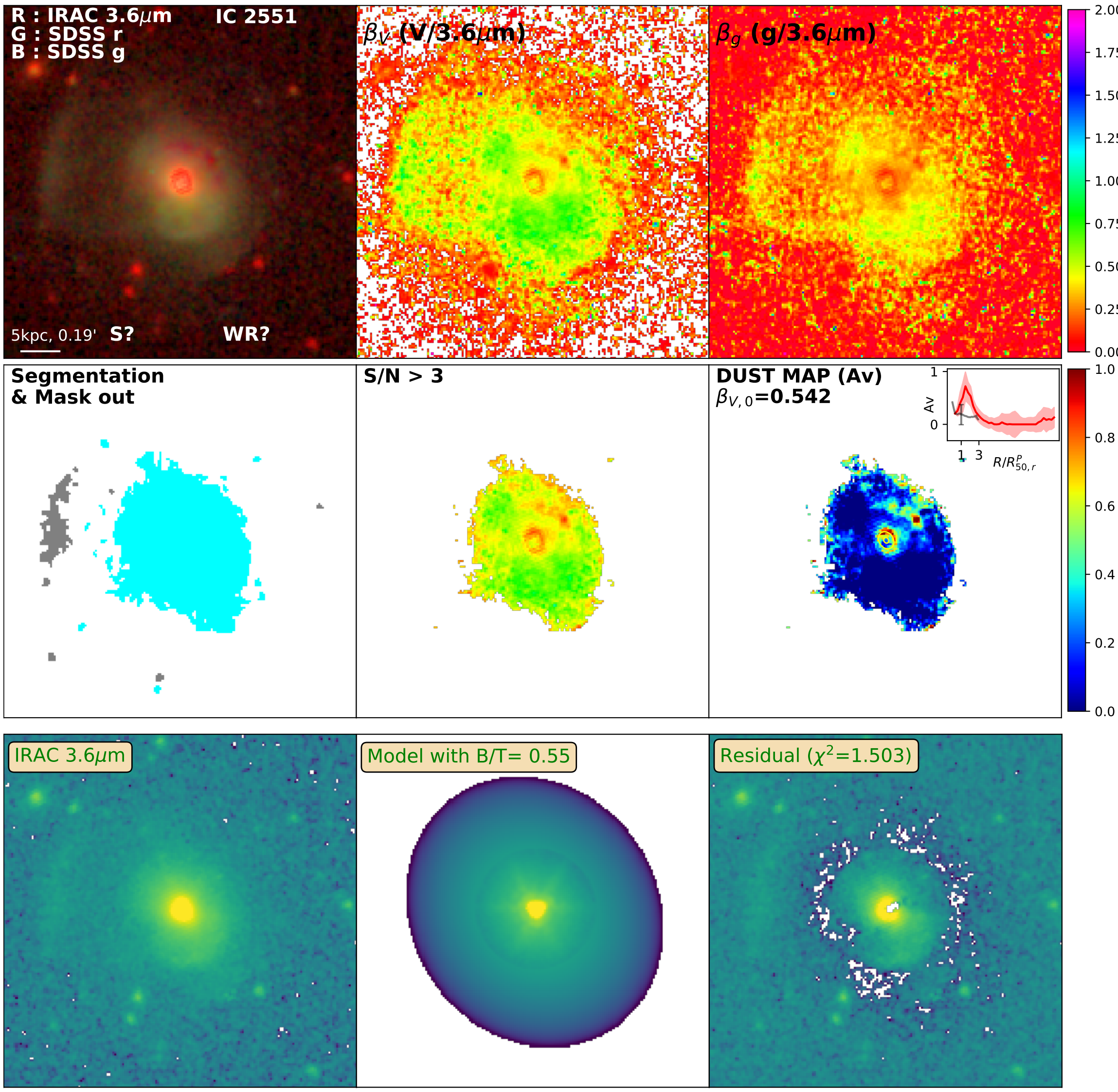

Figure D.72: Same as Figure 3.2 for IC2551

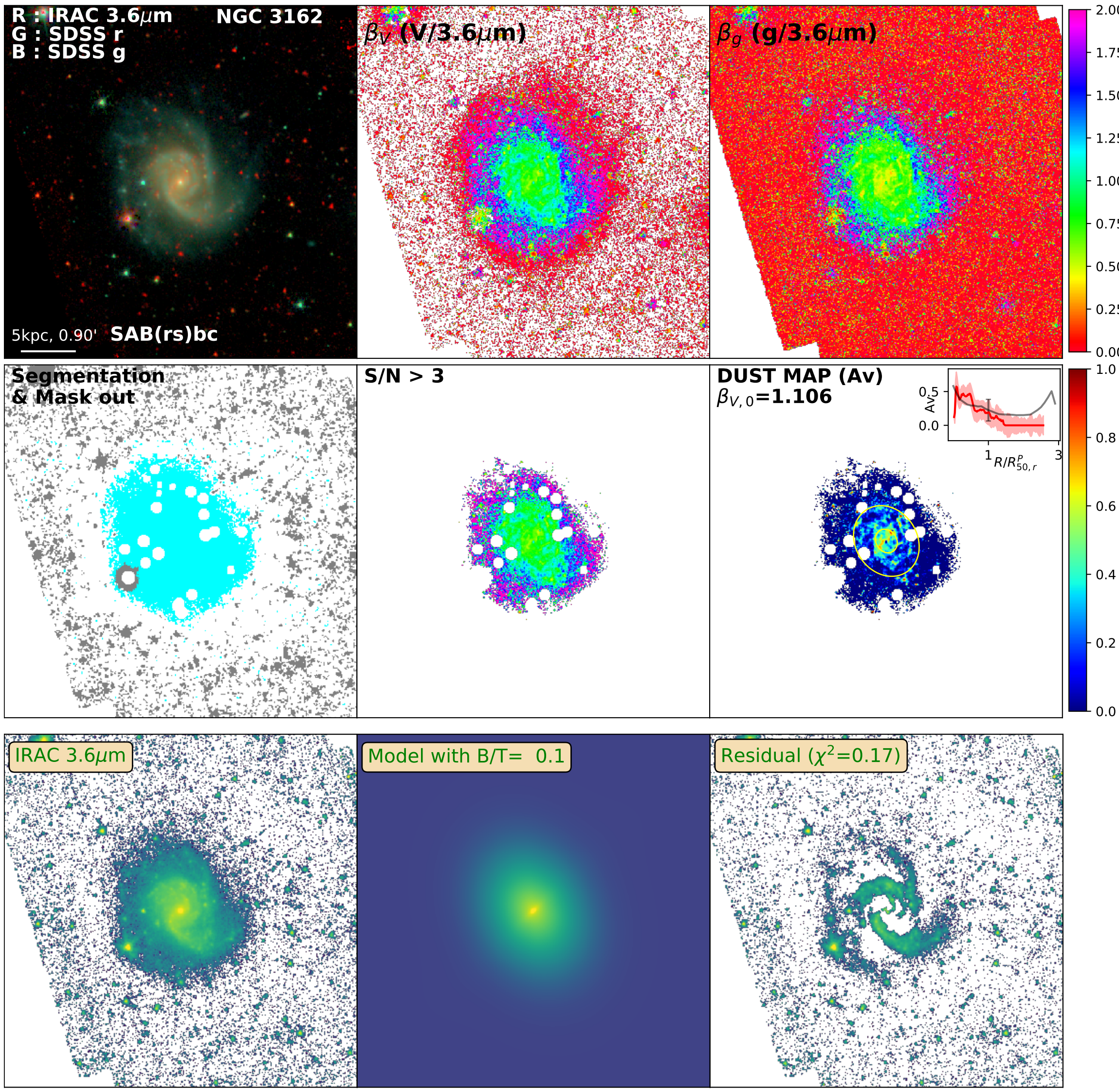

Figure D.73: Same as Figure 3.2 for NGC3162

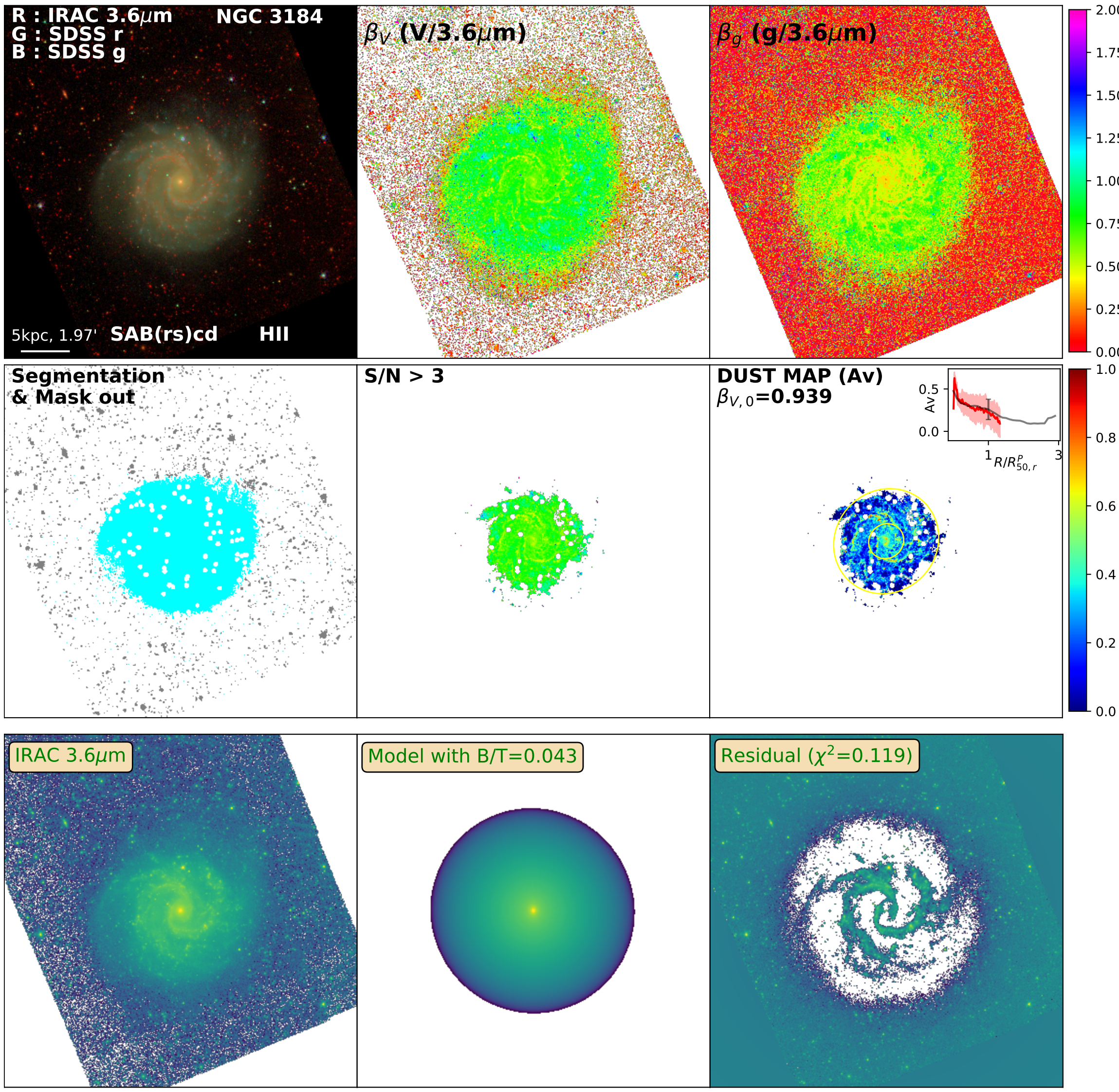

Figure D.74: Same as Figure 3.2 for NGC3184

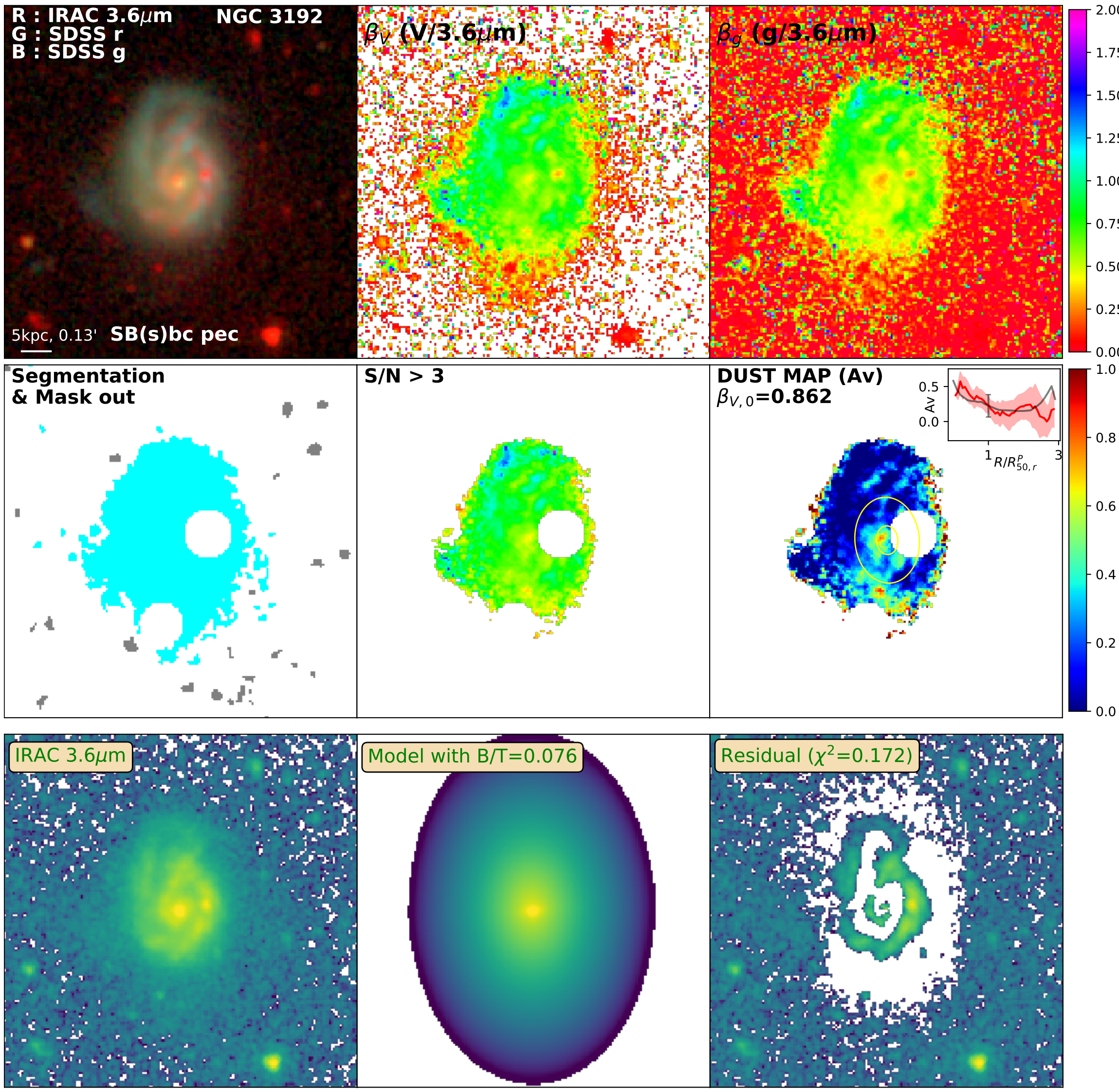

Figure D.75: Same as Figure 3.2 for NGC3192

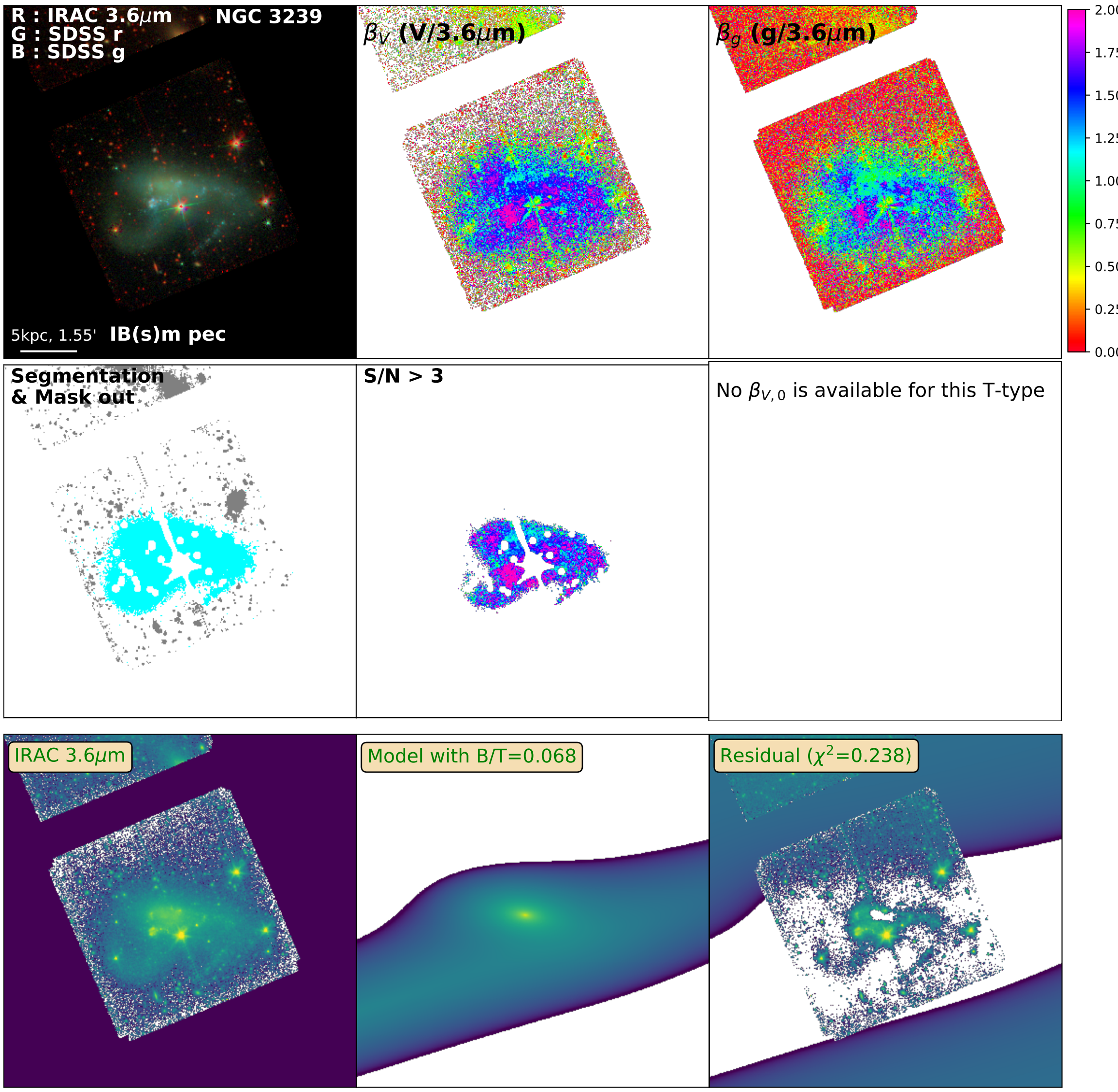

Figure D.76: Same as Figure 3.2 for NGC3239

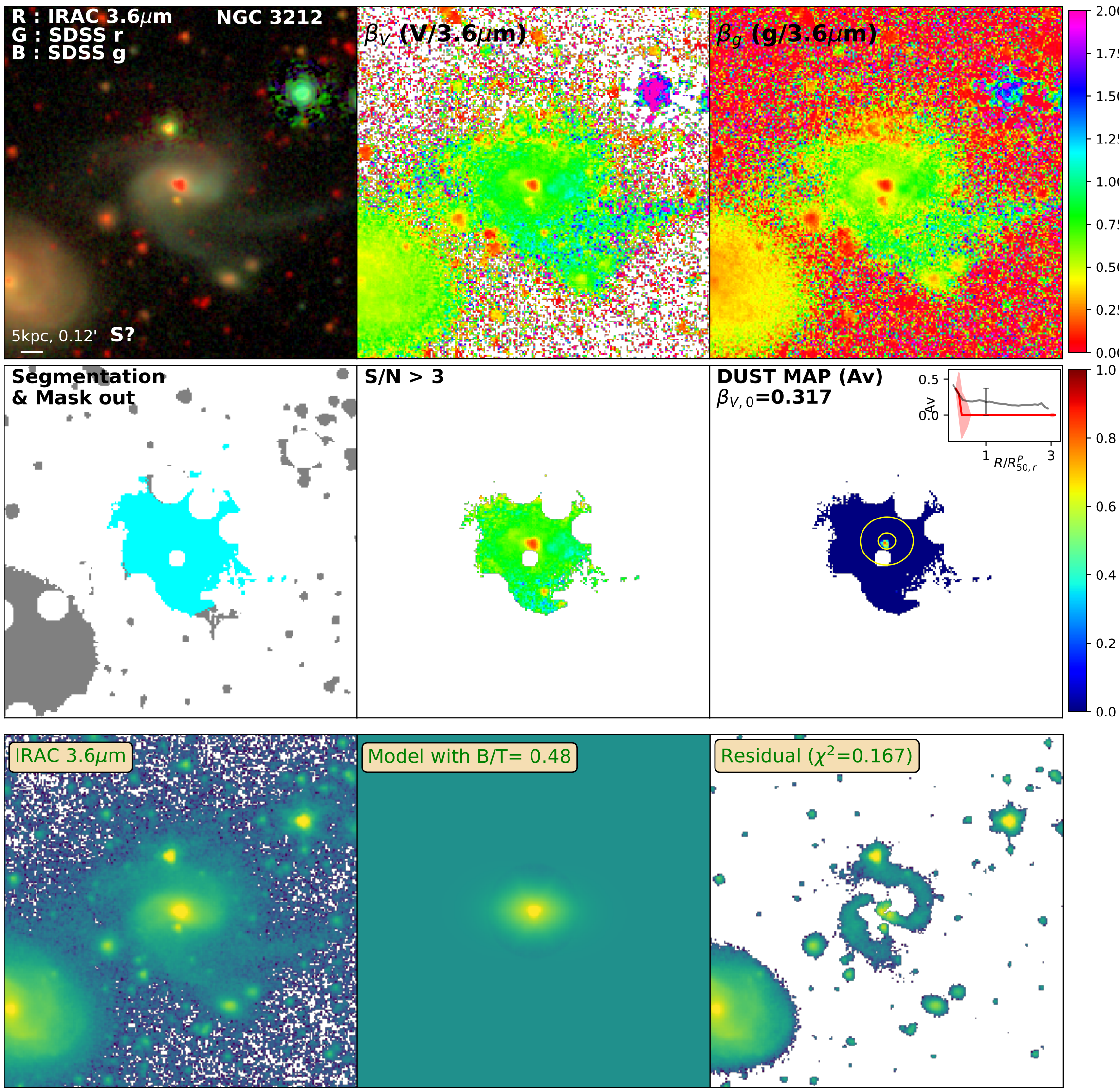

Figure D.77: Same as Figure 3.2 for NGC3212

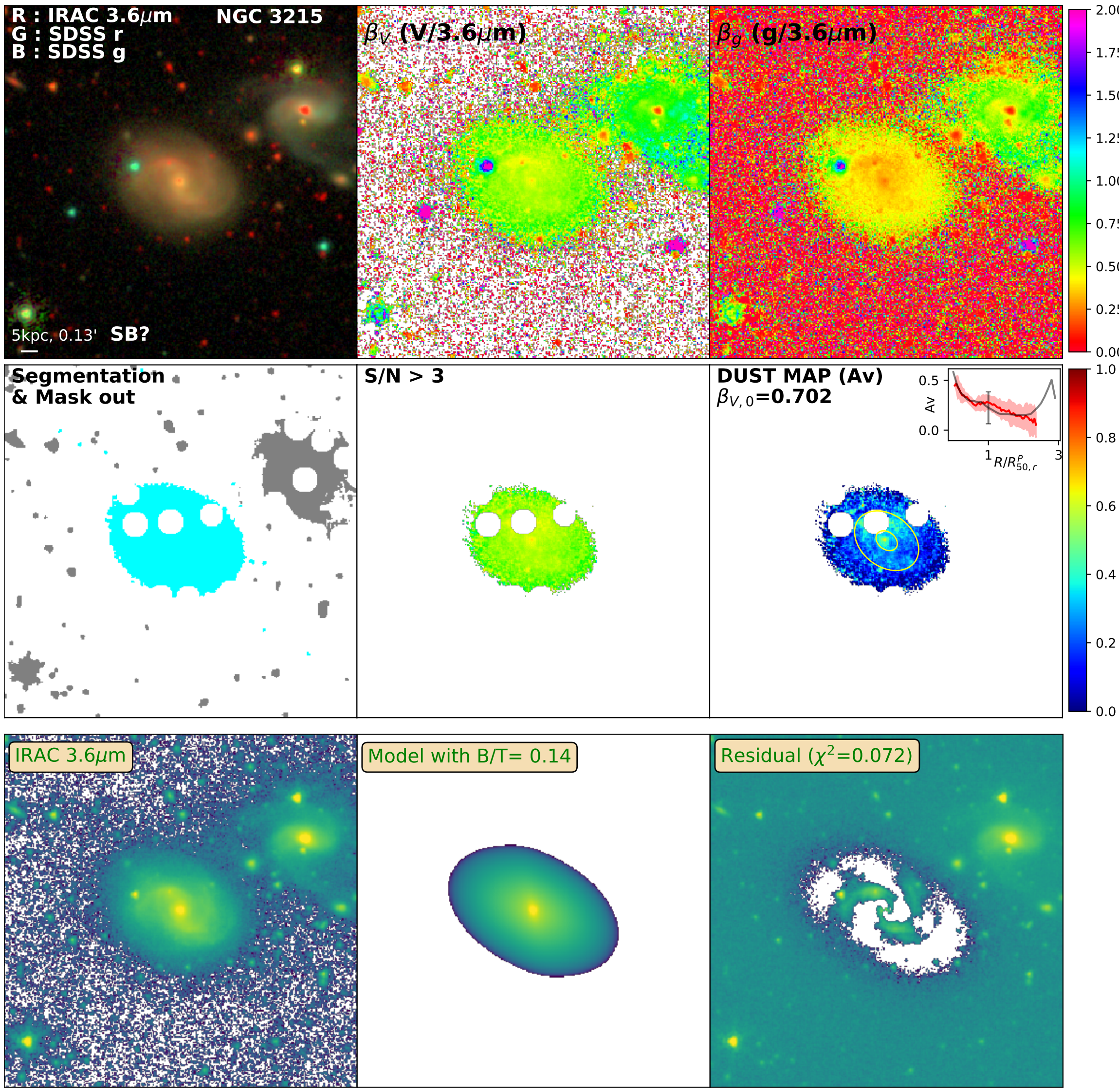

Figure D.78: Same as Figure 3.2 for NGC3215

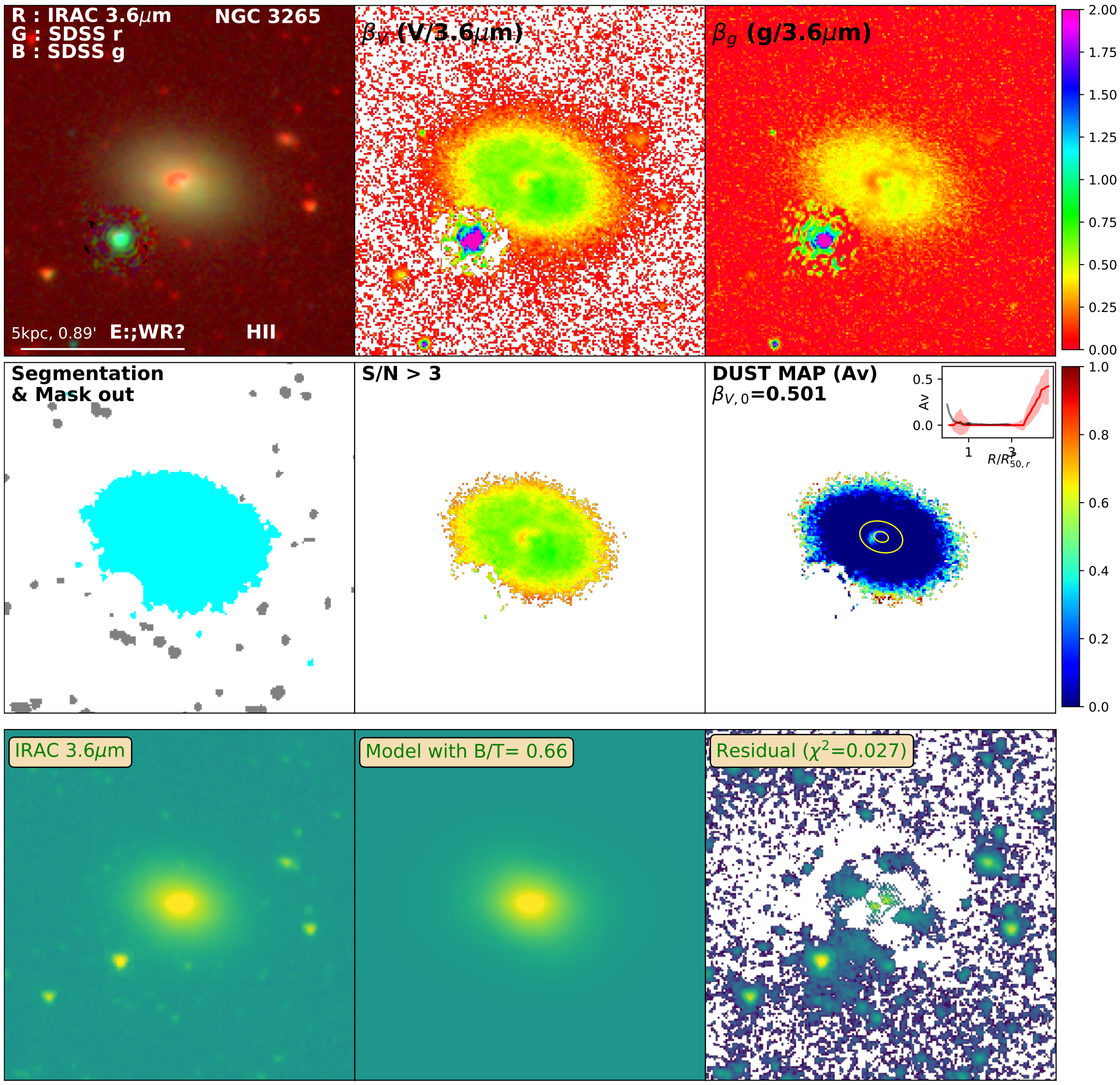

Figure D.79: Same as Figure 3.2 for NGC3265

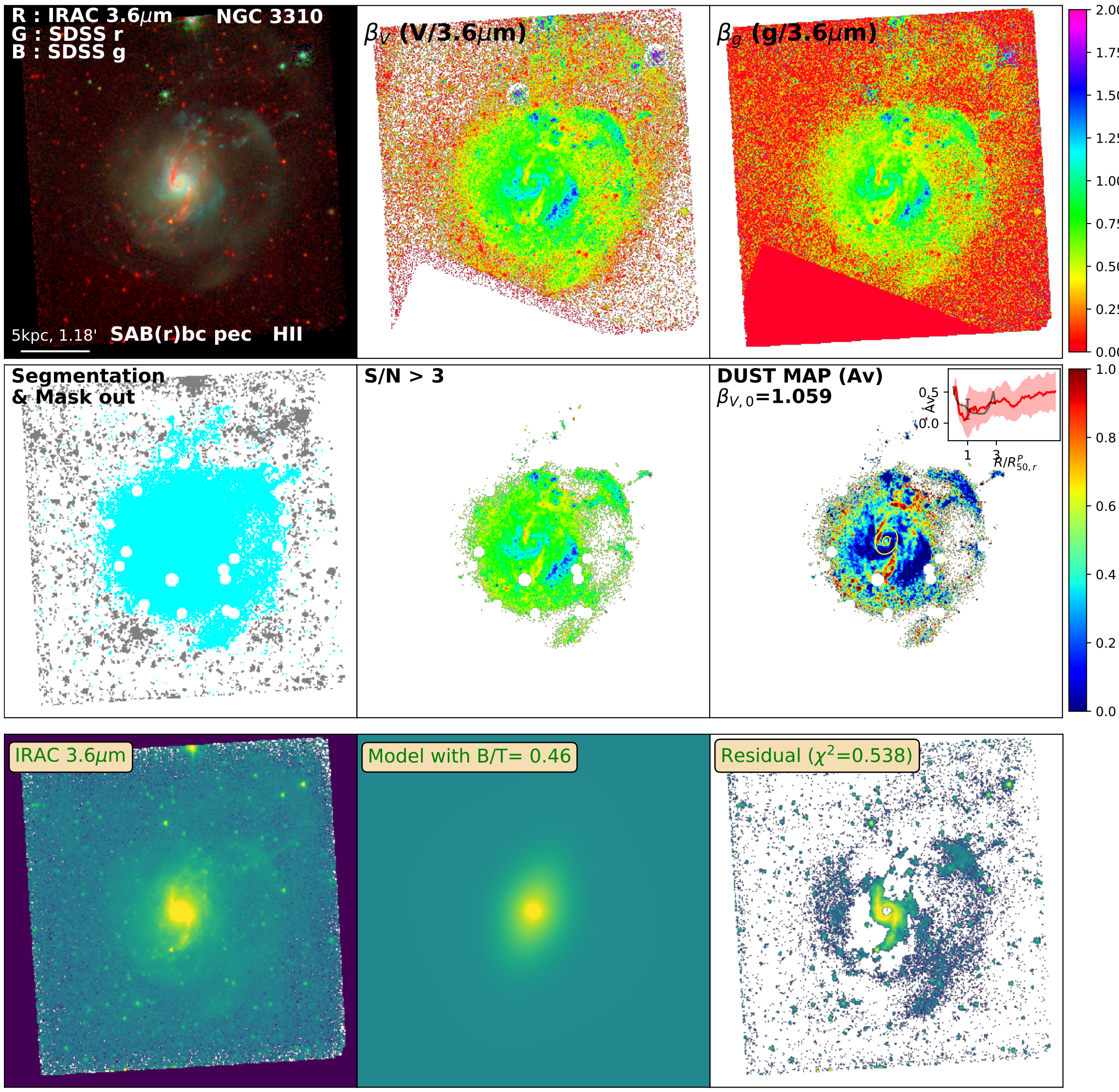

Figure D.80: Same as Figure 3.2 for NGC3310

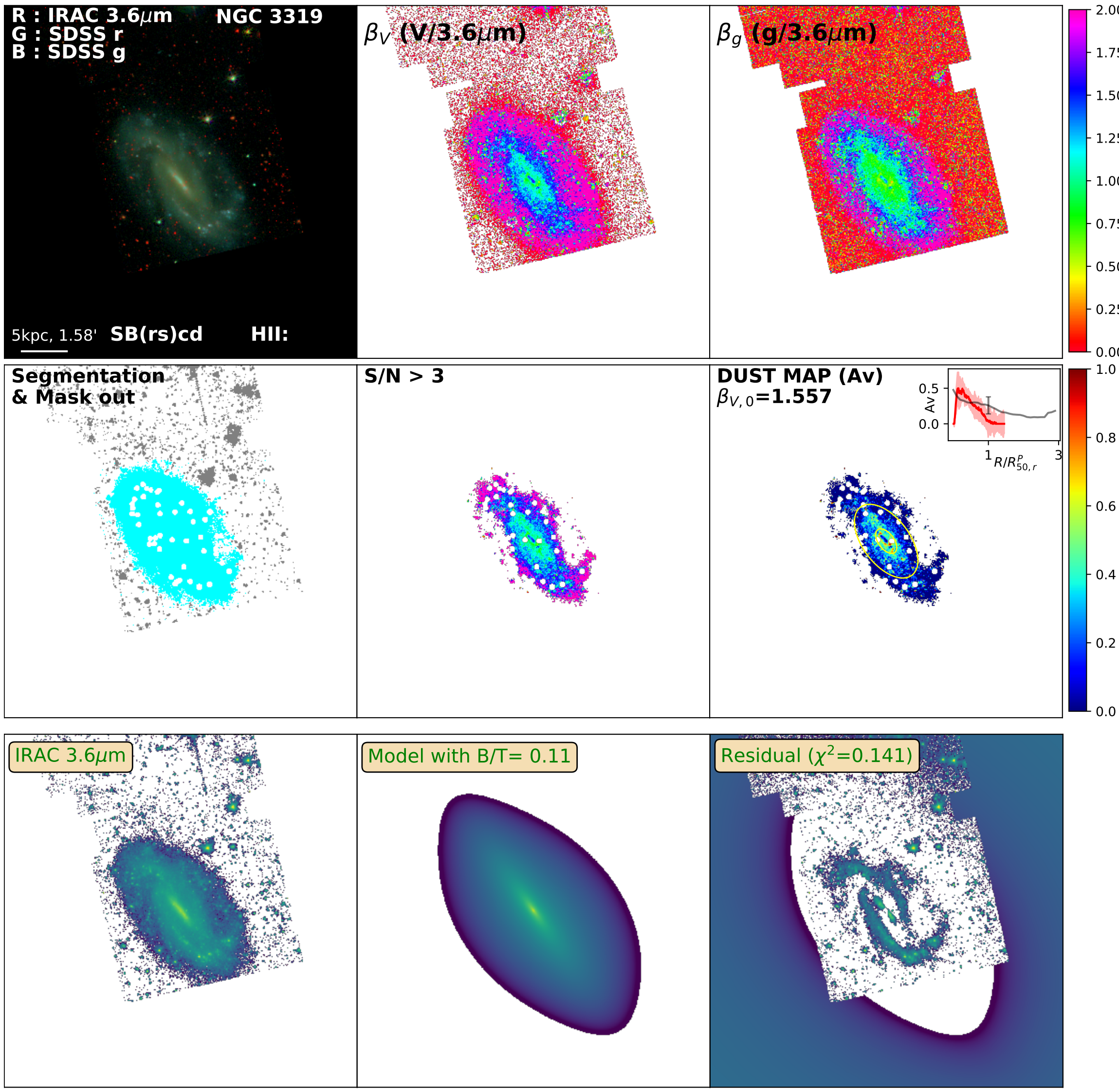

Figure D.81: Same as Figure 3.2 for NGC3319

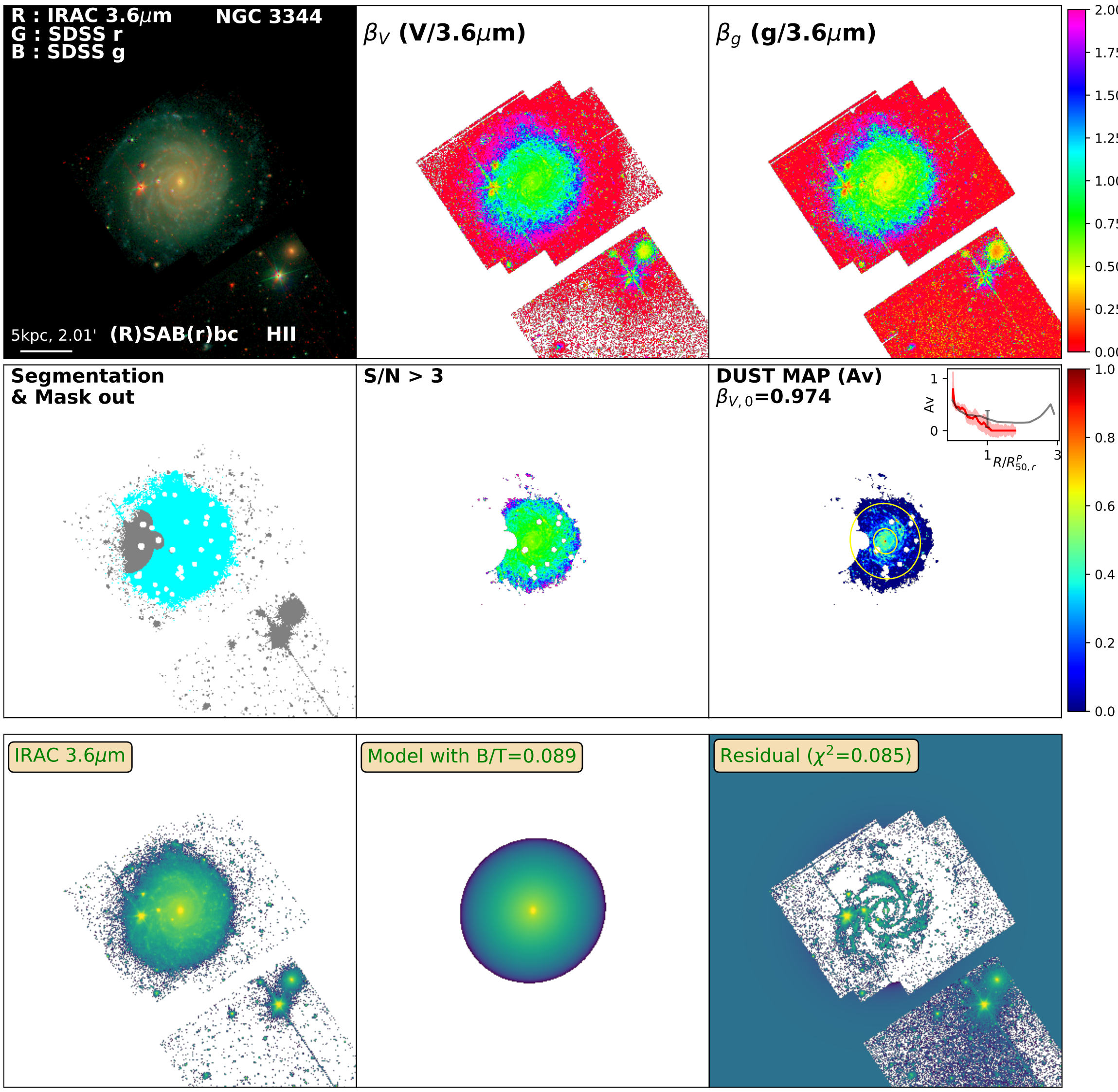

Figure D.82: Same as Figure 3.2 for NGC3344

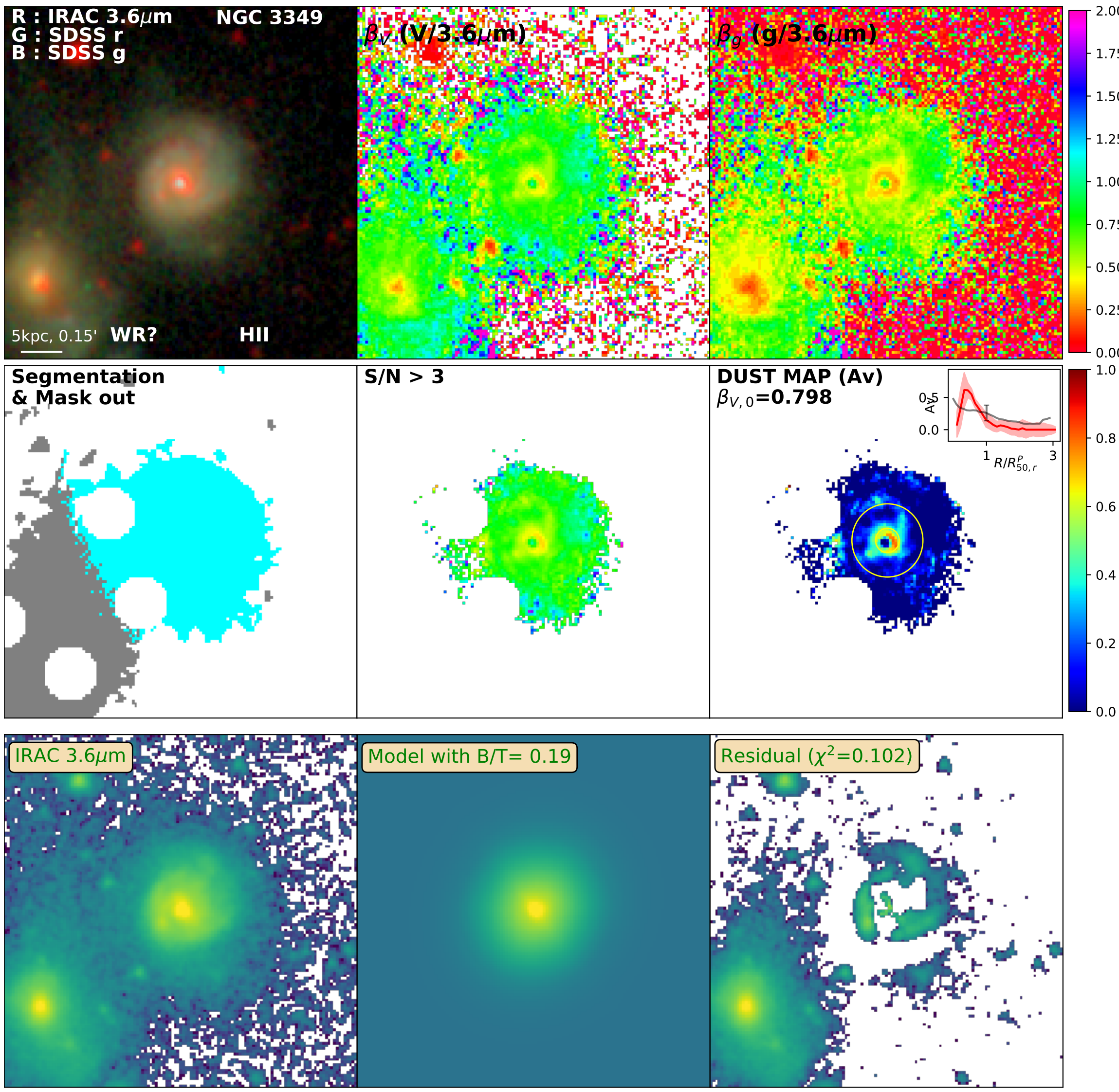

Figure D.83: Same as Figure 3.2 for NGC3349

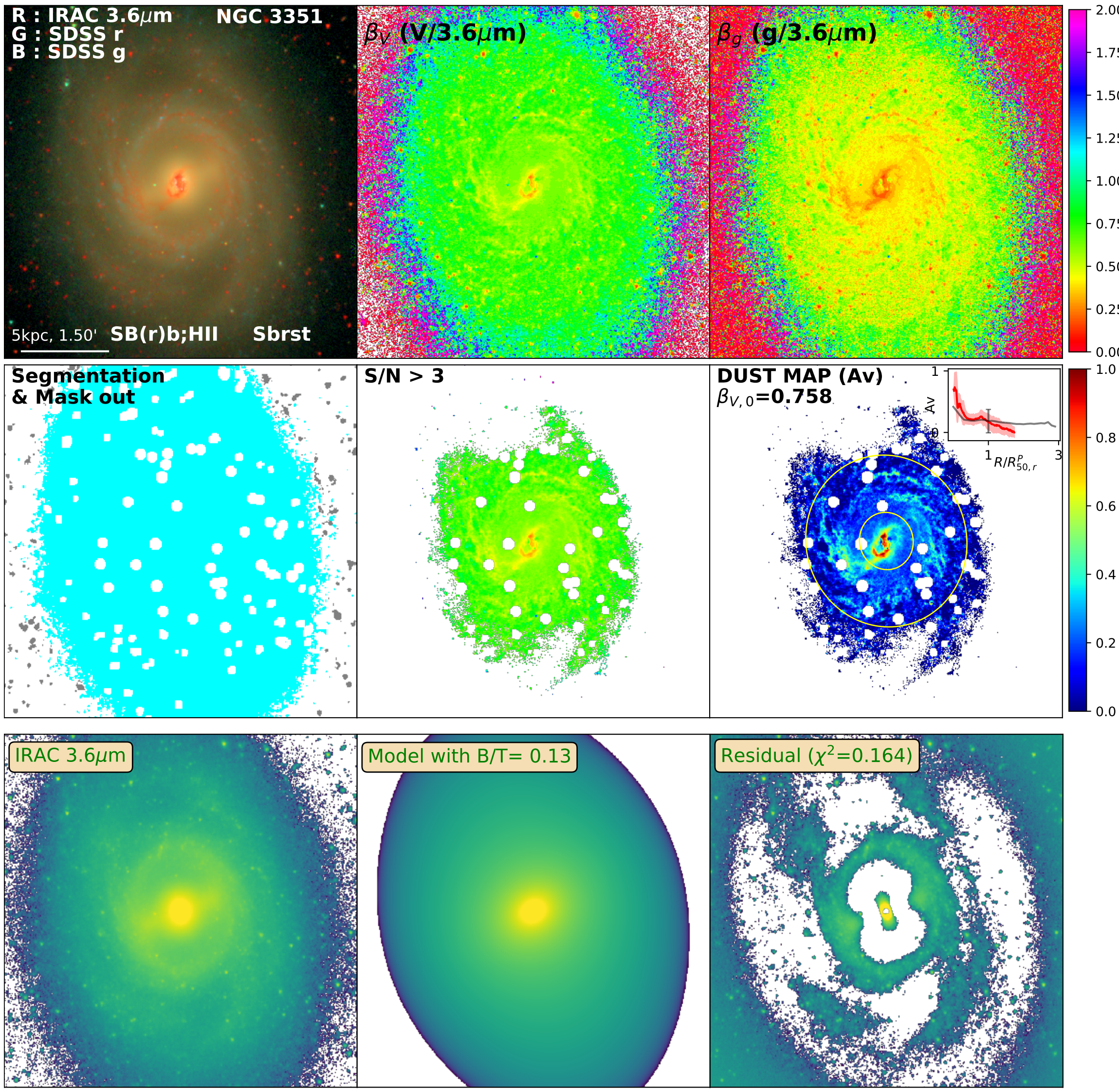

Figure D.84: Same as Figure 3.2 for NGC3351

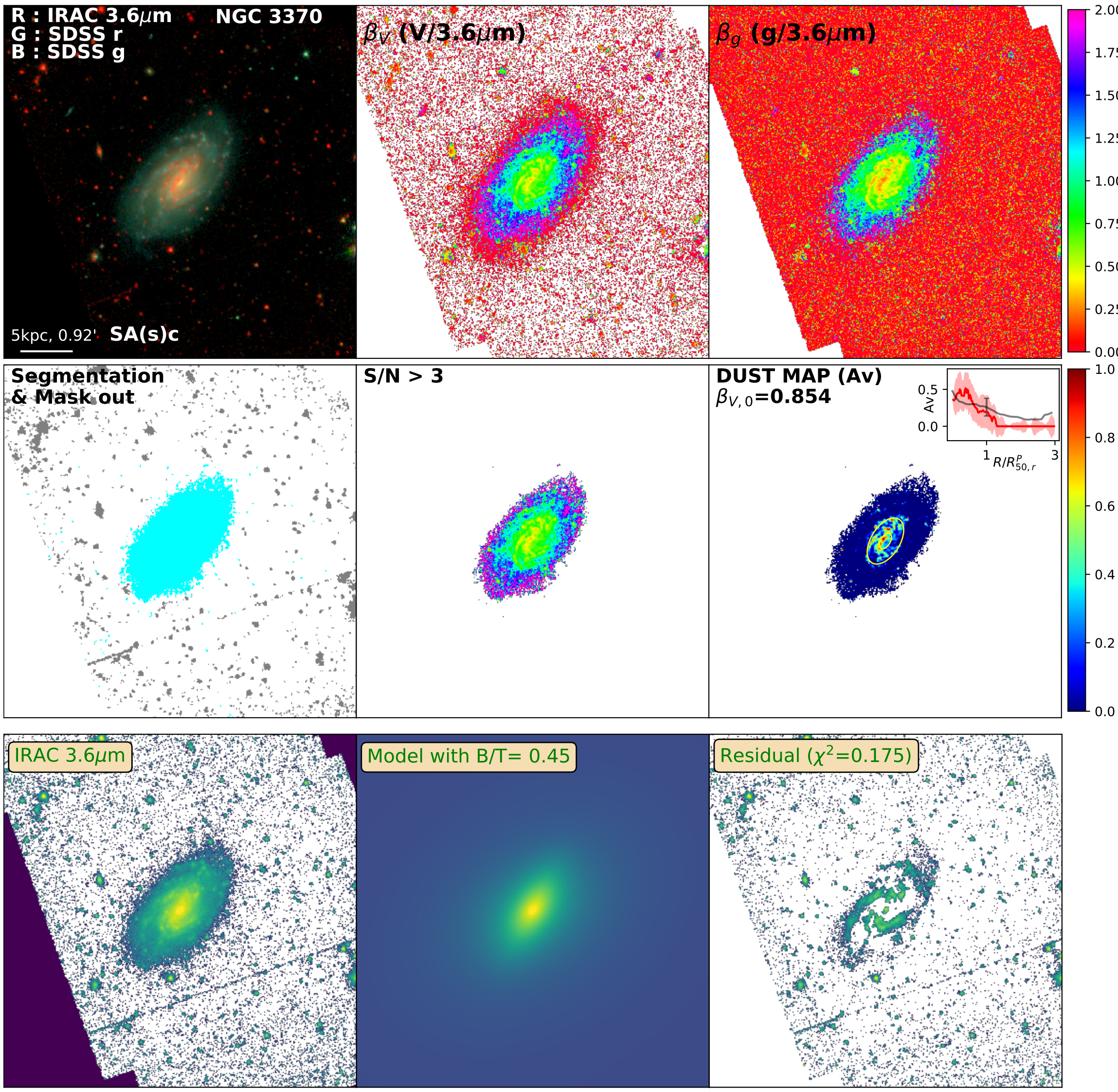

Figure D.85: Same as Figure 3.2 for NGC3370

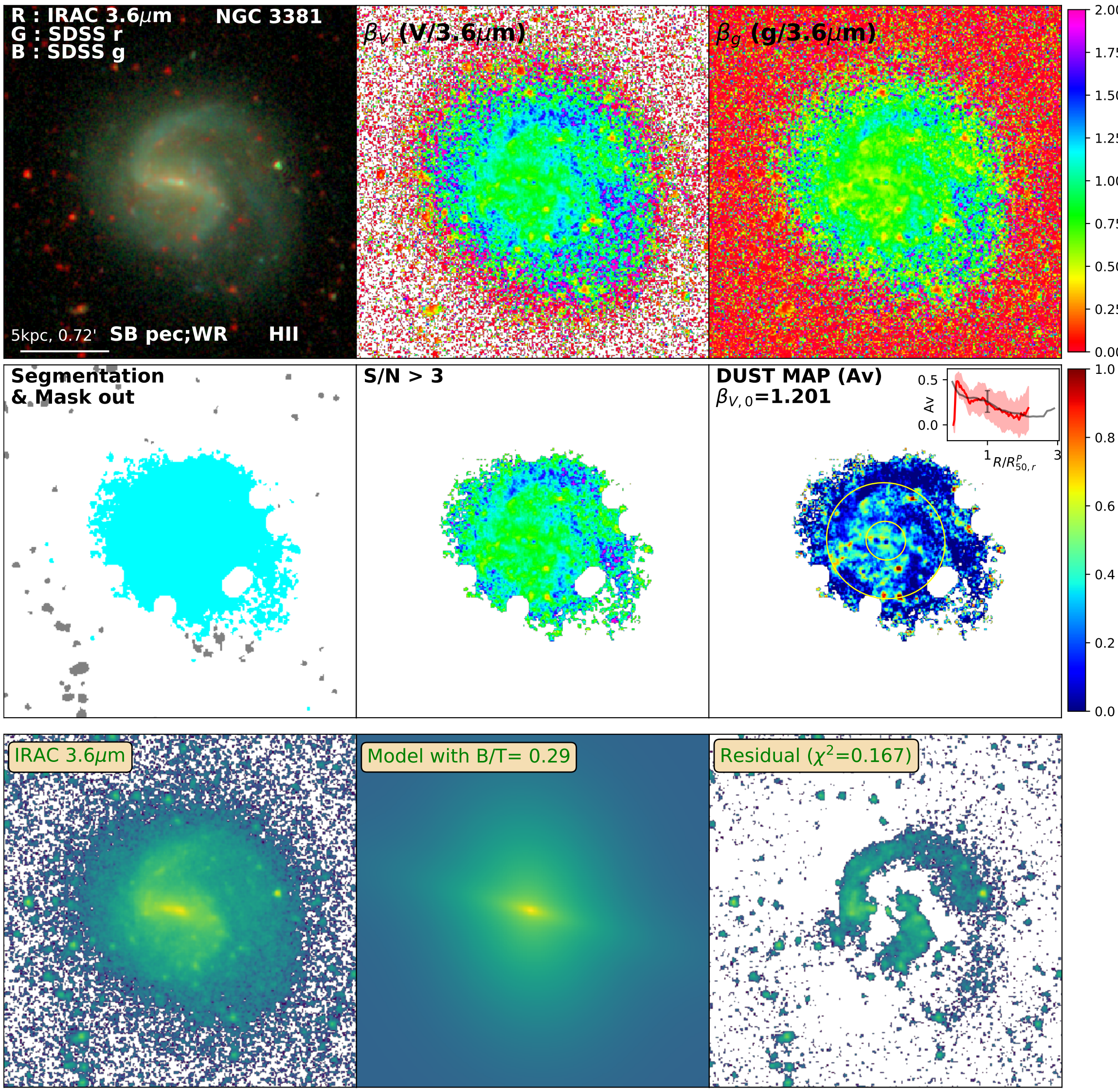

Figure D.86: Same as Figure 3.2 for NGC3381

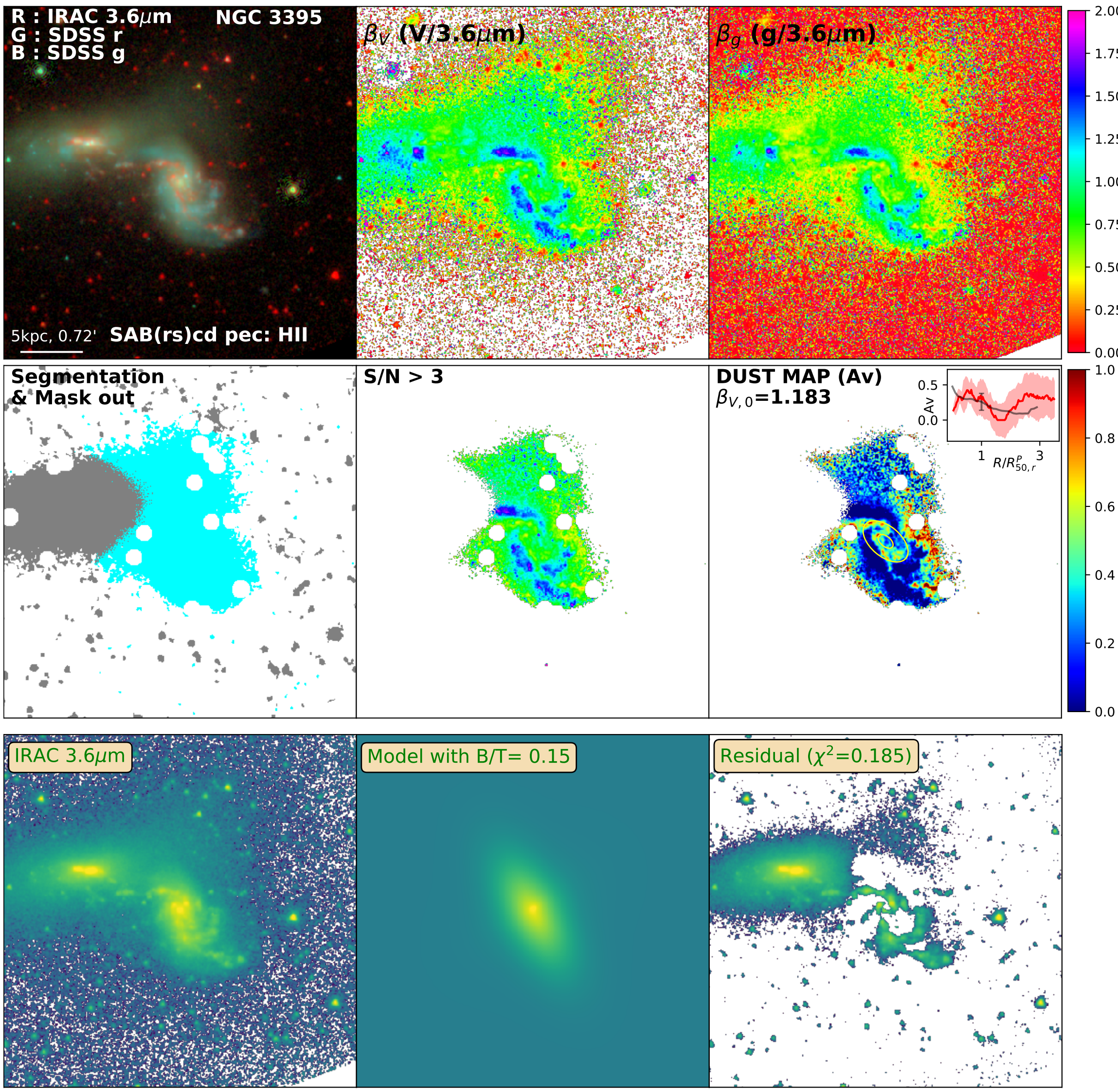

Figure D.87: Same as Figure 3.2 for NGC3395

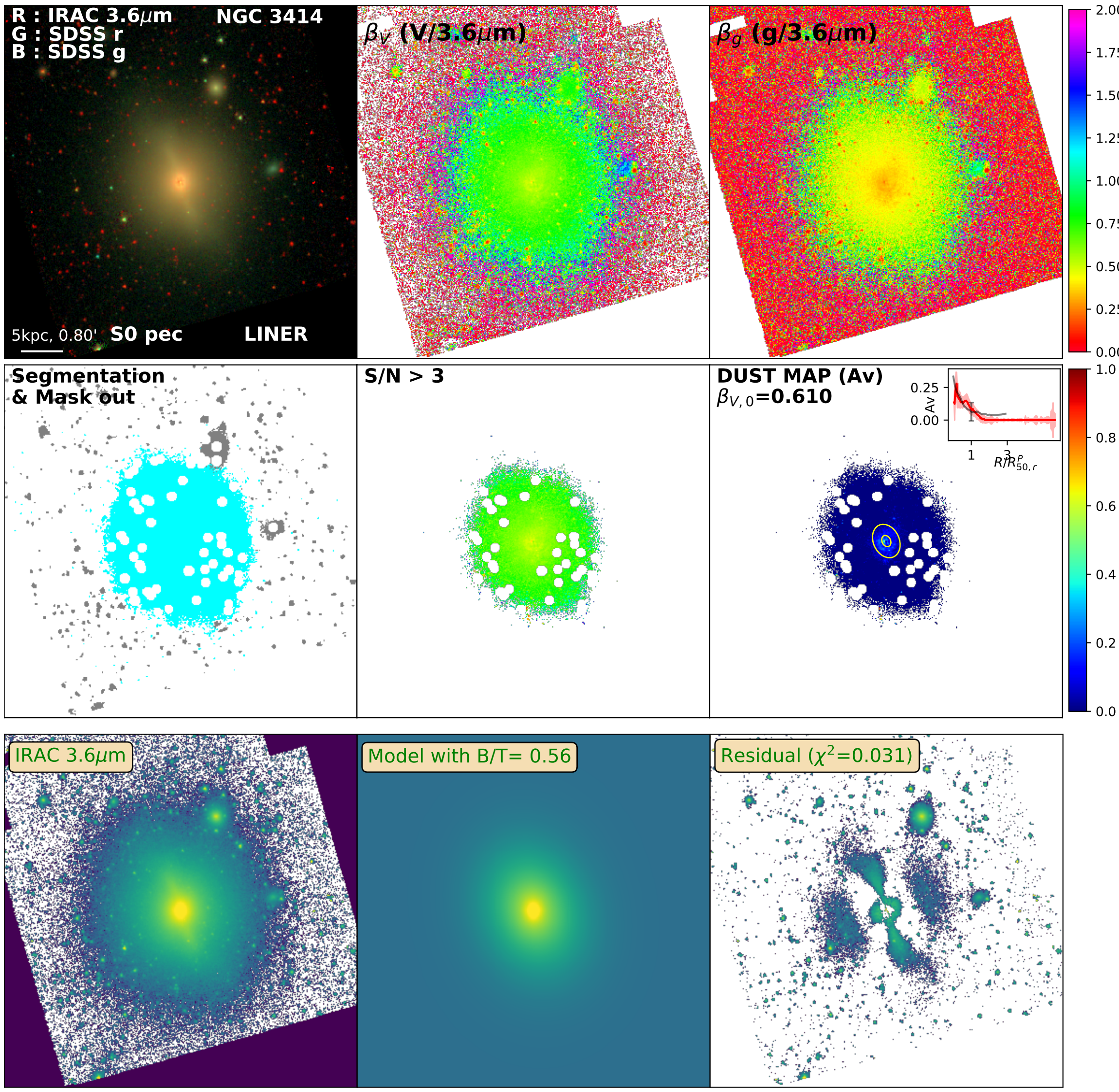

Figure D.88: Same as Figure 3.2 for NGC3414

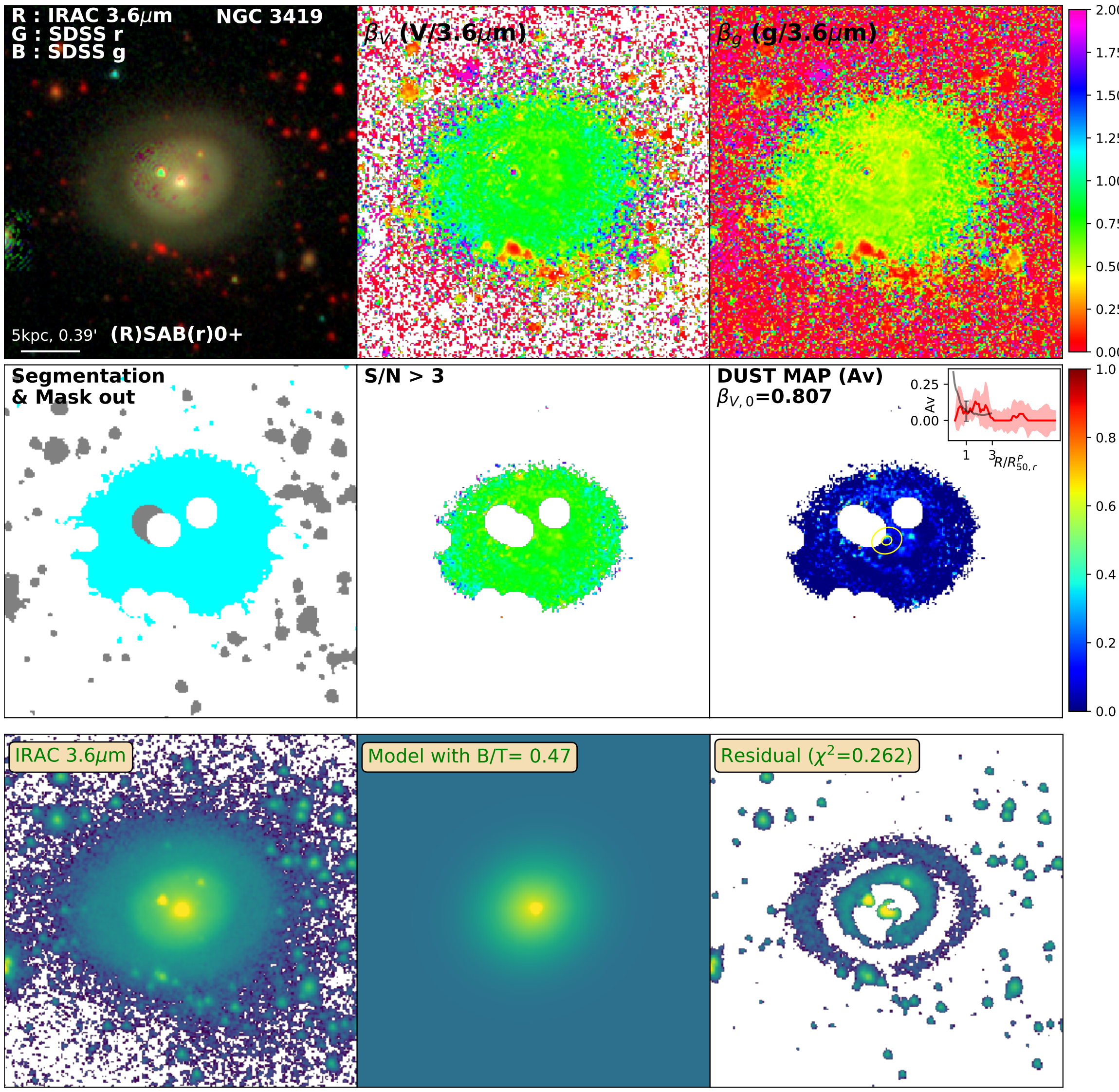

Figure D.89: Same as Figure 3.2 for NGC3419

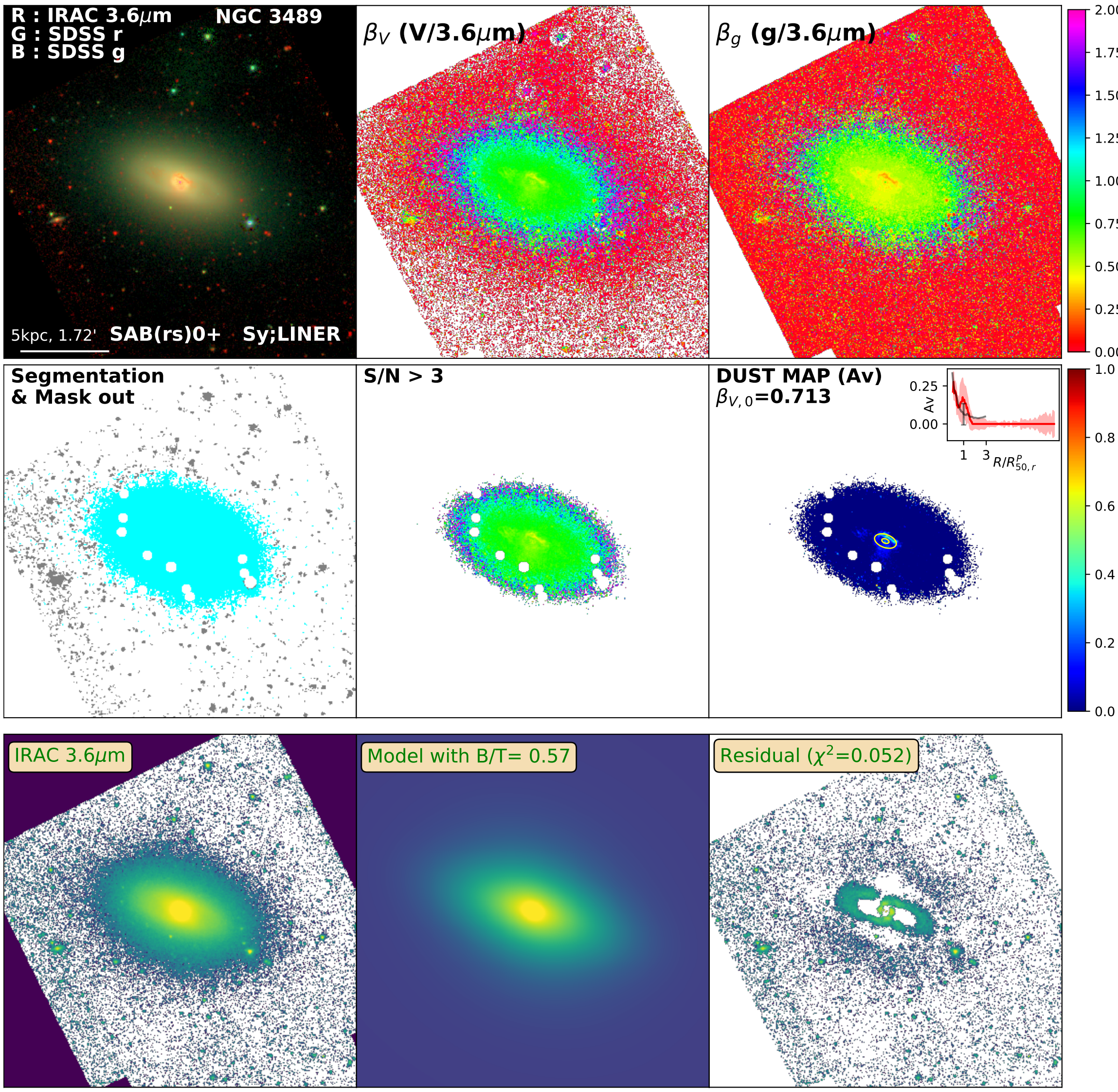

Figure D.90: Same as Figure 3.2 for NGC3489

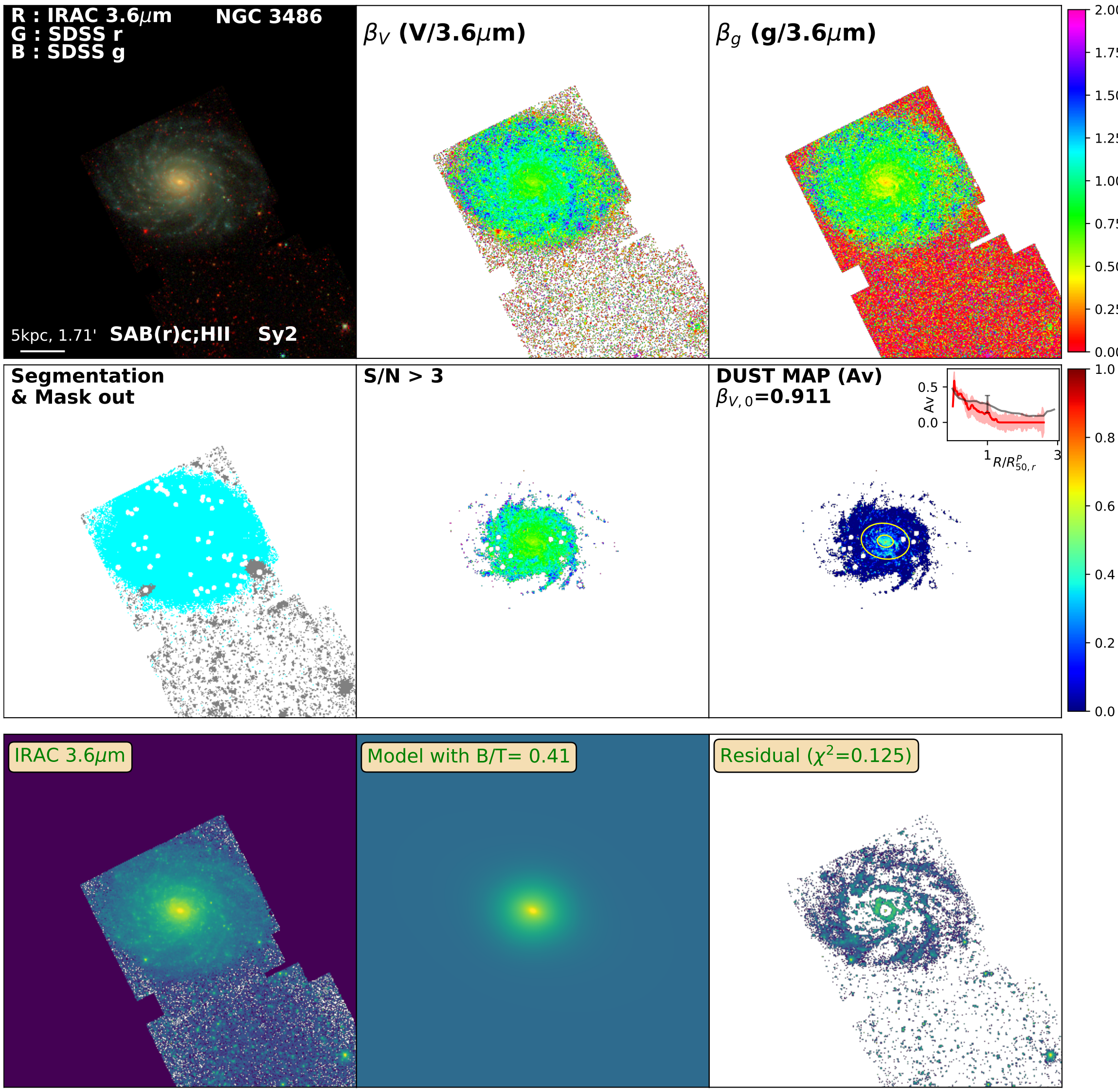

Figure D.91: Same as Figure 3.2 for NGC3486

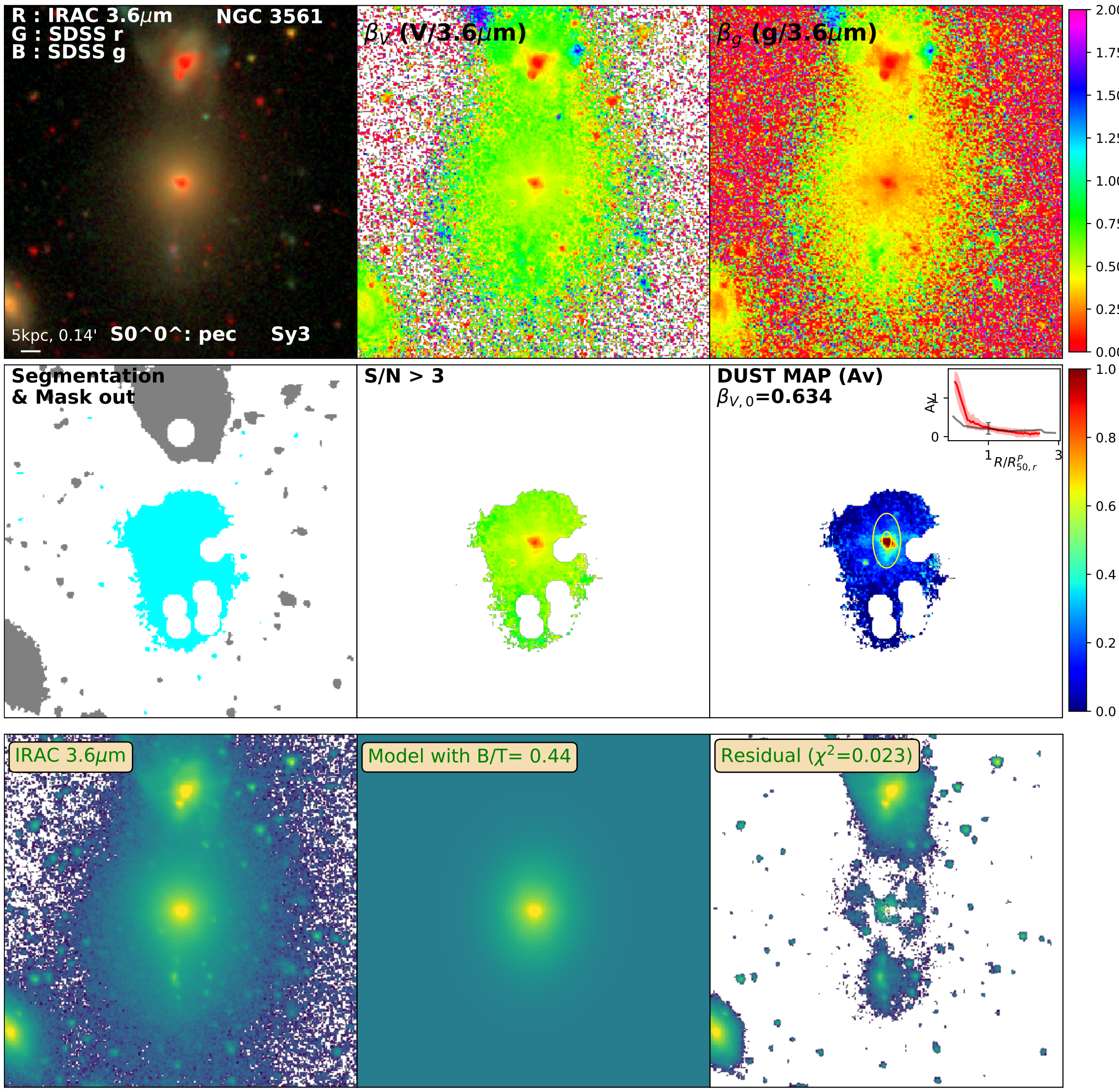

Figure D.92: Same as Figure 3.2 for NGC3561

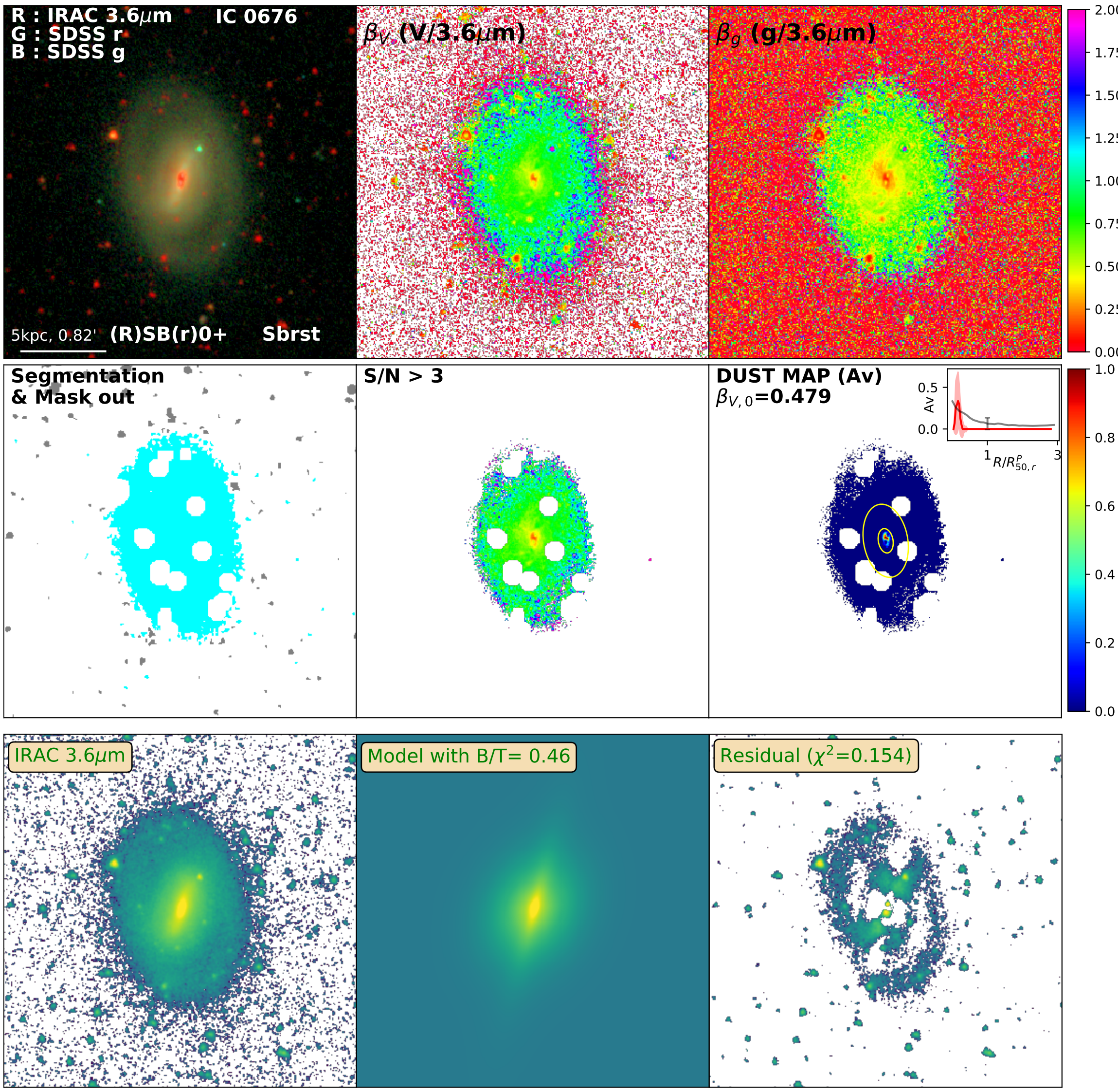

Figure D.93: Same as Figure 3.2 for IC0676

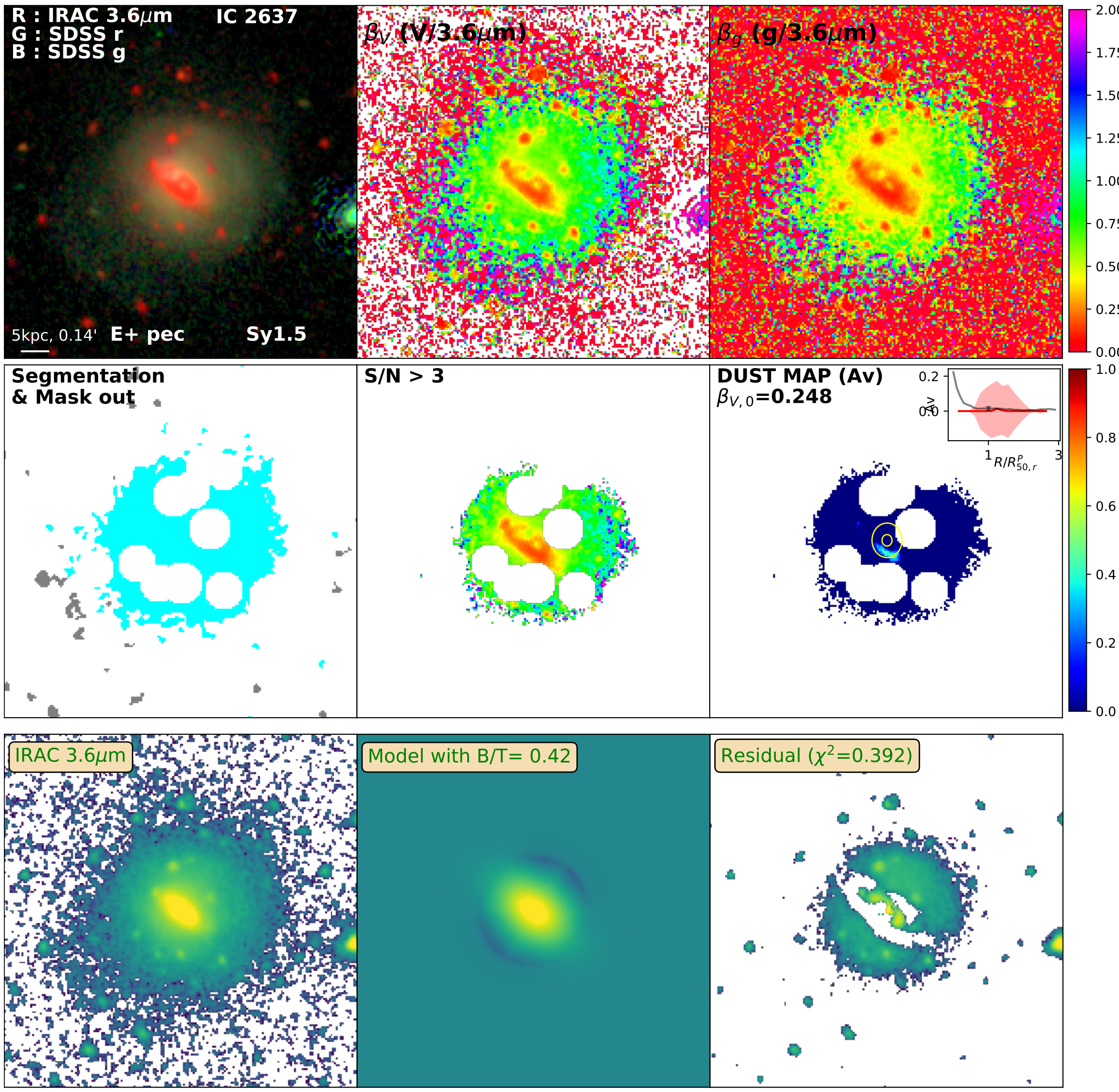

Figure D.94: Same as Figure 3.2 for IC2637

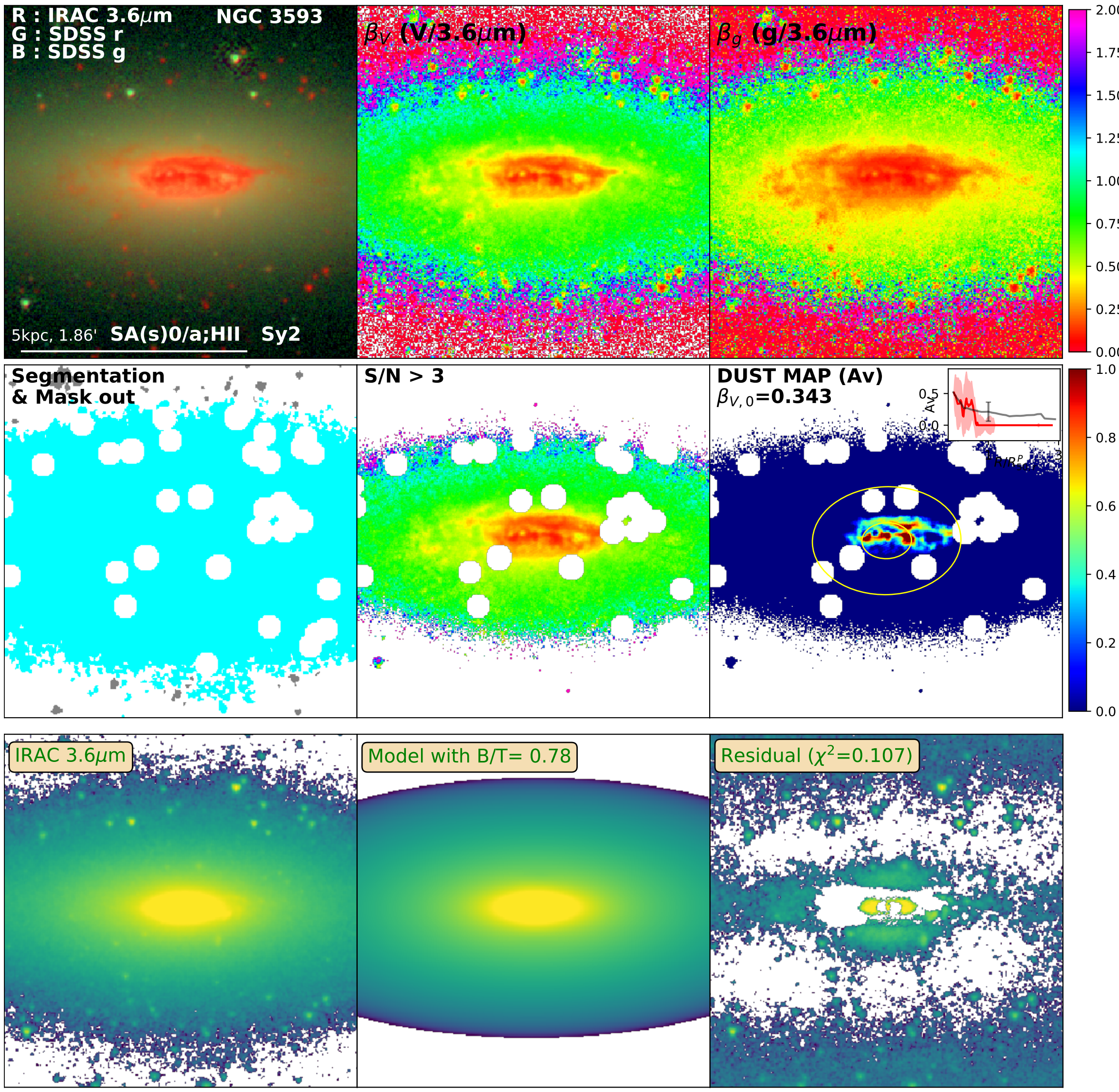

Figure D.95: Same as Figure 3.2 for NGC3593

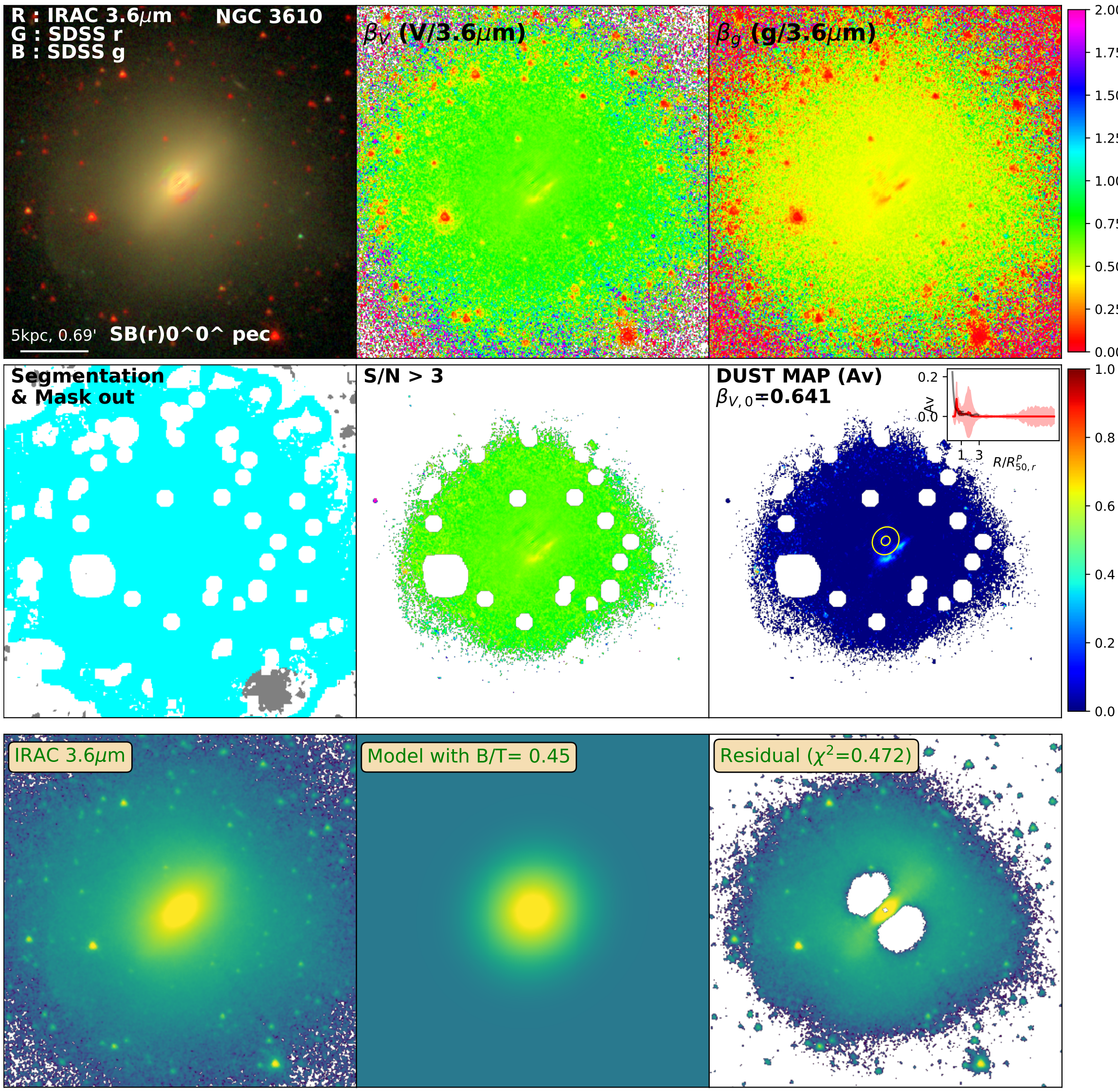

Figure D.96: Same as Figure 3.2 for NGC3610

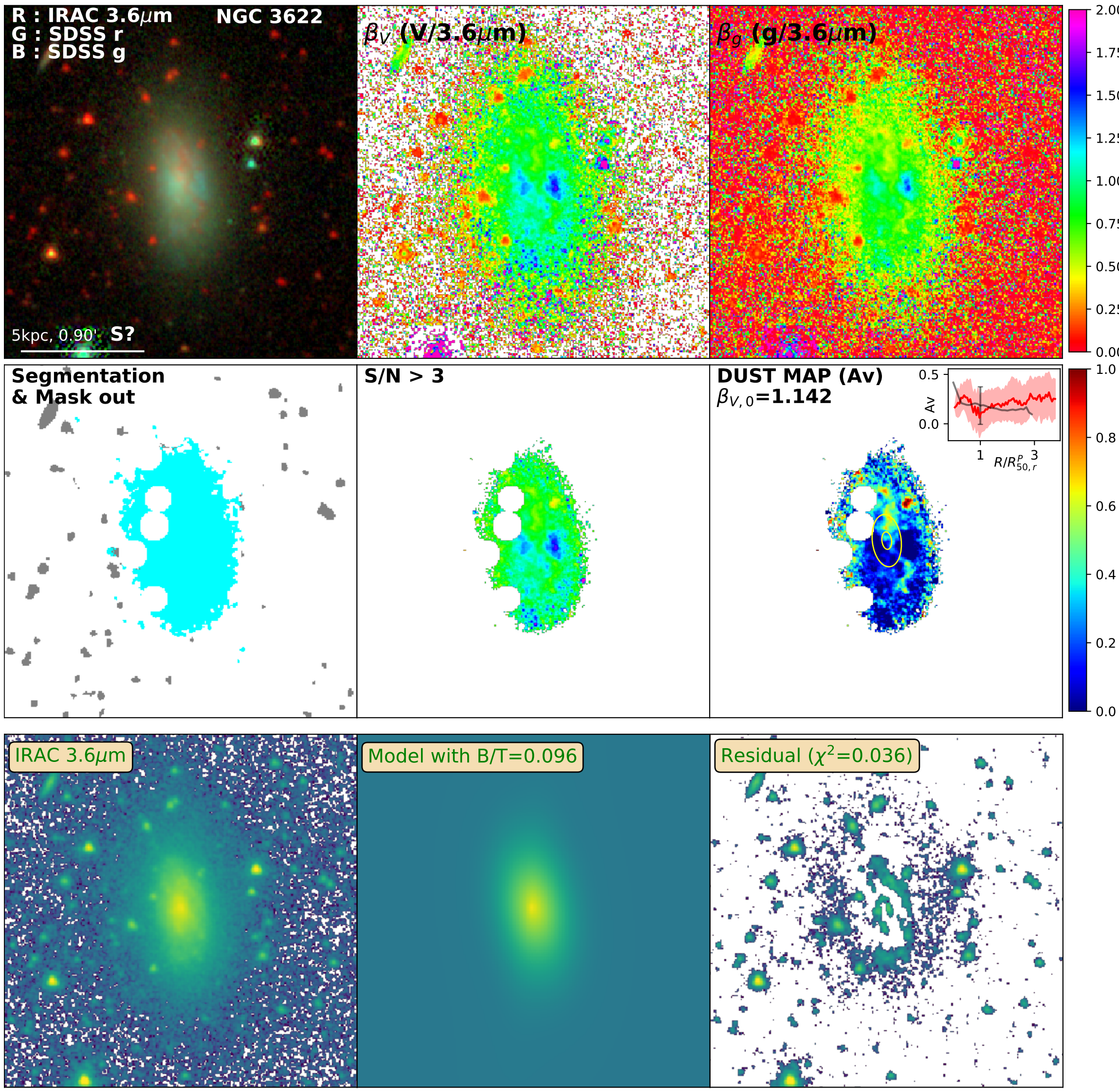

Figure D.97: Same as Figure 3.2 for NGC3622

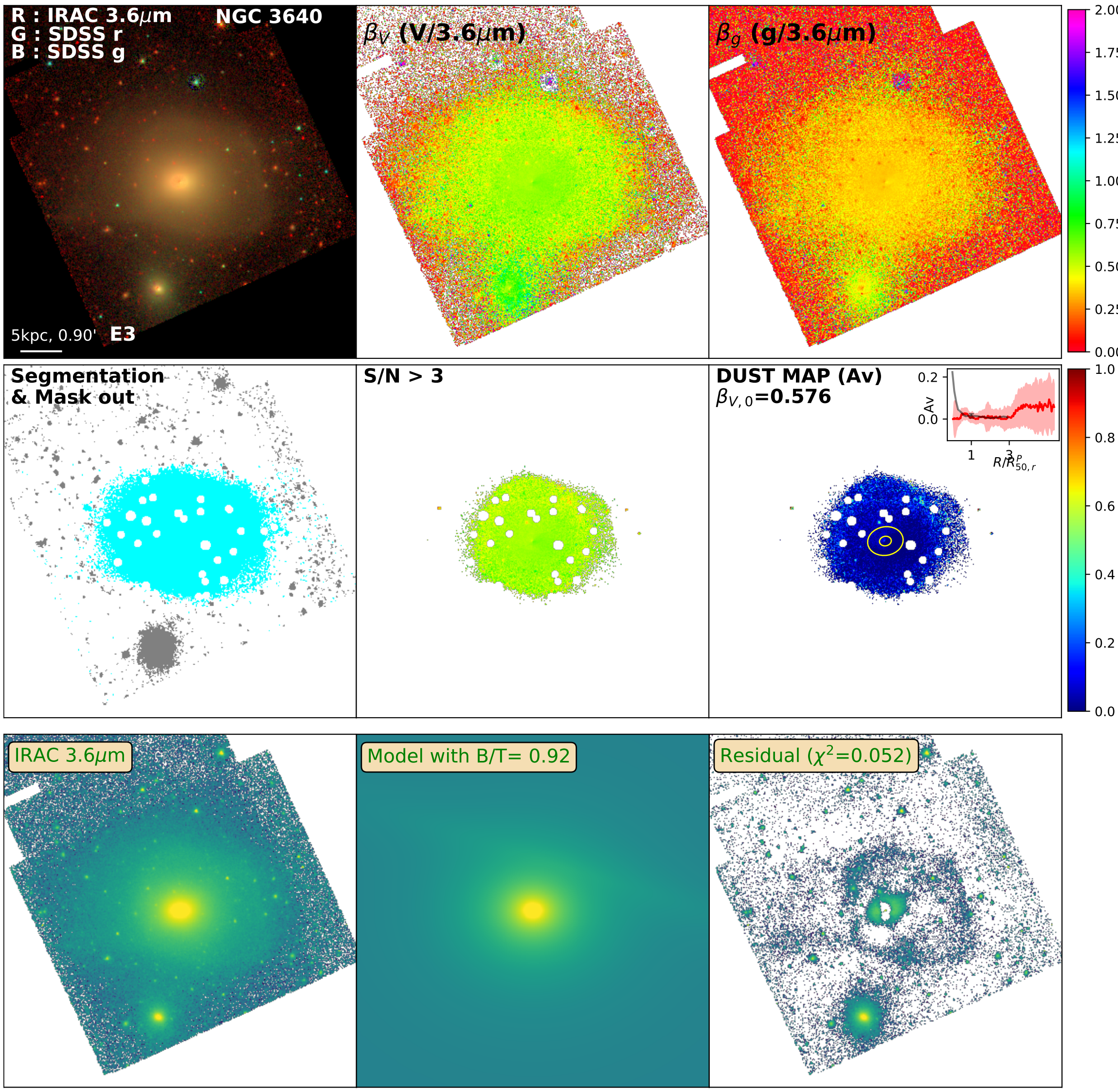

Figure D.98: Same as Figure 3.2 for NGC3640

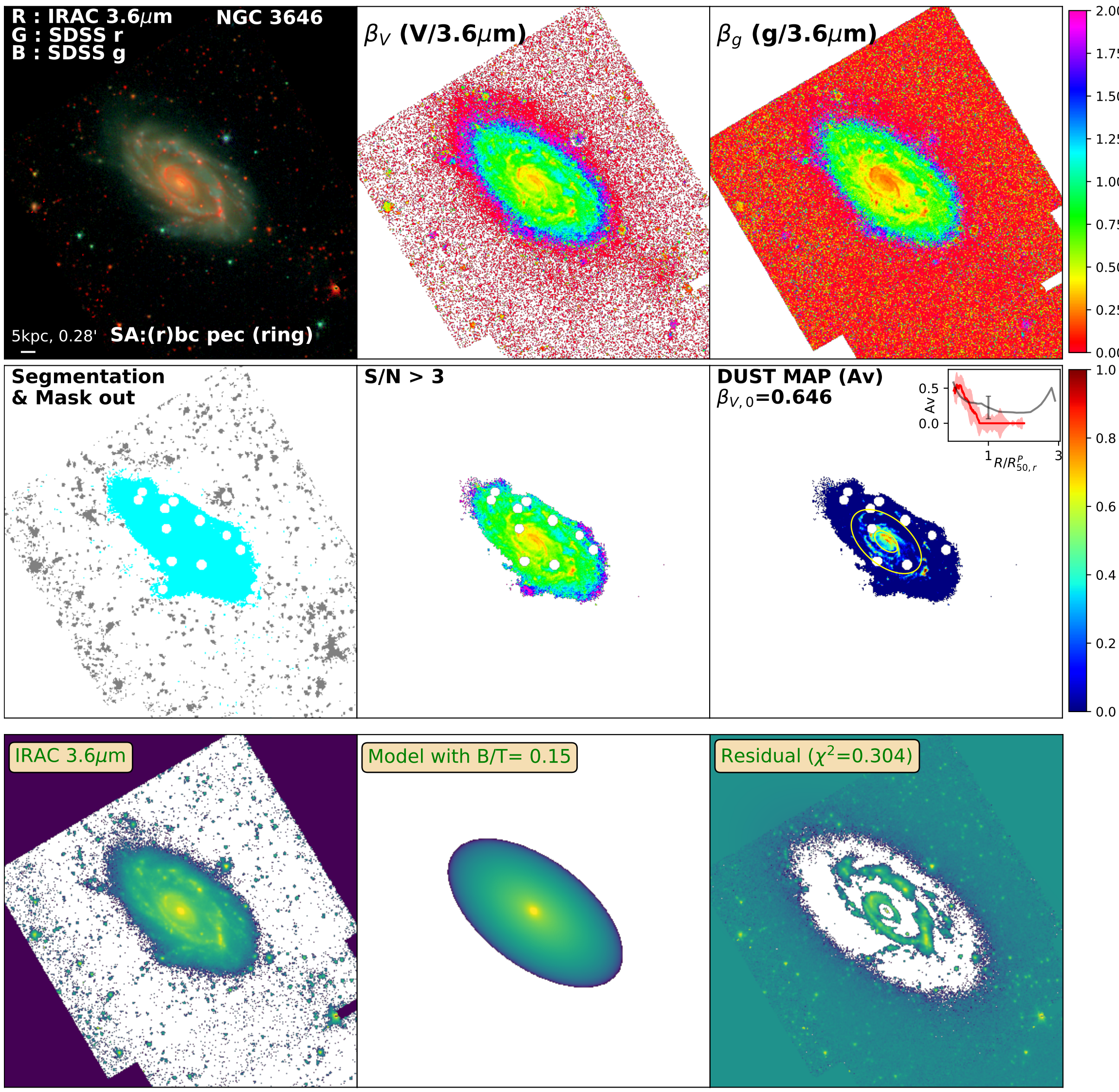

Figure D.99: Same as Figure 3.2 for NGC3646

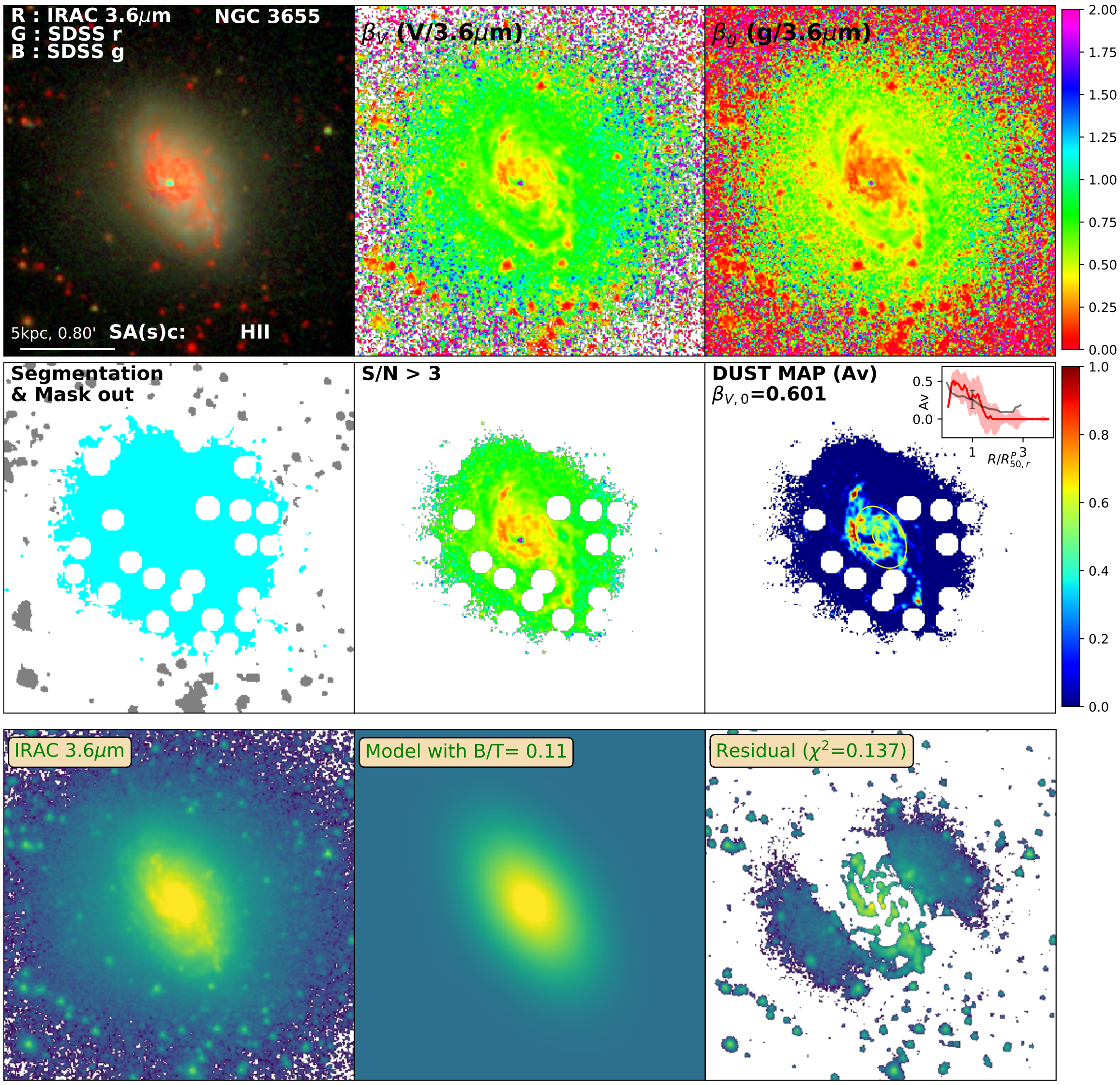

Figure D.100: Same as Figure 3.2 for NGC3655

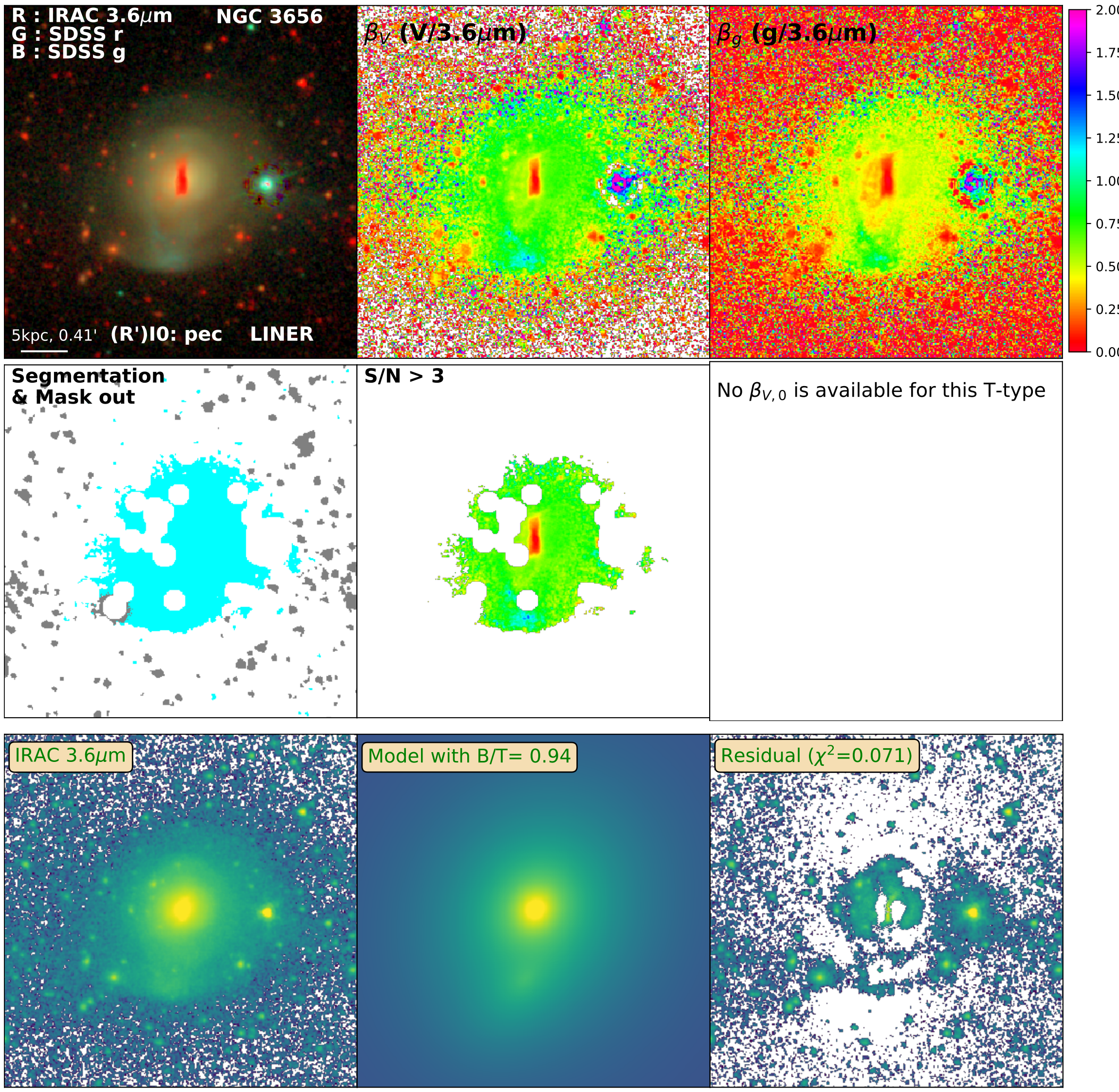

Figure D.101: Same as Figure 3.2 for NGC3656

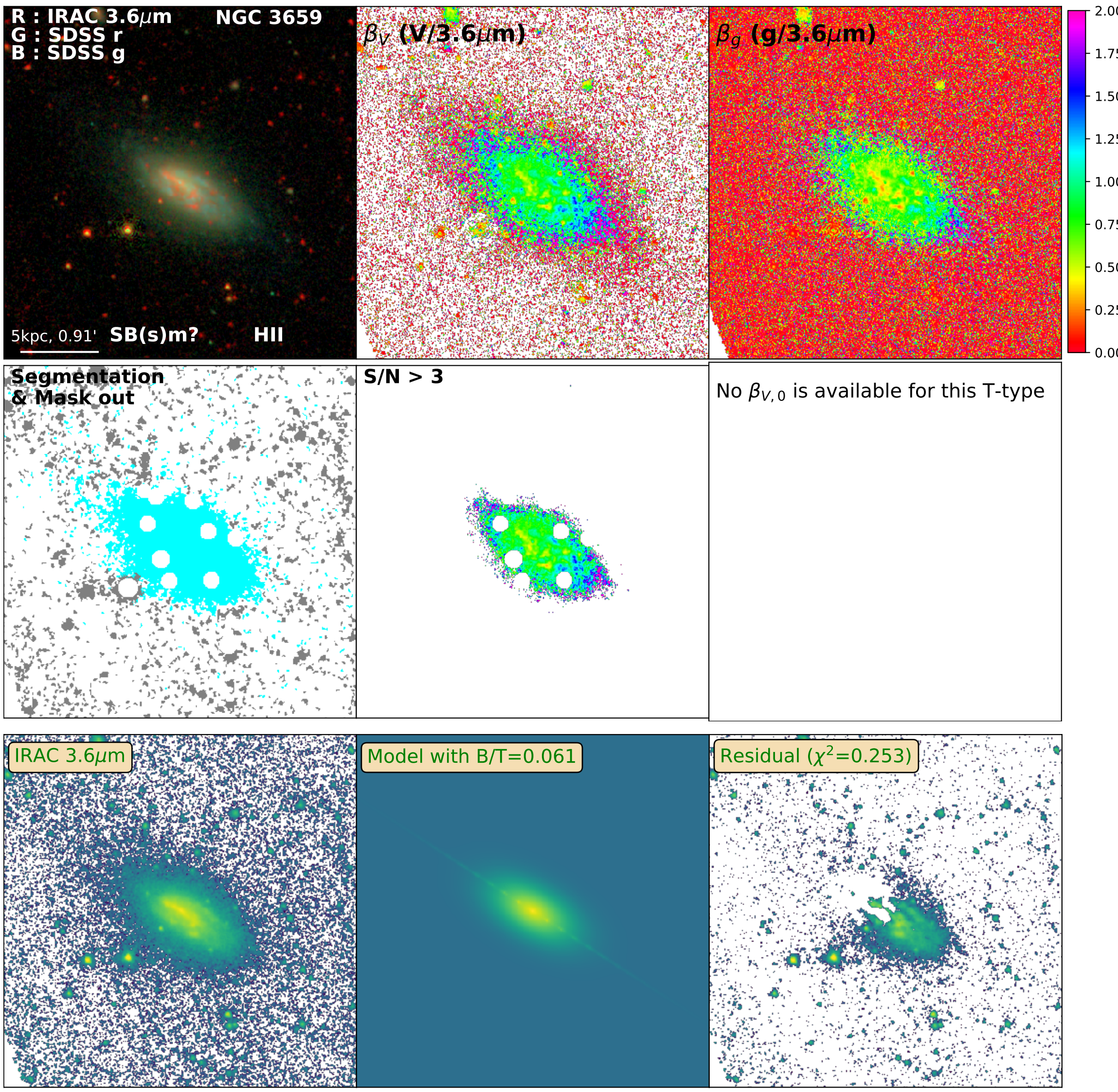

Figure D.102: Same as Figure 3.2 for NGC3659

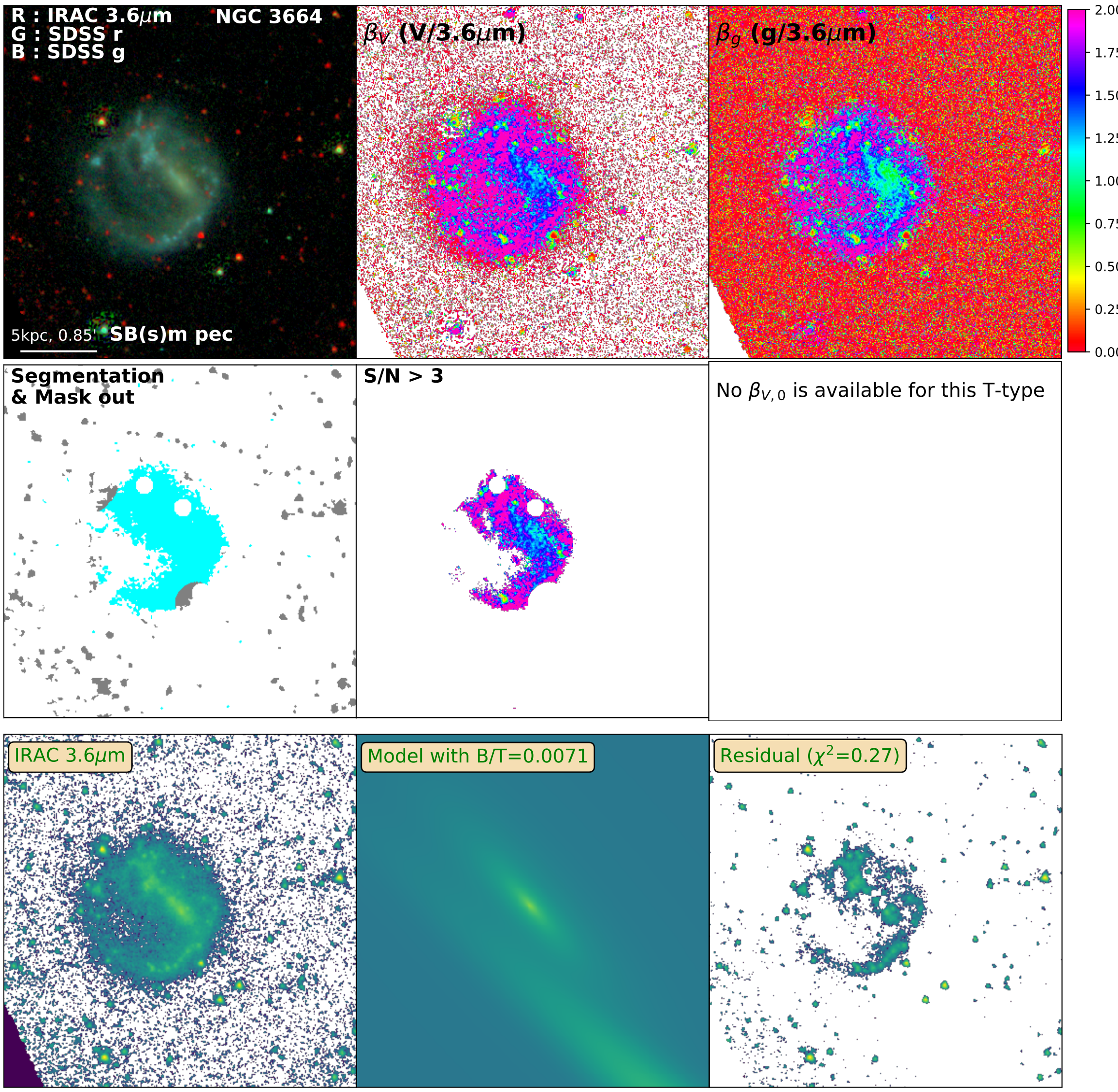

Figure D.103: Same as Figure 3.2 for NGC3664

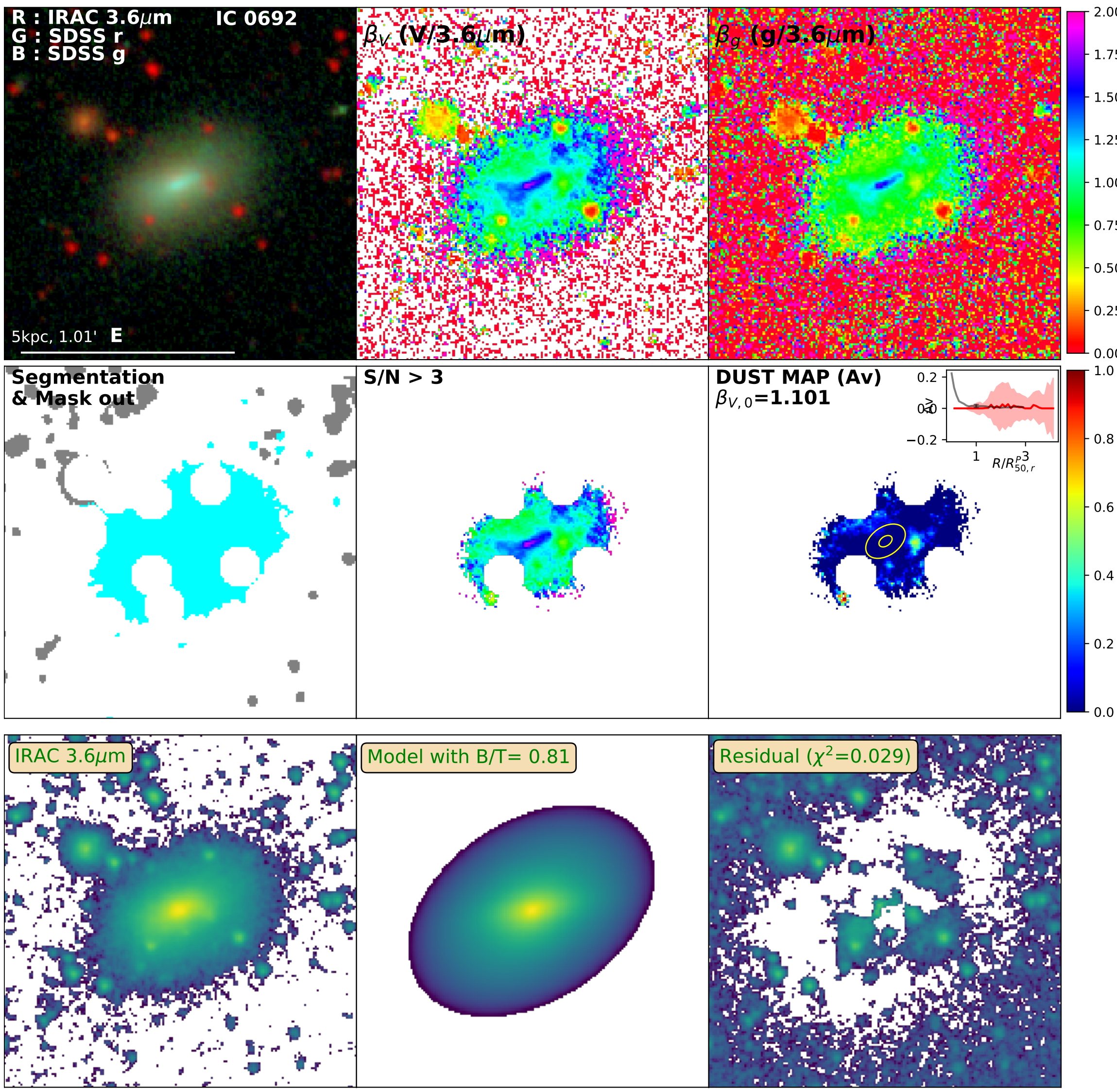

Figure D.104: Same as Figure 3.2 for IC0692

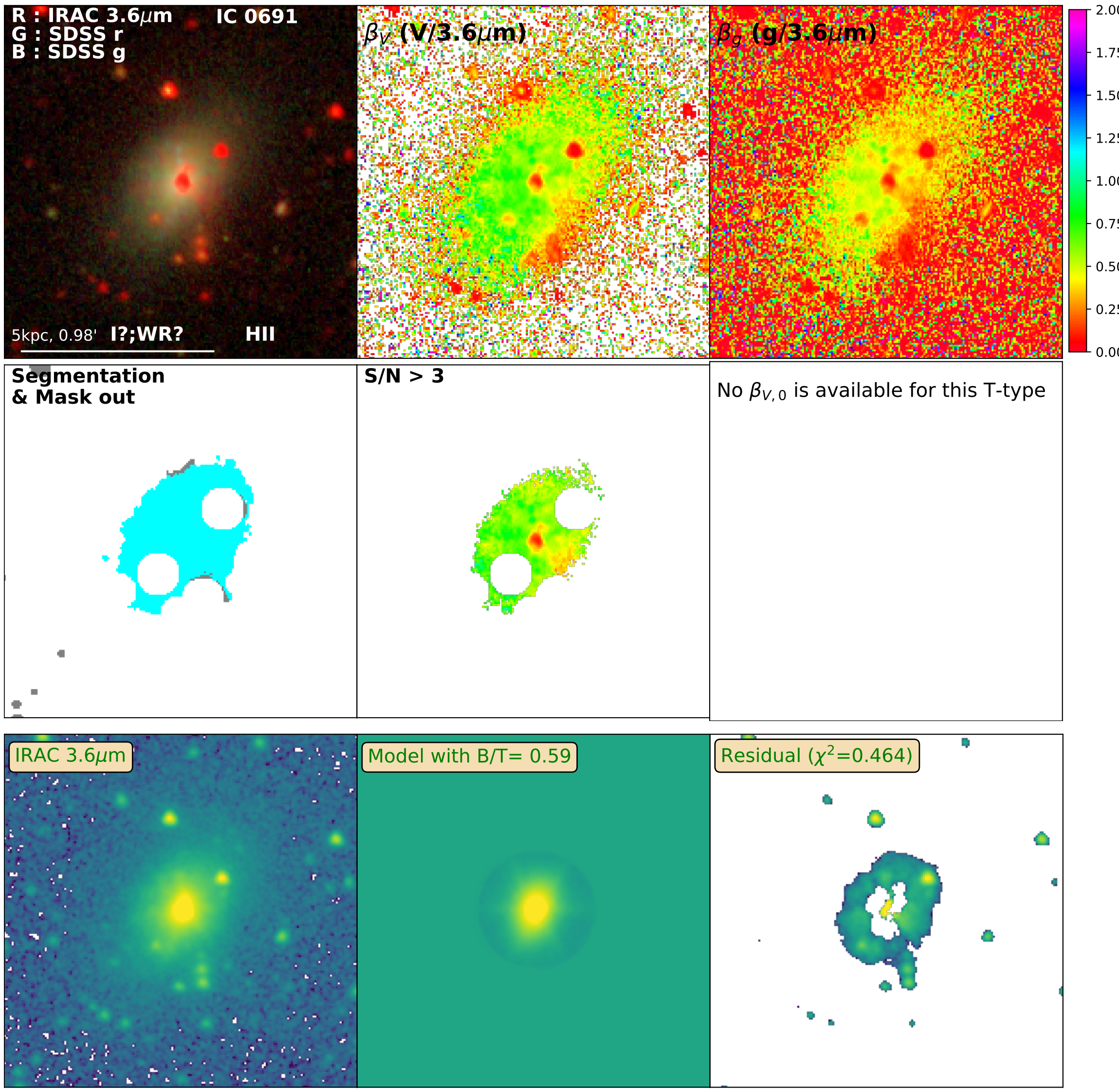

Figure D.105: Same as Figure 3.2 for IC0691

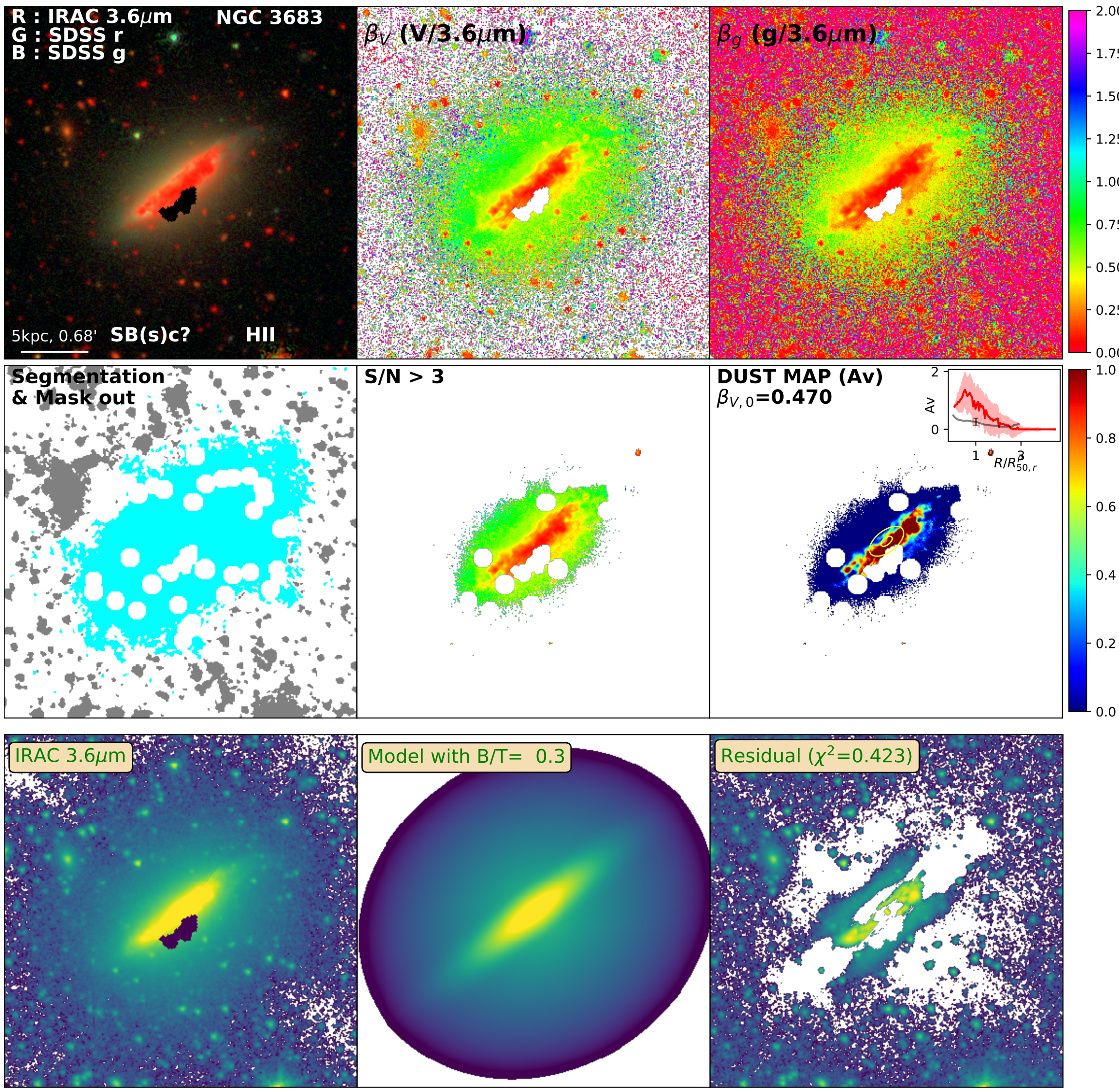

Figure D.106: Same as Figure 3.2 for NGC3683

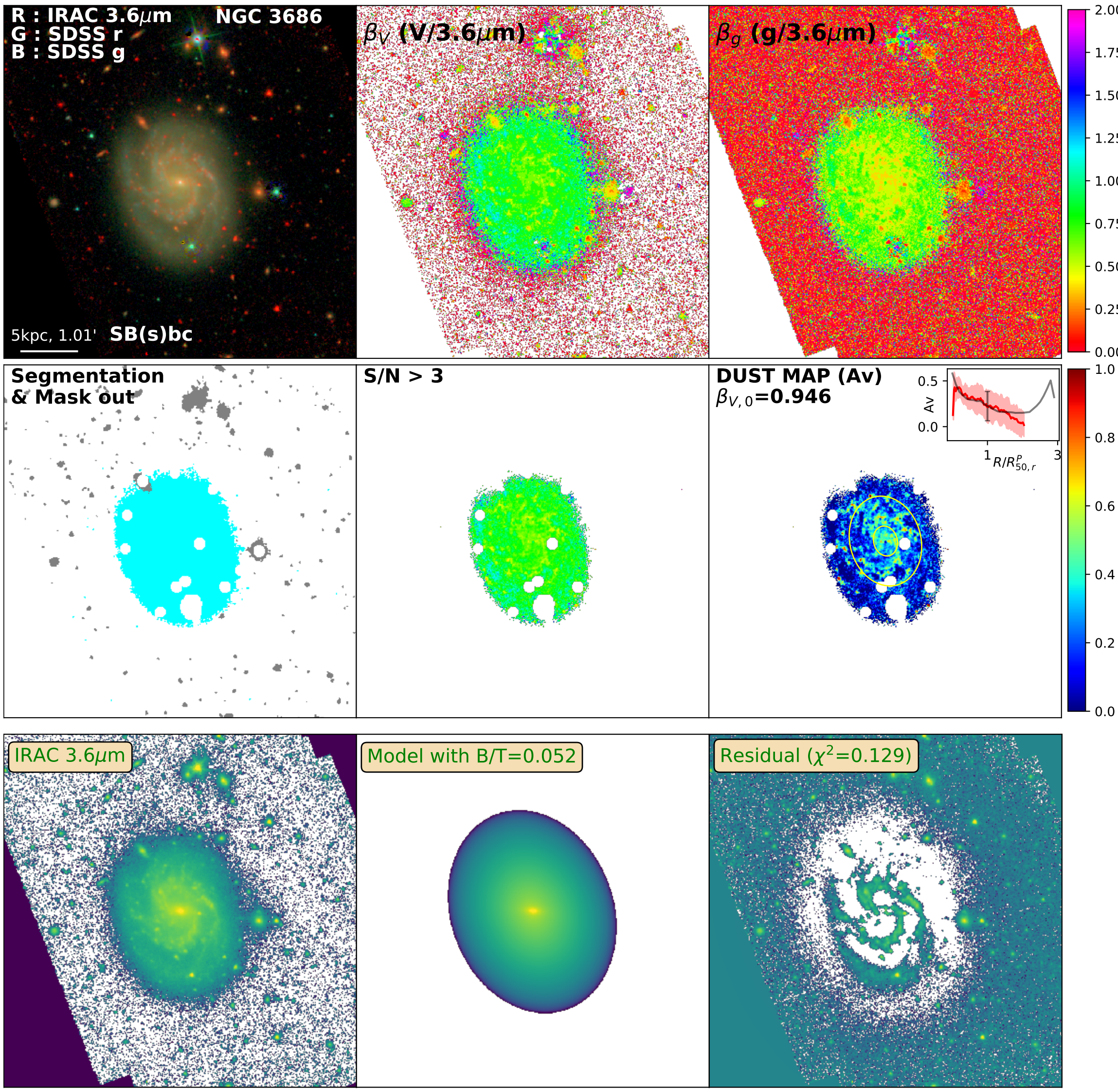

Figure D.107: Same as Figure 3.2 for NGC3686

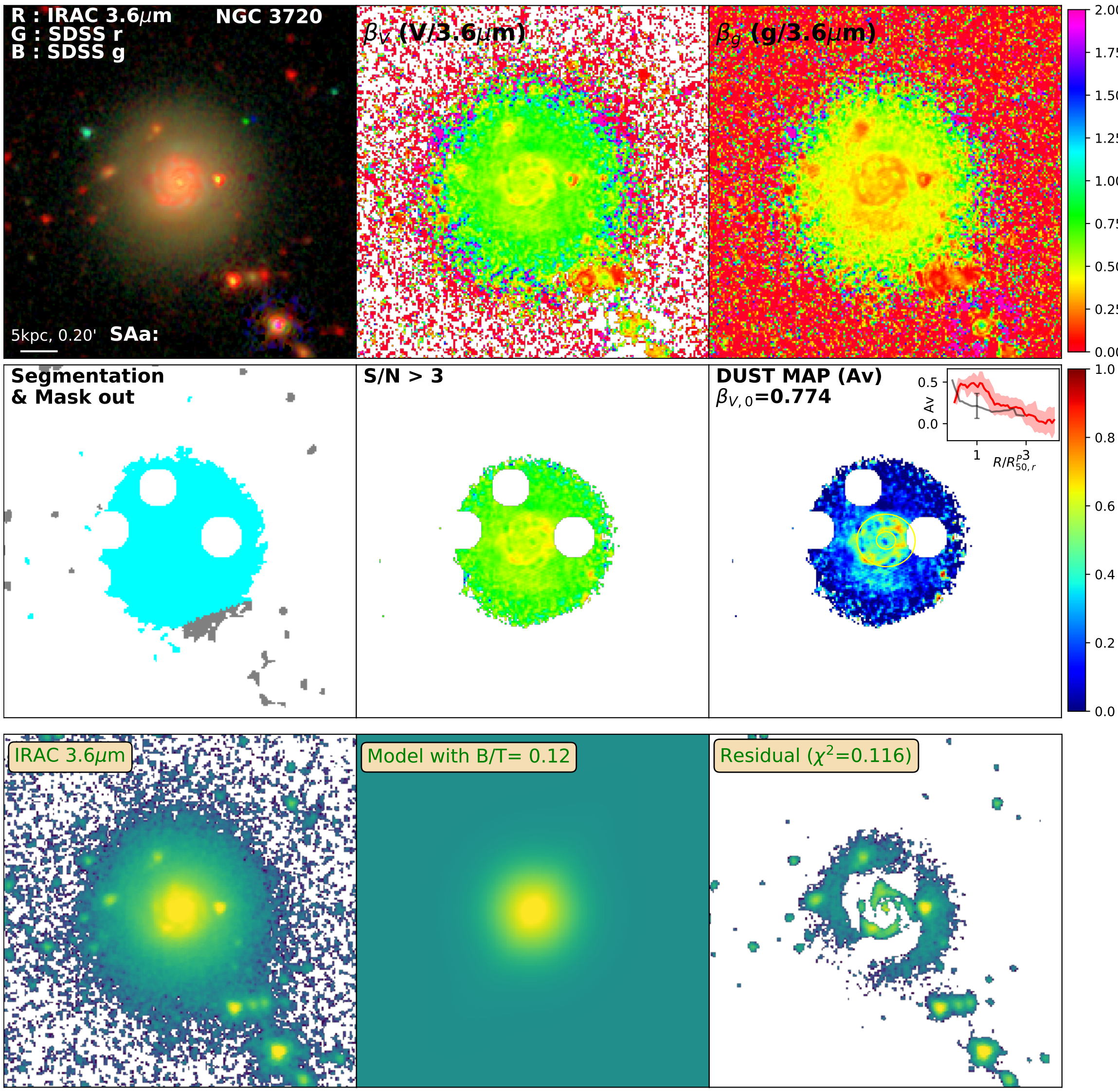

Figure D.108: Same as Figure 3.2 for NGC3720

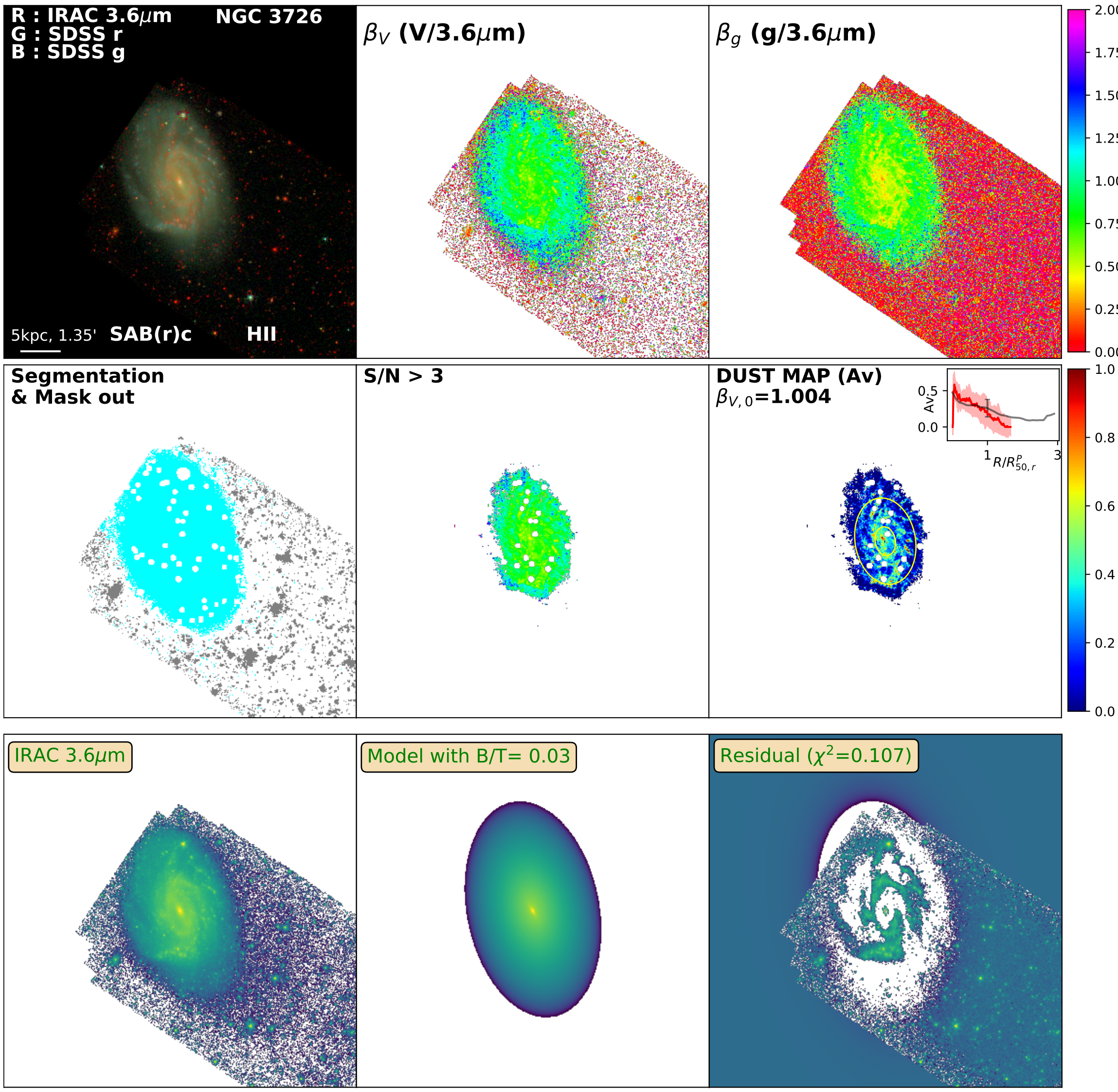

Figure D.109: Same as Figure 3.2 for NGC3726

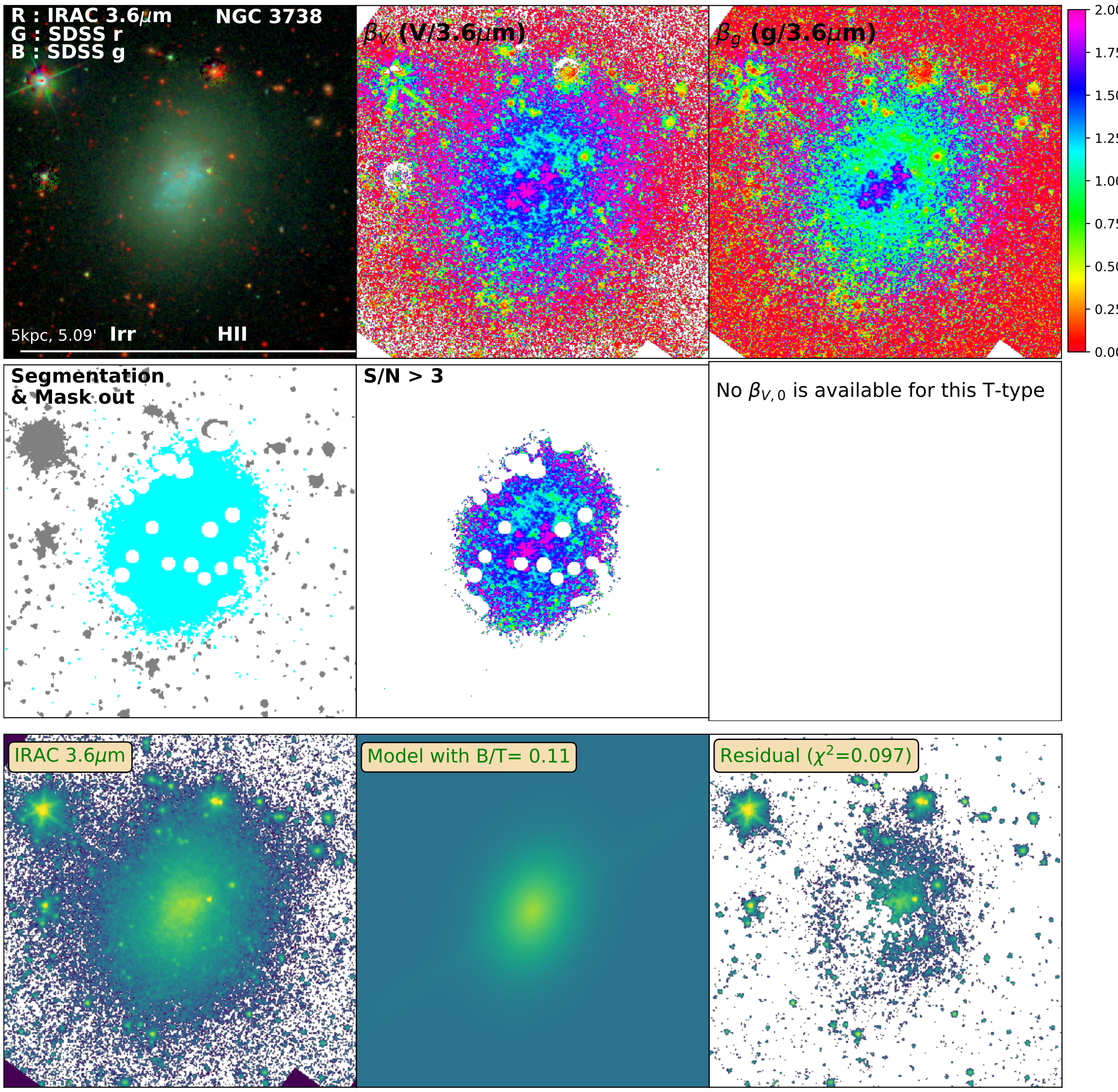

Figure D.110: Same as Figure 3.2 for NGC3738

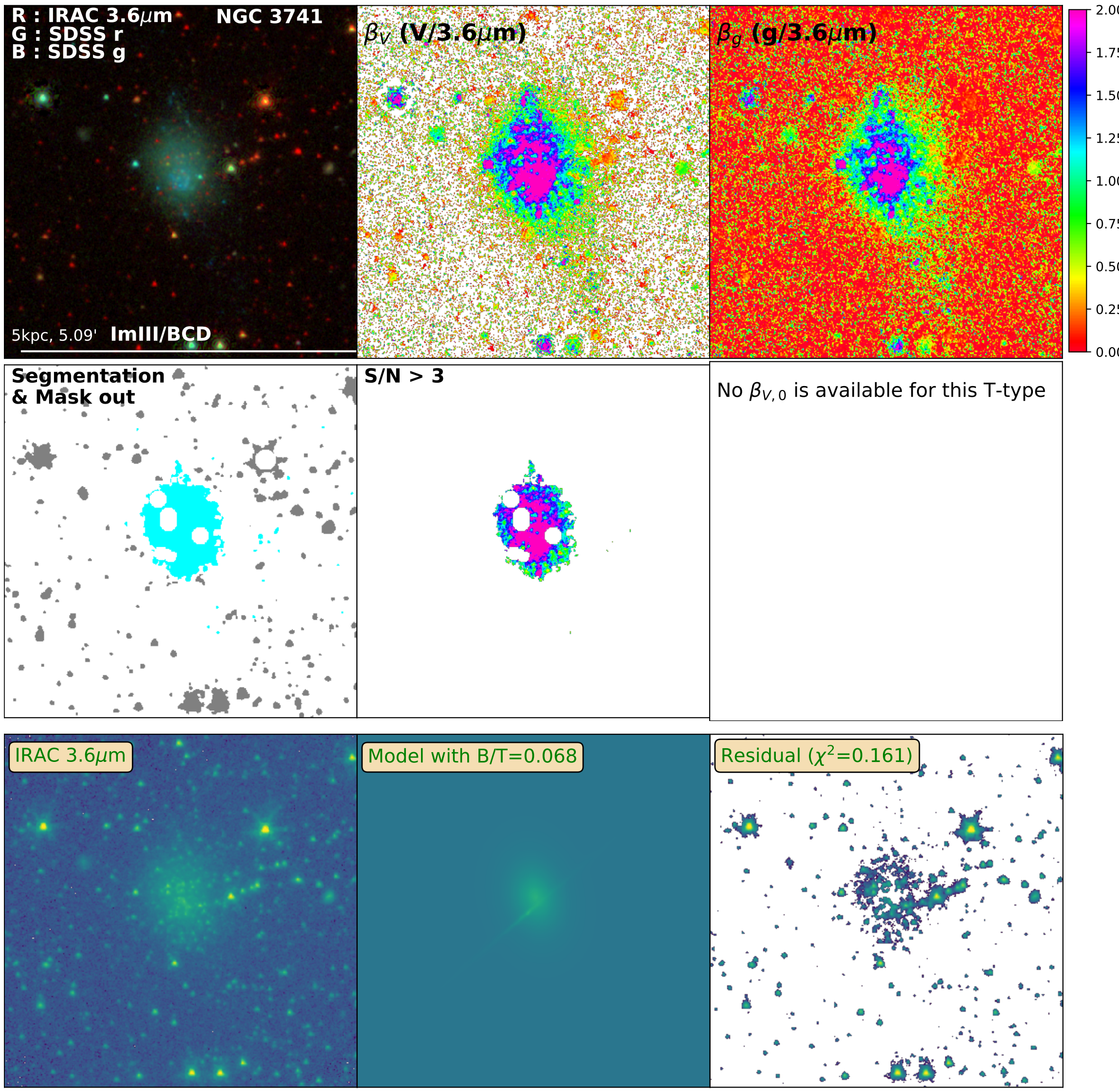

Figure D.111: Same as Figure 3.2 for NGC3741

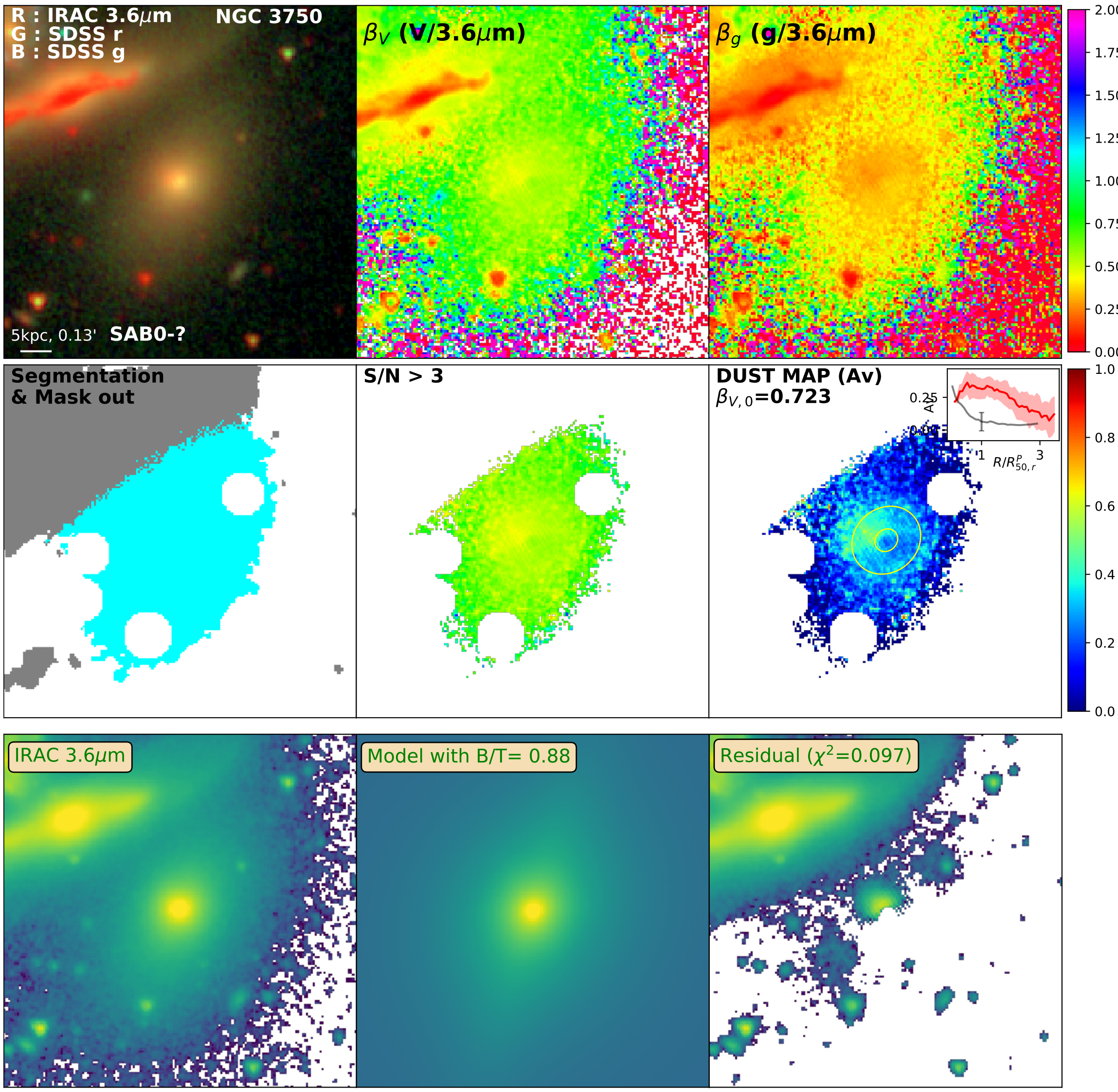

Figure D.112: Same as Figure 3.2 for NGC3750

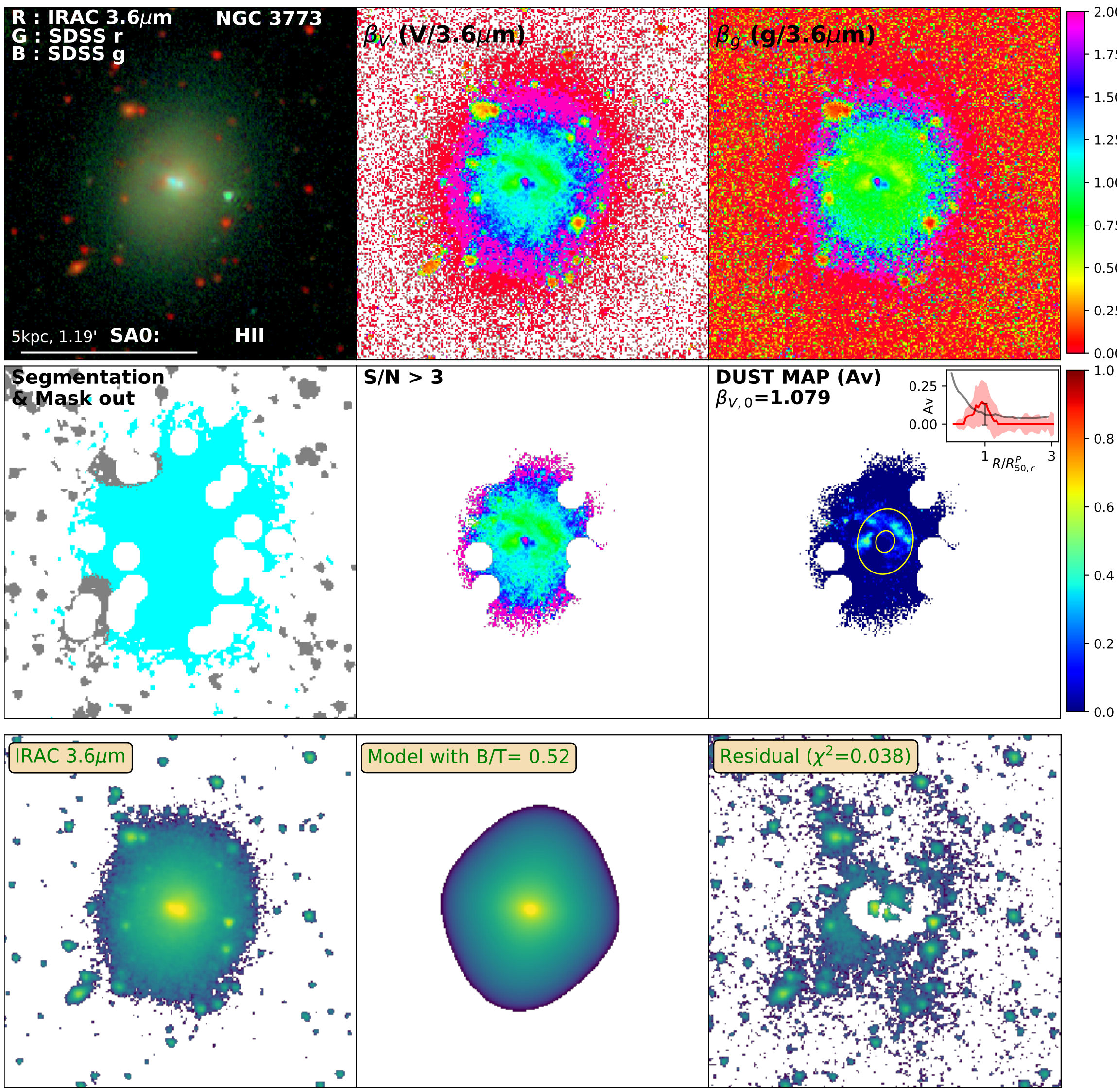

Figure D.113: Same as Figure 3.2 for NGC3773

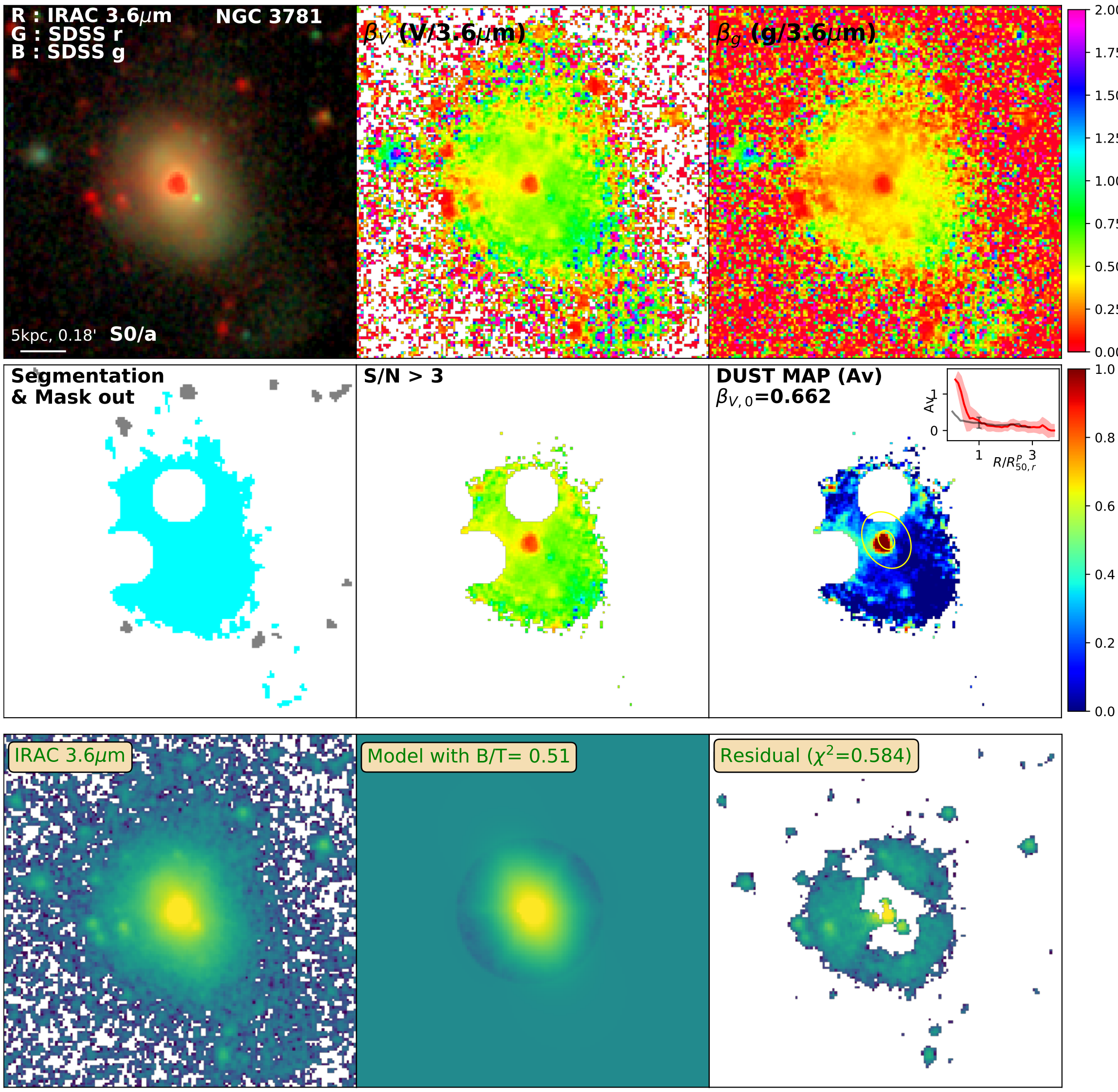

Figure D.114: Same as Figure 3.2 for NGC3781

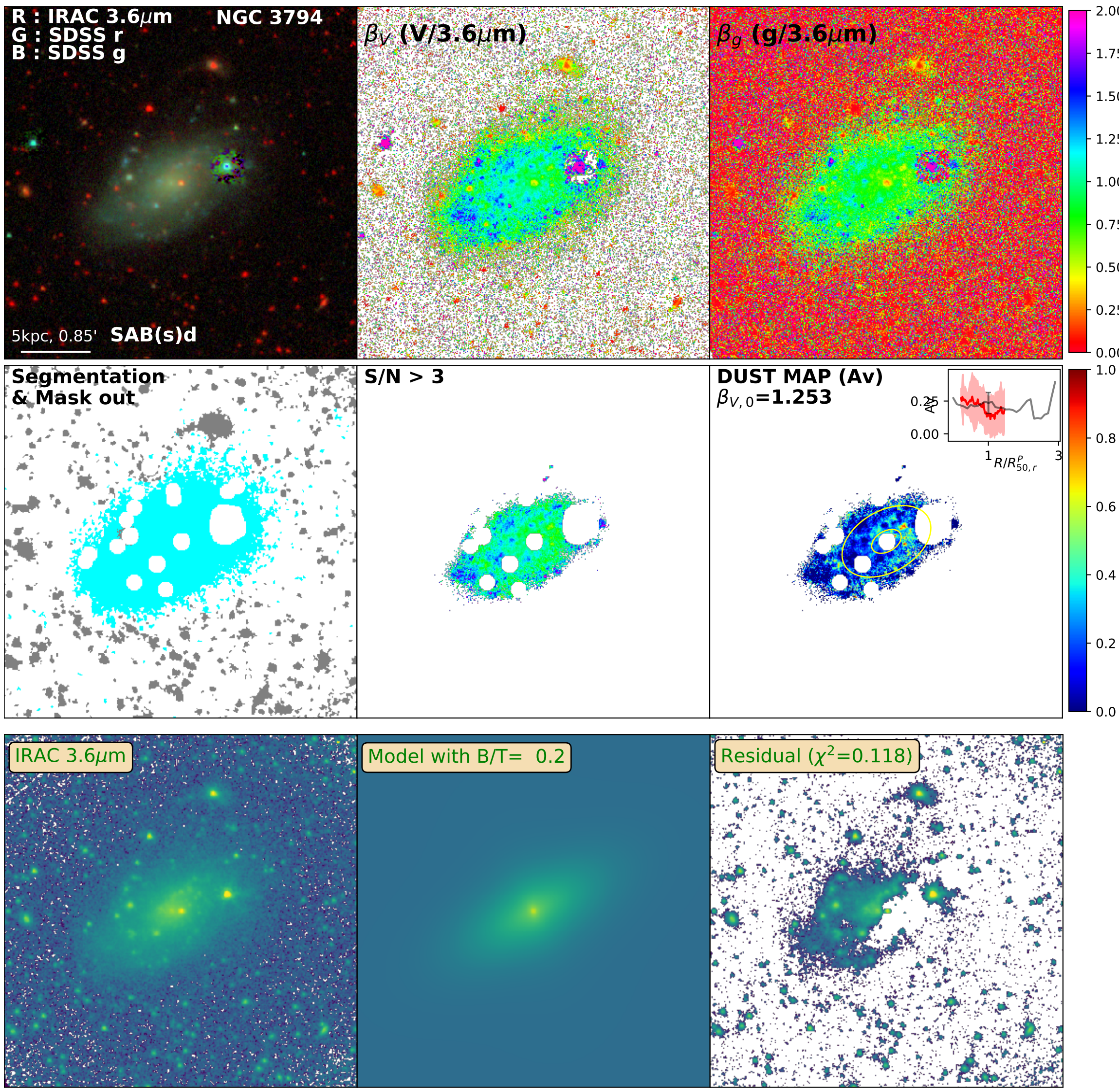

Figure D.115: Same as Figure 3.2 for NGC3794

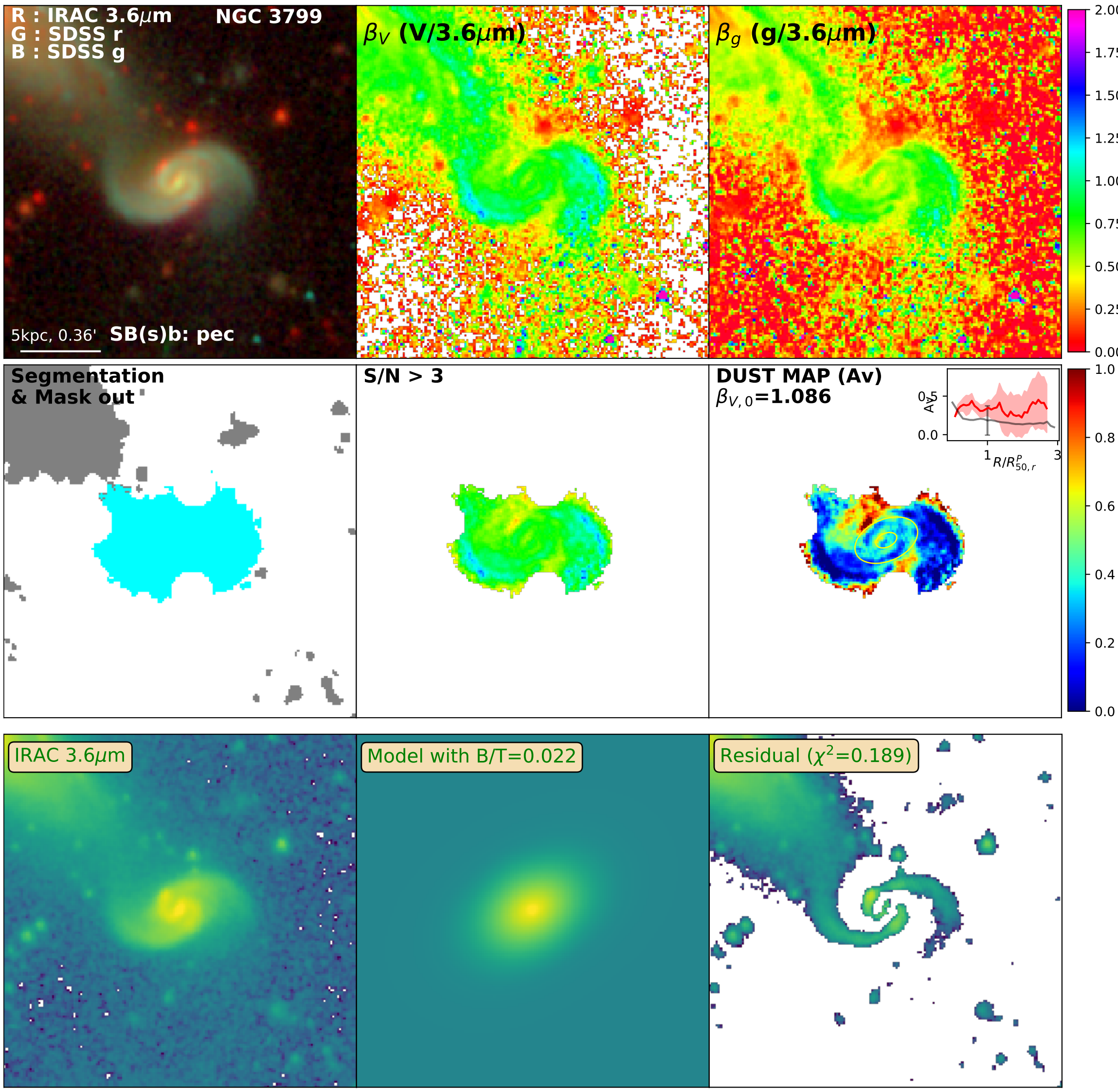

Figure D.116: Same as Figure 3.2 for NGC3799

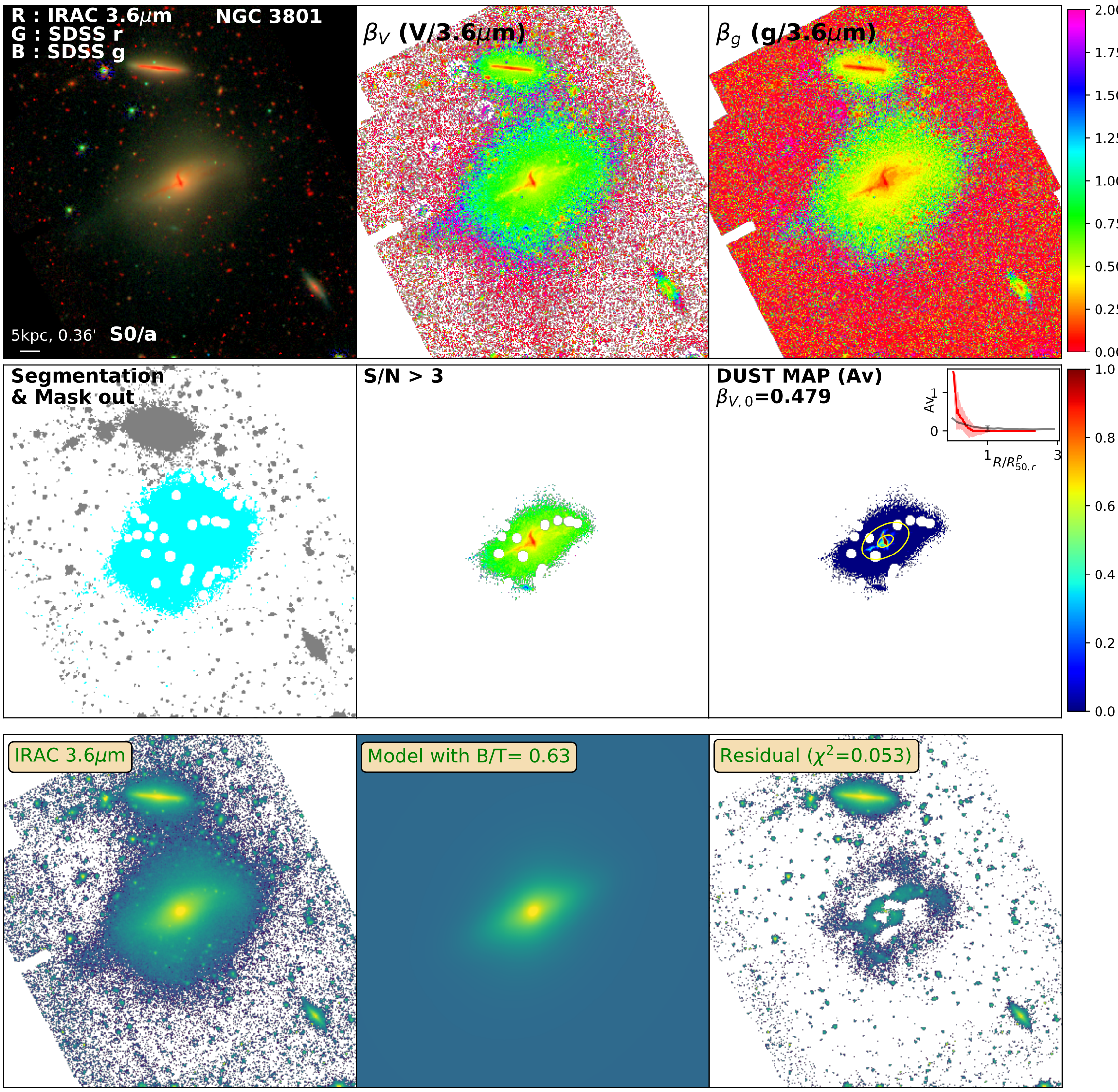

Figure D.117: Same as Figure 3.2 for NGC3801

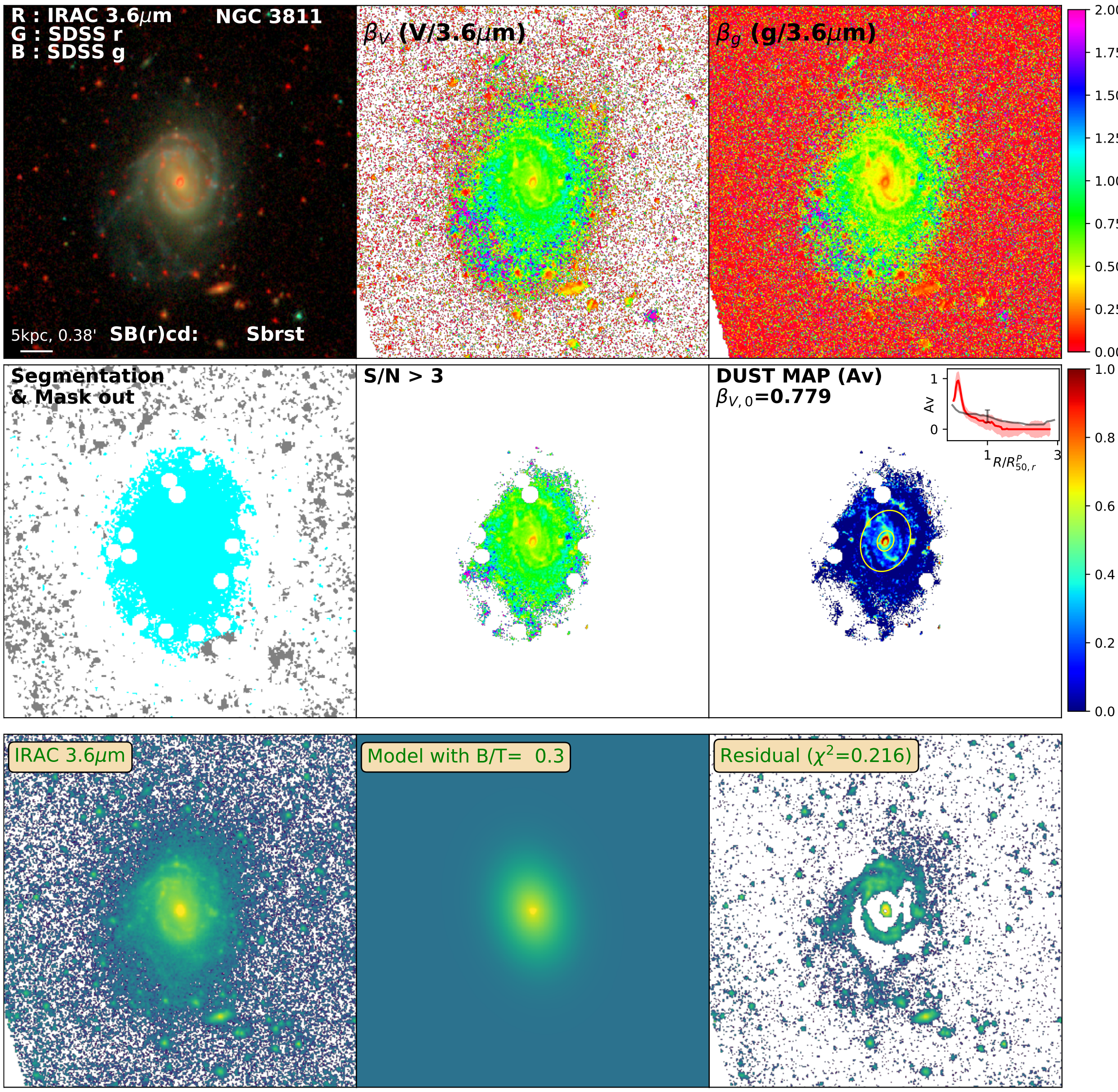

Figure D.118: Same as Figure 3.2 for NGC3811

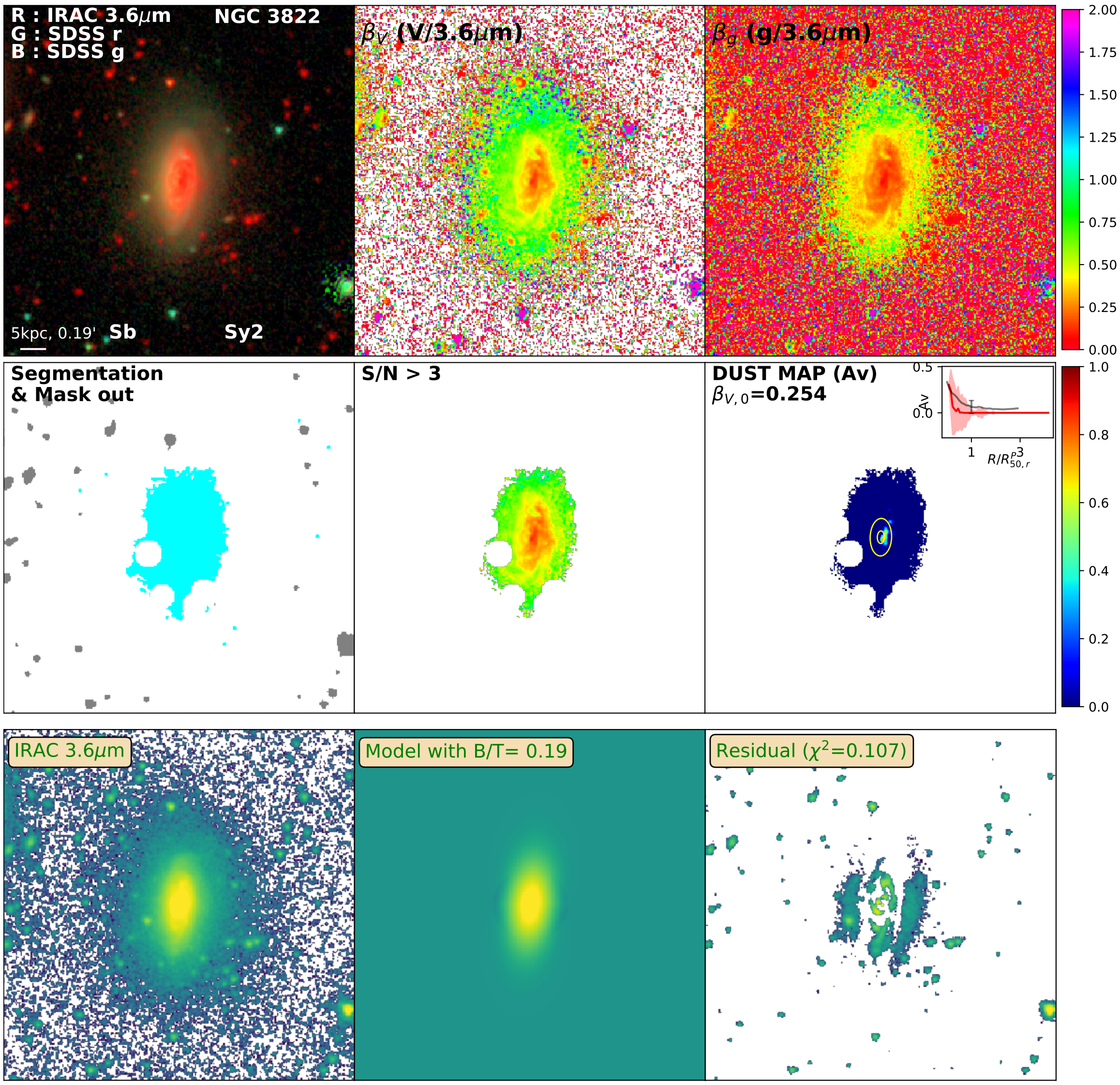

Figure D.119: Same as Figure 3.2 for NGC3822

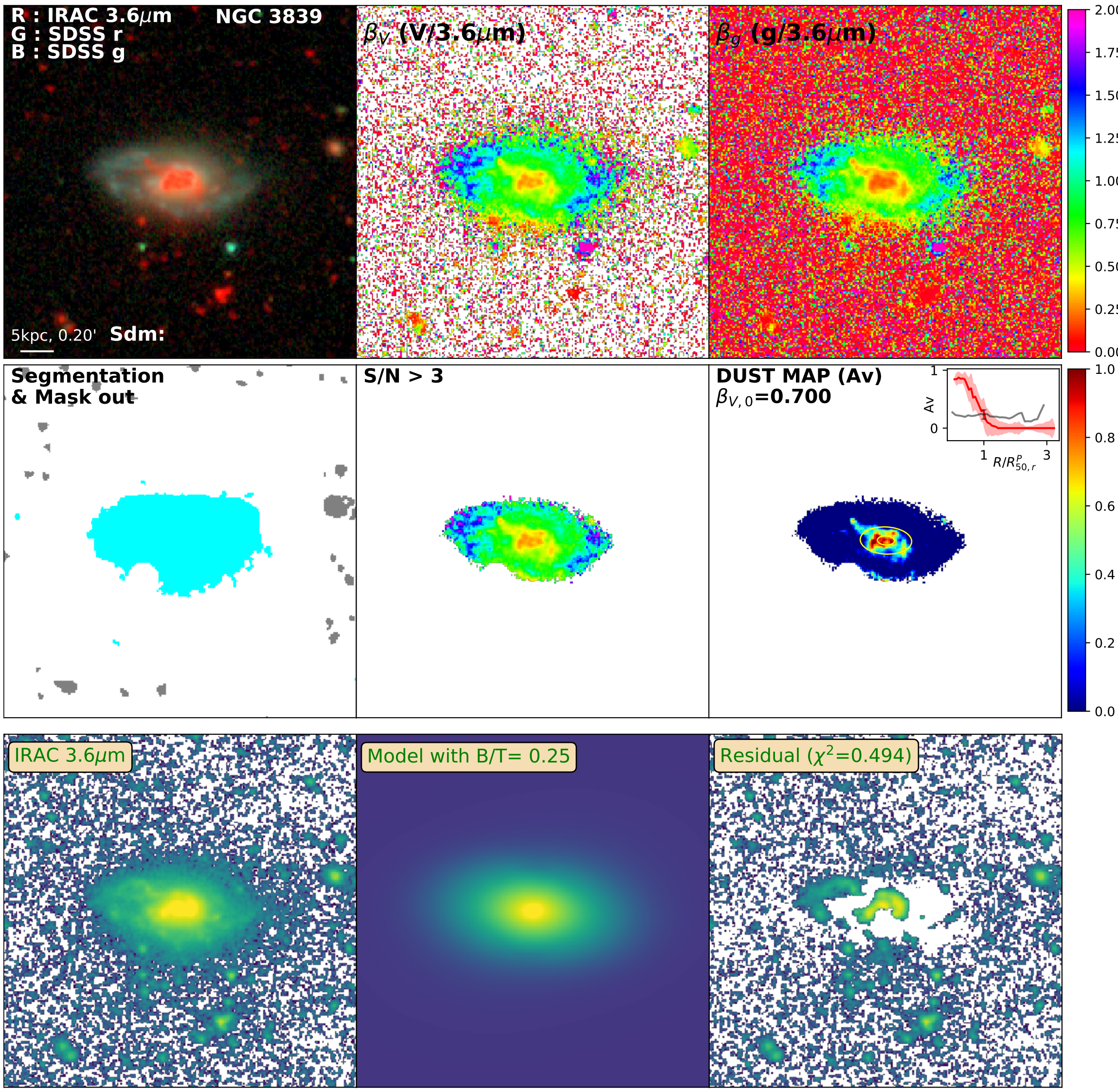

Figure D.120: Same as Figure 3.2 for NGC3839

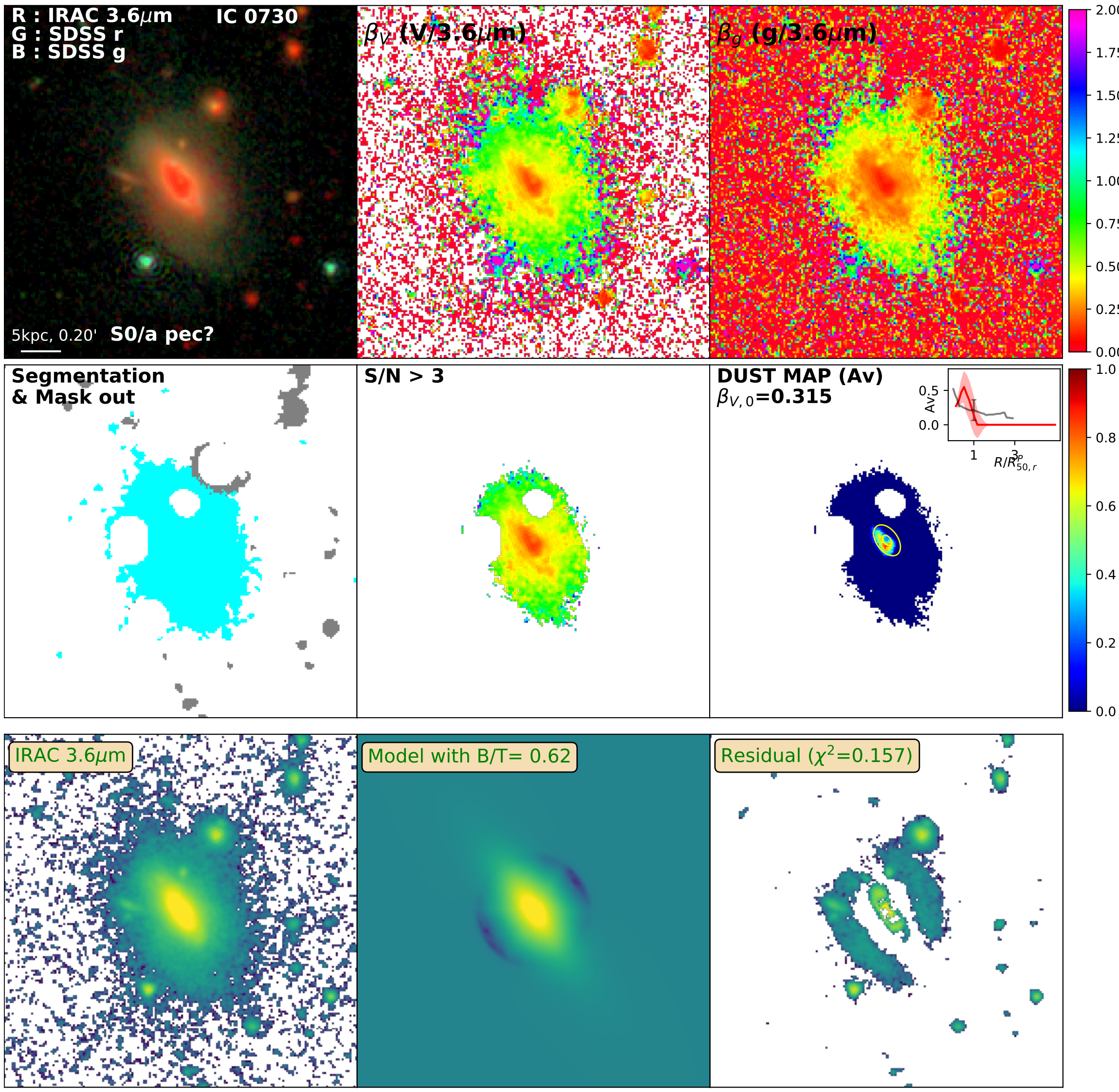

Figure D.121: Same as Figure 3.2 for IC0730

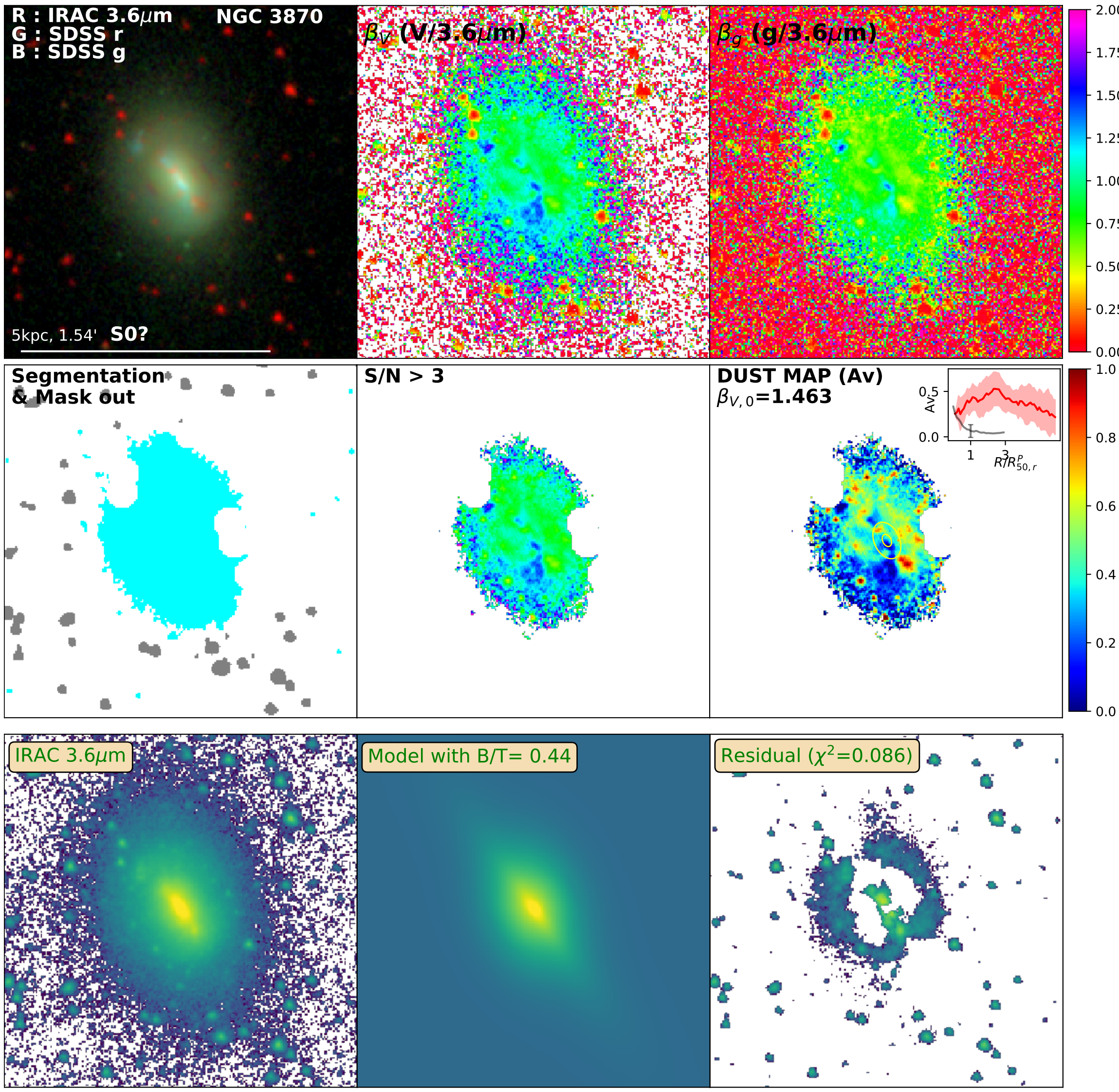

Figure D.122: Same as Figure 3.2 for NGC3870

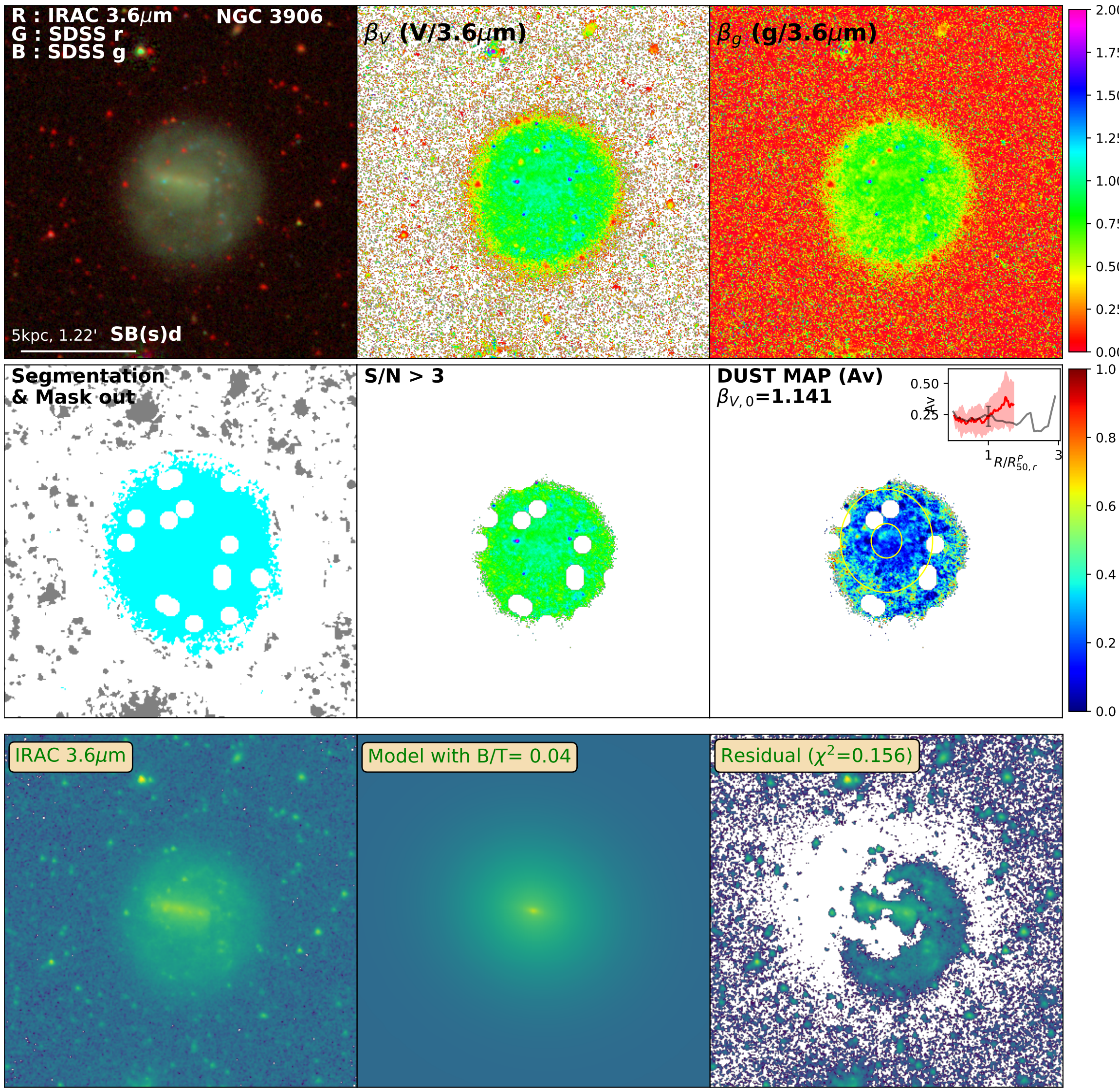

Figure D.123: Same as Figure 3.2 for NGC3906

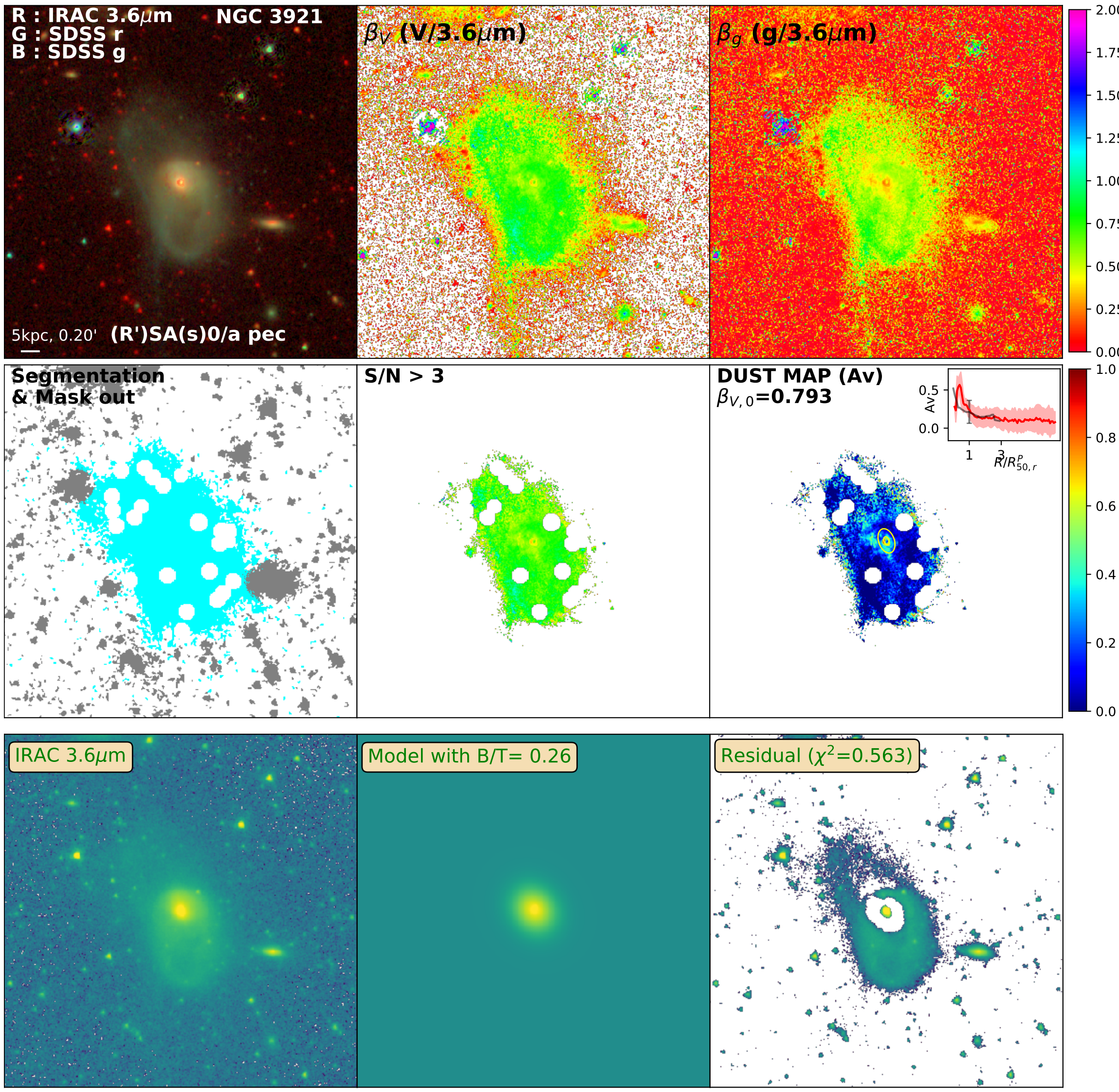

Figure D.124: Same as Figure 3.2 for NGC3921

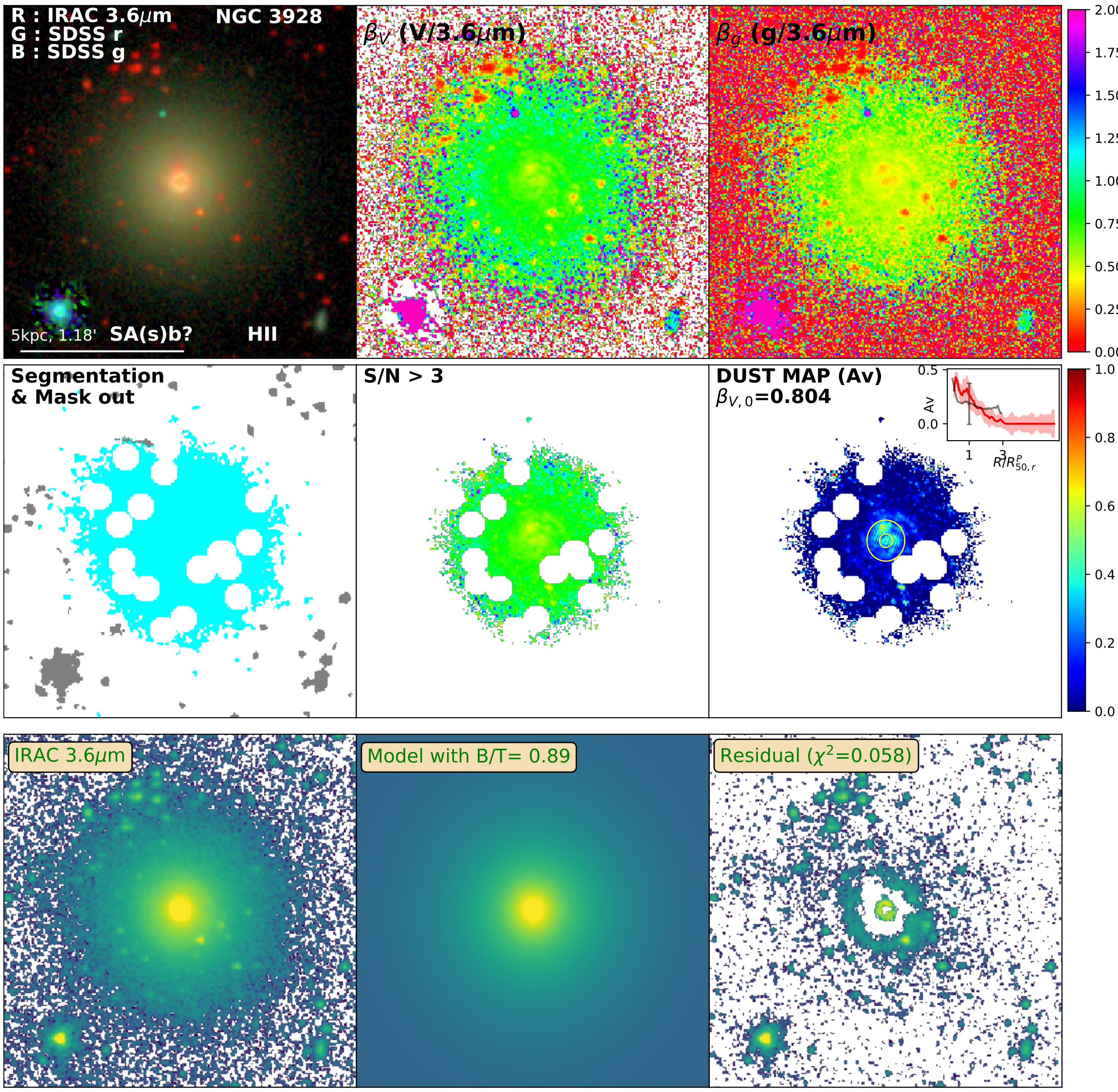

Figure D.125: Same as Figure 3.2 for NGC3928

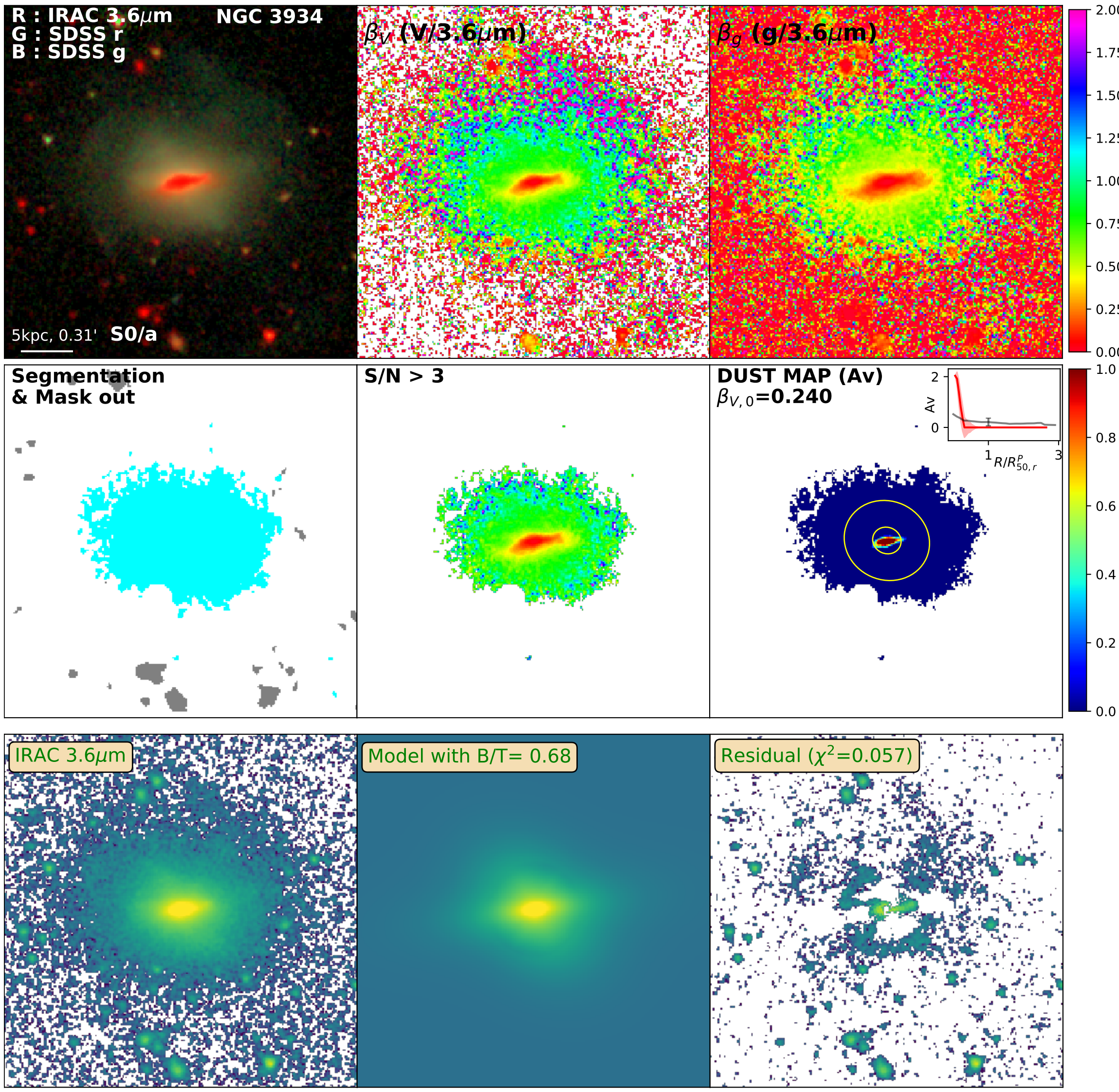

Figure D.126: Same as Figure 3.2 for NGC3934

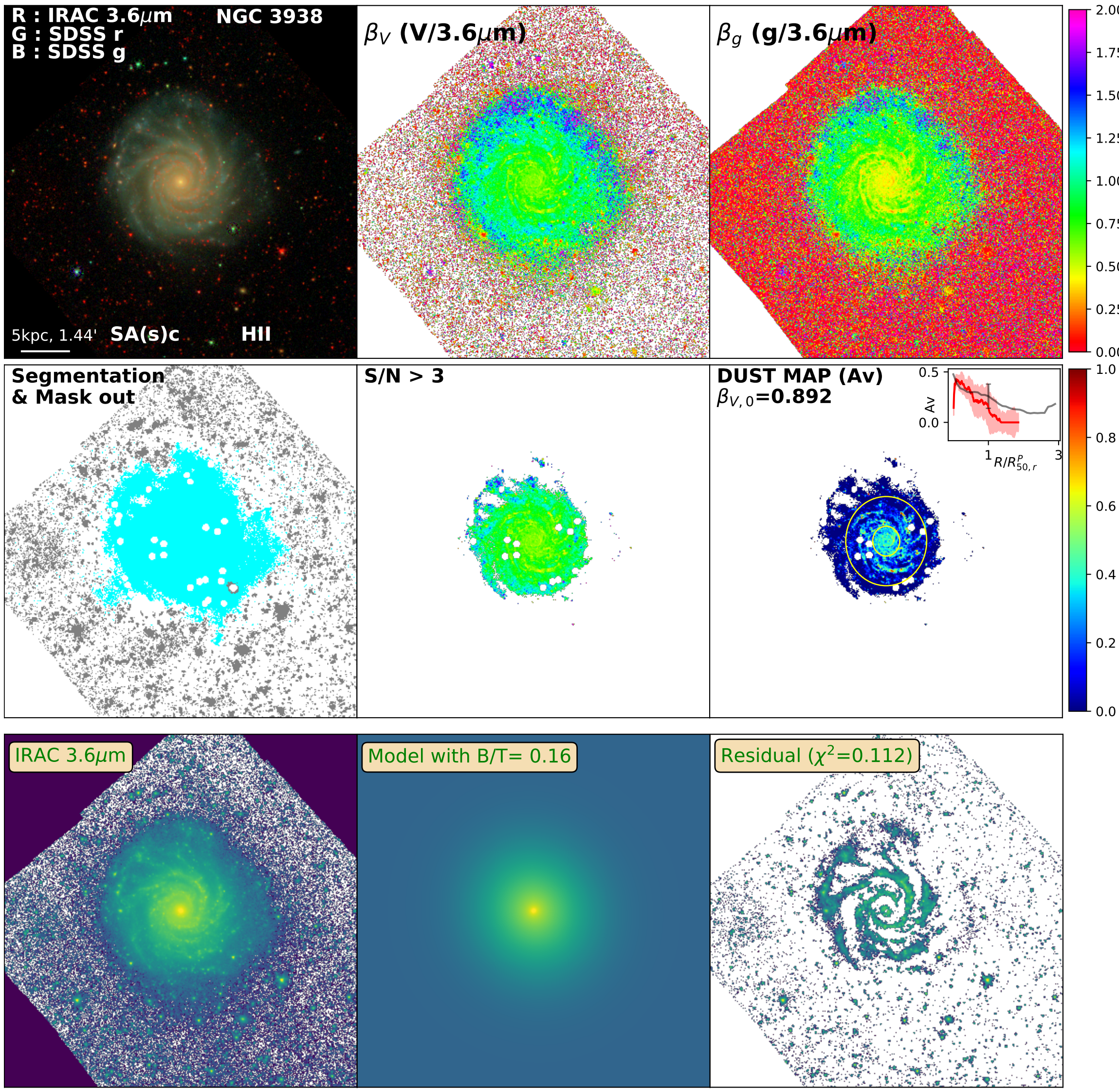

Figure D.127: Same as Figure 3.2 for NGC3938

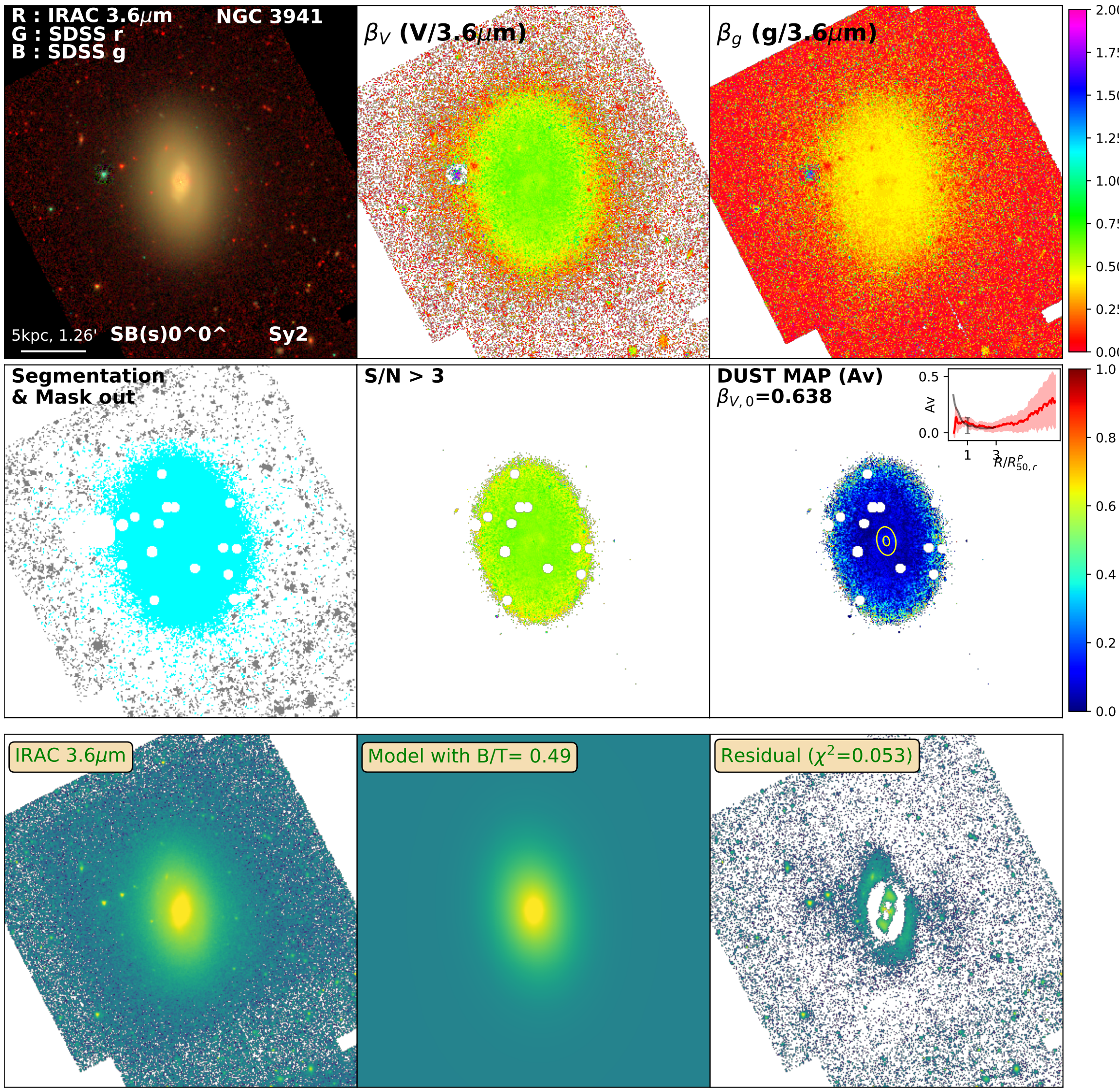

Figure D.128: Same as Figure 3.2 for NGC3941

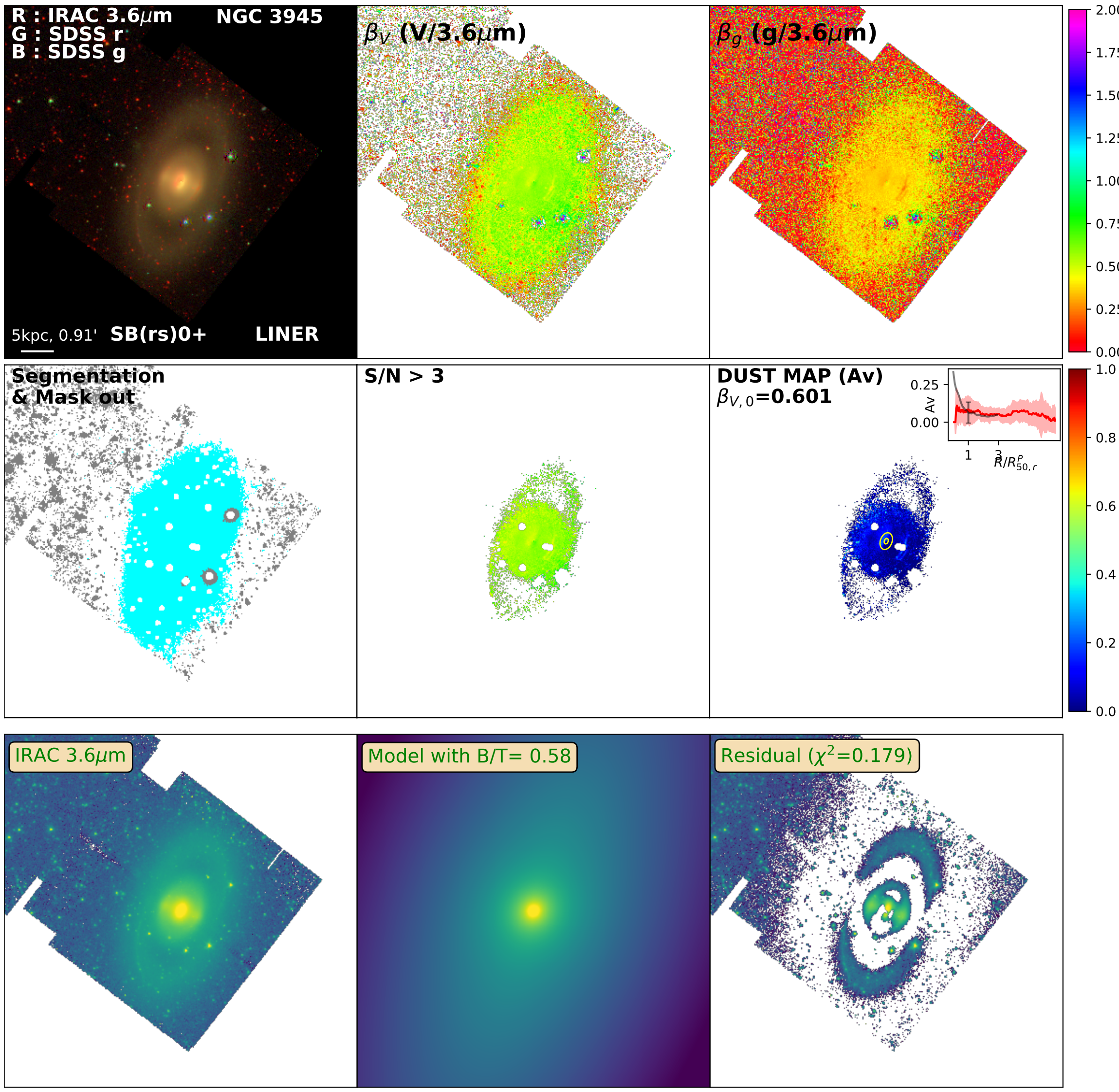

Figure D.129: Same as Figure 3.2 for NGC3945

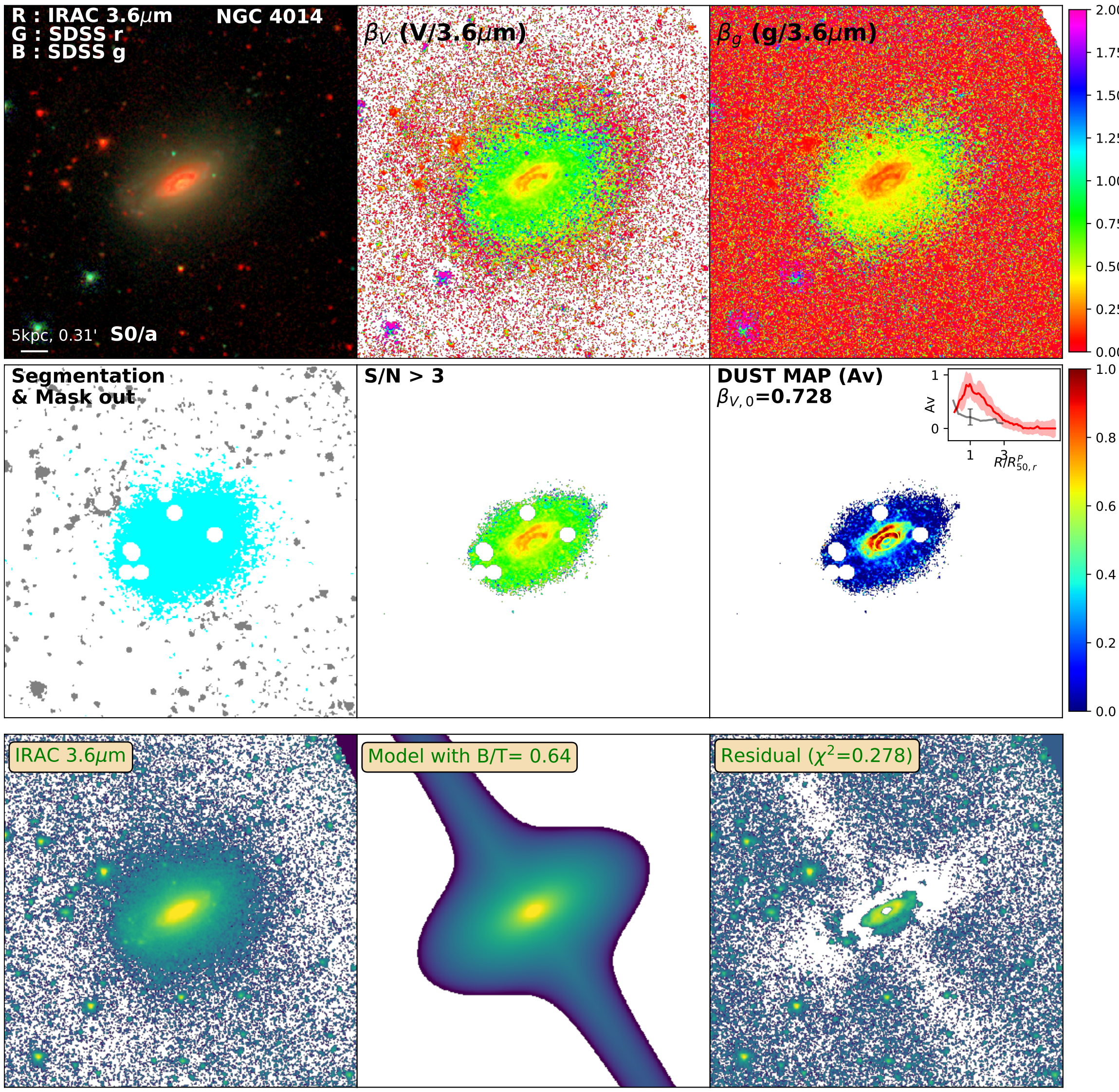

Figure D.130: Same as Figure 3.2 for NGC4014

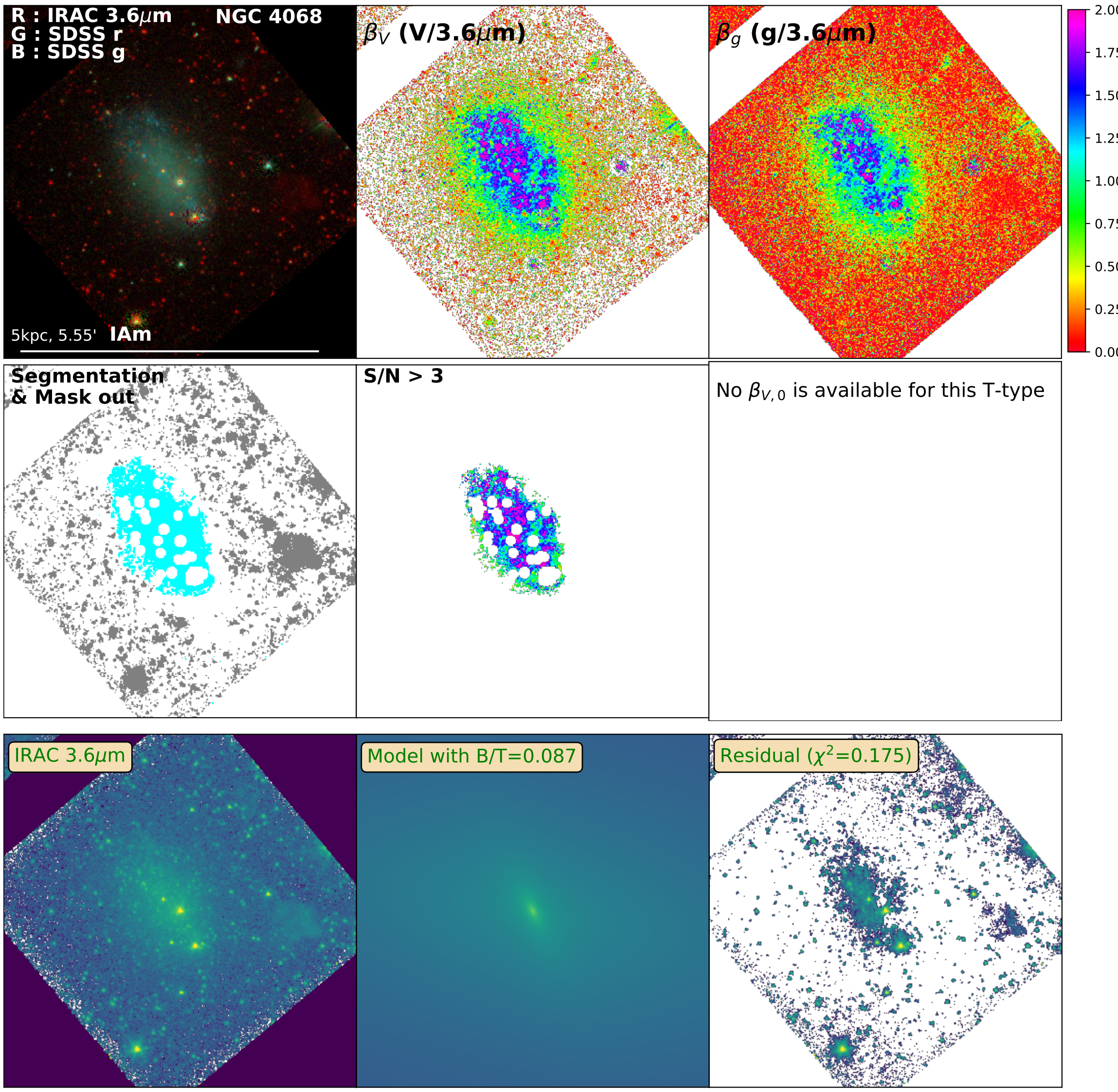

Figure D.131: Same as Figure 3.2 for NGC4068

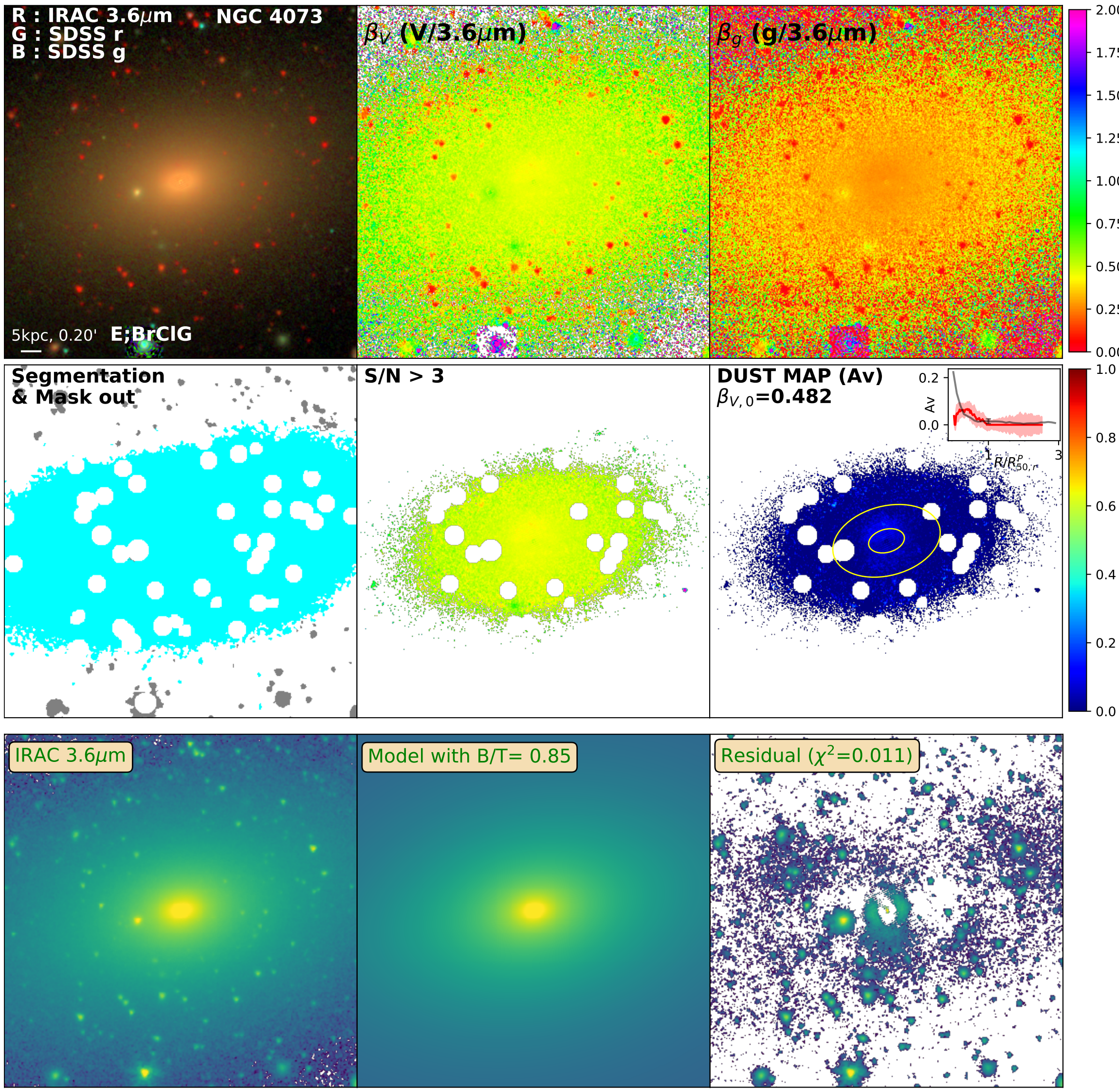

Figure D.132: Same as Figure 3.2 for NGC4073

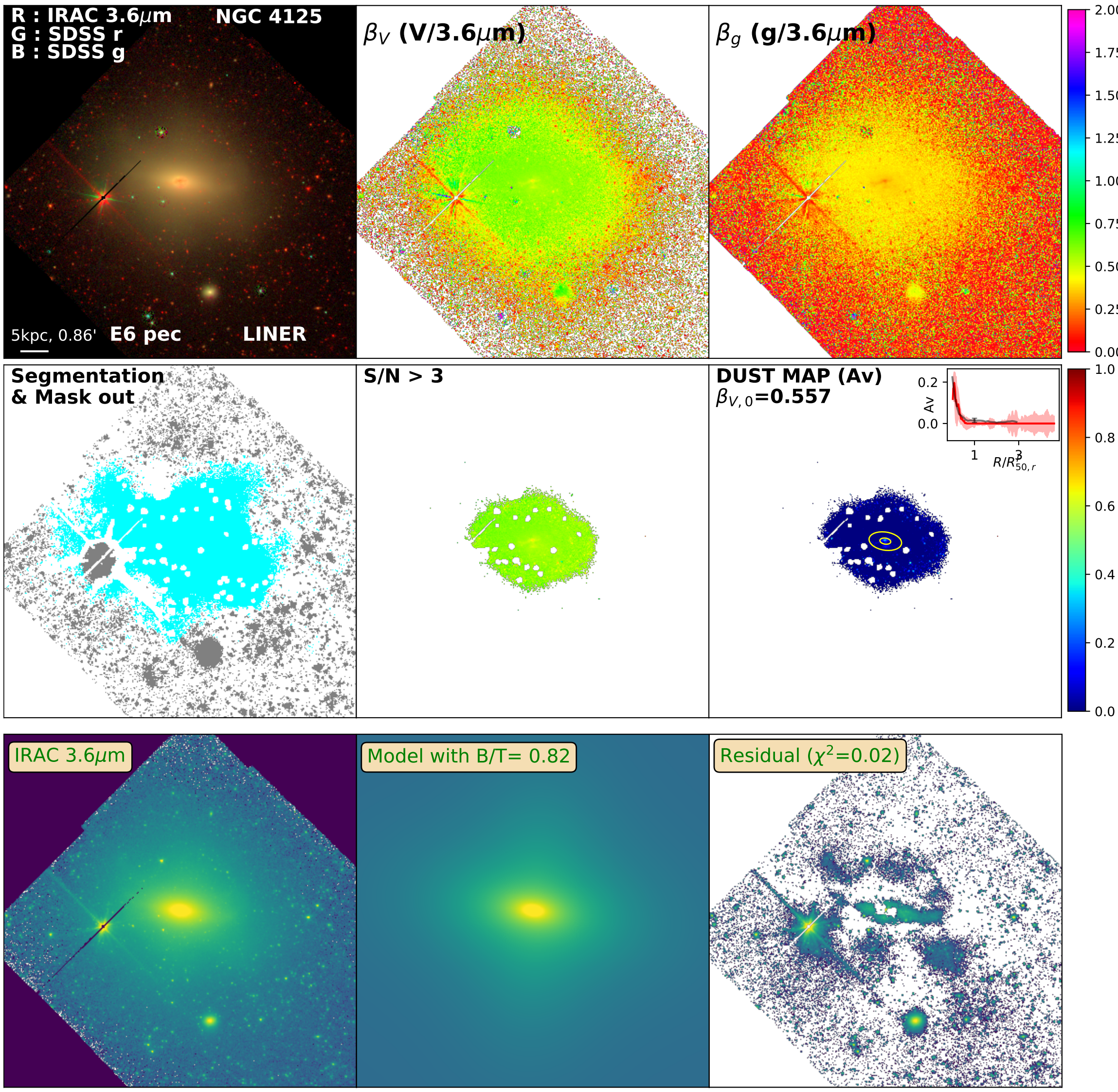

Figure D.133: Same as Figure 3.2 for NGC4125

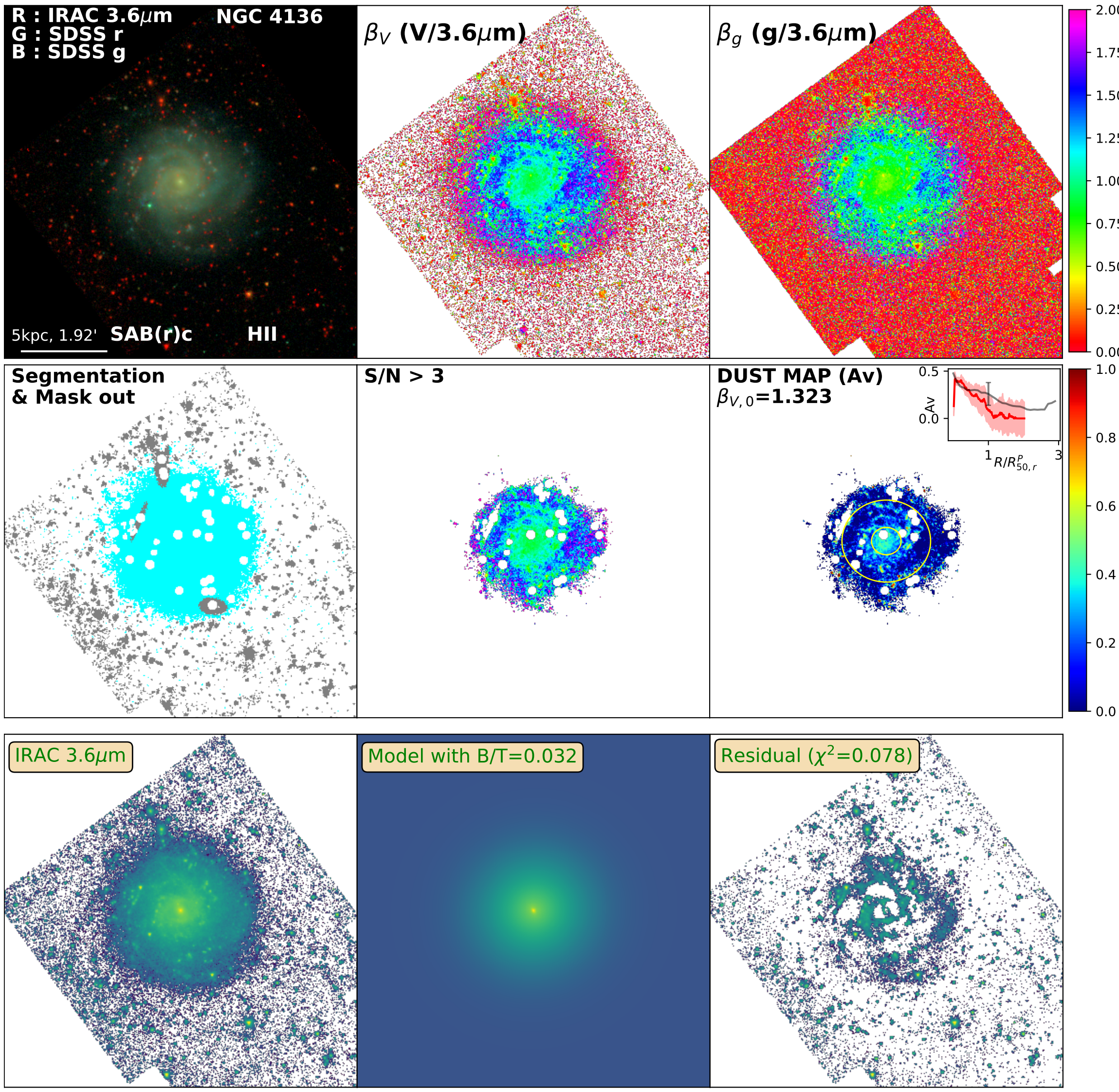

Figure D.134: Same as Figure 3.2 for NGC4136

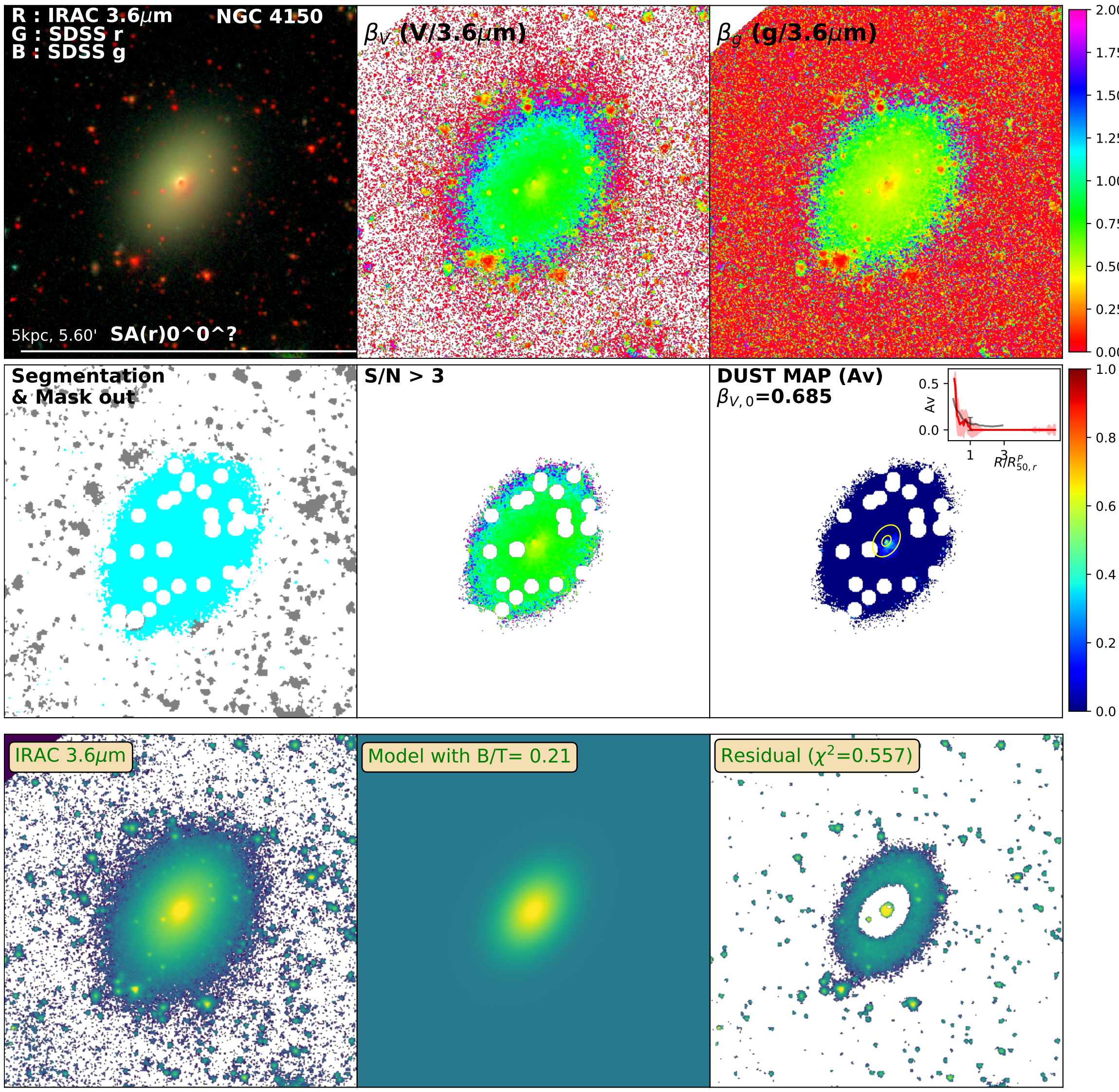

Figure D.135: Same as Figure 3.2 for NGC4150

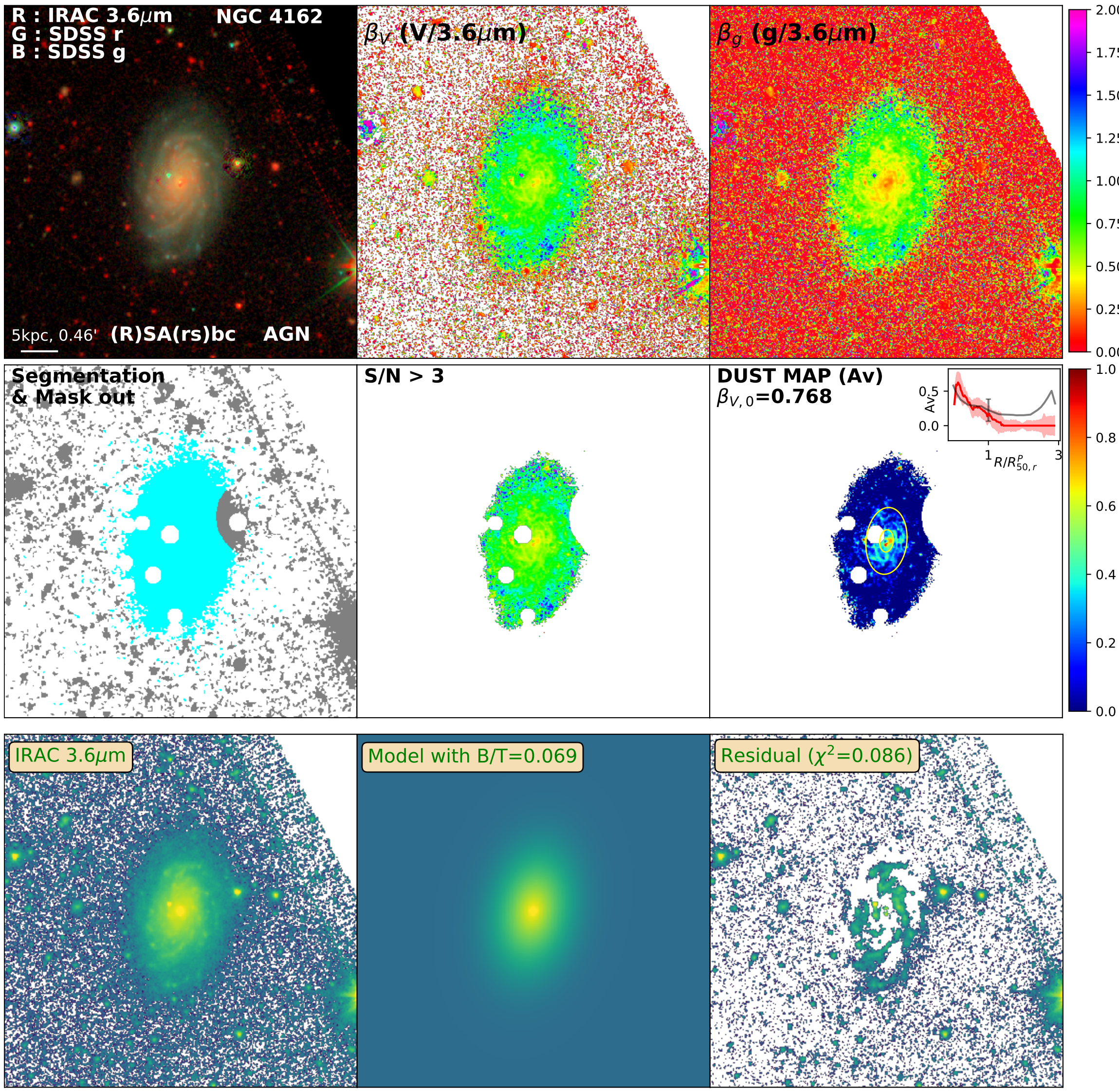

Figure D.136: Same as Figure 3.2 for NGC4162

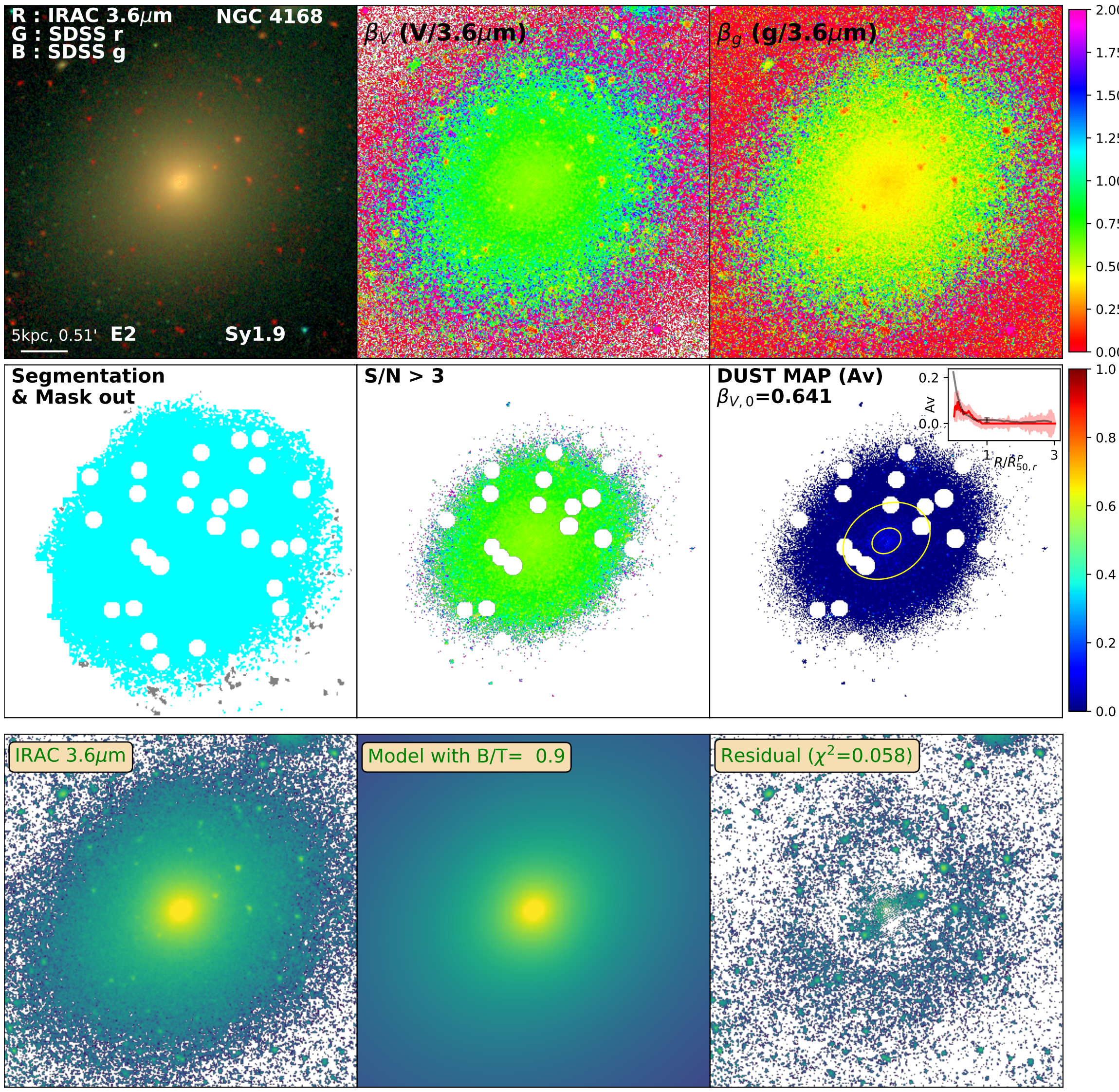

Figure D.137: Same as Figure 3.2 for NGC4168

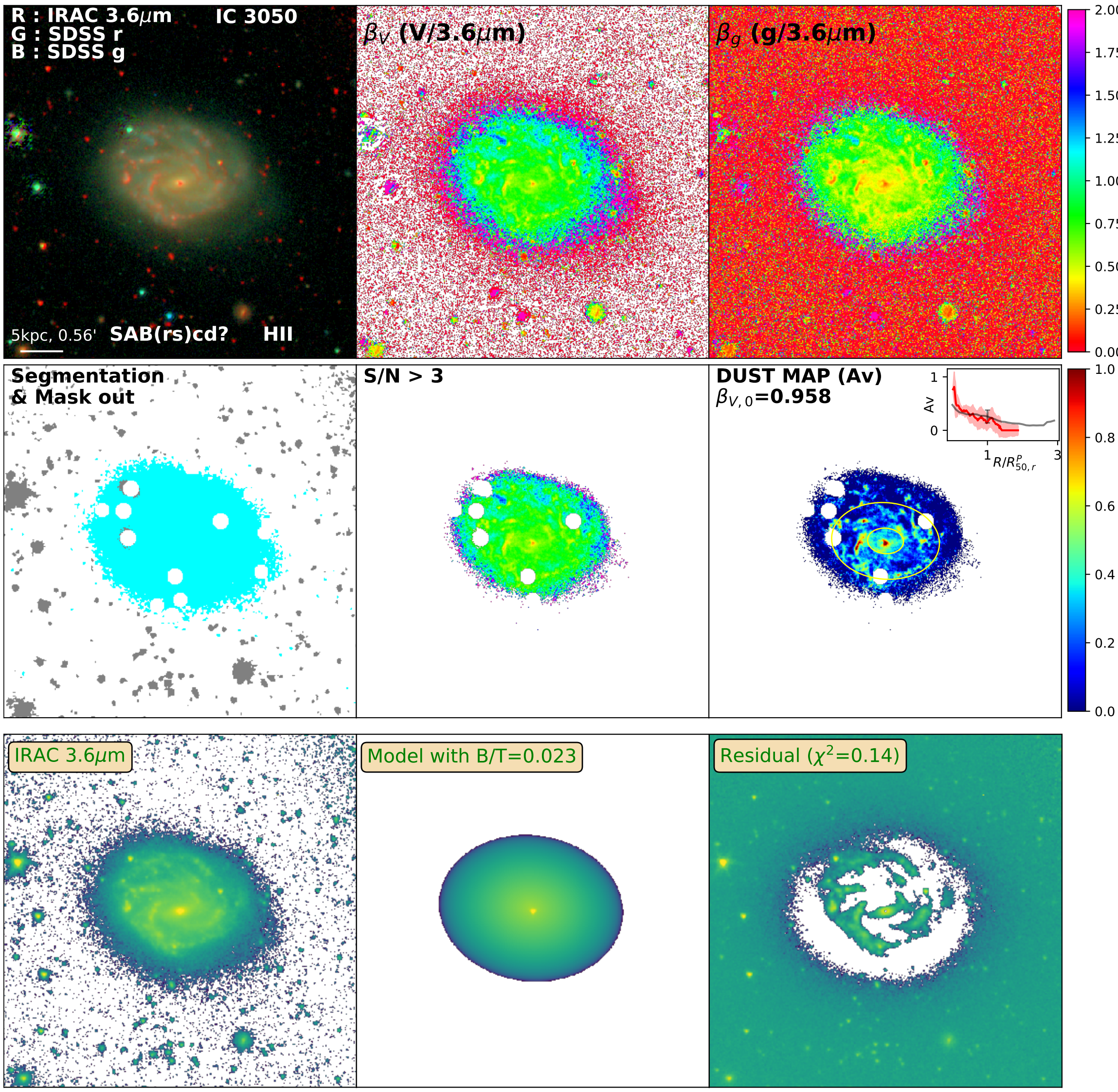

Figure D.138: Same as Figure 3.2 for IC3050

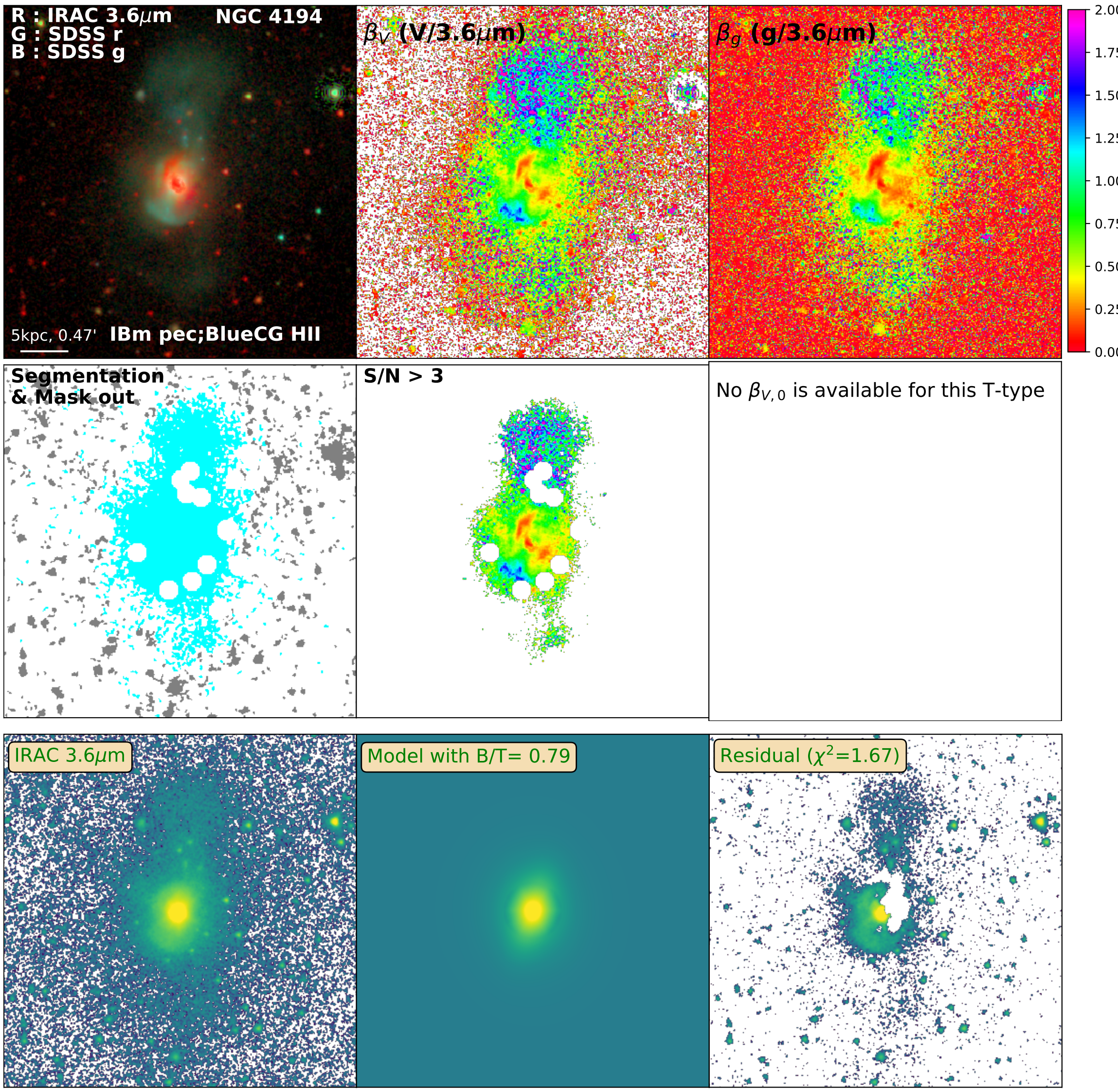

Figure D.139: Same as Figure 3.2 for NGC4194

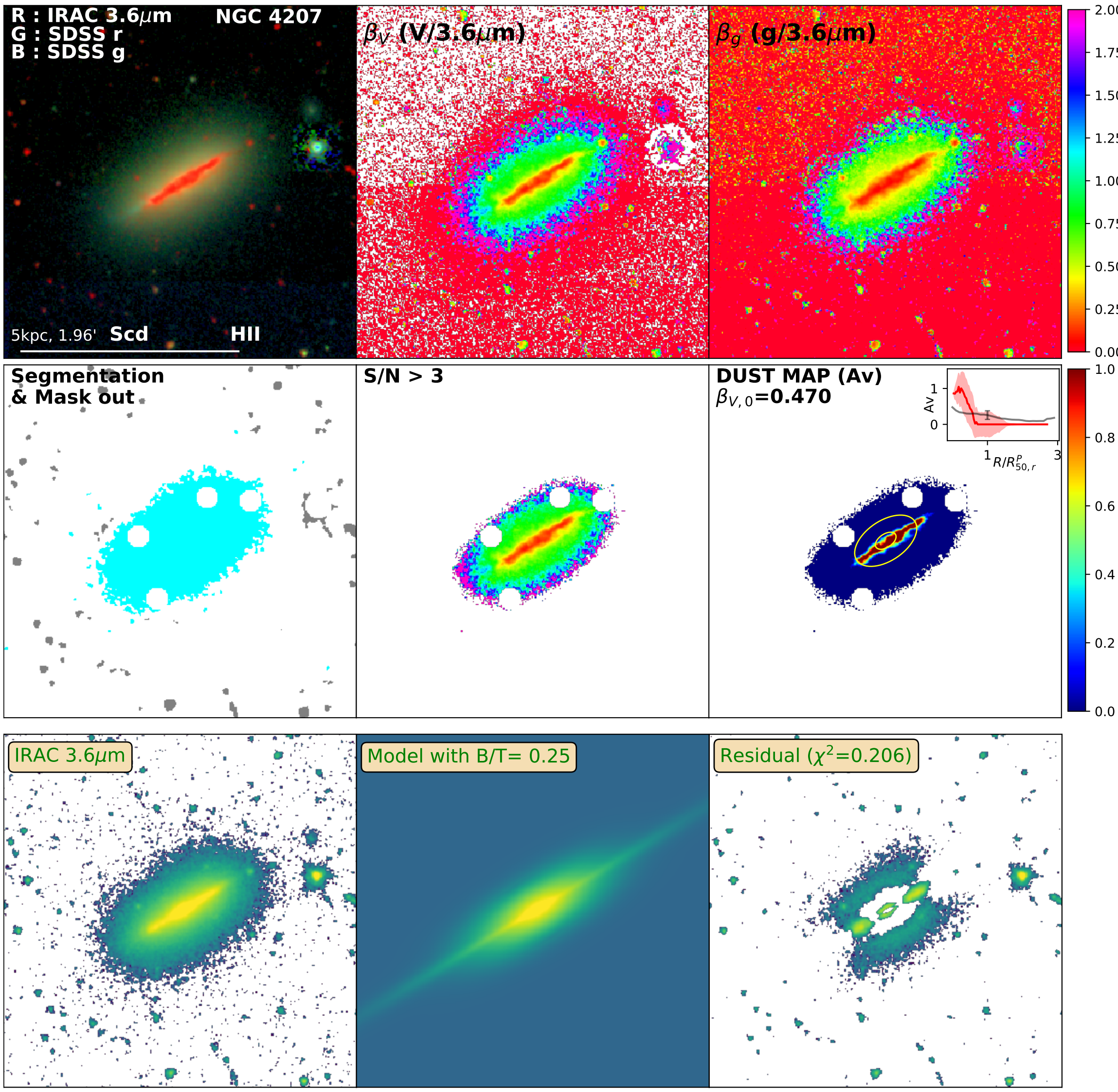

Figure D.140: Same as Figure 3.2 for NGC4207

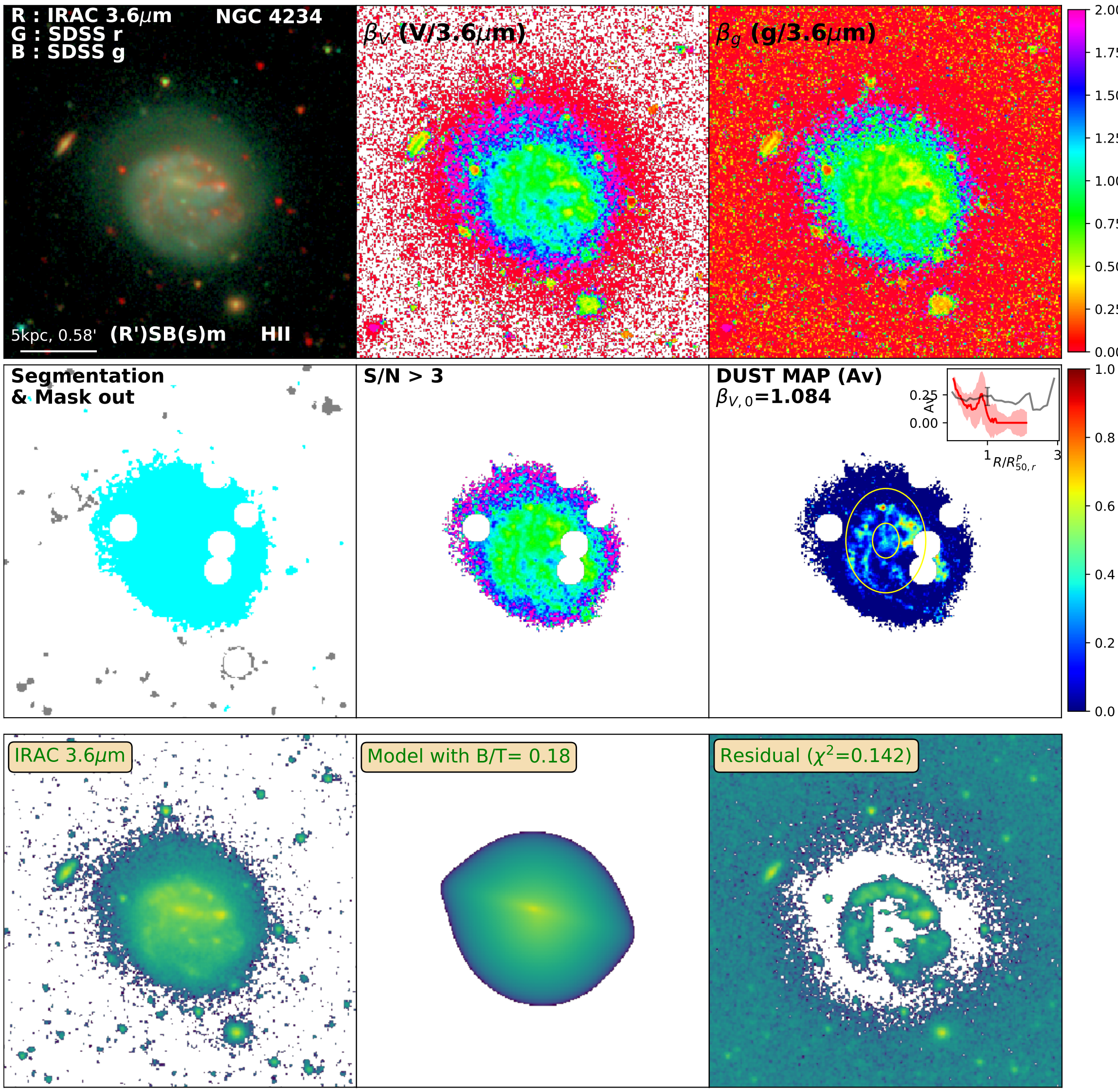

Figure D.141: Same as Figure 3.2 for NGC4234

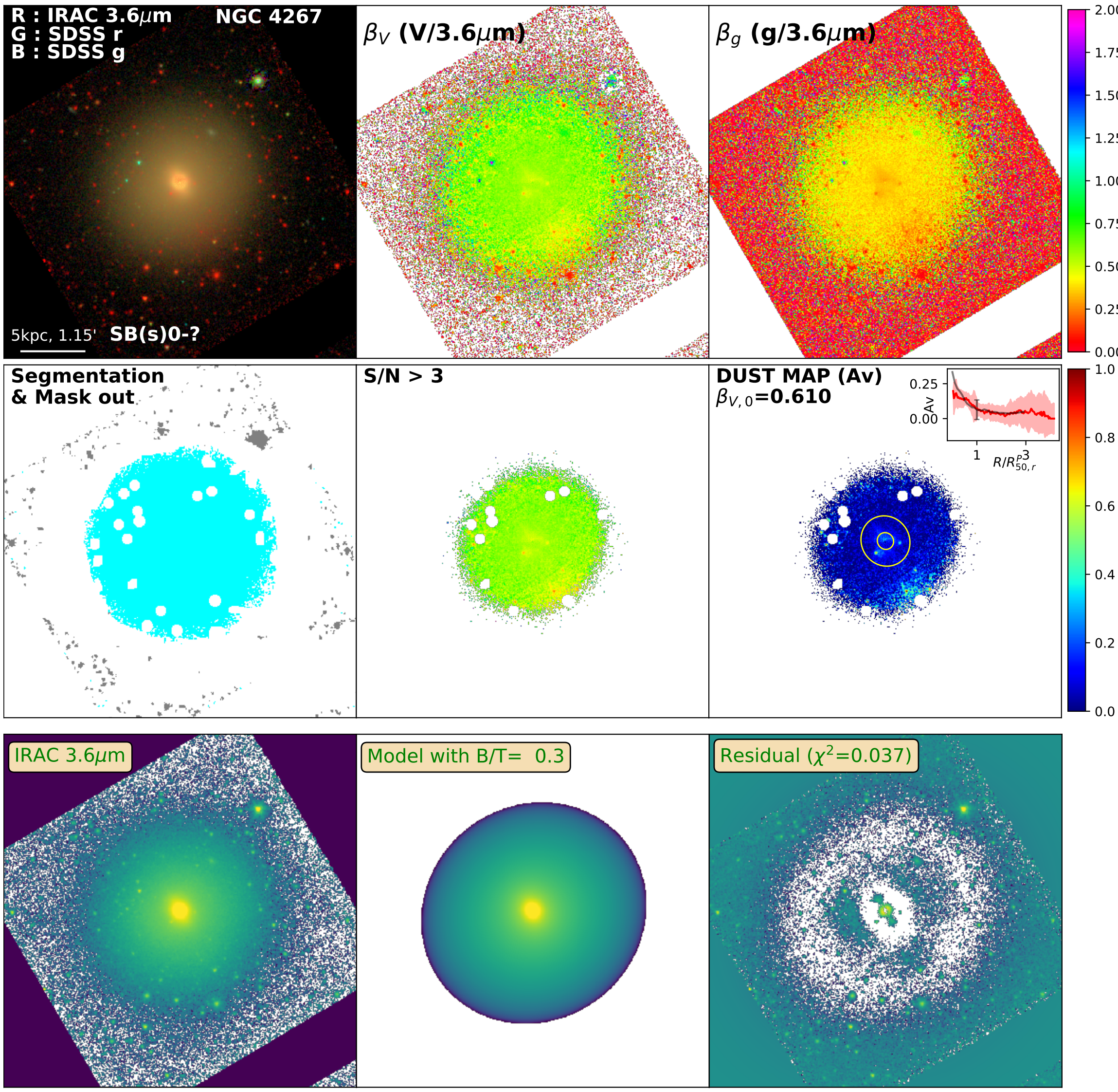

Figure D.142: Same as Figure 3.2 for NGC4267

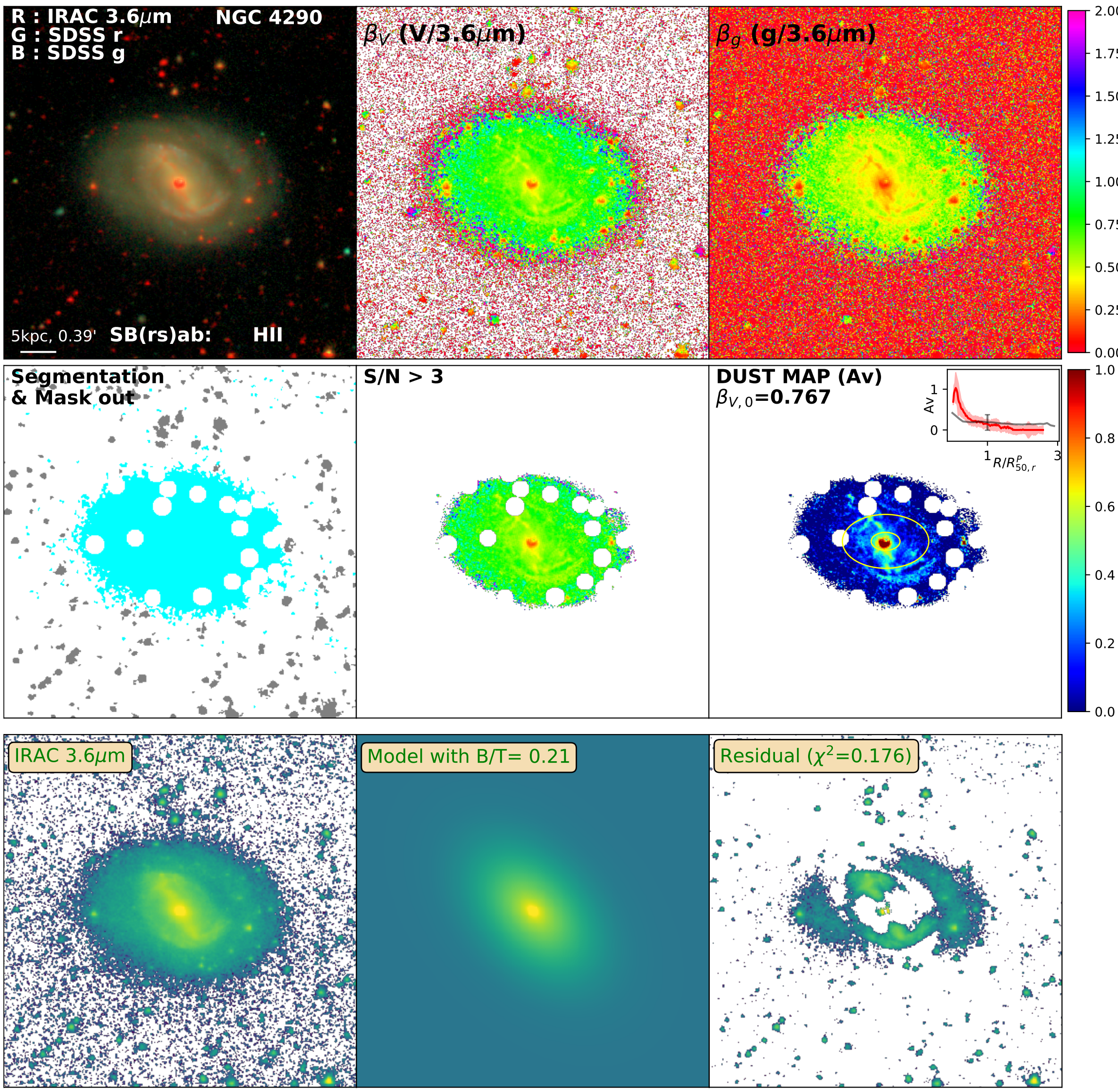

Figure D.143: Same as Figure 3.2 for NGC4290

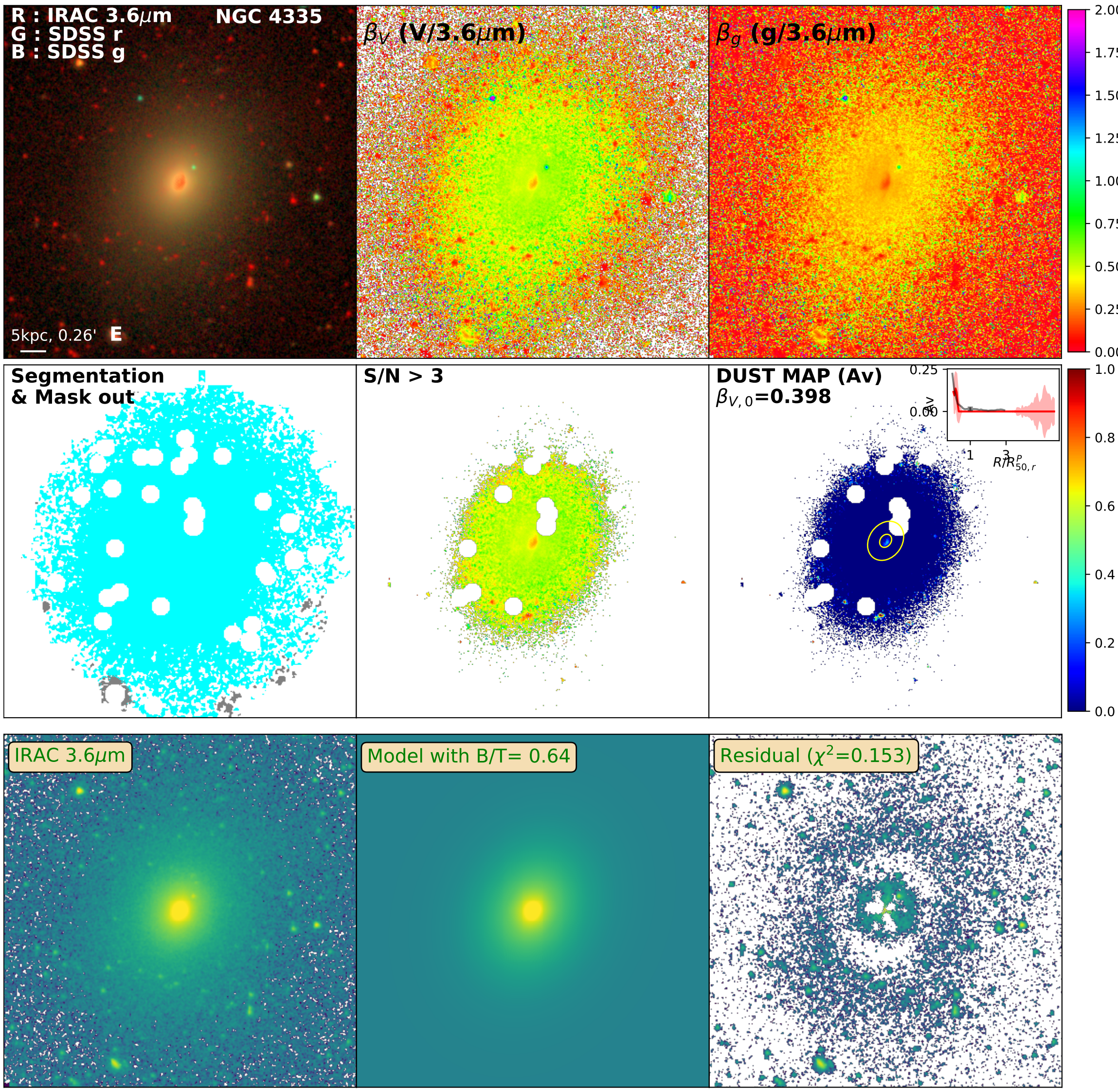

Figure D.144: Same as Figure 3.2 for NGC4335

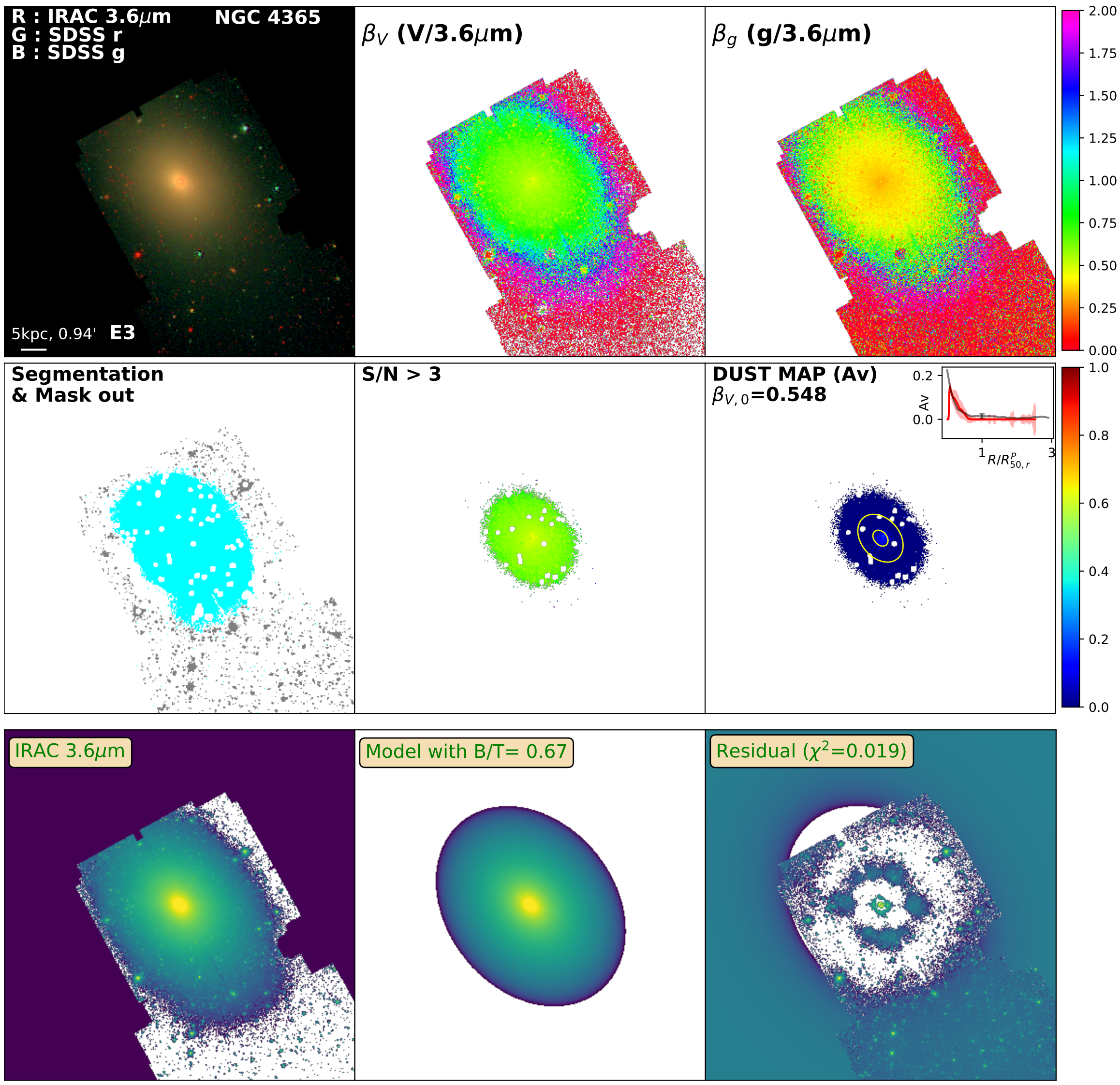

Figure D.145: Same as Figure 3.2 for NGC4365

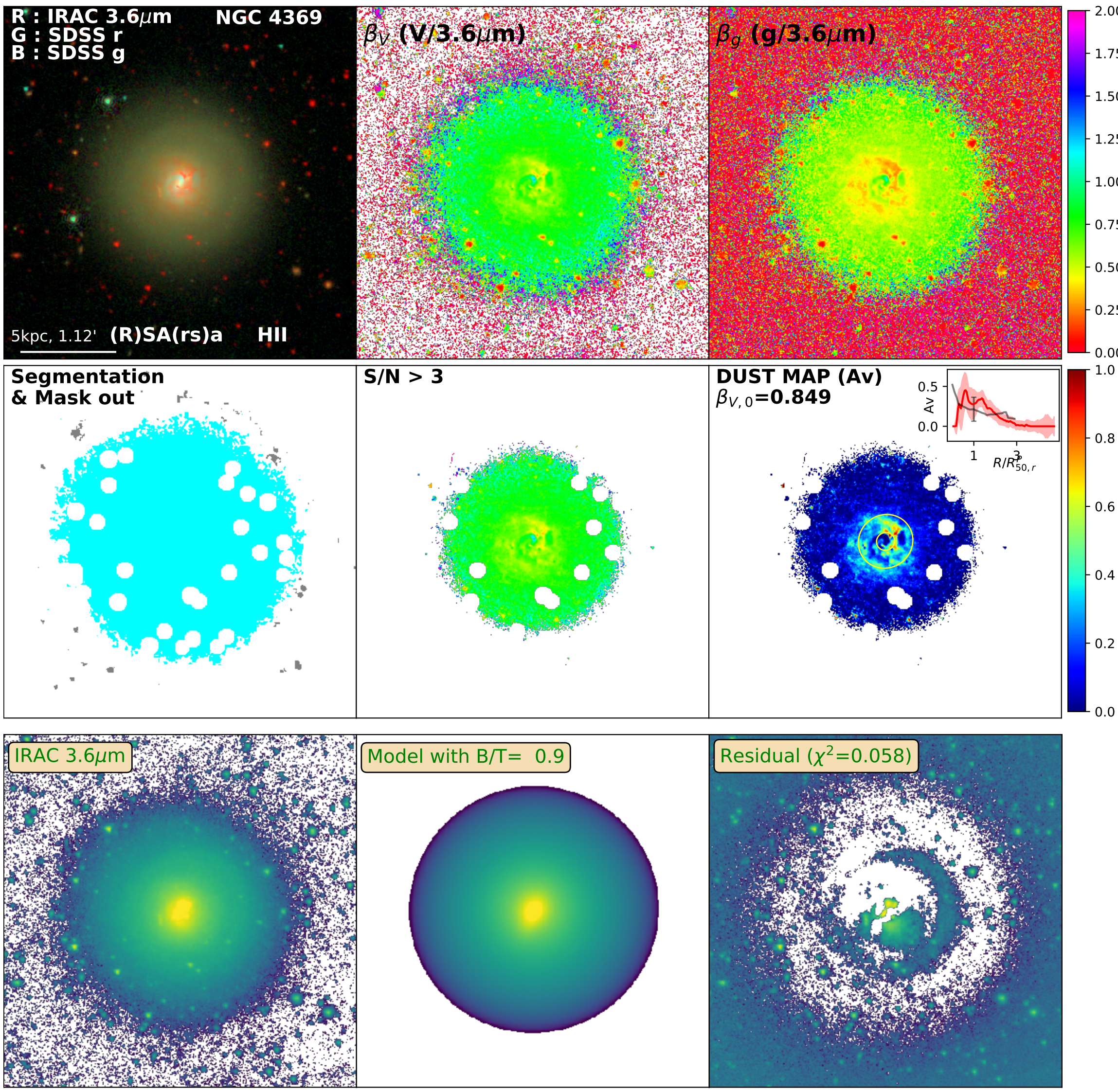

Figure D.146: Same as Figure 3.2 for NGC4369

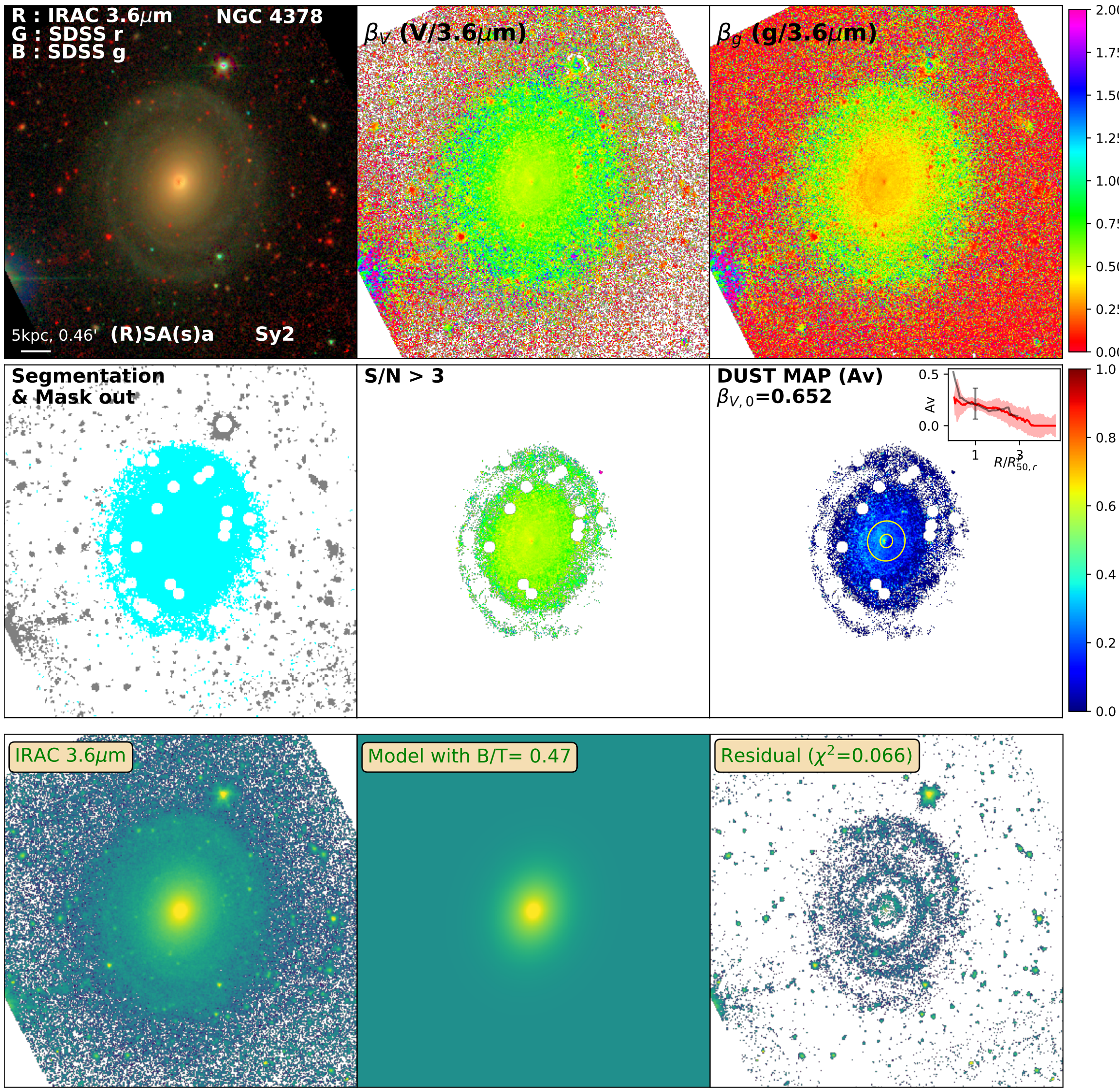

Figure D.147: Same as Figure 3.2 for NGC4378

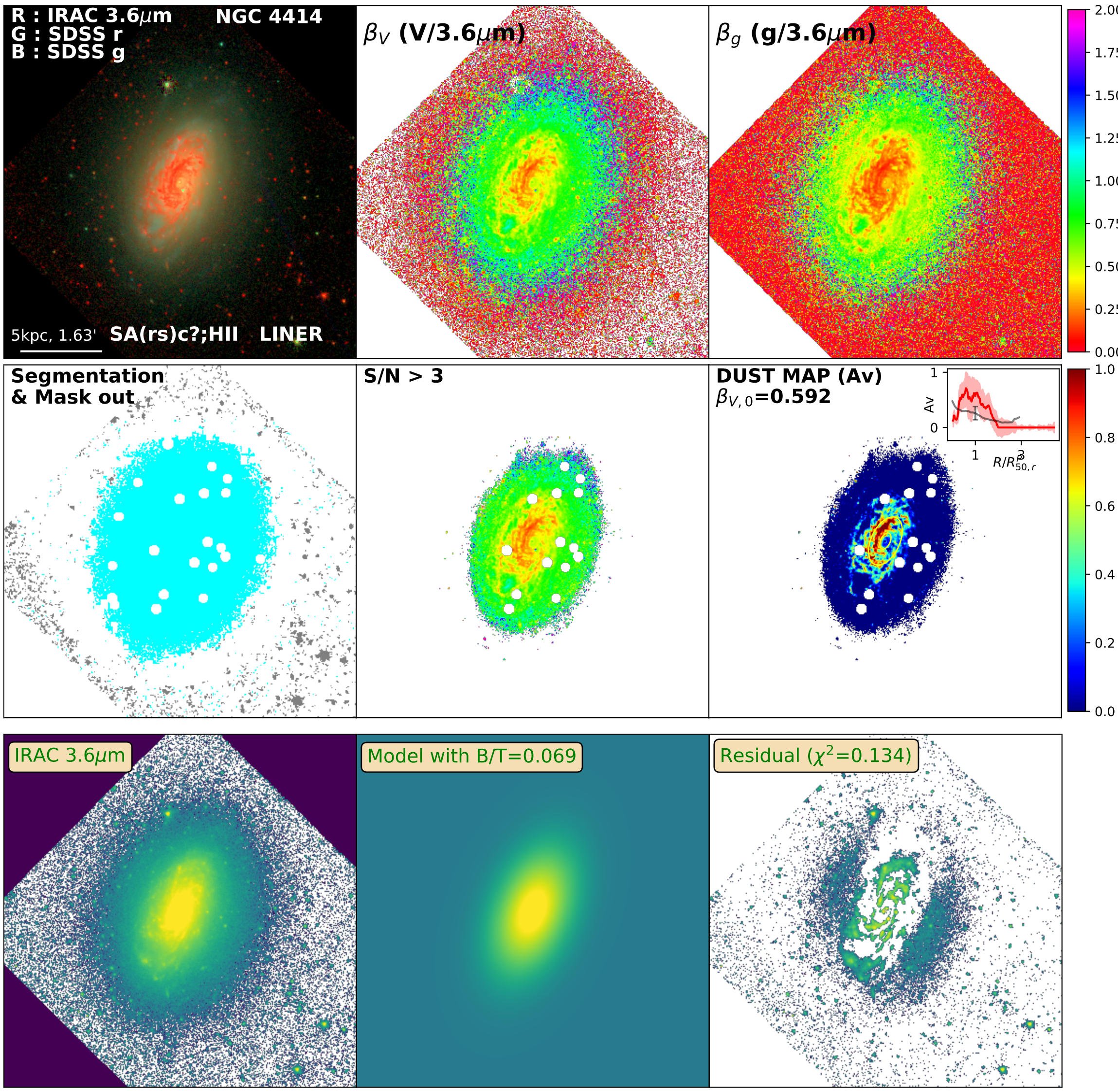

Figure D.148: Same as Figure 3.2 for NGC4414

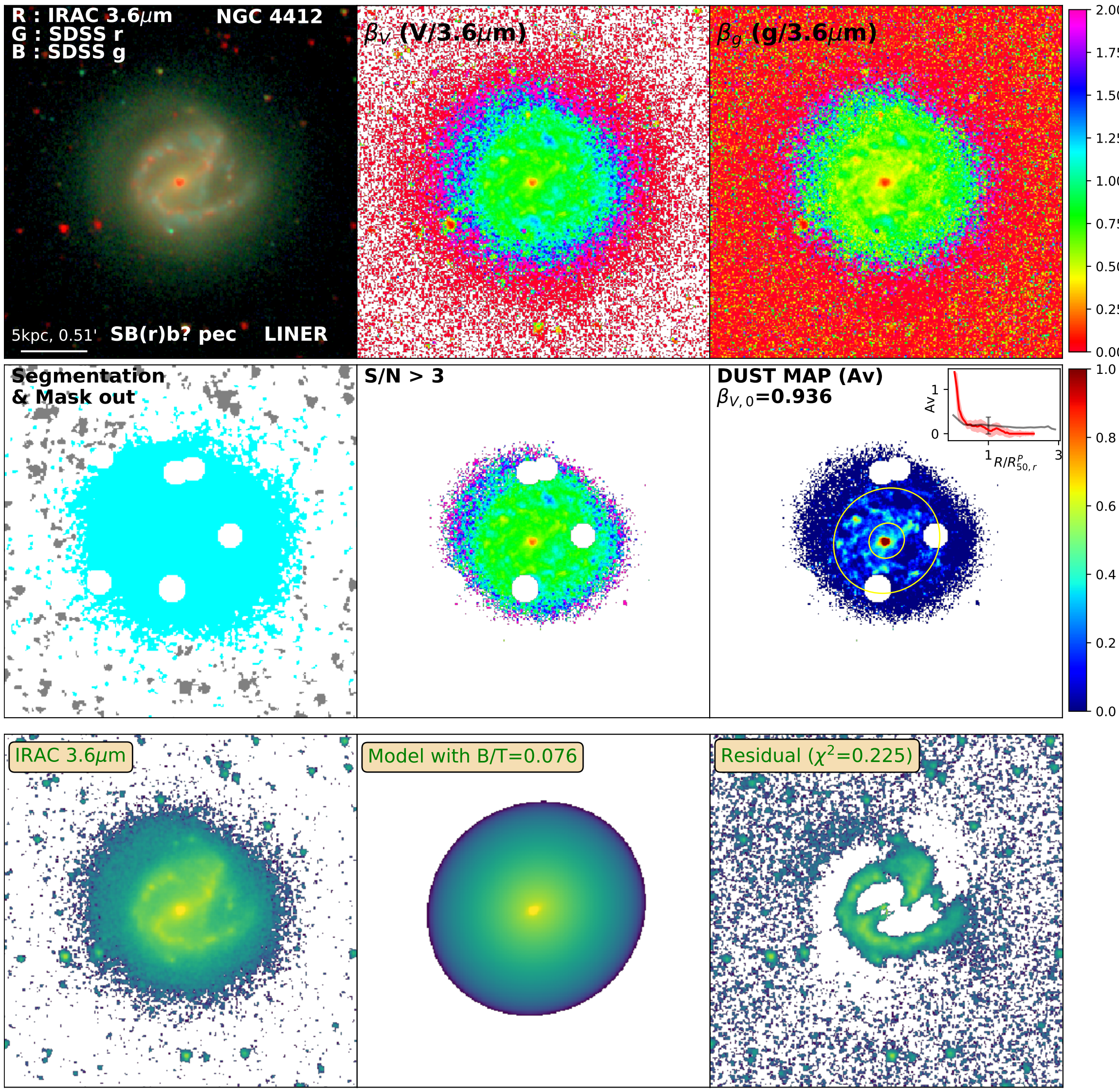

Figure D.149: Same as Figure 3.2 for NGC4412

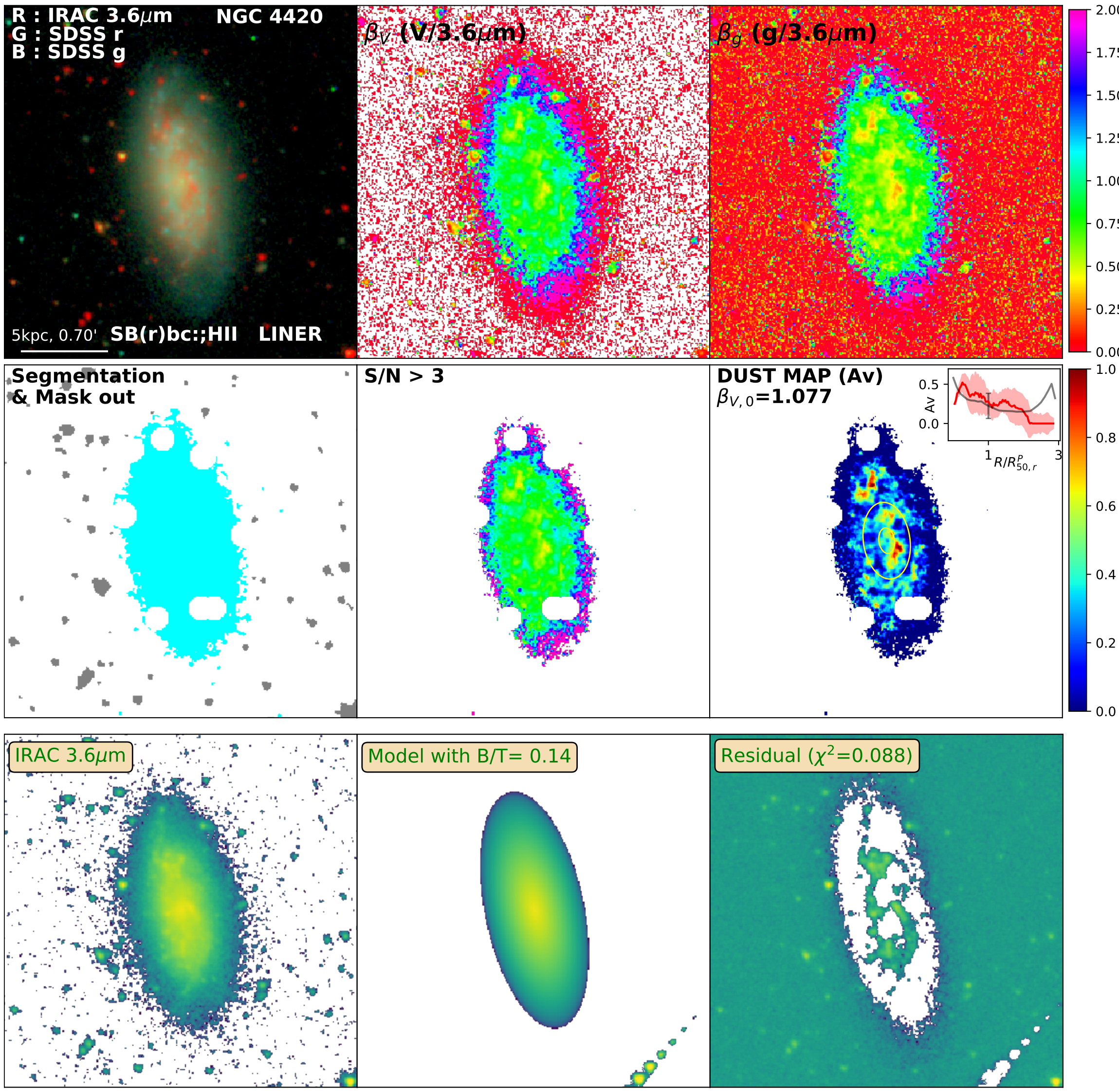

Figure D.150: Same as Figure 3.2 for NGC4420

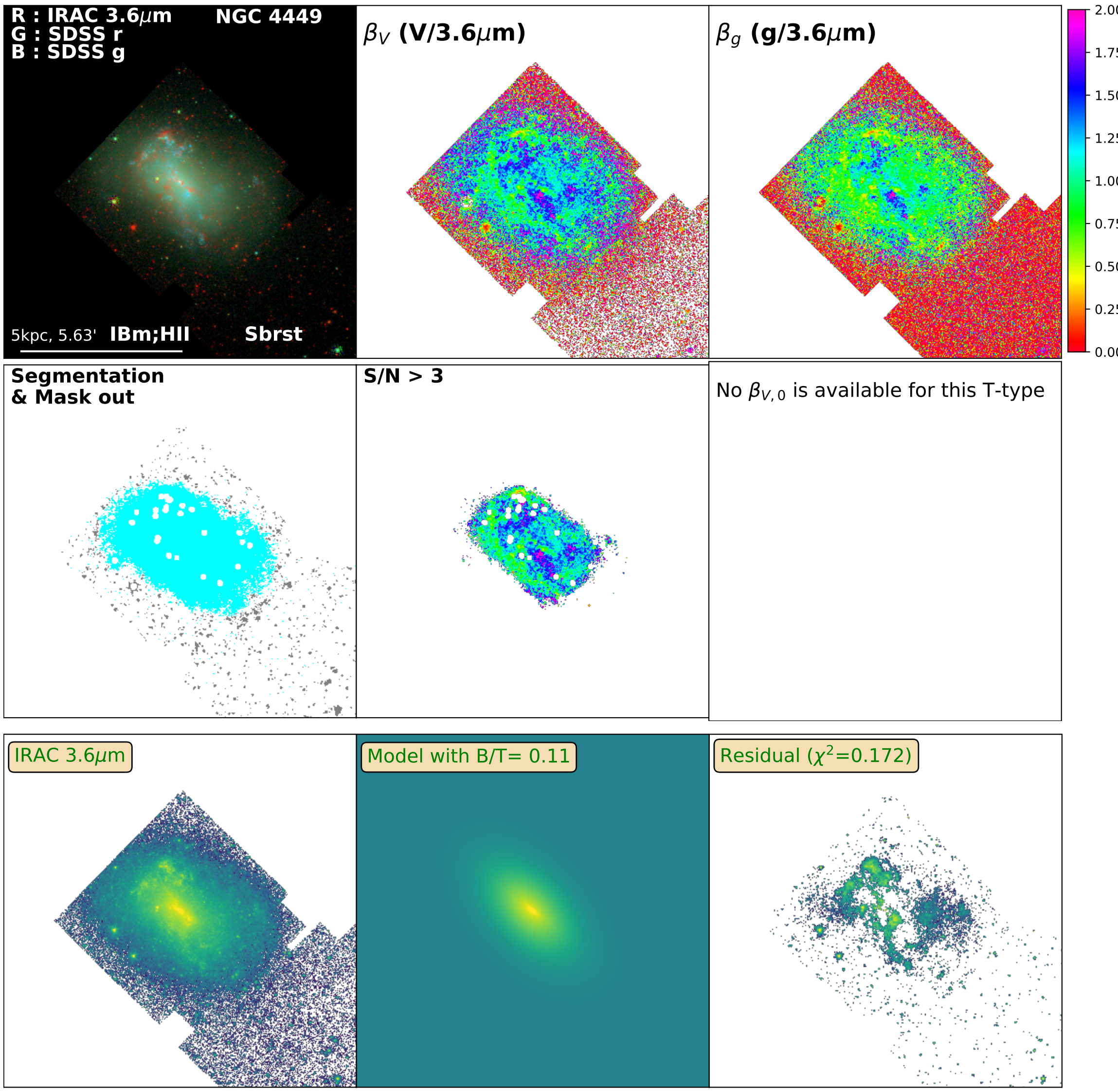

Figure D.151: Same as Figure 3.2 for NGC4449

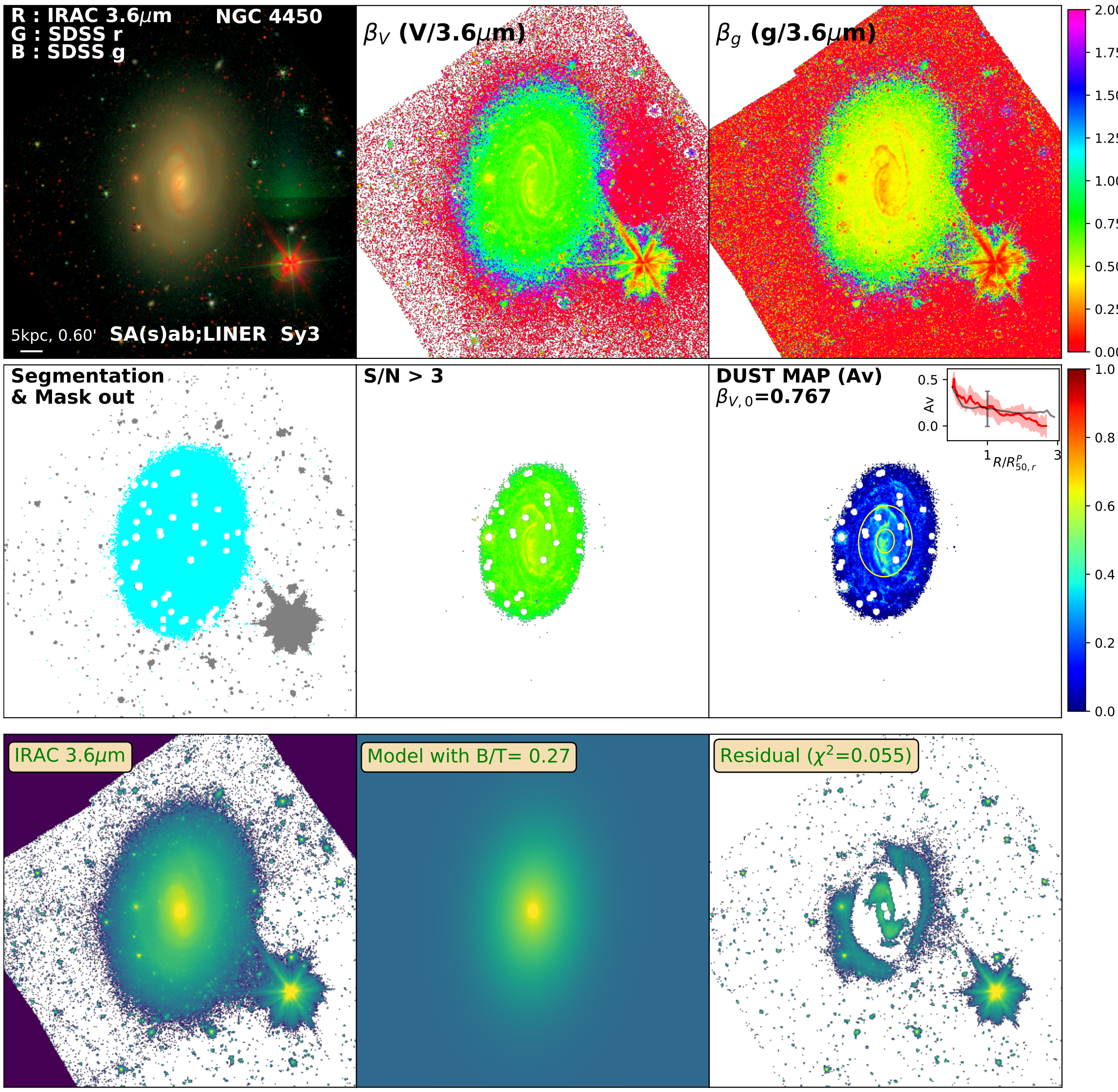

Figure D.152: Same as Figure 3.2 for NGC4450

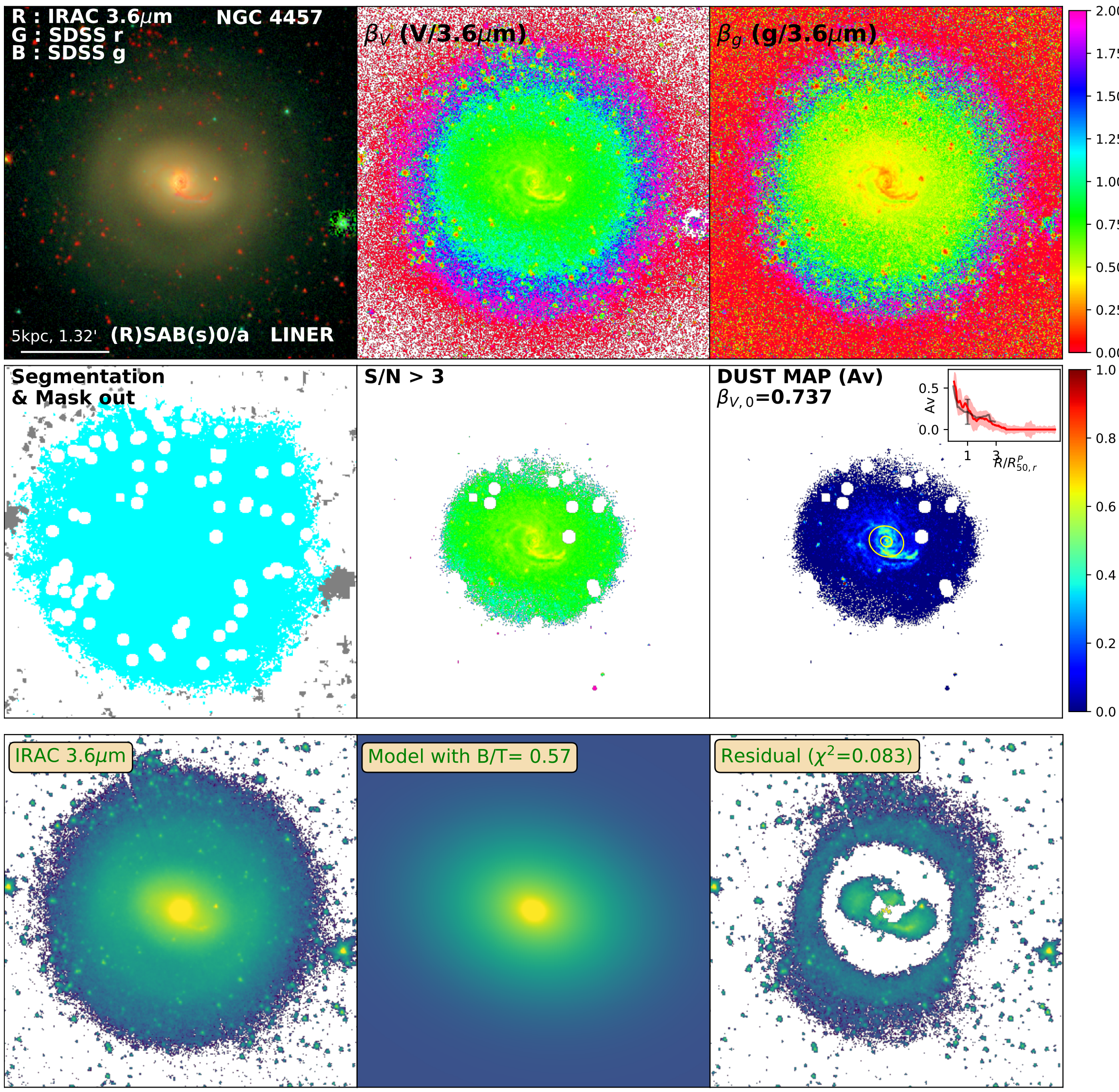

Figure D.153: Same as Figure 3.2 for NGC4457

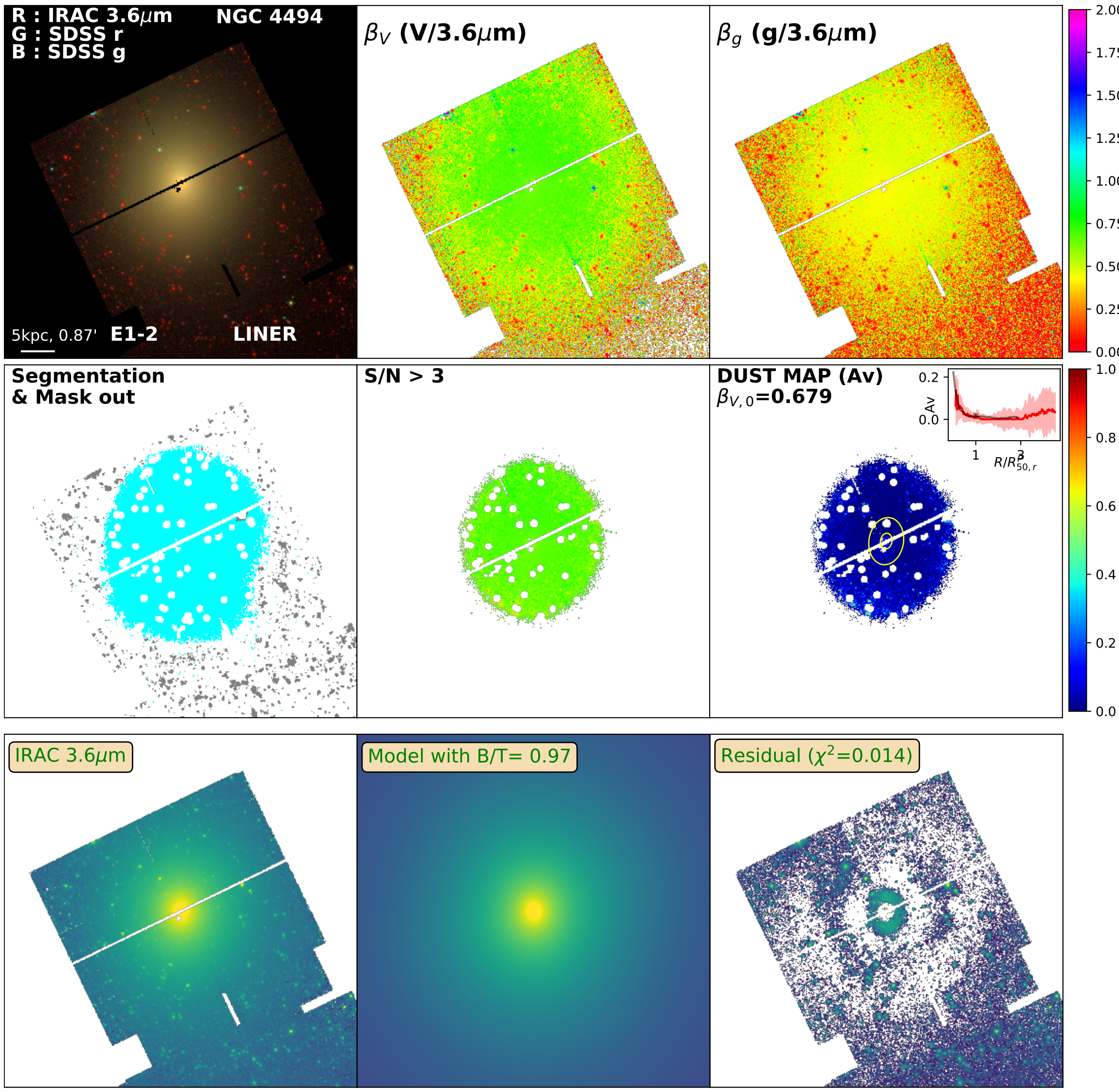

Figure D.154: Same as Figure 3.2 for NGC4494

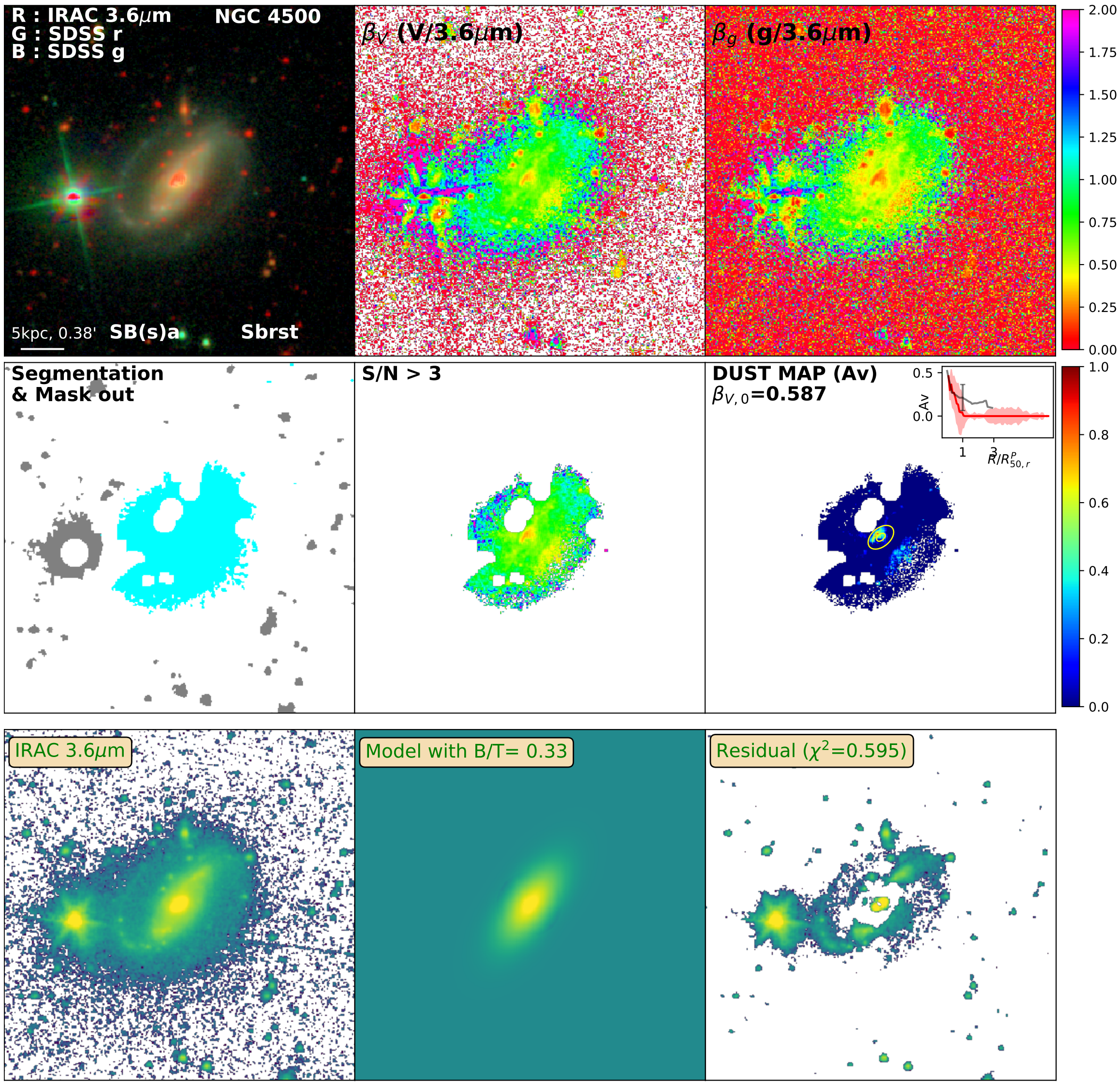

Figure D.155: Same as Figure 3.2 for NGC4500

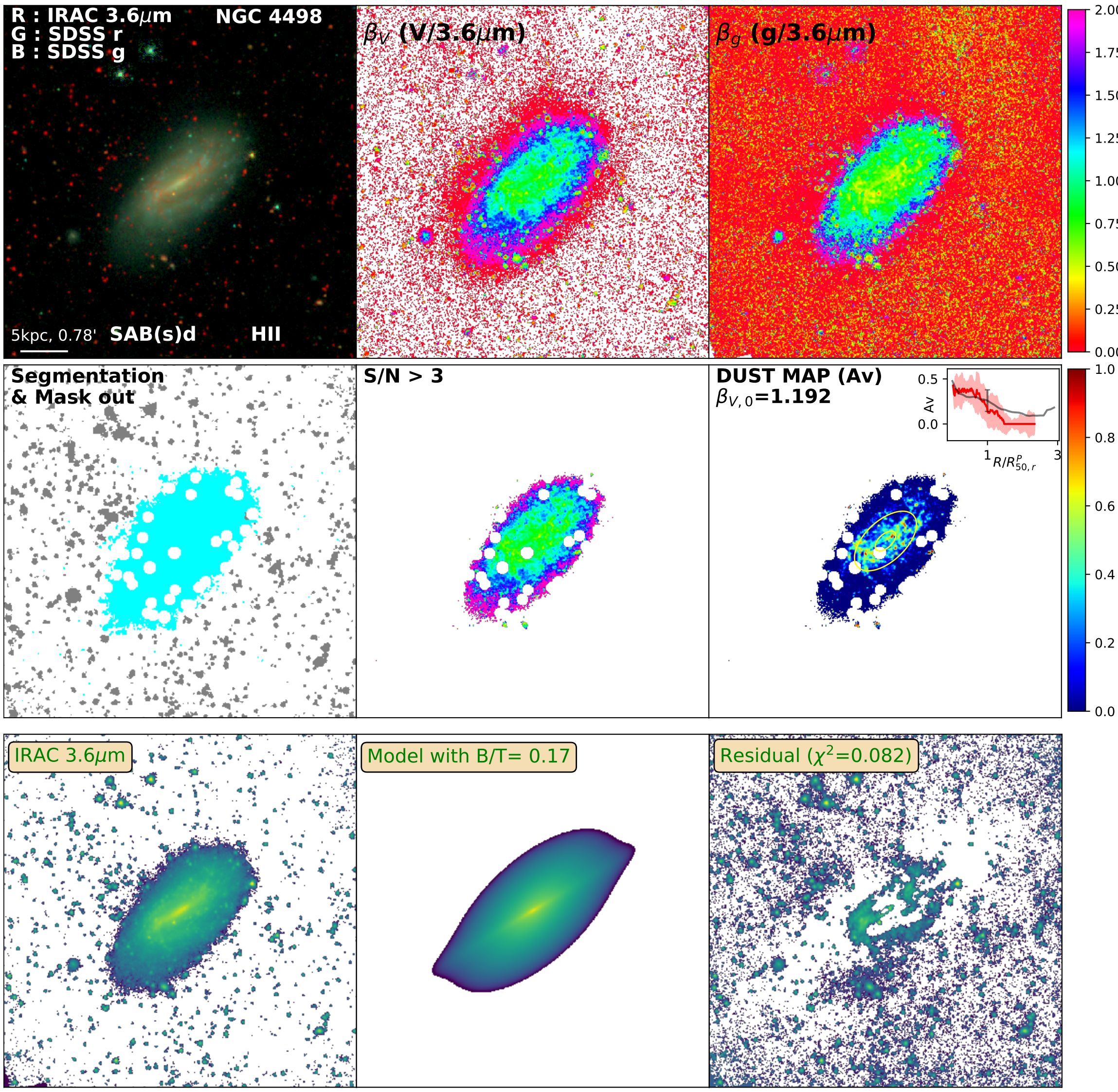

Figure D.156: Same as Figure 3.2 for NGC4498

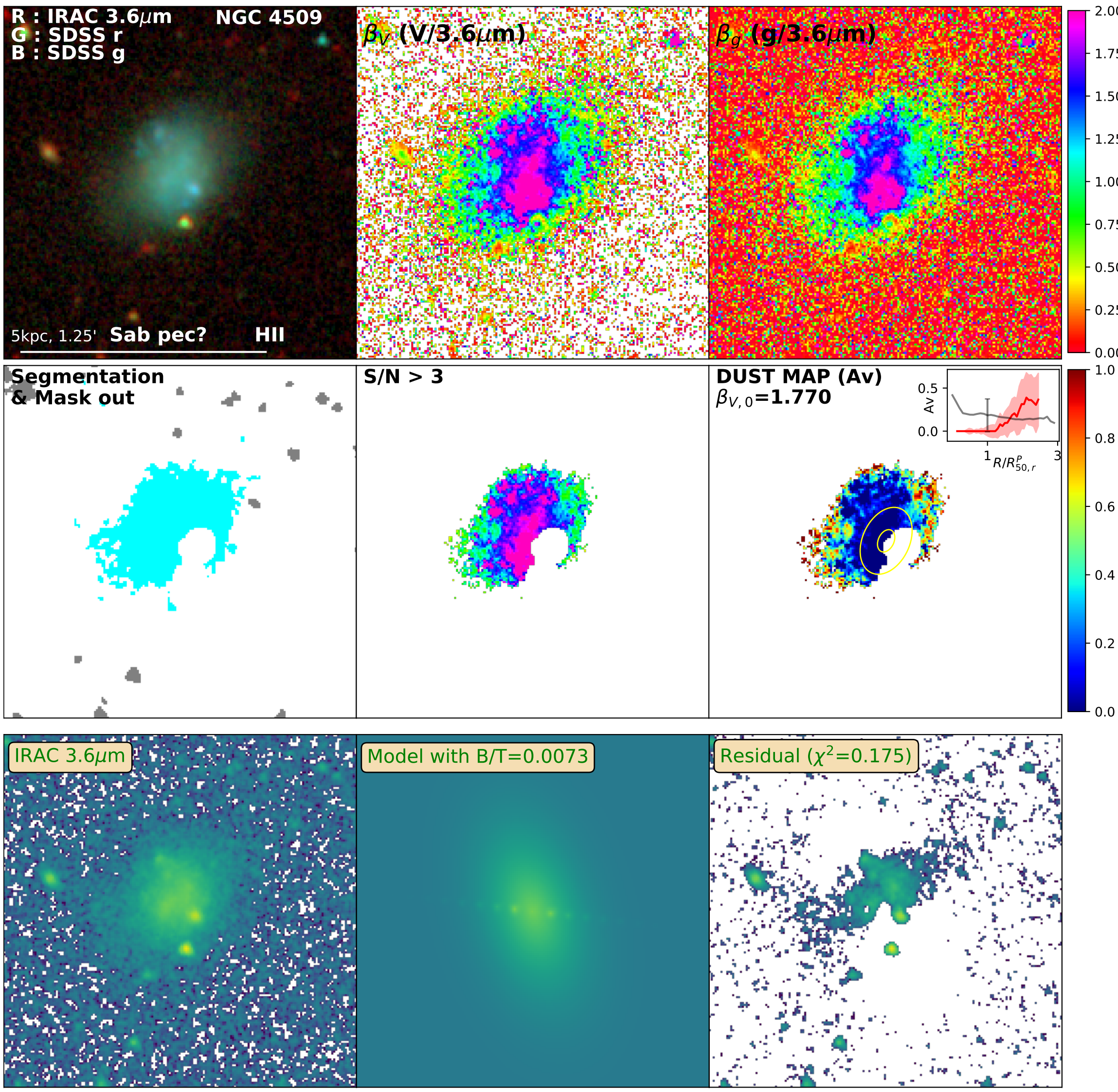

Figure D.157: Same as Figure 3.2 for NGC4509

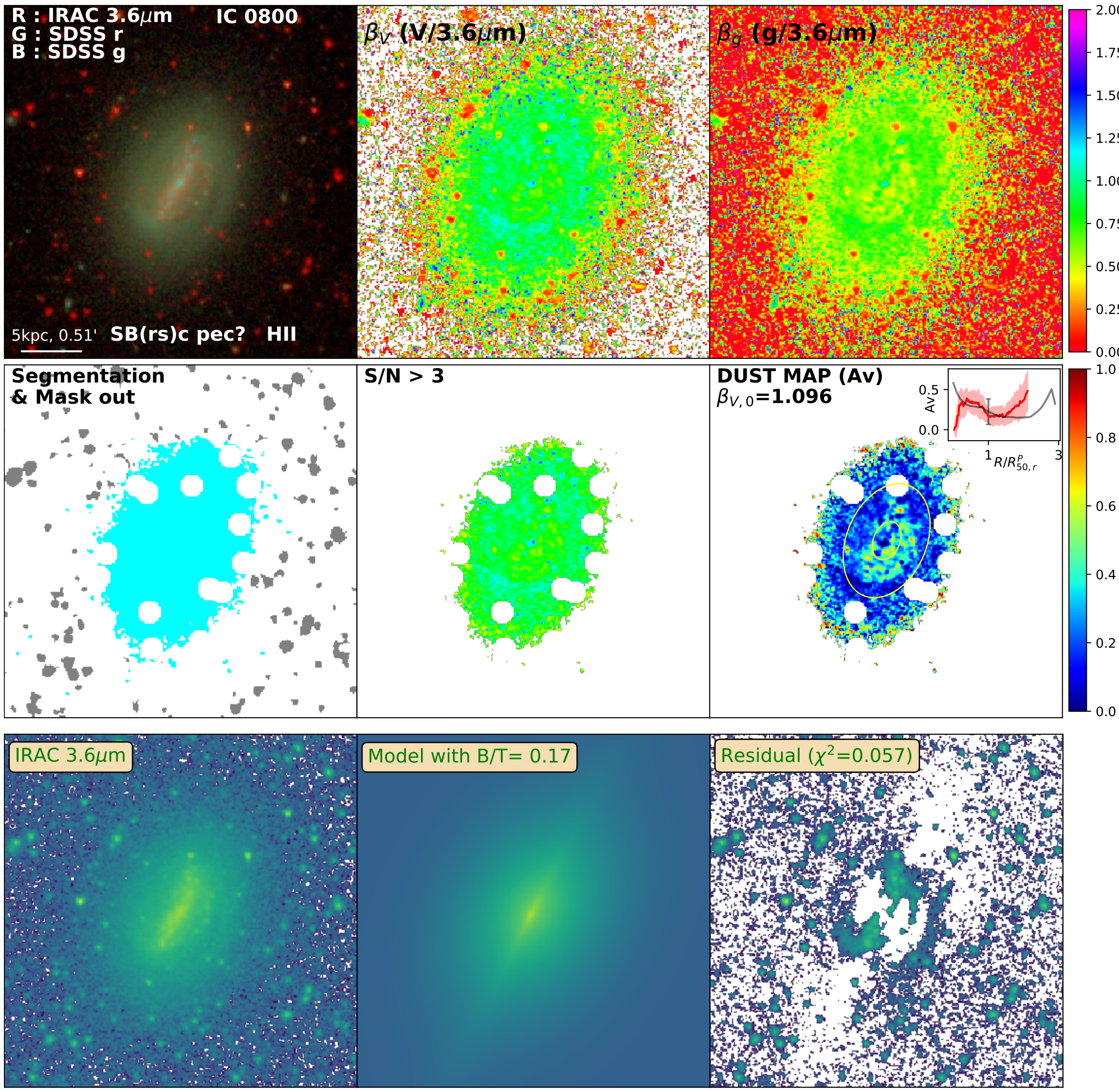

Figure D.158: Same as Figure 3.2 for IC0800

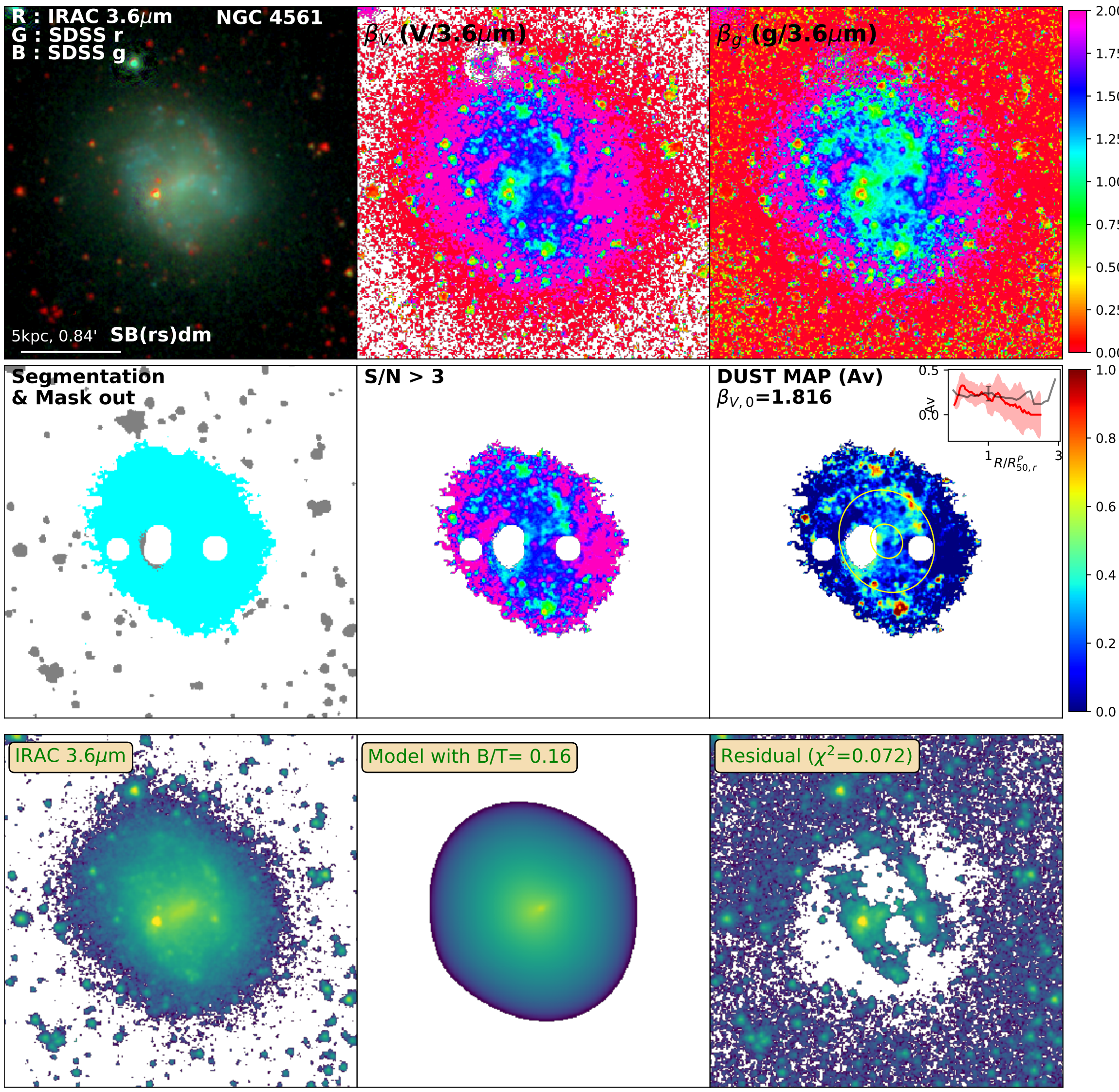

Figure D.159: Same as Figure 3.2 for NGC4561

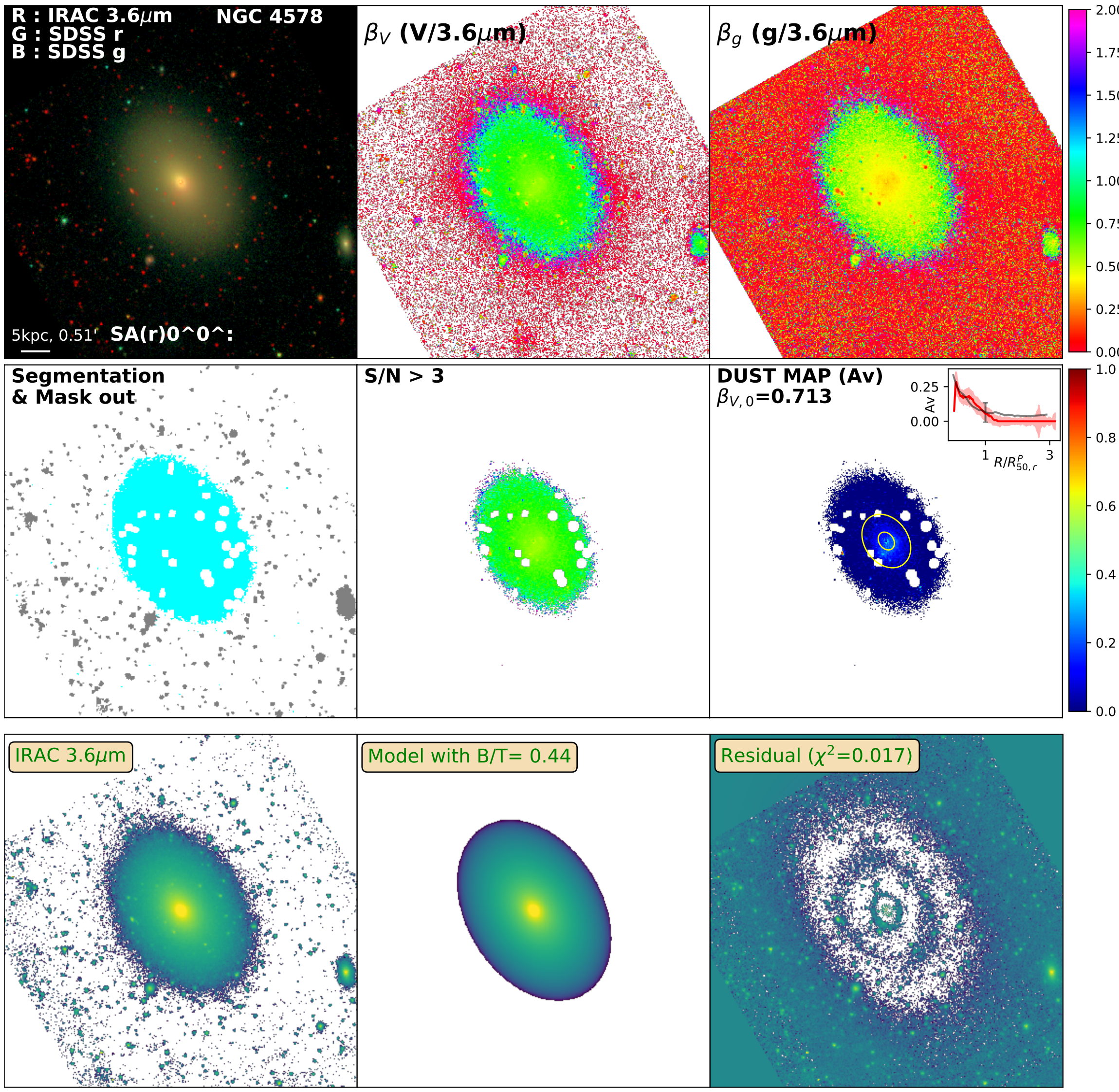

Figure D.160: Same as Figure 3.2 for NGC4578

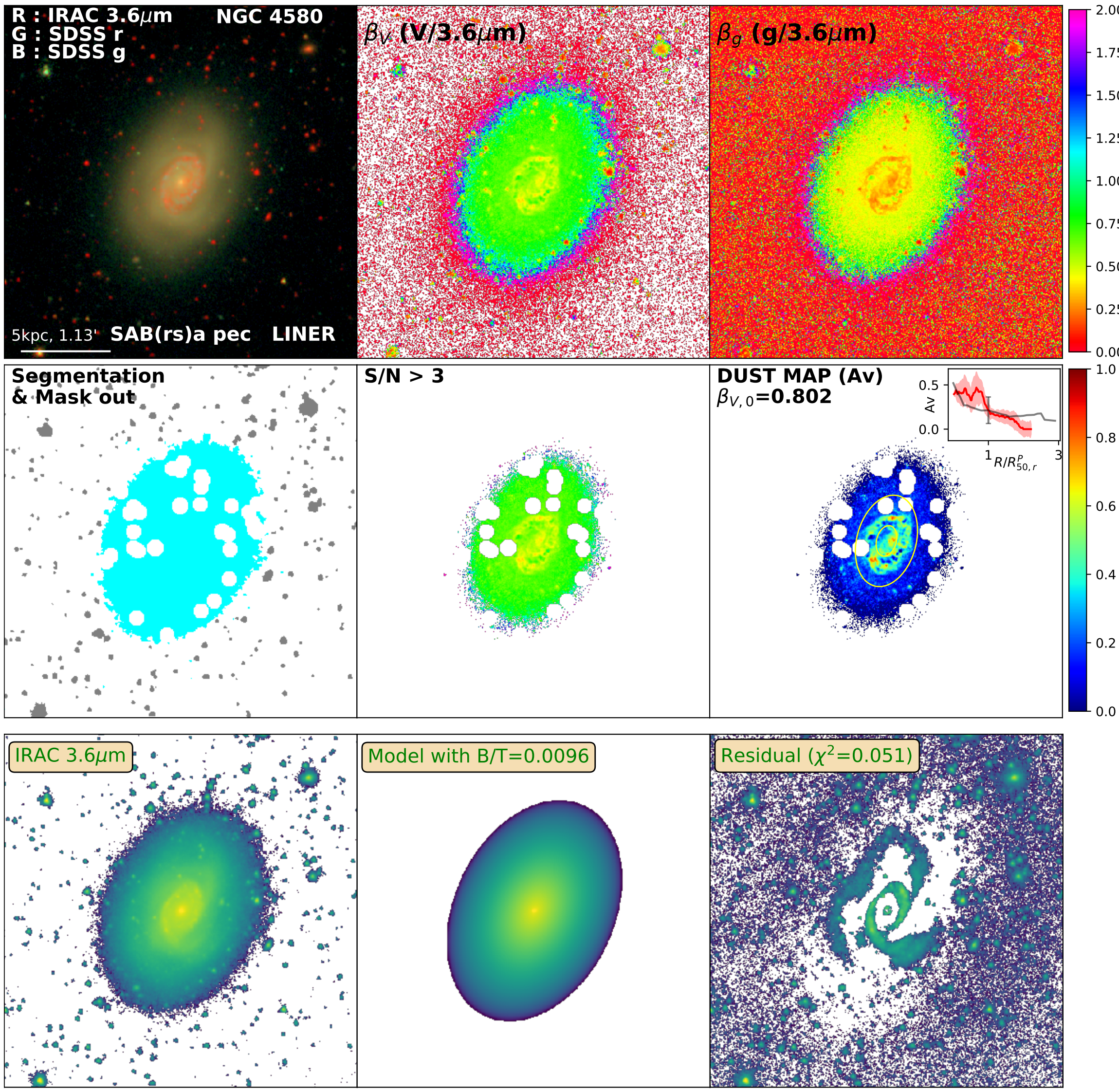

Figure D.161: Same as Figure 3.2 for NGC4580

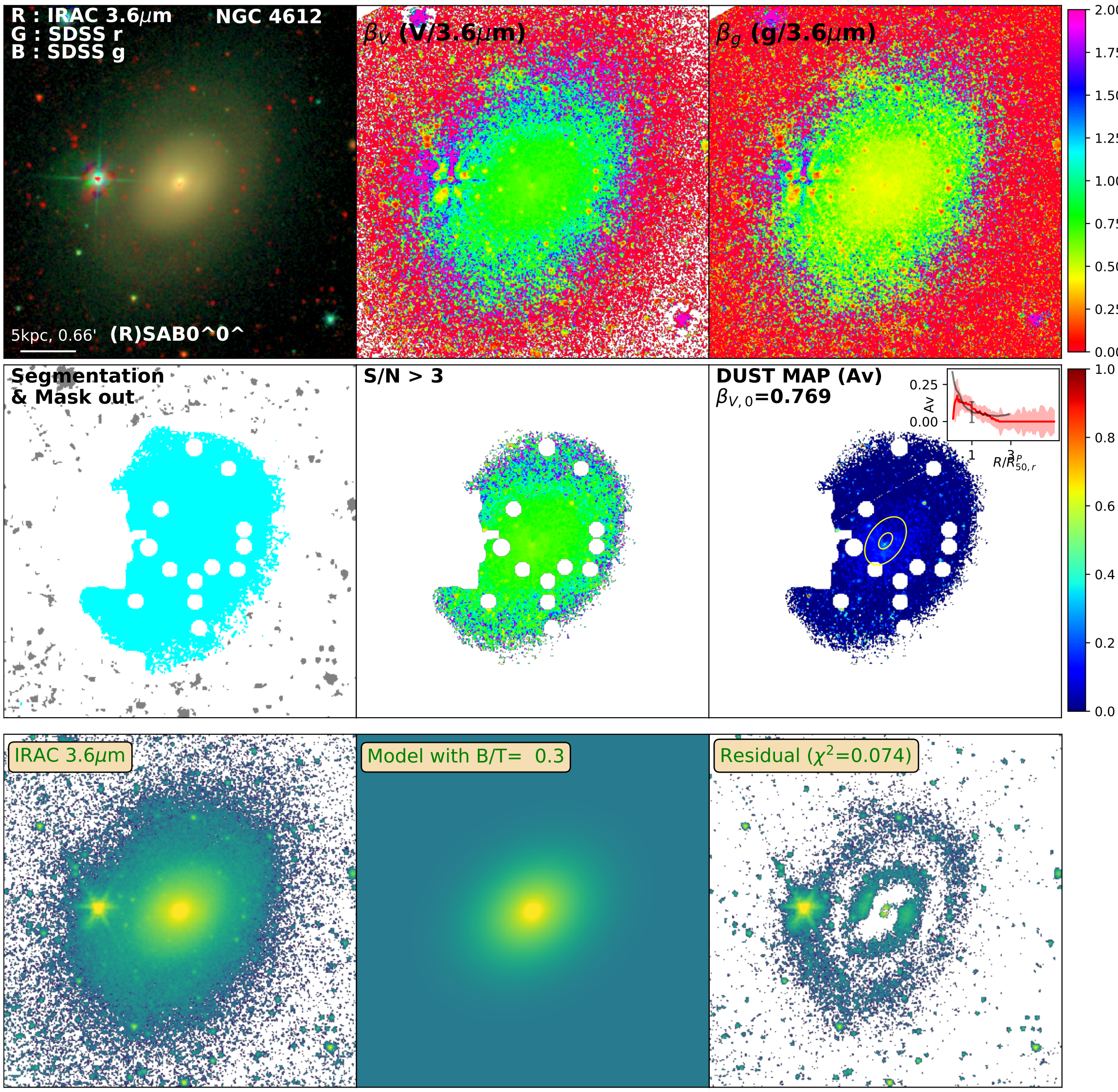

Figure D.162: Same as Figure 3.2 for NGC4612

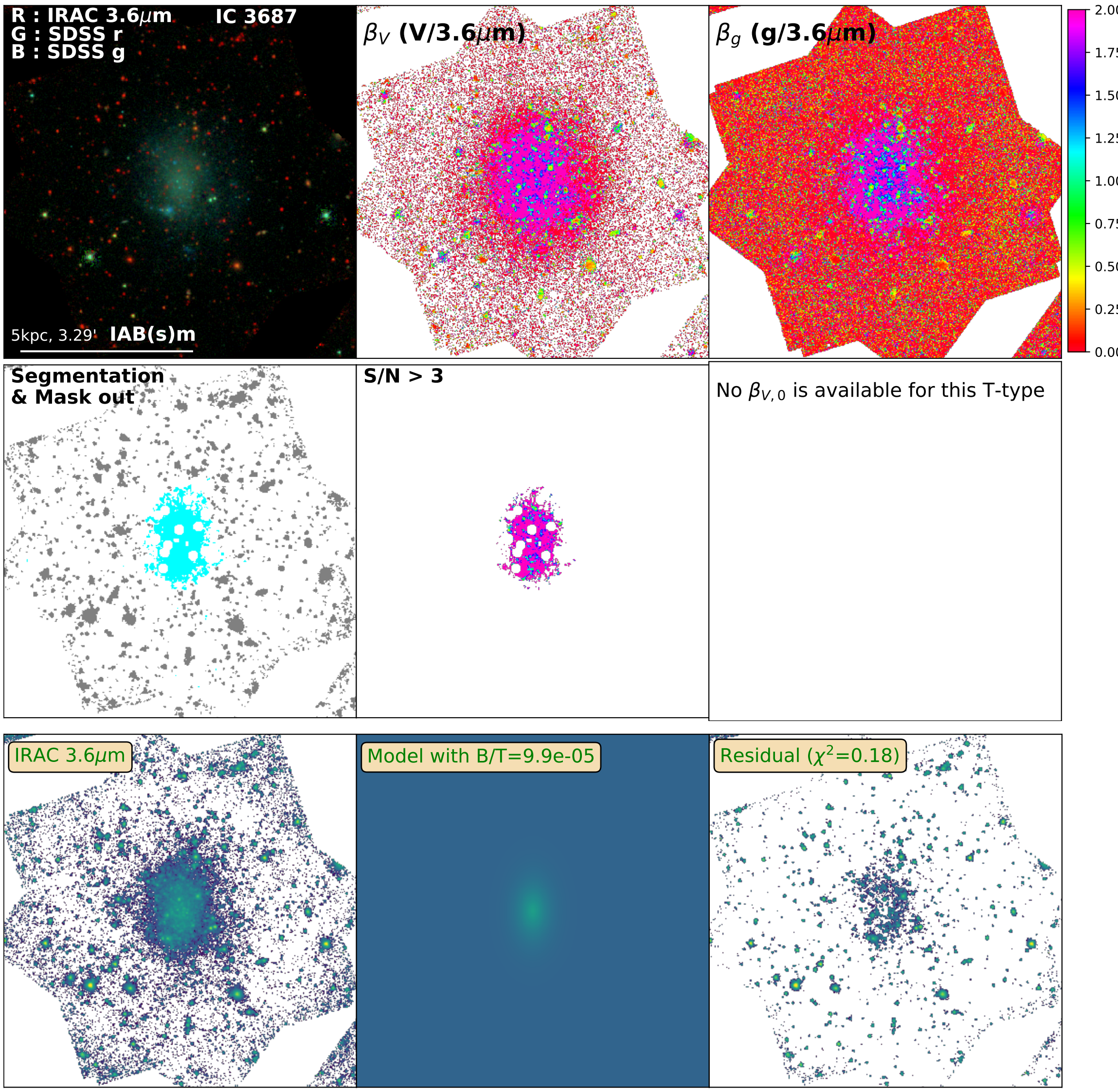

Figure D.163: Same as Figure 3.2 for IC3687

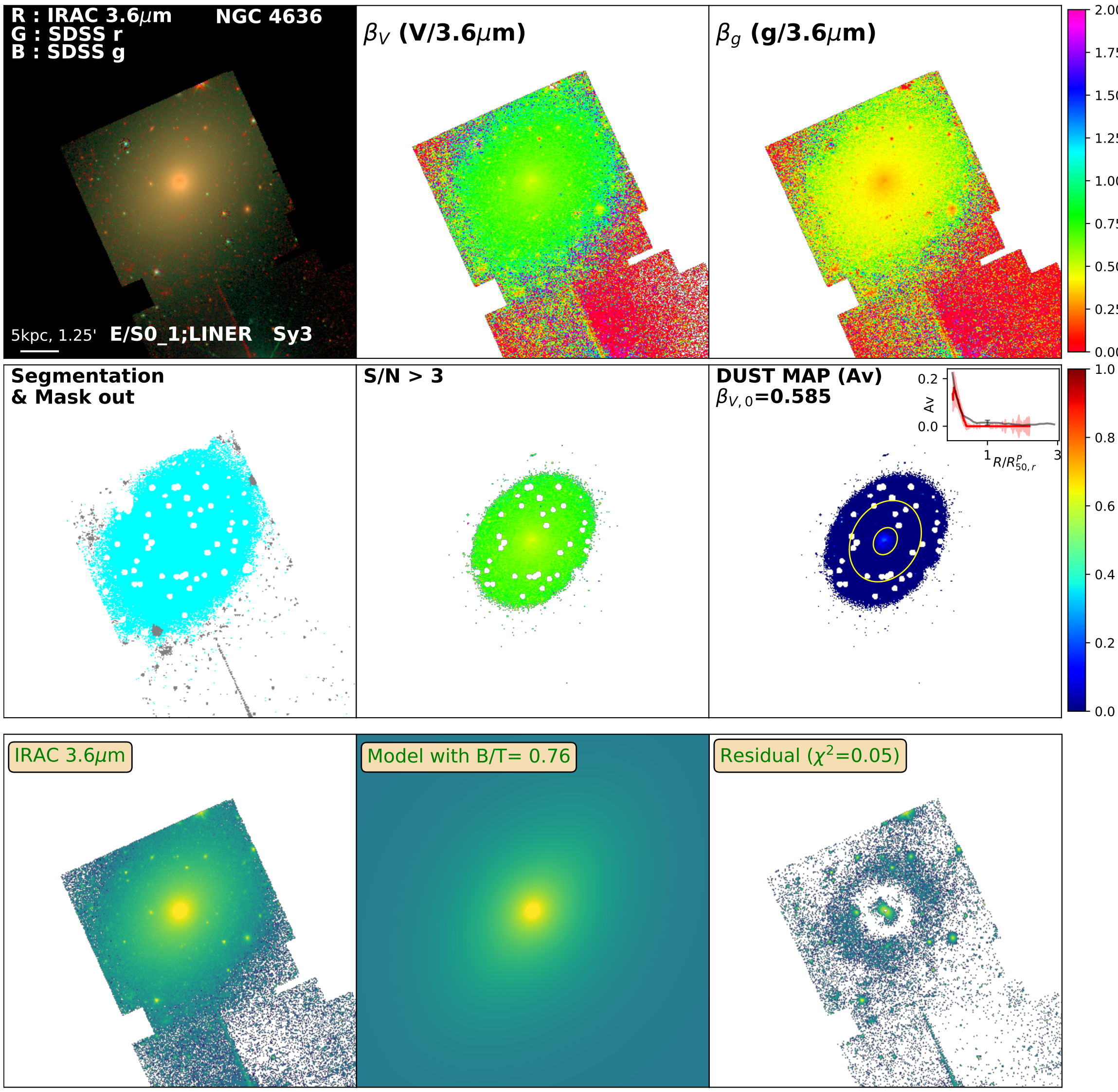

Figure D.164: Same as Figure 3.2 for NGC4636

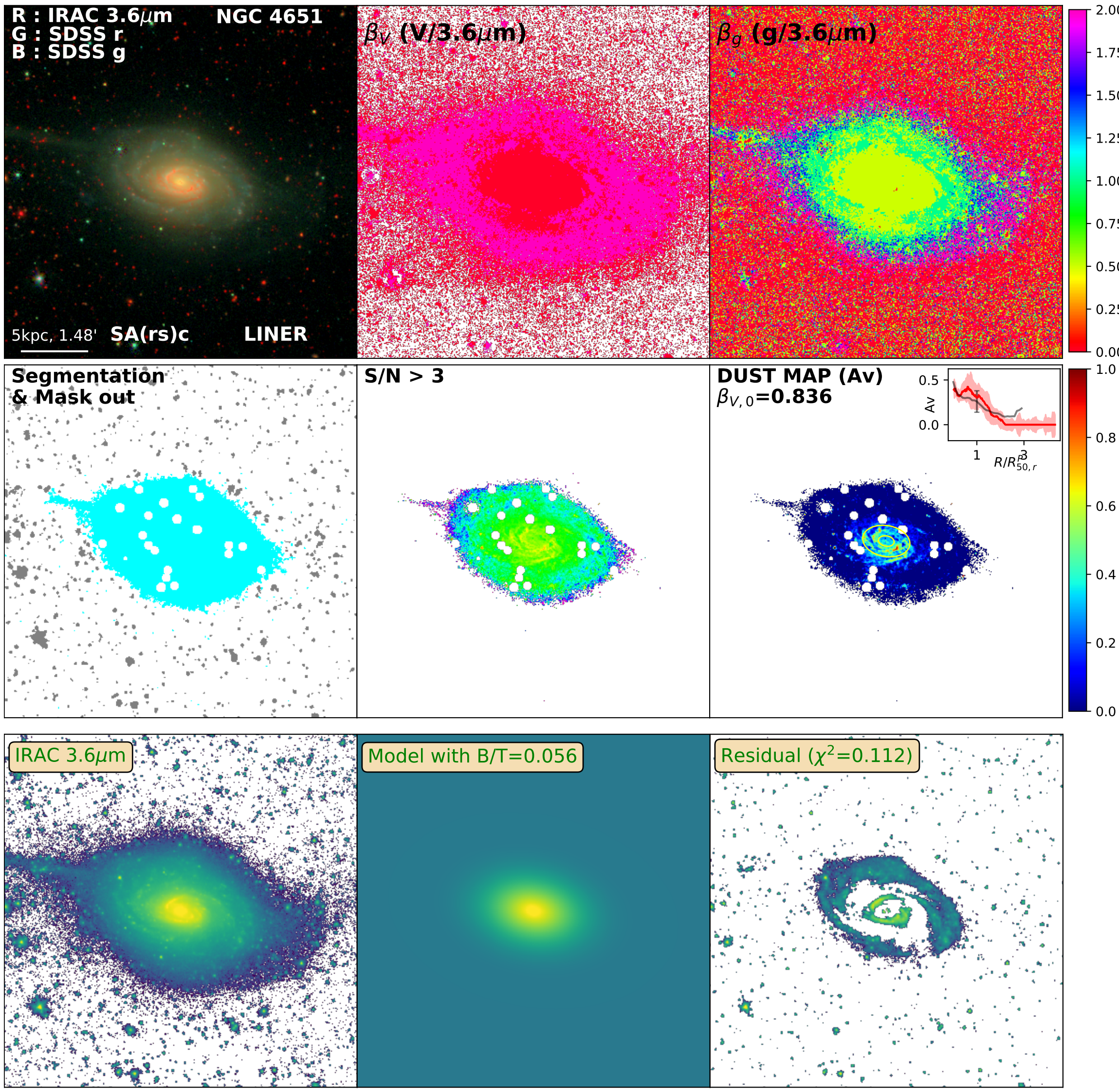

Figure D.165: Same as Figure 3.2 for NGC4651

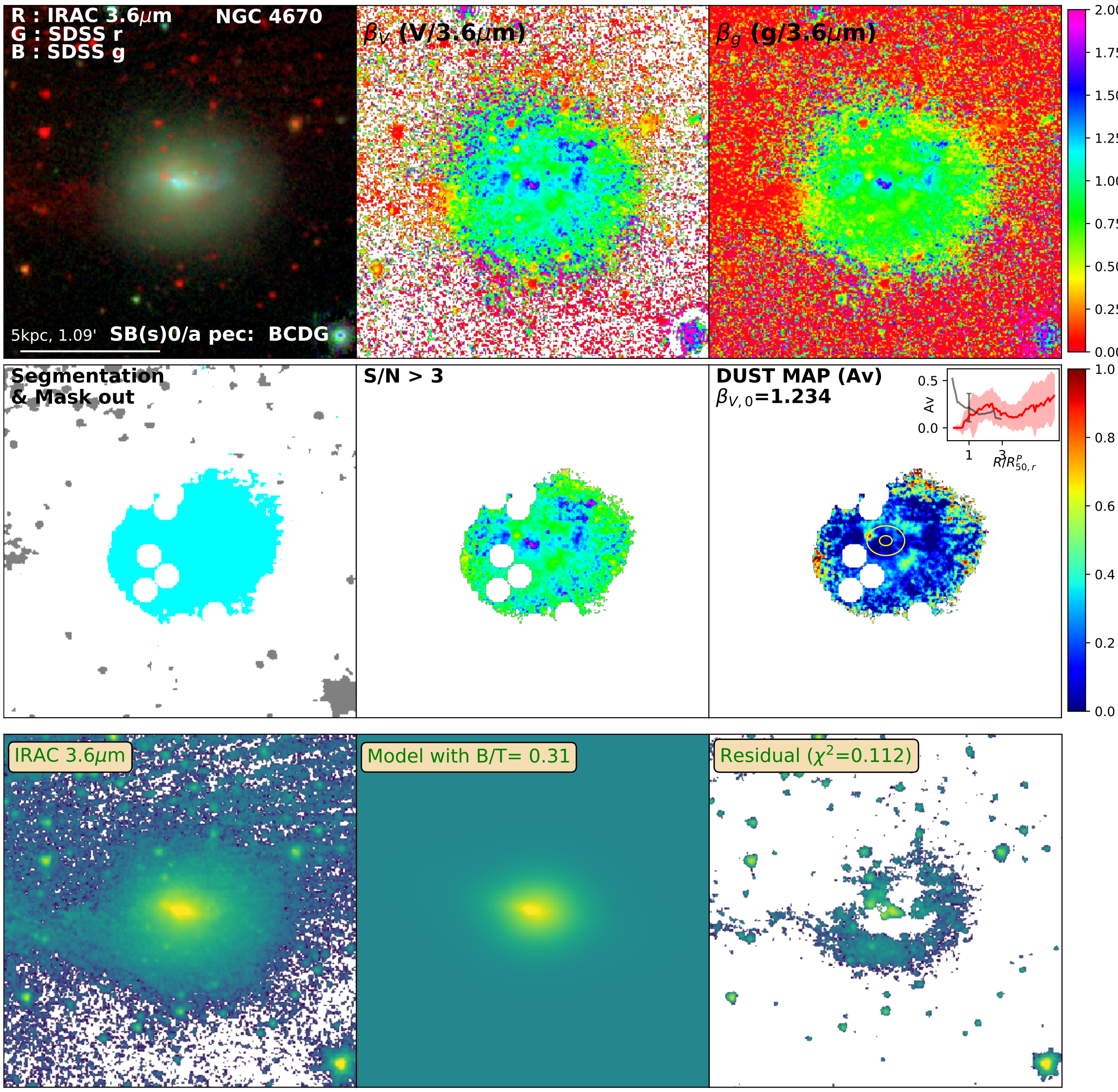

Figure D.166: Same as Figure 3.2 for NGC4670

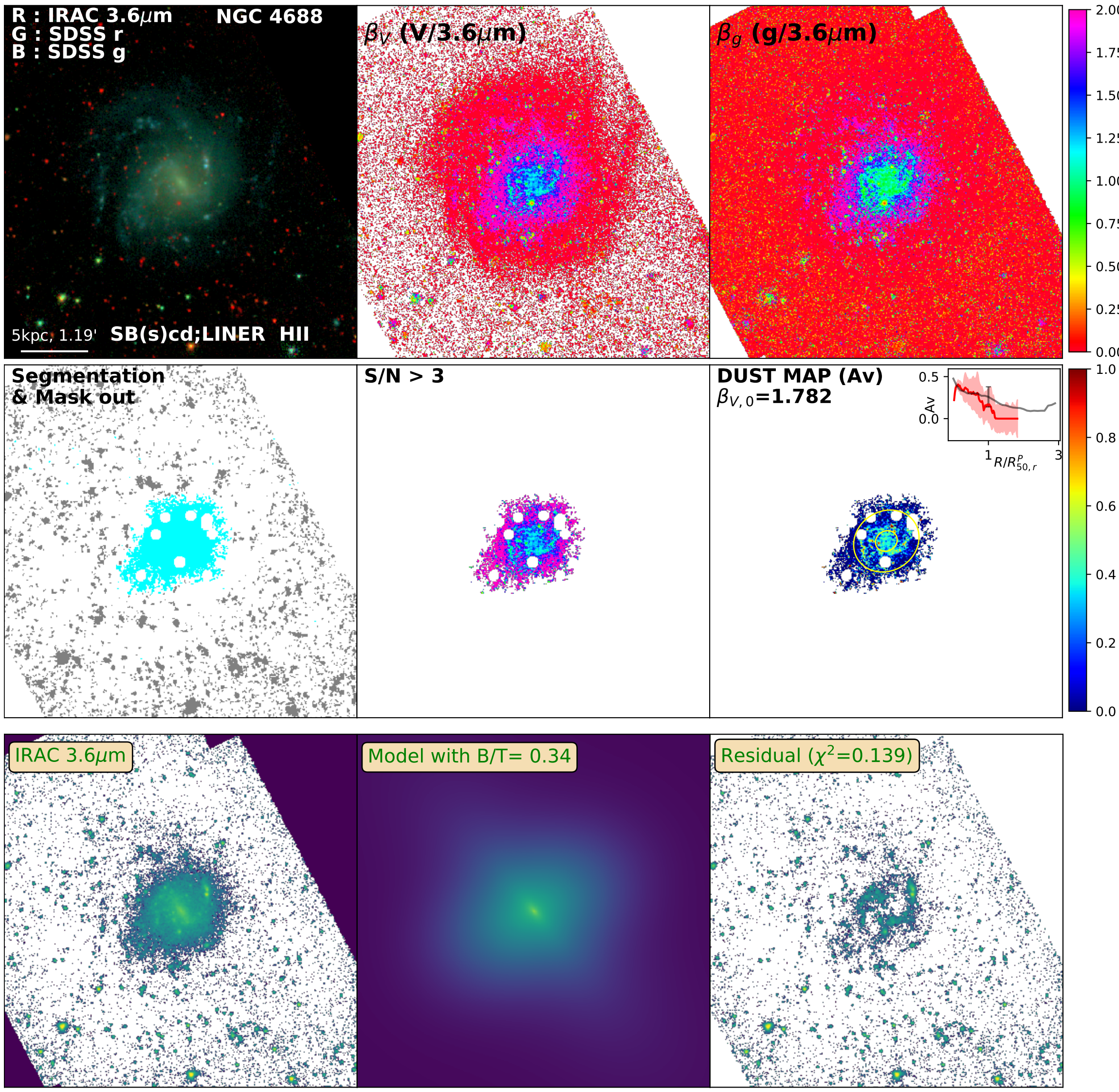

Figure D.167: Same as Figure 3.2 for NGC4688

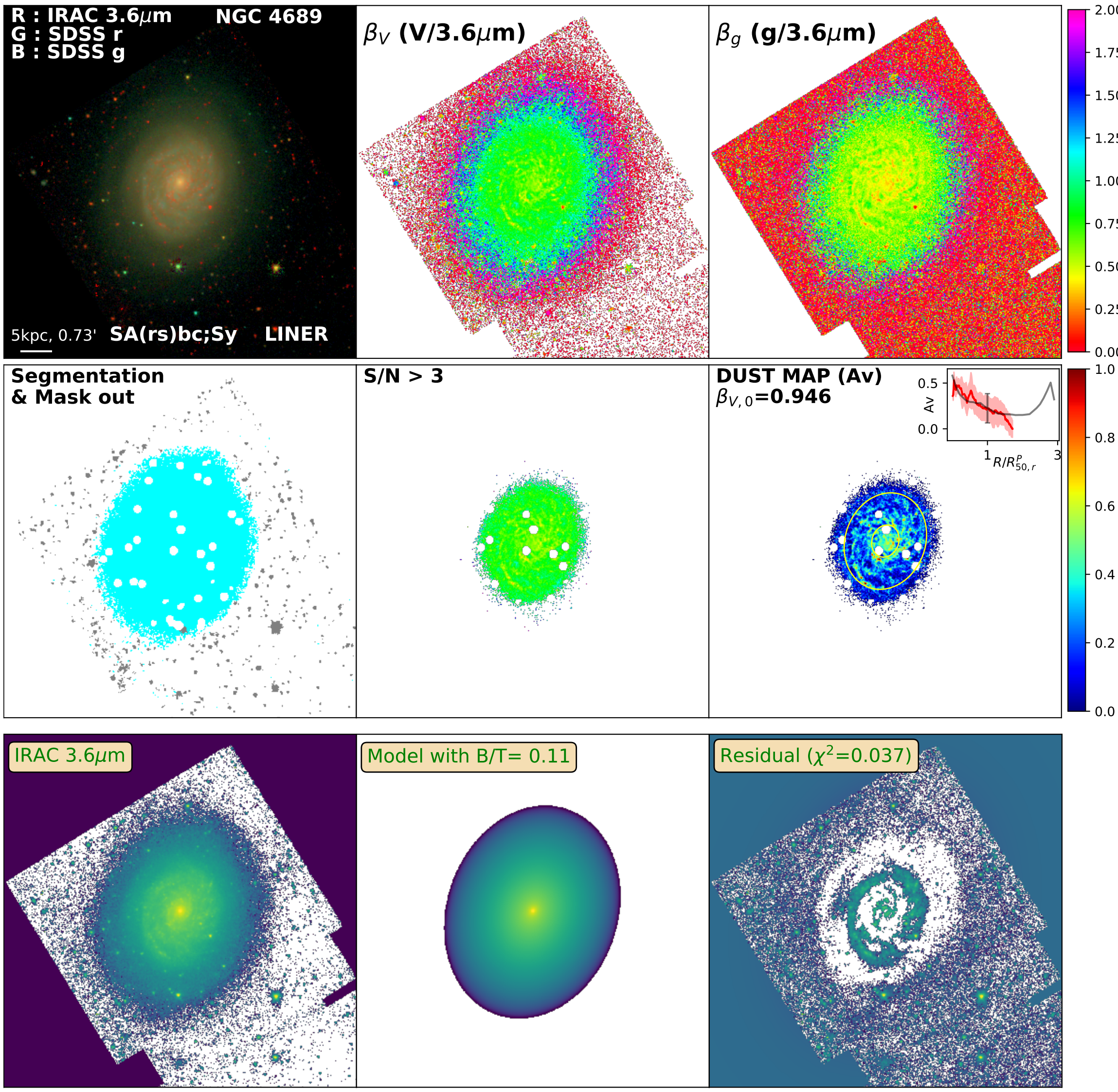

Figure D.168: Same as Figure 3.2 for NGC4689

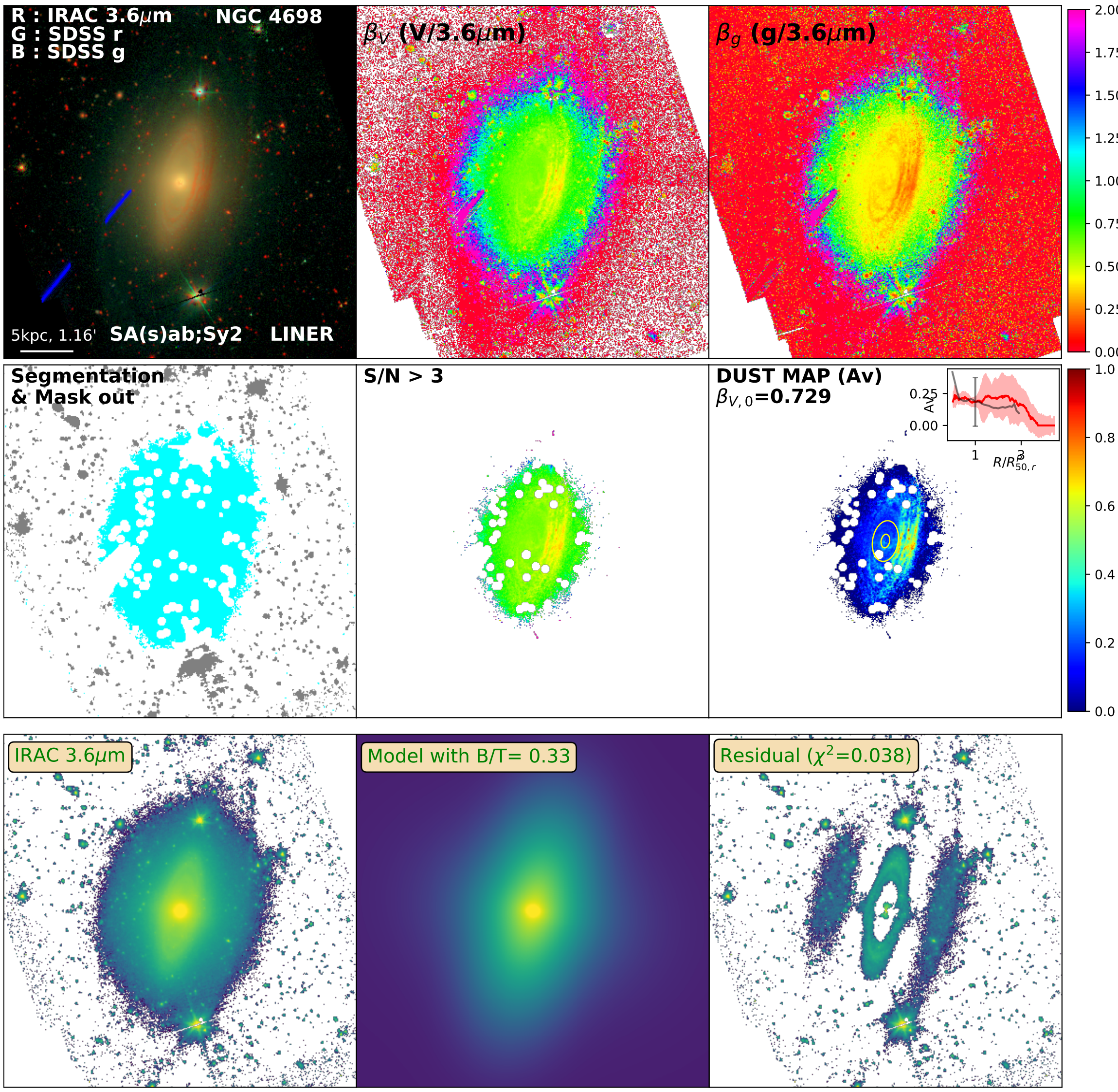

Figure D.169: Same as Figure 3.2 for NGC4698

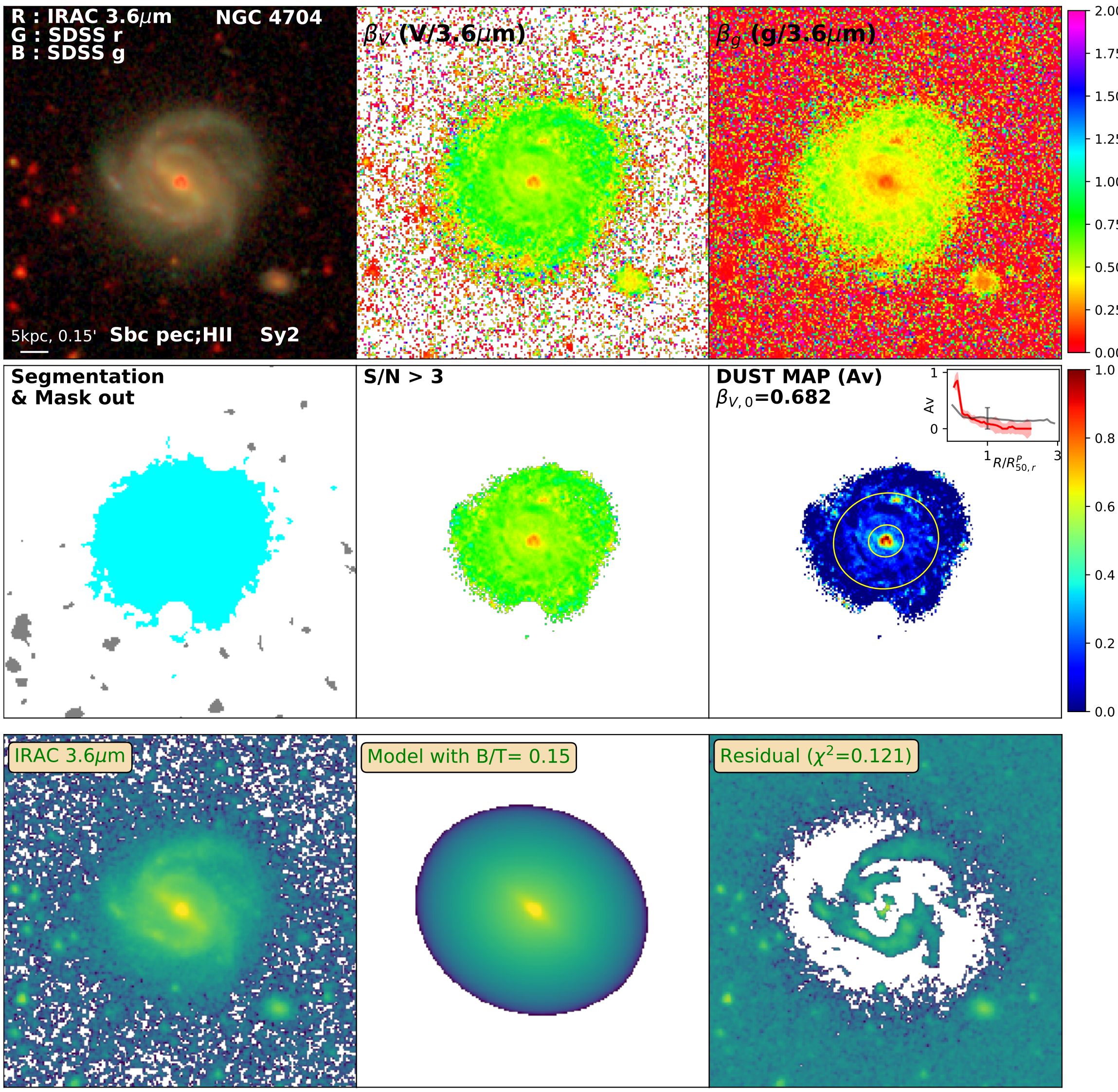

Figure D.170: Same as Figure 3.2 for NGC4704

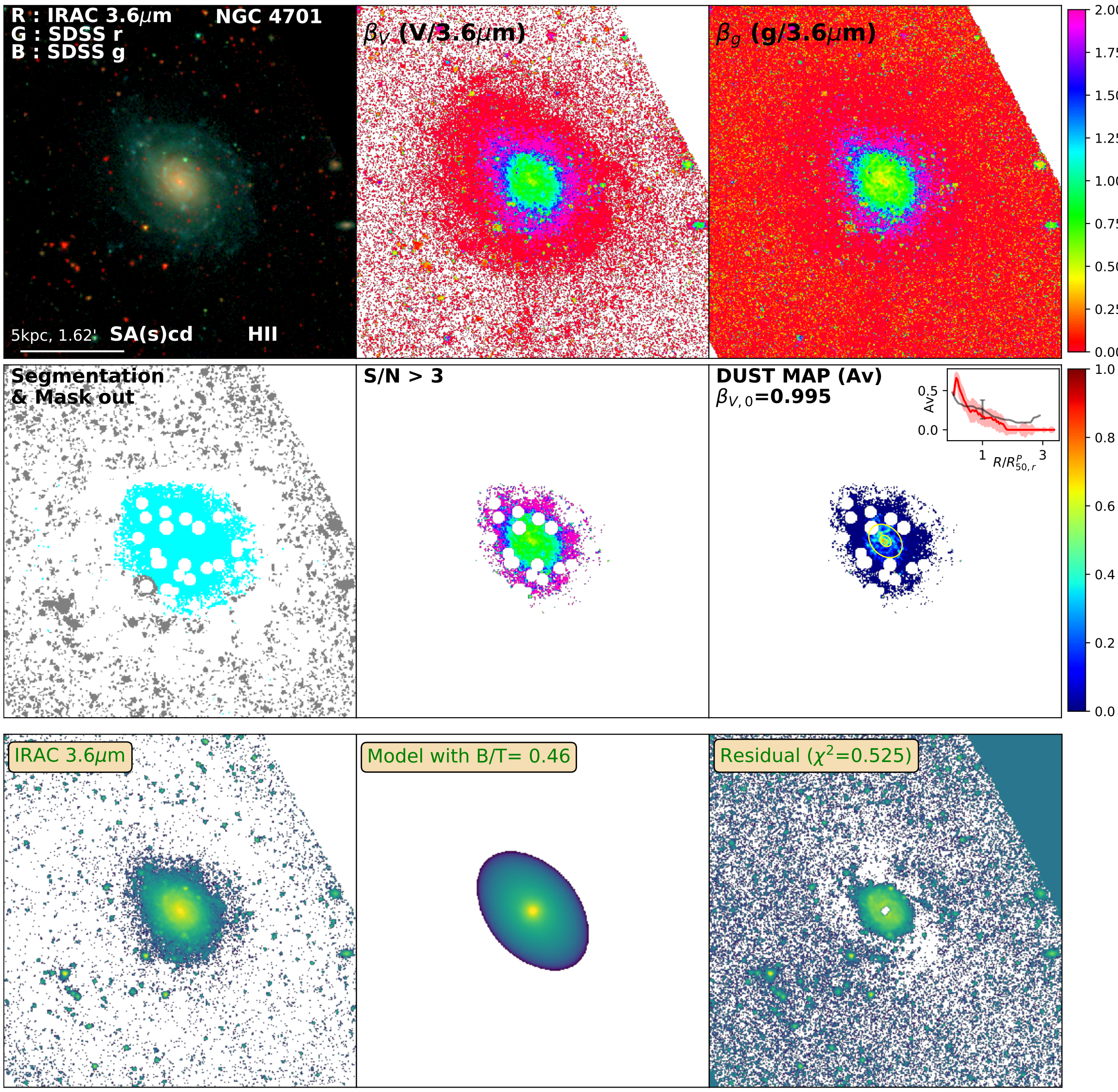

Figure D.171: Same as Figure 3.2 for NGC4701

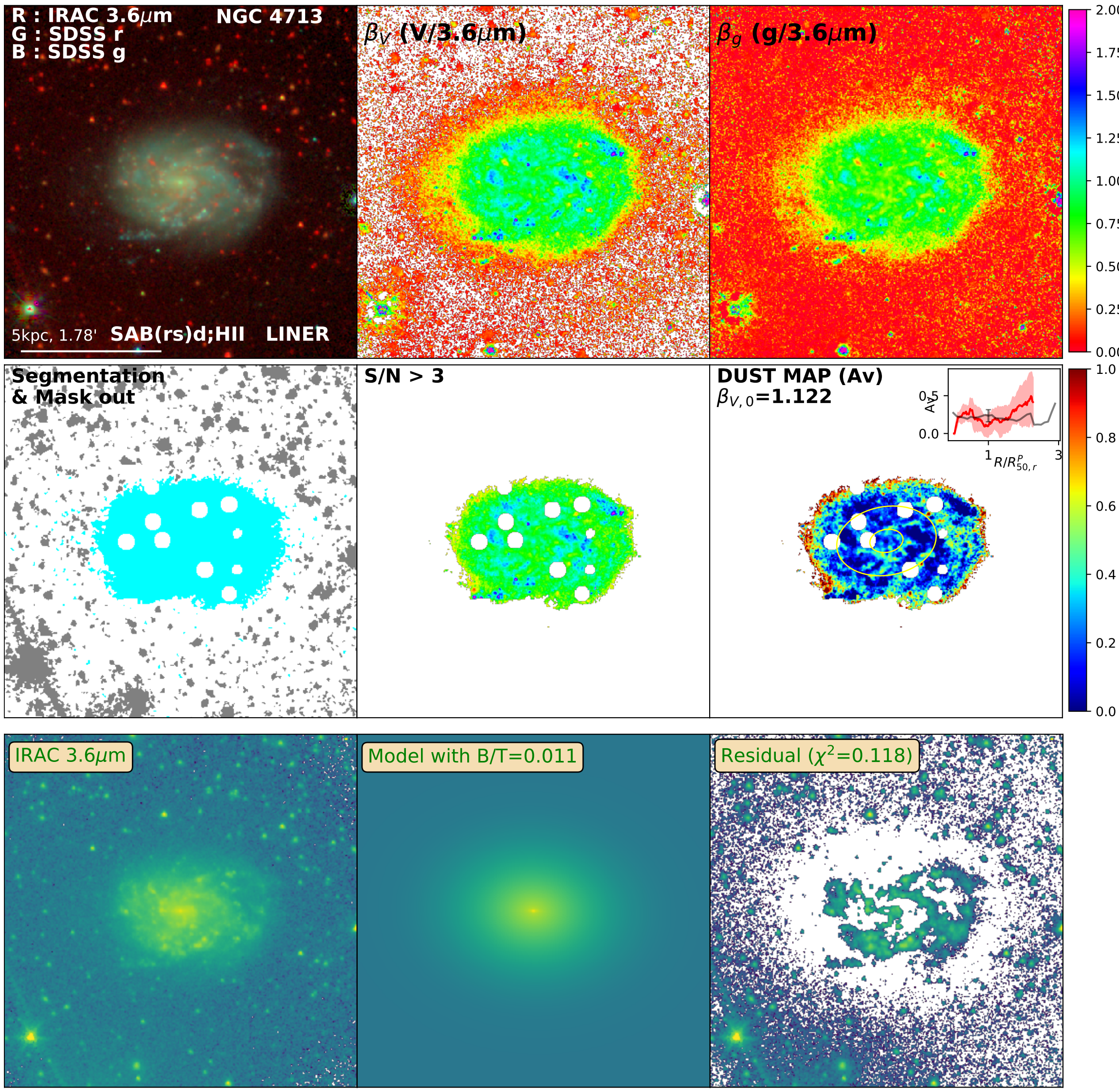

Figure D.172: Same as Figure 3.2 for NGC4713

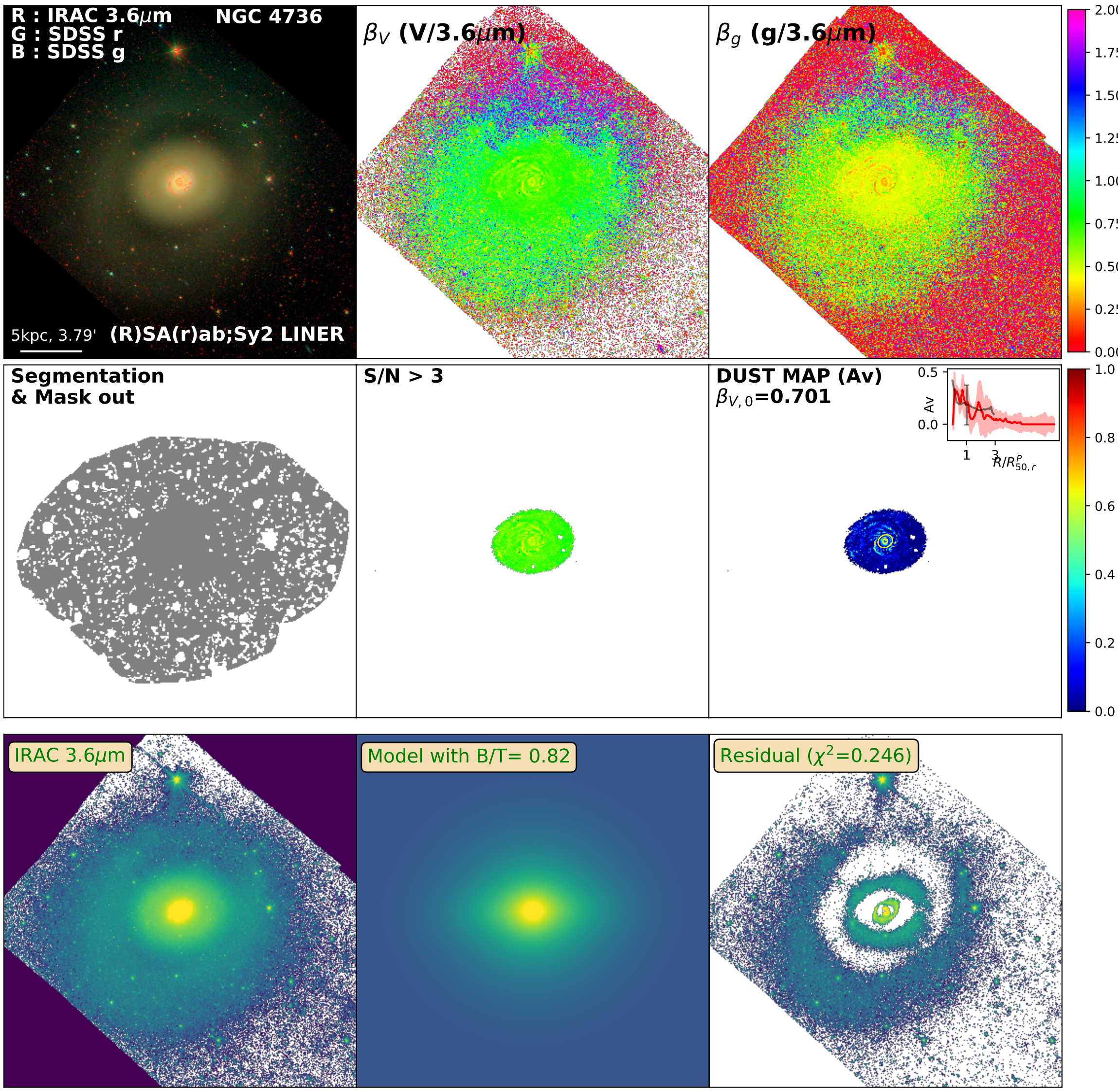

Figure D.173: Same as Figure 3.2 for NGC4736

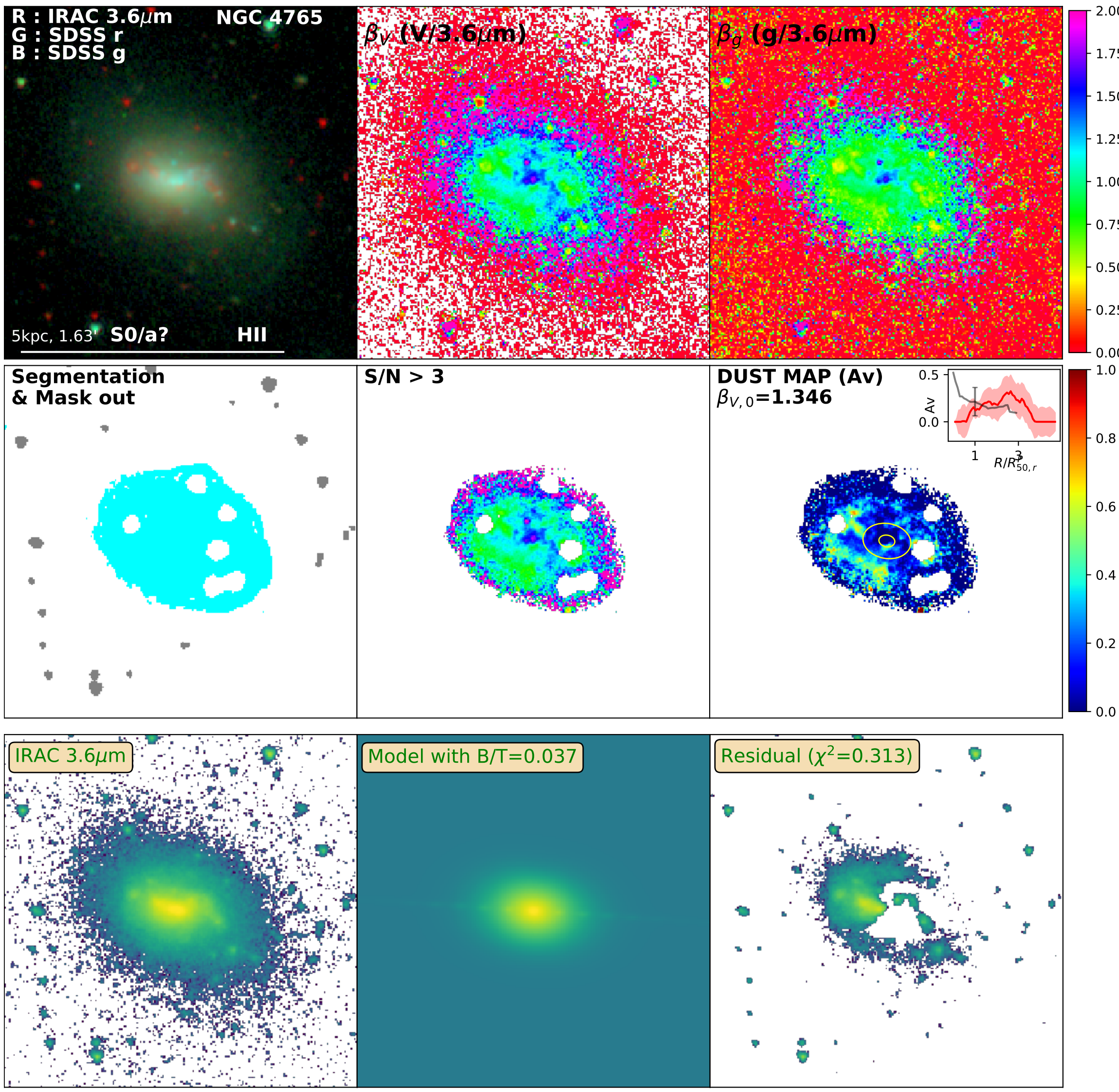

Figure D.174: Same as Figure 3.2 for NGC4765

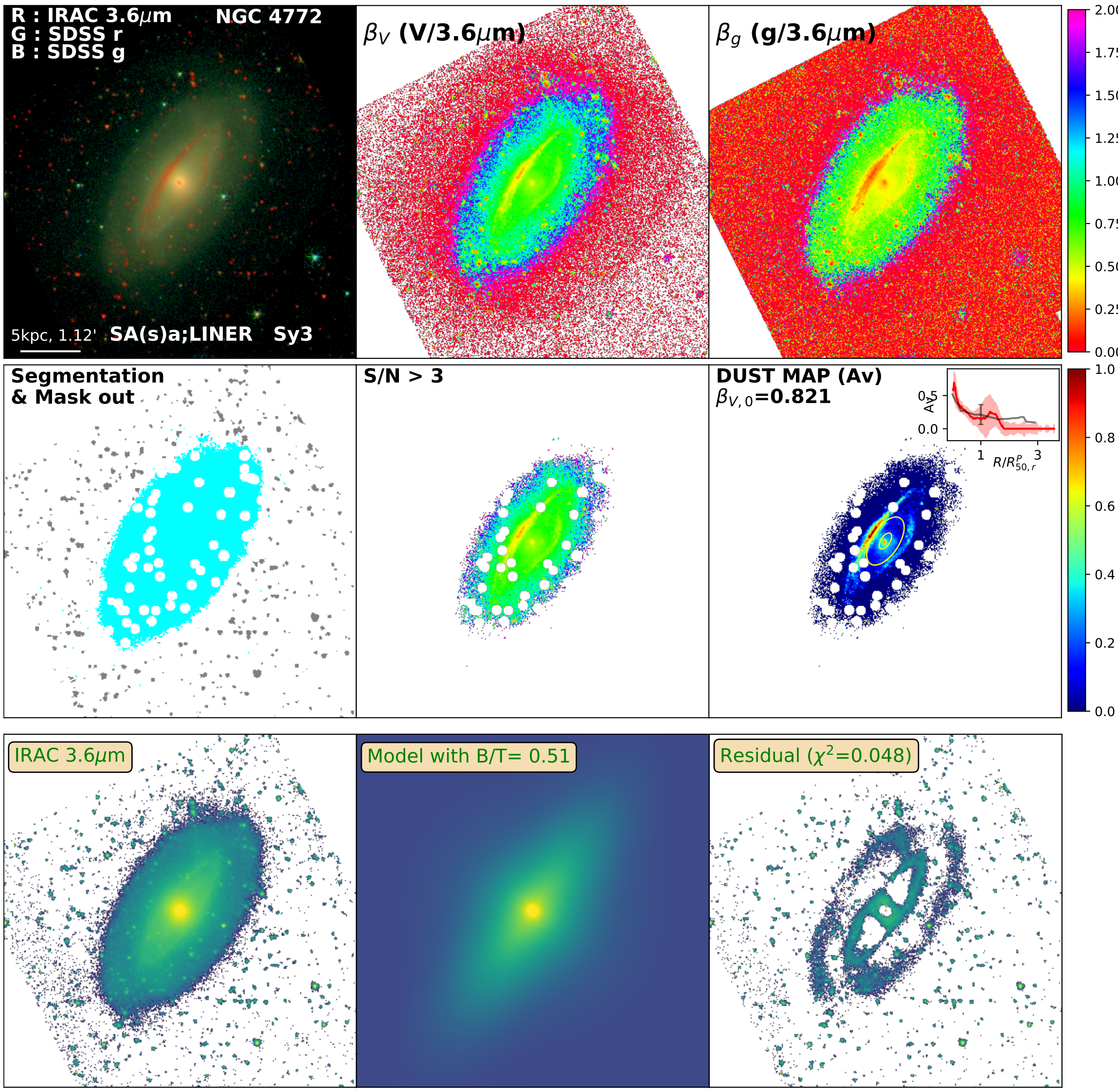

Figure D.175: Same as Figure 3.2 for NGC4772

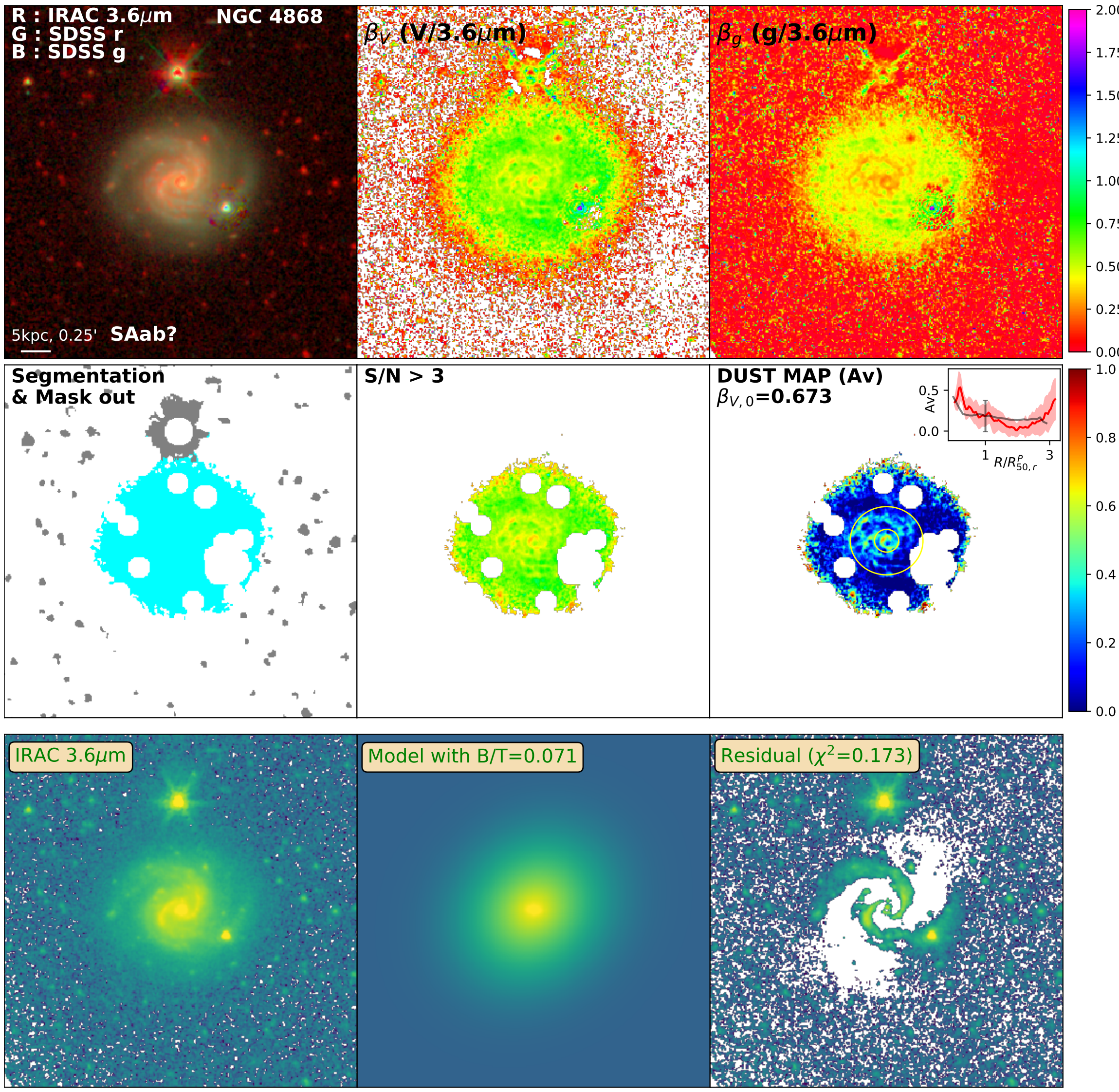

Figure D.176: Same as Figure 3.2 for NGC4868

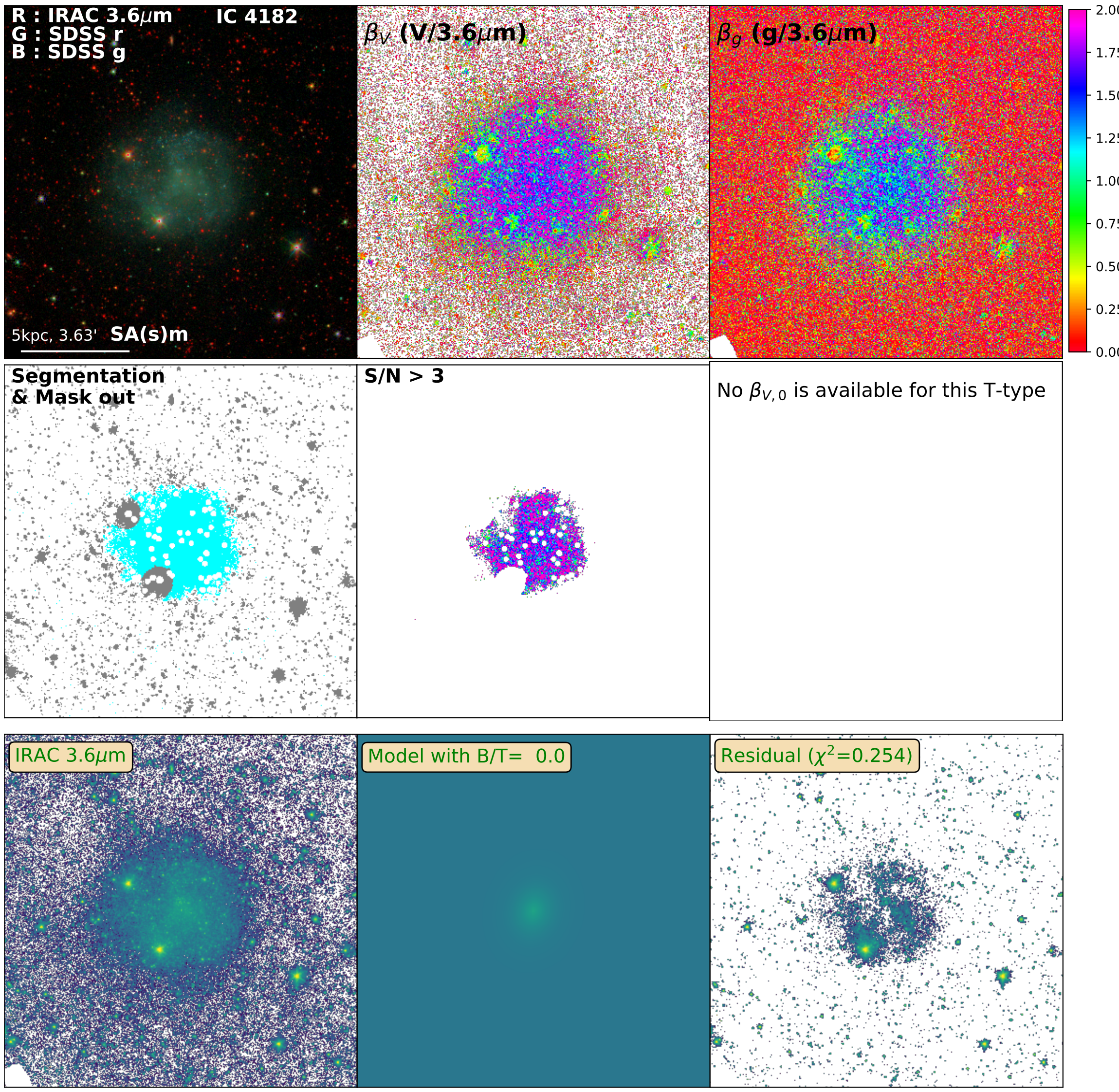

Figure D.177: Same as Figure 3.2 for IC4182

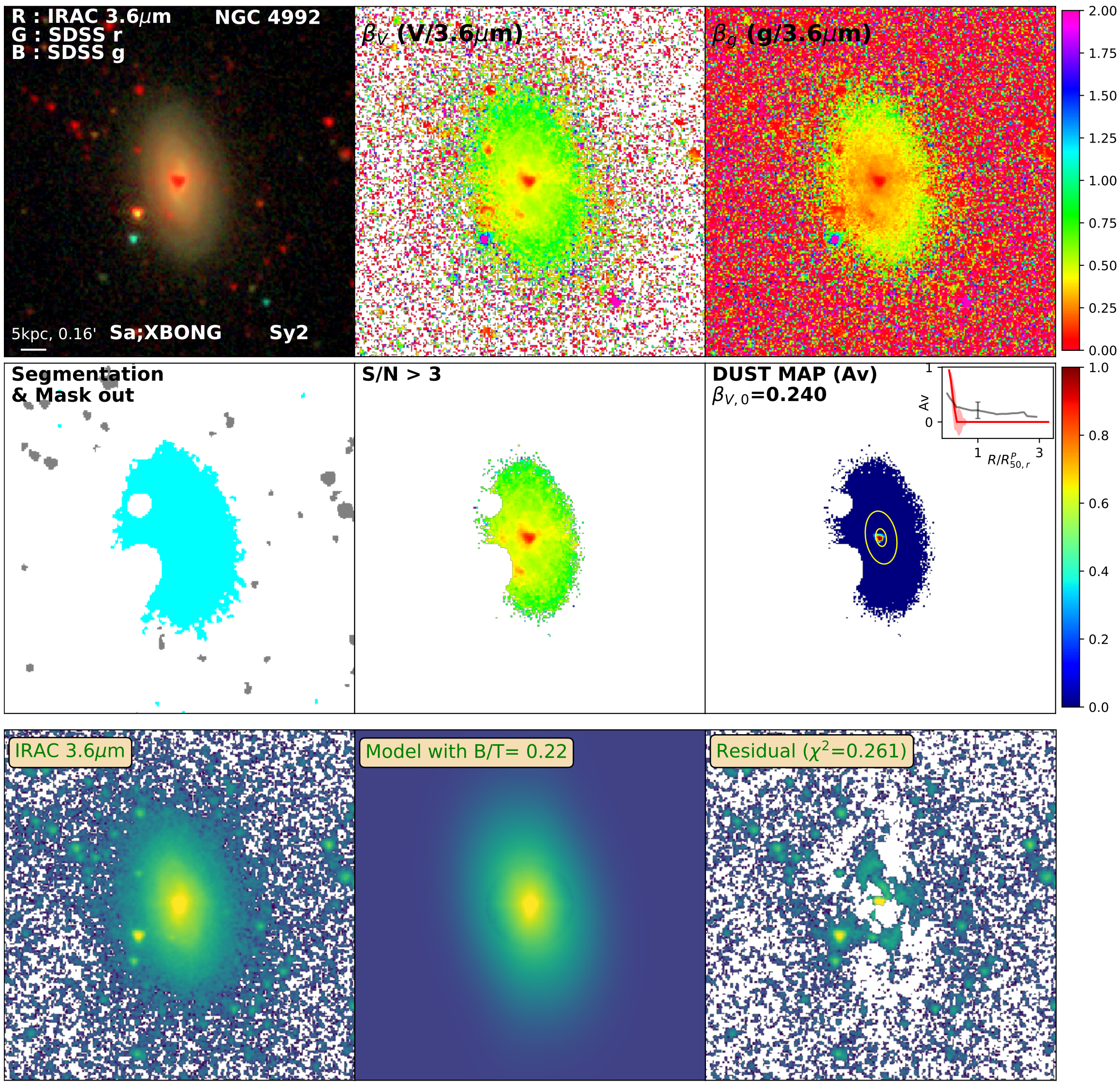

Figure D.178: Same as Figure 3.2 for NGC4992

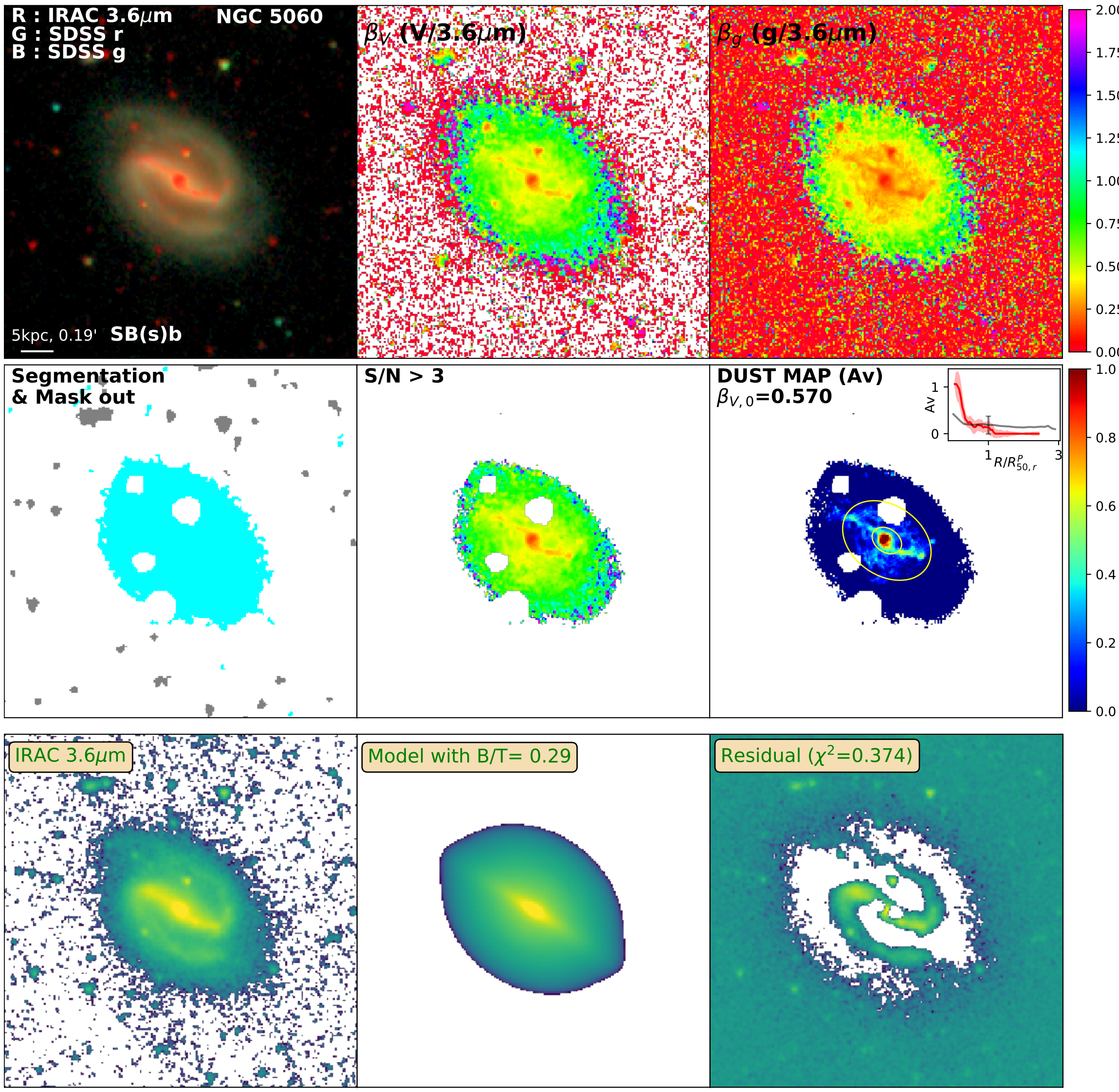

Figure D.179: Same as Figure 3.2 for NGC5060

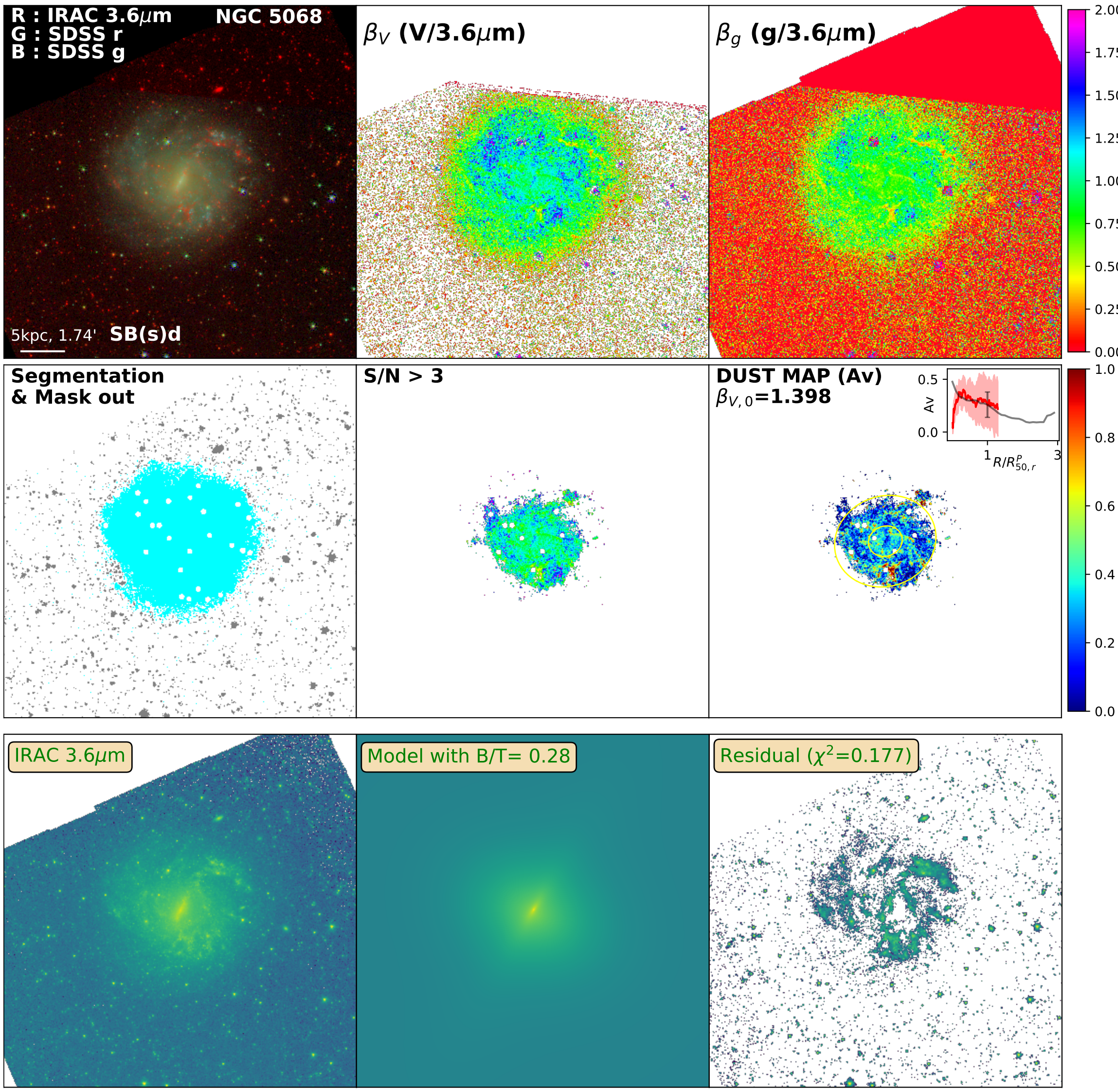

Figure D.180: Same as Figure 3.2 for NGC5068

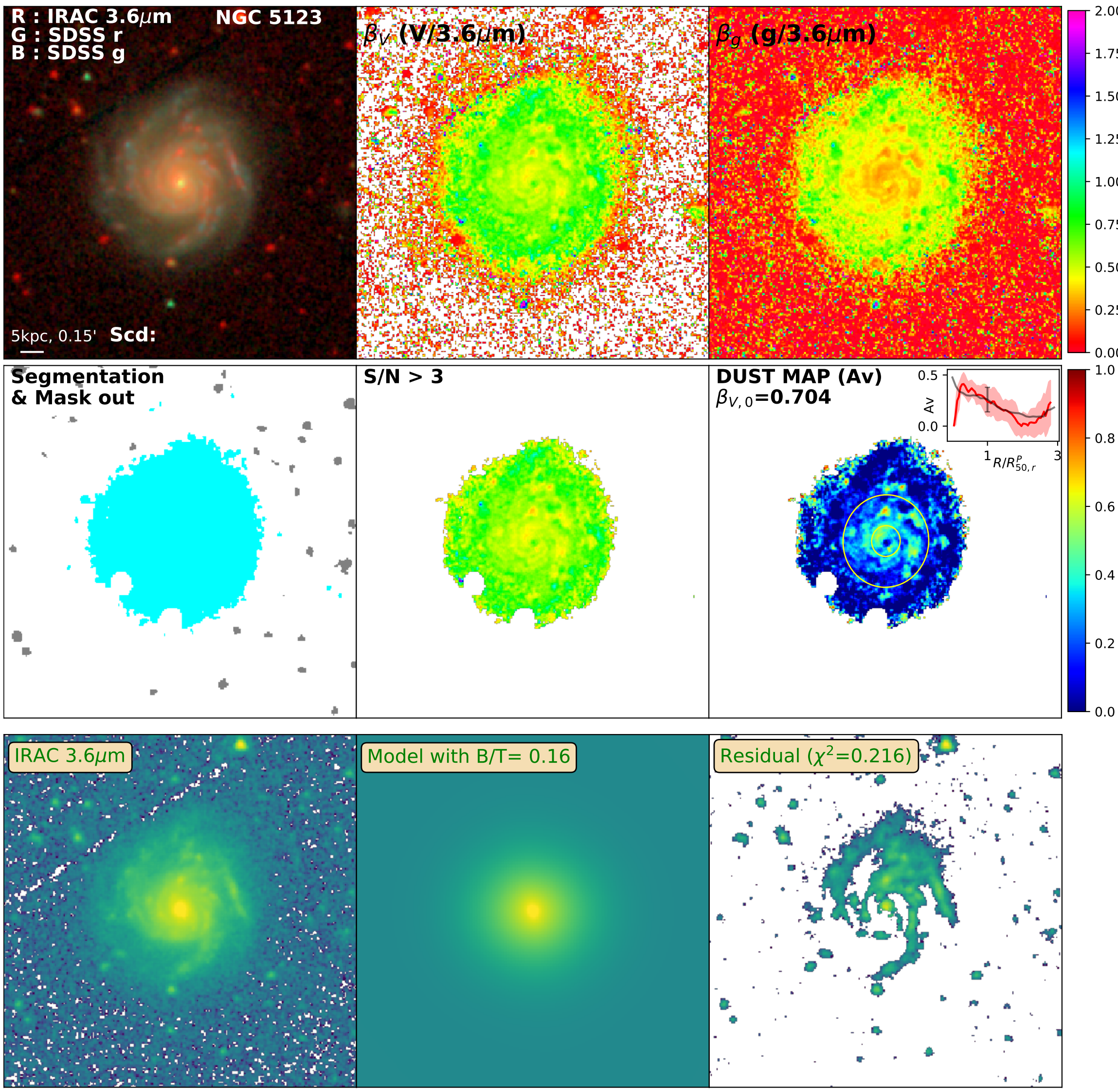

Figure D.181: Same as Figure 3.2 for NGC5123

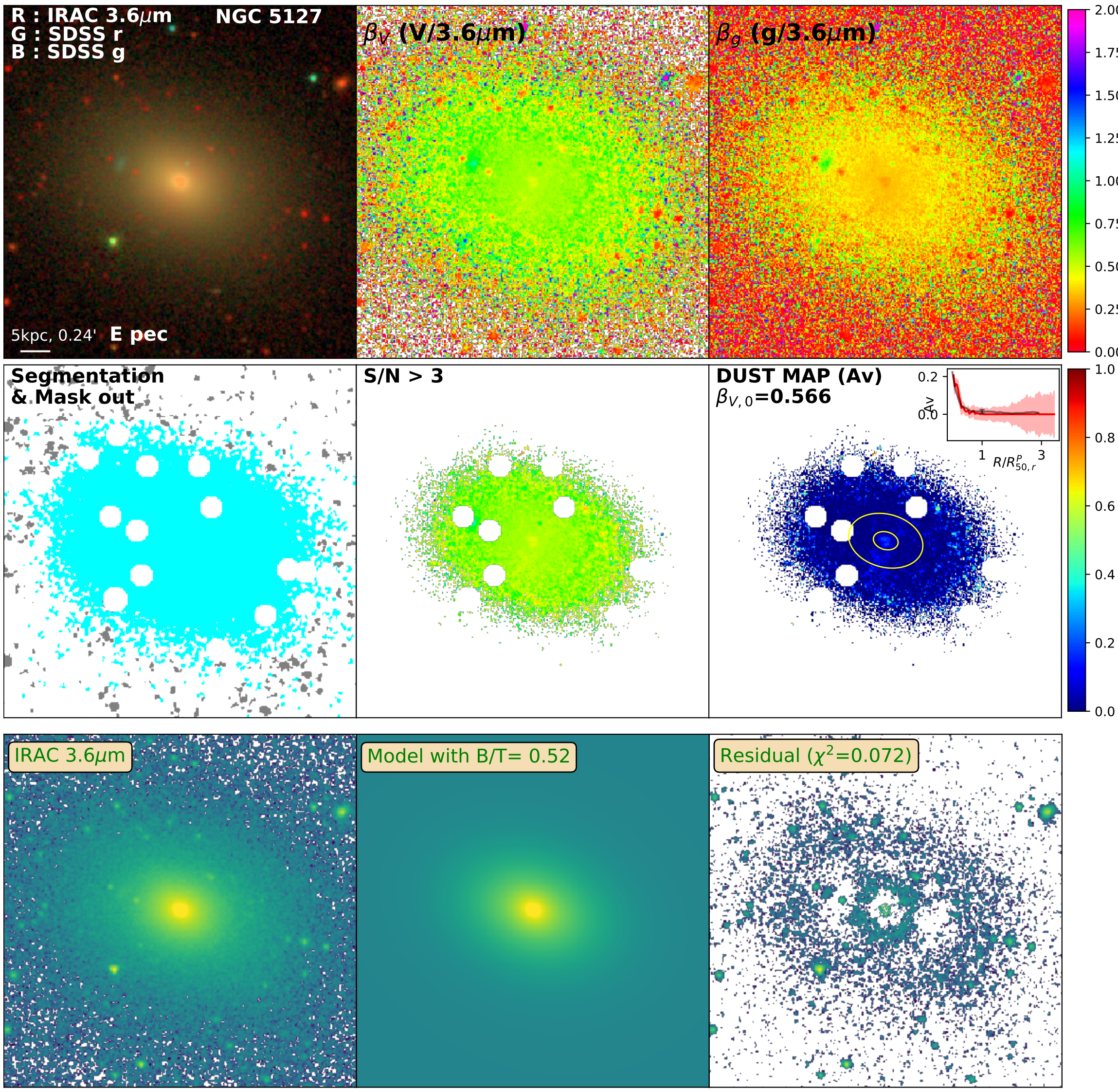

Figure D.182: Same as Figure 3.2 for NGC5127

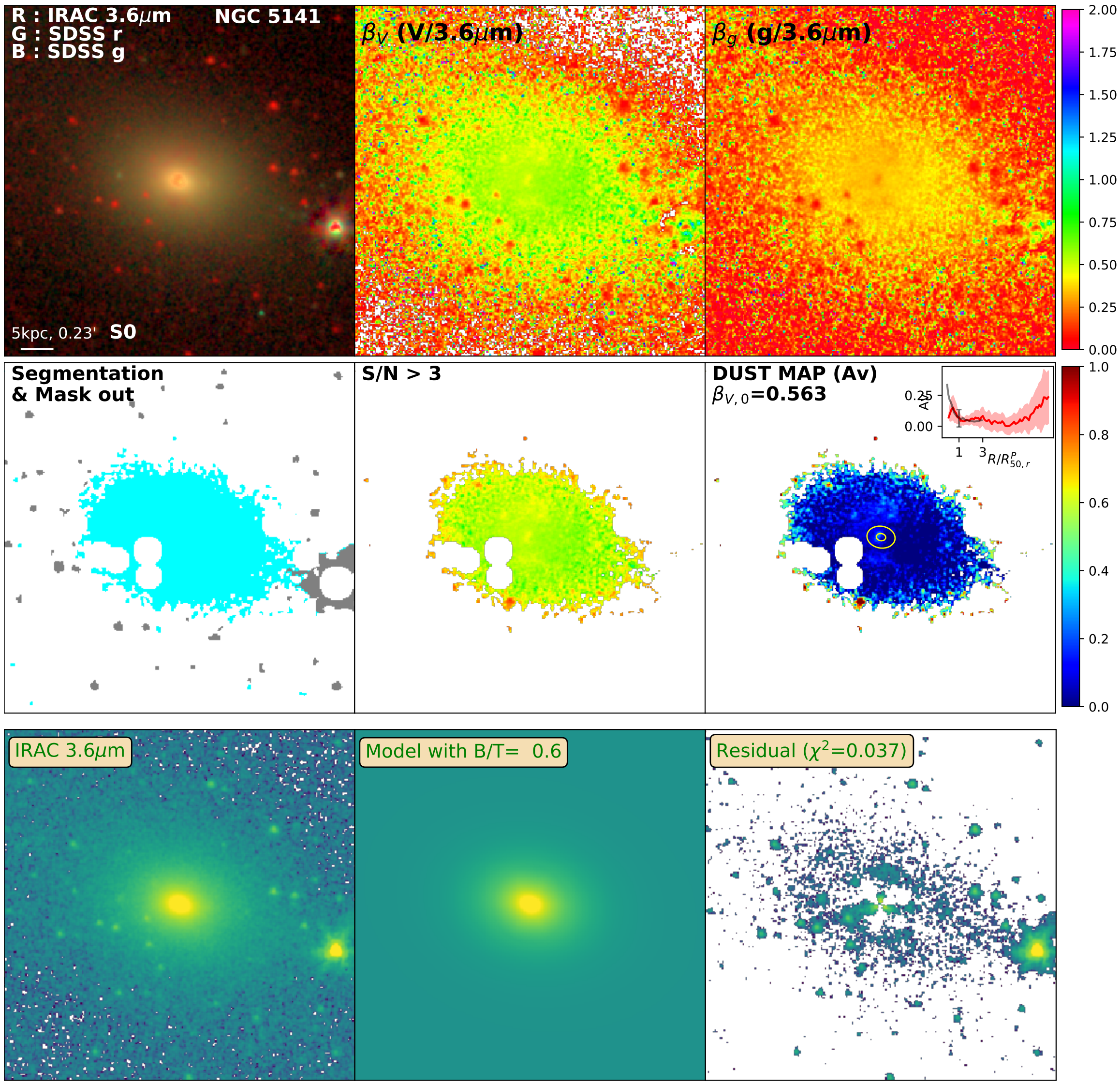

Figure D.183: Same as Figure 3.2 for NGC5141

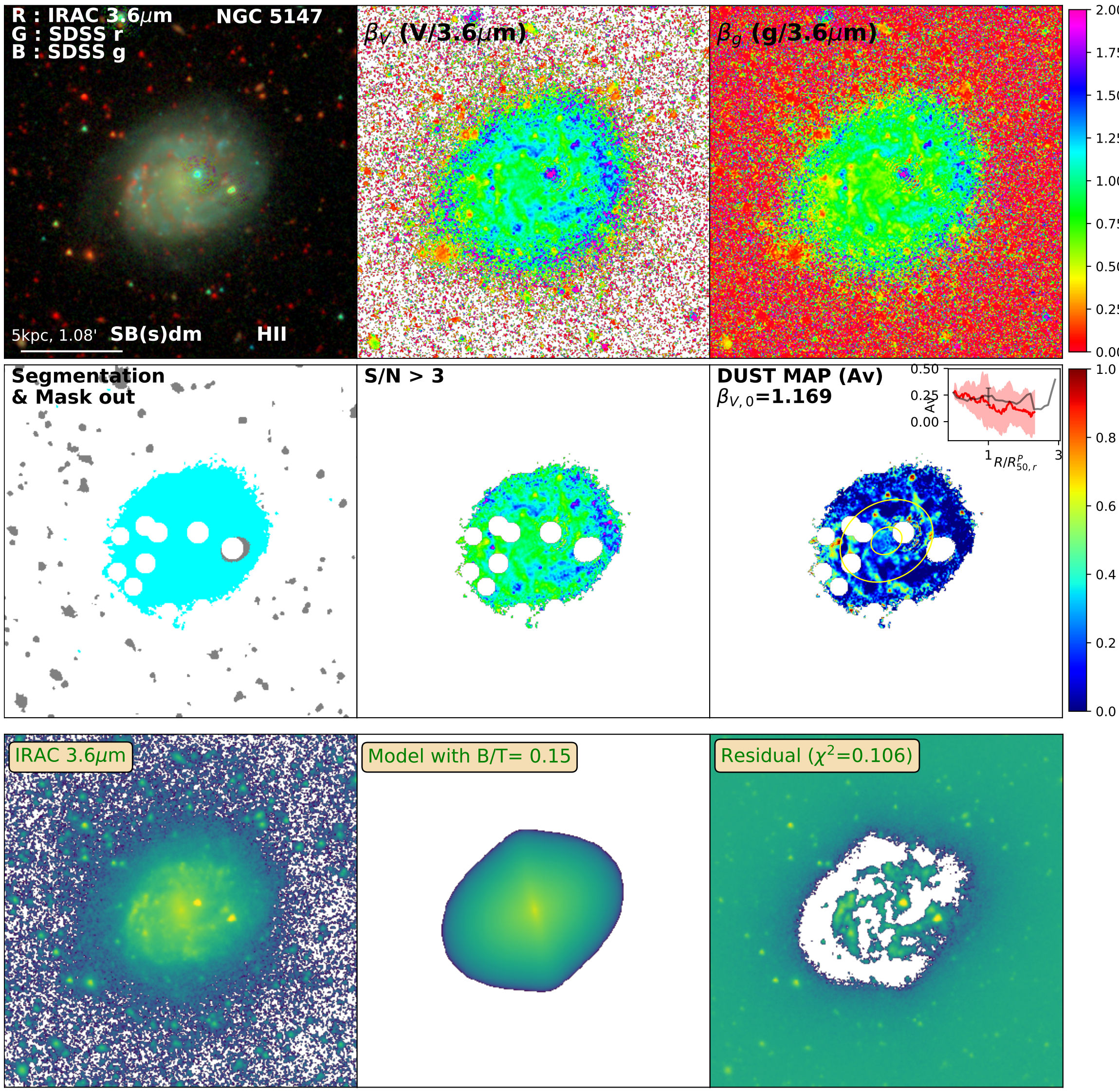

Figure D.184: Same as Figure 3.2 for NGC5147

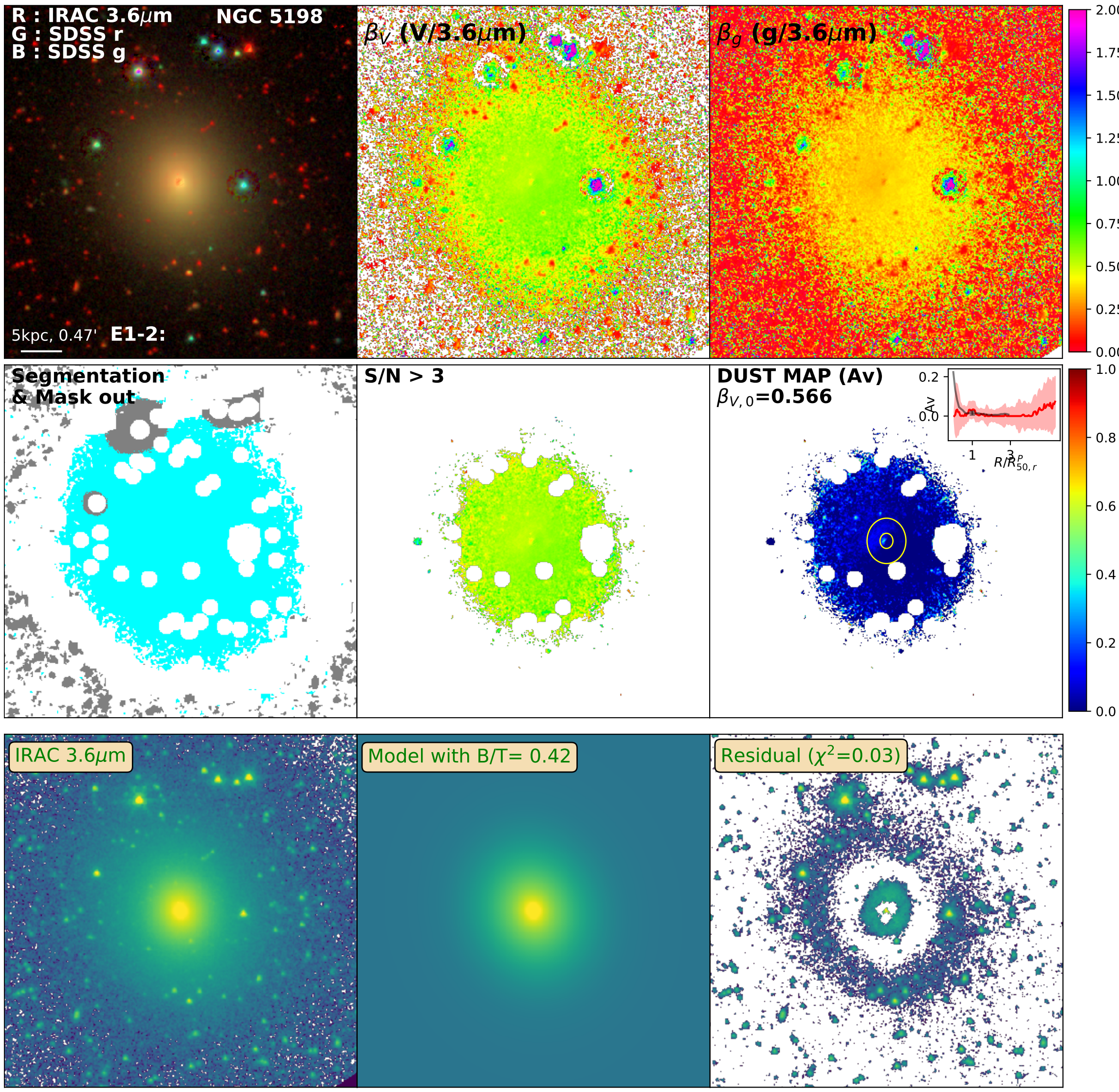

Figure D.185: Same as Figure 3.2 for NGC5198

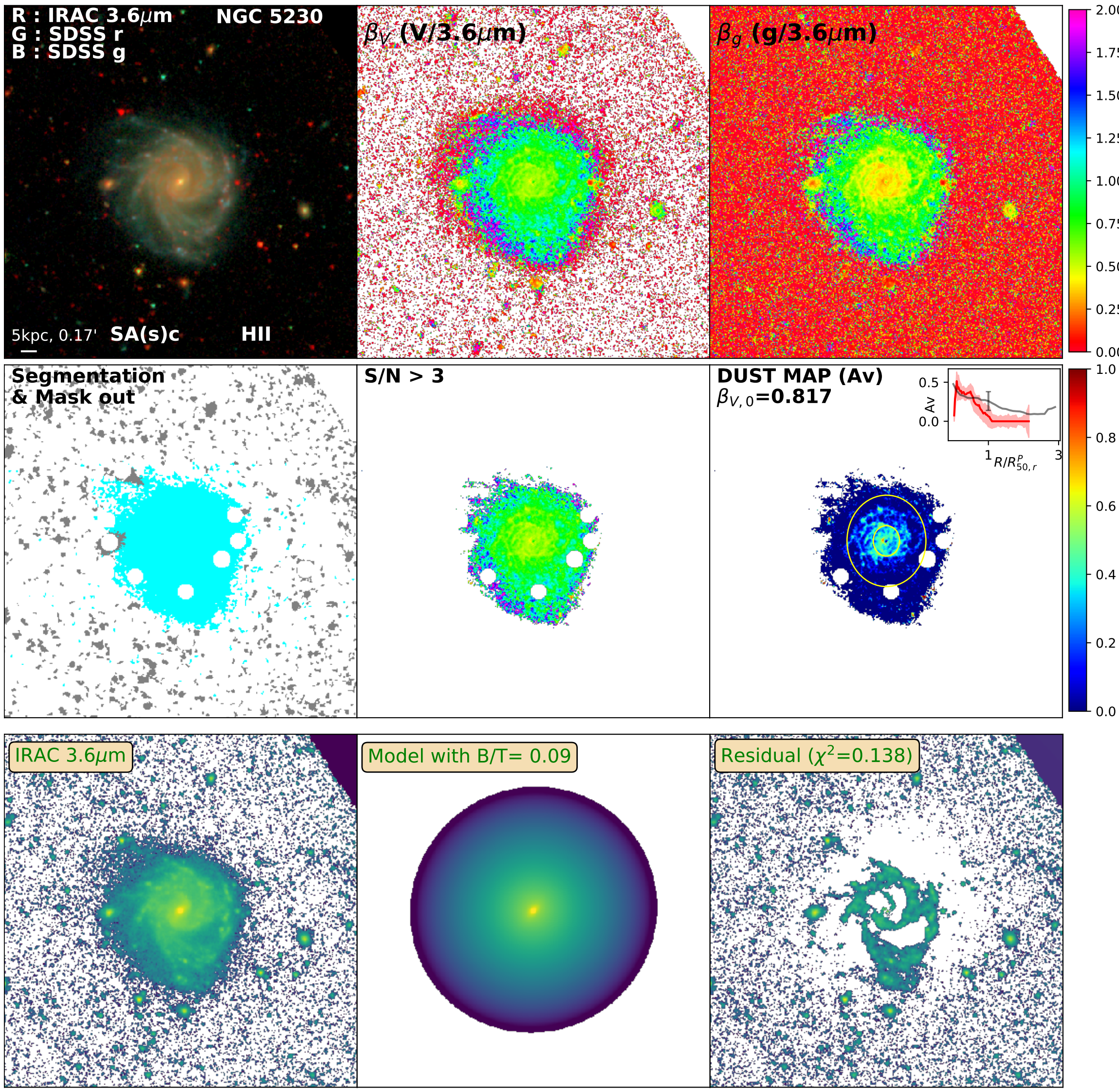

Figure D.186: Same as Figure 3.2 for NGC5230

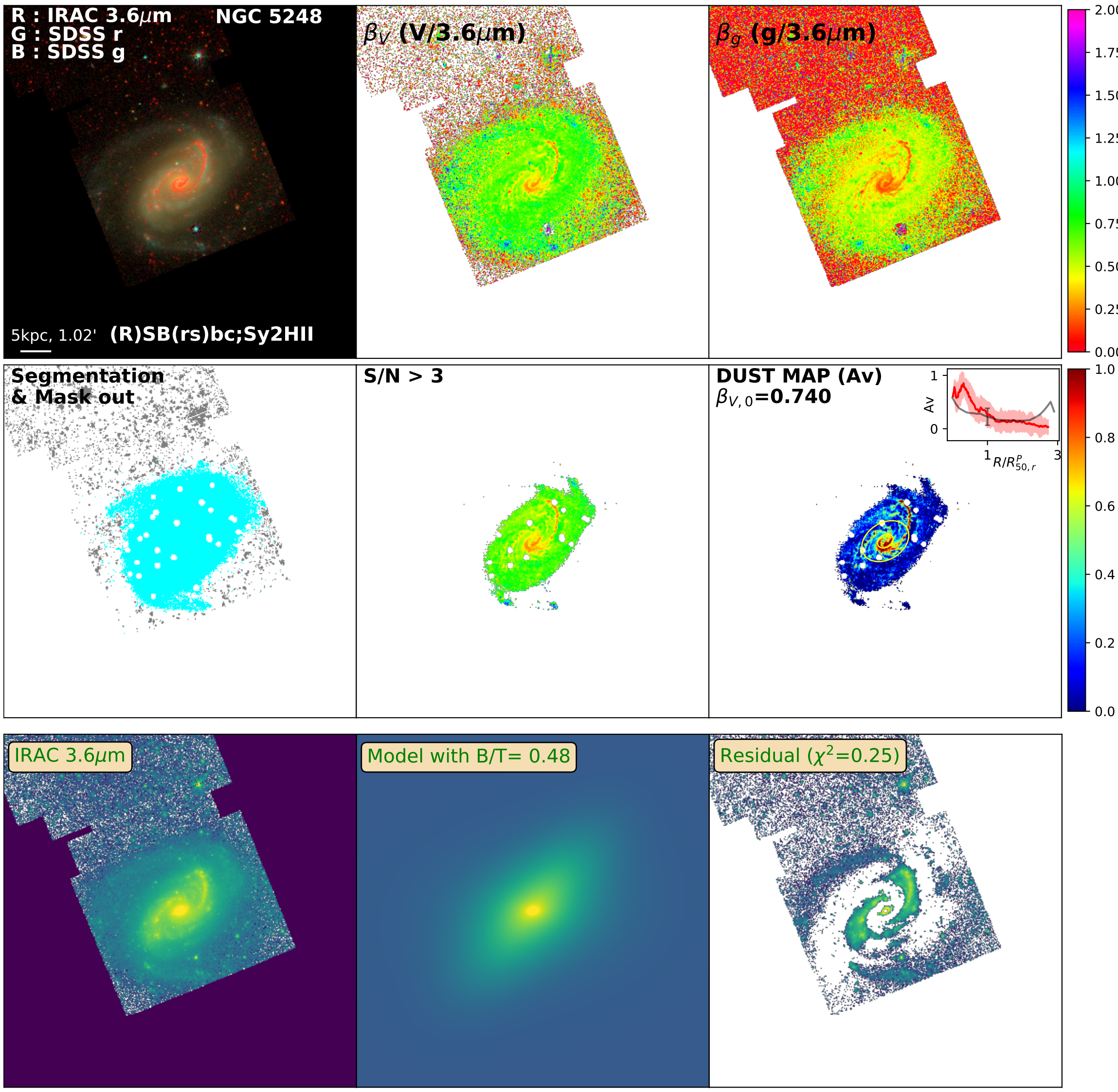

Figure D.187: Same as Figure 3.2 for NGC5248

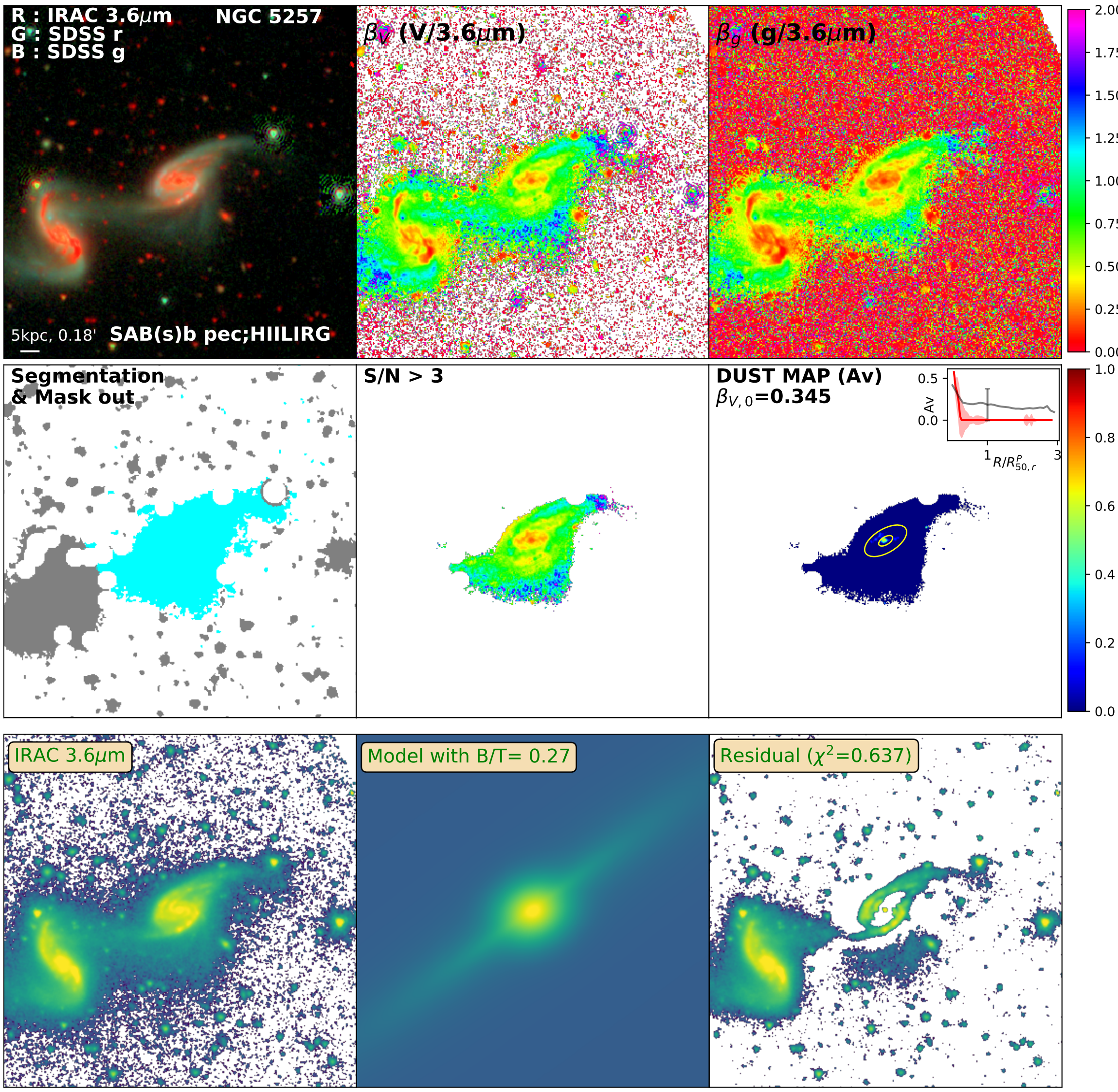

Figure D.188: Same as Figure 3.2 for NGC5257

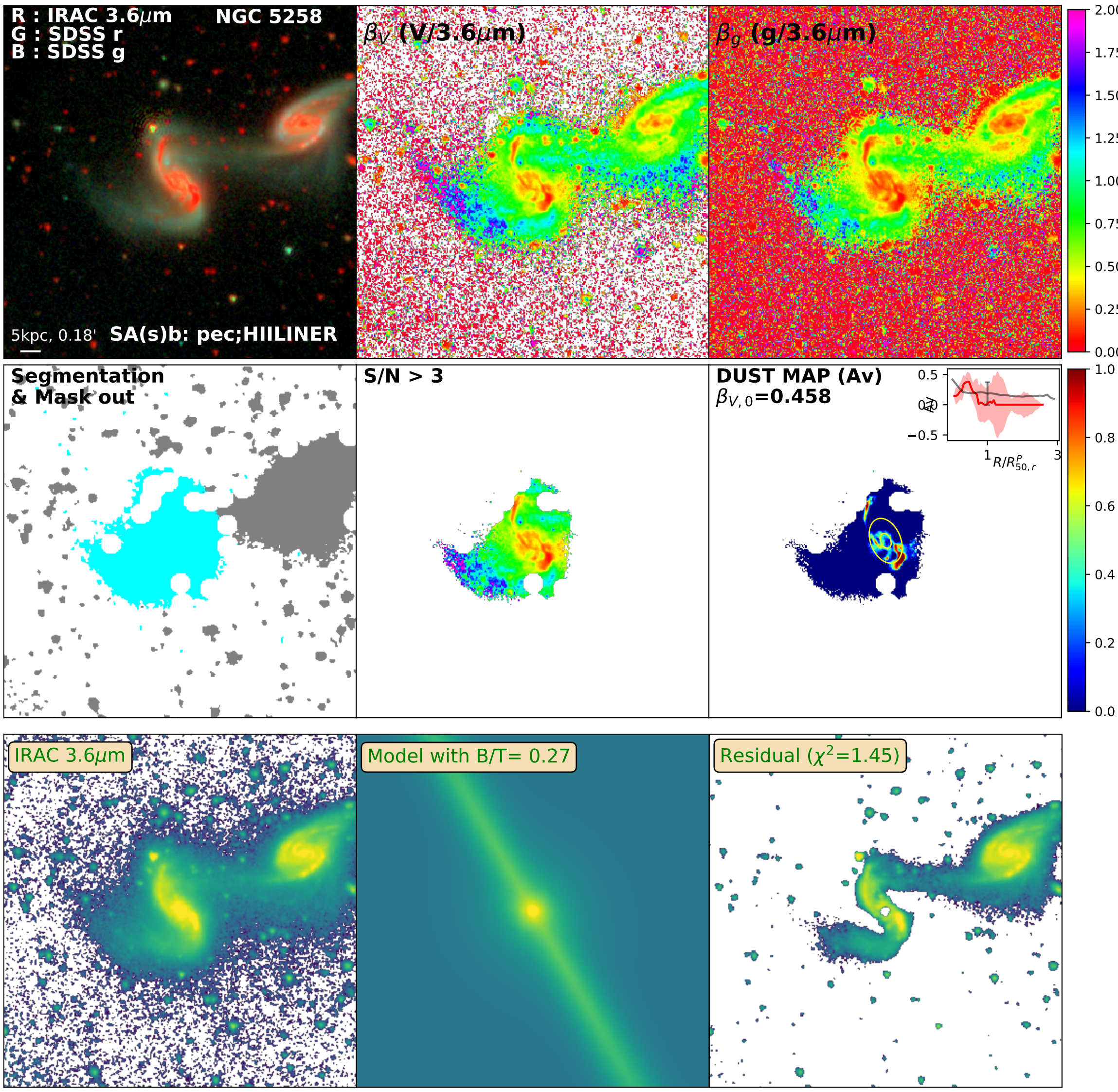

Figure D.189: Same as Figure 3.2 for NGC5258

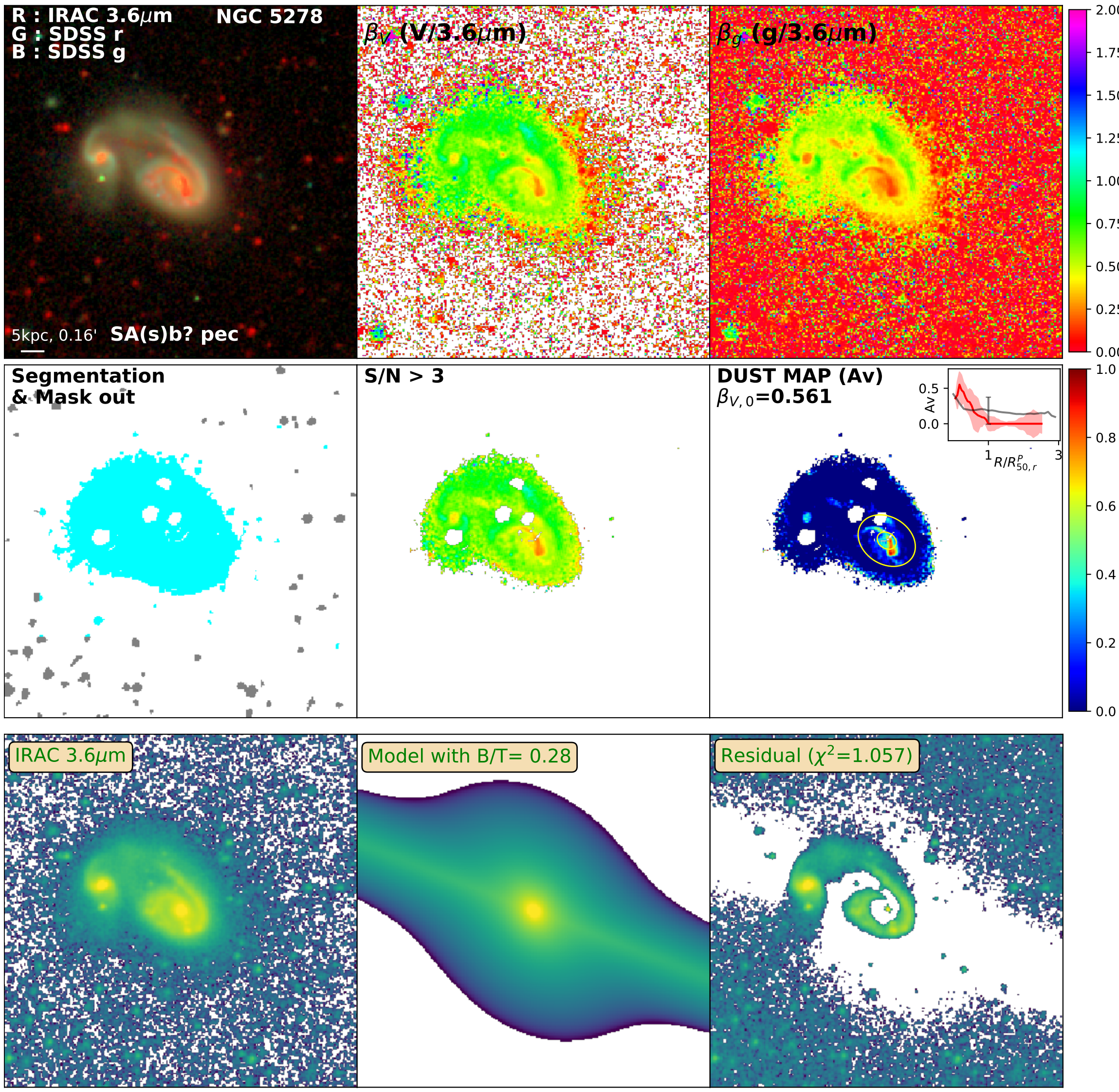

Figure D.190: Same as Figure 3.2 for NGC5278

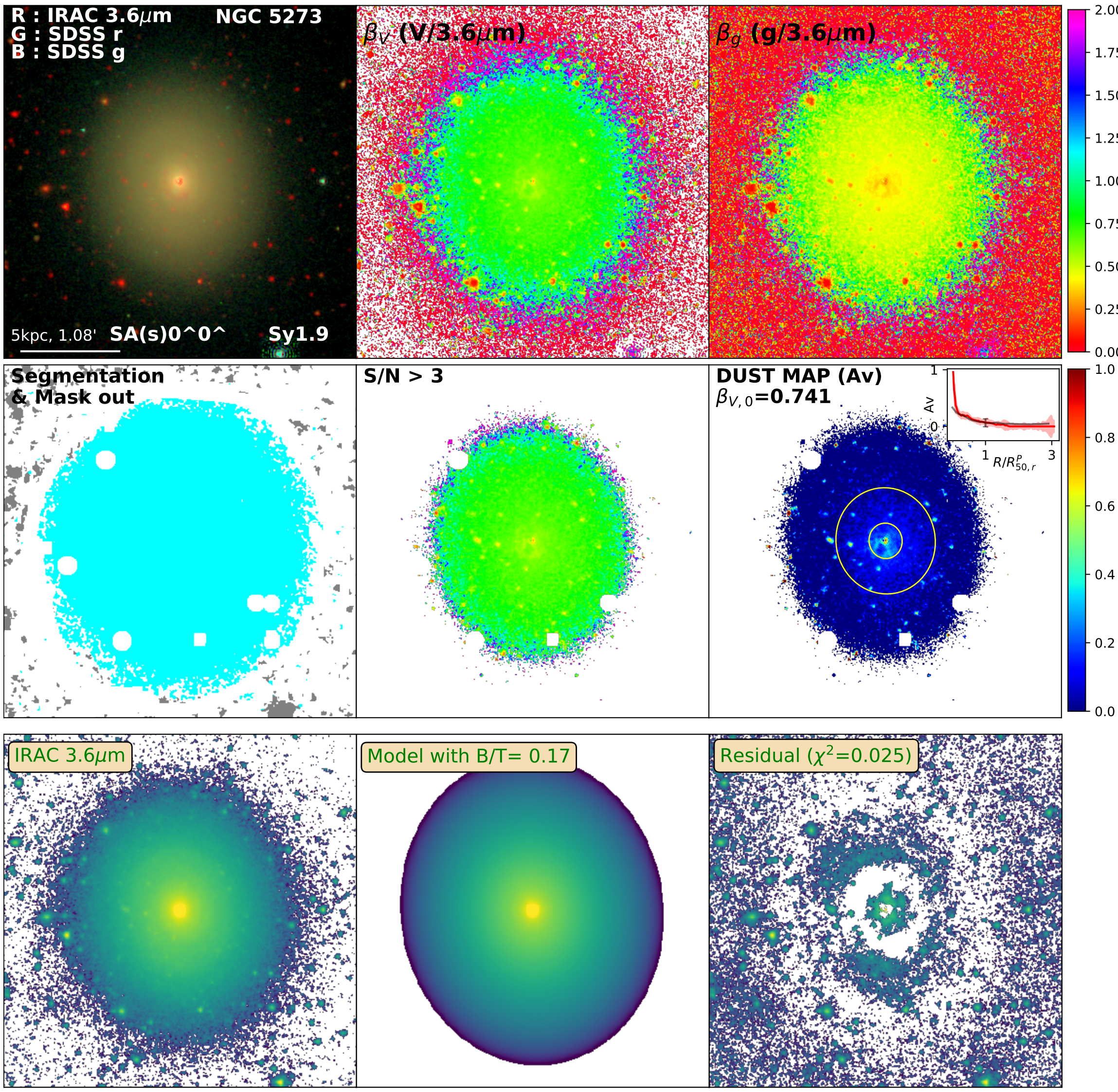

Figure D.191: Same as Figure 3.2 for NGC5273

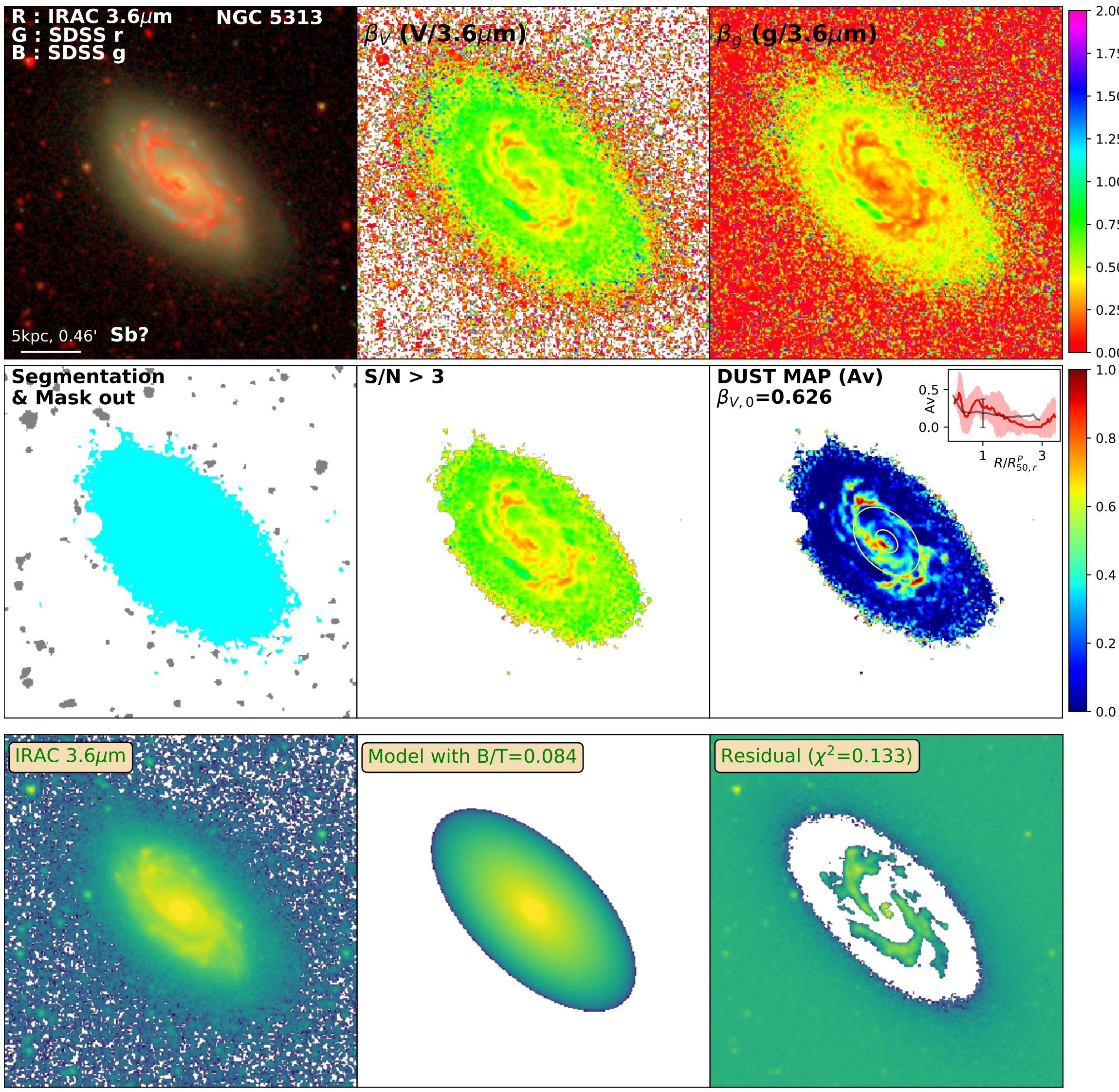

Figure D.192: Same as Figure 3.2 for NGC5313

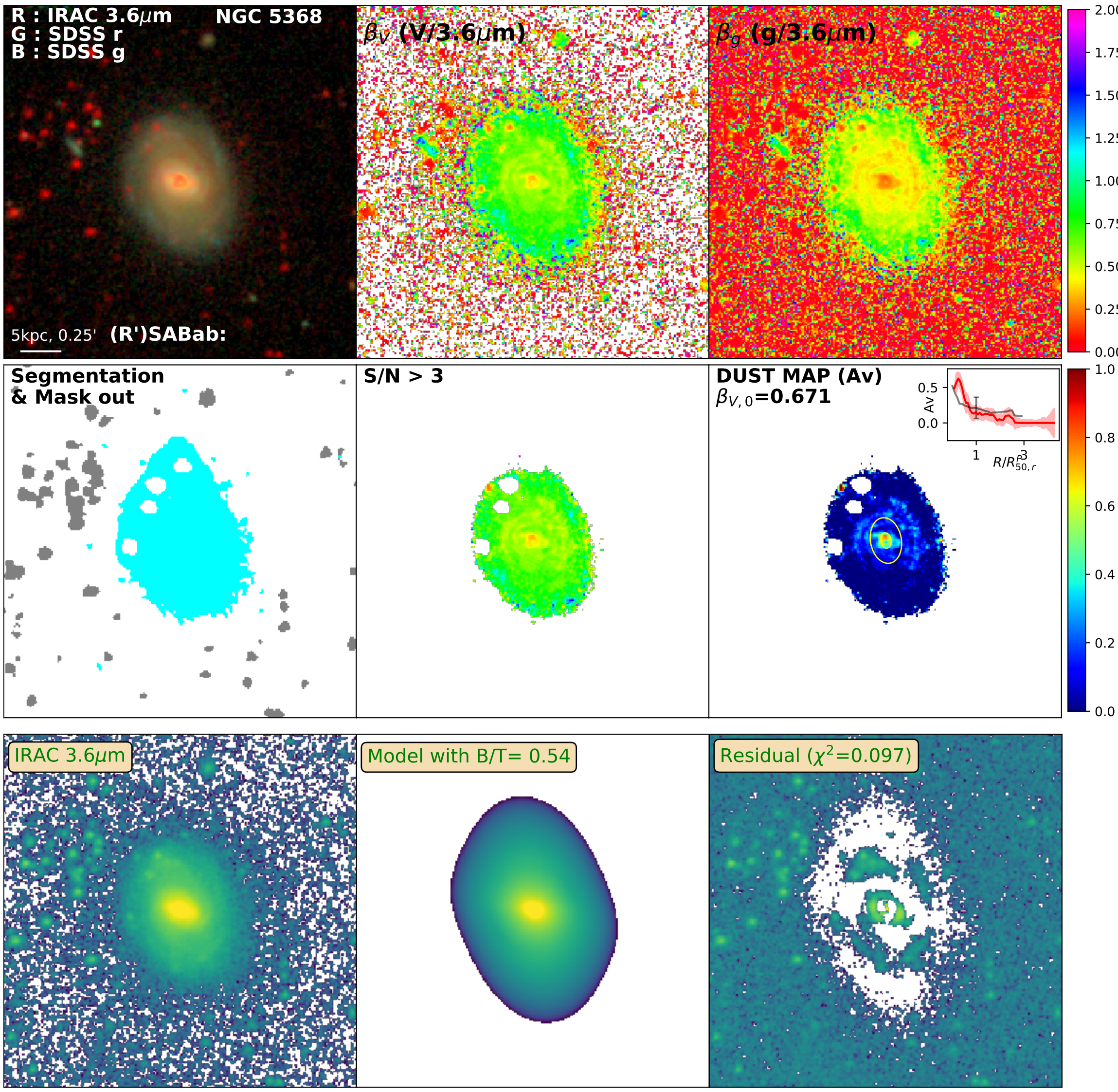

Figure D.193: Same as Figure 3.2 for NGC5368

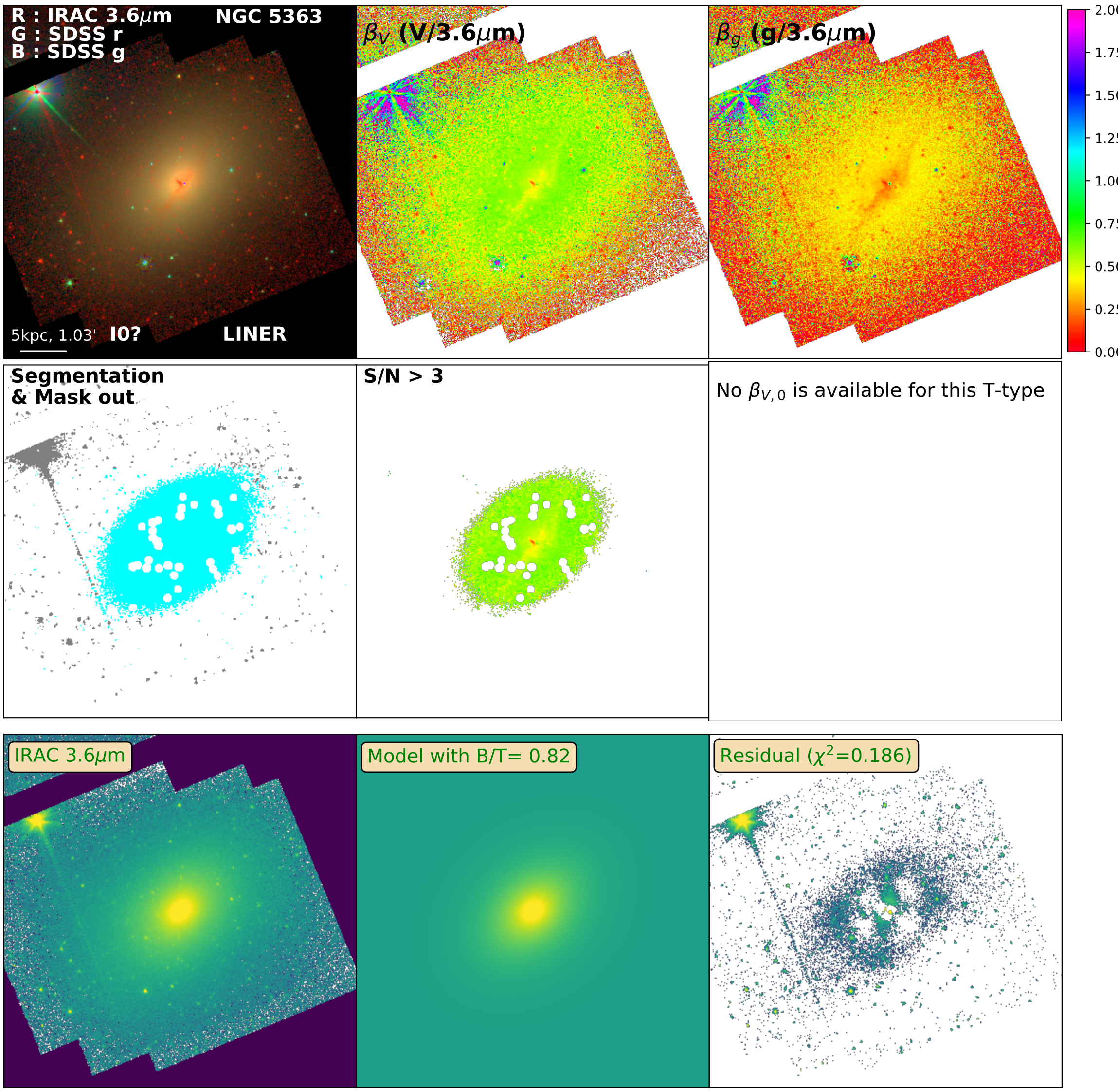

Figure D.194: Same as Figure 3.2 for NGC5363

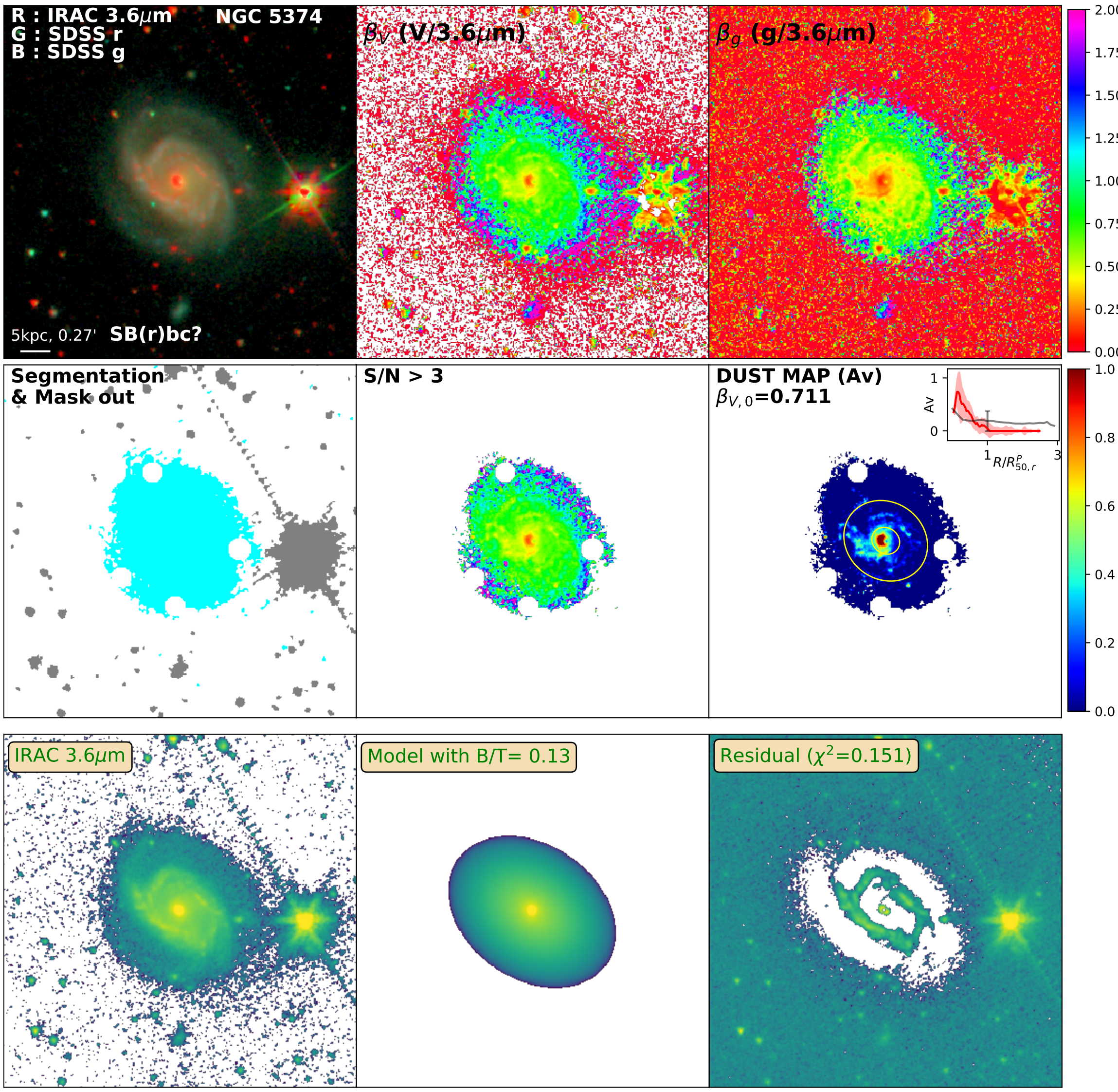

Figure D.195: Same as Figure 3.2 for NGC5374

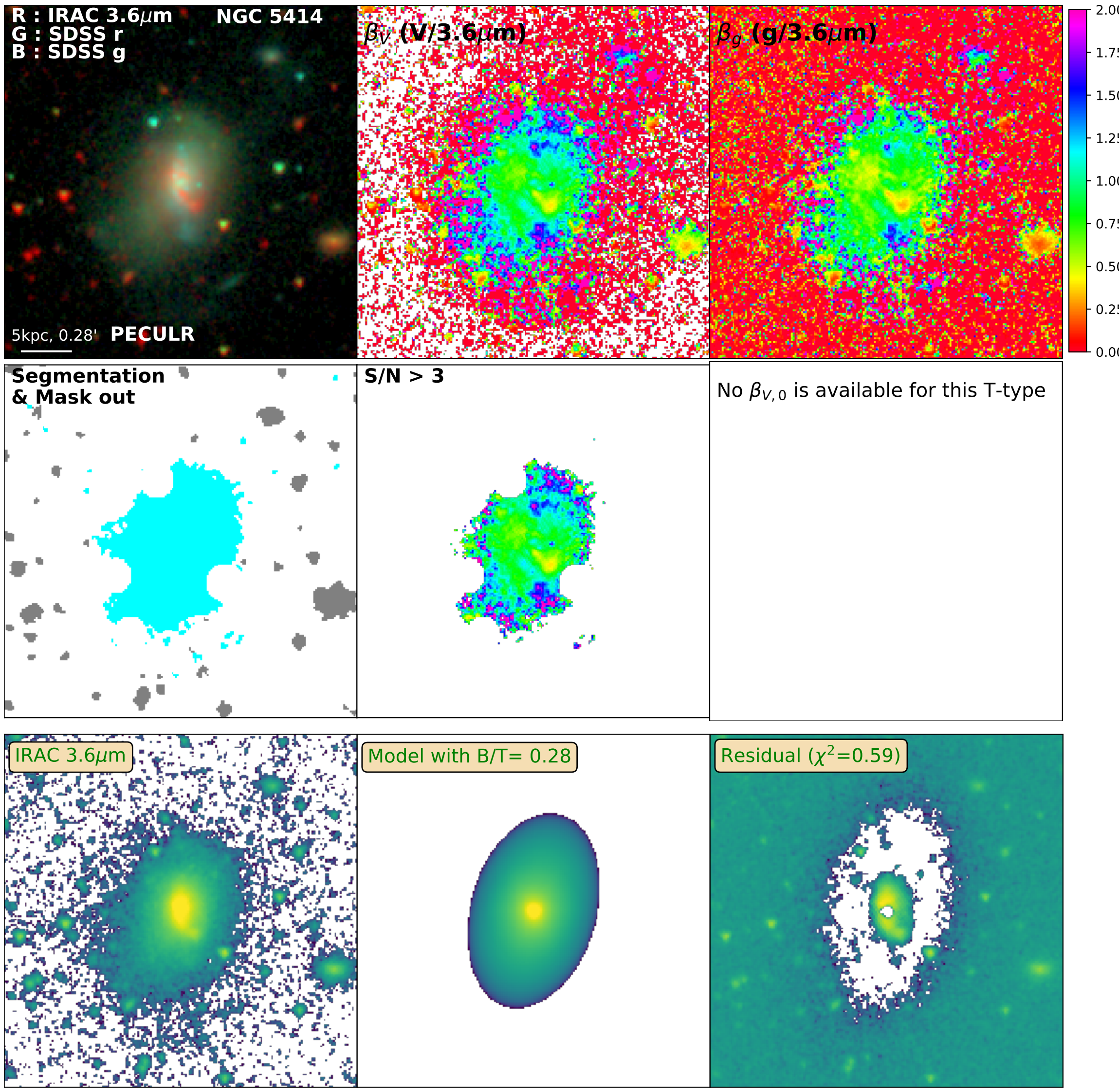

Figure D.196: Same as Figure 3.2 for NGC5414

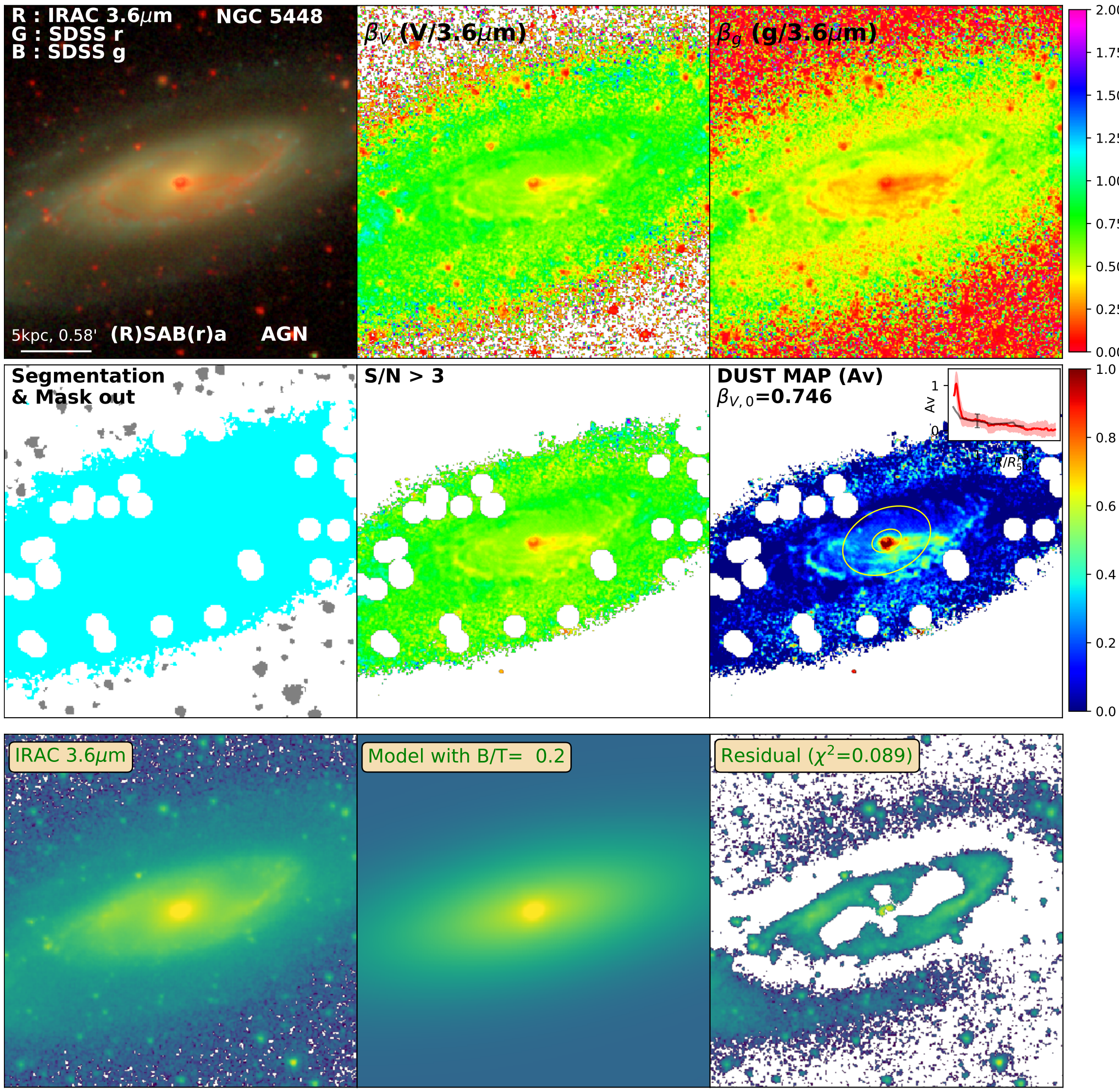

Figure D.197: Same as Figure 3.2 for NGC5448

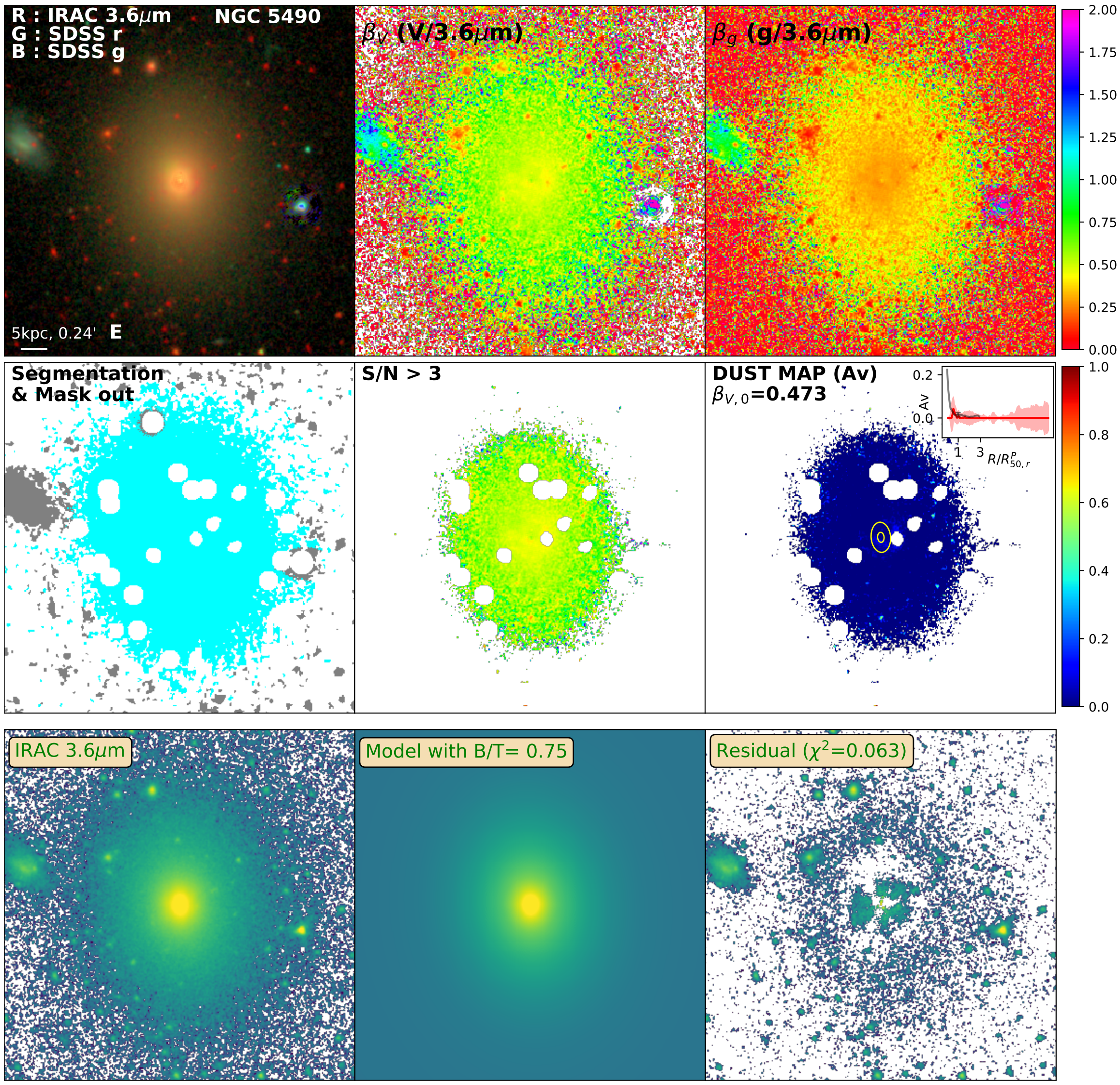

Figure D.198: Same as Figure 3.2 for NGC5490

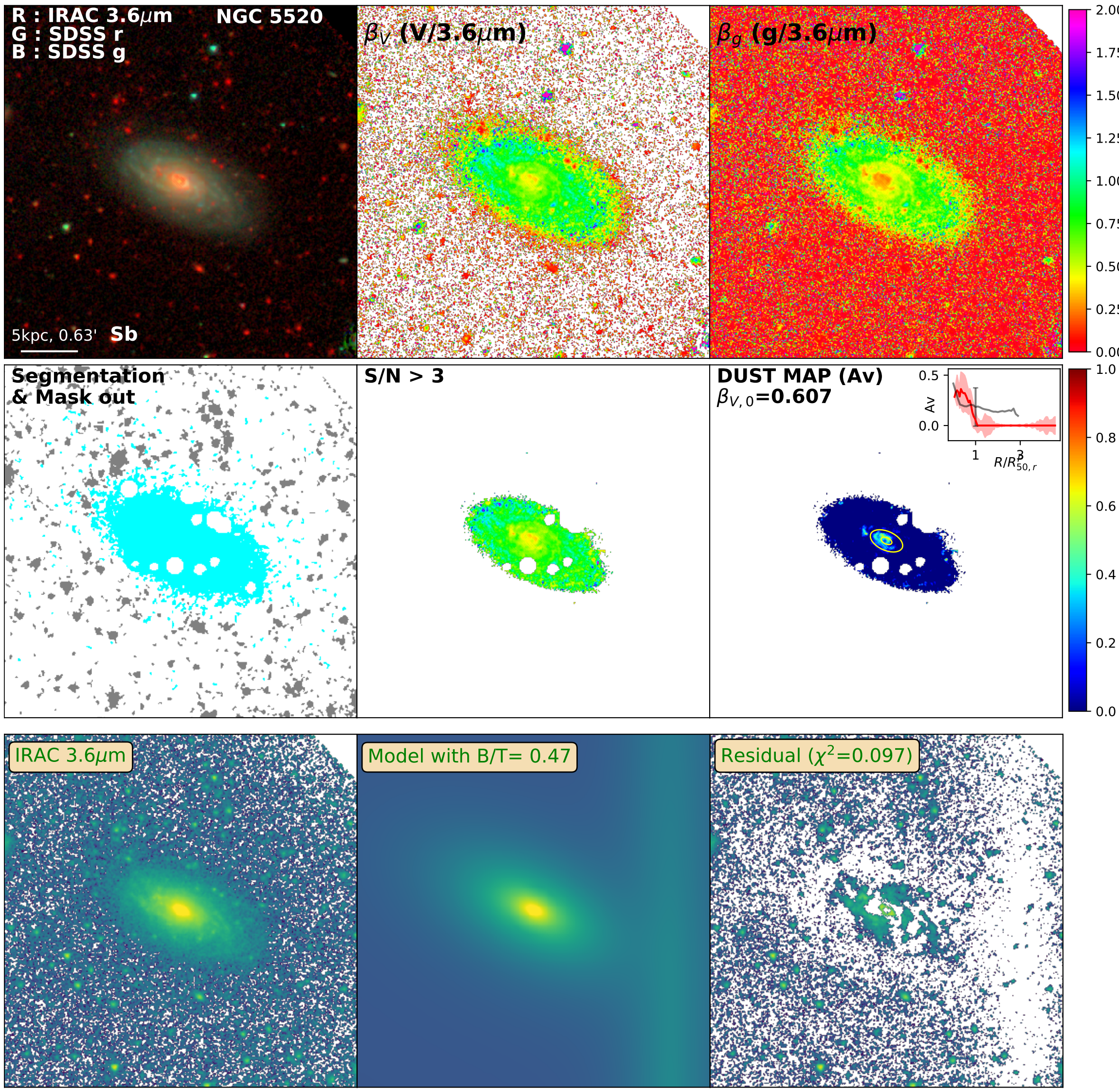

Figure D.199: Same as Figure 3.2 for NGC5520

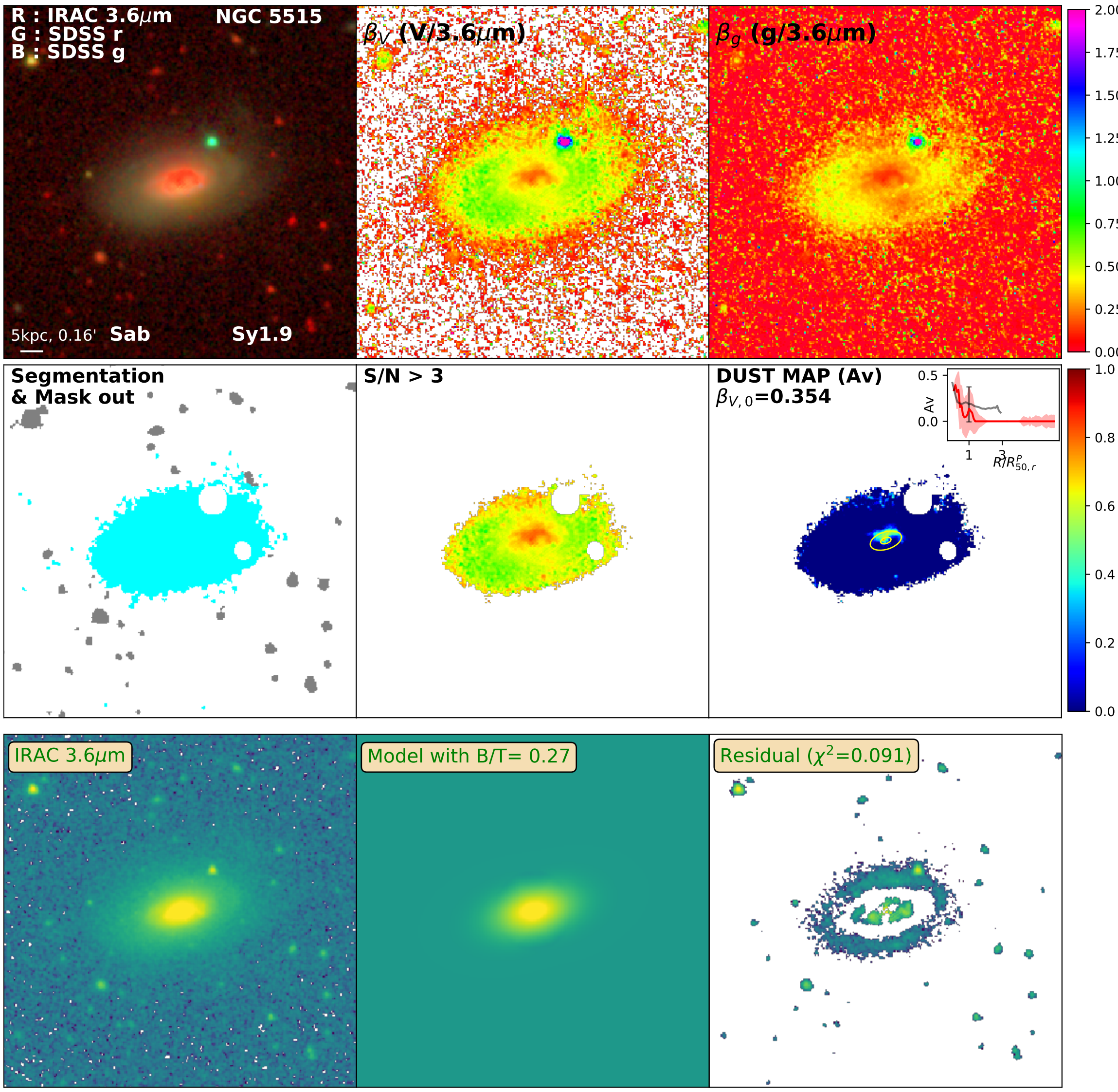

Figure D.200: Same as Figure 3.2 for NGC5515

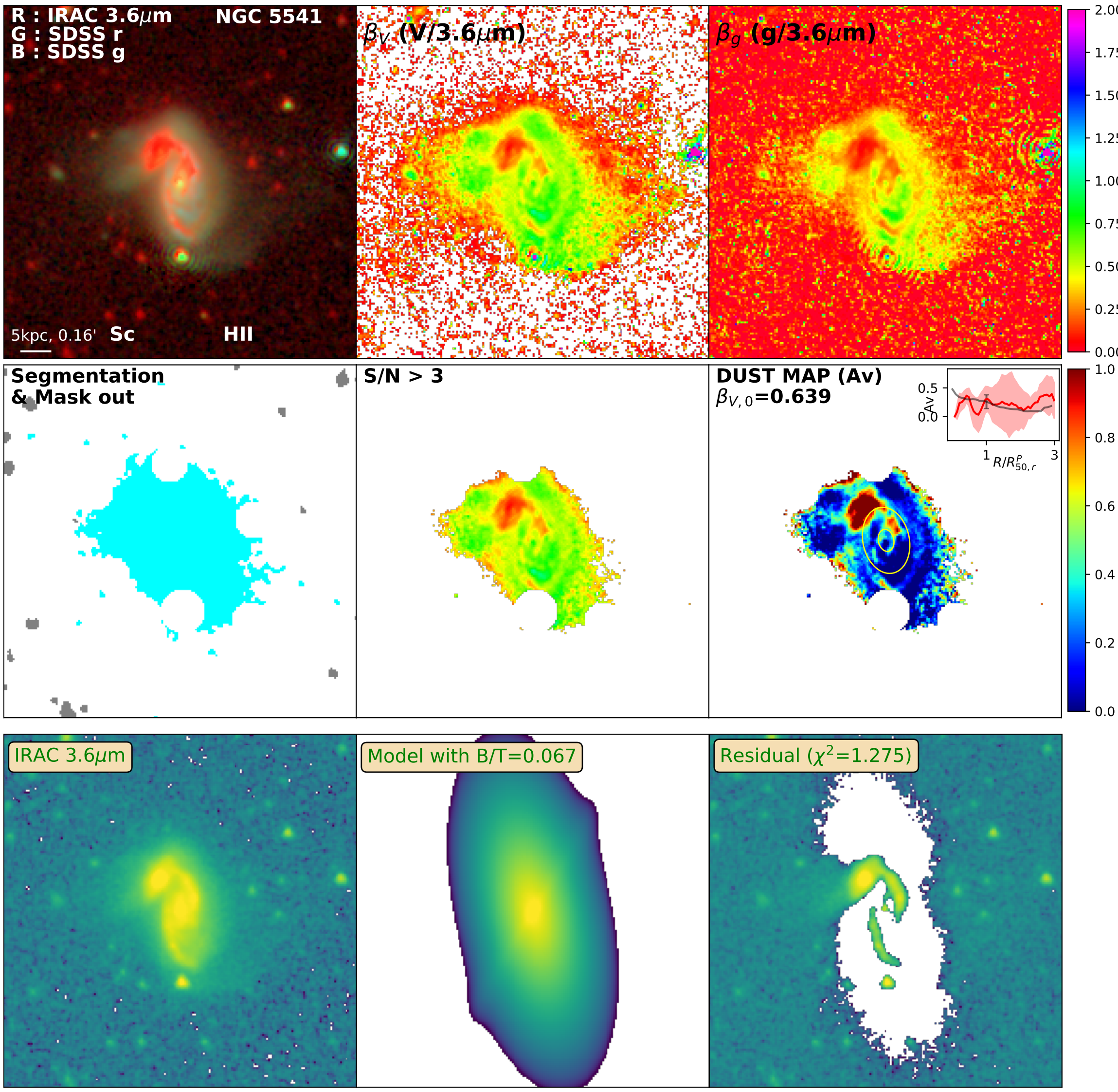

Figure D.201: Same as Figure 3.2 for NGC5541

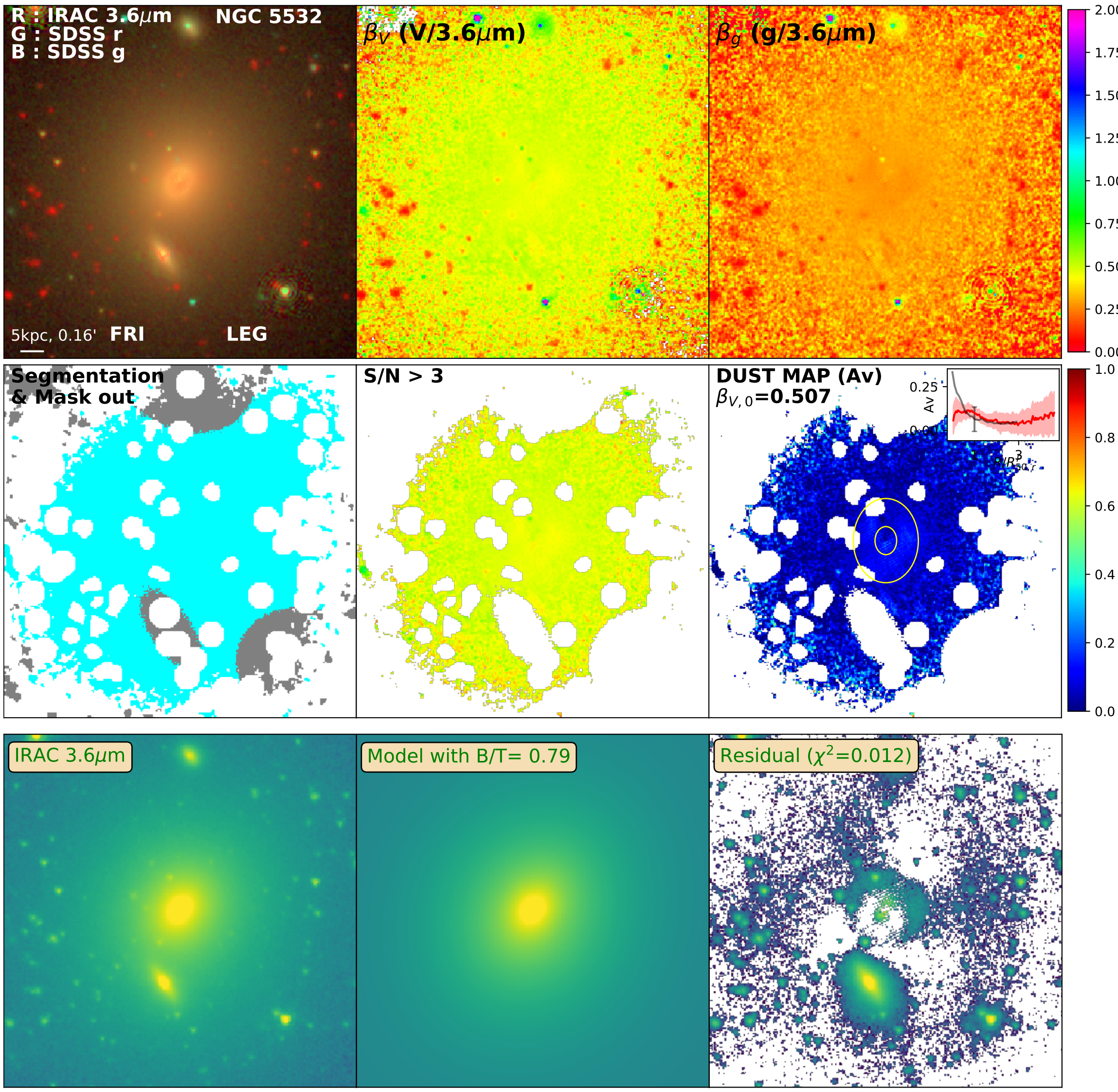

Figure D.202: Same as Figure 3.2 for NGC5532

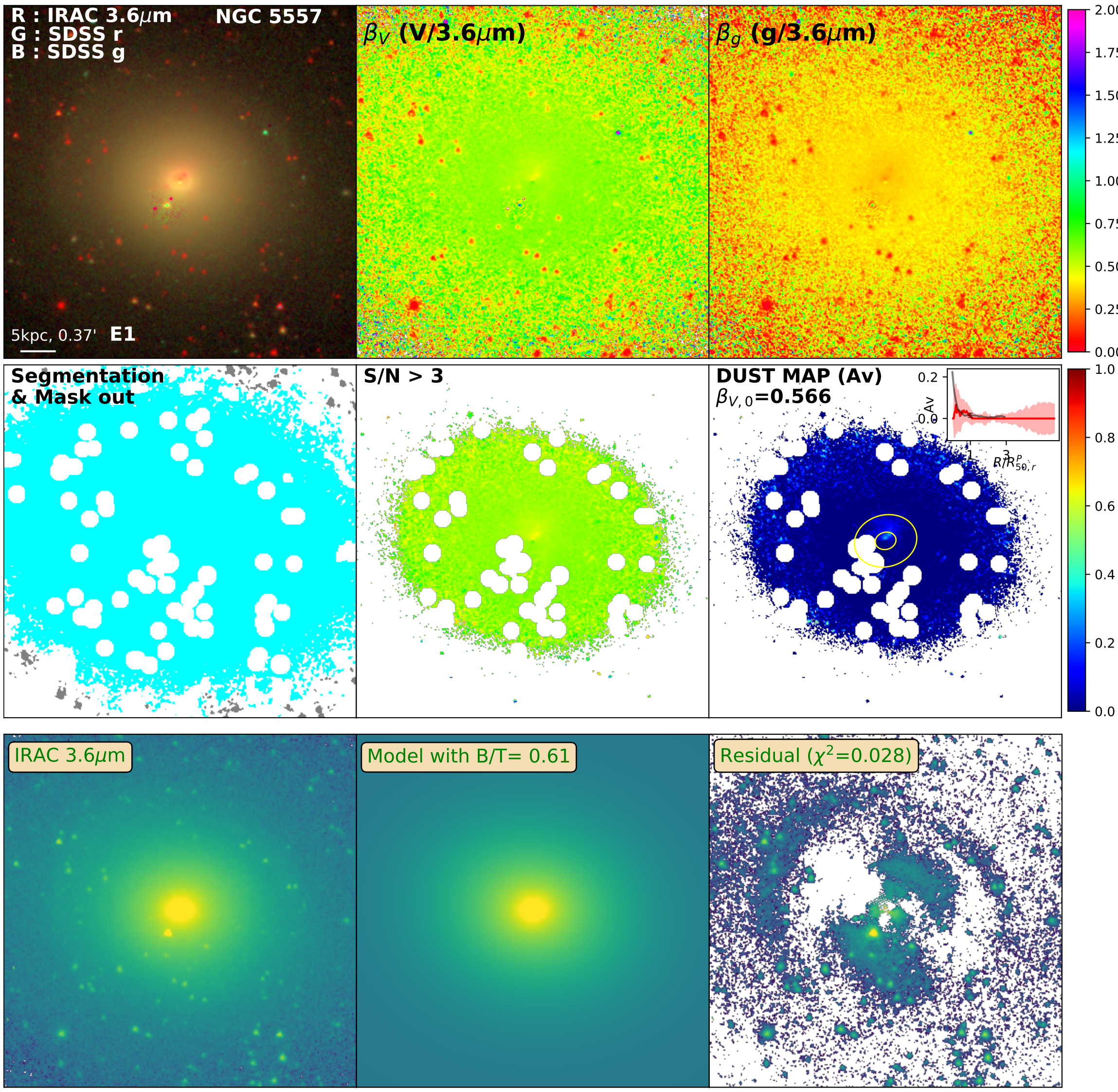

Figure D.203: Same as Figure 3.2 for NGC5557

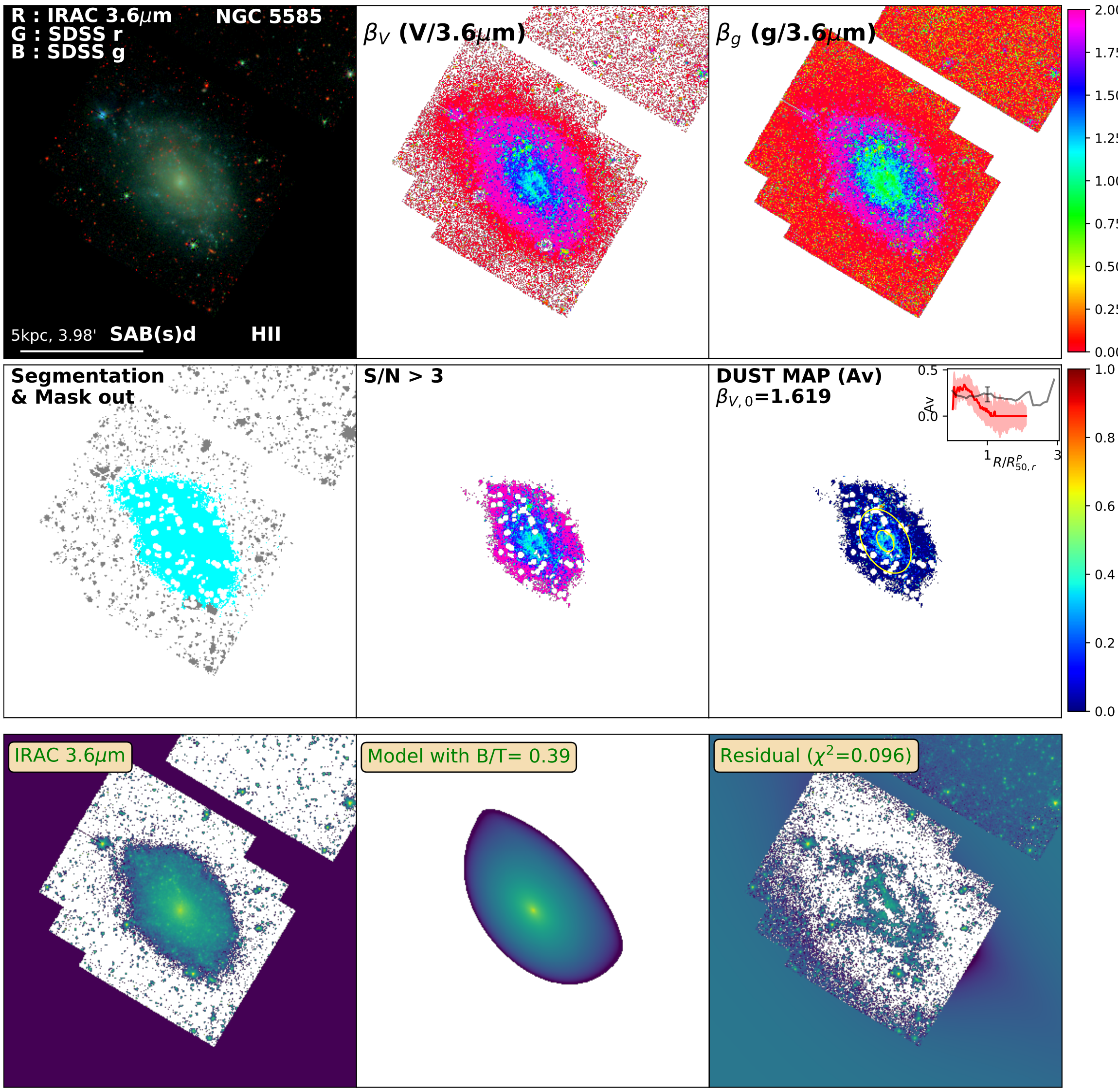

Figure D.204: Same as Figure 3.2 for NGC5585

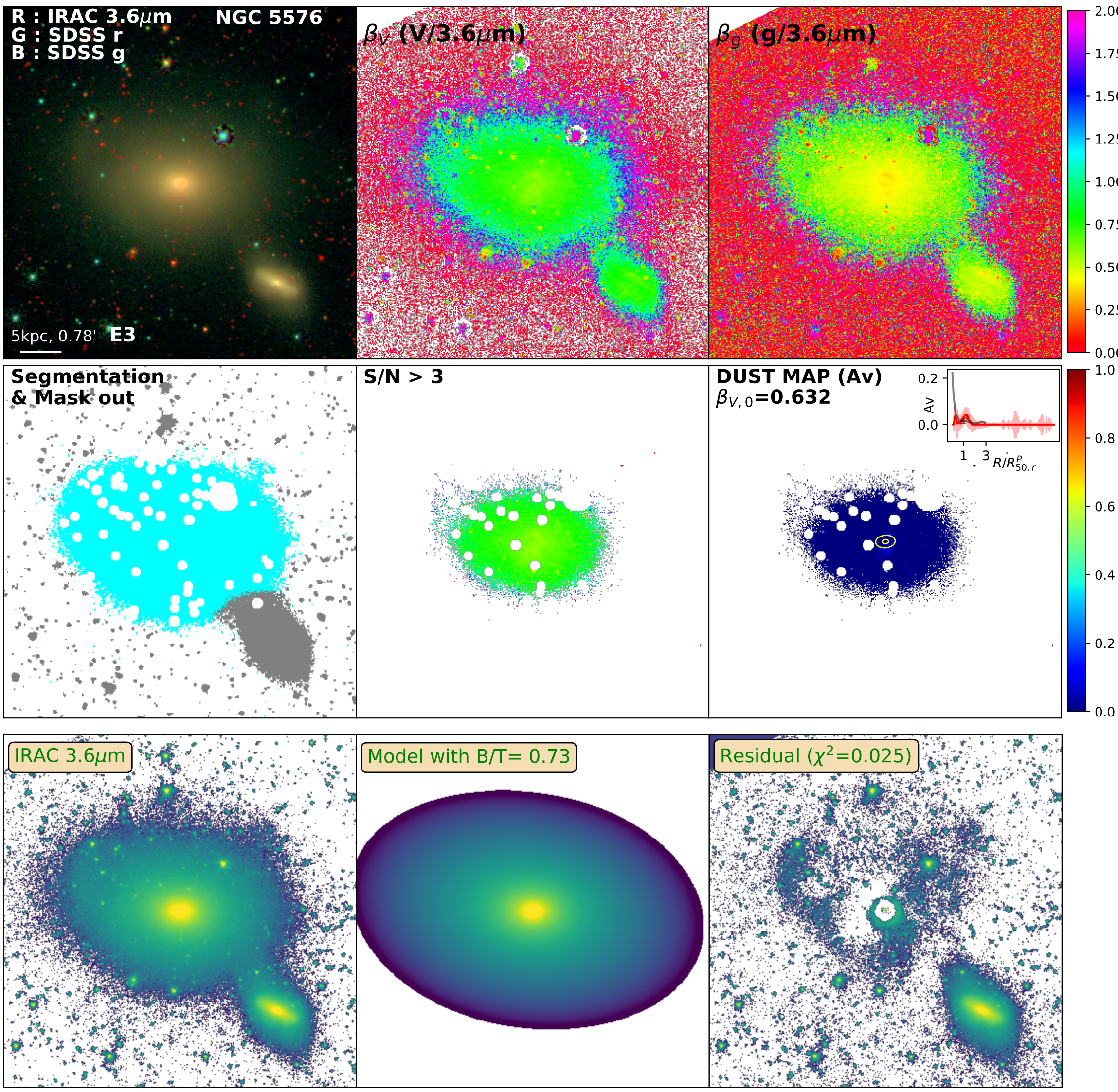

Figure D.205: Same as Figure 3.2 for NGC5576

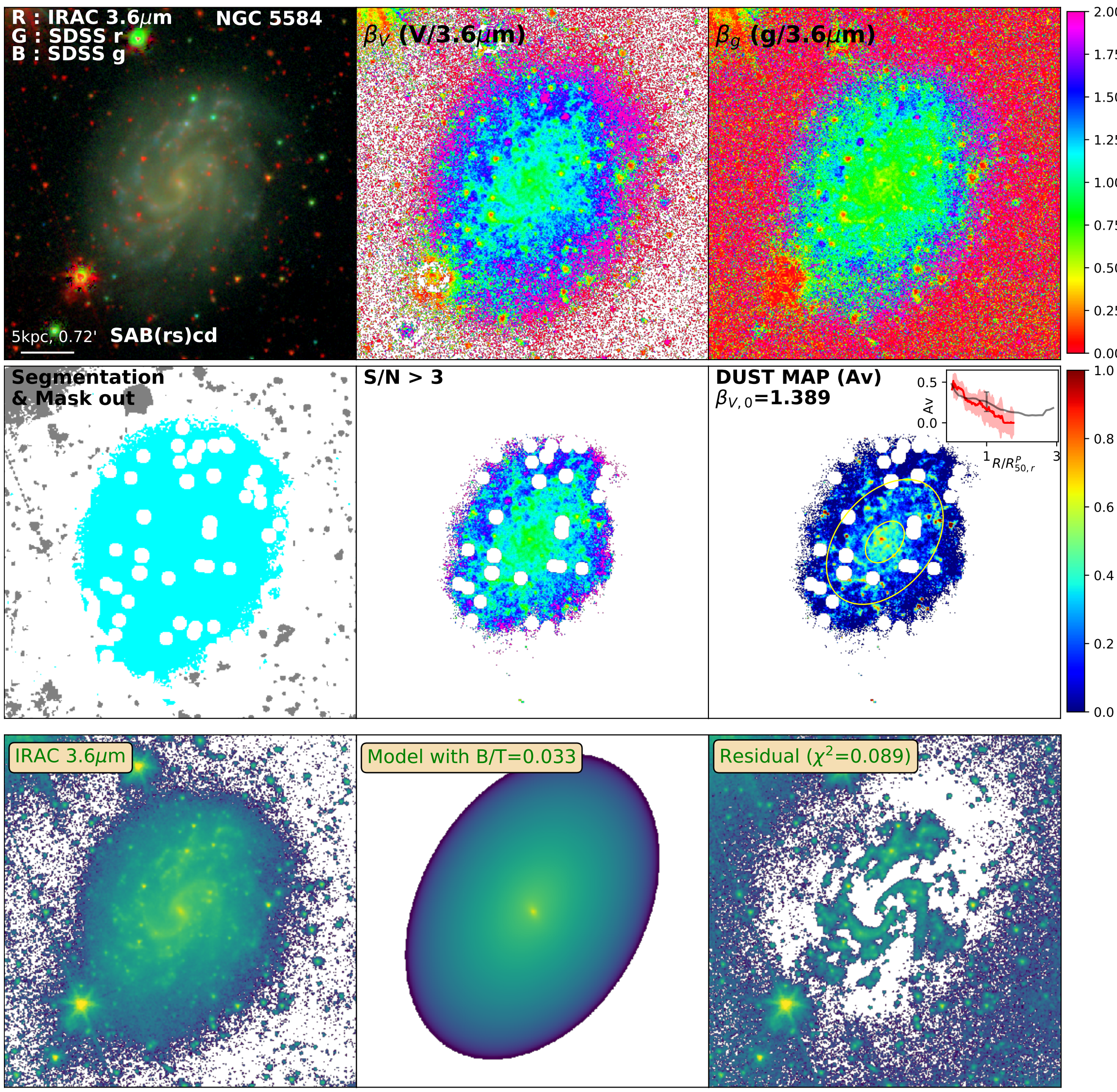

Figure D.206: Same as Figure 3.2 for NGC5584

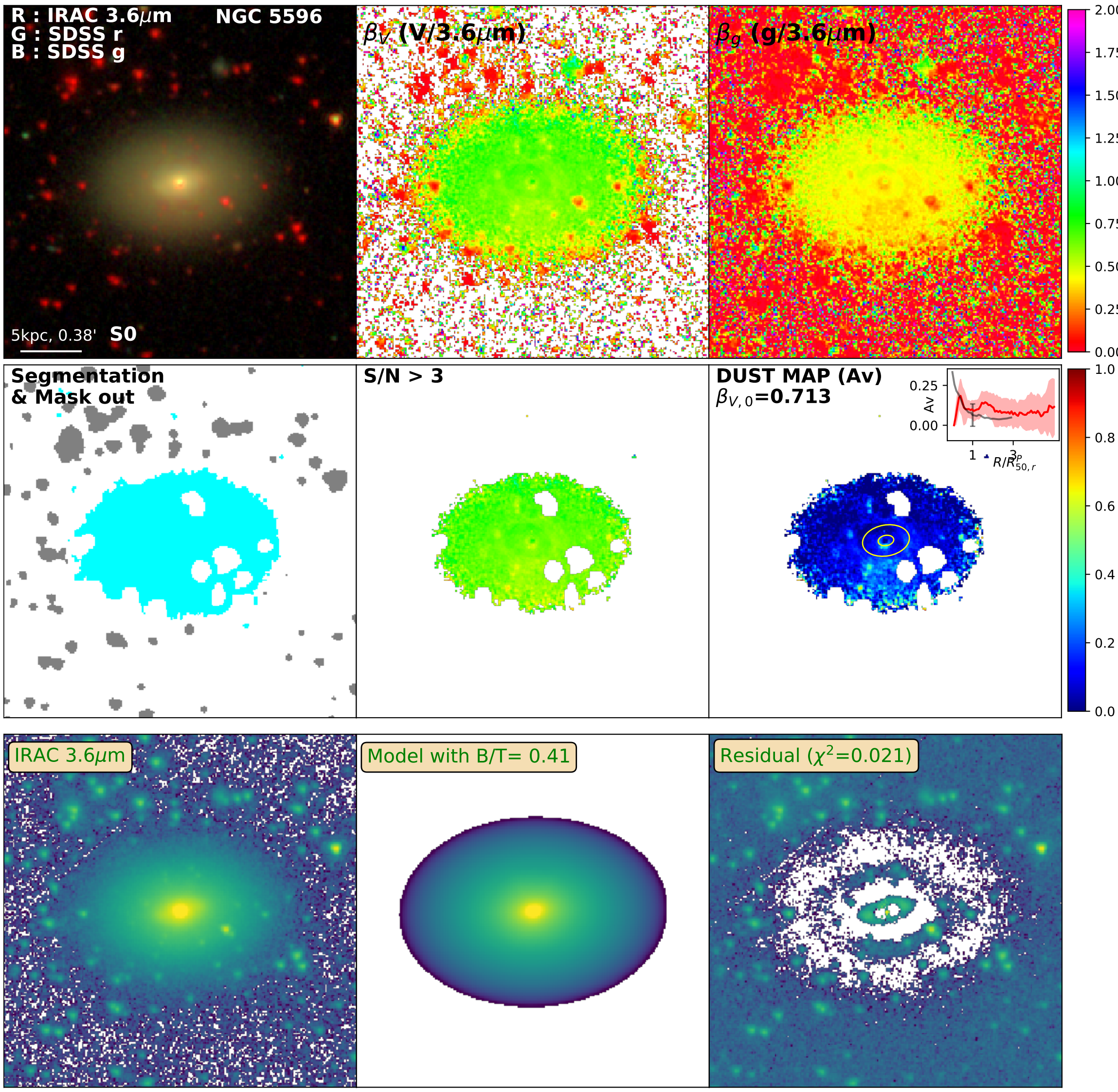

Figure D.207: Same as Figure 3.2 for NGC5596

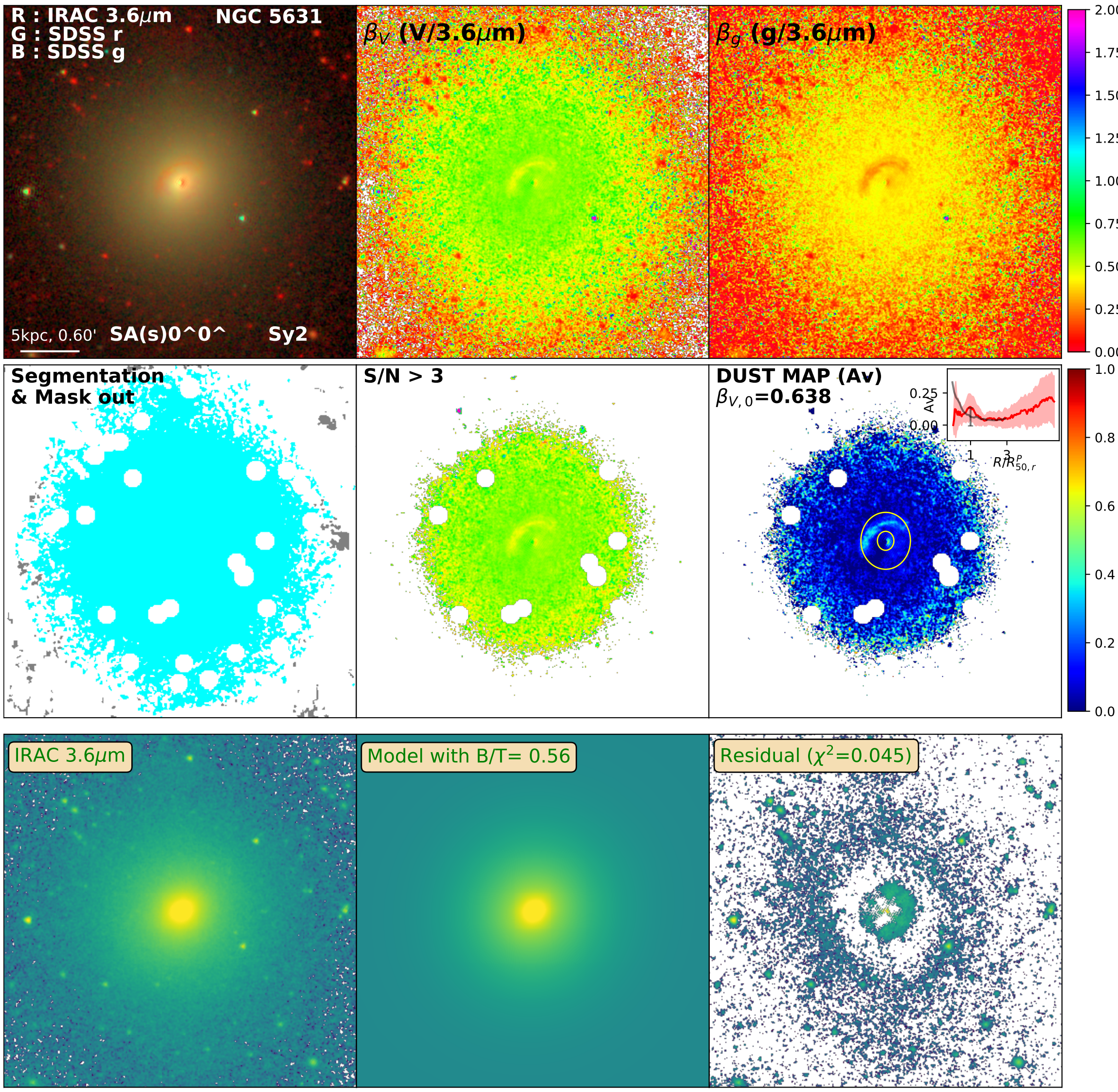

Figure D.208: Same as Figure 3.2 for NGC5631

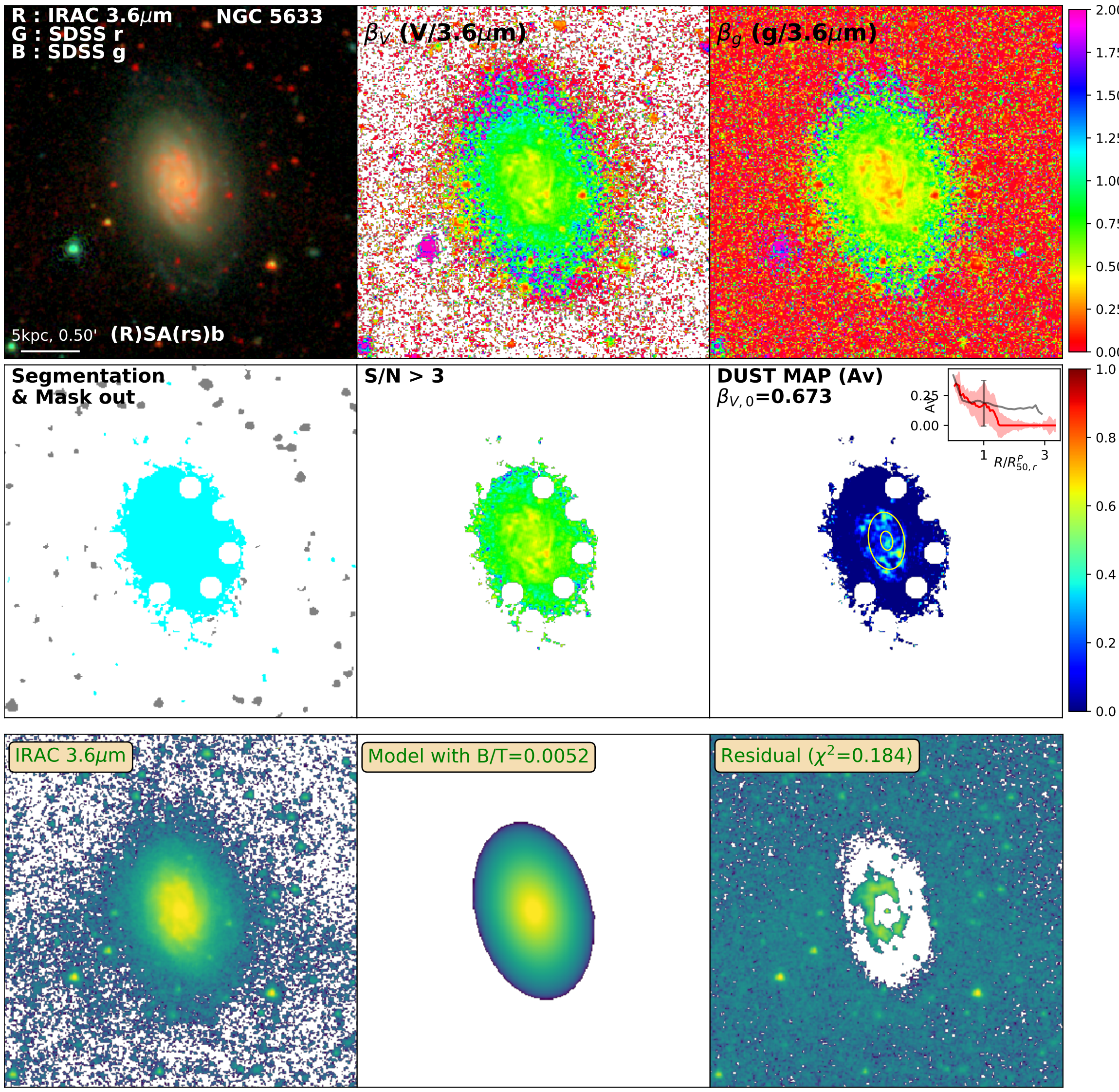

Figure D.209: Same as Figure 3.2 for NGC5633

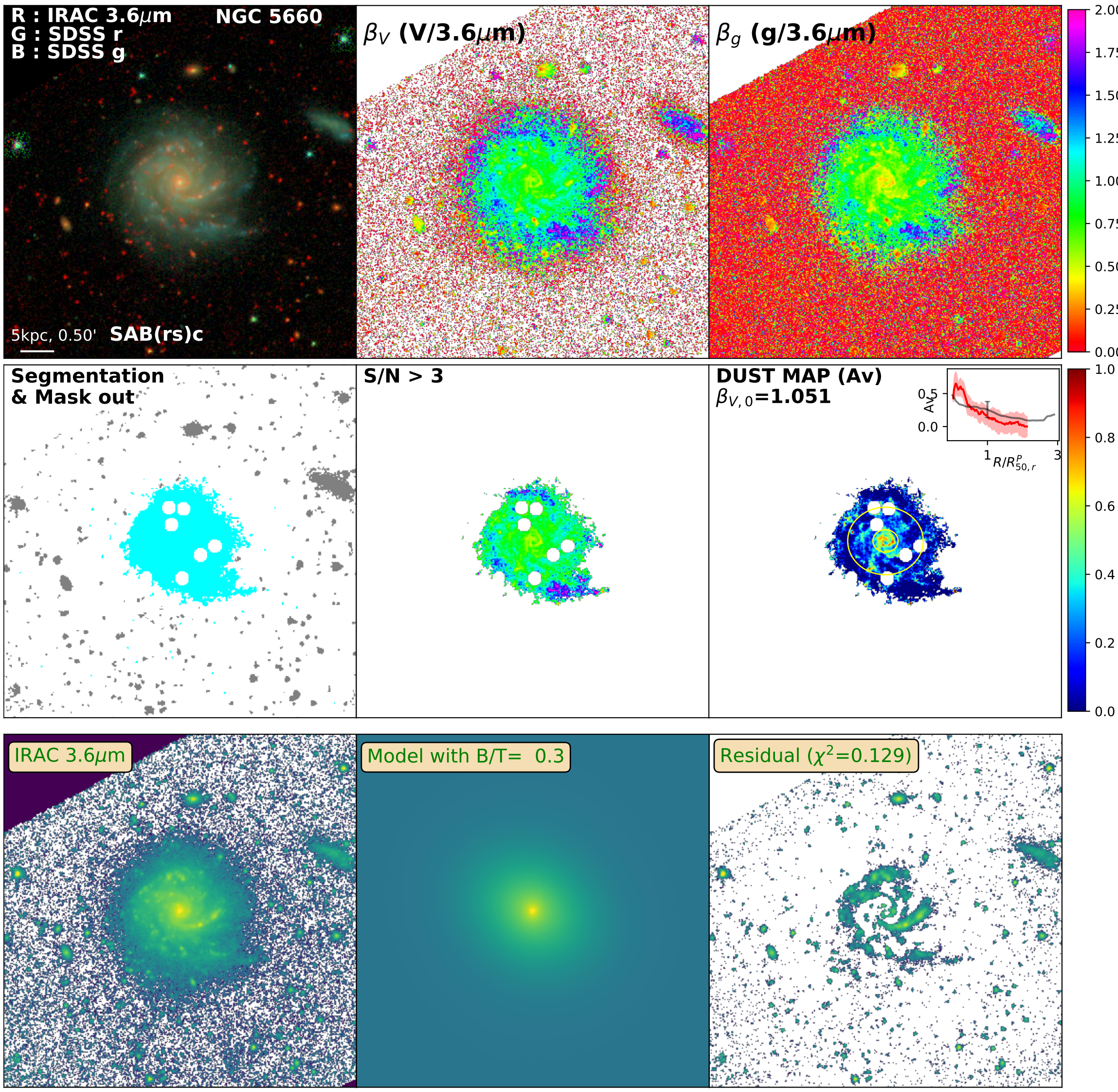

Figure D.210: Same as Figure 3.2 for NGC5660

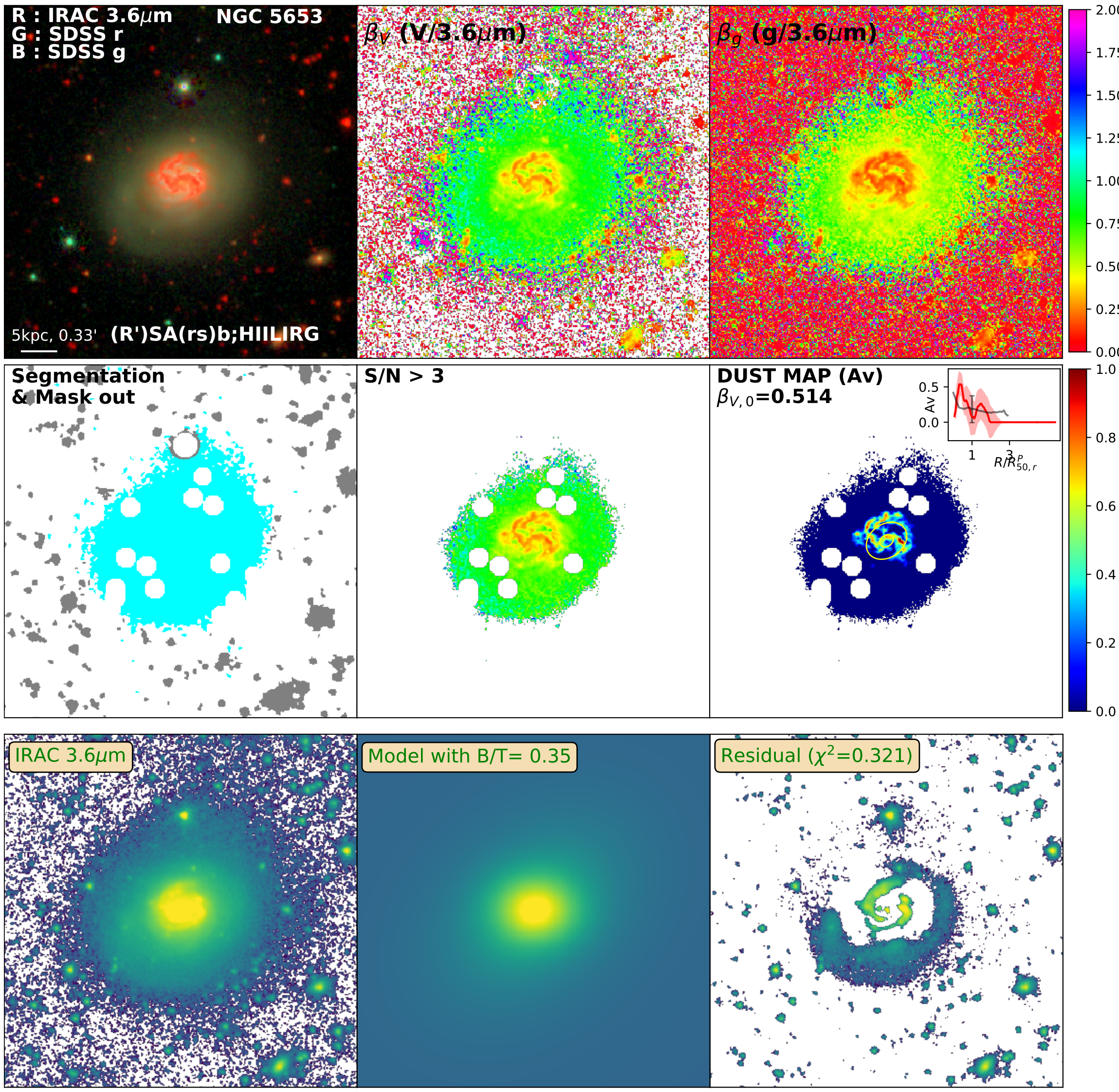

Figure D.211: Same as Figure 3.2 for NGC5653

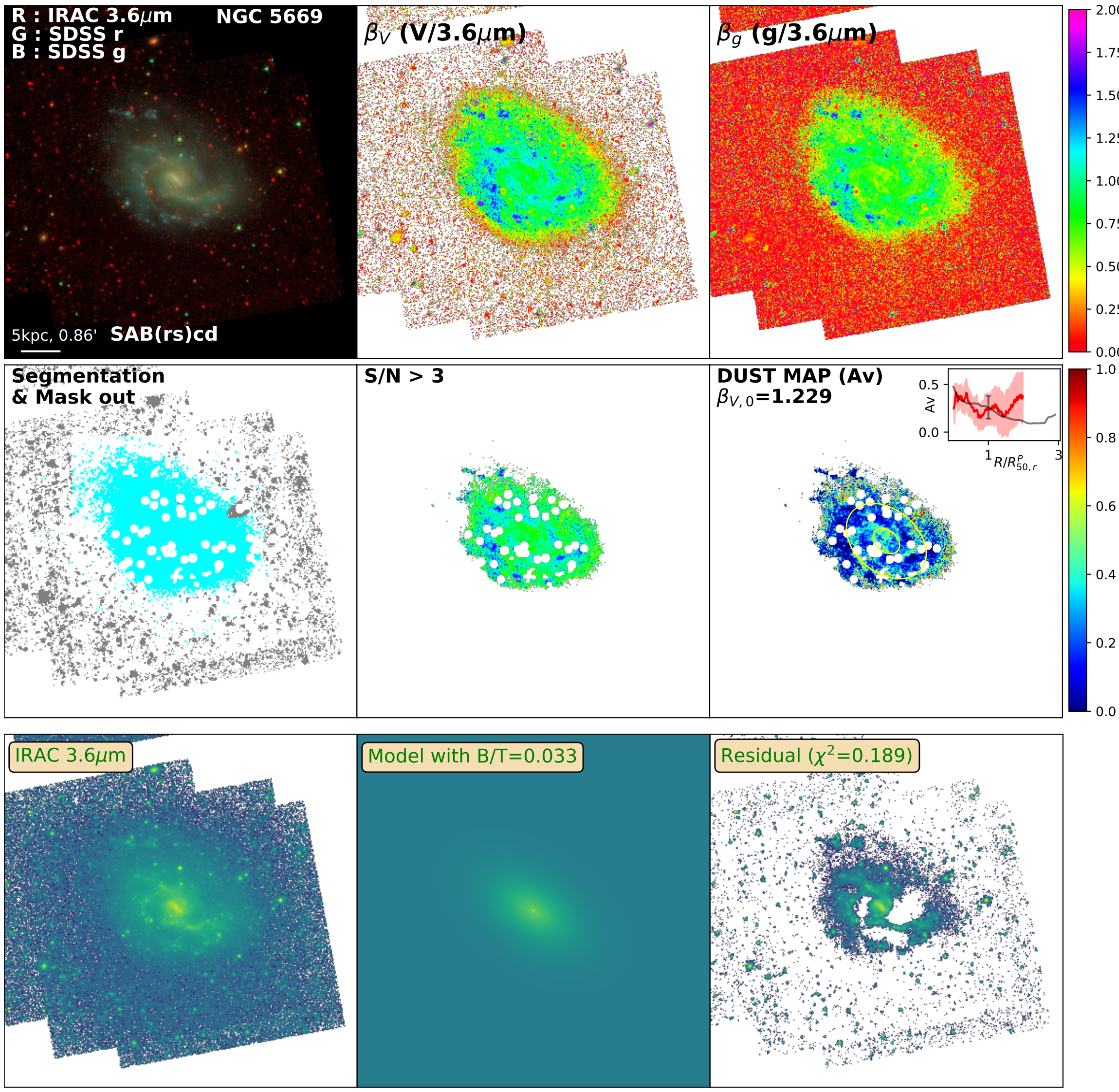

Figure D.212: Same as Figure 3.2 for NGC5669

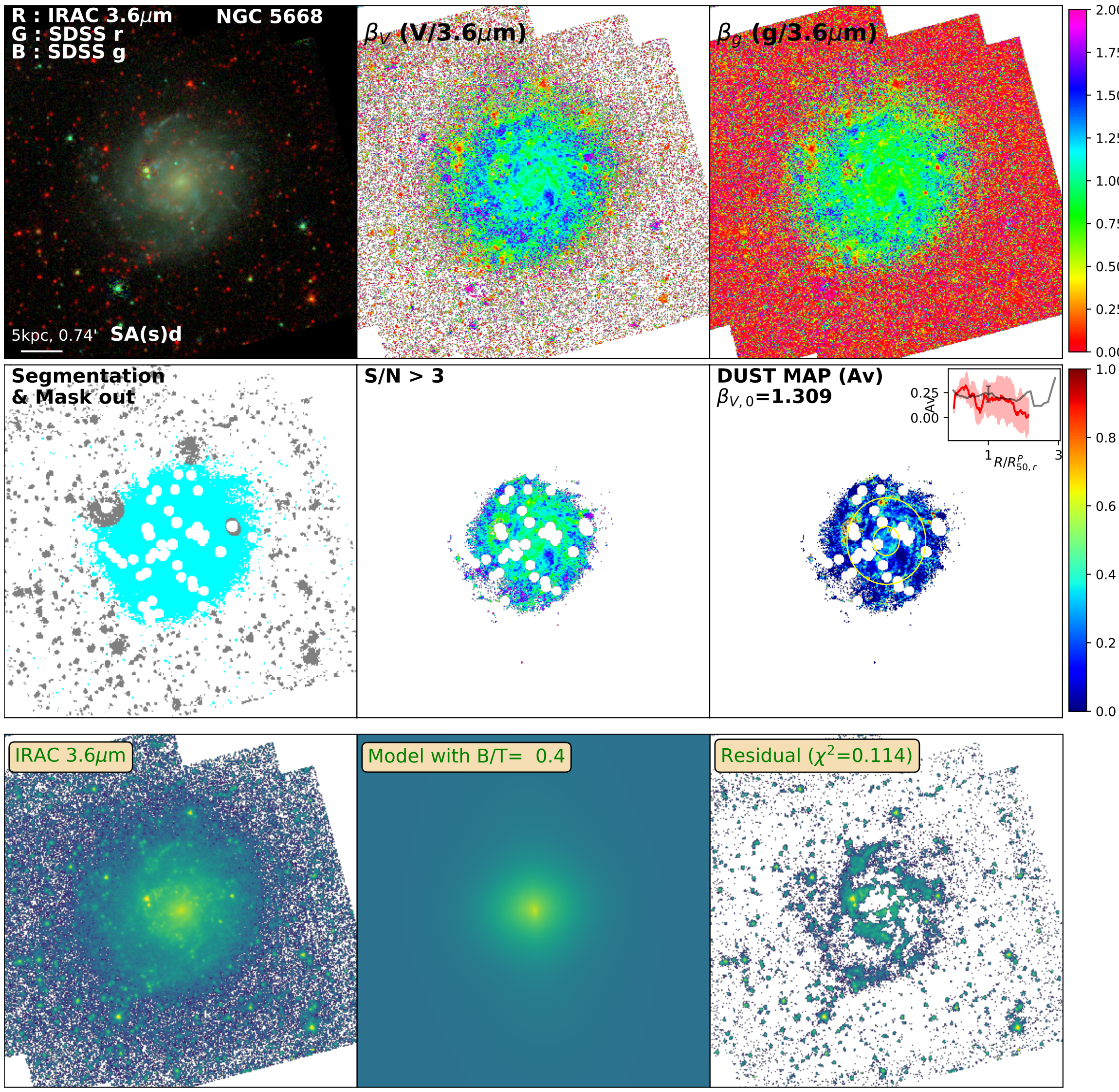

Figure D.213: Same as Figure 3.2 for NGC5668

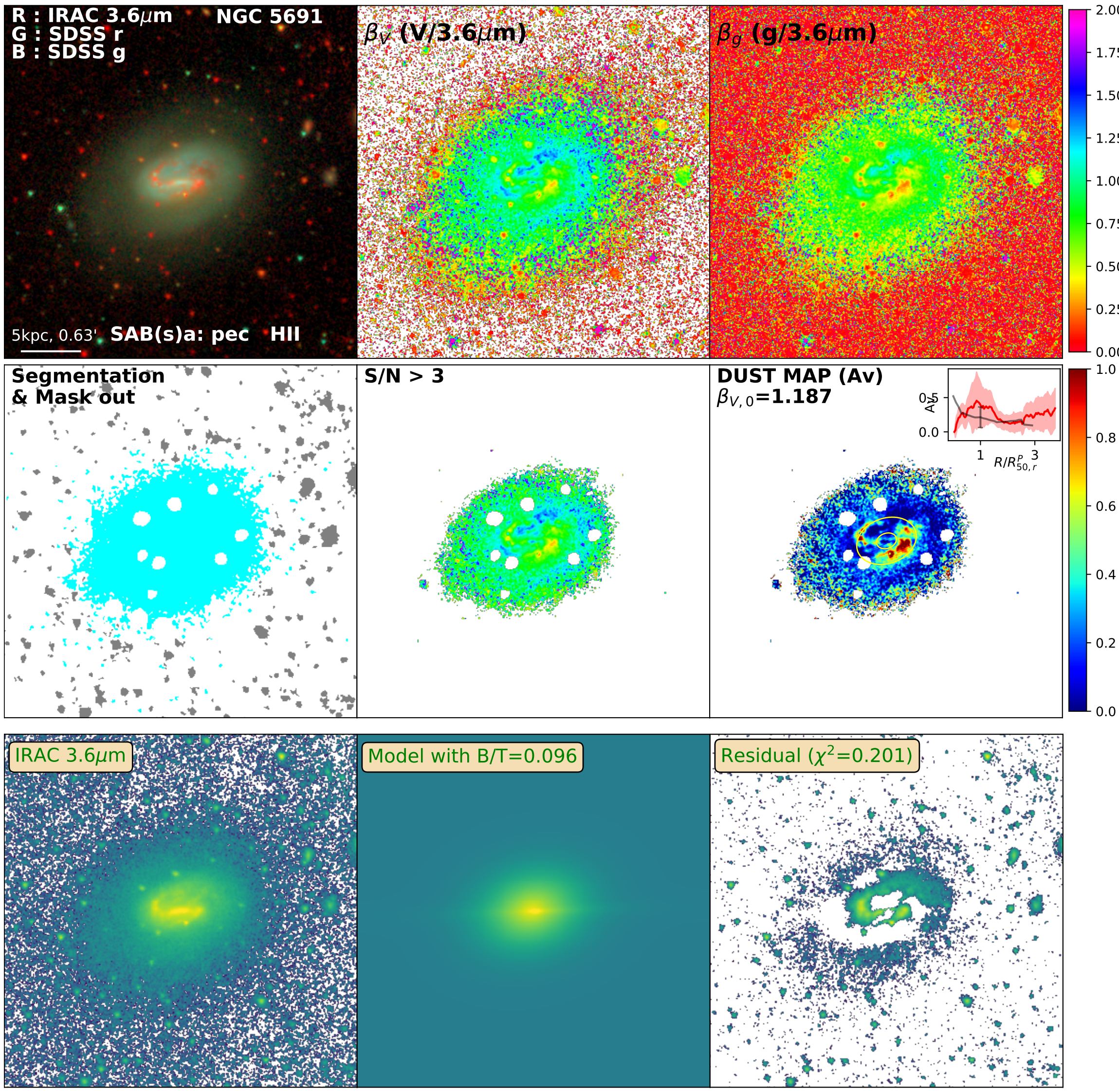

Figure D.214: Same as Figure 3.2 for NGC5691

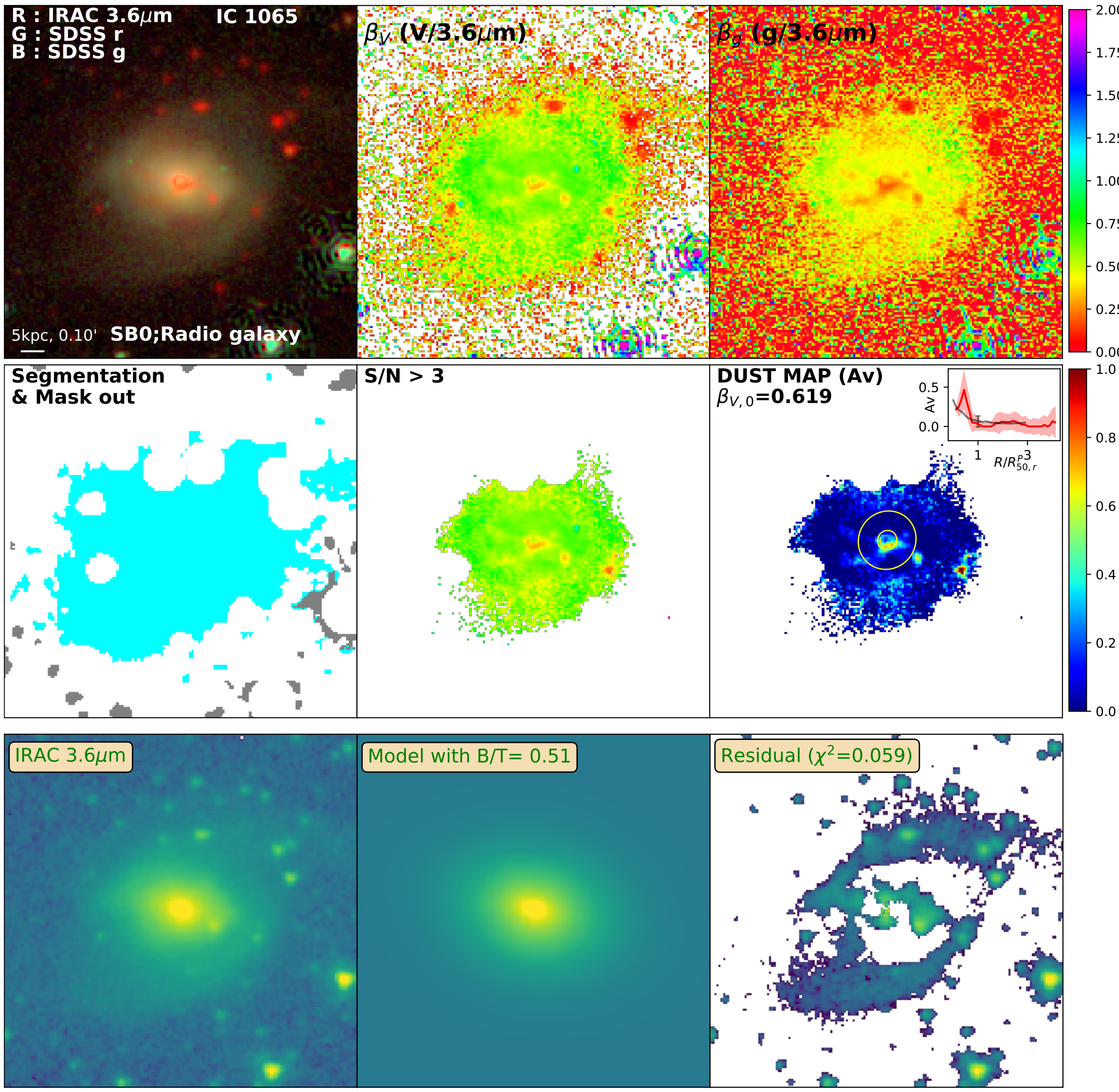

Figure D.215: Same as Figure 3.2 for IC1065

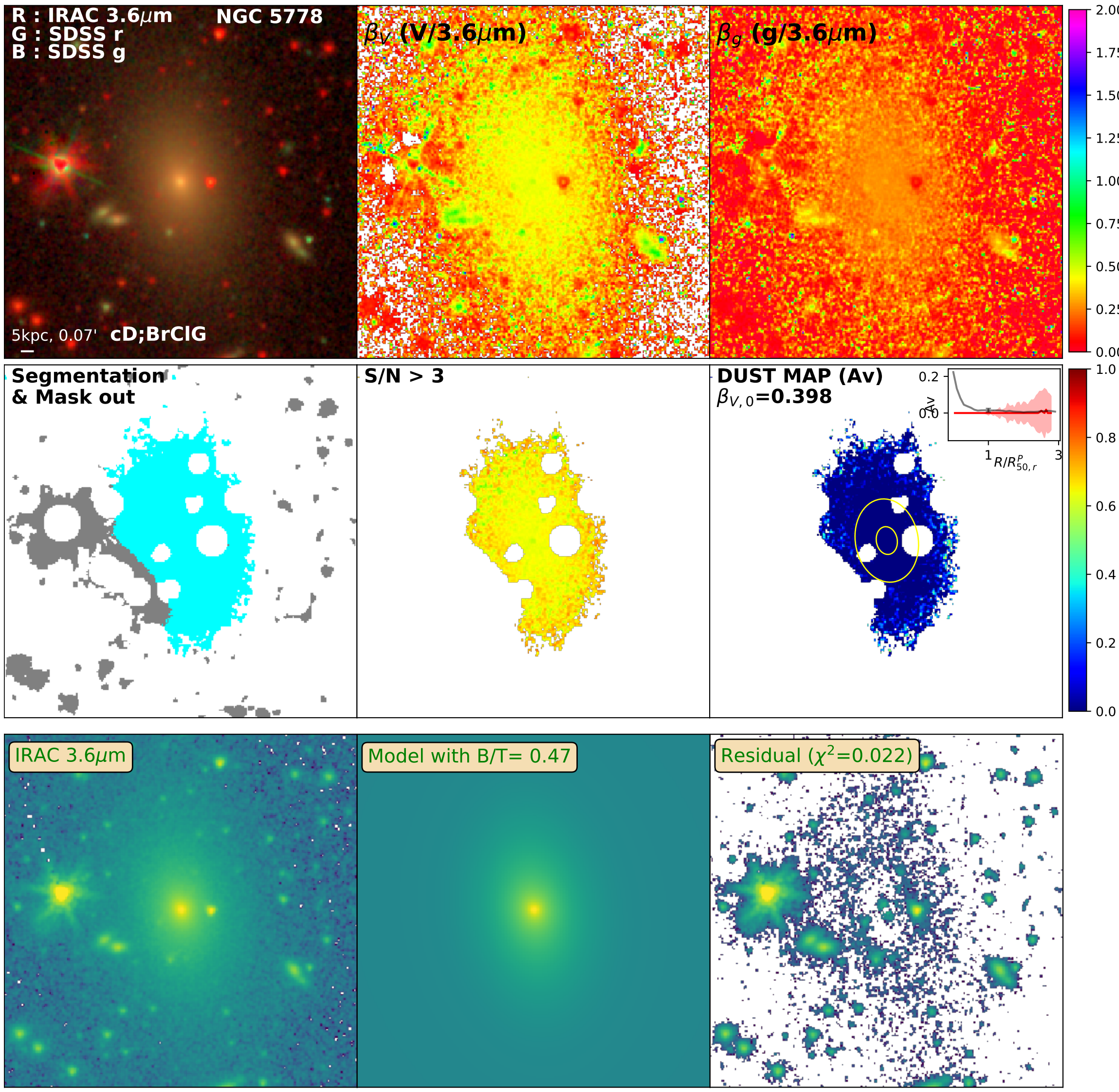

Figure D.216: Same as Figure 3.2 for NGC5778

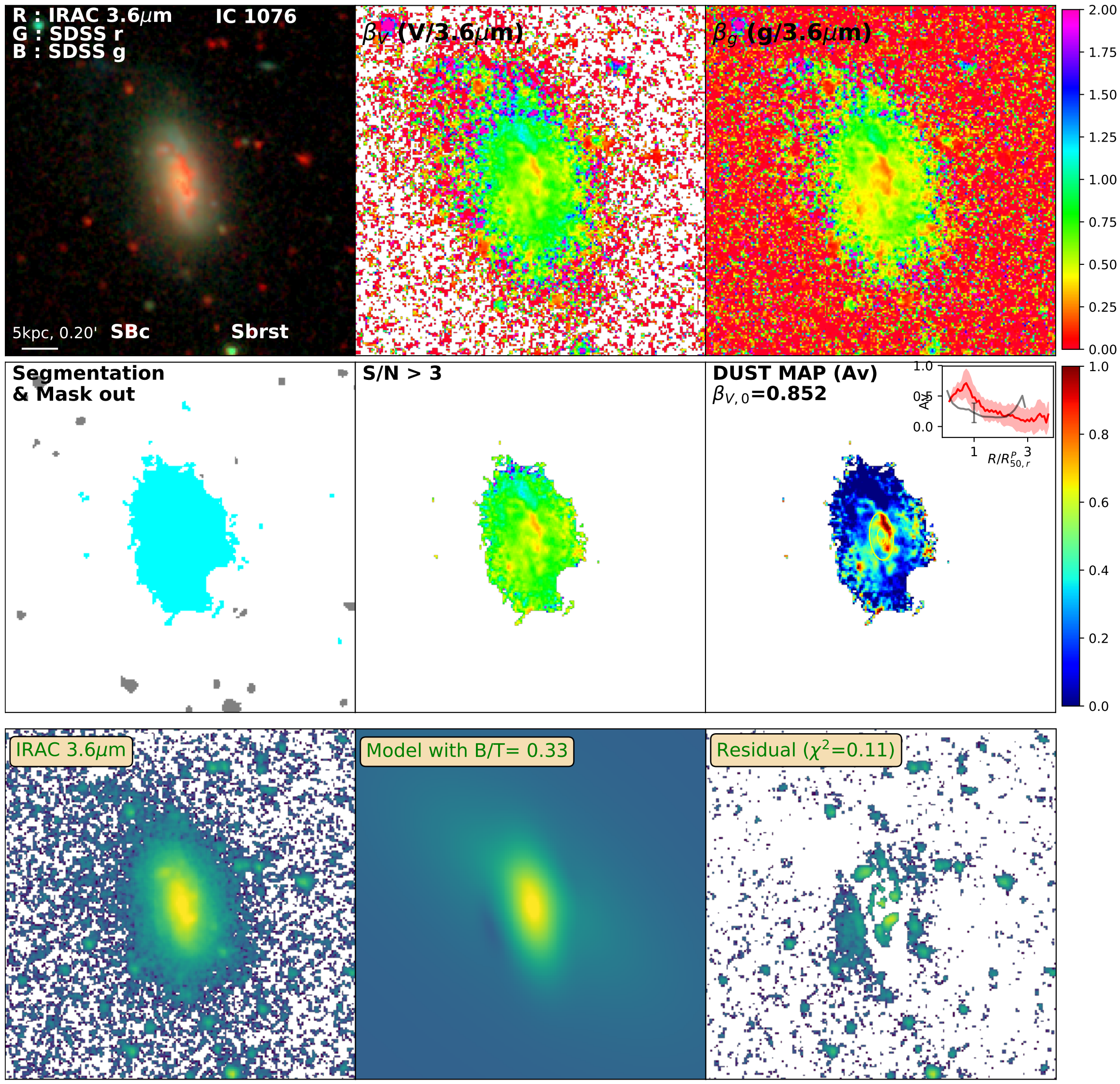

Figure D.217: Same as Figure 3.2 for IC1076

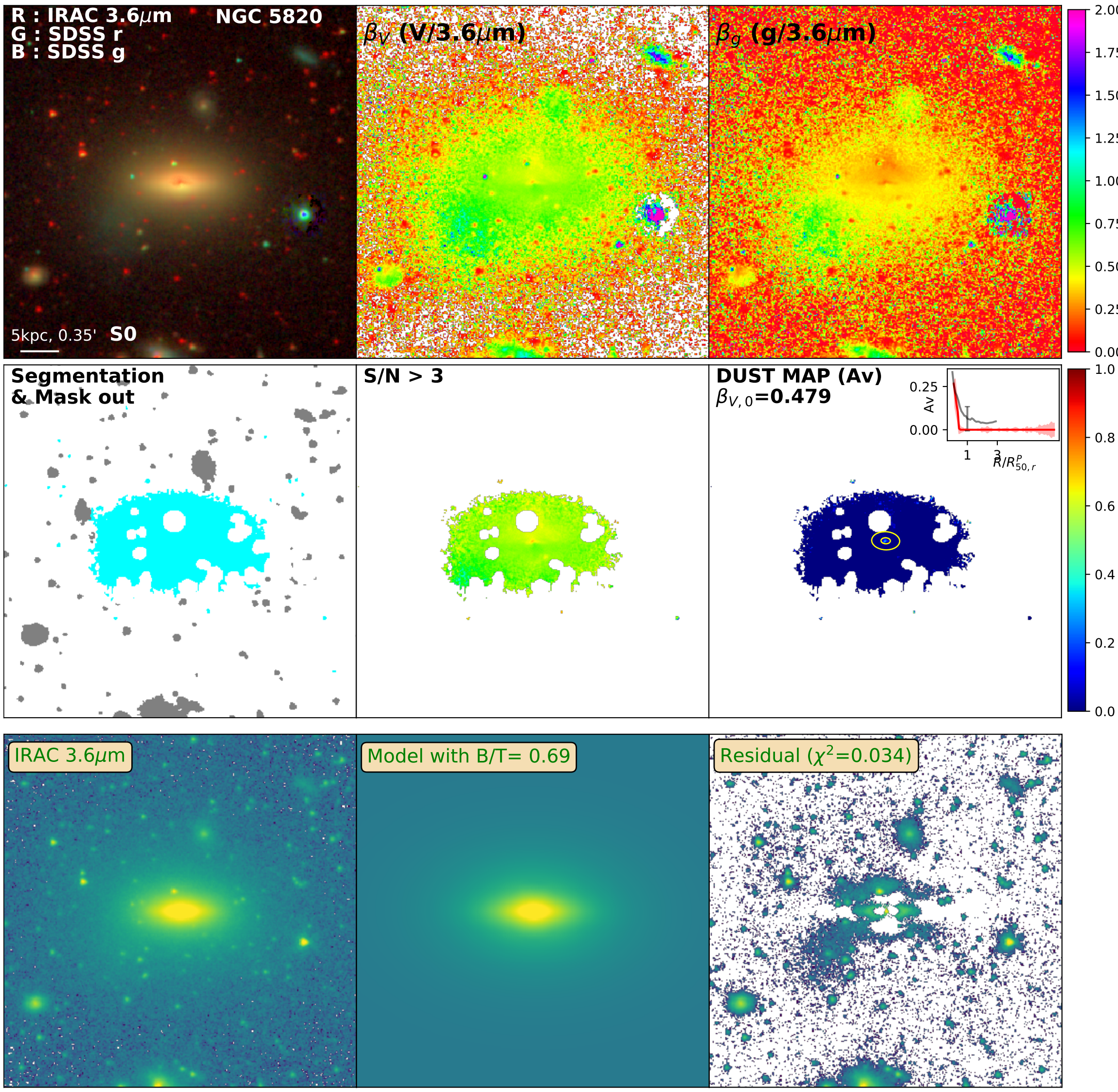

Figure D.218: Same as Figure 3.2 for NGC5820

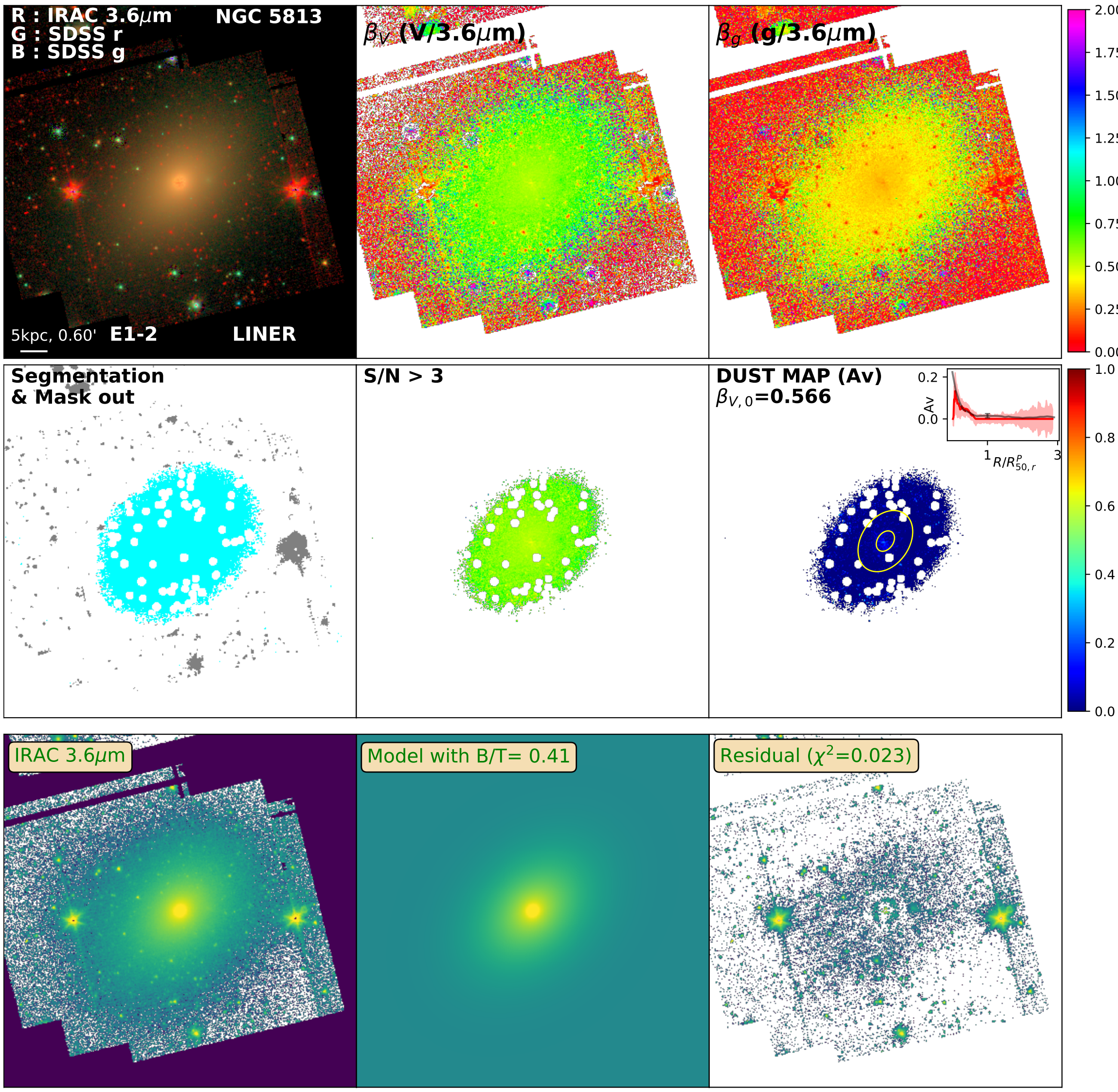

Figure D.219: Same as Figure 3.2 for NGC5813

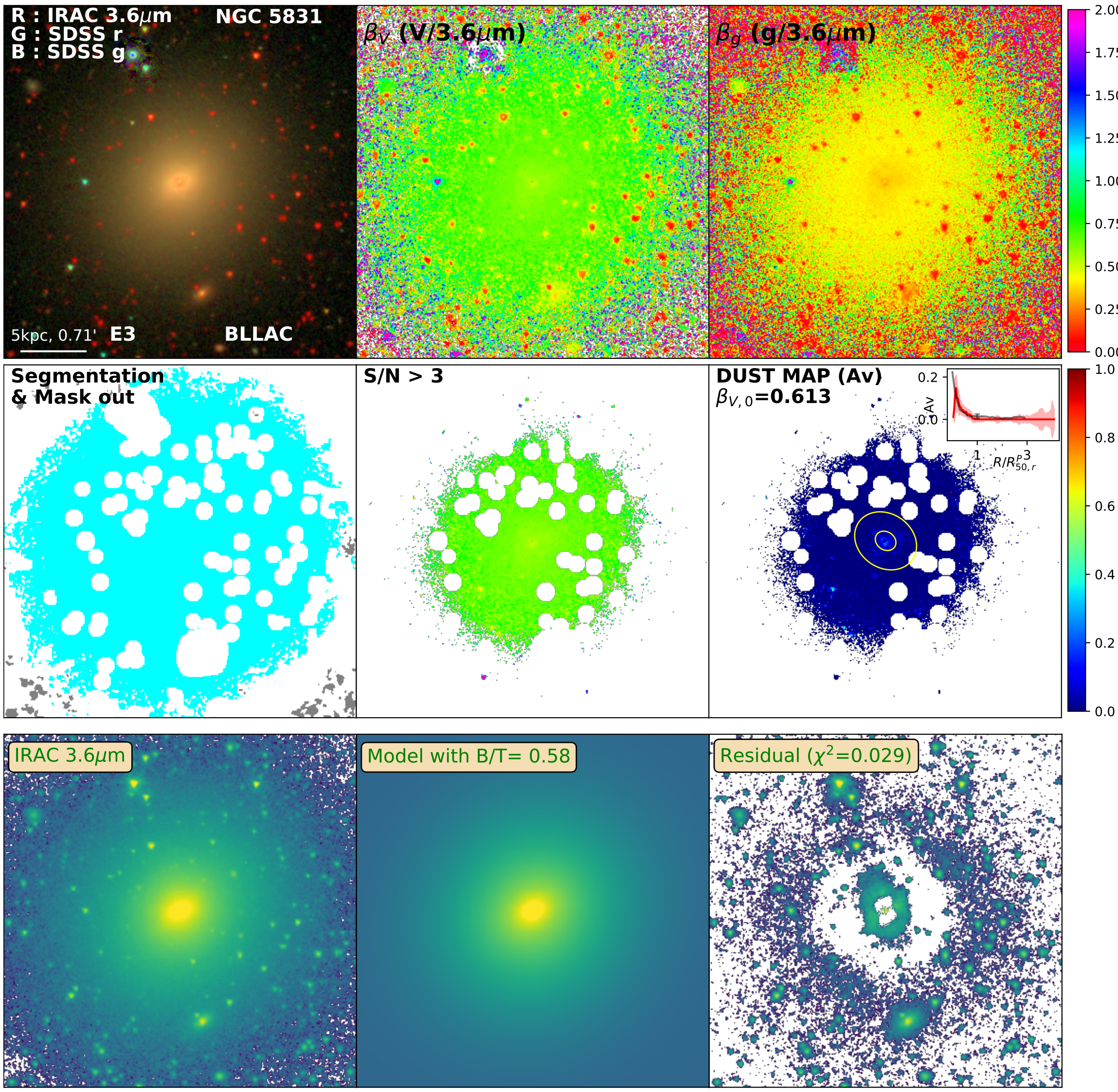

Figure D.220: Same as Figure 3.2 for NGC5831

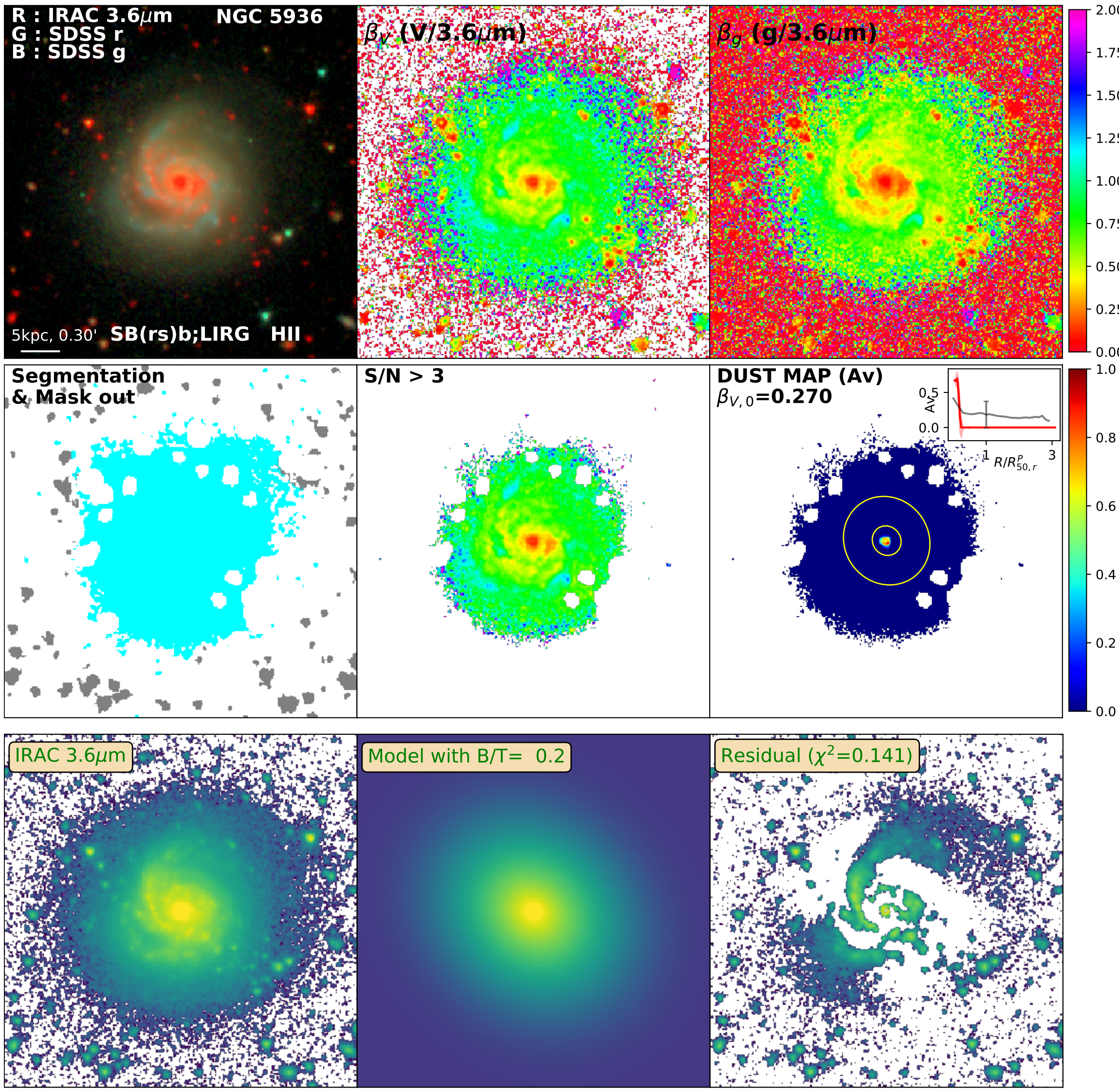

Figure D.221: Same as Figure 3.2 for NGC5936

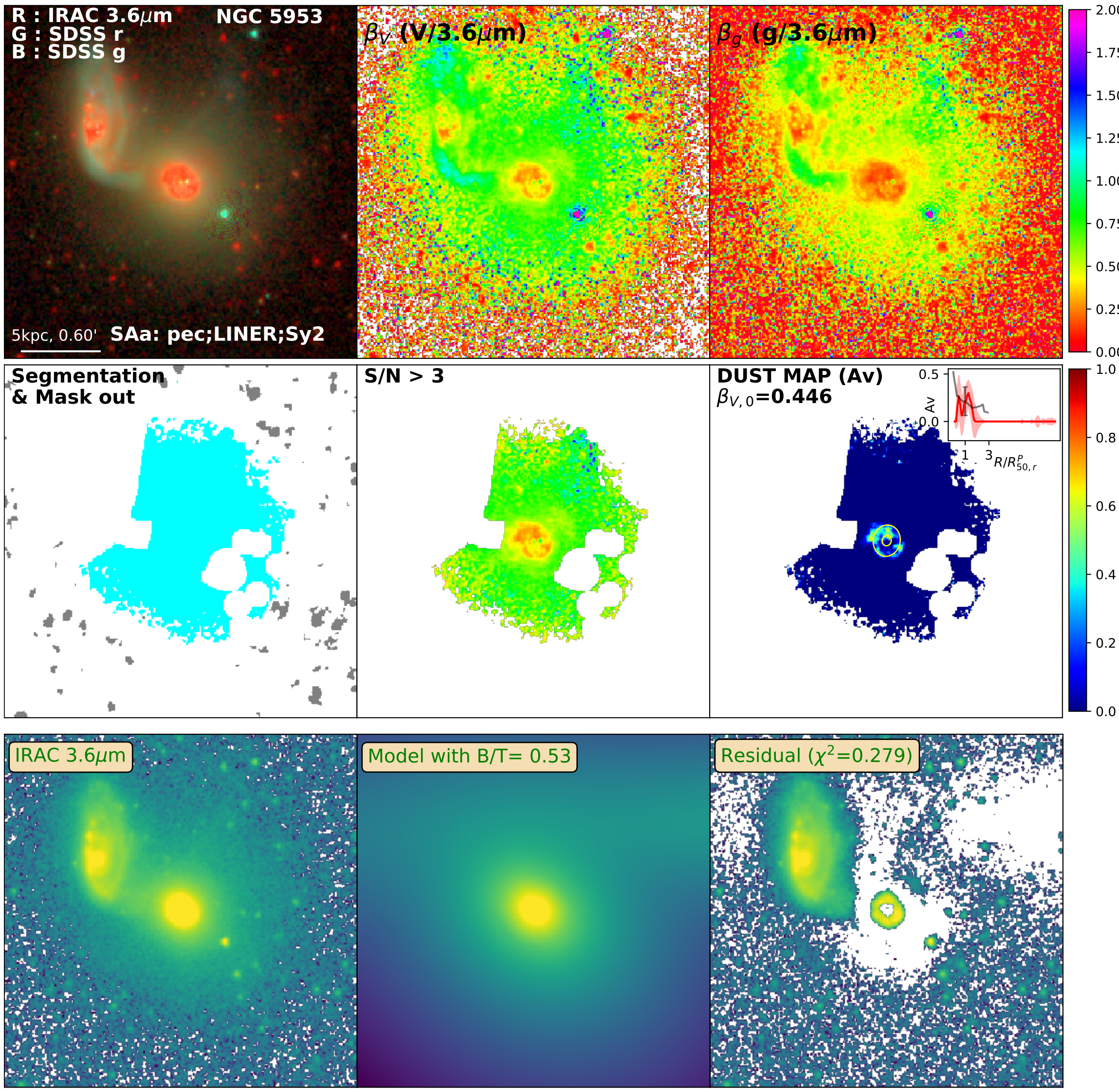

Figure D.222: Same as Figure 3.2 for NGC5953

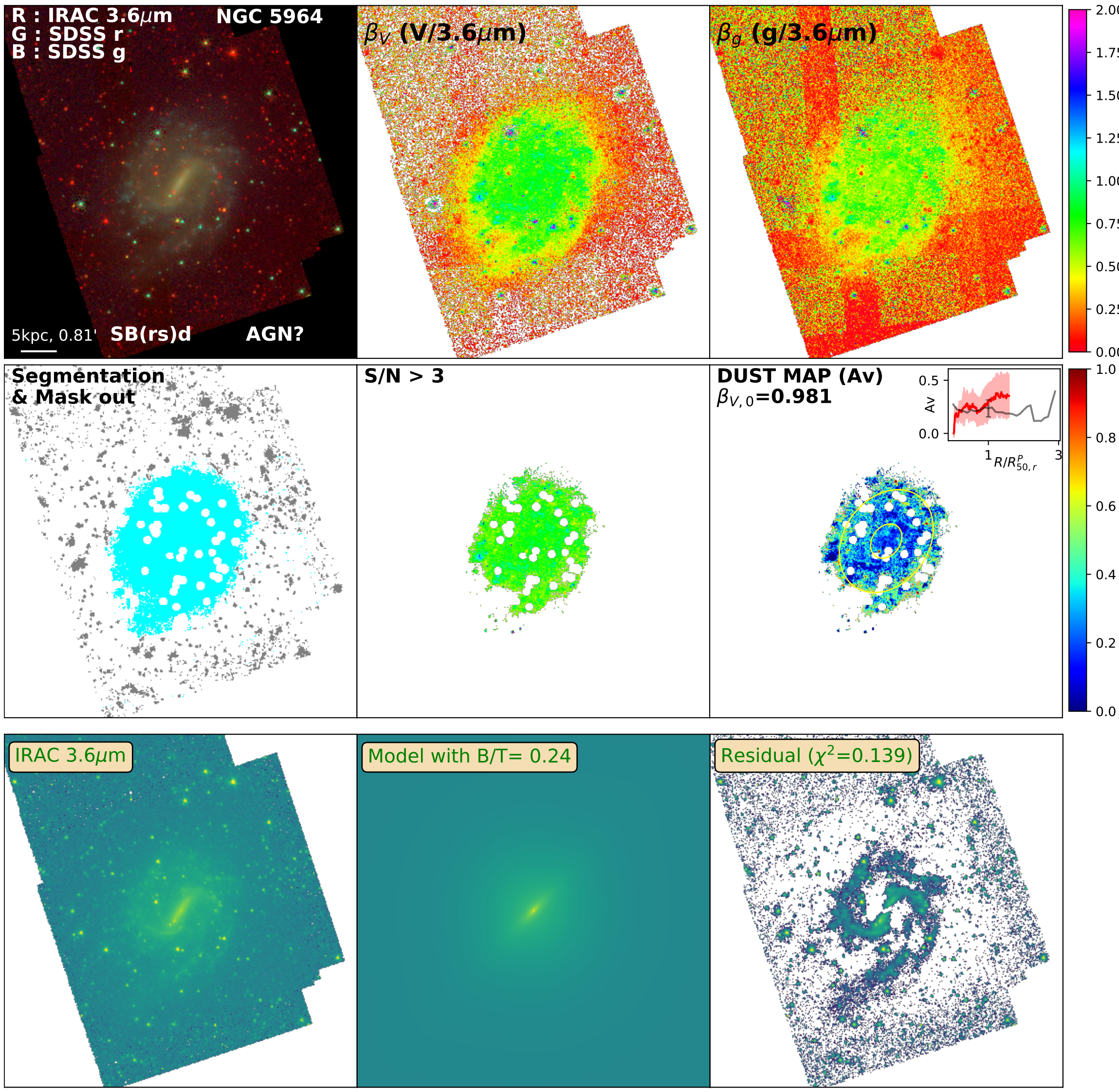

Figure D.223: Same as Figure 3.2 for NGC5964

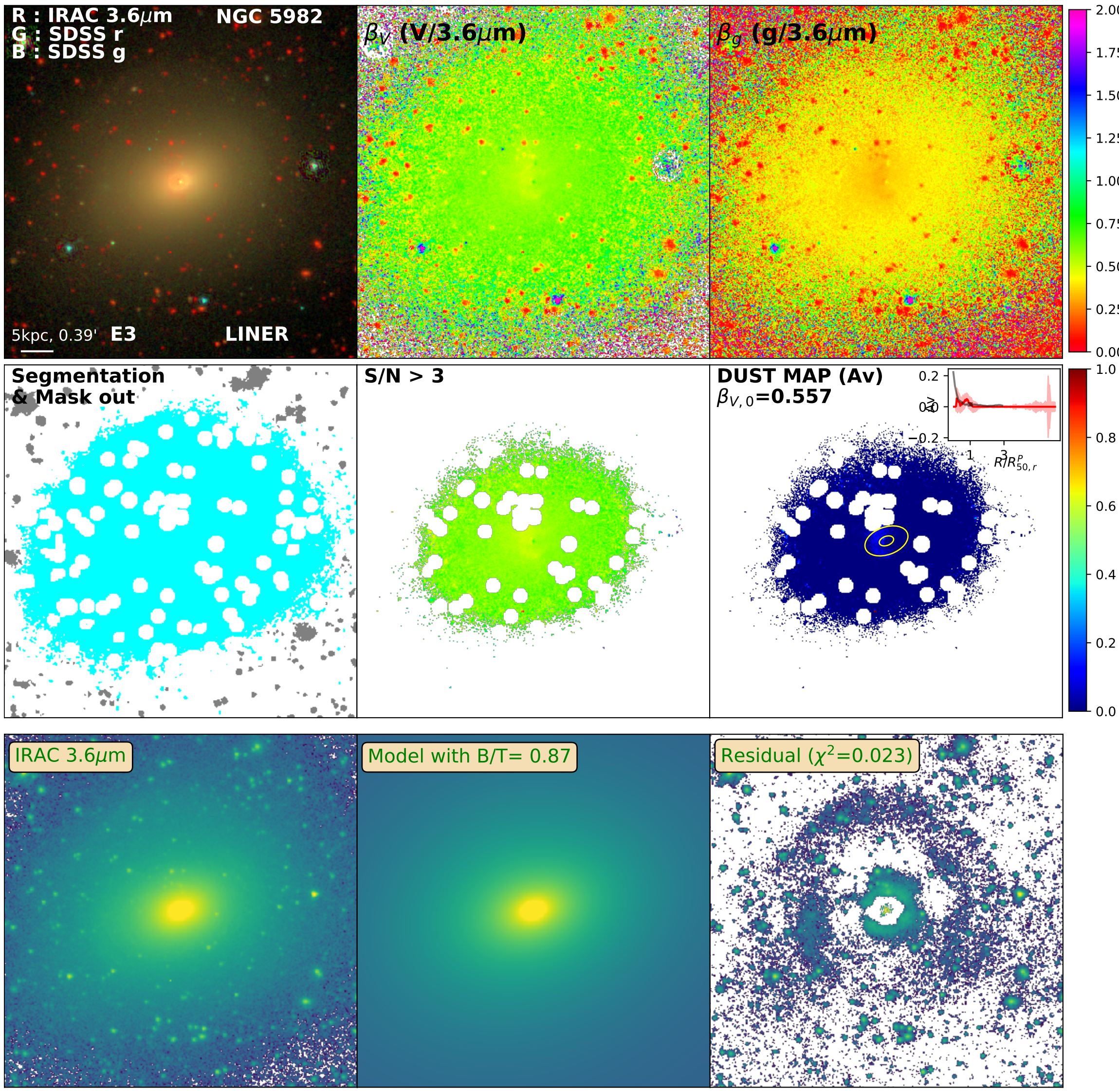

Figure D.224: Same as Figure 3.2 for NGC5982

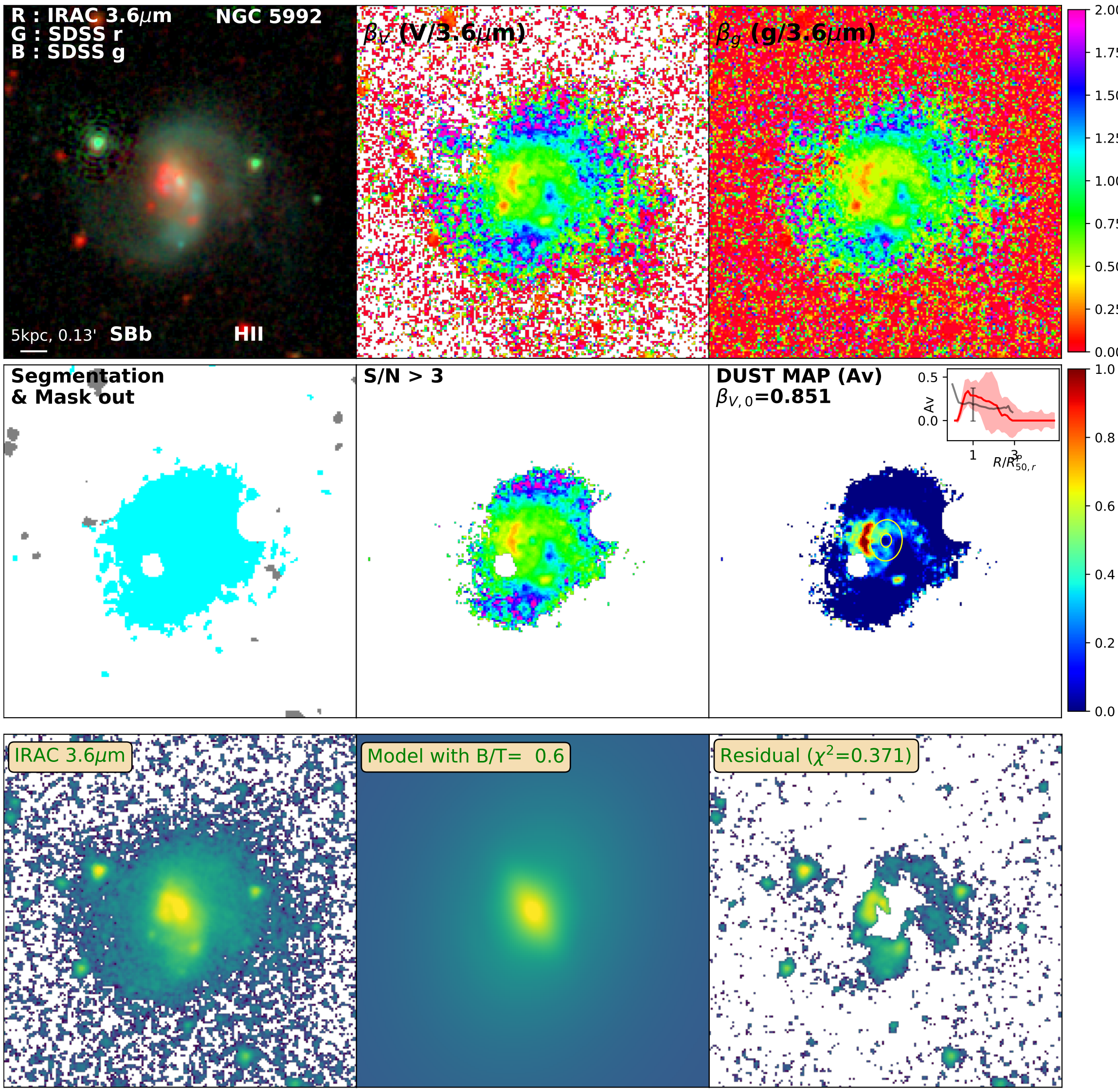

Figure D.225: Same as Figure 3.2 for NGC5992

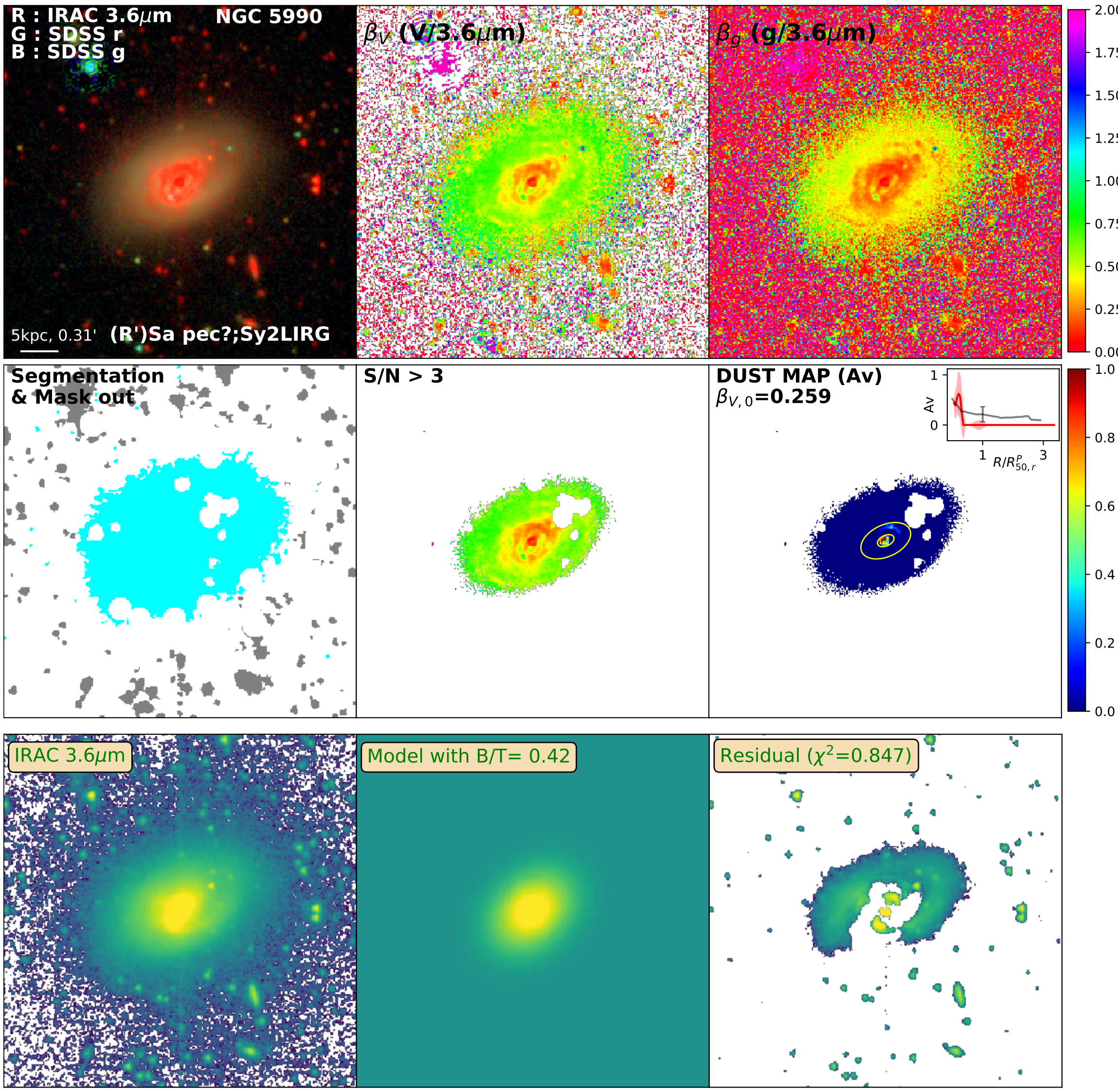

Figure D.226: Same as Figure 3.2 for NGC5990

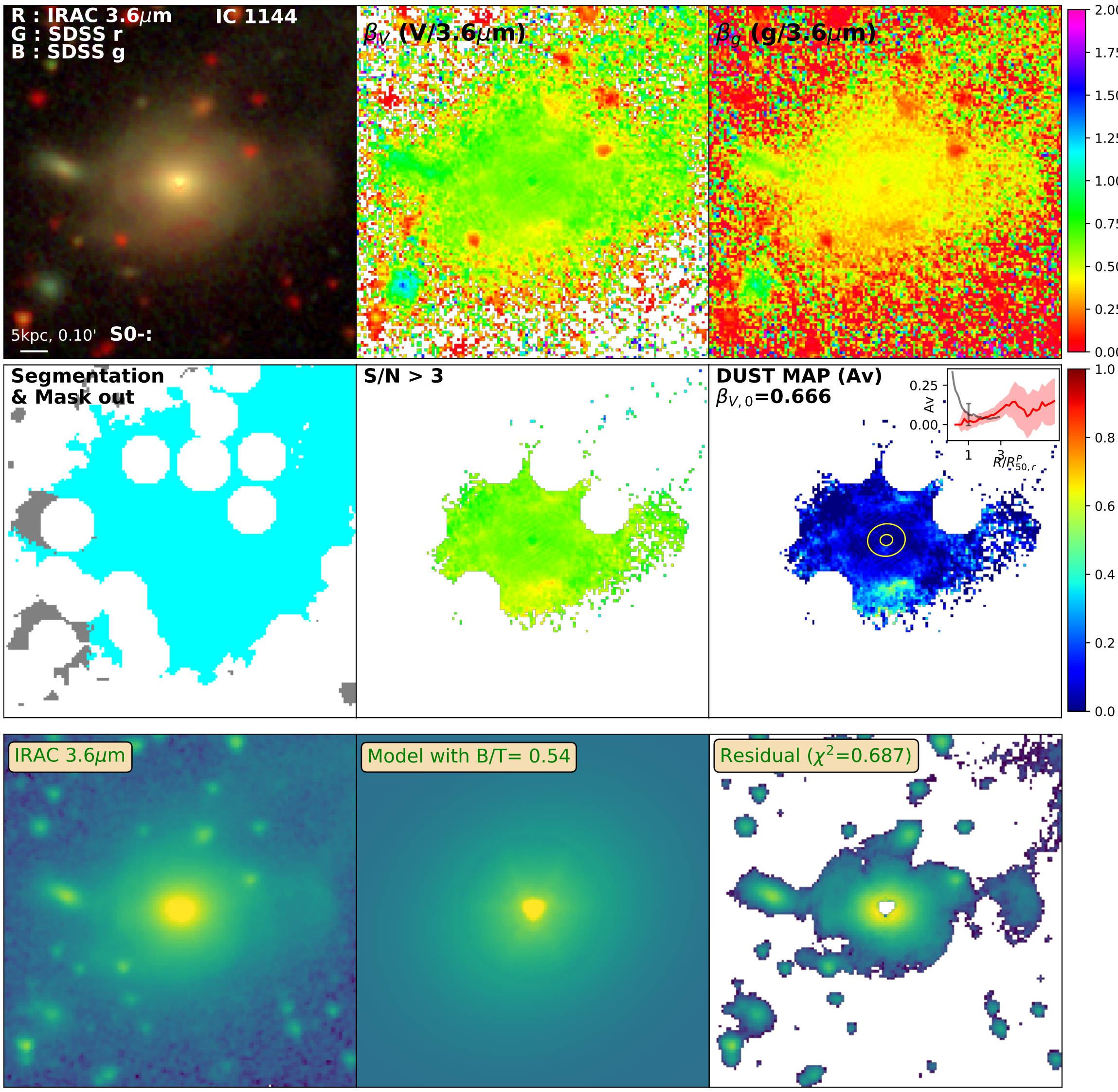

Figure D.227: Same as Figure 3.2 for IC1144

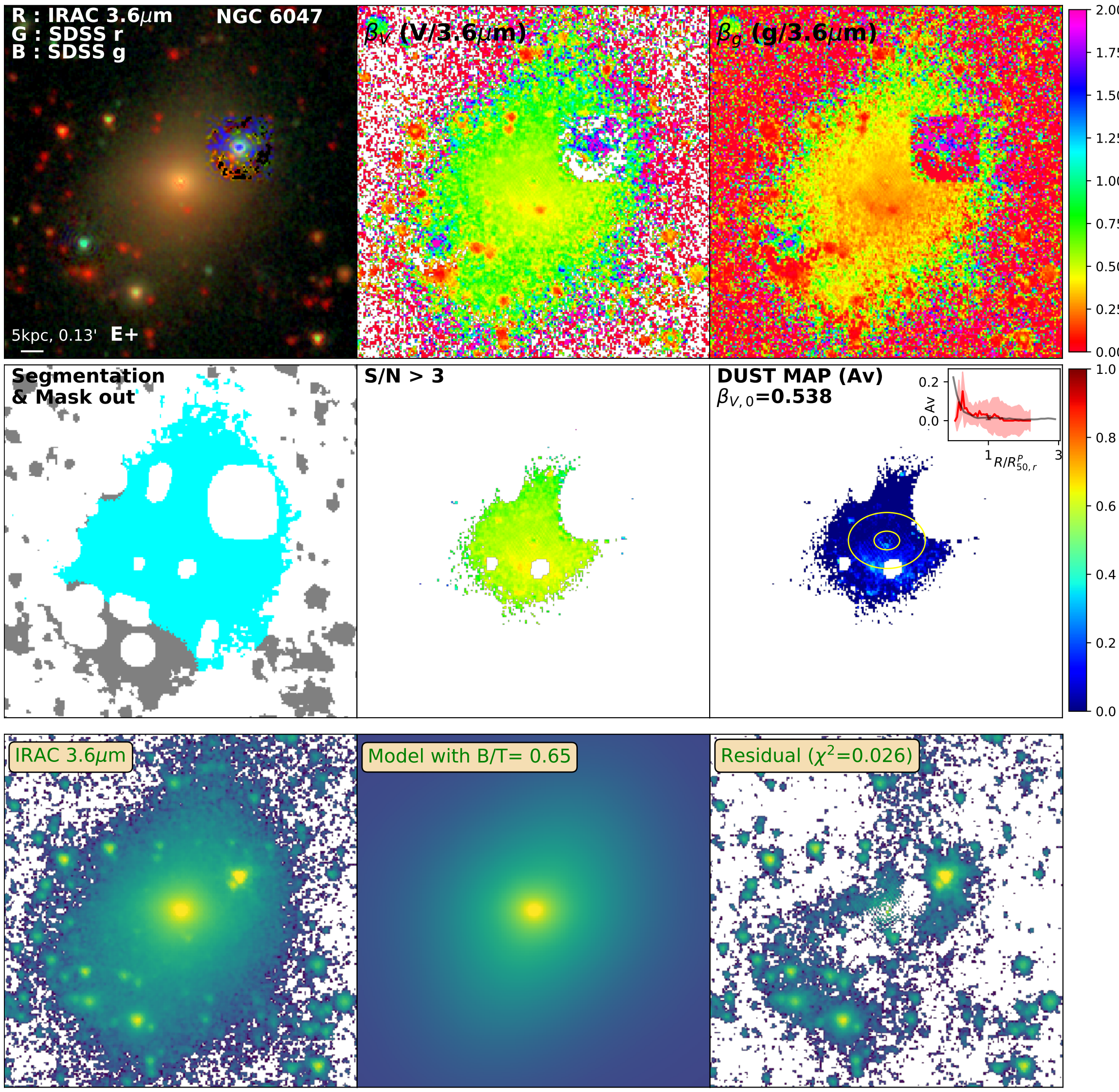

Figure D.228: Same as Figure 3.2 for NGC6047

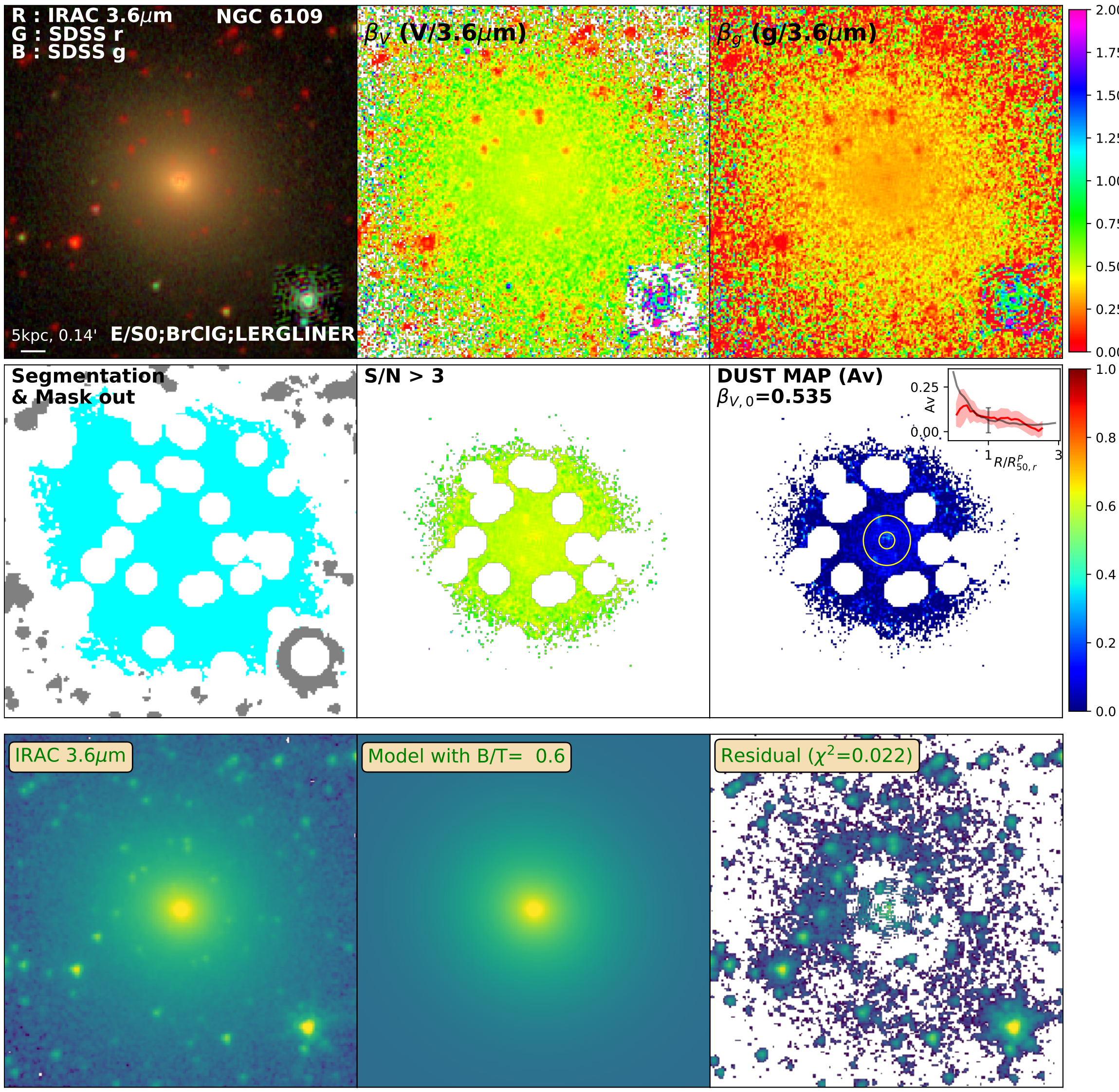

Figure D.229: Same as Figure 3.2 for NGC6109

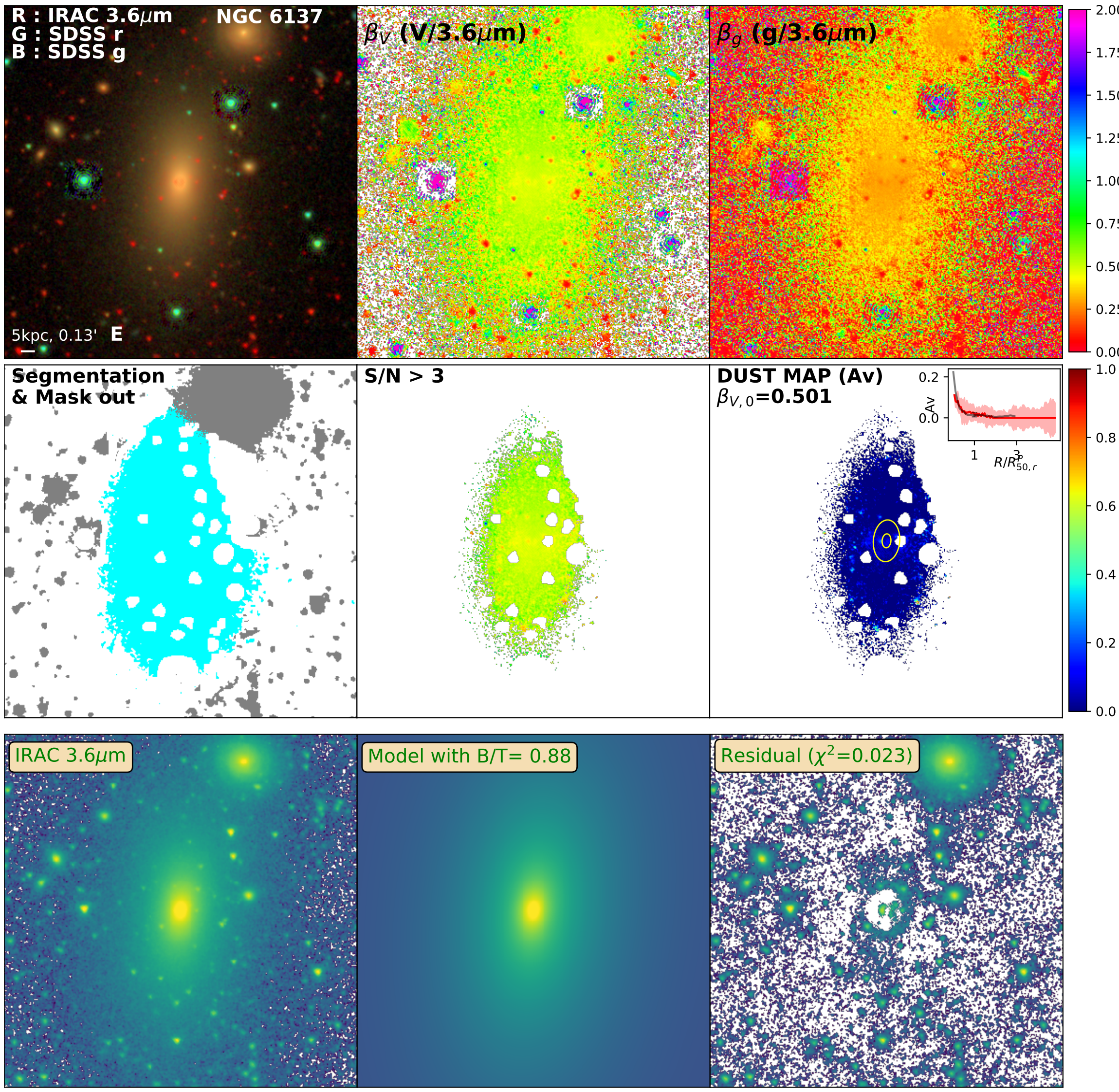

Figure D.230: Same as Figure 3.2 for NGC6137

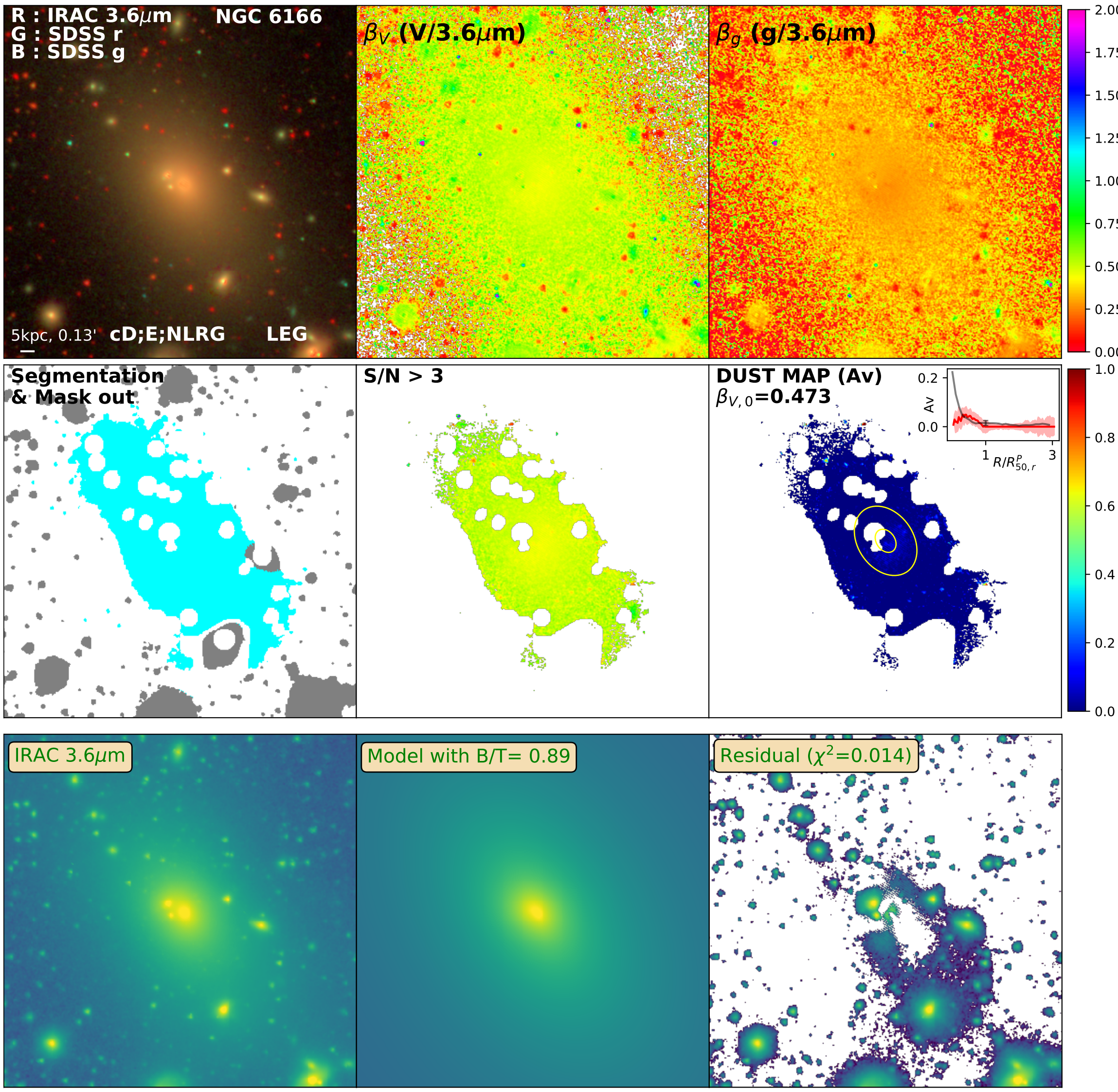

Figure D.231: Same as Figure 3.2 for NGC6166

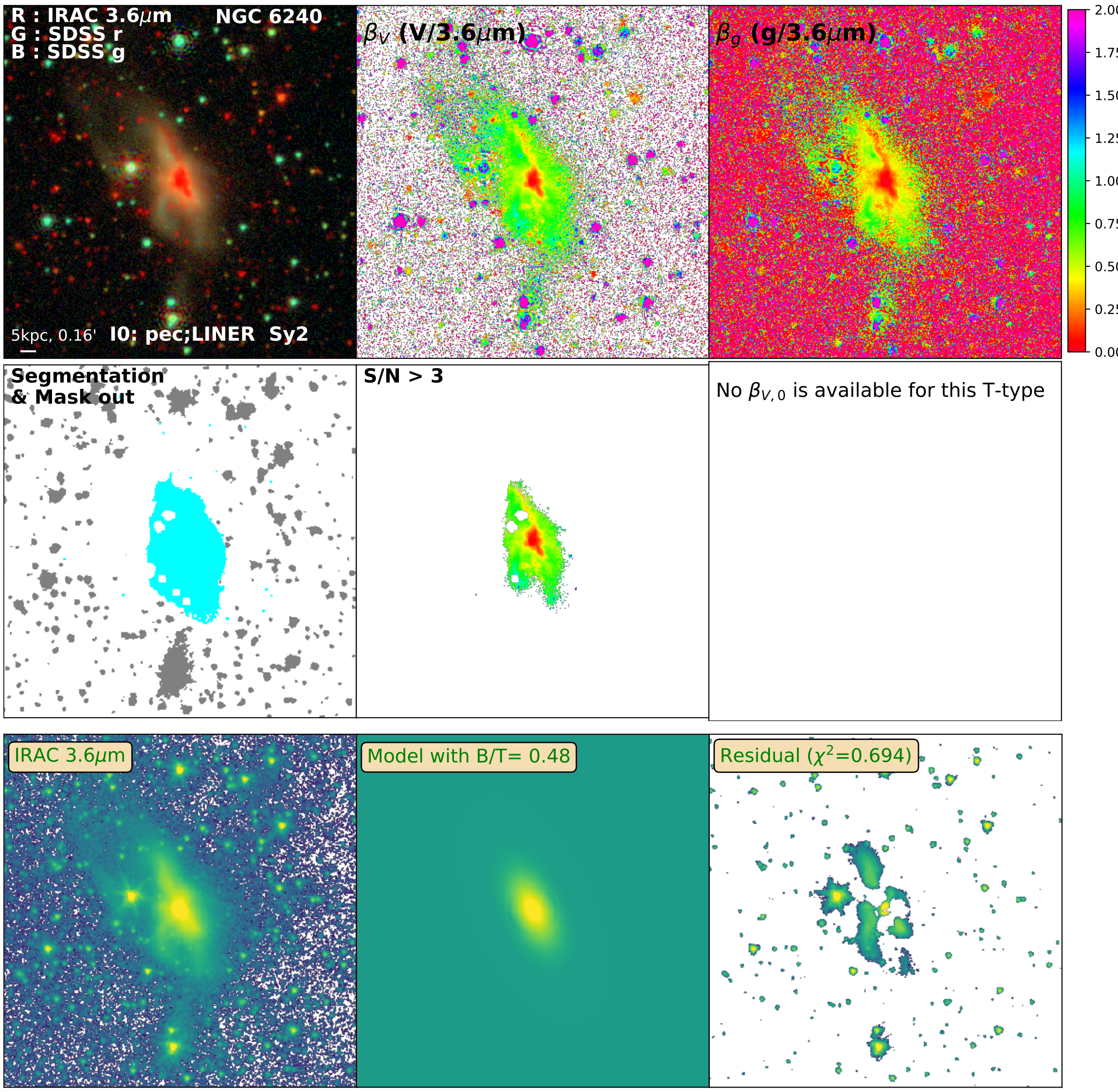

Figure D.232: Same as Figure 3.2 for NGC6240

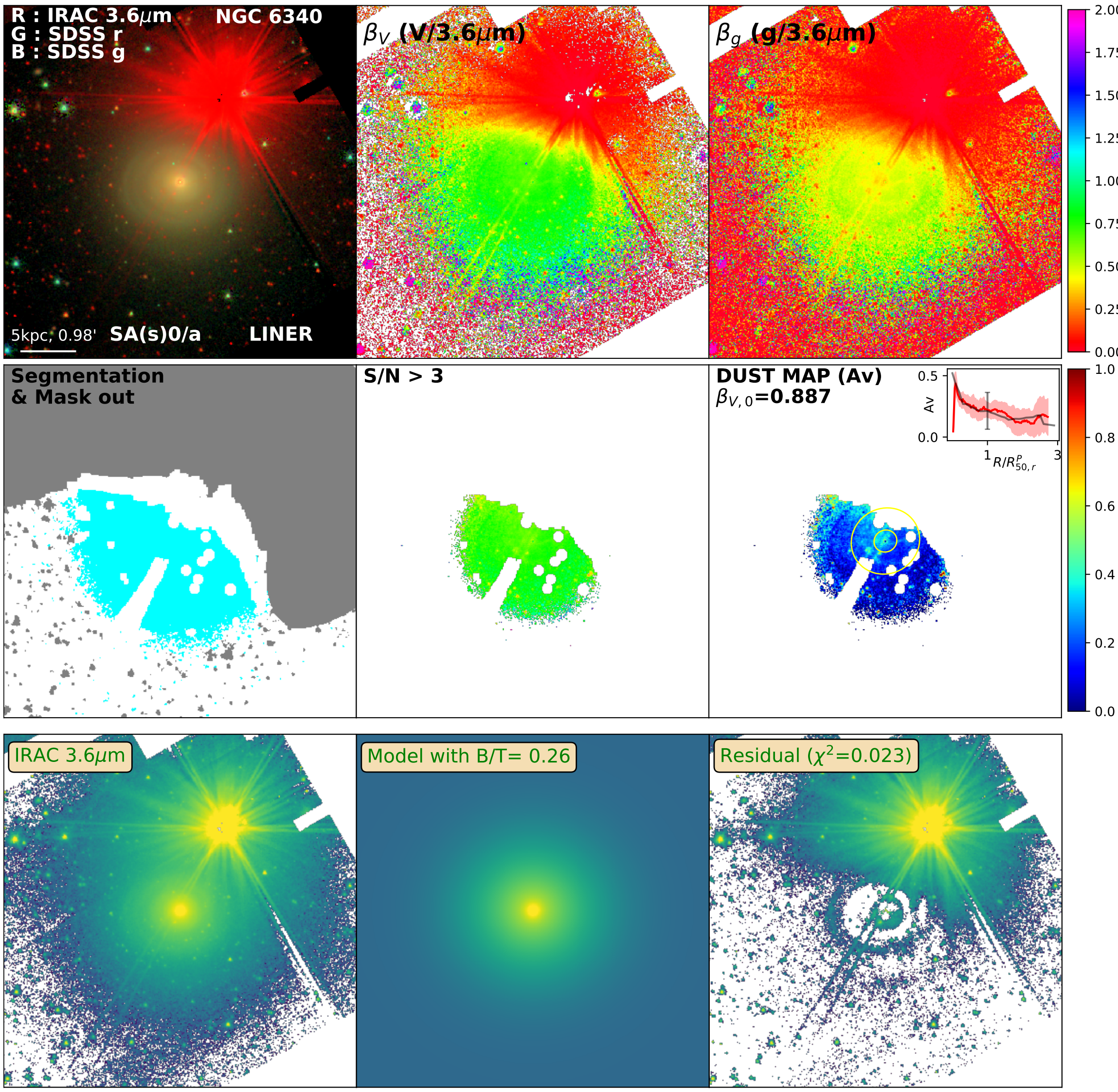

Figure D.233: Same as Figure 3.2 for NGC6340

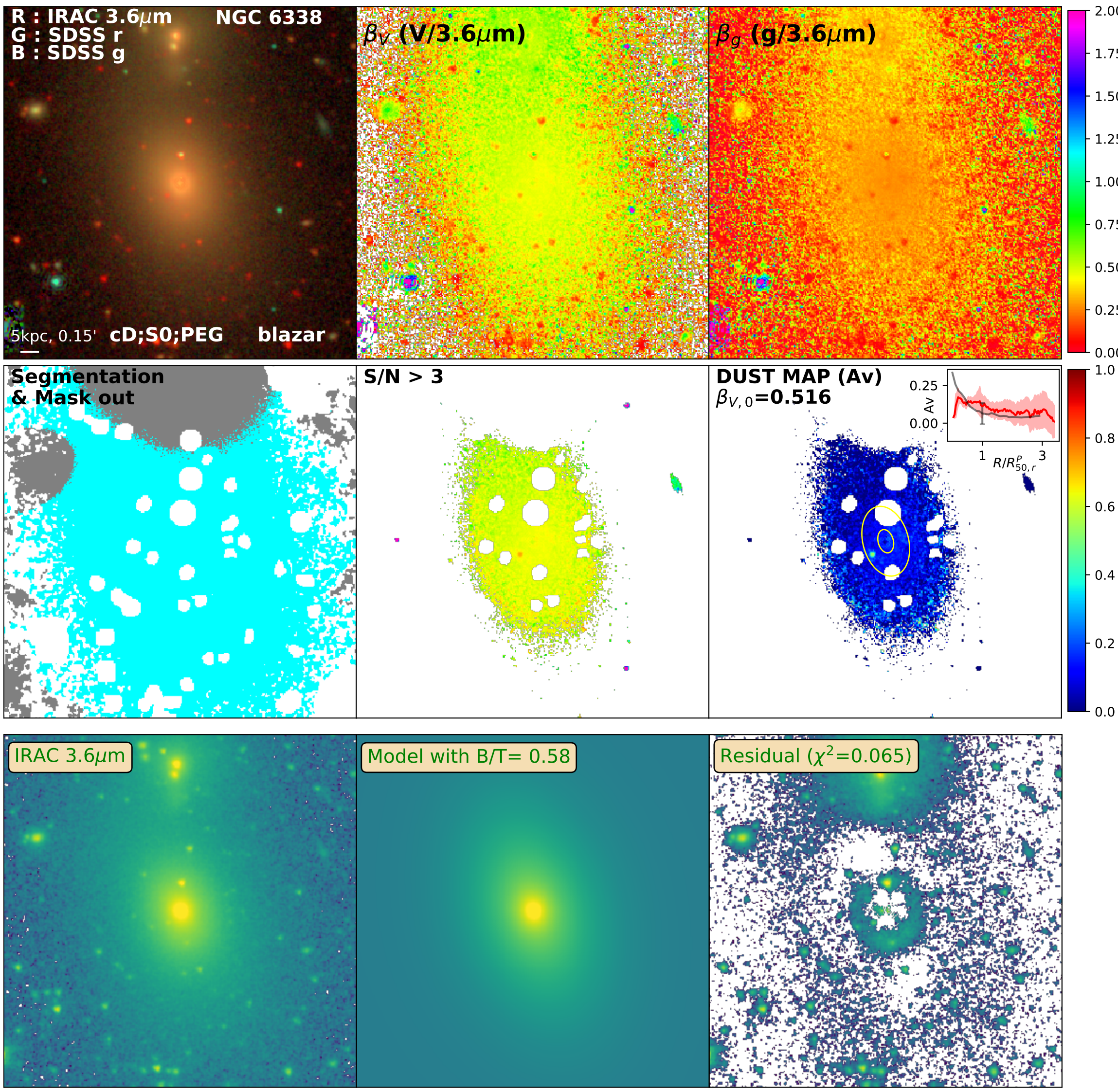

Figure D.234: Same as Figure 3.2 for NGC6338

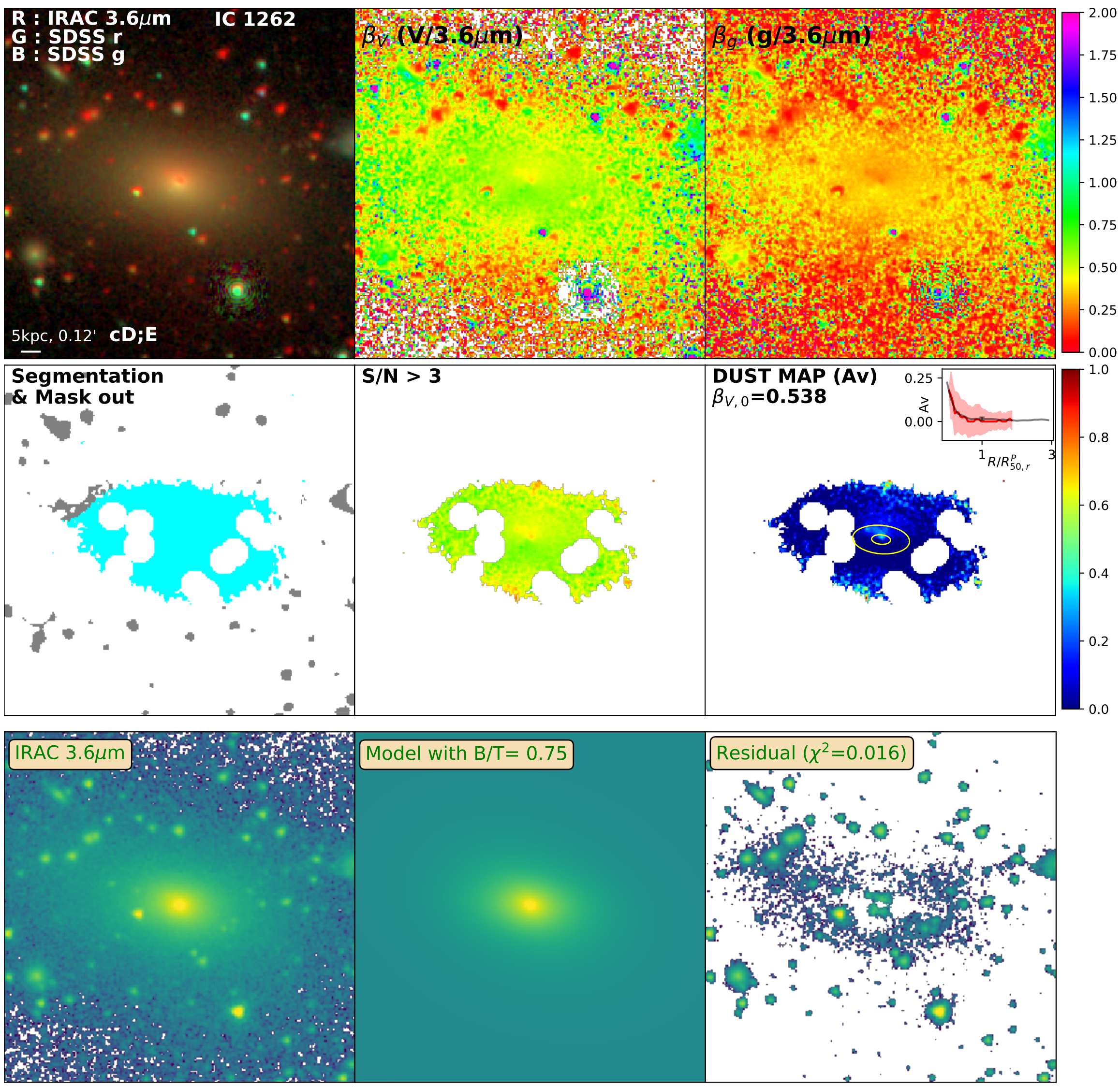

Figure D.235: Same as Figure 3.2 for IC1262

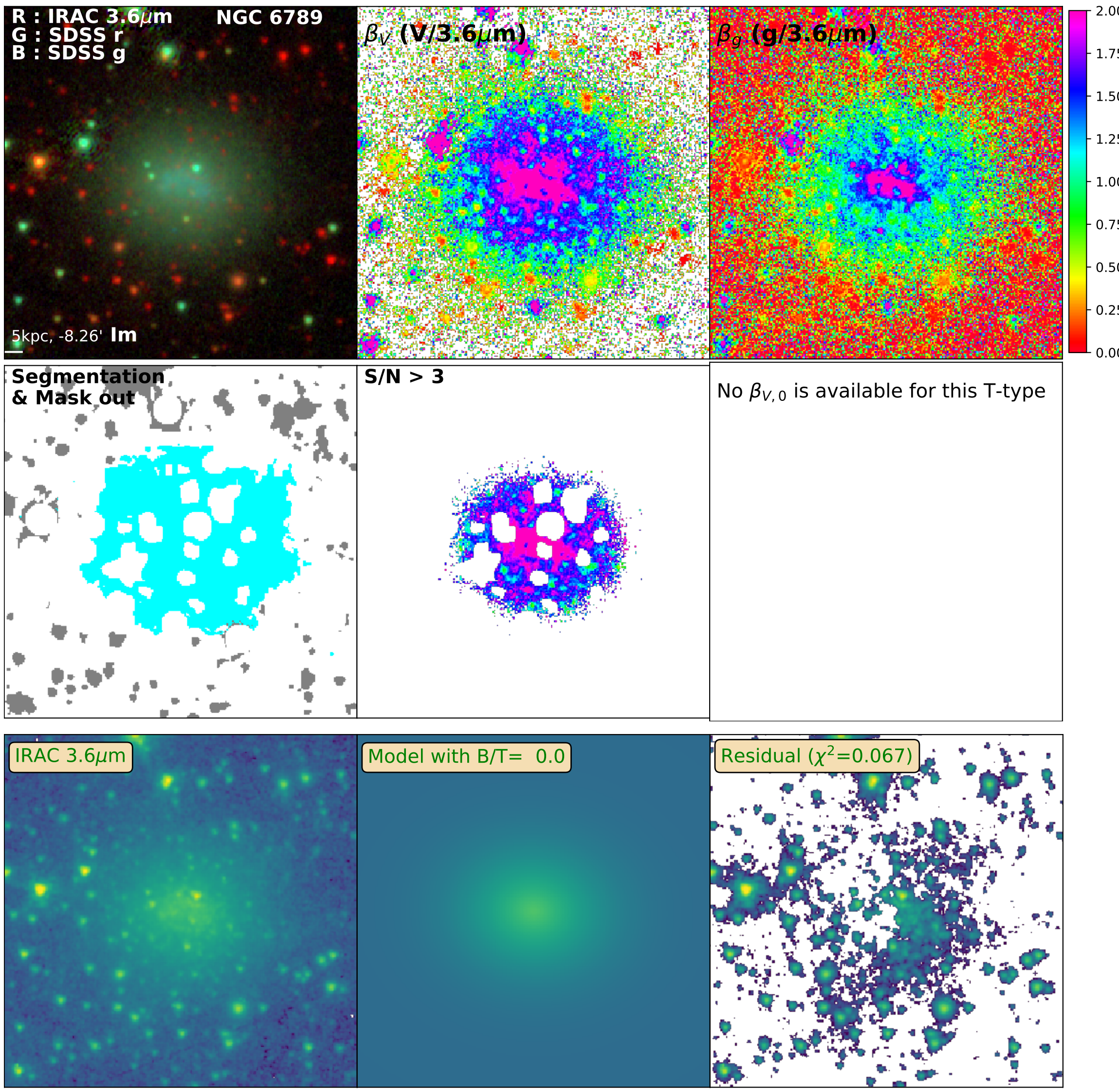

Figure D.236: Same as Figure 3.2 for NGC6789

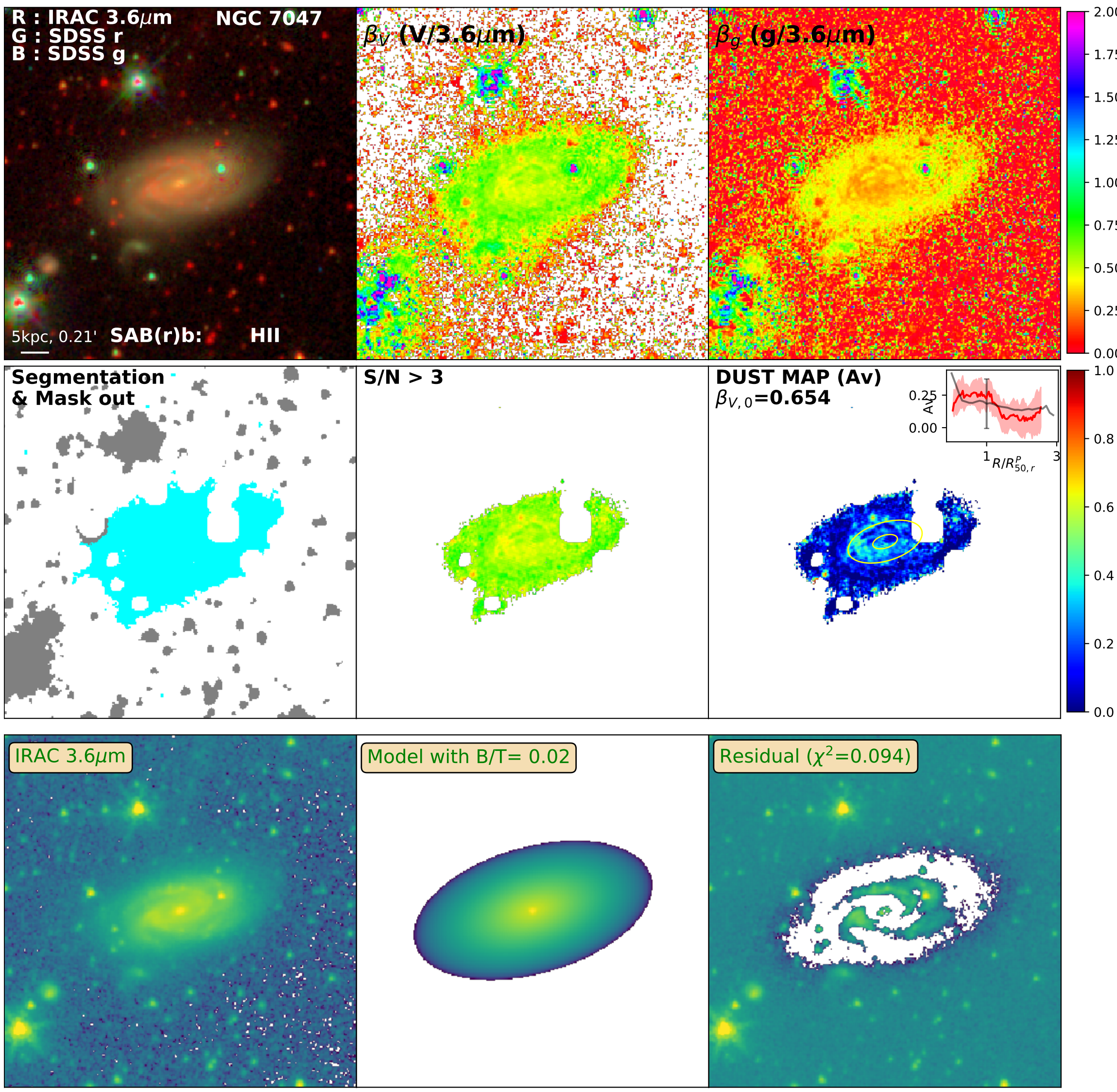

Figure D.237: Same as Figure 3.2 for NGC7047

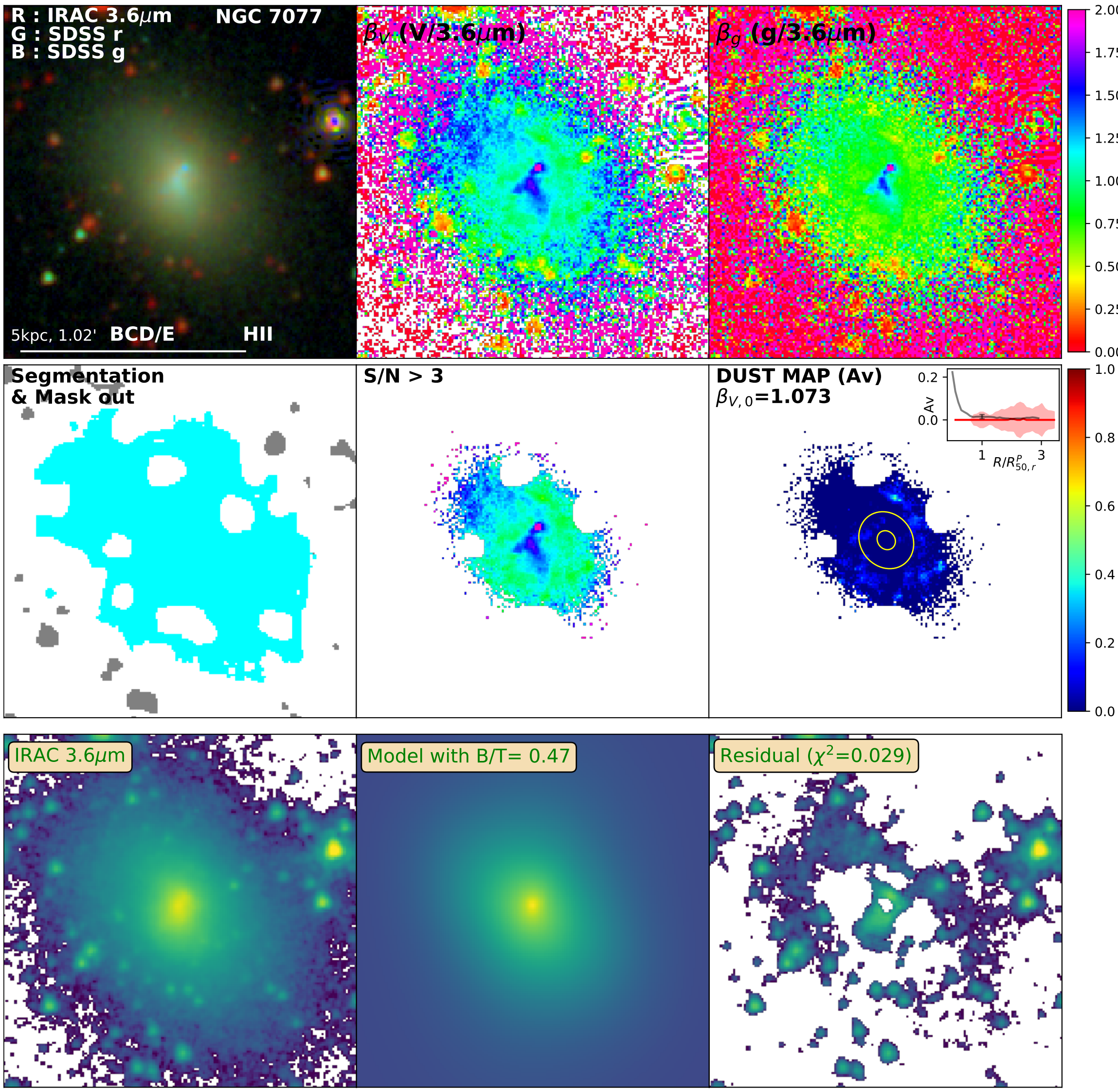

Figure D.238: Same as Figure 3.2 for NGC7077

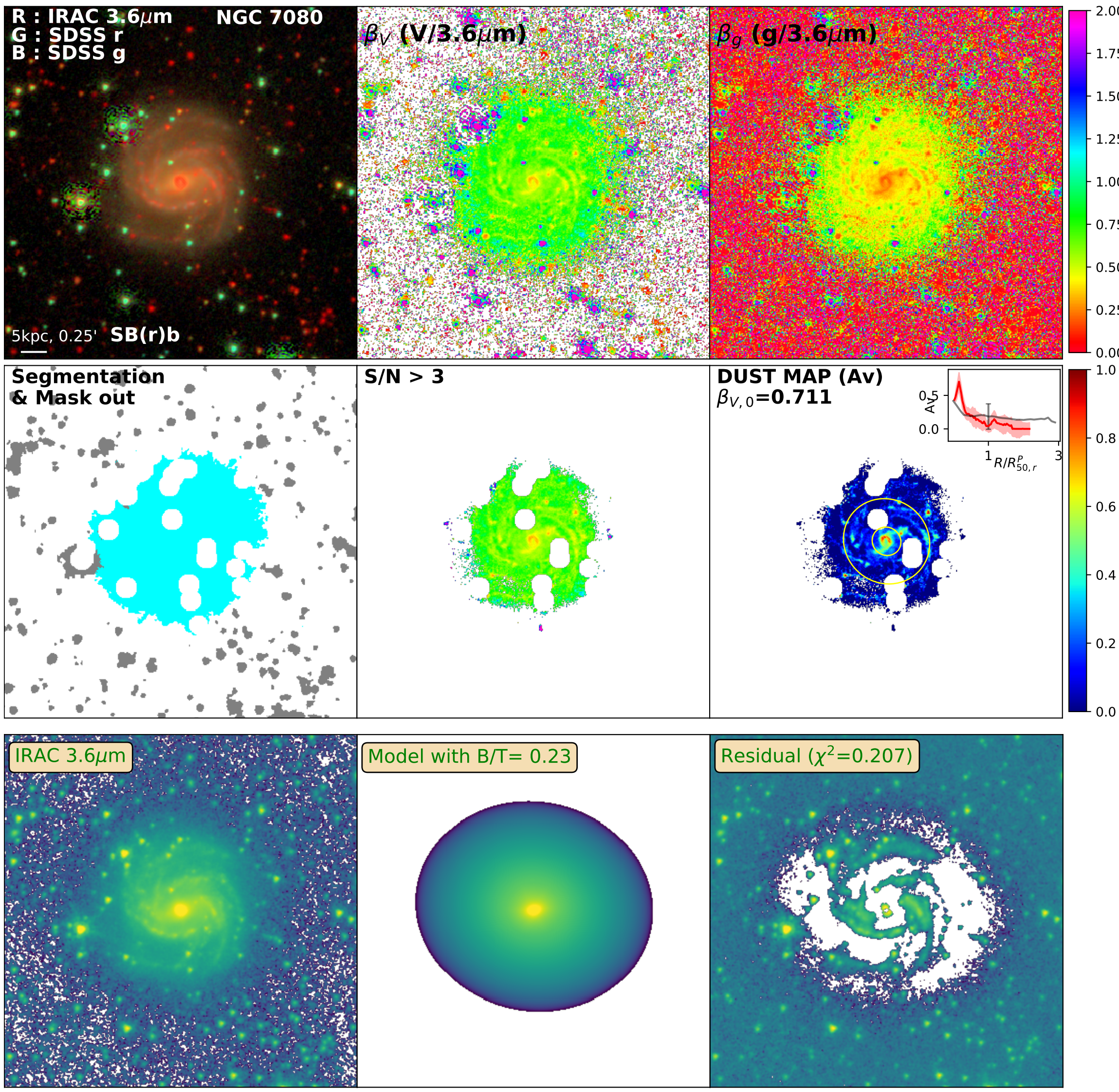

Figure D.239: Same as Figure 3.2 for NGC7080

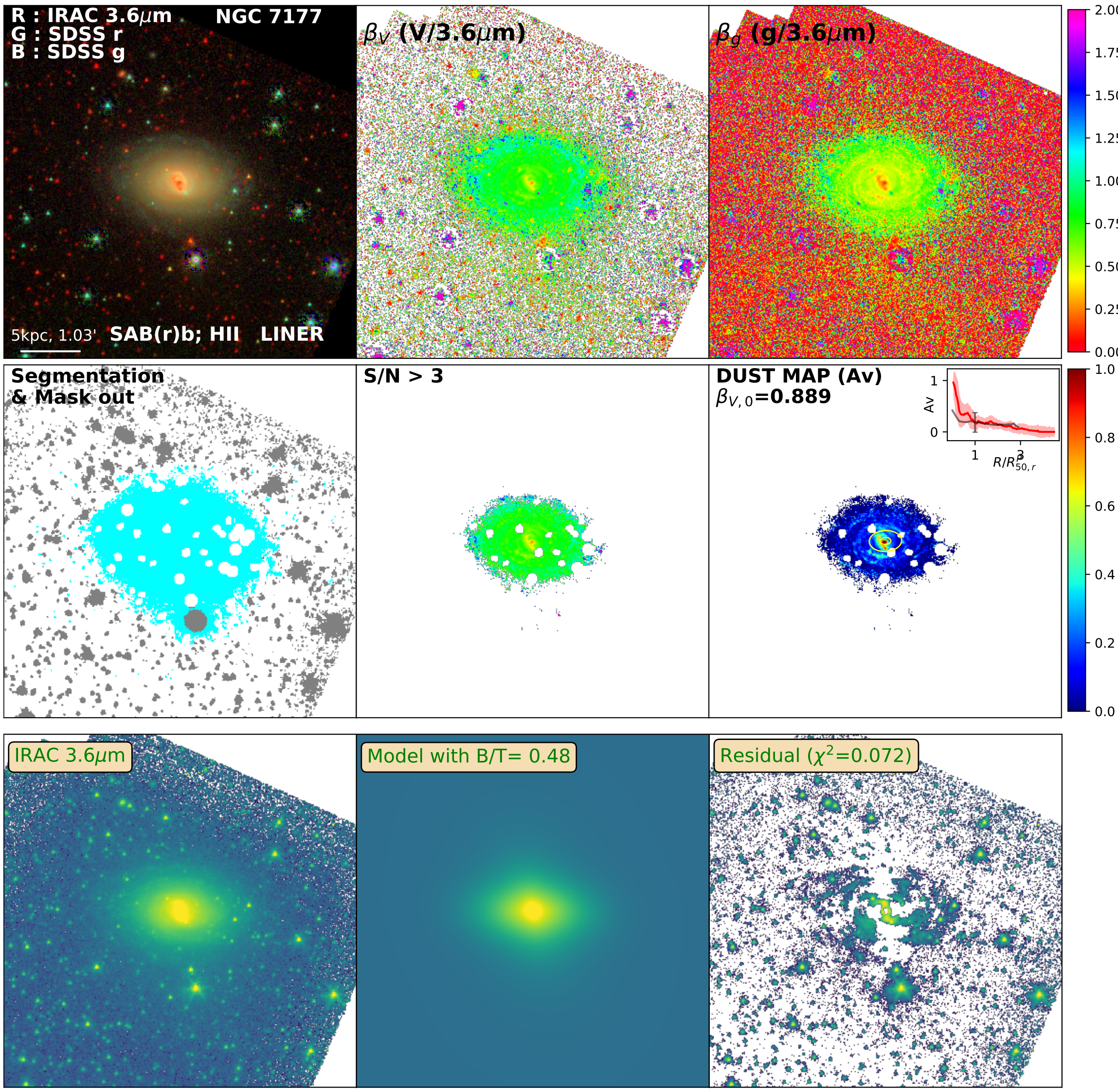

Figure D.240: Same as Figure 3.2 for NGC7177

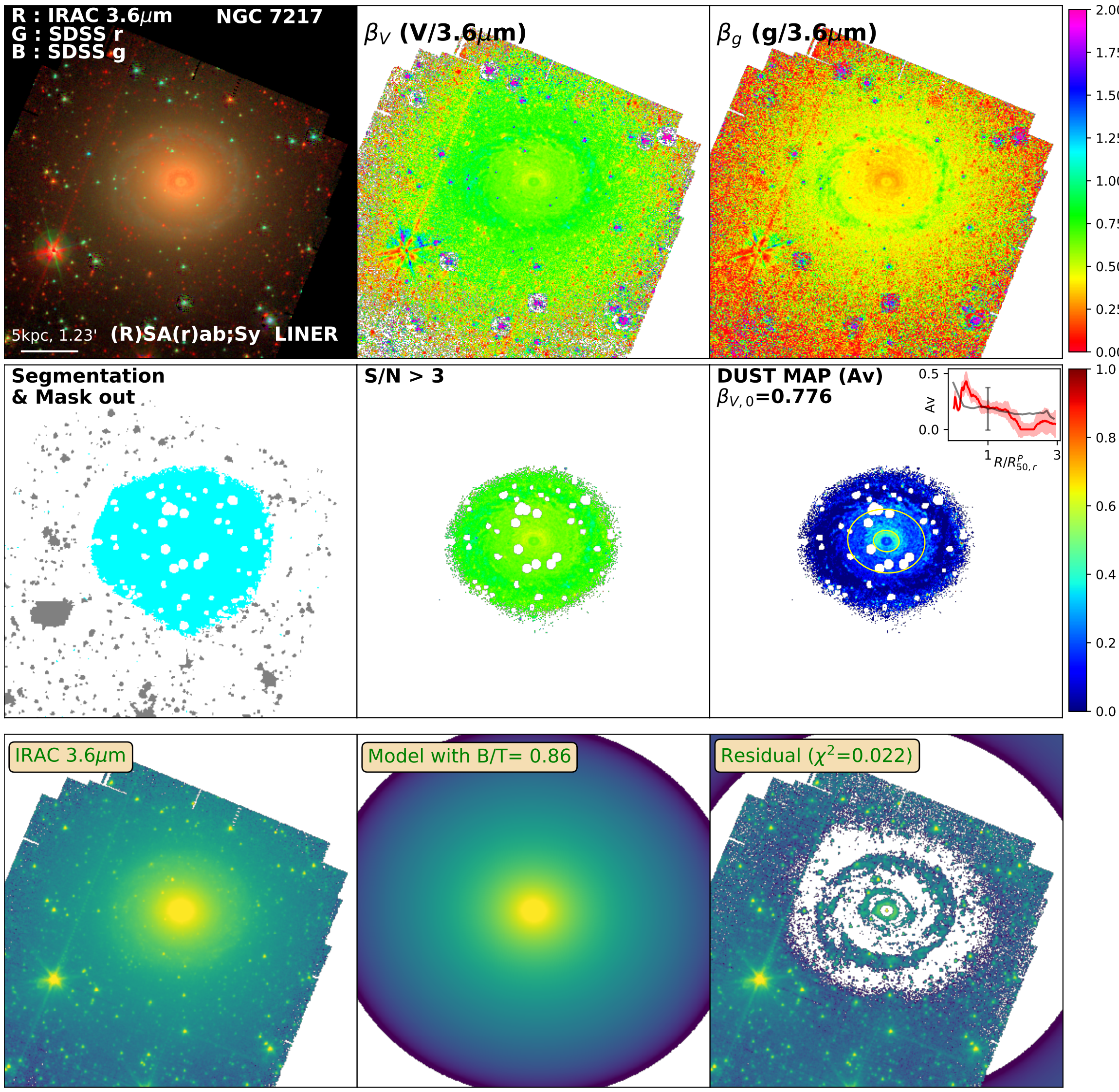

Figure D.241: Same as Figure 3.2 for NGC7217

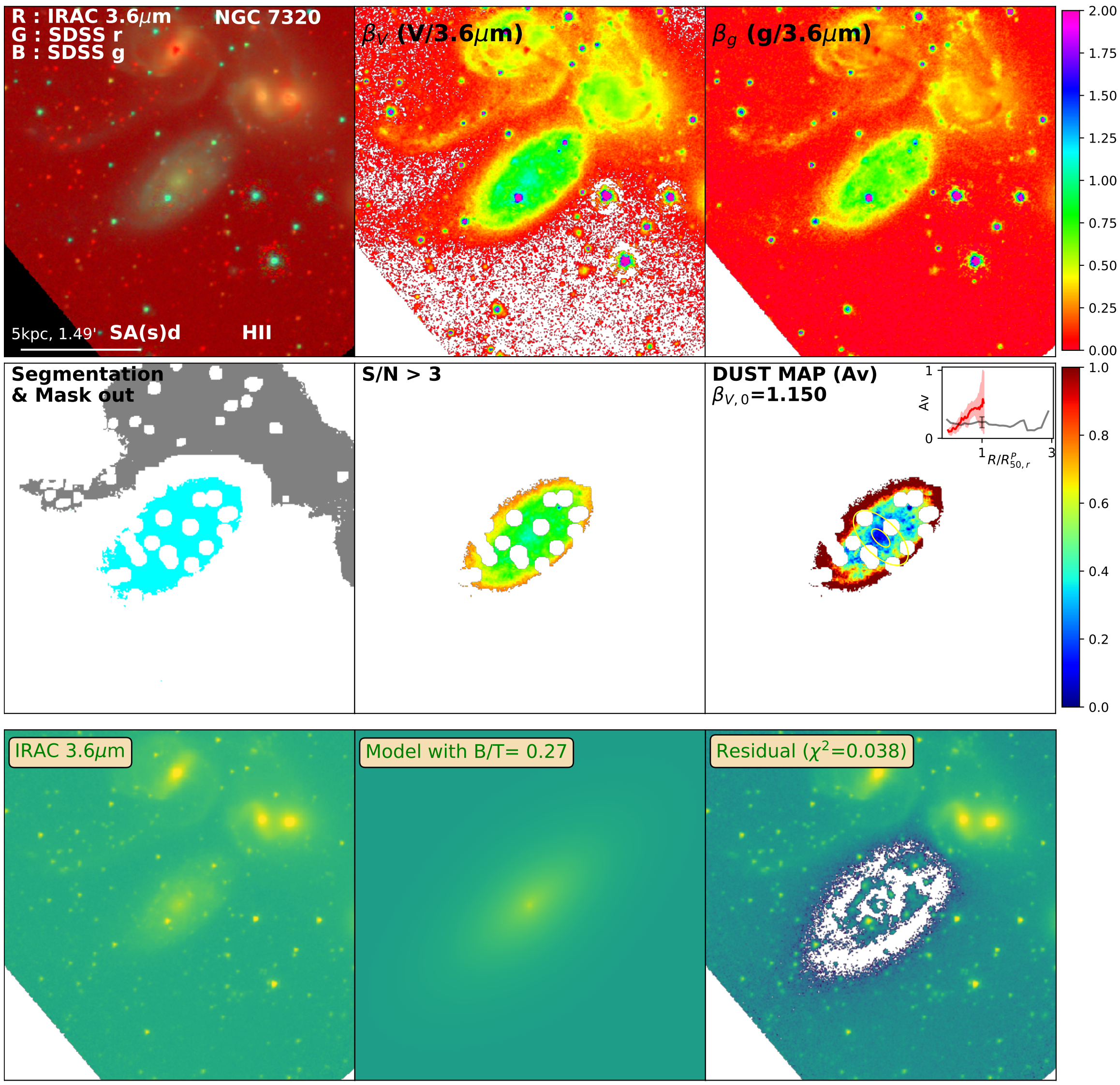

Figure D.242: Same as Figure 3.2 for NGC7320

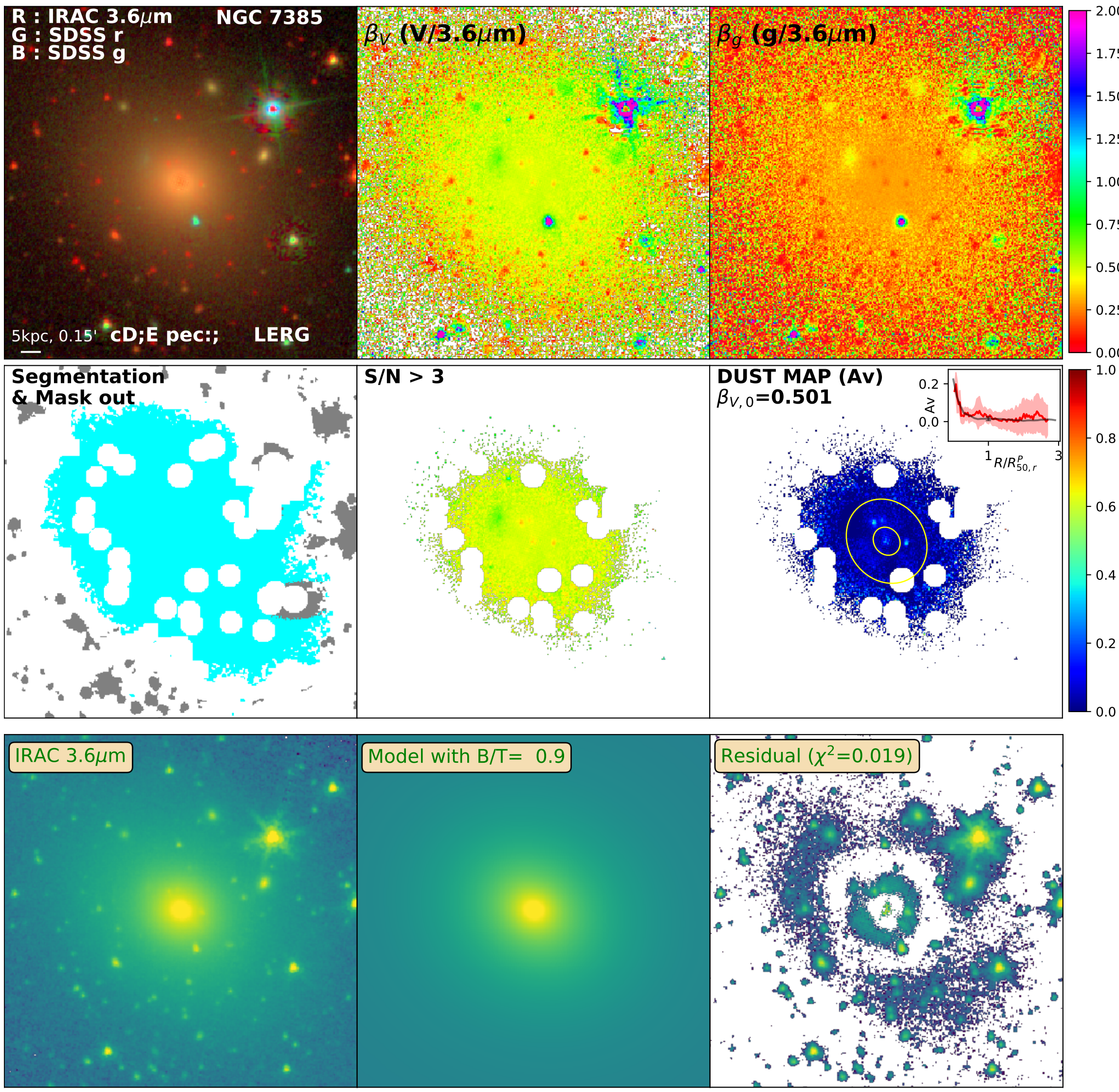

Figure D.243: Same as Figure 3.2 for NGC7385

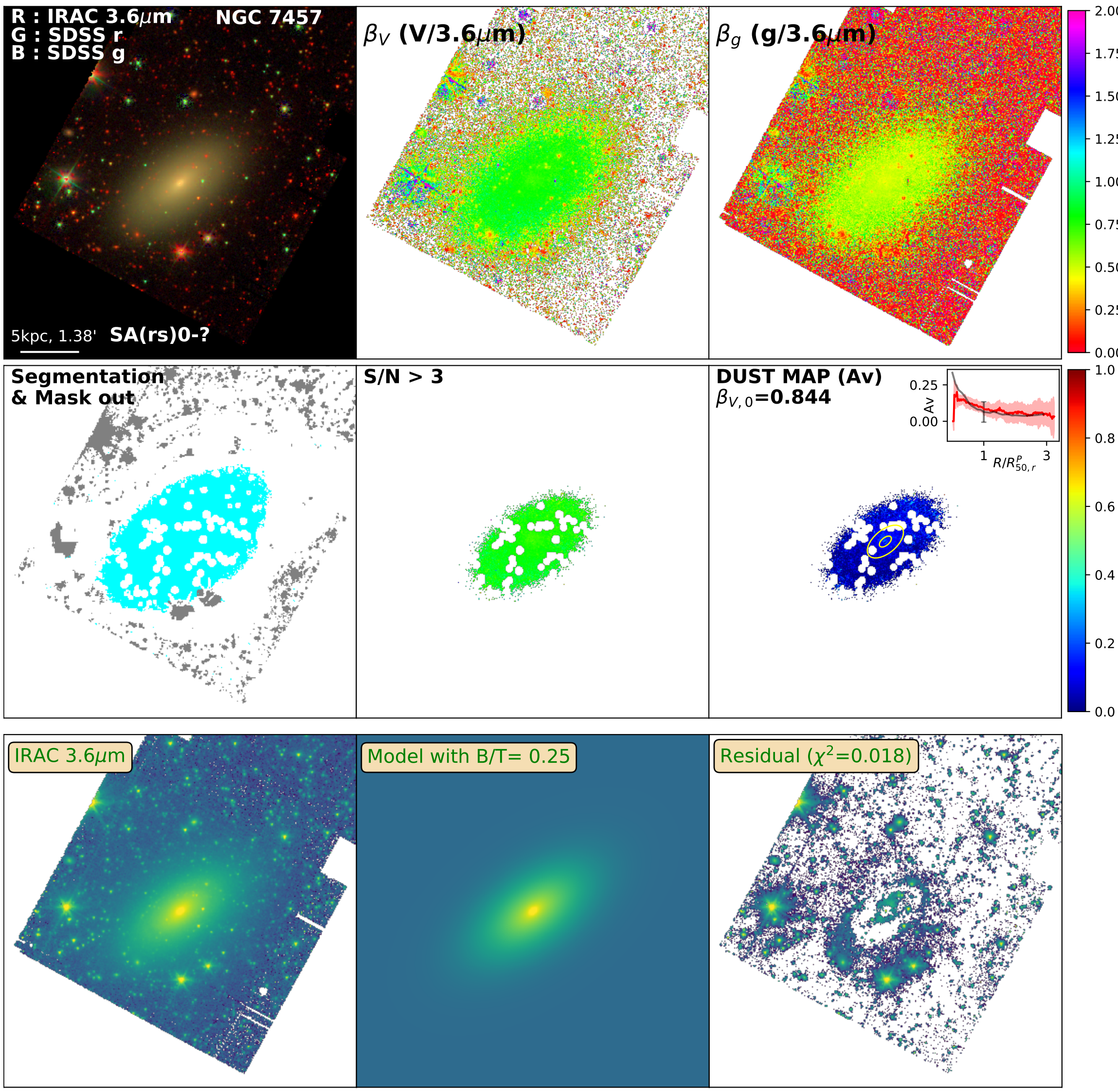

Figure D.244: Same as Figure 3.2 for NGC7457

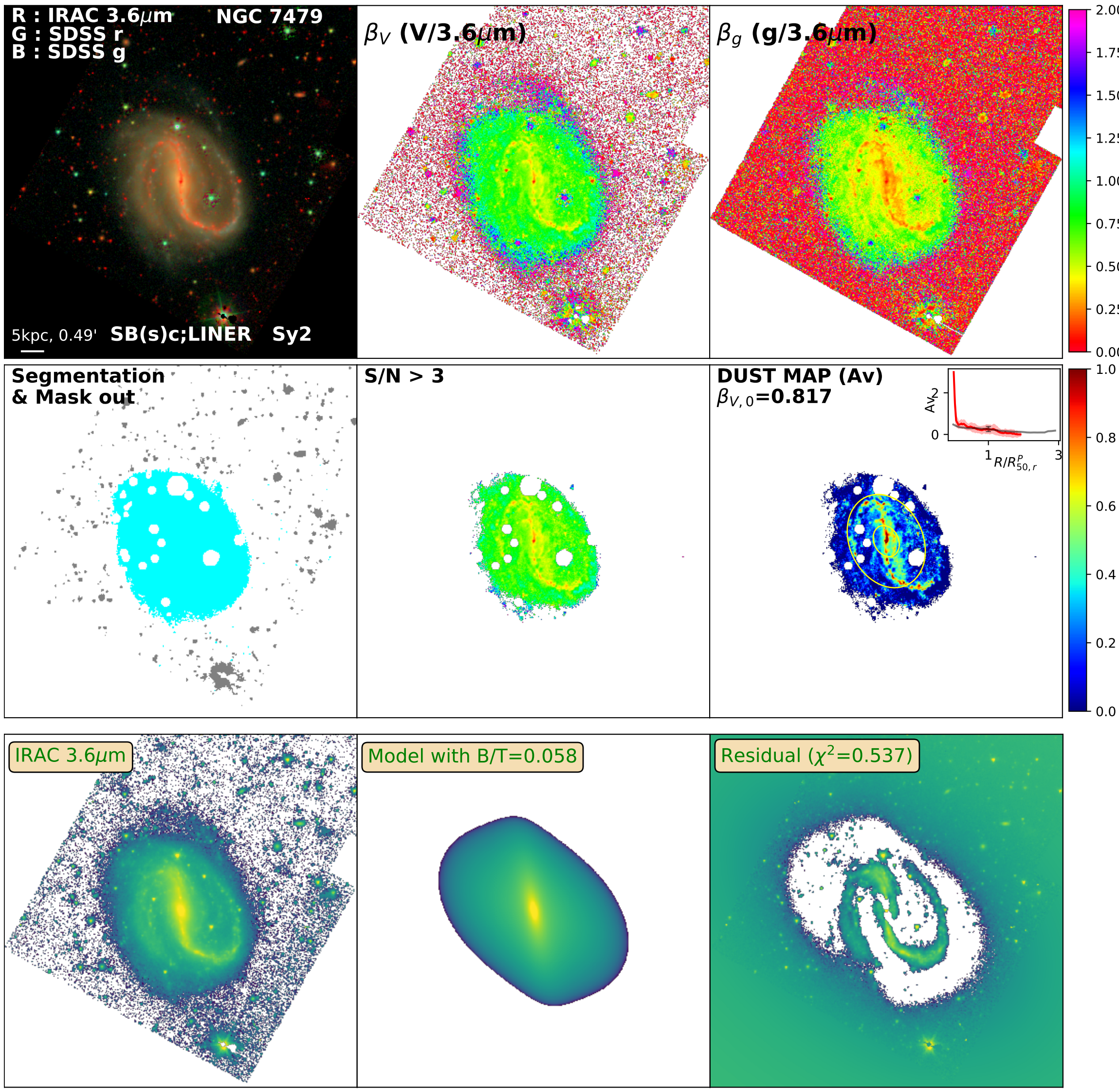

Figure D.245: Same as Figure 3.2 for NGC7479

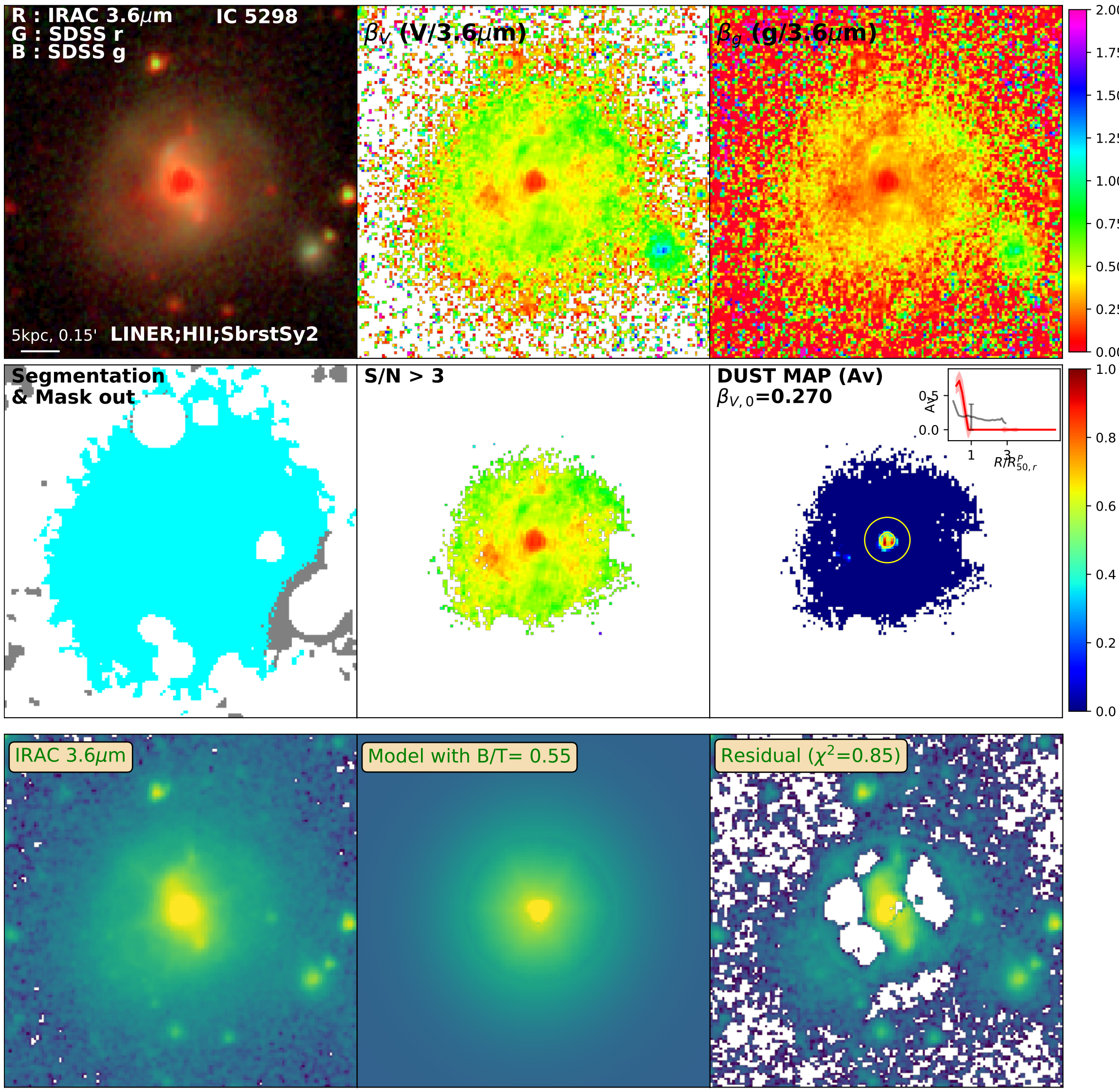

Figure D.246: Same as Figure 3.2 for IC5298

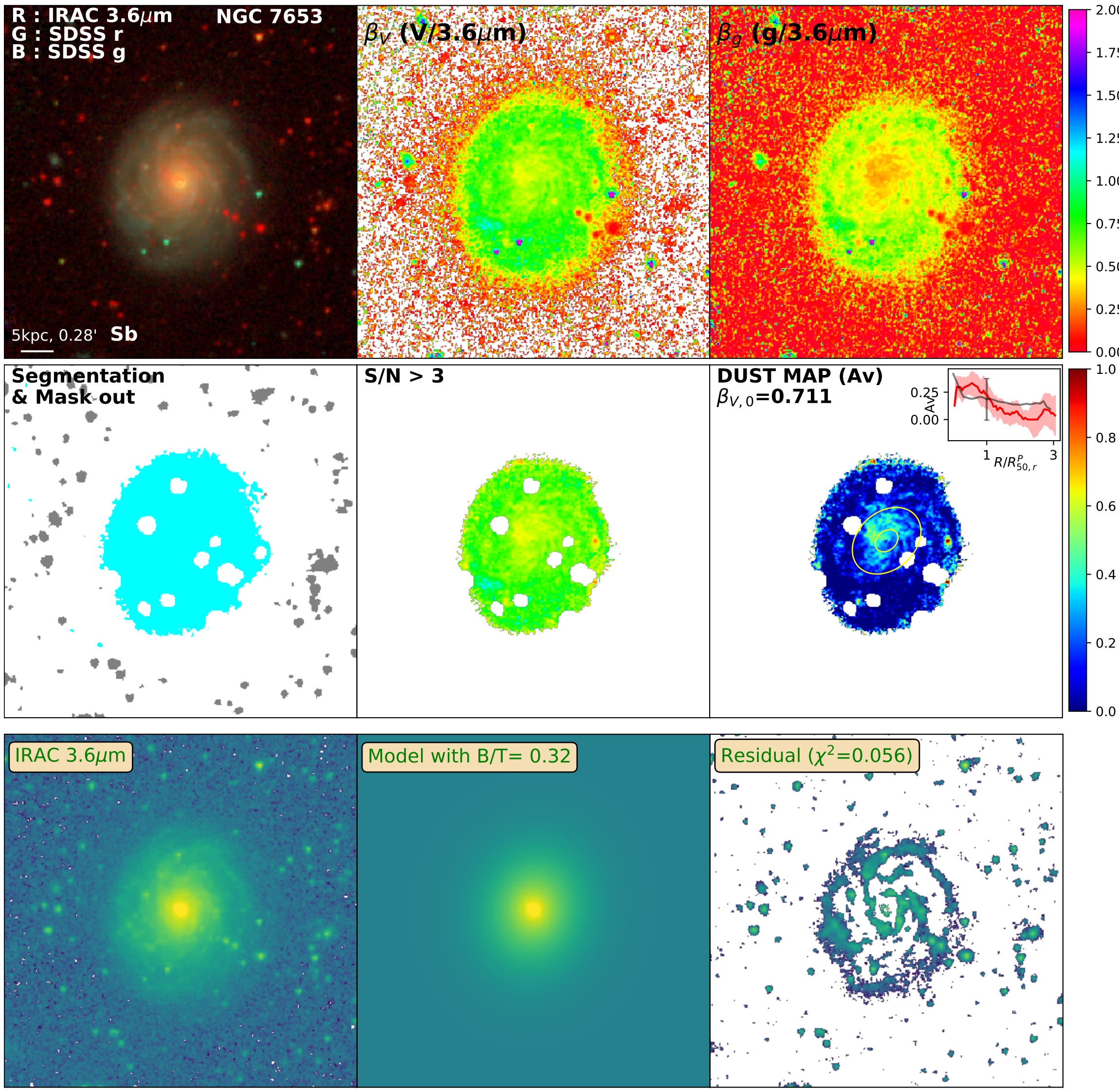

Figure D.247: Same as Figure 3.2 for NGC7653

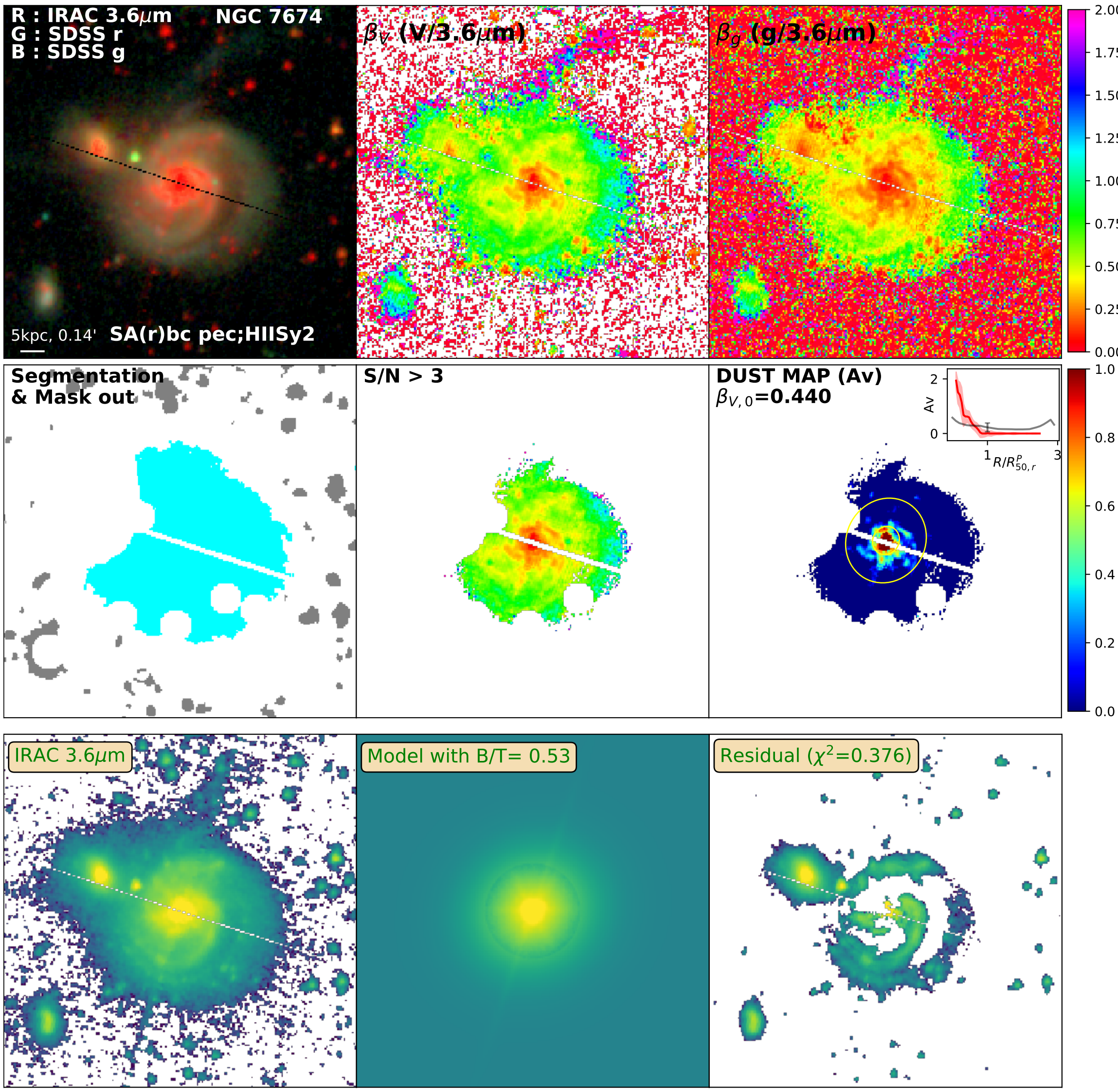

Figure D.248: Same as Figure 3.2 for NGC7674

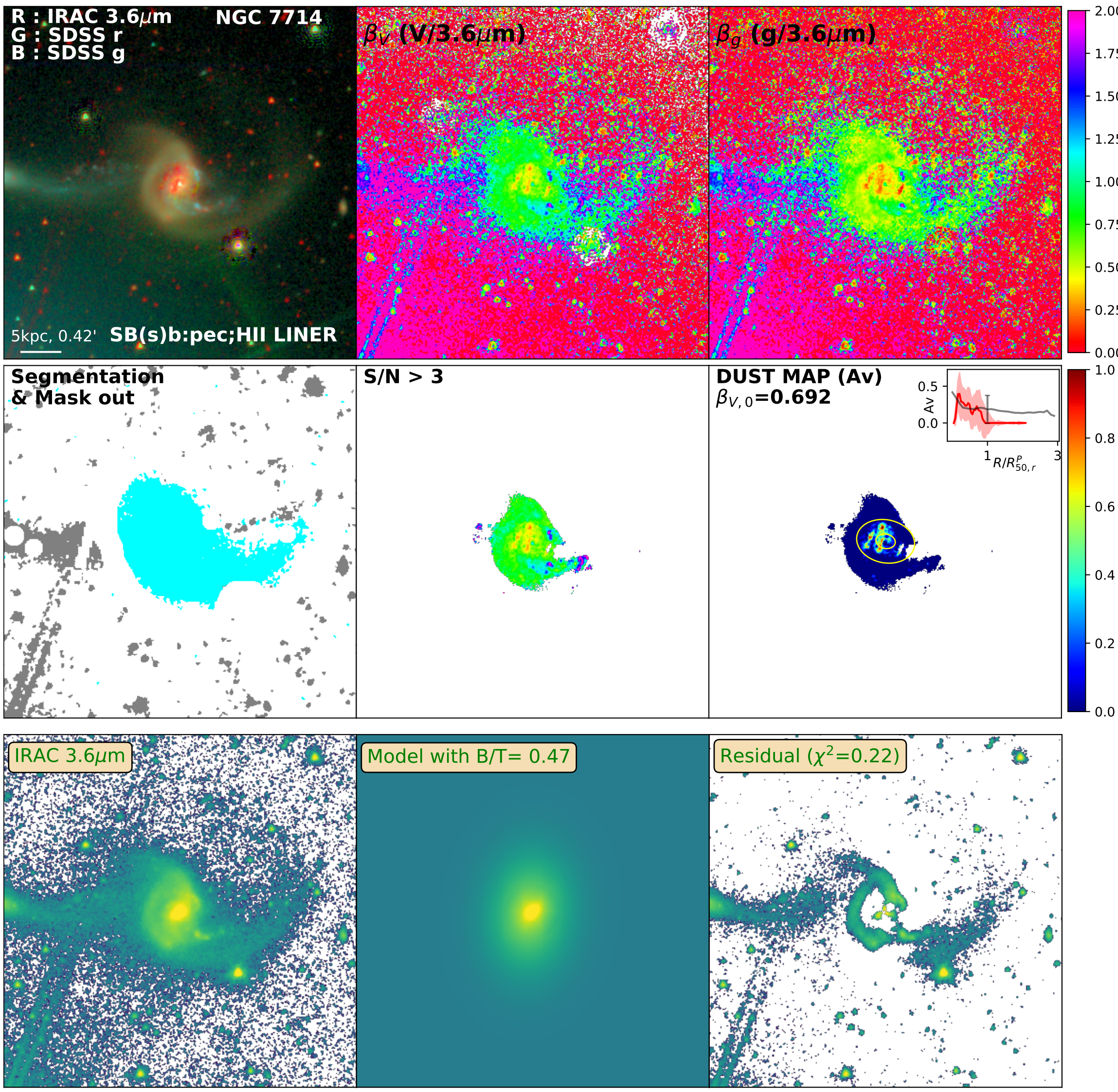

Figure D.249: Same as Figure 3.2 for NGC7714

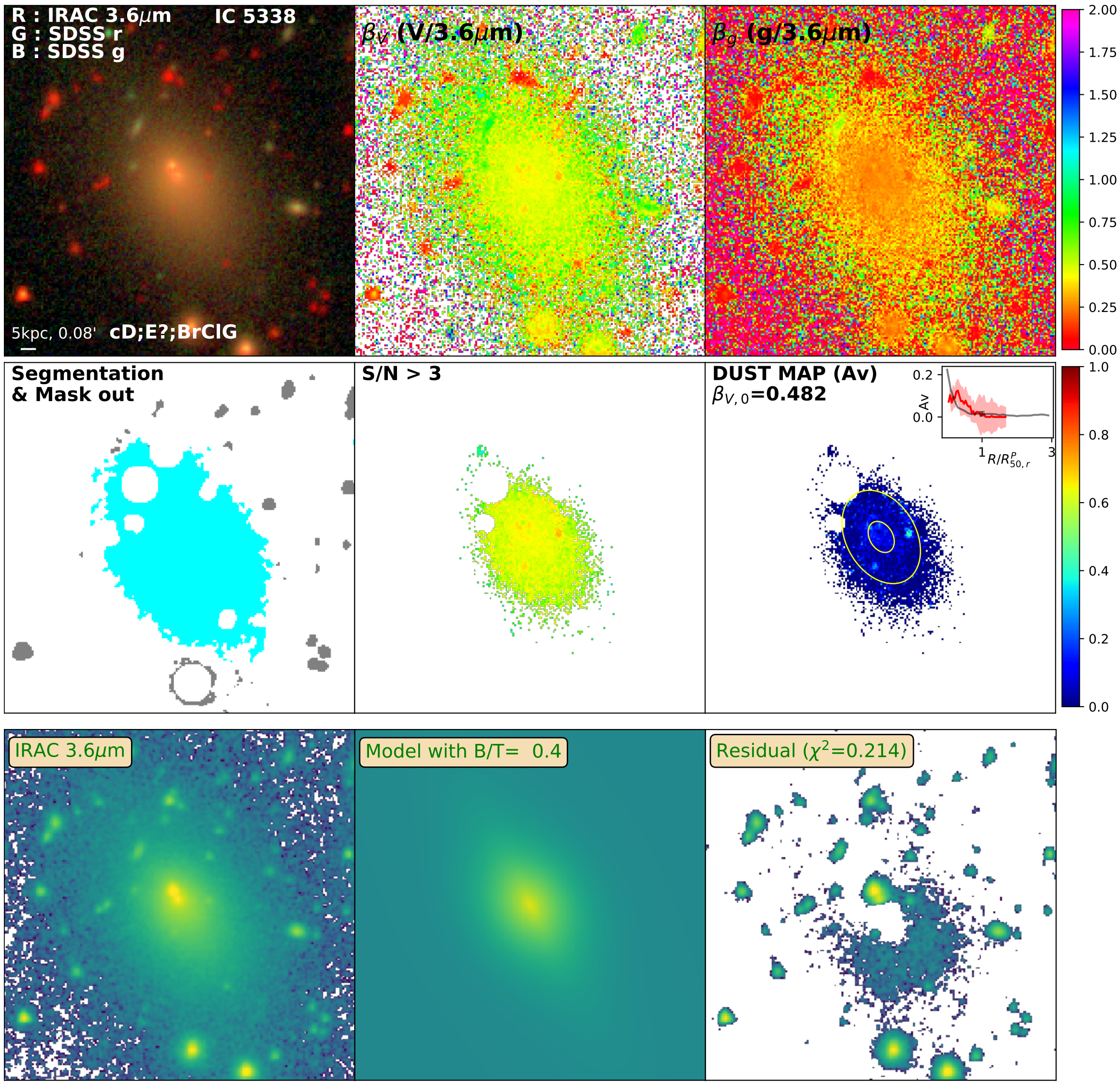

Figure D.250: Same as Figure 3.2 for IC5338

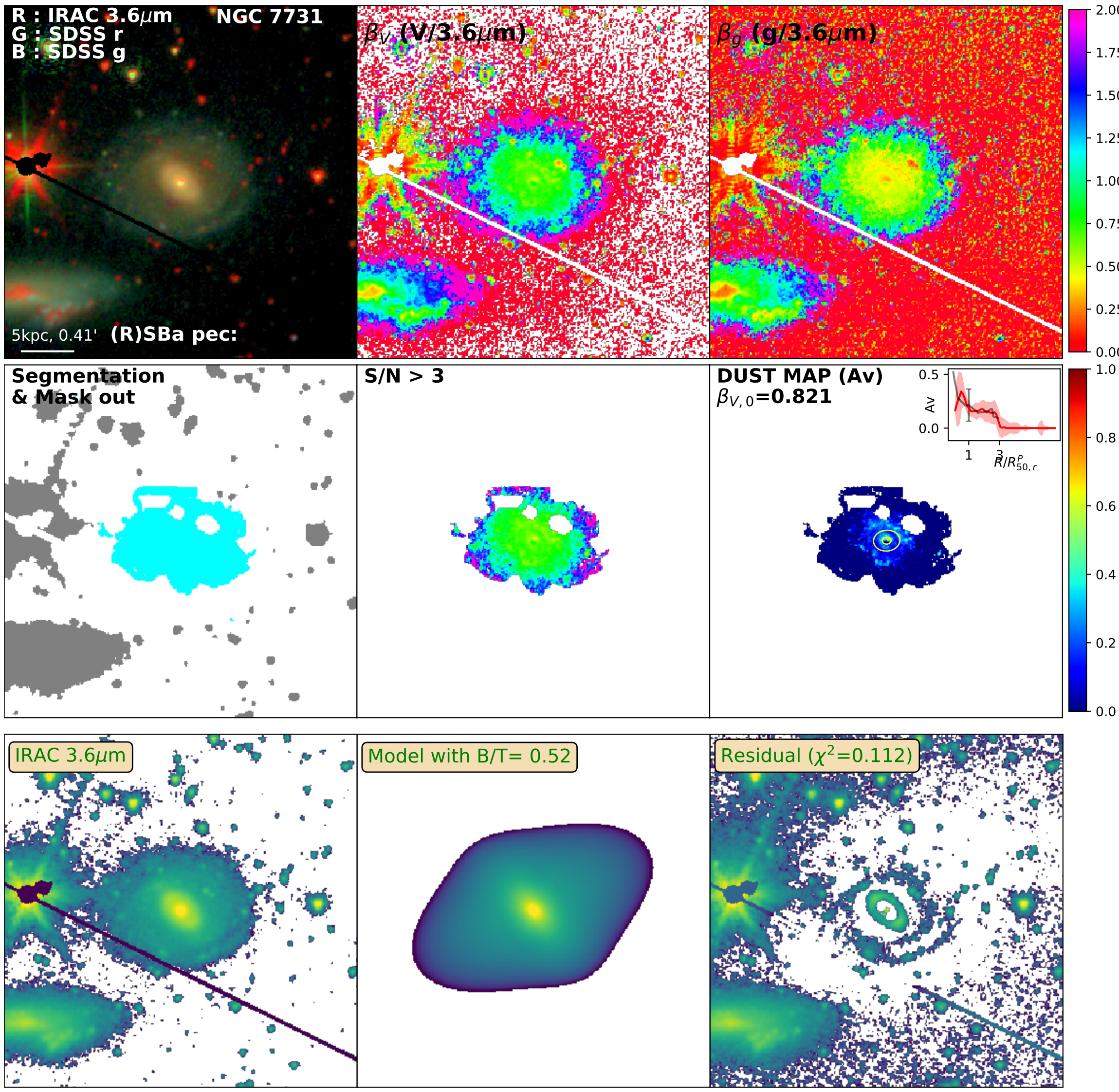

Figure D.251: Same as Figure 3.2 for NGC7731

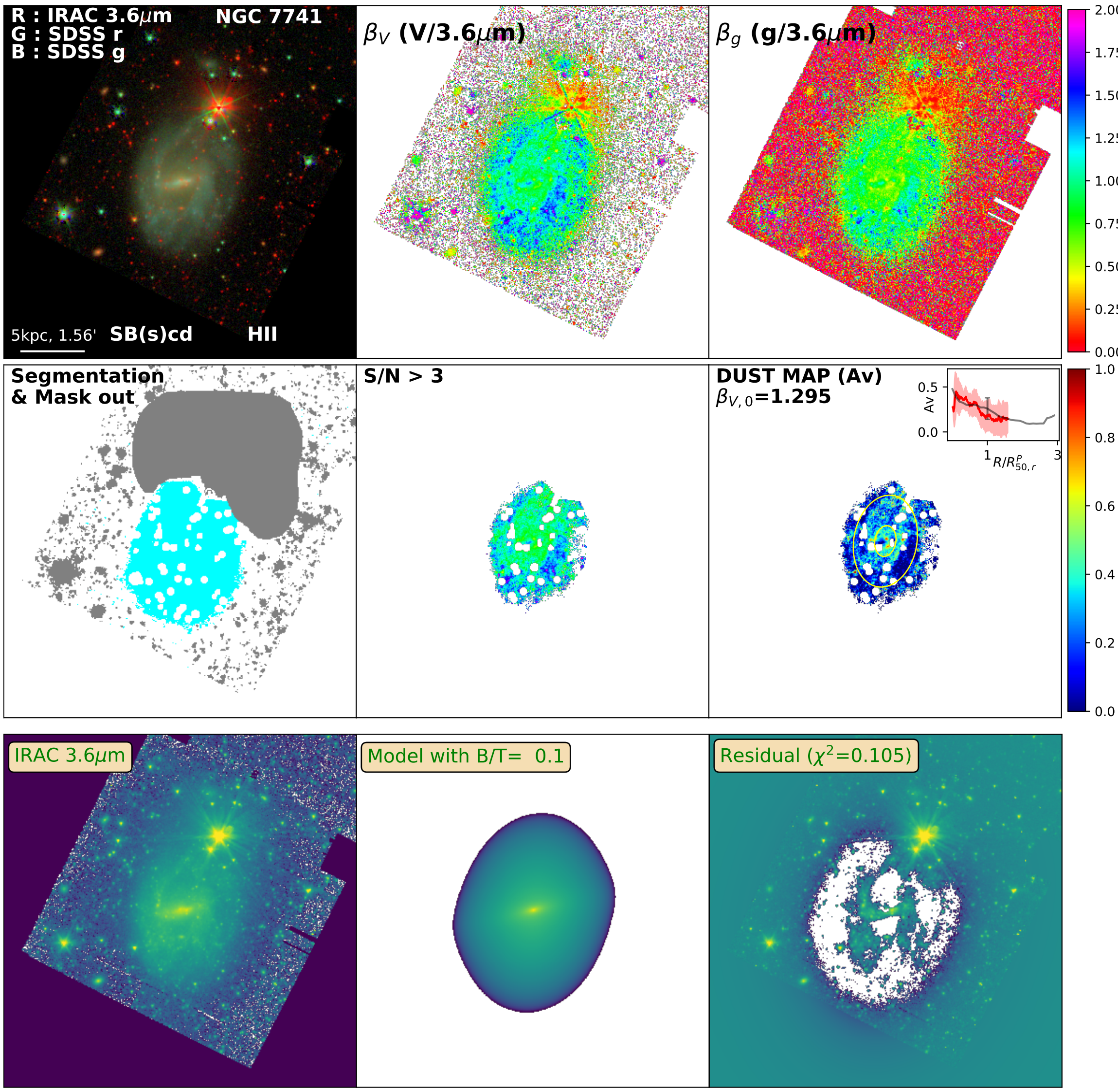

Figure D.252: Same as Figure 3.2 for NGC7741

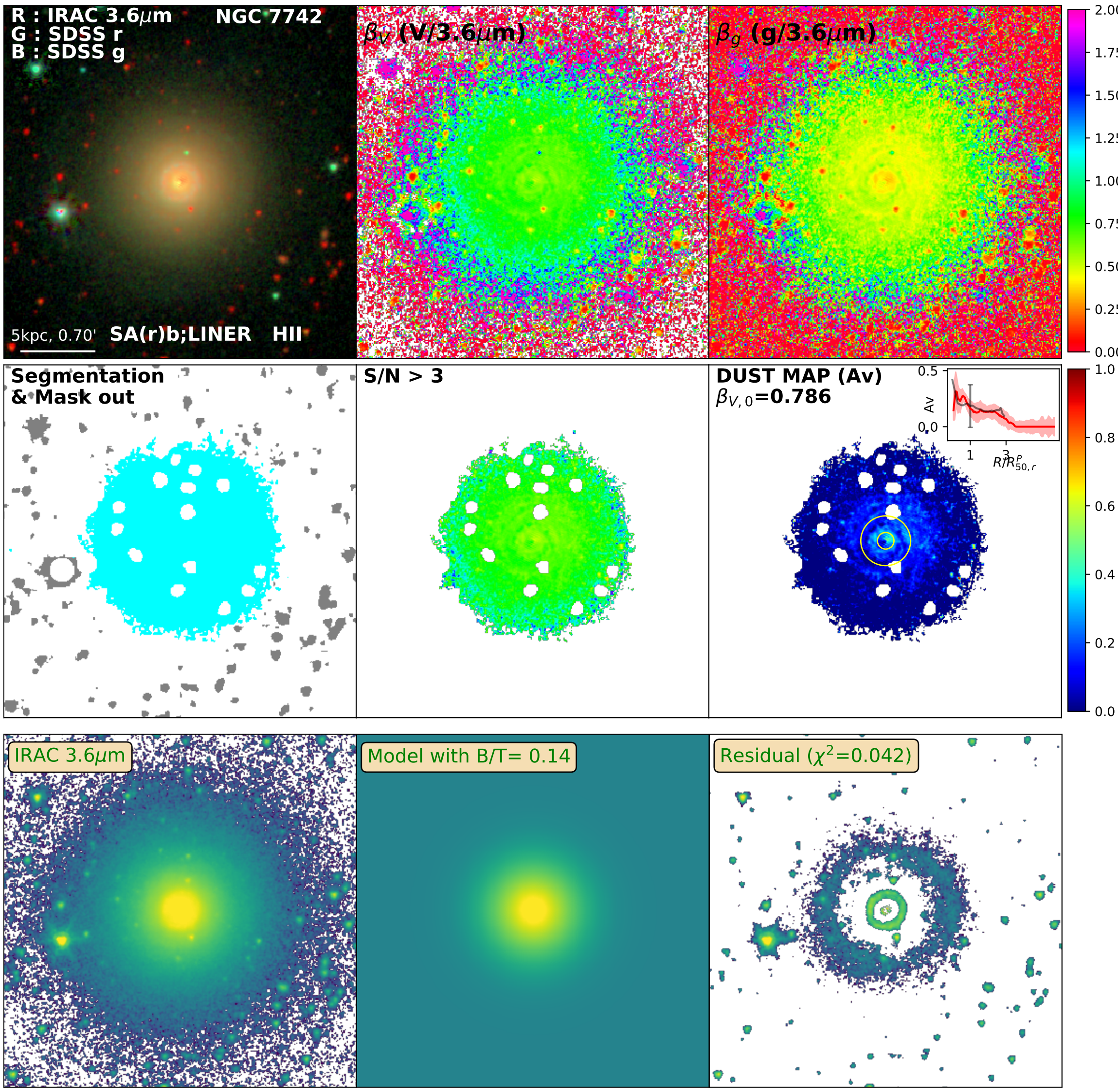

Figure D.253: Same as Figure 3.2 for NGC7742

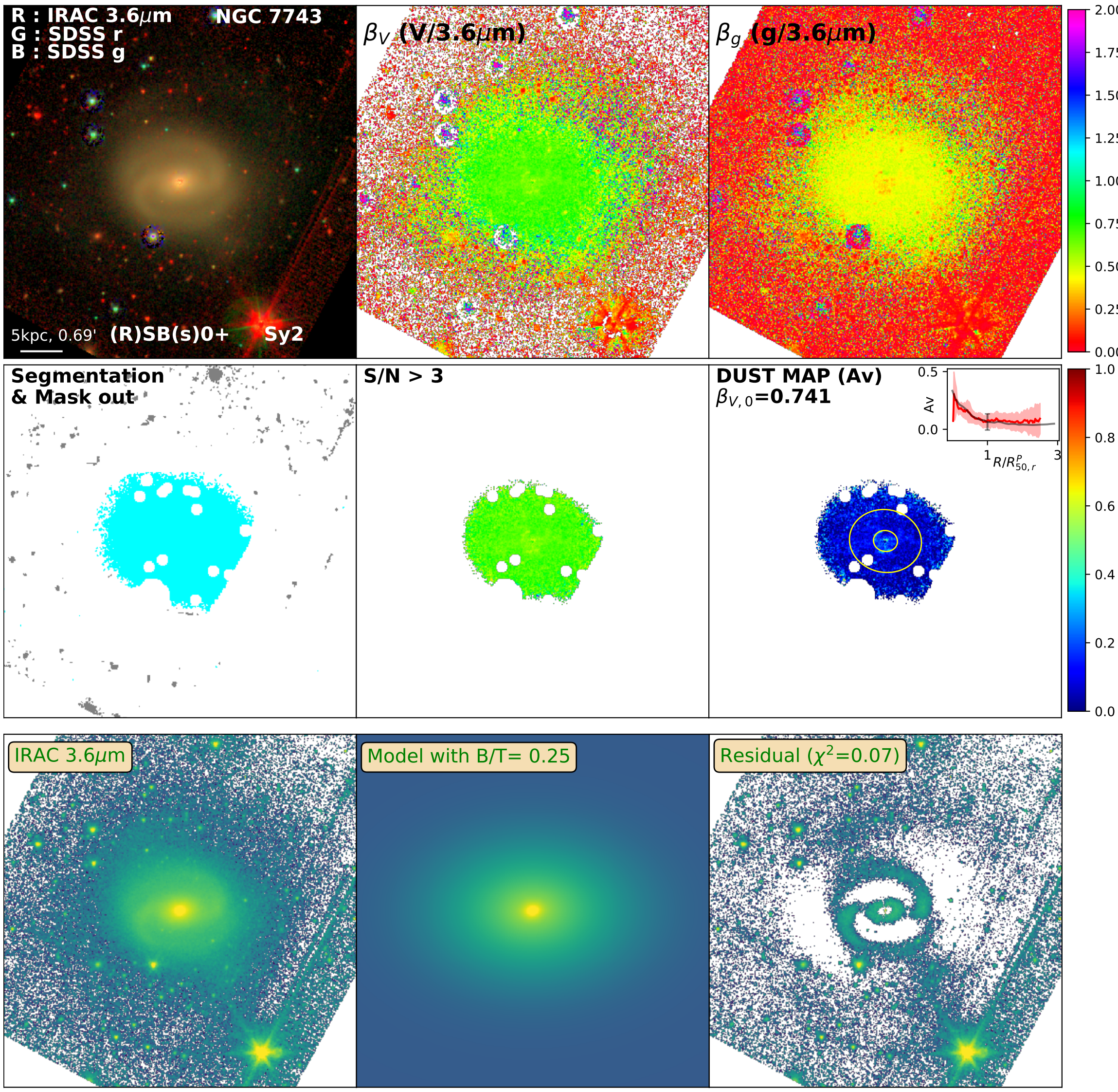

Figure D.254: Same as Figure 3.2 for NGC7743

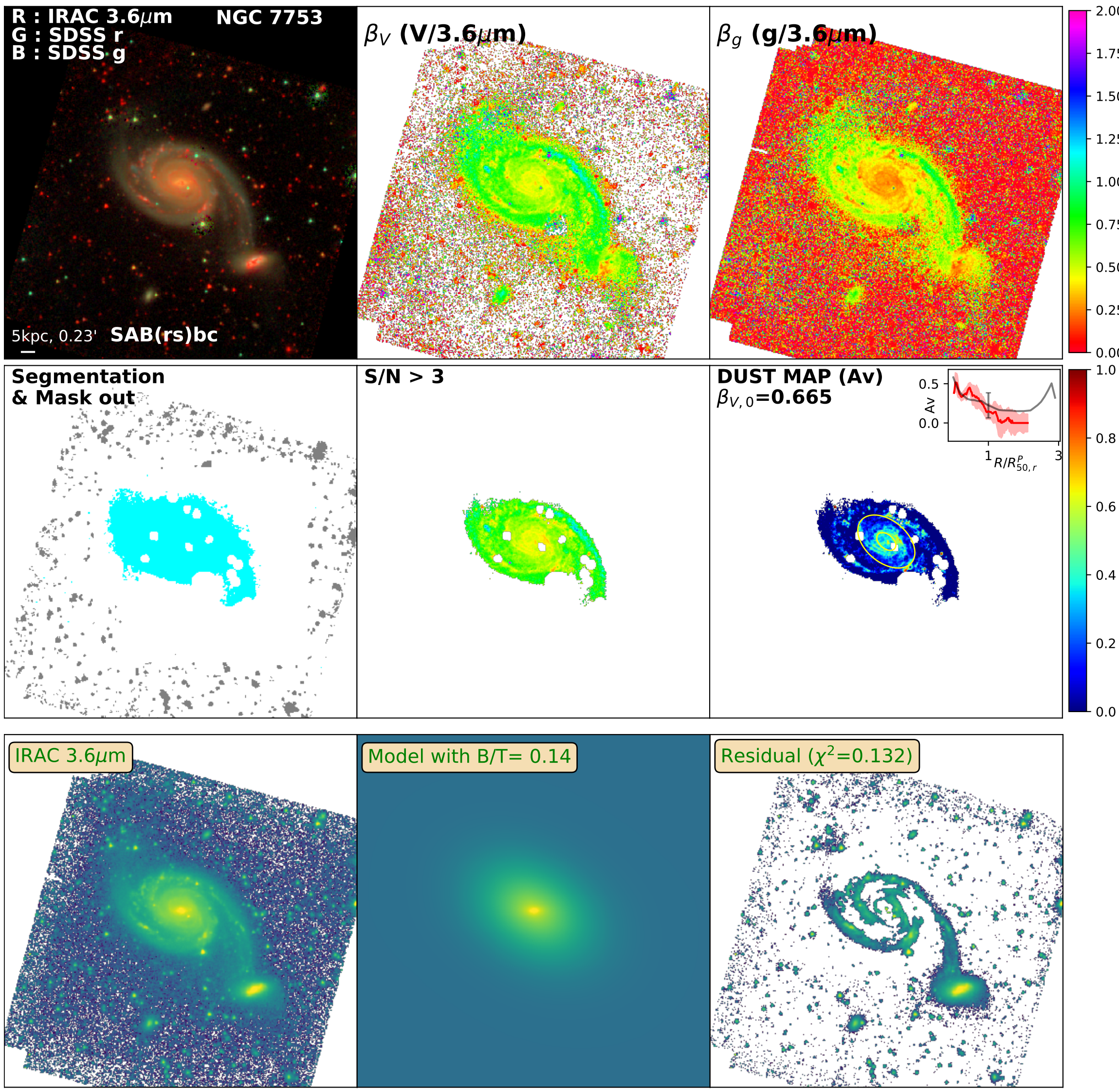

Figure D.255: Same as Figure 3.2 for NGC7753

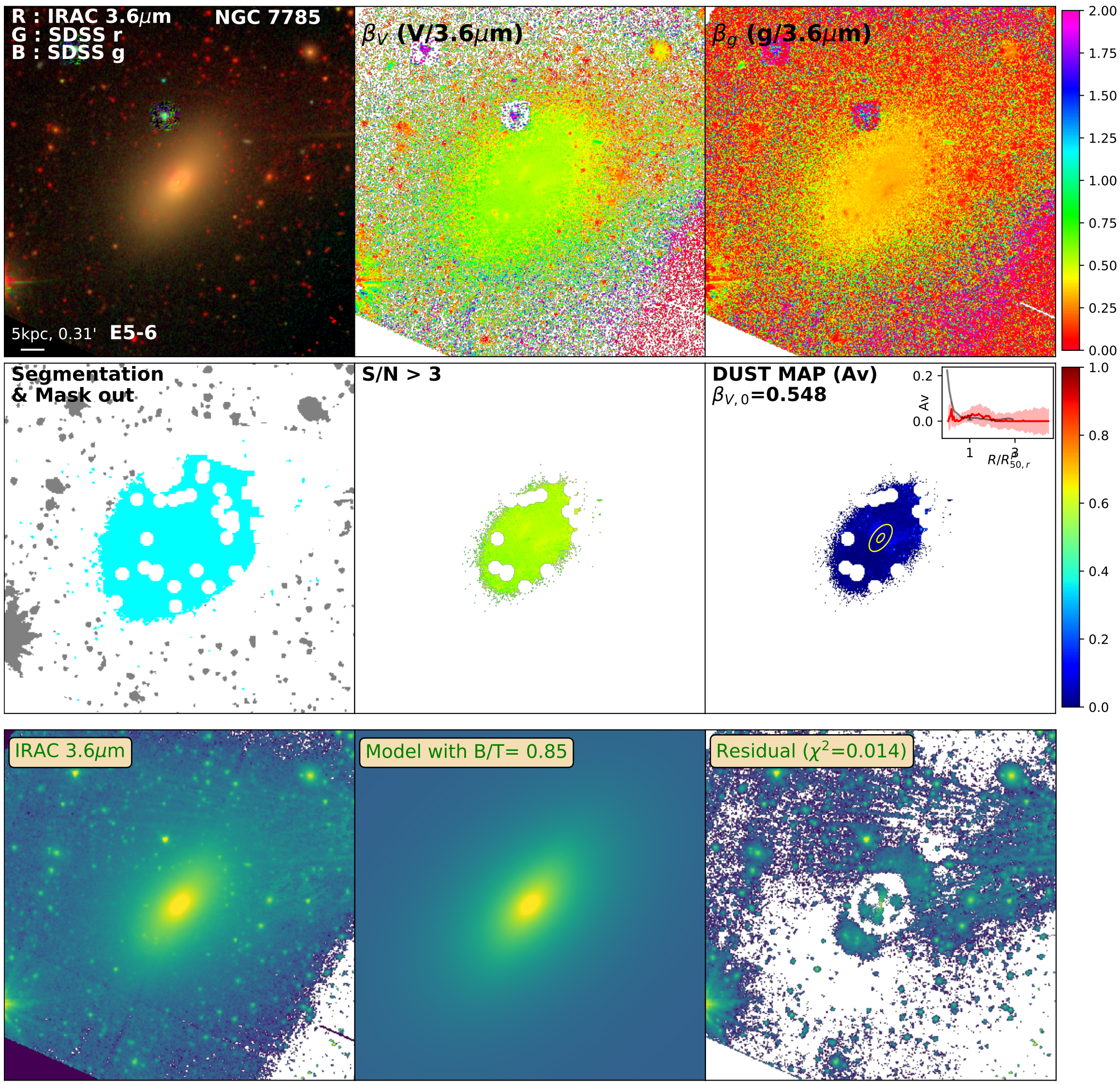

Figure D.256: Same as Figure 3.2 for NGC7785

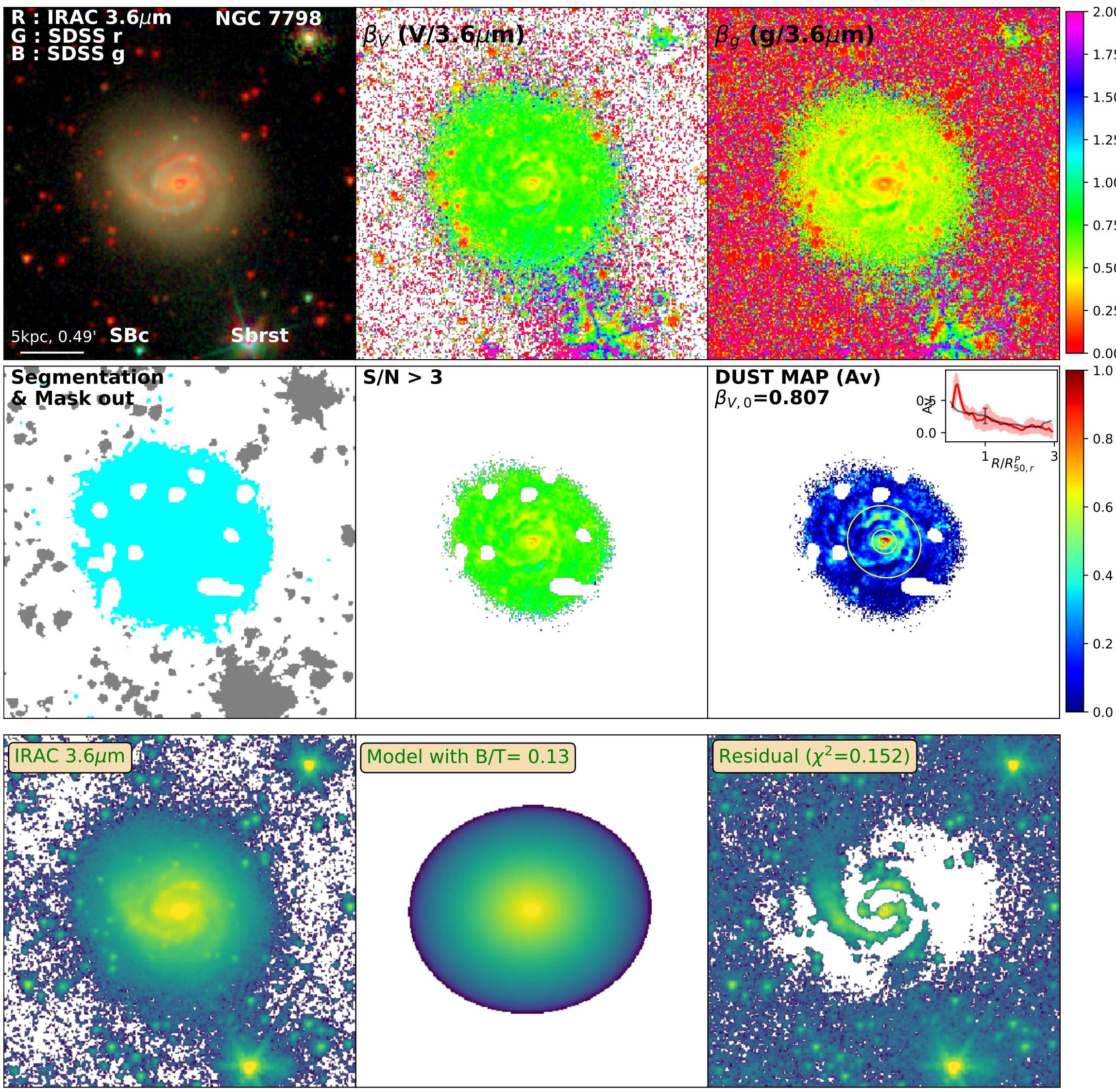

Figure D.257: Same as Figure 3.2 for NGC7798